The first steps toward an eye transplant *p. 1194*

Paying for nature's services: Getting the science right *p. 1206*

How Ebola may lead to a measles epidemic *p. 1240*

Science

$10
13 MARCH 2015
sciencemag.org

AAAS

Synthesis simplified

Automated small-molecule assembly from modular blocks

pp. 1190 & 1221

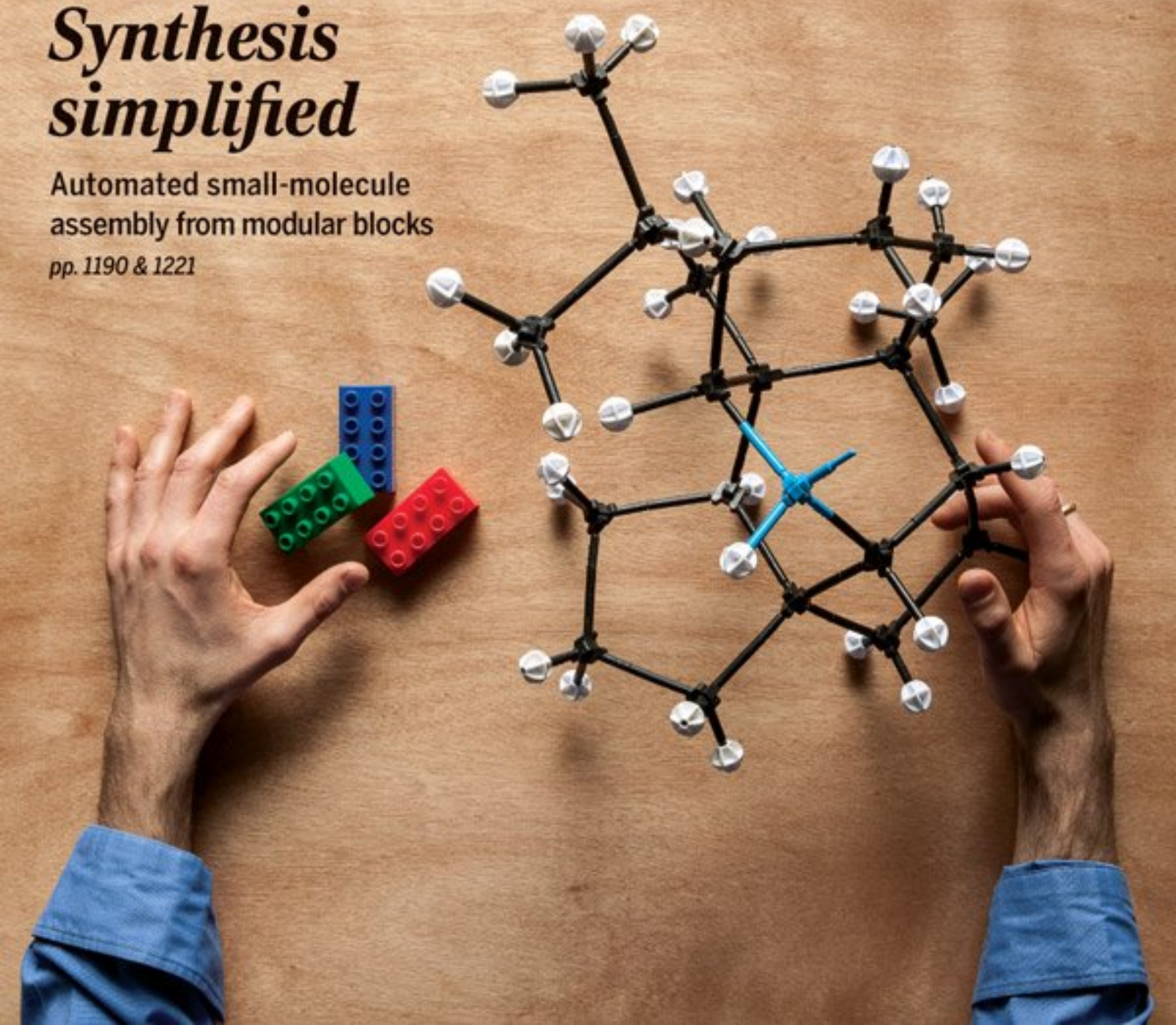

CONTENTS

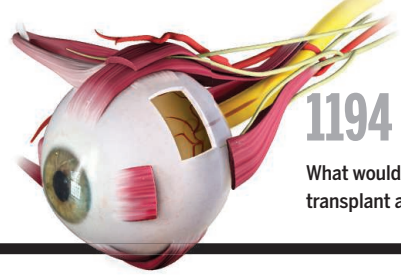

1194 What would it take to transplant an eye?

13 MARCH 2015 • VOLUME 347 • ISSUE 6227

NEWS

IN BRIEF

IN DEPTH

FEATURES

INSIGHTS

PERSPECTIVES

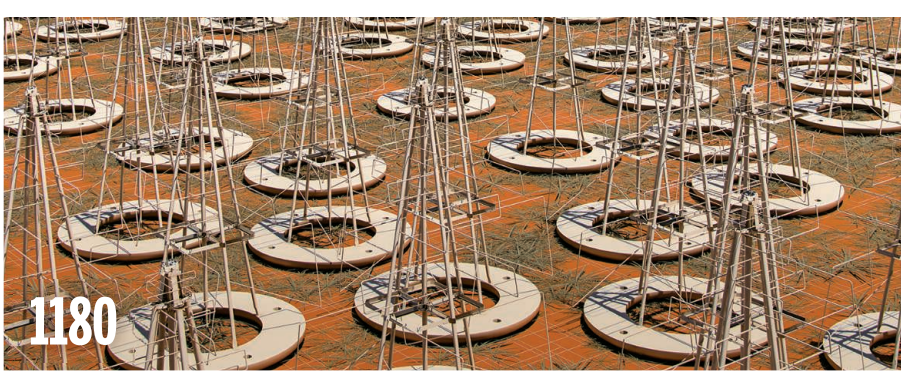

BOOKS *ET AL.*

LETTERS

Published by AAAS

CONTENTS

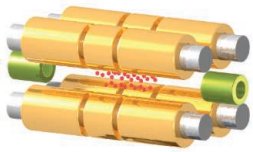

1233 Setting a trap for highly charged ions

13 MARCH 2015 • VOLUME 347 • ISSUE 6227

RESEARCH

IN BRIEF

REVIEW

RESEARCH ARTICLE

REPORTS

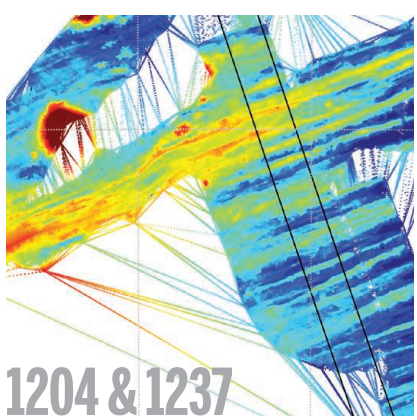

1204 & 1237

1282

DEPARTMENTS

ON THE COVER

Models highlighting a simple and modular approach for making the complex secodaphnane natural product core. Synthesizing small molecules of such complexity has remained a customized and therefore slow and rarely automated process. Li *et al.* discovered that many different types of complex small molecules, including this one, can be made via automated assembly of a well-constrained set of readily available building blocks. See pages 1190 and 1221. *Photo: © Chris Brown/ www.chrisbrownphoto.com*

SCIENCE (ISSN 0036-8075) is published weekly on Friday, except the last week in December, by the American Association for the Advancement of Science, 1200 New York Avenue, NW, Washington, DC 20005. Periodicals mail postage (publication No. 484460) paid at Washington, DC, and additional mailing offices. Domestic individual membership and subscription (51 issues): $153 ($74 allocated to subscription). Domestic institutional subscription (51 issues): $1282; Foreign postage extra: Mexico, Caribbean (surface mail) $55; other countries (air assist delivery) $85. First class, airmail, student, and emeritus rates on request. Canadian rates with GST available upon request, GST #1254 88122. Publications Mail Agreement Number 1069624. **Printed in the U.S.A.**
Change of address: Allow 4 weeks, giving old and new addresses and 8-digit account number. **Postmaster:** Send change of address to AAAS, P.O. Box 96178, Washington, DC 20090–6178. **Single-copy sales:** $10.00 current issue, $15.00 back issue prepaid includes surface postage; bulk rates on request. The identification code for *Science* is 0036-8075. *Science* is indexed in the *Reader's Guide to Periodical Literature* and in several specialized indexes.

Published by AAAS

Science
AAAS
1200 New York Avenue, NW, Washington, DC 20005
Bateman House, 82-88 Hills Road, Cambridge, UK CB2 1LQ

SUBSCRIPTION SERVICES For change of address, missing issues, new orders and renewals, and payment questions: 866-434-AAAS (2227) or 202-326-6417, FAX 202-842-1065. Mailing addresses: AAAS, P.O. Box 96178, Washington, DC 20090-6178 or AAAS Member Services, 1200 New York Avenue, NW, Washington, DC 20005

INSTITUTIONAL SITE LICENSES 202-326-6755 **REPRINTS:** Author Inquiries 800-635-7181 **COMMERCIAL INQUIRIES** 803-359-4578 **PERMISSIONS** 202-326-6765, permissions@aaas.org **AAAS Member Services** 202-326-6417 or http://membercentral.aaas.org/discounts

Science serves as a forum for discussion of important issues related to the advancement of science by publishing material on which a consensus has been reached as well as including the presentation of minority of conflicting points of view. Accordingly, all articles published in *Science*—including editorials, news and comment, and books reviews—are signed and reflect the individual views of the authors and not official points of view adopted by AAAS or the institutions with which the authors are affiliated.

INFORMATION FOR AUTHORS See pages 678 and 679 of the 6 February 2015 issue or access www.sciencemag.org/about/authors

Published by AAAS

EDITORIAL

Chemistry embraced by all

Chemistry is the great enabler. For two centuries, it has played a key role in conquering diseases, solving energy problems, addressing environmental challenges, and providing discoveries that have spawned new industries. To meet the demands of the future, this mature science must expand into new frontiers, a move that will be facilitated if the public and policy-makers understand its pivotal role in every facet of life. Such support will not be forthcoming from those who associate chemistry with harm—intentional or not—to people and the biosphere. Addressing the disparity between those perceptions and the reality of chemistry's contributions to society will garner broader support for spurring innovations in the 21st century. How can chemistry ensure that it has this support?

Chemistry is connected to the physical and biological worlds, underpinning progress across sectors. Too often, the benefits of chemistry have been overshadowed by harmful effects, such as the toxicity of drugs and food additives, environmental contaminants, and chemical warfare. Consequently, chemistry and its practitioners are held in relatively low esteem by society. The good news is that when 2011 was declared the International Year of Chemistry, the chemistry community boosted its engagement with the public. All stakeholders, including educators, researchers, the chemical industry, and the professional bodies and academies, must join forces and continue to build on that momentum. Major international meetings, such as the one this month convened by the American Chemistry Society (ACS) in Colorado, are good venues to forge discussions among those in the field about changing how the field is perceived by potential learners, practitioners, policy-makers, the public, and the media. Equally important are outreach events that include the public, media, and policy-makers. Outreach is already part of large scientific meetings and can serve as a good model for this type of interaction. Obviously, communication and education are key to more-positive public engagement. Chemists must continue to improve their conversations with the public, using language that is accessible to explain the relevance of their work to everyday life. Cultivating a better reputation means not only promoting the good, but also acknowledging the bad—an honest dialogue.

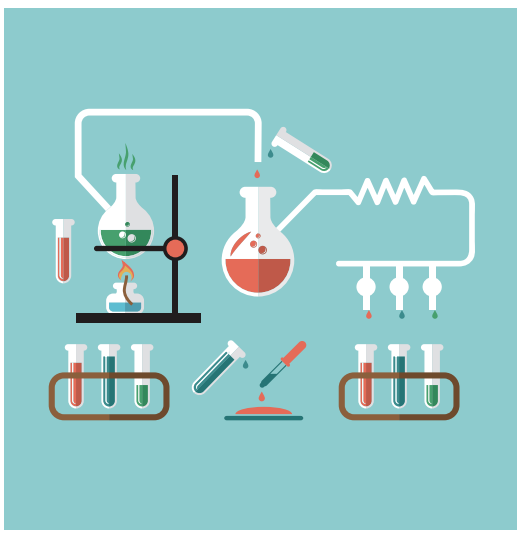

"Too often, the benefits of chemistry have been overshadowed by harmful effects..."

Redesigns and reforms within the community are needed as well. Chemistry educators should assess how teaching and learning at all levels can be improved to inspire the next generation of chemists. Meetings such as the forthcoming Gordon Research Conference this summer (Chemistry Education as an Agent in Global Progress) are good ways to focus on how to achieve a chemistry literacy that is relevant to people's lives. Many of the field's major national and international associations require sweeping reforms to balance their focus on the professional advancement of their members with an active role in bolstering recognition, respect, and understanding for chemistry from the public. Changing this balance will require breaking very long-standing traditions of many of these associations, and champions at both leadership and grassroots levels must step forward and press the case for reforms.

As a critical constituent of the chemistry community, industry could do its part by wholeheartedly embracing ethical rules and practices and engaging in responsible chemicals management and responsible innovation. Industry must become less removed from their consumers and have frank conversations with a society that demands transparency and has deep concern about risks. Here, academia could work with industry to clearly explain the science, applications, and impacts. Society faces many emerging global challenges. Broadening support for chemistry will enable the next generation of solutions to tackle them.

– **Stephen Matlin, Goverdhan Mehta, Henning Hopf**

Stephen Matlin is Adjunct Professor at the Institute of Global Health Innovation, Imperial College London, UK, and Head of Strategic Development for the International Organization for Chemical Sciences in Development. E-mail: s.matlin@imperial.ac.uk

Goverdhan Mehta is National Research Professor and Lilly-Jubilant Chair in the School of Chemistry, University of Hyderabad, India. He has served as president of the Indian National Science Academy and the International Council for Science. E-mail: gmehta43@gmail. com

Henning Hopf is a professor at the Institute of Organic Chemistry, Technische Universität Braunschweig, Germany. He has served as president of the German Chemical Society. E-mail: h.hopf@tubraunschweig.de

10.1126/science.aab0690

NEWS

> “We were told not to use the terms ‘climate change,’ ‘global warming’ or ‘sustainability.’”
>
> **Attorney Christopher Byrd,** formerly with Florida’s Department of Environmental Protection, to *The Miami Herald*. Some former employees say the state banned the terms’ use in reports and e-mails in 2011.

IN BRIEF

Climate change turning Atacama mummies into black ooze

Some Chinchorro mummies at a Chilean museum are beginning to rapidly degrade.

Mummies made by the Chinchorro culture in Chile and Peru have survived for more than 7000 years. So when several specimens at the University of Tarapacá’s archaeological museum in Arica, Chile, started to turn into black ooze, scientists knew something was wrong. The museum sent samples of damaged and undamaged mummy skin to Harvard University, where researchers cultured the microorganisms growing on each kind of skin. They then transferred the cultures to pig skin and ran tests to determine the conditions under which the microbes started munching away. It turns out that when the humidity is high, the mummies’ microbiome kicks into high gear—something the Chinchorro didn’t have to worry about, living in and around the extremely arid Atacama Desert. In recent years, however, Arica has become increasingly humid, possibly due to global climate change. Stringently controlling the humidity inside the museum’s collection is a relatively easy fix, but the changing climate in northern Chile may damage the hundreds of mummies likely buried in shallow graves around Arica, the researchers warn—and archaeologists may find themselves digging up little more than black ooze.

AROUND THE WORLD

Big science faces dark days?

SYDNEY, AUSTRALIA | Facilities across Australia as diverse as telescopes, supercomputers, a synchrotron, and marine observation networks may fall victim to budget politics. The government has linked operational funding for 27 major research facilities—AU$150 million in fiscal year 2015 to 2016—to the passage of controversial and unrelated education legislation, which is now stalled in the country’s senate. Since the National Collaborative Research Infrastructure Strategy (NCRIS) was established in 2004, successive governments have committed more than AU$2 billion to the facilities. In a 4 March letter to Prime Minister Tony Abbott, the heads of 15 of the country’s major scientific research organizations warned of “immense” damage to domestic and international research if the facilities close. They noted that some 35,000 Australian and overseas researchers use the NCRIS facilities, which employ more than 1700 scientists, support, and management staff.

Low-cost x-rays for all

LAUSANNE, SWITZERLAND | Medical imaging equipment is too frail and expensive for most hospitals in developing countries—an x-ray machine designed for an air-conditioned hospital “would last 3 months in Chad,” says Klaus Schönenberger, leader of the GlobalDiagnostiX project at the Swiss Federal Institute of Technology in Lausanne. On 9 March, GlobalDiagnostiX unveiled its new x-ray machine prototype that the team

A radiography device in a Cameroon hospital.

PHOTOS: (LEFT TO RIGHT) COURTESY OF VIVIEN STANDEN; © SYLVAIN LIECHTI

Published by AAAS

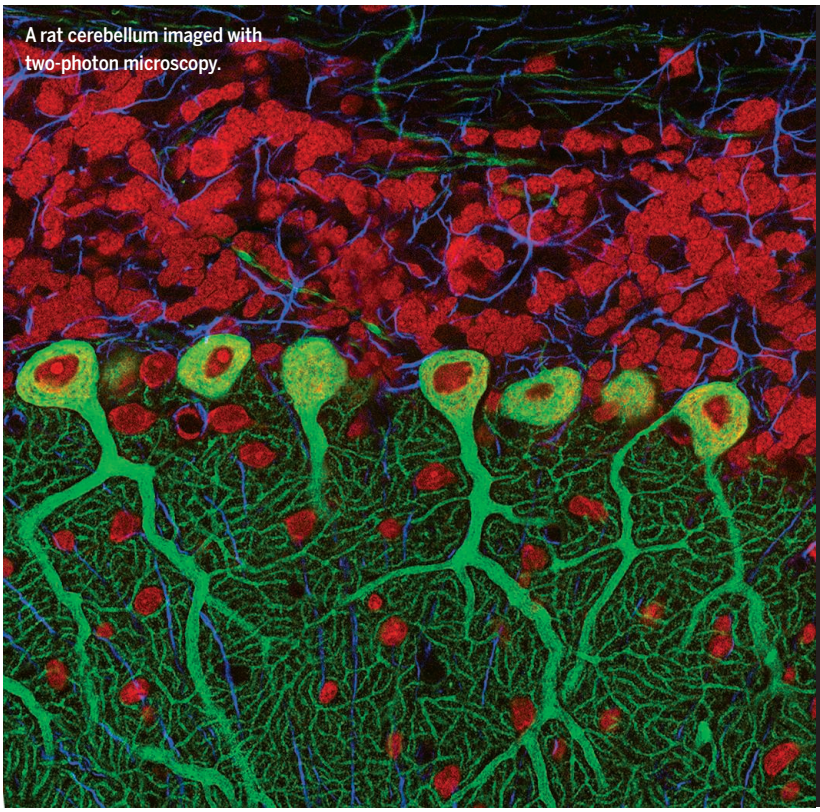

A rat cerebellum imaged with two-photon microscopy.

PHOTO: © THOMAS DEERINCK/VISUALS UNLIMITED/CORBIS

Brains that fluoresce

Shoot the brain repeatedly with gentle, focused bursts of light, and its fine structures will appear in luminous detail. That's the principle behind two-photon microscopy, an imaging technique honored with the €1 million Brain Prize this week. Traditional fluorescence microscopy creates an image by shining light on cells labeled with fluorescent molecules. By contrast, the two-photon method, first developed by Winfried Denk in 1990, uses two consecutive pulses of relatively lower energy infrared light to elicit a glow from the fluorescent molecules. The weaker and less scattered light illuminates a smaller area and penetrates deeper into tissue, allowing researchers to focus on tiny details such as the structure and interaction of neurons. The Grete Lundbeck European Brain Research Foundation selected four scientists involved in the technique's development to split the winnings: Denk, now at the Max Planck Institute of Neurobiology, shares the prize with Arthur Konnerth of the Technische Universität München, Karel Svoboda of the Howard Hughes Medical Institute's Janelia Research Campus, and David Tank of Princeton University.

says is "completely rethought" to suit the needs of developing countries. The machine can weather heat, dust, and humidity and an unreliable electricity supply—at a tenth of the cost of current equipment, including 10 years of maintenance, but with high image quality, Schönenberger claims. He hopes that the product will be on the market in 2 or 3 years.

Reforms urged for brain project

LAUSANNE, SWITZERLAND | Two reports have urged for drastic and urgent reforms at the embattled Human Brain Project (HBP), a collaboration selected to receive up to €1 billion in funding from the European Commission and E.U. member states that has caused deep rifts among neuroscientists. In an open letter published last year, hundreds of researchers threatened to boycott the project unless the European Commission stepped in to demand an overhaul. Both an anonymous review panel working for the commission and a mediation committee led by Wolfgang Marquardt, head of the Jülich Research Center in Düren, Germany, concluded that the HBP needs to overhaul its management, scientific priorities, and communication style. (Summaries of both reports were published on 6 March and 9 March, respectively.) HBP is working to implement the advice, says Philippe Gillet, president of HBP's board of directors, including the mediators' recommendation to transform HBP into an international, CERN-like organization.
http://scim.ag/HBPreviews

USDA promises better oversight

WASHINGTON, D.C. | New research projects have been halted at a controversial U.S. Department of Agriculture (USDA) facility, USDA Secretary Tom Vilsack announced 9 March. The agency's Meat Animal Research Center in Clay Center, Nebraska, has come under fire for allegedly causing suffering and death while trying to create larger and more fecund farm animals. Last month, Congress proposed new protections for farm animals, backing a bill called the AWARE Act that would expand the Animal Welfare Act (*Science*, 13 February, p. 696). A draft of a USDA report released 9 March says "no instances of animal abuse, misuse, or mistreatment were observed" at the facility, but that the center had not provided proper oversight of animal care. Vilsack said no new research would be conducted until oversight is improved.

NEWSMAKERS

Cancer institute head steps down

Harold Varmus, the Nobel Prize–winning cancer biologist who has directed the U.S. National Cancer Institute (NCI) for nearly 5 years, is stepping down on 31 March. While leading the $4.9 billion NCI during a time of flat budgets, Varmus promoted cancer genomics, global health, and studies of little-explored questions in cancer. He

BY THE NUMBERS

2.9 million

The first estimate of the number of large whales killed and processed by industrial whaling during the 20th century, as reported in *Marine Fisheries Review*.

13.4%

Clinical trials of medical products that reported basic results in the public ClinicalTrials.gov database within the 1-year window required by the U.S. Congress, according to a study in *The New England Journal of Medicine*.

Published by AAAS

A scaled-back radio array

The consortium that will build the world's biggest radio telescope, the Square Kilometer Array (SKA), this week announced the final plan for the €650 million first phase of the project, due to begin construction in 2018 and be completed by 2023. The first phase, SKA1, was scaled back to stay within available funding, but will still achieve its two key scientific goals. The first is to detect metronomic signals from rapidly spinning neutron stars, or pulsars, and use them to track the passage of gravitational waves. The second is to map out the faint signal of neutral hydrogen gas back to the time of the earliest formation of stars and galaxies. SKA1's final plan has two components: a midfrequency array with about 200 (down from 250) dish antennas in South Africa; and a low-frequency array in Australia made up of about 130,000 (down from 250,000) so-called dipole antennas (similar to a rooftop TV aerial). SKA's phase 2 will be built between 2023 and 2030. The final instrument will have dishes and antennas stretching across most of southern Africa as well as Australia and will have a total collecting area of a square kilometer. **http://scim.ag/SKAback**

Dipole antennas of SKA's proposed low-frequency telescope in Australia.

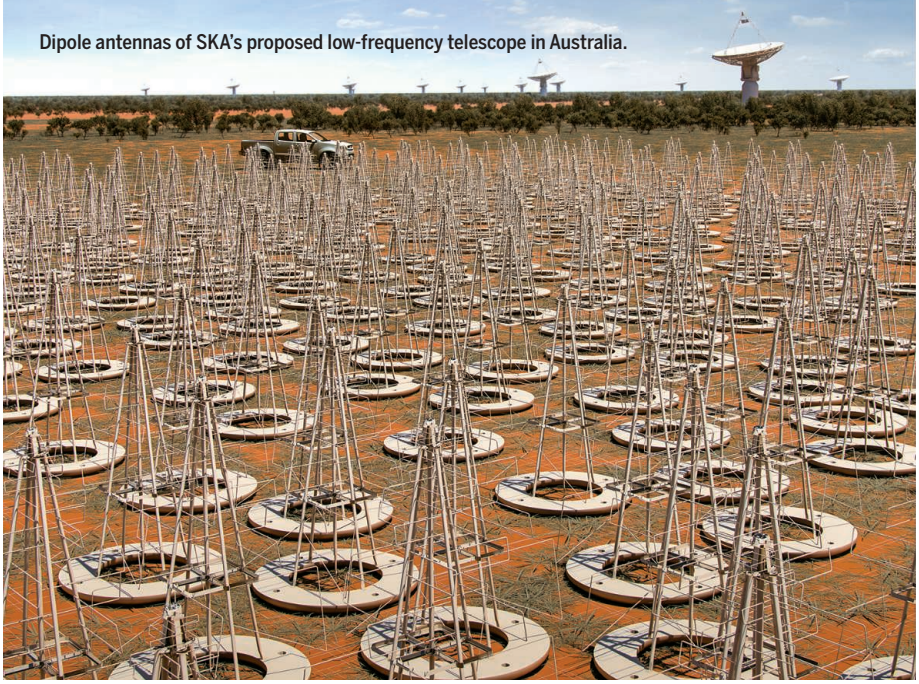

pushed for changes in how scientists are evaluated and launched a new award to give investigators stable long-term support. Varmus, 75, a former director of the National Institutes of Health, will head a lab at Weill Cornell Medical College in New York City and work with the New York Genome Center. Douglas Lowy, who now serves as NCI's deputy director, will become acting director. **http://scim.ag/Varmus**

French higher ed official departs

The French secretary of state for higher education and research, **Geneviève Fioraso**, has stepped down for health reasons, the French government announced last week. Fioraso became minister for higher education and research in May 2012; her role was downgraded to secretary of state last year in a Cabinet reshuffle. Limited by France's austerity policies, Fioraso had few budget increases to offer and came under fire from groups that hoped she would make a more radical break with the policies of the right-wing government of Nicolas Sarkozy. Fioraso's main achievement was a law, passed in 2013, that aimed to simplify France's higher education and research landscape and give the nation a stronger strategic research agenda. The minister in charge of national education, higher education, and research, Najat Vallaud-Belkacem, will temporarily take over her duties. **http://scim.ag/Fioraso**

Embattled RIKEN chief exits

Ryoji Noyori plans to resign as president of RIKEN, the network of Japanese national labs that spent much of the past year embroiled in a fraud scandal, Japanese news outlets reported last week. Noyori, 76, won a Nobel Prize in chemistry in 2001 and became head of RIKEN in October 2003. He has 3 years remaining in his third 5-year term as president. Some reports said he was retiring due to age, but some mentioned his desire to end a long drama over fraudulent papers on stem cells. In January 2014, a group led by Haruko Obokata of RIKEN's Center for Developmental Biology in Kobe reported in two papers in *Nature* to have found a new, simple way, dubbed STAP, to make pluripotent stem cells. The papers were retracted in July after investigators found them riddled with manipulated images and plagiarized text. Obokata was found guilty of research misconduct and resigned; another author committed suicide. In December, investigators concluded that the STAP cells never existed. **http://scim.ag/Noyori**

FINDINGS

Sponge shows evolutionary split

The evolution of the sponge (phylum Porifera) has long been a mystery. Some scientists think the first sponges emerged in the Cambrian period, between 541 million and 485 million years ago; others say they emerged during the Precambrian as early as 760 million years ago, based on some genetic analyses of modern sponges. But claims for fossils that early have been met with skepticism due to their poor preservation. Now, a research team reporting online this week in the *Proceedings of the National Academy of Sciences* claims that the millimeter-wide 600-million-year-old fossil pictured below is the oldest known poriferan. The new discovery indicates that the common ancestor of sponges and most other animals (called Eumetazoa) lived much earlier than many scientists assumed. And because today's sponges and eumetazoans differ in key genetic features, the team says, the find could also help date the first appearance of genes key to the evolution of most animals living today.

PHOTOS: (TOP TO BOTTOM) SKA; ZONGJUN YIN

Technicians have redone 10,170 splices in the superconducting wire in the LHC's magnets.

PHOTO: MAXIMILIEN BRICE/© 2014 CERN

PARTICLE PHYSICS

Excitement, anxiety greet LHC restart

Some worry the massive accelerator could produce nothing besides the Higgs boson

By **Adrian Cho**

Later this month, scientists at the European particle physics lab, CERN, near Geneva, Switzerland, will reawaken their slumbering giant, the Large Hadron Collider (LHC), after 2 years of repairs. They are hoping that the past is not prologue. In July 2012, physicists at CERN scored the field's crowning achievement by discovering the Higgs boson, the particle key to explaining how other fundamental particles get their mass and the last missing piece in a 40-year-old theory called the standard model. But in its 3-year first run, the LHC also produced nothing that would point to a deeper theory. For decades, in fact, atom smashers haven't produced anything the standard model can't explain. So some physicists worry that the LHC won't find anything besides the Higgs—for many, the nightmare scenario.

"The likelihood for this to happen is, honestly, not very small, because we haven't seen anything new so far," says Maurizio Pierini, a physicist at CERN who works on CMS, one of four massive particle detectors fed by the LHC. But Michael Peskin, a theorist at SLAC National Accelerator Laboratory in Menlo Park, California, says it's too early to fret. The LHC should have three runs over the next 15 years, he notes. "I think most people in the community were disappointed that we did not see new particles," he says. "Before we worry about this too much, let's see what the next run of the LHC has to say."

The LHC was designed to smash counter-circulating beams of protons at energies of 14 trillion electron volts (TeV), enough to produce particles dozens of times as massive as the Higgs or the top quark, the heaviest known particles. So far it has run at 8 TeV or less and has produced less than 1% of the expected data. That energy limit was imposed after the LHC broke down catastrophically in September 2008, just 9 days after first smashing protons, when a soldered electrical connection between two of its 1695 superconducting magnets melted. The LHC didn't take data until March 2010.

Technicians have now reworked the electrical connections—10,170 of them—so that they can safely carry the 13,000 amps of current required when the LHC runs all out. Researchers also aim to crank up the rate at which the LHC smashes protons, from 360 million to 700 million collisions per second.

In that torrent, physicists hope to find something beyond the standard model, which they say must be incomplete. For example, it doesn't account for the force of gravity. It also doesn't explain *why* nature uses the so-called Higgs mechanism to give other particles their mass. Fundamental particles gain mass by interacting with a field of Higgs bosons lurking "virtually" in the vacuum. But the standard model assumes the field exists without explaining its origins.

Physicists' list of things to look for first resembles the one they had in 2010, but the emphases have evolved. Most prominently, the quest to find the Higgs boson has grown into a program to study it. "Obviously, the number one thing that we are going to do is to measure the Higgs's properties as well as we can," says Marcela Carena, a theorist at the University of Chicago and Fermi National Accelerator Laboratory in Batavia, Illinois. "Any deviations [from the standard model predictions] will point to new physics."

For example, the standard model predicts the probabilities with which the Higgs decays into combinations of other known particles, such as a massive bottom quark and its antimatter partner. Having studied just a few thousand Higgses, physicists have only begun to measure those probabilities. Researchers will also search for multiple Higgs bosons, which many theories that attempt to expand the standard model predict.

The prime candidates for new particles remain those predicted by a concept called supersymmetry, which posits that every standard model particle has a heavier partner with a different amount of spin. Supersymmetry would solve a conceptual puzzle. If new, more-massive particles exist, then as they lurk in the vacuum they should interact with the Higgs boson to cause its mass to skyrocket. That doesn't happen, so the new particles must come with just the right

combination of properties to keep the Higgs light. In supersymmetry that would happen "naturally," as the effects of partnered particles on the Higgs mass would cancel because of the difference in their spins.

Unfortunately for physicists, those superpartners didn't show up in the LHC's first run. So now researchers are focusing mainly on finding the "stop squark," the superpartner of the top quark, the standard model particle that most influences the Higgs's mass. Even those searches are looking a bit iffy, as the failure to see the stop so far shows that it must weigh more than 0.7 TeV, a value that strains the theory. Still, Sanjay Padhi of the University of California, San Diego, says he's optimistic. "I will start to worry if the stop is not found up to 1.5 TeV," says Padhi, who works on CMS, one of the detectors that discovered the Higgs.

Interest is also rising in trying to blast out particles of dark matter—the mysterious stuff whose gravity binds the galaxies. Cosmological measurements show that it makes up 85% of all matter in the universe. "We know there is something beyond the Higgs," says Stephanie Majewski, a physicist at the University of Oregon in Eugene who works on the ATLAS particle detector, which also discovered the Higgs. "We know that there is dark matter, and we ought to be able to produce it with the LHC."

The dark matter particles themselves would not be directly detectable. To deduce their presence, physicists will look for lopsided "mono-X" events: proton-proton collisions that send a standard model particle or a jet of them flying in one direction and nothing detectable going the opposite way—an absence that would reveal a hidden particle. But John Ellis, a theorist at King's College London, cautions that dark matter particles could have different, more complicated signatures.

If nothing new shows up in the next few years, people may drift away from the LHC, Pierini says. But Ellis says physicists have a good decade before they should worry. CERN plans to upgrade the LHC's particle detectors in 2018 and the accelerator itself around 2022, to boost its intensity.

A bigger concern, Pierini says, is that experimenters might inadvertently overlook a new effect. To keep the data rate manageable, physicists rely on computerized "triggers" to sift out the few encounters between countercirculating bunches of protons that contain interesting proton-proton collisions. The triggers toss data from all but a few of every 100,000 bunch crossings. "It's really terrifying to think that there is something there but that we didn't discover it because we just didn't look for it," Pierini says. "That's what keeps me up at night." ■

ATMOSPHERIC SCIENCE

California fogs are thinning

Warming linked to urbanization prevents low clouds from forming, Los Angeles area study shows

By **Cally Carswell**

For years, sun worshippers have flocked to southern California's coast, only to be disappointed each spring when the weather turns drab and foggy, a phenomenon locals call "May Gray" and "June Gloom." But the low-hanging marine clouds responsible for that gloom have declined dramatically over the past 60 years, a new study concludes. It fingers the growth of cities and their heat-retaining concrete as a prime cause.

The research, recently published online in *Geophysical Research Letters*, offers insight into how increasing urbanization may erode coastal fog banks in the future, with potentially serious consequences for people and ecosystems. It's "the first definitive look at how fog might change for a specific coastal region," says Travis O'Brien, a research scientist at Lawrence Berkeley National Laboratory in California, who was not involved in the research.

To understand how California's coastal fog might be changing, some 6 years ago lead author Park Williams, now a bioclimatologist at Columbia University's Lamont-Doherty Earth Observatory in Palisades, New York, began assembling data from 24 southern California airports, which keep hourly records of fog conditions. He hoped to identify key climate variables influencing fog, such as sea surface temperatures and wind patterns. He revisited the data for years, but was unable to spot any notable trends.

Last year, however, Rachel Schwartz, a Ph.D. candidate at the Scripps Institution of Oceanography in San Diego, California, sent Williams a study she was finishing. It showed that low clouds had declined slightly over the past 60 years from coastal California to Alaska. But fog had nearly disappeared at the Los Angeles and Long Beach airports over a similar period, earlier studies by another researcher concluded.

Those contrasting results gave Williams an idea: Perhaps the low clouds had not disappeared, exactly, but gained height. He realized that he had lumped together two potentially distinct data sets on stratus clouds, which form between the cool sea surface and a warm, stable inversion. The clouds can form close to the ground, as fog, which tends to burn off by afternoon; they can also sit higher in the sky and linger all day. Reanalyzing his data, Williams saw—at last—some intriguing trends.

The lowest tier of clouds, it turned out, was heavily influenced by land use—and changing more dramatically than the higher clouds. At some airports, fog was becoming a threatened species; at one strip in Ontario, California, the average height of the summer clouds lifted by 170 meters between 1950 and 2014. That amounted to an 87% decline in the lowest clouds; summer fog that once regularly cloaked nearby mountains in moisture now visits them rarely. Overall, the Los Angeles region showed a 64% reduction in

Foggy days are an increasingly rare sight in Los Angeles.

PHOTO: © SUPERSTOCK/CORBIS

fog. In contrast, the San Diego area saw less dramatic declines, and Santa Barbara saw little change.

To explain the variability, Williams tried comparing the trends with land use data. "The scatterplot came out, and everything just lined up," he recalls. The airports that experienced the greatest fog declines tended to sit within the landscapes that had undergone the most development since 1950. That urbanization led to a marked increase in nighttime air temperatures, a result of all that concrete and asphalt absorbing heat during the day and slowly radiating it after dark. The warmth pushed up the elevation at which air cools enough for water vapor to condense—effectively eliminating fog.

Williams says this warming mechanism could eventually squeeze out stratus clouds, which form only below about 800 meters, especially in inland regions, where the ocean's cooling effect is smaller. Indeed, in his study, though the lowest clouds changed most dramatically, overall cloud cover in the Los Angeles region declined as well.

Such changes could have implications for both regional ecosystems and humans. Fog is likely a key source of water in the arid forests and chaparral that ring Los Angeles, notes Christopher Still of Oregon State University, Corvallis. Loss of the moisture could result in "a lot of plant mortality and … ecological change," he says. And although clearer conditions could increase the region's ability to produce solar energy, they might also bump up temperatures in existing urban "heat islands," leading to greater energy use for cooling and raising health issues related to heat stress.

What Williams's study portends for global fog trends is less clear. He found, for example, that even as the cloud layer lifted inland, it slipped to lower altitudes off the California coast over the Channel Islands, increasing fog there. Without the urban heat island effect, he says, "this same trend might have been seen over L.A. and San Diego." And how marine clouds might change in a warming world is murky. Rising sea surface temperatures would tend to reduce stratus cloud cover, notes Katinka Bellomo, a doctoral candidate at the University of Miami in Florida, who is using ship records to study clouds over the Pacific and Indian oceans. But climate models also project changes in the lower atmosphere that would increase the clouds. So far, she says, "we don't know which one prevails."

In California, however, everyday concerns are often more parochial. When people learn she studies the clouds that cause May Gray and June Gloom, Schwartz says they often ask: "You're trying to figure out how to get rid of them, right?" She politely tells them no. ■

PHOTO: SUZANNE BOTT

The arches and statues of Hatra in northern Iraq stood for 2000 years, but now may be gone.

ARCHAEOLOGY

Militants leave trail of destruction at Iraqi sites

The Islamic State group strikes one valuable archaeological site after another, destroying priceless ruins and artifacts

By **Andrew Lawler**

The ancient city of Hatra fended off two Roman emperors and repulsed a ruler of Persia's powerful Sassanid dynasty. But late last week, local people near the ornate ruins about 110 kilometers southwest of the Iraqi city of Mosul heard massive explosions that likely marked the demise of the 2000-year-old city and its spectacular, well-preserved sculptures and stone architecture.

While inflicting misery on the people of northern Iraq, supporters of the Islamic State group have also attacked one ancient site after another in the past 2 weeks, systematically taking sledgehammers and drills to artifacts. Other reports say that the forces of the group, increasingly known by its Arabic acronym Daesh, are using bulldozers to demolish ancient buildings. By last week the toll included the statues in the Mosul Museum, the classical site of Hatra, and the ancient Assyrian capitals of Nineveh, Nimrud, and Khorsabad, famed for their massive protective deities in the form of human-headed winged bulls. Assur, a 4500-year-old temple-studded Assyrian city where kings and queens were laid to rest for centuries, is likely the next target, say archaeologists, who are desperately trying to piece together the extent of the damage.

The unprecedented wave of destruction has prompted a small protest march in Washington, D.C., as well as statements of outrage from archaeologists and museum curators around the world. U.N. officials have said that the events constituted a war crime. "Those barbaric, criminal terrorists are trying to destroy the heritage of mankind and Iraq's civilization," said Iraqi Prime Minister Haider al-Abadi. He spoke during a ceremony on 28 February in which his government reopened Baghdad's long-shuttered Iraq Museum as a way of reaffirming the importance of the country's heritage.

Outside experts feel the losses keenly, because northern Iraqi sites have been largely off-limits to study since the start of the first Gulf War a quarter-century ago. "Assyria was the first true empire in world history," says Yale University Assyriologist Eckart Frahm. Its "scholarly exploration is far from complete." For example, many of the inscriptions at Nimrud have yet to be properly documented, he says.

Representatives and publications from the Islamic State group have said that statues and reliefs of animals and humans are anathema to their brand of Sunni Islam. "We were ordered by our prophet to take down idols and destroy them," explained an unidentified Daesh representative in a video widely distributed earlier this month, which showed men pushing intricately carved statues off their plinths and smashing the remains with sledgehammers. Another video image showed a man using an electric drill to destroy the human face of a huge winged bull standing at a gate at Nineveh.

Independent Iraqi archaeologist Lamia al-Gailani, based in London, identified the location of the destroyed statues as the Mosul Museum and said that 26 of the 30 statues in the museum's Hatra hall were originals, made during Hatra's heyday at the start of the common era. She adds that 21 of 24 Assyrian reliefs and statues from Nineveh and Nimrud in the museum were also originals.

The militants spare some artifacts because sales serve as an important source of revenue, according to organizations tracking the illicit antiquities trade. Irina Bokova, the head of the United Nations Educational, Scientific and Cultural Organization, said that officials are examining images that showed looted material from Nimrud, about 30 kilometers southeast of Mosul, "put on big trucks" and transported, possibly for sale.

After looting Nimrud, the capital of the sprawling Assyrian Empire in the 8th century B.C.E., Islamic State forces reduced some or all of it to rubble. Abdul Amir Hamdani, an Iraqi archaeologist at Stony Brook University in New York, spoke with a colleague in Mosul familiar with the situation and reports that Islamic State forces occupied Nimrud for several days before bulldozing it from noon to late evening on 5 March.

The next day, explosions were heard at Hatra, though the extent of damage at the statue-filled site remains uncertain. Then on 8 March, the Iraqi government said that Islamic State supporters demolished Khorsabad, another ancient Assyrian capital about 15 kilometers northeast of Mosul. Hamdani and other archeologists fear that Assur, nearly 100 kilometers south of Mosul, is next, although that site lacks the large sculptures that have previously drawn Daesh's attention.

In an 8 March press conference in Baghdad, Adel Fahad al-Shershab, Iraq's minister of tourism and antiquities, lamented the lack of international action. "We request aerial support" from the United States, he said. American bombers carried out a dozen airstrikes in the region this past weekend, but it was not clear if protecting the sites was part of the mission. American bombers are striking Islamic State forces involved in the destruction and looting, including machinery like bulldozers and earth excavators, said U.S. Defense Department spokesperson Kim Michelsen. "But we don't have troops on the ground to protect the sites—and that might make them even more of a target," he said.

U.S. spy satellites, however, could provide important data on the exact extent of damage. The U.S. State Department made a "high-priority request for new satellite imagery," according to a source there. Real-time imaging could conceivably be used to follow the trucks that left Nimrud, and so track looted material. But such requests will likely take a back seat to ongoing military operations, including a battle now unfolding around Tikrit. Meanwhile, Sunni Islam's leading institution, al-Azhar in Cairo, put out a statement declaring that the destruction "is forbidden in Islam and rejected in total ... [and is] a major crime against the whole world."

For Near Eastern archaeologists, the news provoked both outrage and a sense of helplessness. Many say they are at a loss about what they could do to reverse—or even assess—the damage. The University of Chicago, long a center of research in the field, said in a statement that the events add "to the growing spiral of despair from both Iraq and Syria." Hamdani expressed his anger by helping organize a small 10 March protest near the White House. "Thousands of years of history are being smashed by the hammers of ignorance," he says. "With each destroyed statue, a story is forgotten." ■

Ancient sites under attack

The world's first empire, that of the Assyrians, lay in what is now northern Iraq. Its monuments, as well as other irreplaceable antiquities, are now being destroyed or sold by the militant movement known as the Islamic state group.

NEUROSCIENCE

Can sound open the brain for therapies?

Ultrasound methods breach blood-brain barrier

By **Emily Underwood**

From imaging babies to blasting apart kidney stones, ultrasound has proved to be a versatile tool for physicians. Now, several research teams aim to unleash the technology on some of the most feared brain diseases.

The blood-brain barrier, a tightly packed layer of cells that lines the brain's blood vessels, protects it from infections, toxins, and other threats but makes the organ frustratingly hard to treat. A strategy that combines ultrasound with microscopic blood-borne bubbles can briefly open the barrier, in theory giving drugs or the immune system access to the brain. In the clinic and the lab, that promise is being evaluated.

This month, in one of the first clinical tests, Todd Mainprize, a neurosurgeon at the University of Toronto in Canada, hopes to use ultrasound to deliver a dose of chemotherapy to a malignant brain tumor. And in some of the most dramatic evidence of the technique's potential, a research team reports this week in *Science Translational Medicine* that they used it to rid mice of abnormal brain clumps similar to those in Alzheimer's disease, restoring lost memory and cognitive functions. If such findings can be translated from mice to humans, "it will revolutionize the way we treat brain disease," says biophysicist Kullervo Hynynen of the Sunnybrook Research Institute in Toronto, who originated the ultrasound method.

Some scientists stress that rodent findings can be hard to translate to humans and caution that there are safety concerns about zapping the brain with even the low-intensity ultrasound used in the new study, which is similar to that used in diagnostic scans. Opening up the blood-brain barrier just enough to get a beneficial effect without scorching tissue, triggering an excessive immune reaction, or causing hemorrhage is the "crux," says Brian Bacskai, a neurologist at Massachusetts General Hospital in Boston who studies Alzheimer's disease and used to work with Hynynen.

Safely and temporarily opening the blood-

brain barrier is a long-sought goal in medicine. About a decade ago, Hynynen began exploring a strategy combining ultrasound and microbubbles. The premise is that ultrasound causes such bubbles to expand and contract, jostling the cells forming the blood-brain barrier and making it slightly leaky.

That could help cancer physicians such as Mainprize deliver chemotherapy drugs into the brain. Hynynen also hypothesized that the brief leakage would rev up the brain's inflammatory response against β amyloid—the toxic protein that clumps outside neurons in Alzheimer's and may be responsible for killing them. Disposing of such debris is normally the role of the microglia, a type of brain cell. But previous studies have shown that when β amyloid forms clumps in the brain, it "seems to overwhelm microglia," Bacskai says. Exposing the cells to antibodies that leak in when the blood-brain barrier is breached could spur them to "wake up and do their jobs," he says. Some antibodies in blood may also bind directly to the β-amyloid protein and flag the clumps for destruction.

Hynynen and others have recently tested the ultrasound strategy in a mouse model of Alzheimer's. In December 2014, for example, he and colleagues reported in *Radiology* that the method reduces amyloid plaques in a strain of mice engineered to develop the deposits, leading to improvements in cognition and spatial learning. Microglia consumed more β amyloid after the treatment, suggesting the cells do play a role in the effect, says neuroscientist Isabelle Aubert, who collaborates with Hynynen at Sunnybrook.

This week, neuroscientist Jürgen Götz of the Queensland Brain Institute in St. Lucia, Australia, and his Ph.D. student Gerhard Leinenga report that they have built on Hynynen and Aubert's protocol, using a different mouse model of Alzheimer's. After injecting these animals with a solution of microscopic bubbles, they scanned an ultrasound beam in a zigzag pattern across each animal's entire skull, rather than focusing on discrete areas as others have done. After six to eight weekly treatments, the team tested the rodents on three different memory tasks. Alzheimer's mice in the control group, which received microbubble injections but no stimulation, showed no improvement. Mice whose blood-brain barriers had been made permeable, in contrast, saw "full restoration of memory in all three tasks," Götz says.

The team also found a two- to fivefold reduction in different types of β-amyloid plaques in the brain tissue of the treated group. The attempt to stoke microglia's appetite appeared to work; Götz and Leinenga found much more β-amyloid protein within the trash-eating cells of treated animals. Yet rousing microglia may not be the only mechanism responsible for the rodents' memory boost, Aubert notes. She and Hynynen recently reported in *Brain Stimulation* that ultrasound also boosts the birth and growth of new neurons in mice.

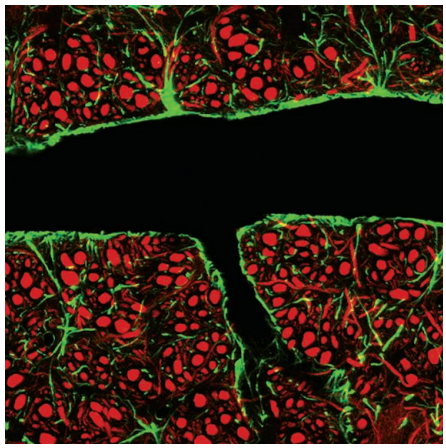

A tightly packed assembly of cells including astrocytes (green) forms the barrier between blood vessels (black) and neurons (red).

Götz and Leinenga next plan to test the whole-brain ultrasound scan method in larger animals with β-amyloid deposits, such as sheep. The approach, which could in theory be used for other brain diseases involving abnormal protein clumps, "is exciting," says Gerald Grant, a neurosurgeon at the Stanford University School of Medicine in Palo Alto, California. "We've been thinking of opening up the blood-brain barrier as a way to get things into the brain, but this pays attention to getting things out."

It's far from settled that eliminating β-amyloid deposits outside of neurons is the key to treating or stopping Alzheimer's disease, however. And Bacskai is skeptical that the mouse results say much about the technique's potential in humans. The range between a mouse that can learn and one that cannot learn "is pretty small," so big gains in behavioral tests in mice may mean nothing in humans, he says. He adds that nonstandardized ultrasound equipment makes it hard to answer basic safety questions: "How long is the blood-brain barrier open? How big are the pores? What's the damage?"

Hynynen, who is working with a medical imaging company to commercialize the technique, notes that ultrasound application to the brains of animals including rabbits and monkeys has produced no negative side effects. And Mainprize's clinical trial may provide more safety data. He hopes to open the blood-barrier to increase chemotherapy delivery to a brain cancer patient just before he operates to remove the tumor. Using Hynynen's technology, he and colleagues will apply ultrasound and microbubbles to tissue in and around the tumor, as well as to several unaffected brain areas. Then they'll examine excised tissue for hemorrhages and to see if the treatment boosted the concentration of the drug. A similar trial is now recruiting participants in France.

If these phase I trials establish safety, "it opens the door for phase II trials looking to see if there's any benefit" to opening the blood-brain barrier, including for conditions beyond cancer, Mainprize says. Despite his doubts, Bacskai can't fully resist the dream driving this fledging field. "Imagine if your grandmother went to the clinic once per year, and it cleared amyloid β and that was all it took—no surgery, no drugs. It would be amazing." ■

A sound way to clean up the brain

Microbubbles injected into the blood vibrate under ultrasound, temporarily forcing cells lining the blood-brain barrier apart. This may allow amyloid-fighting antibodies to slip into brain tissue (shown) or rouse cells that clean up the protein.

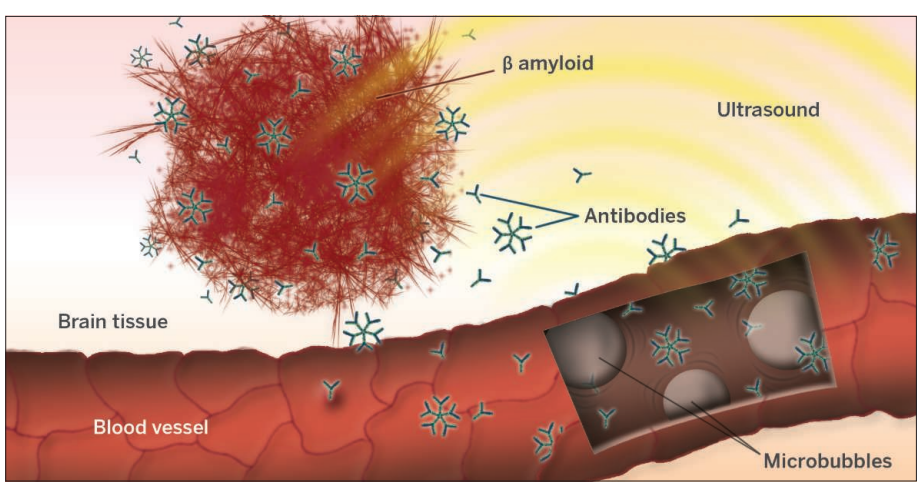

CREDITS: (IMAGE) C. J. GUERIN, MRC TOXICOLOGY UNIT/SCIENCE SOURCE; (ILLUSTRATION) EMMANUEL THEVENOT/LAB OF ISABELLE AUBERT; COURTESY OF SUNNYBROOK RESEARCH INSTITUTE

VIROLOGY

Bird flu virus's promiscuity raises red flags

Novel variants of H7N9 and other strains are arising at alarming rate

By **Dennis Normile**

The most worrisome of the avian flu viruses to emerge in recent years is looking even more menacing. Since it first began killing people in eastern China 2 years ago, the H7N9 virus has infected poultry throughout the country and could be poised to spill into Central Asia. Worse, strains of H7N9 are promiscuously swapping DNA with other avian viruses in circulation, report virologist Yi Guan of the University of Hong Kong and colleagues this week in *Nature*. That could increase the chance that a pandemic strain will emerge.

Mindful of how predictions a decade ago of an imminent H5N1 pandemic proved shrill, public health officials are advising calm while heightening vigilance for any signs of H7N9 evolving into a form that could spread rapidly among people. In a document released last month, *Warning signals from the volatile world of influenza viruses*, the World Health Organization (WHO) notes that four new H5 avian flu viruses have emerged in the past 2 years. "The diversity and geographical distribution of influenza viruses currently circulating in wild and domestic birds are unprecedented," WHO warns. "The world needs to be concerned." As a first step, Guan and other experts are renewing calls to close China's live poultry markets, where most victims catch H7N9—and where animals can contract multiple virus strains, allowing them to swap genetic material.

Based solely on case mortality rate—38%—the H7N9 virus is not as nasty as H5N1, a bird flu strain that has killed 55% of people known to have contracted it since 2003 (see table). But in just 2 years, H7N9 has infected 602 humans, running almost neck and neck with H5N1. "Humans seem more susceptible" to H7N9 infection, Guan says. Two mysteries about H7N9 deepen the concerns. Researchers still don't know where or if the virus circulates in nature, and infected poultry show no or very mild symptoms, confounding surveillance.

Still, H7N9 is clearly spreading (*Science*, 29 November 2013, p. 1031). The first human cases were in Anhui province and Shanghai, along China's east coast, in early 2013. By the following year, H7N9 had been reported in 11 provinces and municipalities. Last fall it popped up in Xinjiang, China's westernmost region. From there, "this virus has the chance to get to other countries," Guan says.

At the same time, it is rapidly diversifying. Guan's team found that all H7N9 samples collected during the spring 2013 outbreak could be grouped in one clade, or phylogenetic branch. Samples collected a year later, from thousands of chickens in 15 cities across China, painted a different picture. Sequencing the viruses showed that H7N9 had split into three clades, as a result of rampant genetic exchange.

Other bird flu viruses are reassorting like mad. The H and N in the nomenclature for flu viruses refer to two surface glycoproteins: hemagglutinin, for which 18 different genes are known, and neuraminidase, which is encoded by 11 different genes. Influenza viruses have shuffled these and six other viral genes into a dazzling array of combinations, and the reassortment "appears to be happening now at an accelerated pace," WHO warns. Guan's team amplifies the warning in their *Nature* paper. The "H5N1 and H9N2 viruses, along with the H7N9 virus, are now reassorting with other viruses in the influenza ecosystem in China," the team writes.

The proliferation of strains over the past 2 years is a particular puzzle. "Something has changed, which made some of these more recent strains more readily able to produce reassortments," says Les Sims, a Melbourne, Australia–based veterinary consultant. The WHO report concludes: "The emergence of so many novel viruses has created a diverse virus gene pool made especially volatile by the propensity of H5 and H9N2 viruses to exchange genes with other viruses. The consequences for animal and human health are unpredictable yet potentially ominous."

Attention focuses on China's live poultry markets, where "we have a lot of different subtypes of avian viruses dynamically reassorting," says George Gao, deputy director-general of the Chinese Center for Disease Control and Prevention. To forestall disaster, "we need to close the live poultry markets now and [halt] live poultry trading," says Gao, who called for such steps last year in Science (18 April 2014, p. 235). As a start, authorities have banned markets from some urban centers. ■

A tale of two bird flus

H7N9 may not be as lethal at present as H5N1, but virologists worry about its pandemic risk because of the number of cases and how fast the virus is mutating.

	H5N1	H7N9
Year identified	1997	2013
Human cases/deaths	777/428 (since 2003)	602/227 (since 2013)
Effect on domestic chickens	Highly pathogenic	No or mild symptoms
Natural host	Aquatic wildfowl	Unknown

China's live poultry markets are hotbeds of viral gene swapping.

PHOTO: STRINGER/IMAGINECHINA/AP IMAGES

Not enough children were immunized against measles in Guinea even before Ebola struck.

INFECTIOUS DISEASES

As Ebola fades, a new threat

With health services devastated in the wake of Ebola, experts are bracing for a deadly measles outbreak in West Africa

By **Leslie Roberts**

As the Ebola epidemic wanes in West Africa, a second health crisis is brewing. The last known Ebola case in Liberia was recorded weeks ago. But there and in Guinea and Sierra Leone, where the epidemic is still smoldering, it has devastated already weak public health systems and curtailed childhood immunizations. On page 1240, researchers warn of what could be a disastrous consequence: a measles outbreak that could, at its worst, kill thousands more people than Ebola has.

"The secondary effects of Ebola are likely to be as bad as or worse than the direct effects," says epidemiologist Justin Lessler of Johns Hopkins Bloomberg School of Public Health in Baltimore, Maryland, who with his collaborators put some sobering numbers on the size of a potential post-Ebola measles outbreak.

Measles is by no means the only or the worst threat in this devastated region. Worried about an upsurge in malaria cases, Doctors Without Borders began distributing drugs for the parasitic disease in late October, for instance. But measles is a sentinel of a broken health system, and it will likely hit early and hard. One of the most contagious viruses on Earth—five to 10 times more infectious than Ebola—measles is among the first diseases to erupt in the wake of a disaster. In humanitarian crises in poor countries, it can kill up to 20% of those infected, usually those weakened by malnutrition and vitamin A deficiency.

Even before Ebola hit, Liberia, Guinea, and Sierra Leone were headed for trouble. Just an estimated 62% to 79% of children were vaccinated against measles in the three countries in 2012 and 2013, according to the Demographic and Health Surveys—and that was with only one dose of the vaccine. Because the virus is so exquisitely transmissible, 95% of the population must be protected with two doses of vaccine to stop measles.

"Measles immunization is chronically weak [in those three countries], but last summer it plummeted," says Steve Cochi, senior adviser in the Global Immunization Division at the U.S. Centers for Disease Control and Prevention (CDC) in Atlanta. Liberia had scheduled a measles campaign for late fall 2014, but it was canceled once Ebola struck. In Guinea and Sierra Leone, planning has been postponed.

> ***"The secondary effects of Ebola are likely to be as bad as or worse than the direct effects."***
>
> **Justin Lessler**, John Hopkins University

In the new study, Lessler and his collaborators set out to see just how bad a post-Ebola measles explosion might be. The multiuniversity team used statistical and geospatial approaches to map the number, age, and location of children who were susceptible to measles before Ebola hit. Then they plugged in various assumptions to project the effects of the disruption in measles immunization after 6, 12, and 18 months.

Their grim projection: A regional measles epidemic post-Ebola would strike roughly twice as many people as a pre-Ebola epidemic, an estimated 227,000 compared with 127,000, and cause 2000 to 16,000 additional deaths. At the high end, the death toll could exceed the nearly 10,000 killed by Ebola to date. Nearly all of those deaths could be averted, Lessler stresses, by effective mass vaccination campaigns. He says the group focused on measles instead of, say, setbacks in maternal mortality, "because this is something we know what to do about, and compared to other interventions it is relatively cheap."

Lessler concedes their scenario may be "a touch" too pessimistic. The team assumed that measles vaccination, through both routine coverage and mass campaigns, dropped 75% after the Ebola outbreak and took 18 months to return to pre-Ebola rates.

"The assumed magnitude of disruption to routine vaccination is fairly arbitrary and open to debate, as the authors acknowledge," says Nicholas Grassly, an epidemiologist at Imperial College London. "But the conclusion and the call to action are not."

In late 2014, CDC did its own model of the size of the susceptible population, says Katrina Kretsinger, who runs the measles team in Cochi's division. Although the CDC group used different assumptions—for instance, a 50% decline in vaccination—it came up with very similar numbers, says Kretsinger, who briefed CDC Director Tom Frieden in early January. "It is a high priority for him," she says.

But Ebola has added a whole new level of difficulty to mounting vaccination campaigns in a region that was challenging to begin with. Cochi asks: Who will deliver the vaccine, when so many health care workers have died? And, given the rumors and distrust of Western medicine, will people accept it? "If you approach people with a measles vaccine, they might think it is an Ebola vaccine," he says.

Even so, Liberia, with help from CDC and other international partners, is pushing ahead, trying to launch a measles campaign as early as May that will target all children between 9 months and 5 years of age. Planning in Sierra Leone and Guinea is further behind, because, for now, the focus remains on stopping Ebola. ■

CREDITS: (PHOTO) JULIEN HARNEIS/FLICKR

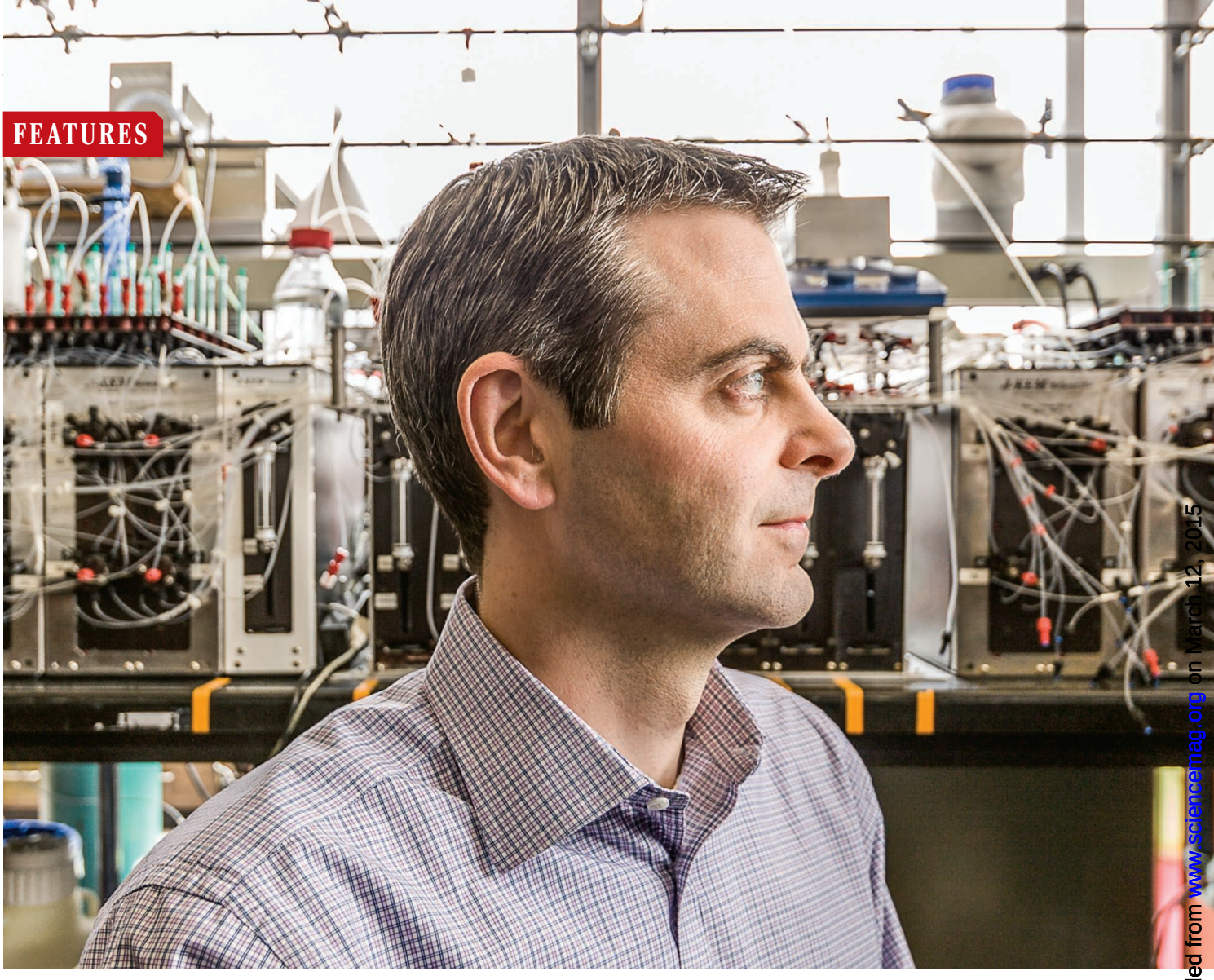

THE SYNTHESIS MACHINE

An automatic device that makes small organic molecules could revolutionize drug discovery

By **Robert F. Service**, *in Urbana, Illinois*

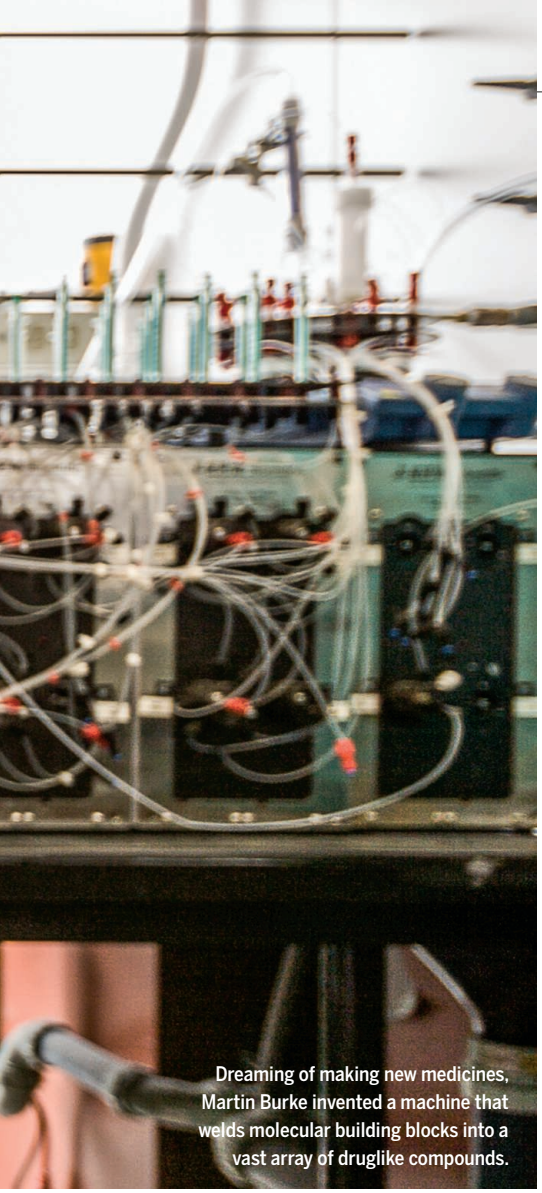

Dreaming of making new medicines, Martin Burke invented a machine that welds molecular building blocks into a vast array of druglike compounds.

Organic chemistry is an ordeal—just ask most science majors. There are the bewildering names of molecules, the elements, bonds, reactions, and reagents. There are the recipes, lab work, and late nights hovering over flasks. There are the separations, purifications, and analysis. Even for experts, making molecules is slow, painstaking work.

"We think we can change that," says Martin Burke, a chemist at the University of Illinois, Urbana-Champaign. And to drive the point home, he offers to transform a chemistry neophyte—me—into a synthetic chemist.

Burke steers me into Room 456 of the Roger Adams Laboratory building and toward a black lab bench holding a contraption about the size of one of those industrial espresso machines you see at Starbucks. Atop it sits two aluminum blocks, drilled through with 2.4-centimeter-wide holes, for holding nine vials. A tangle of thin tubes connects all the different pieces. But its basic principle is simple: It's a chemistry version of a highway cloverleaf, intended to steer ingredients from one place to another. Burke and his students call it simply "The Machine."

Michael Schmidt, a second-year graduate student in Burke's lab, gives me a recipe for crocacin C, an antifungal compound first synthesized in 2000 by three Australian chemists. Plastic vial number 1, which contains a pinch of a white crystalline powder, goes in slot number 1. Vial number 2, with a different white crystalline powder, goes in slot number 2, and so on. Schmidt has me connect a few spaghetti-width tubes to feed in water, organic solvent, air, and nitrogen gas. Then I press "run" on the Dell laptop below the lab bench, and my work is done.

But The Machine is just getting started. With a soft whir, it proceeds through dozens of steps: preparing, reacting, purifying, washing, preparing, reacting, purifying, washing, and on and on. Two days later, Burke sends word by e-mail that my first total synthesis is complete. The result: 8.6 milligrams of an off-white, powdery crocacin C.

Crocacin C is just one of a host of organic molecules that Burke's machine can make. On page 1221 of this issue, Burke and his colleagues report that they've used their automated synthesizer to produce a wide variety of molecules—stringlike linear compounds, rings, and bowls—all with bonds twisting this way and that. Like an automated DNA synthesizer, the new machine works by snapping together premade building blocks. And because thousands of such building blocks are already sold commercially, the machine could speed the production of potentially billions of different organic compounds that can be tested as new drugs, agricultural compounds, and materials.

"This is an amazing technology," says Cathleen Crudden, an organic chemist at Queen's University in Kingston, Canada. "It's a huge advance in small-molecule synthesis." Peter Seeberger of the Max Planck Institute of Colloids and Interfaces in Potsdam, Germany, agrees. "It's an important milestone, and there will be more to come," says Seeberger, who pioneered his own automated synthesizer for a different kind of molecule, the oligosaccharide sugar chains that cap many proteins and lipids. Improved automation, he and others say, will give biologists and many other researchers unprecedented access to compounds they need, while freeing organic chemists to pursue projects more challenging than churning out molecules they already know how to make. "The better we make this tool and the more we make it available, the more it will enhance science," Seeberger says.

ORGANIC CHEMISTRY has largely resisted automation since the first organic molecules were synthesized in the 1820s. The primary exception has been biopolymers, molecules made with a small number of building blocks that are all linked with the same type of chemical bond. That single bond acts like a train hitch capable of linking boxcars together in any desired order. Today, dedicated synthesizers churn out three such biopolymers: DNA fragments called oligonucleotides, protein fragments called peptides, and oligosaccharides.

This automation has produced powerful results. According to the business research firm MarketsandMarkets, by 2019 the oligonucleotide synthesis business will be worth $1.7 billion. Synthetic peptide-based drugs, meanwhile, already account for more than $14 billion in sales annually. "If you could do similar things with small molecules, it would have a huge impact," says Richard Whitby, an organic chemist at the University of Southampton in the United Kingdom. That's because these molecules not only represent the backbone of the pharmaceutical industry, but are also used in countless other products such as dyes, agricultural chemicals, light emitters, and biological probes.

That hasn't been possible, because small molecules assume a near-infinite variety of shapes. One recent report, for example, calculated that small molecules containing just carbon, oxygen, and nitrogen could be assembled in 10^{60} different ways, more than the number of atoms in the universe. "You need a lot of reactions to put together complex molecules," Crudden says.

Making organic molecules has always been less like linking boxcars than like building furniture. Woodworkers can use many kinds of wood, linked with a variety of joints: mortise and tenon, dovetail, lap joints, and so on. And like craftsmen joining pieces of wood, organic chemists must ensure that each bond is oriented in the proper direction. Attach a carbon atom facing away from the core of the molecule instead of inward, and the biological result could be as useless as a chair with one leg jutting skyward. As a result, except for automating several common industrial reactions, organic chemists tend to rely on complex recipes to forge bonds one at a time, slowly building their molecules in dozens or hundreds of steps. Most synthetic chemists consider that methodical approach the only way to ensure they make exactly what they want. "That has been the dogma for 180 years," Burke says.

BURKE HAS THE TALL and trim build of a long-distance runner and something of a marathoner's persistence. In November 1998, as an M.D.-Ph.D. student at Harvard University, he met a 22-year-old patient with cystic fibrosis, a disease caused by the lack of a protein that normally forms an ion channel in cell membranes. Without the channel, the salt balance in patients' lung tissue is disrupted, making sufferers prone to infections. The patient, a bright and inquisitive young woman, asked Burke ever more detailed questions about the disease, and he described the exact genetic mutation at fault. Finally, she asked: If doctors knew so much about her disease, why couldn't they fix it? "That conversation changed my life," Burke says.

Burke knew that modern medicines are tailored to block overactive proteins, not to create missing ones. But he also knew that, in some cases, small drug molecules may be able to substitute for them. He had learned about one such molecule in one of his early organic chemistry classes at Harvard. Amphotericin B (Amph B) is an antifungal compound made by bacteria. The molecule links up with multiple copies of itself, along with cell membrane molecules called sterols, to create an ion channel. Researchers had long believed—though not proven—that Amph B kills fungi by punching holes in their cells. Whatever the mechanism, Amph B was a lifesaving drug for patients with dangerous fungal infections. Unfortunately, the drug is also highly toxic, causing such severe side effects that patients often refer to it as "amphiterrible."

As Burke was finishing his M.D.-Ph.D. in 2005, he hoped to confirm Amph B's cell-killing mechanism and then tweak the compound to make it less toxic. But his long-range vision was even bolder: He wanted to harness the molecule's channel-making properties to help cystic fibrosis patients. If it worked, it could serve as a sort of molecular prosthetic device for ensuring the proper salt balance in lung tissues—perhaps not as good as the real thing, but good enough to improve patients' lives.

The initial hope was short-lived. "We quickly realized that the bottleneck was synthesis," Burke says. Amph B is a complicated molecule containing more than 38 carbon atoms, and the only known synthesis, published in 1987, involved more than 100 steps. Making enough of the molecule—along with near-variants of it—to figure out the biology of pore formation would take years, if not decades.

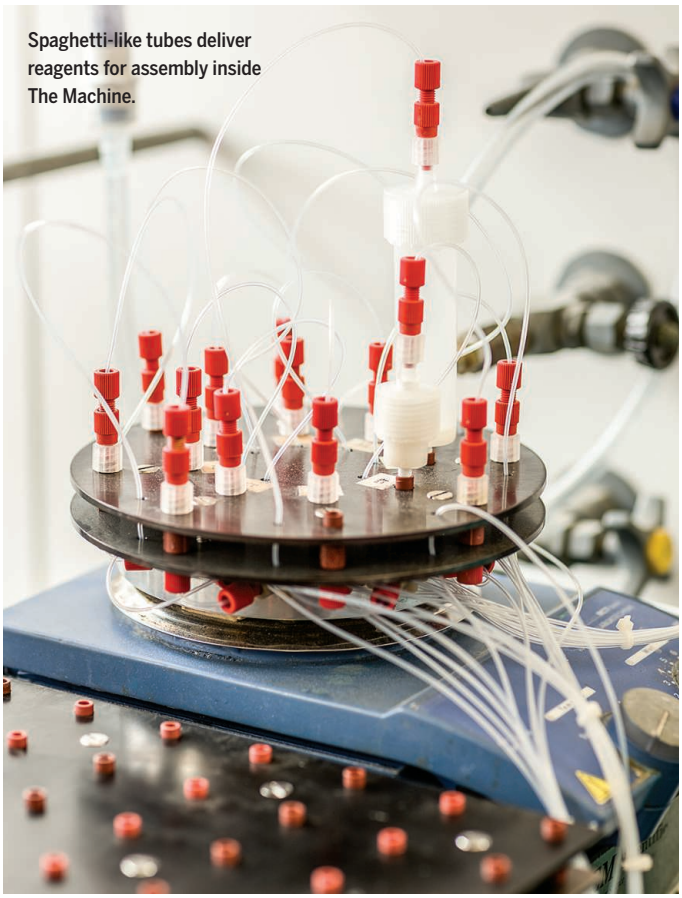

Spaghetti-like tubes deliver reagents for assembly inside The Machine.

"This is an amazing technology. It's a huge advance in small-molecule synthesis."

Cathleen Crudden, Queen's University

Burke envied his close friend and fellow Harvard Ph.D. student, Rahul Kohli, who was studying the biological activity of large ring-shaped peptides. At the end of each week, Kohli and Burke got together at The Cellar, a Cambridge, Massachusetts, bar, to catch up over a beer. "I was blown away at how fast his research was moving," Burke says. Kohli's advantage boiled down to the automated synthesizer that churned out a library of peptides for him to study. "While we were drinking, some machine was making more [peptides] for him. I became insanely jealous, and wondered 'How can we do the same thing for small molecules?' "

Burke realized that many of the amino acid building blocks Kohli's synthesizer was assembling are structurally complex. They come in a wide variety of shapes and sizes, some with single- or double-ringed sidecars, others without. Yet a machine readily strings them together, using a single kind of bond. "The complexity is all in the building blocks, and you buy those in a bottle," Burke says.

Could that same strategy work for small molecules? After getting his degree, Burke decided to find out. He put together a proposal for a research program, as he searched for an academic job. The day he interviewed at Illinois, Burke says, "they gave me an offer and I accepted on the spot." He's been working to fulfill his vision ever since.

THE FIRST TASK was to identify the best reaction to link building blocks together. The answer seemed clear. In the 1970s, a Japanese chemist named Akira Suzuki from Hokkaido University discovered a way to use palladium metal as a catalyst to link carbon atoms on two separate molecules, while leaving everything else about those molecular pieces untouched. Suzuki's trick was to adorn a carbon atom on one of the two molecules with a so-called boronic acid: a boron atom attached to two alcohols $(OH)_2$. To a carbon on the other molecule he attached an element such as iodine or bromine, known in chemistry parlance as halogens. When the palladium brings the two couplers together, it links the carbon tied to the boronic acid with the carbon joined to the halogen and throws away the boronic acid and halogen. Today, says Max Planck's Seeberger, this so-called Suzuki coupling is one of the most powerful and widely useful reactions in all of organic chemistry.

Burke had his connector. By synthesizing building blocks with a boronic acid group on one side and a halogen on the other, he could snap them together like a ball and hitch. But he needed one more critical piece: a way to control the reaction, so the catalyst would not go on linking building blocks in random combinations ad infinitum. To build a molecule step by step, Burke says, "we needed a switch."

In 2007, he and his colleagues found it: a molecule called MIDA that wraps itself around the boron and shuts down its reactivity. Now, Burke's team could start with one building block that did not contain a halogen but had an exposed boronic acid, then add a second building block that had both a halogen and a boronic acid capped

with MIDA. Because the capped boronic acid couldn't react, the setup forced the halogen on the second building block to react with the exposed boronic acid on the first. Presto, the two were linked. Burke's team could then remove MIDA from the just-forged tandem, add another building block with a halogen and capped boronic acid, and repeat the process (see diagram, below).

The strategy worked. In 2012, Burke's team reported in the *Proceedings of the National Academy of Sciences* that they had used their technique to make a derivative of Amph B, which could not make ion channels but still killed fungal cells. The result proved that the conventional wisdom was wrong: Amph B kills fungal cells not by poking holes in them but by binding the sterols that cells need for their membrane proteins to work properly, among other functions. Without the sterols, the cells can't survive. Beyond Amph B, in 2008 Burke and colleagues reported in the *Journal of the American Chemical Society* (*JACS*) that they had used their technique to make a wide variety of druglike compounds called polyenes. Later, they calculated that just 12 MIDA boronate building blocks would enable them to synthesize more than 75% of the 2839 polyenes known to be made by natural organisms. They were off and running.

THE TROUBLE WAS, THEY WERE STILL doing all of their assembly work by hand. To automate it, they needed to solve new problems. The biggest was finding a way to purify whatever tandem molecules they made—separating finished molecules from partially completed ones, unused building blocks, and leftover reagents.

Automated peptide, DNA, and oligosaccharide synthesizers can do that because the building blocks for each class of these biopolymers have a chemical handle in common. Using that handle, researchers tether the molecules they are building to a solid anchor such as a plastic bead. Between synthetic steps, the machines just hang on to the beads and wash the excess reagents away. But no such common handle exists for small molecules. Then, in 2008, by chance, Burke's team discovered that MIDA boronates stick to sandlike silica particles when two organic solvents—methanol and ether—are both present but then drop off when a different solvent, known as THF, is added. The technique gave the researchers a way to catch and release their compounds at will. Now, to purify compounds, they could simply run them through a silica-containing vial—no beads involved. This simple solution was "the key discovery" that enabled them to automate their chemistry, says Southampton's Whitby.

Burke and his students pushed on to make their machine. It took a couple of years of designing and redesigning the apparatus, working with engineers in the university's machine shop to create the parts, and writing the computer code needed to follow each recipe step by step. Along the way, they added other steps to link building blocks in different orientations and turn some of their linear chain-like compounds into more rigid ringed molecules, both key advances in making a broader array of natural products.

~260 thousand
Known small-molecule natural products

70–75
Percentage that could be made with 5000 MIDA boronate building blocks

~200
MIDA boronate building blocks now commercially available

FOR NOW, IT'S UNCLEAR how many small organic molecules Burke's synthesis machine can make. With about 5000 building blocks, he estimates, it could make 70% to 75% of the nearly 260,000 small-molecule natural products known to exist. "If we can do that, we can shift the rate-limiting step from synthesis to understanding function," Burke says. "I think organic chemistry is hungry for this."

Still, many organic chemists remain resistant to using automation, Seeberger says. "Some people feel threatened." And so far, only about 200 building blocks with both the crucial halogen and MIDA-capped boronic acid linkers are commercially available. Thousands more, however, sport just the boronic acid or the halogen and can be used by the machine as the first or last building block. Nevertheless, for the technology to reach its potential, other chemists will have to embrace it and produce many more full-fledged building blocks.

Burke is not waiting. He is using the synthesizer to return to his favorite compound, Amph B. He says his team has already made a derivative that kills fungi but leaves human cells alone. Fungi and human cells rely on different sterols to make their cell membranes, and in a 2013 paper in *JACS*, Burke's team reported making an Amph B derivative that binds the fungal sterol, called ergosterol, but not cholesterol, the human version. That selectivity has already yielded a less toxic version of the drug, at least in cell culture. Last month, the team passed much of that work on to a new biotech startup that Burke co-founded, Revolution Medicines, which has also acquired the intellectual property for commercializing Burke's synthesis machine.

Burke says he has also begun to use his new synthesis machine to return to his dream of making molecular prosthetics to help cystic fibrosis patients and others. He says his team is already working to make new Amph B derivatives capable of forming the ion channels that cystic fibrosis patients lack. The end of that story remains to be written. But the potential of a new approach to automating organic chemistry is just starting to unfold. ■

A huge chemical menu, from standardized ingredients

To make a small molecule, The Machine links a carbon attached to a boronic acid (○) to a carbon attached to a halogen (⊃). A MIDA group (⌐) stops the reaction. Then the MIDA group is removed and another component added.

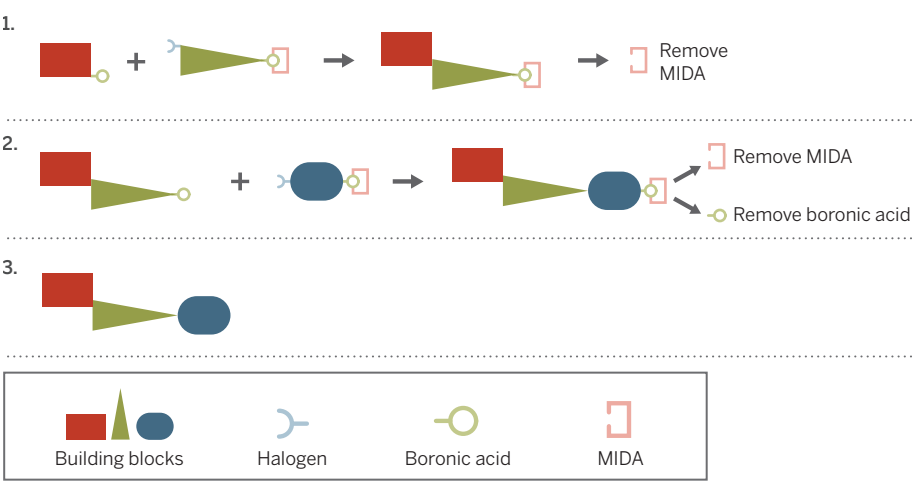

ILLUSTRATION: G. GRULLON/*SCIENCE*

SECOND SIGHT

Eye transplants are science fiction. A team of researchers wants to change that

By **Jennifer Couzin-Frankel**

In his first-floor lab at the University of Pittsburgh Medical Center (UPMC) in Pennsylvania, Vijay Gorantla is hunched over a blind pig. Under the glare of an operating room light, he's venturing into a shadowy landscape.

Gorantla's terrain is an elegant, tightly controlled 7.5-gram bundle of cells: the eye. Pigs and humans share similar ocular anatomy, and Gorantla, a plastic and reconstructive surgeon, has sliced this animal's optic nerve in two. Now the question is, can he help it see again?

When an eye is lost, darkness reigns. And those who treat eye trauma and disease are, in a sense, groping in the dark themselves. They have little to offer the young girl who tripped while trick-or-treating one Halloween night, cracking her skull and severing the optic nerve, or the 60-year-old who sees only light and shadows, because glaucoma has destroyed cells in that same conduit.

Physicians have transplanted hearts and lungs, faces and hands, a uterus, the abdominal wall. Now, Gorantla wants the eye on that list. He and his colleagues have their work cut out for them. The most daunting challenge is coaxing nerves to regenerate and connect the donor eye to the recipient's brain. But they must also establish blood flow to a transplanted eye; control how the immune system responds to it; and preserve the intricate mechanisms that keep the eye moist, blinking, and able to focus. No one has achieved success even in an animal, and Gorantla is starting from humble beginnings: removing a pig's eye and reattaching it.

Those holding the purse strings are ready to gamble. Last fall, the Department of Defense (DOD) awarded $1.25 million over 2 years to three centers, including Gorantla's, to develop animal models for whole-eye transplantation. In 2013, the National Eye Institute (NEI) in Bethesda, Maryland, announced the winner of its "audacious goal initiative," a reachable but ambitious target for eye research. The choice—"regenerate neurons and neural connections in the eye and visual system"—encompasses eye transplants, though isn't limited to them, says Paul Sieving, director of NEI. "Science fiction becomes reality eventually, doesn't it?"

Or, as Gorantla puts it, "if you don't think about something being a possibility, nothing can happen."

GORANTLA HAS HELD TIGHT to that motto since at least 1998, when he flew from Manchester, U.K., to Louisville, Kentucky. Fresh from surgical training in England, he was en route to one of the world's premier hand surgery programs. In the Manchester airport before his departure, Gorantla grabbed a copy of *Time*—and was startled to learn that his new home was gearing up for what would be the world's first successful hand transplant. The 15-hour surgery took place 6 months later, in January 1999, on a 37-year-old who had lost his hand in a fireworks accident.

Hand transplants were very different from the organ transplants that preceded them. "With a solid organ, the minute you transplant it" and reconnect the blood vessels, "it starts functioning," Gorantla explains. "All it needs is a blood supply." Hands include nerves, skin, bones, and bone marrow. Each of these needs to work for a transplant to succeed. Peripheral nerves connecting the new hand to the rest of the body have to regenerate—which they do, albeit just 1 millimeter a day. In Louisville, Gorantla assisted in two hand transplant surgeries and followed the patients for years afterward. "It was a process of self-education and discovery," he remembers. "I was right there in front of the patient every day, understanding how rejection happens … understanding how patients adapt."

In 2006, he relocated to UPMC to establish a hand transplant program there. Face transplants were just beginning, and

Restoring vision

Because of the eye's complex anatomy and its connection to the brain, transplants come with a host of hurdles.

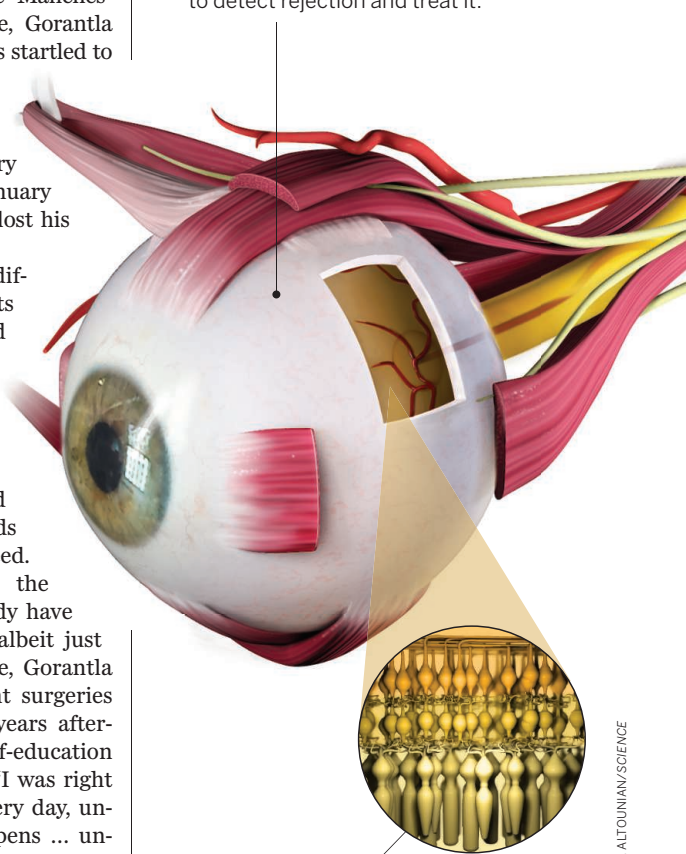

REJECTION
The donor eye is likely to be attacked as foreign; doctors need to understand how to detect rejection and treat it.

CELL SURVIVAL
Scientists have to preserve cells in the retina, which can die quickly in the time between donation and transplant.

ILLUSTRATION: V. ALTOUNIAN/*SCIENCE*

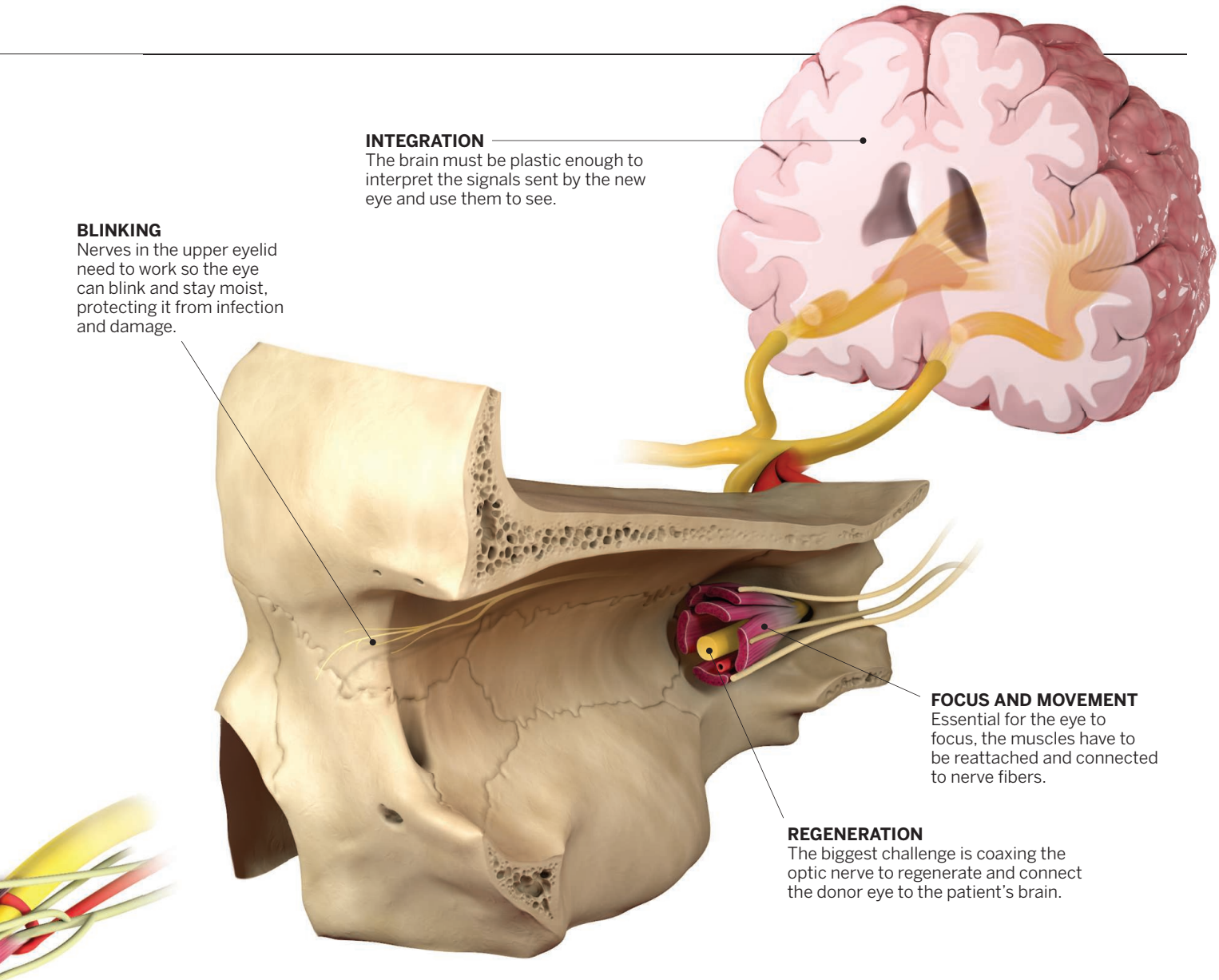

Gorantla wondered whether he might take them on. The candidates he met were often Iraq War veterans, their faces blown away.

Although Gorantla could offer these veterans a new face, many had lost their eyes as well, and he couldn't restore their sight. For them, as for other blind people, the preferred strategy for navigating the world is a Seeing Eye dog. "We've outsourced it," says Andrew Huberman, a neuroscientist at the University of California, San Diego (UCSD). "That's the best thing we've got."

So rather than dive into face transplants, Gorantla focused on vision. About 5 years ago, he began broaching the subject of eye transplants with ophthalmologists. "I thought, 'It's crazy,' " remembers Joel Schuman, director of the eye center at UPMC. "The barriers to success are very high." The greatest: Parts of the eye belong to the central nervous system, and unlike peripheral nerves in the hands and face, the central nervous system was thought incapable of repairing itself. Gorantla was eager to defy dogma. "People said I was too disruptive; they distanced themselves from me," he recalls.

He turned to history. Digging into medical archives, Gorantla uncovered illustrations and handwritten notes from 1885, when a Parisian ophthalmologist had transplanted a rabbit's eye into a young girl. Other efforts followed. All failed miserably, of course—"the rabbit eye was rejected immediately," Gorantla says. But still, the early attempts "really gave me confidence to get back on track. … I was not being completely stupid" to consider this.

MORE THAN A MILLION retinal ganglion cells form a layer in the retina of the human eye. Running from each is a nerve fiber called an axon that stretches back into the brain. Together, these fibers assemble into the optic nerve, "a cable of 1 million phone wires," as NEI's Sieving describes it.

In *Nature* in 2011, Harvard University neuroscientist Zhigang He and his colleagues described crushing the optic nerve of mice and deleting two genes in their retinal ganglion cells. Losing those two genes helped neurons sense stress and proliferate, and, remarkably, they activated a host of others that prompted at least 10% of the nerves to regenerate. The work was replicated by other labs, confirming that "it's possible to get mouse axons to regenerate long distance," says Ben Barres, a neuroscientist at Stanford University in Palo Alto, California, who wasn't directly involved.

But did the newly sprouted nerve fibers travel to the right place? In 2012, Harvard neuroscientist Larry Benowitz, working independently, supplied early evidence that they did, at least partially: The axons reached into visual centers of the brain. Preliminary data hinted that the pupils of the mice responded to light, suggesting they had regained some vision, albeit a minuscule amount. In a dif-

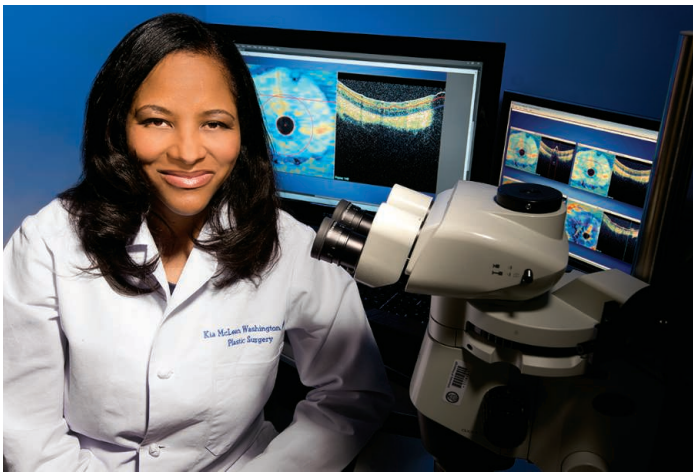

Surgeons Kia Washington and Vijay Gorantla (*right*) at the University of Pittsburgh are hoping pigs and rats will offer an eye transplant road map.

ferent Harvard lab, He is studying how the regenerated nerves function, performing electrophysiology on the cells and behavior studies on his animals.

Also unknown is how many nerve cells must regenerate so the eyes can see. "The brain is exceptionally good at taking relatively deprived input and making the most of it," says UCSD's Huberman, but no one knows what the minimum number is. When cochlear implants were introduced to restore hearing, many scientists were shocked that they work with as few as 16 electrodes applied to the auditory nerve. "Everyone thought it would take thousands of electrodes to stimulate thousands of nerve fibers for this to happen," says John Dowling, a neuroscientist at Harvard who studies the retina.

The discovery that the optic nerve can regenerate has raised hopes, and not just for transplants: Eye transplants are far in the future, and they'll be appropriate for only a subset of blind individuals. But even if the transplants never succeed, the regeneration studies could help drive "all sorts of spinoff science and technology," says Jeffrey Goldberg, a neuroscientist and ophthalmologist at UCSD. Those might include ways to combine regenerative techniques with treatments for vision loss like retinal prostheses, gene therapy, or stem cells to replace cells that have been lost.

In 2012, Benowitz and Goldberg, who also works in optic nerve regeneration, were invited to speak at the University of Pittsburgh's Fox Center for Vision Restoration. "Vijay was in the audience," Benowitz says. Afterward, the surgeon approached the neuroscientist to evangelize on eye transplants.

The following year, the three began to collaborate. Quickly, the group expanded to include other neuroscientists, surgeons, and ophthalmologists. Researchers at nine institutions joined with Pitt. To augment their funding from DOD, they're seeking grant money from foundations and government sources. It's "like our moonshot," Pitt ophthalmologist Schuman says, recalling the famous speech by John F. Kennedy in 1961, when Schuman was 2 years old. Transplanting an eye may take longer to achieve than the decade Kennedy promised for the moon landing, he acknowledges, "but I'm sure that we're going to reach" it, too.

Even some of the doubters have come around. Fifteen years ago José-Alain Sahel, director of the Vision Institute in Paris, regarded his countrymen's failed rabbit eye experiments 130 years ago as the first and last word on the matter. A gifted student of his was desperate to graft an eye; Sahel told her the project was outlandish and, with no other goals in mind, she quit science after finishing her Ph.D. Now he's collaborating with the researchers at Pitt, Harvard, and UCSD. "All of this is no longer deemed impossible, it is just a huge, huge crazy effort," he says.

EARLY STEPS TO BRIDGE fantasy and reality are being plotted in a lab not far from Gorantla's, where a young plastic and reconstructive surgeon, Kia Washington, is transplanting the eyes and faces of rats. It's the first eye transplant model in a warm-blooded animal. Washington is focused on reattaching dozens of blood vessels, muscle fibers, and the optic nerve. Many of the fibers are less than a millimeter in diameter. To keep immune reactions at bay, she uses genetically identical rats as donors and recipients, much like the first successful kidney transplant in 1954 from a brother to his identical twin.

"It doesn't look like there's function" in the rat eyes, Washington says, but she isn't surprised, because she hasn't tried to induce nerve regeneration. Using cutting-edge optical imaging with Schuman's help, she's found that the transplanted eyes look healthy—even if, practically speaking, they're useless. "You can actually see blood flow in the eye and in the retina," she says, and MRIs suggest the eyes produce moisture as they're supposed to. As her work progresses, Washington expects to team up with her neuroscientist collaborators to stimulate optic-nerve regeneration. Assessing the outcome will require new kinds of imaging tools, such as measuring how retinal cells grow in real time. NEI plans to release $5 million to fund several imaging awards this spring.

A rat eye is too small to transplant on its own, so Washington combines it with facial tissue from the same donor. This is how Gorantla imagines the first eye transplants: a combination of face and eye for a patient who's lost both. "You have nothing to lose," because immunosuppressants are already part of the face transplant package, Gorantla notes. The team is readying its first paper, describing Washington's rat eye transplants, for publication. And Washington is about to shift to genetically diverse animals, so she can study how to manage the expected immune response to the transplant.

For his part, Gorantla is ramping up his pig model—and, thinking far ahead, considering where human donor eyes might come from. "The common criteria for organ donors is brain death," he says, and "most of the donors have significant brain trauma or head trauma." That's worrying when it comes to eyes, because brain damage can inflict injury on the optic nerve. One group of collaborators, at the L V Prasad Eye Institute in Hyderabad, India, is testing eye function in brain-dead individuals on ventilators in an intensive care unit. Gorantla is also considering how best to preserve the eye once it's removed—right now, a human retina lives only about 4 hours outside the body.

"There's so much we don't know," Gorantla says. "We don't even know what we don't know." In a way, that's what excites him the most. ■

INSIGHTS

Immune therapies for sepsis *p. 1201*

Meeting demand for rare earth minerals *p. 1209*

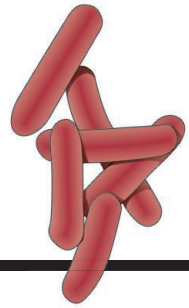

PERSPECTIVES

CHEMISTRY

Toward substitution with no regrets

Advances in chemical design are needed to create safe alternatives to harmful chemicals

By **Julie B. Zimmerman** *and* **Paul T. Anastas**

Vast numbers of synthetic chemicals are used in everyday consumer products. Many are safe, but some can have unintended biological or environmental effects. For example, phthalates are widely used to increase the flexibility of plastics but also disrupt hormonal balance (*1*). Organophosphates are highly effective insect repellents but cause severe neurotoxicity to mammals (*2*). In many cases, chemicals of concern have been replaced by other chemicals that are functionally equivalent and believed to be of less concern (see the photo). However, the need for expedient substitution can lead to the use of chemicals that are no less harmful than those they replace. How can such "regrettable substitutions" be avoided?

There have been many examples of regrettable substitution over the years. The example gaining most attention recently is the substitution of bisphenol S (BPS) for bisphenol A (BPA) (see the figure, panel A). BPA is widely used to make clear and rough plastics, used in water bottles, sports equipment, and CDs and DVDs; it is also used in food and beverage can coatings (where it helps to protect food from contamination and spoilage)

Replacement troubles. In many plastic baby bottles, bisphenol A (BPA) has been replaced with bisphenol S (BPS), but the latter compound may also have adverse health effects.

PHOTO: LAWRENCE LAWRY/SCIENCE SOURCE/PHOTO RESEARCHERS

and in thermal paper (such as till receipts). Numerous studies suggest that BPA may act as an endocrine disruptor—a substance that mimics hormonal function and could cause developmental and reproductive problems in animal and human offspring, perhaps even affecting future generations (*3*). Rising public concern led to a voluntary withdrawal of BPA from many children's products even before regulatory action was taken (see the photo). One substance among many emerged as a replacement: BPS could expe-

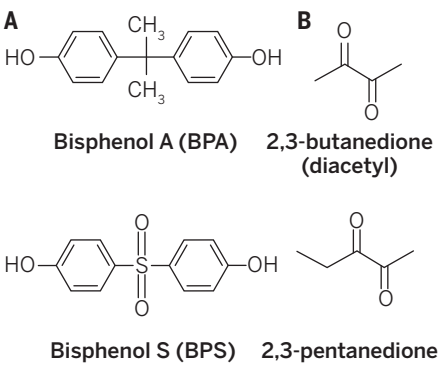

Regrettable substitutions. Because of toxicological concerns, BPA has been replaced with BPS in some applications (**A**). Similarly, diacetyl has been replaced with 2,3-pentanedione (**B**). However, these replacement compounds are chemically similar to the ones they replace, causing concerns about possible toxicological effects.

diently serve as a drop-in replacement for products that could be labeled "BPA free." Yet recent studies have identified toxicological concerns with BPS, suggesting that one hazardous chemical was substituted for another (*4*).

Several other examples are similarly attracting attention, including the case of diacetyl (2,3-butanedione), a naturally occurring chemical that gives butter its characteristic aroma and taste and that is produced industrially for use as a butter flavoring. Diacetyl has been linked to lung cell damage via inhalation exposure, as evidenced by epidemiological studies of factory workers diagnosed with obliterative bronchiolitis (*5*). In response to the publicity deriving from these reports, a number of major food companies voluntarily stopped using diacetyl and began to use alpha-diketone (2,3-pentanedione) as a flavoring substitute for diacetyl (see the figure, panel B). However, toxicology results indicate that acute inhalation exposure to 2,3-pentanedione can cause airway epithelial damage that is similar to that caused by diacetyl (*6*).

School of Engineering and Applied Science, Yale University, New Haven, CT 06511, USA. E-mail: julie.zimmerman@yale.edu

Further studies have raised concerns that the toxicological effects of diacetyl may be shared with this and other alpha-diketones, which are close structural analogs (*7*).

Given the growing number of regrettable substitution examples, as exemplified by BPA and diacetyl, the National Research Council (NRC) recently released a report calling for "informed substitution" (*8*). As the Environmental Protection Agency notes, practicing informed substitution is meant to "minimize the likelihood of unintended consequences, which can result from a precautionary switch away from a chemical of concern without fully understanding the profile of potential alternatives, and to enable a course of action based on the best information—on the environment and human health—that is available or can be estimated" (*9*). In practice, this can be achieved through an alternatives assessment, a process of comparing functionally equivalent chemicals based on a variety of factors, including performance, costs, potential adverse effects to human health and the environment, and societal impacts (*8*). However, alternatives assessments tend to only consider chemical substitutes that have been commercialized, can be readily obtained, and, typically, have known physiochemical properties or information about their effects (*8*).

Cases in which viable alternatives are available can often be attributed to chemical design innovations that view reduced hazard as part of the performance criteria (*10*). An example of informed substitution is the replacement of chromated copper arsenate (CCA), used for wood preservation, with alkaline copper quaternary (ACQ). CCA contains both arsenic and chromium and is associated with increased cancer risks following environmental exposure (*11*). ACQ instead relies on a bivalent copper complex and a quaternary ammonium compound and offers equivalent performance against biological impacts, such as decay and termite attack. In North America, CCA has been widely replaced with ACQ and other newer, more benign wood preservatives for most residential applications. ACQ wood products are expected to reduce soil contamination and limit impacts from construction and debris landfills, but questions remain about the amount of copper released from ACQ-treated wood, with potential implications for aquatic ecotoxicity (*12*). Thus, even though this example is largely regarded as successful, it shows that design decisions must be revisited and continuously improved as new toxicity information and assays become available.

In many other cases, alternatives that can serve the desired function and have the desired toxicity profile have not been invented, discovered, or even imagined. Alternatives assessment then merely identifies an alternative that meets minimal functional requirements while offering a satisfactory profile in terms of cost and potential hazards.

One route to chemical products and processes that reduce or eliminate the use and generation of hazardous substances is provided by green chemistry (*13*). This approach uses insights into the critical stages of biological activity—absorption, distribution, metabolism, and excretion (ADME), and molecular initiation—as an important piece of the design framework. By using physiochemical properties and structural motifs along with an understanding of mechanistic toxicology, it is possible to devise chemical design rules for reduced toxicity. There are many examples of chemicals designed to avoid specific undesirable or hazardous aspects, such as persistence (*14*), use of depleting feedstocks, and cytotoxicity (*15*); however, we will not have plentiful examples of systematic design for reduced hazard until we routinely view the task as a systems issue. Safer substitutions require scientific advances in toxicity data generation and curation, computational models, and systems insight that lead to intentional design.

As stated in the NRC report (*8*), rational design of our next-generation molecules will not be easy. The report calls for more research on property-toxicity relationships and greater elucidation of toxicological mechanisms of action at the molecular level. Substantial resources are devoted to identifying and measuring the problem of hazardous chemicals in society, but at least the same resources need to be available for the molecular designs of safer chemicals. It is only through this process that we can hope to avoid future regrettable chemical substitutions. ■

REFERENCES

1. T. Colborn, F. S. vom Saal, A. M. Soto, *Environ. Health Perspect.* **101**, 378 (1993).
2. D. L. Sudakin, W. R. Trevathan, *Clin. Toxicol.* **41**, 831 (2003).
3. B. S. Rubin, *J. Steroid Biochem. Mol. Biol.* **127**, 27 (2011).
4. S. Eladak *et al.*, *Fertil. Steril.* **103**, 11 (2015).
5. K. Kreiss *et al.*, *N. Engl. J. Med.* **347**, 330 (2002).
6. A. F. Hubbs *et al.*, *Am. J. Pathol.* **181**, 829 (2012).
7. S. E. Anderson, J. Franko, J. R. Wells, E. Lukomska, B. J. Meade, *Food Chem. Toxicol.* **62**, 373 (2013).
8. National Research Council, *A Framework to Guide Selection of Chemical Alternatives* (National Academies Press, Washington, DC, 2014).
9. U.S. Environmental Protection Agency, *EPA's DfE Standard for Safer Products* (2012); www.epa.gov/dfe/pubs/projects/gfcp/standard-for-safer-products.pdf.
10. A. M. Voutchkova, T. G. Osimitz, P. T. Anastas, *Chem. Rev.* **110**, 5845 (2010).
11. P. J. Landrigan, C. A. Kimmel, A. Correa, B. Eskenazi, *Environ. Health Perspect.* **112**, 257 (2004).
12. M. Velleux *et al.*, *Environ. Sci. Technol.* **46**, 6723 (2012).
13. P. T. Anastas, J. C. Warner, *Green Chemistry: Theory and Practice* (Oxford Univ. Press, Oxford, 1998).
14. R. S. Boethling, E. Sommer, D. DiFiore, *Chem. Rev.* **107**, 2207 (2007).
15. J. Hoque *et al.*, *Langmuir* **28**, 12225 (2012).

10.1126/science.aaa0812

PHYSICS

A walk across a quantum lattice

A simple two-atom system is used to probe complex quantum phenomena

By **Artur Widera**

Quantum effects emerge from an intricate interplay of the wave nature of massive particles, quantum statistics, and interactions in many-body systems. Each individual aspect can lead to nonclassical behavior and is often well understood; in many-body systems, however, it can be hard to identify the mutual influence of these three aspects on a single-particle level. On page 1229 of this issue, Preiss *et al.* (*1*) present an experimental study illustrating the effect of quantum statistics as well as of various interaction strengths on the matter wave quantum dynamics of two ultracold atoms. Starting from the matter wave dynamics of a single atom, adding a second atom allows them to observe the two-body dynamics of interacting bosons. By controlling the interparticle interaction, they are able to bring the atoms into the strongly interacting regime, where the system resembles two weakly interacting fermions. The work by Preiss *et al.* allows the role of different quantum mechanisms to be identified. It also constitutes a step toward the study of more complex quantum systems in a controlled fashion, where the level of complexity is not accessible to classical simulations.

Since the early days of quantum theory, the wave nature of particles has been essential for the description of single-particle properties in the quantum regime. It lies at the heart of modern electron microscopes, where the resolution can be adjusted via the electrons' small de Broglie wavelength. In a periodic potential, such as for electrons moving in the periodic potential of ion cores, matter wave interference has surprising consequences. The first is Bloch oscillations, which are oscillations of a quantum particle within a small length scale in position space when it is exposed to an external force. In typical solid-state systems, scattering of electrons off impurities destroys such quantum oscillations. In pure systems, however, such as cold atoms in optical traps (*2*) they have been observed. Preiss *et al.* demonstrate such Bloch oscillations, showing a dispersion of the atomic probability distribution in position space that subsequently refocuses to its initial position after one oscillation period, yielding an illustrative example of particle-wave duality. Furthermore, matter wave interference in a periodic potential also modifies the diffusion properties of a quantum particle. For a diffusion time t, the probability of finding a classical particle at a specific distance from the starting position on a line grows as $\sqrt{t}$; for a quantum system, the probability grows proportional to t. It is this difference in the time dependence that is responsible for the speed-up of quantum search algorithms relative to classical search algorithms. Preiss *et al.* use the quantum walk, which has been observed in various systems, including single neutral atoms (*3*), to study the influence of quantum statistics and interactions in a two-body quantum system (see the figure).

> ***"Since the early days of quantum theory, the wave nature of particles has been essential for the description of single-particle properties in the quantum regime."***

With additional identical particles added to the system, two effects must be taken into account: (i) in the absence of interactions, quantum statistics determining the distribution of particles across the quantum states available; and (ii) attractive or repulsive interactions between particles. Quantum statistics divides the many-body properties of indistinguishable particles into two classes, depending on the value of their total spin. Particles with half-integer spin value, fermions, obey Pauli's exclusion principle, imposing a total antisymmetric wave function of a many-body system under exchange of any two particles. In contrast, particles with integer spin value, bosons, have symmetric wave functions under particle exchange. The consequences of the wave function's symmetry are dramatic: Electrons in the conduction band of a metal have much higher energies than expected from the metal's

Atoms undergoing a quantum walk in an optical lattice

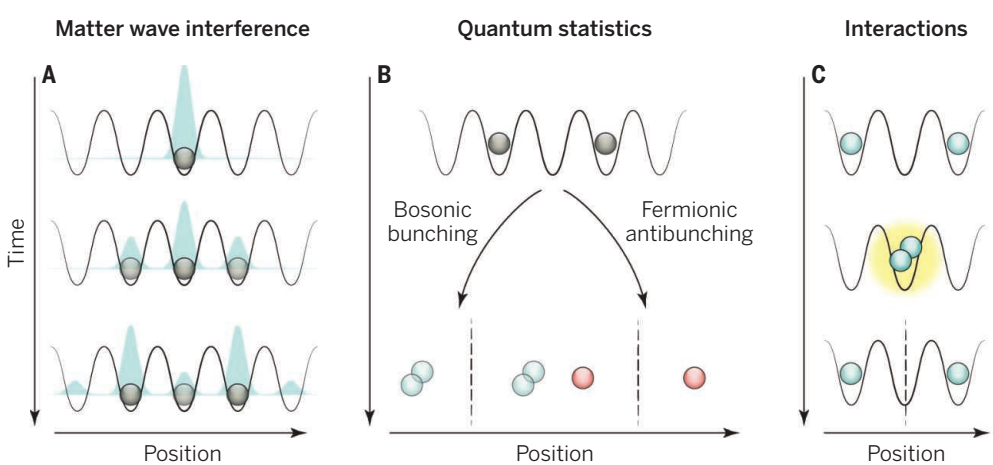

Walking and interacting. (**A**) A single atom undergoing a quantum walk. The probability of finding the atom at a specific lattice position is dominated by matter wave interference. (**B**) The effect of quantum statistics on the dynamics of two particles. Bosons tend to bunch and can be found close to each other, while fermions antibunch and avoid each other. (**C**) Strong interactions can mimic an exclusion principle for bosons. For strong repulsion, the atoms avoid each other and can be described as weakly interacting fermions.

ILLUSTRATION: ADAPTED BY P. HUEY/*SCIENCE*

Physics Department and State Research Center, Kaiserslautern University, 67663 Kaiserslautern, Germany. E-mail: widera@physik.uni-kl.de

temperature, because all lower-lying energy levels are already occupied and thus further occupation is forbidden. For a measurement of position correlations, the antisymmetry of the wave function results in an apparent antibunching, where fermions seem to avoid each other. Bosons, in contrast, experience an increase in the probability of reaching a state already occupied by other bosons. That is, bosons tend to bunch together. For small systems of particles, the consequences of quantum statistics were exploited in fermionic (*4*) as well as bosonic (*5*) systems. Preiss *et al.* observe this effect of bunching in the position correlations of two identical atoms undergoing a quantum walk.

Surprisingly, although this behavior due to quantum statistics seems to be fundamentally fixed, interactions between particles can in fact turn bosonic bunching into fermionic antibunching and vice versa. This has been seen, for example, by association of two fermionic atoms to a bosonic molecule that can undergo Bose-Einstein condensation (*6*), or pairing of fermions in a many-body system showing superfluid behavior similar to Cooper pairs in a superconductor (*7*). Preiss *et al.* go the other way: By increasing repulsive interaction more and more, the bosonic atoms under investigation start to mimic the behavior of weakly interacting fermions, as was observed in one-dimensional Bose gases in the so-called Tonks-Girardeau regime (*8*, *9*). With their superb position resolution, Preiss *et al.* can track the crossover from the quantum statistics–dominated bosonic bunching to the interaction-dominated antibunching, again extracting position correlations of two atoms doing a quantum walk.

The system presented by Preiss *et al.* allows the study of the interplay of all these aforementioned aspects in a rather simple, paradigmatic system comprising all these effects: two identical, interacting atoms. Beyond the illustration of quantum physics, their system can serve as a basic building block for a bottom-up approach to engineering of complex quantum states atom by atom. ■

REFERENCES

1. P. M. Preiss *et al.*, *Science* **347**, 1229 (2015).
2. M. Ben Dahan, E. Peik, J. Reichel, Y. Castin, C. Salomon, *Phys. Rev. Lett.* **76**, 4508 (1996).
3. M. Karski *et al.*, *Science* **325**, 174 (2009).
4. A. N. Wenz *et al.*, *Science* **342**, 457 (2013).
5. A. M. Kaufman *et al.*, *Science* **345**, 306 (2014).
6. M. Greiner, C. A. Regal, D. S. Jin, *Nature* **426**, 537 (2003).
7. M. W. Zwierlein, J. R. Abo-Shaeer, A. Schirotzek, C. H. Schunck, W. Ketterle, *Nature* **435**, 1047 (2005).
8. T. Kinoshita, T. Wenger, D. S. Weiss, *Science* **305**, 1125 (2004).
9. B. Paredes *et al.*, *Nature* **429**, 277 (2004).

10.1126/science.aaa6885

IMMUNOLOGY

Getting sepsis therapy right

Is decreasing inflammation or increasing the host immune response the better approach?

By **Richard S. Hotchkiss**[1] *and* **Edward R. Sherwood**[2]

Sepsis—a complication of infection—is a factor in at least a third of all hospital deaths—a sobering statistic (*1*). Patients with sepsis frequently present with fever, shock, and multiorgan failure. Because of this dramatic clinical scenario, investigators have generally assumed that sepsis mortality is due to unbridled inflammation (*2*). Research in animal models, in which administration of the cytokines tumor necrosis factor–α (TNF-α) and interleukin-1 (IL-1) reproduced many features of sepsis, supported that assertion. Yet, over 40 clinical trials of agents that block cytokines, pathogen recognition, or inflammation-signaling pathways have universally failed (*3*, *4*). However, on page 1260 of this issue, Weber *et al.* (*5*) show that blocking a cytokine—specifically, IL-3—can indeed be protective against sepsis.

IL-3 is a pleiotropic cytokine that induces proliferation, differentiation, and enhanced function of a broad range of hemopoietic cells (blood cells derived from the bone marrow). Using a mouse abdominal sepsis model, Weber *et al.* identified IL-3 as a critical driving force of sepsis. The authors observed that the cytokine caused proliferation and mobilization of myeloid cells that generated excessive proinflammatory cytokines, thereby fueling systemic inflammation, organ injury, and death. Blocking IL-3 (by treating wild-type mice with an antibody that blocks the receptor for IL-3 or using IL-3–deficient mice) prevented sepsis-induced increases in the number of circulating neutrophils and inflammatory monocytes and decreased the amount of circulating inflammatory cytokines, thus ameliorating organ injury and improving survival. Additionally, the authors showed a correlation between mortality in septic patients and elevated blood IL-3 concentrations.

The findings of Weber *et al.* are mechanistically analogous to that of another study in which intravenous injection of mesenchymal stem cells (also known as bone marrow stromal cells) into a mouse model of sepsis led to reprogramming of immune cells toward a less inflammatory phenotype, thereby decreasing organ injury and mortality (*6*). In this scenario, mesenchymal stem cells released factors that reprogrammed monocytes and macrophages; the downstream effect was to prevent a damaging, unrestrained immune response. Thus, IL-3 blockade and mesenchymal stem cell–based therapy represent potential approaches for sepsis treatment because of their ability to broadly reshape early immune responses from a proinflammatory, damaging reaction to a more balanced and effective one.

However, a few cautionary caveats should be considered before adopting this approach. A phase II clinical trial of granulocyte-macrophage colony-stimulating factor (GM-CSF), a cytokine that increases production, maturation, and function of monocytes, macrophages, and neutrophils, thereby mimicking selected properties of IL-3, was efficacious in treating sepsis and, indeed, a large multicenter trial of GM-CSF in sepsis is under way (*7*). This is contrary to the findings of Weber *et al.* that blocking IL-3 can ameliorate sepsis. Two other highly promising agents that are likely to enter clinical trials in sepsis are IL-7 (which promotes $CD4^+$ and $CD8^+$ T lymphocyte proliferation and maturation) and an antibody to programmed death–ligand 1 [(PD-L1), an immunosuppressive protein] (*8*, *9*). Both IL-7 and anti-PD-L1 antibody are immunostimulatory agents that reverse key immunologic defects in lymphocytes and monocytes from septic patients ex vivo and are highly effective in multiple animal models of sepsis (*9*). Emerging evidence shows correlations between lymphopenia (decrease in lymphocytes) and impaired leukocyte functions with late mortality in patients with sepsis (*8*, *9*). Thus, there is rationale for using approaches that selectively enhance antimicrobial immunity during sepsis.

> ***"Which approach to sepsis... is correct? ...there are several clues..."***

[1]*Department of Anesthesiology, Medicine, and Surgery, Washington University School of Medicine, St. Louis, MO, USA.* [2]*Department of Anesthesiology and Pathology, Microbiology and Immunology. Vanderbilt University School of Medicine, Nashville, TN, USA. E-mail: hotch@wustl.edu; edward.r.sherwood@vanderbilt.edu*

Immunoinflammatory response in sepsis

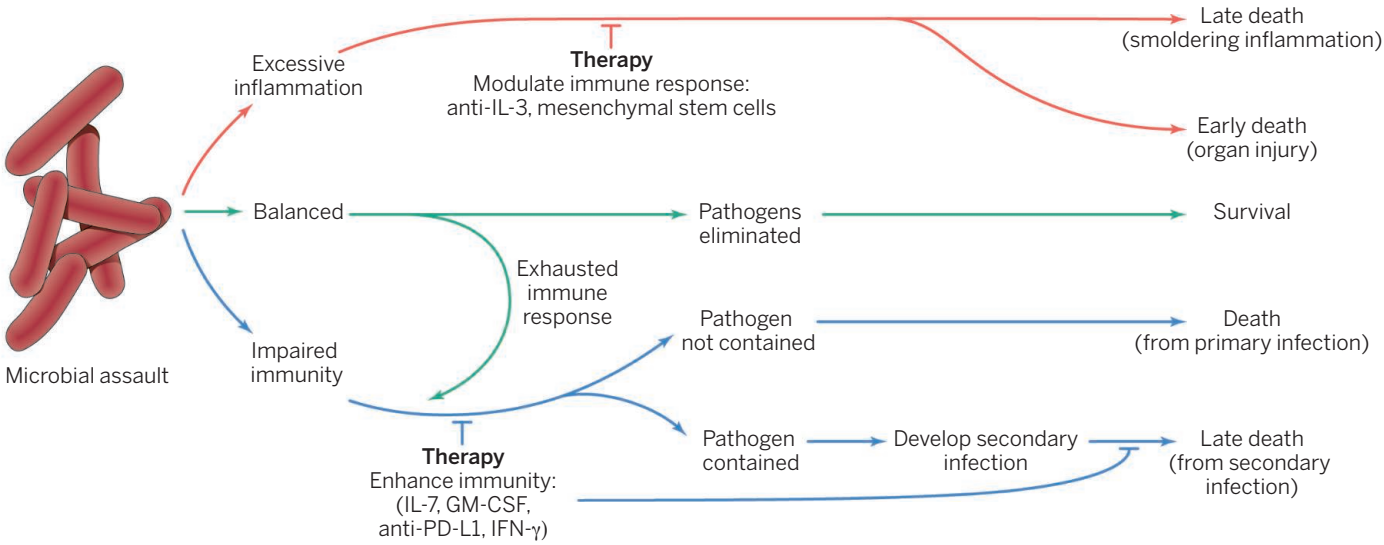

Inflammatory response to sepsis. Potential immune therapies can modulate immune responses that provoke excessive inflammation or enhance immunity if there is an impaired immune response to microbial infection. IFN-γ, interferon-γ.

Which approach to sepsis—decreasing excessive inflammation versus boosting host immunity—is correct? The answer to this question is critical and there are several clues (see the figure). Immunologic status is highly dependent on the age and general health of the individual. Although young, previously healthy individuals acquire virulent infections, early inflammatory deaths are becoming less common in developed countries because of improved surveillance and advances in supportive care. In the United States, 75% of the deaths in sepsis occur in patients over the age of 65 (*10*). The immune system in the elderly is substantially impaired and renders them susceptible to infection. Patients with major comorbidities, including chronic renal and liver failure, also are immunosuppressed, rendering them more vulnerable to developing and dying from sepsis. Thus, the patient populations that represent the highest proportion of sepsis deaths are likely to require therapy that augments immunity. By contrast, the number of sepsis patients with overwhelming inflammation, who may benefit from therapies that reduce early hyper-release of proinflammatory cytokines ("cytokine storm"), is declining.

Another caveat affecting treatment selection is timing (*11*). Patients rapidly transition from the initial cytokine storm to a predominant immunosuppressed state as sepsis persists. This shift to an immunosuppressed state occurs for many reasons, including massive sepsis-induced death of immune cells, development of T cell exhaustion, and generation of T regulatory and myeloid-derived suppressor cells. A postmortem study of intensive care unit patients, in which spleens and lungs were harvested rapidly after death, showed that compared to patients dying of causes other than sepsis, immune effector cells from septic patients were massively depleted (*12*). Most of the sepsis deaths occurred after a prolonged course in the intensive care unit. This protracted septic course is difficult to reproduce in animal models. For example, animal sepsis mortality reported by Weber *et al.* generally occurred within 24 to 48 hours after sepsis onset (during the hyperinflammatory phase) and is therefore not reflective of most clinical deaths in sepsis.

Recent studies provide compelling evidence for this immunologic evolution. In patients admitted with sepsis, "late" positive blood and tissue cultures were detected in ~28% of patients, and over half of these infections were due to fungi or weakly virulent bacteria considered to be "opportunistic" pathogens (*13*). In addition, use of latent viral reactivation as a surrogate marker of loss of immunocompetence (*14*) showed that over 42% of septic patients had reactivation of two or more viruses. The amount of viral reactivation in septic patients was comparable to that occurring in organ transplant patients on immunosuppressive therapy, further evidence of the remarkable degree of impaired immunity in patients with sepsis.

So, how should sepsis be treated? The cornerstone of sepsis therapy remains drainage and/or removal of the infected site, fluid resuscitation, and rapid antibiotic administration. Although anti-inflammatory therapies, such as blocking IL-3, may be beneficial in selected patients, history has not been kind to such approaches. It may be that restorative immunotherapy, in which adjuvants that stimulate host immunity would be the centerpiece for response modification, offers the most promise. To guide sepsis immunotherapy, new methods to determine the health of the various components of a patient's immune system are being developed and may direct the application of targeted immune-adjuvant therapies in the future (*15*). ■

REFERENCES AND NOTES

1. V. Liu *et al.*, *JAMA* **312**, 90 (2014).
2. R. S. Hotchkiss, I. E. Karl, *N. Engl. J. Med.* **348**, 138 (2003).
3. J. Cohen *et al.*, *Lancet Infect. Dis.* **12**, 503 (2012).
4. D. C. Angus, *JAMA* **306**, 2614 (2011).
5. G. F. Weber *et al.*, *Science* **347**, 1260 (2015).
6. K. Németh *et al.*, *Nat. Med.* **15**, 42 (2009).
7. C. Meisel *et al.*, *Am. J. Respir. Crit. Care Med.* **180**, 640 (2009).
8. R. S. Hotchkiss *et al.*, *Lancet Infect. Dis.* **13**, 260 (2013).
9. F. Venet *et al.*, *J. Immunol.* **189**, 10 (2012).
10. G. S. Martin, D. M. Mannino, M. Moss, *Crit. Care Med.* **34**, 15 (2006).
11. J. Leentjens *et al.*, *Am. J. Respir. Crit. Care Med.* **187**, 1287 (2013).
12. J. S. Boomer *et al.*, *JAMA* **306**, 2594 (2011).
13. G. P. Otto *et al.*, *Crit. Care* **15**, R183 (2011).
14. A. H. Walton *et al.*, *PLOS ONE* **9**, e98819 (2014).
15. J. L. Vincent, L. Teixeira, *Am. J. Respir. Crit. Care Med.* **190**, 1081 (2014).

ACKNOWLEDGMENTS

R.S.H. has been on the advisory boards of Bristol-Myers Squibb (BMS), GlaxoSmithKline (GSK), and Merck, on immunotherapy for sepsis (he speaks on the topics of IL-7, anti-PD-1, anti-PD-L1, IL-15, IFN-γ, and GM-CSF). He is a paid consultant to BMS, GSK, Merck, and MedImmune on immunotherapy for sepsis. He collaborates with Revimmune on a trial of IL-7 in sepsis and with BMS on a trial of anti-PD-L1 in sepsis. He receives funding from BMS and MedImmune for studies with anti-PD-1 and anti-PD-L1 and from GSK to test immunomodulators in sepsis.

10.1126/science.aaa8334

ILLUSTRATION: ADAPTED BY P. HUEY/*SCIENCE*

Catalysis by nickel in its high oxidation state

A Ni^{IV} catalyst couples carbon atoms to oxygen, sulfur, and nitrogen atoms

By **Charles G. Riordan**

> ***"...involvement of a thoroughly characterized organonickel^{IV} in carbon-heteroatom bond formation opens vistas for constructing new types of molecules and materials under mild conditions."***

An oxidation state is a numerical value, assigned to an atom in a compound or ion, based on a set of rules such that the sum of the oxidation states equals the overall charge on the entity. The transfer of valence electrons changes the oxidation state of an atom, so oxidation states can help predict chemical reactivity. Nowhere is this concept more exploited than in catalysis with transition metals, which can readily access a variety of oxidation states. Small molecules or ions that bind to the metal as ligands influence the metal's molecular and electronic geometries, and the resulting changes in oxidation state can drive reactions of these ligands. On page 1218 of this issue, Camasso and Sanford (*1*) report an exquisite example of tuning the reactivity of a nickel (Ni) catalyst by the introduction of ligands and oxidants suitable to access an uncommon oxidation state, Ni^{IV} (*2*). They used the high oxidation state of Ni to drive the formation of carbon bonds to heteroatoms, specifically oxygen, sulfur, and nitrogen.

Metal-promoted cross-coupling reactions have a diverse history, ranging from the work a century ago of Grignard with magnesium halides to the more recent palladium (Pd) reagents (*3*). The latter are widely used because of their efficacy and functional-group tolerance—that is, the facility to construct new carbon-carbon and carbon-heteroatom bonds with reactants bearing functional groups that could potentially interfere with the reaction. Applications of Pd cross-coupling include transformations seminal to DNA sequencing technologies (*4*), pharmaceuticals (*5*), and electronic device construction (*6*).

There is a need to develop non–Pd-based catalysts for several reasons. In particular, catalysts that use non-heavy metals are attractive from an economic perspective (*7*), including Ni, the lighter congener of Pd in the periodic table. Further, there are compelling examples from nature and synthetic chemistry that portend success for nickel-based cross-coupling. Two enzymes found in ancient bacteria make use of Ni ions at their active sites to choreograph bond-forming or bond-breaking reactions that exploit the metal's redox activity. Acetyl coenzyme A synthase promotes C–C and C–S bond formation similar to the Monsanto acetic acid process at a $Ni_2Fe_4S_4$ cluster (*8*), whereas methyl coenzyme M reductase (*9*) cleaves a C–S bond during methane biosynthesis in a reaction fundamental to the global carbon cycle. Because these enzymes are found in anaerobes that live in oxygen-poor environments, it is not surprising that the metal accesses a number of lower oxidation states: Ni^{I}, Ni^{II}, Ni^{III}, and perhaps even Ni^{0} (*10*).

Synthetic organonickel complexes enjoy a rich history dating back half a century, including Ni^{0} π-complexes and organonickel^{II} species. Catalytic mechanisms have often invoked cycling between the 0 and 2+ oxidation states, but odd-electron states [i.e., Ni^{I} and Ni^{III}] have been suggested (*11*). Indeed, one of the perceived limitations of nickel catalysis is that one-electron redox catalysis that proceeds through the formation of radicals competes with two-electron events; this is believed to provide less control over product formation and distribution.

Nonetheless, nickel cross-coupling catalysis is undergoing a renaissance that will be further enhanced by definitive evidence that an organonickel^{IV} species is competent in carbon-heteroatom cross-coupling. The approach of Camasso and Sanford depends on organometallic complexes in their higher oxidation states being inherently susceptible to reductive elimination of cis-positioned ligands. Indeed, such oxidatively induced reductive elimination has proven an effective strategy, most recently in Pd^{IV} catalysis (*12*). Given the lower kinetic and thermodynamic stabilities of first-row metal-ligand bonds relative to their second- and third-row congeners, there are few examples of isolable organonickel^{IV} complexes. However, addition of potent oxidants that introduce either a "F^{+}" or "CF_3^{+}"

Ni^{IV} at work: Making bonds to carbon

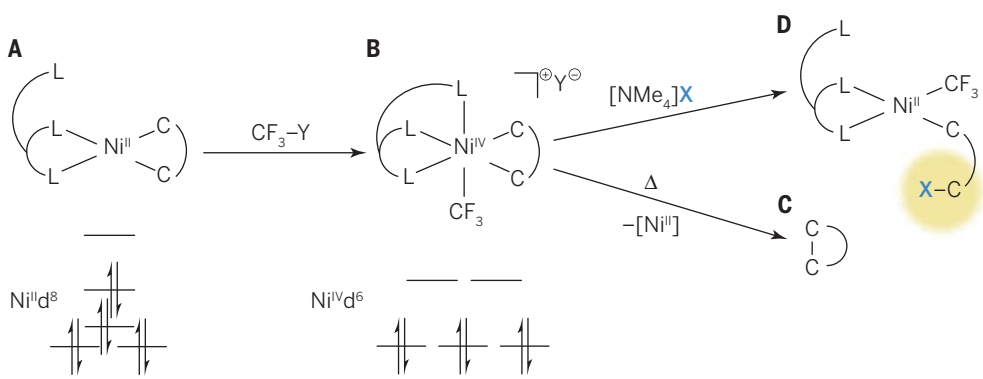

Upping the oxidation state. In the synthetic route devised by Camasso and Sanford, (**A**) a Ni^{II} complex in a d^8 electronic configuration binds a tridentate ligand L at two of three sites and an organic substrate through two of its carbon atoms. (**B**) Reaction with a CF_3^{+} oxidant forms a cationic Ni^{IV} d^6 complex (along with its anion Y); the Ni^{IV} now binds to the third ligand donor, L. Reductive elimination can occur (**C**) by heating, which releases the organic product, or (**D**) by reaction with a tetramethyl ammonium (NMe_4^{+}) complexed nucleophilic anion bearing a heteroatom X. The anion forms a C–X bond with the organic substrate.

Department of Chemistry and Biochemistry, University of Delaware, Newark, DE 19716, USA. E-mail: riordan@udel.edu

equivalent to organonickel^{II} precursors leads to oxidatively induced C–C reductive elimination.

By combining an organonickel^{II} precursor supported by a ligand that coordinates the nickel with three heteroatom donors with a CF_3^+ oxidant, isolable organonickel^{IV} complexes were obtained. These complexes were partners for formation of C–X bonds (where X denotes oxygen-, sulfur-, and nitrogen-based reagents) in excellent yields and under mild reaction conditions. Preliminary kinetic experiments support a mechanistic pathway in which an organonickel^{IV} bond is attacked by the heteroatom nucleophile. The high oxidation state of the metal serves to ensure the bound carbon atom is highly electrophilic and susceptible to facile C–X bond formation.

Although further mechanistic details remain to be unraveled, the involvement of a thoroughly characterized organonickel^{IV} in carbon-heteroatom bond formation opens vistas for constructing new types of molecules and materials under mild conditions. Key aspects of these transformations include the ability to use an economically more attractive metal as the catalyst; exploitation of the lability of the nickel-ligand bonds to promote selective reactions under mild conditions; and the formation of new C–X bonds in which the carbon atom is sp^3-hybridized, which constitutes the most challenging reaction of this class. Future opportunities will entail exploring and developing a fundamental understanding of the range of ligands and oxidants that can successfully partner to facilitate nickel^{IV} cross-coupling reactions. The utility of this work will be greatly enhanced if the efficacy of other oxidants, ideally O_2 (*13*), could be demonstrated. ■

REFERENCES AND NOTES

1. N. M. Camasso, M. S. Sanford, *Science* **347**, 1218 (2015).
2. H.-F. Klein, A. Bickelhaupt, T. Jung, G. Cordier, *Organometallics* **13**, 2557 (1994).
3. R. F. Service, *Science* **330**, 308 (2010).
4. J. Bowers *et al.*, *Nat. Methods* **6**, 593 (2009).
5. C. E. Garrett, K. Prasad, *Adv. Synth. Catal.* **346**, 889 (2004).
6. P.-L. T. Boudreault *et al.*, *J. Am. Chem. Soc.* **129**, 9125 (2007).
7. The market value of Pd per troy ounce is more than 1500 times that of nickel, as of February 2015.
8. G. Bender, E. Pierce, J. A. Hill, J. E. Darty, S. W. Ragsdale, *Metallomics* **3**, 797 (2011).
9. Y. Z. Zhou, D. A. Sliwa, S. W. Ragsdale, in *Handbook of Porphyrin Science with Applications to Chemistry, Physics, Materials Science, Engineering, Biology and Medicine, Vol. 19: Biochemistry of Tetrapyrroles*, K. M. Kadish, K. M. Smith, R. Guilard, Eds. (World Scientific, Singapore, 2012), pp. 1–44.
10. P. A. Lindahl, *J. Biol. Inorg. Chem.* **9**, 516 (2004).
11. V. B. Phapale, D. J. Cárdenas, *Chem. Soc. Rev.* **38**, 1598 (2009).
12. P. Sehnal *et al.*, *Chem. Rev.* **110**, 824 (2010).
13. M. T. Kieber-Emmons, C. G. Riordan, *Acc. Chem. Res.* **40**, 618 (2007).

10.1126/science.aaa7553

OCEANS

How climate influences sea-floor topography

Sea-floor hills show the same periodicity as glacial cycles

By **Clinton P. Conrad**

Earth's sea floor is created along great volcanic ridges that spread at rates of a few centimeters per year beneath every ocean basin. The volcanic and tectonic processes at these mid-ocean ridges ultimately determine the characteristics of the sea floor and the oceanic crust beneath it. These processes occur beneath several kilometers of rock and seawater, seemingly far removed from climatic variations above sea level. Thus, it is surprising that both Crowley *et al.* (*1*), on page 1237 in this issue, and Tolstoy (*2*) found ice age periodicity in hilly topography on the flanks of ridges submerged beneath the Southern and Pacific Oceans.

After its creation at the mid-ocean ridges, Earth's sea floor forms the abyssal hills (see the figure). If we could view this terrain without its cover of water, it would appear as gentle rolling hills hundreds of meters high and spaced kilometers apart. The abyssal hills are oriented roughly parallel to the ridges where they are formed and are carried across the ocean basins by sea-floor spreading.

Over the course of tens of millions of years, the abyssal hills become buried by sediments, but they are nevertheless observable in bathymetric surveys across vast expanses of sea floor (*3*). This coverage makes the abyssal hills the most extensive geological feature on Earth, but their remoteness means that they remain largely unexplored and poorly understood. Detailed bathymetric surveys, obtained using sonar that images a swath of sea floor beneath a ship, have only been obtained for a small portion of the sea floor. Close examination of these images informs our understanding of how the abyssal hills are created. In particular, extensional faults associated with mid-ocean ridge rifting are thought to be important (*4*). Such faults are observable in bathymetric surveys of newly created abyssal hills near ridge crests and are prevalent in computer models of rifting (*5*).

Comprehensive bathymetry of the Australian-Antarctic ridge south of Tasmania, observed from a South Korean icebreaker, allowed Crowley *et al.* to examine an unusually long record of abyssal hill fabric. They found that the abyssal hills exhibit characteristic spacing of about 23,000, 41,000, and 100,000 years. Working separately but concurrently, Tolstoy also detected 100,000-year periodicity in the abyssal hill fabric of the East Pacific Rise, a ridge west of South America (*2*).

"...the diversity of abyssal hill fabrics observed on the sea floor may result from a range of interactions between climate-induced melting variations and tectonic deformation processes."

These periods are familiar to paleoclimatologists: They are the primary Milankovitch cycles of cooling and warming of Earth's surface climate. Caused by periodic fluctuations in Earth's rotation, obliquity, and orbit, respectively, the Milankovitch cycles result from changes in the amount and location of radiation reaching Earth's surface and can produce large climate swings between ice ages and warm interglacial periods. For example, Earth has warmed since the last Ice Age, which peaked between 20,000 and 30,000 years ago. The ice sheets that once covered much of North America and Eurasia have melted, causing sea level to rise by about 120 m.

How do Milankovitch cycles induce topographic variations on the sea floor? Oceanic crust is formed from magma produced as hot rocks rise toward the ridge crest, where decreased pressure causes them to melt. The eruption and refreezing of this magma produces the oceanic crust,

Department of Geology and Geophysics, School of Ocean and Earth Science and Technology, University of Hawaii, Honolulu, HI 96822, USA. E-mail: clintc@hawaii.edu

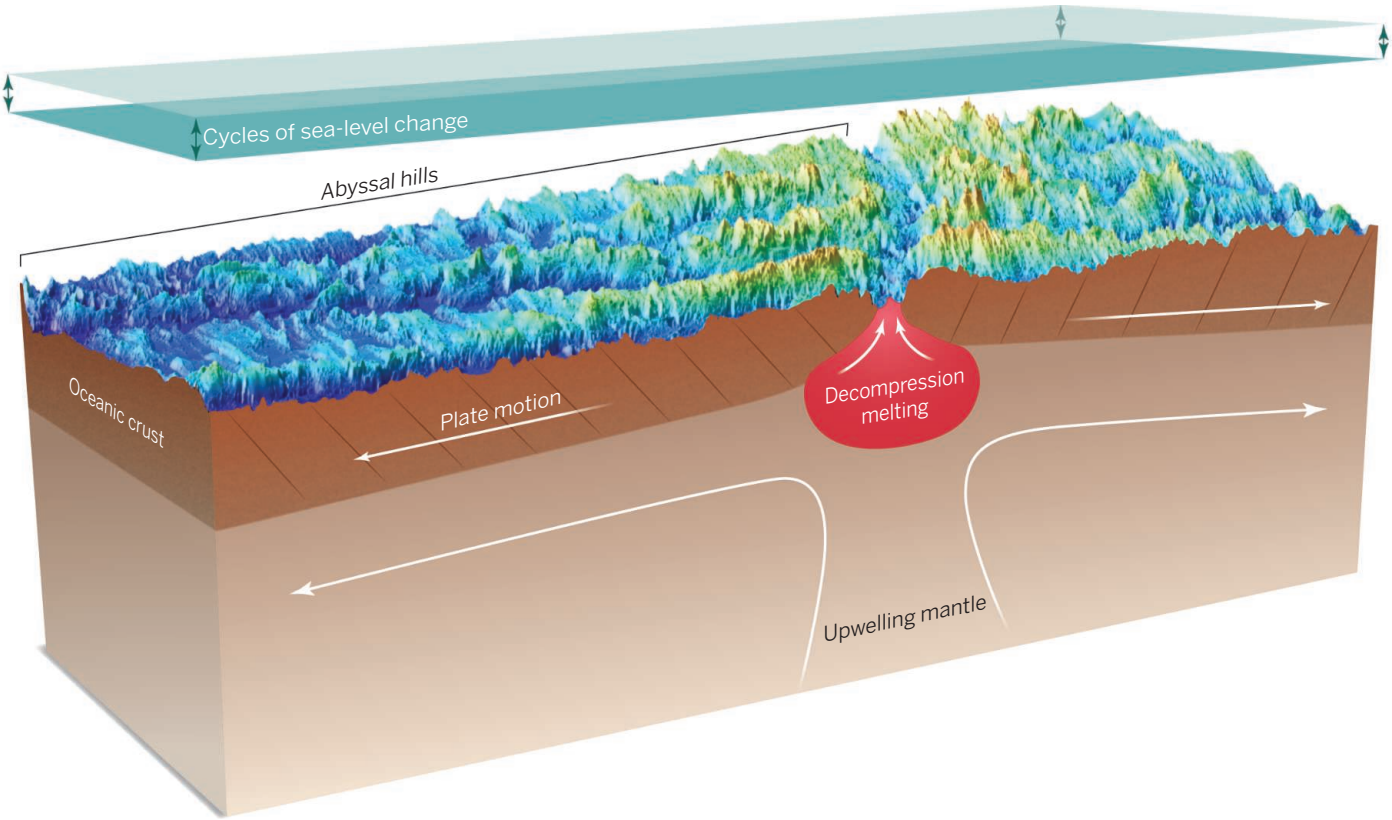

How the sea floor gets its hills. High-resolution bathymetry (*10*) of the North Atlantic's mid-ocean ridge (near 26°N, 46°W), showing the abyssal hills that form near the ridge axis and are carried across the ocean basin by sea-floor spreading. Crowley *et al.*'s observations suggest that Ice Age cycles of sea-level rise and fall cause sea-floor pressure changes that induce periodic variations in rates of decompression melting beneath the ridge. These variations change rates of ridge-axis volcanism and contribute to the abyssal hill fabric.

but the temperatures involved are much larger than those associated with climate change; seawater temperature variations should thus not affect submarine volcanism. Instead, climate change can affect volcanism by changing belowground pressures, which affect the melting behavior of rocks (*6*, *7*). Indeed, periods of increased volcanic activity in Iceland have been associated with deglaciation and the resulting decompression melting of rocks (*8*).

Both Crowley *et al.* and Tolstoy (*2*) attribute their observations of Milankovitch cycles in the abyssal hills to a similar mechanism. As the climate cools and ice sheets form, the associated sea-level drop causes pressure to decrease at the mid-ocean ridges. This accelerates melting there, which causes more magma to erupt at the ridge. The result is a region of thicker oceanic crust, which is observed as an abyssal hill. Conversely, periods of warming climate lead to the valleys between the abyssal hills.

Crowley *et al.* show that the 100-m variations in sea level associated with Milankovitch cycles can produce hundreds of meters of bathymetric relief, sufficient to explain the observed height of the abyssal hills. Such large variations are possible because changes in the rate of melt production depend on rates of sea-level change, which were indeed rapid in the past: The last major deglaciation produced 100 m of sea-level rise over 10,000 years, an average rate of 1 cm/year. For comparison, sea level is currently rising 3 mm/year and accelerated to this rate only during the past century (*9*). Such rates would need to be sustained for thousands of years to perceptibly affect the abyssal hills currently forming along Earth's mid-ocean ridges.

Because sea-level changes are global in nature, climatic variations are likely to influence abyssal hill fabrics along every ridge. Of course, Crowley *et al.* studied a location where the climatic signal is likely to be strongest. The Australian-Antarctic ridge exhibits little complicating topography, such as volcanic seamounts or transform faults, and has a spreading rate of 3 cm/year—fast enough to separate crustal thickness variations, but slow enough to avoid wide lava flows that might smear them. Detection of Milankovitch cycles in the abyssal hills of other sea floor will be challenging and may be complicated by other processes, such as extensional faulting. Indeed, the diversity of abyssal hill fabrics observed on the sea floor may result from a range of interactions between climate-induced melting variations and tectonic deformation processes. Furthermore, the Milankovitch climate fluctuations may themselves be affected by variations in CO_2 emissions associated with volcanic pulsations at the mid-ocean ridges (*2*). Understanding these interactions will require new high-resolution observations of the abyssal hills, examined in the light of past climate change. ■

ILLUSTRATION: ADAPTED BY P. HUEY/*SCIENCE*

REFERENCES

1. J. W. Crowley, R. F. Katz, P. Huybers, C. H. Langmuir, S.-H. Park, *Science* **347**, 1237 (2015).
2. M. Tolstoy, *Geophys. Res. Lett.* 10.1002/2014GL063015 (2015).
3. J. A. Goff, W. H. F. Smith, K. M. Marks, *Oceanography* **17**, 24 (2004).
4. K. C. Macdonald, P. J. Fox, R. T. Alexander, R. Pockalny, P. Gente, *Nature* **380**, 125 (1996).
5. W. R. Buck, A. N. B. Poliakov, *Nature* **392**, 272 (1998).
6. P. Huybers, C. Langmuir, *Earth Planet. Sci. Lett.* **286**, 479 (2009).
7. D. C. Lund, P. D. Asimow, *Geochem. Geophys. Geosyst.* **12**, Q12009 (2011).
8. J. Maclennan, M. Jull, D. McKenzie, L. Slater, K. Grönvold, *Geochem. Geophys. Geosyst.* **3**, 1 (2002).
9. C. C. Hay, E. Morrow, R. E. Kopp, J. X. Mitrovica, *Nature* **517**, 481 (2015).
10. W. B. F. Ryan *et al.*, *Geochem. Geophys. Geosyst.* **10**, Q03014 (2009).

ACKNOWLEDGMENTS

I thank P. Wessel for helpful comments. Supported by NSF grant EAR-1151241.

10.1126/science.aaa6813

ENVIRONMENT AND DEVELOPMENT

Get the science right when paying for nature's services

Few projects adequately address design and evaluation

By **S. Naeem***, **J. C. Ingram**, **A. Varga**, **T. Agardy**, **P. Barten**, **G. Bennett**, **E. Bloomgarden**, **L. L. Bremer**, **P. Burkill**, **M. Cattau**, **C. Ching**, **M. Colby**,† **D. C. Cook**, **R. Costanza**, **F. DeClerck**, **C. Freund**, **T. Gartner**, **R. Goldman-Benner**, **J. Gunderson**, **D. Jarrett**, **A. P. Kinzig**, **A. Kiss**, **A. Koontz**, **P. Kumar**, **J. R. Lasky**, **M. Masozera**, **D. Meyers**, **F. Milano**, **L. Naughton-Treves**, **E. Nichols**, **L. Olander**, **P. Olmsted**, **E. Perge**, **C. Perrings**, **S. Polasky**, **J. Potent**, **C. Prager**, **F. Quétier**, **K. Redford**, **K. Saterson**†, **G. Thoumi**, **M. T. Vargas**, **S. Vickerman**, **W. Weisser**, **D. Wilkie**, **S. Wunder**

Payments for Ecosystem Services (PES) mechanisms leverage economic and social incentives to shape how people influence natural processes and achieve conservation and sustainability goals. Beneficiaries of nature's goods and services pay owners or stewards of ecosystems that produce those services, with payments contingent on service provision (*1*, *2*). Integrating scientific knowledge and methods into PES is critical (*3*, *4*). Yet many projects are based on weak scientific foundations, and effectiveness is rarely evaluated with the rigor necessary for scaling up and understanding the importance of these approaches as policy instruments and conservation tools (*2*, *5*, *6*). Part of the problem is the lack of simple, yet rigorous, scientific principles and guidelines to accommodate PES design and guide research and analyses that foster evaluations of effectiveness (*4*). As scientists and practitioners from government, nongovernment, academic, and finance institutions, we propose a set of such guidelines and principles.

POLICY

Because PES mechanisms directly link payments to environmental performance, they are often viewed as more efficient alternatives and complements to traditional regulatory or protection-based conservation approaches (*5*). Unlike the polluter-pays principle common to many environmental interventions, in PES, beneficiaries pay. PES beneficiaries can be governments, nongovernmental organizations, or private entities; owners or stewards can be governments, private, or communal land holders. PES interventions are increasingly used for securing nature's services while conserving species, curtailing deforestation, mitigating climate change, and pursuing social objectives such as sustainable livelihoods and poverty alleviation (*3*). Given the centrality of the ecosystem service framework to the Intergovernmental Platform for Biodiversity and Ecosystem Services (IPBES), the Convention on Biological Diversity, and the United Nations Sustainable Development Goals, and the expectation of innovative financing mechanisms to achieve the Aichi Targets (*6*), ensuring the scientific integrity of PES will be extraordinarily important.

SCIENCE, PRACTICE, AND THE GAP. Irrespective of scale or complexity, whether national [e.g., Costa Rica's PES program (*7*)], regional [e.g., New York City's and Munich's water supply (*8*)], or smaller-scale efforts [e.g., community-scale biodiversity conservation in Cambodia (*9*)], identifying whom to compensate, what to pay (i.e., money or other forms of incentives), how much to pay, the mechanisms for payment, and verification of service delivery are essential social and economic components to PES (*10*, *11*).

Although getting the social science right is critical for PES, we focus on the natural science because of growing concerns over scientific weaknesses (*2*, *5*, *6*, *12*). Success of PES initiatives is reliant upon scientific knowledge of the ecosystem services of interest, methods for verifying delivery of services, establishing a relationship between natural resource practices and the generation of a service, the spatial and temporal scale at which the service is produced, and factors that may threaten the service or trade-offs with other beneficial nontarget services (*13*). If any of these basic principles are not considered, the ability of PES mechanisms to generate ecological and social benefits may be undermined (*3*, *14*).

However, the scientific content of PES programs and projects varies enormously. Some of this is due to environmental urgency or social and political expediency that can promote implementation in advance of scientific analyses (*13*, *15*), the lack of sufficient scientific knowledge and data, or weak capacity and resources to monitor results and assess compliance (*4*, *9*). Practitioners are frequently better attuned than scientists to limited budgets, available technical capacity in environmental science, and knowledge gaps. Thus, disconnects often exist between science and practices developed by the research community and what is accessible and feasible in the field.

Reviews of designs, metrics, analytical methods, and perceptions of PES interventions reveal a need for greater coordination among scientific researchers, practitioners, ecosystem service providers, and beneficiaries (*5*). Collecting metrics for ecosystem services varies enormously in cost, utility, and complexity. Without tools for identifying the best and most affordable metrics, PES proponents may struggle to collect scientifically meaningful, cost-effective baseline data and implement effective monitoring programs.

We developed a framework for integrating natural science into PES based on six natural science principles encompassing 33 guidelines (see the table and the supplementary materials). Based on the work on these issues in Asia, Africa, Europe, North America, South America, and Australia, the principles are designed to be applicable across a range of ecological and social contexts. Although these principles were developed with a focus on PES, they may be useful for a range of market-based conservation instruments hampered by limited scientific evidence and empirical data on effectiveness (*6*). Many may apply to ecosystem service projects that do not include payment or incentives mechanisms.

We examined the degree to which active PES projects spanning several types of ecosystem services followed the principles and guidelines (see the supplementary materials). Of the 118 projects we examined, 60% lacked adherence to the four principles (see table) deemed essential to ensuring scientific integrity in environmental interventions: (i) baseline data, (ii) monitoring of key environmental factors and services, (iii) recognizing that ecosystems are dynamic, and (iv) inclusion of metrics, specifically on risks such as climate change or invasive species.

The context-specific nature and market uncertainties surrounding PES (*16*) may make accommodating even these basic principles difficult. Consideration of the principles is recommended even if resources or capacity do not permit extensive scientific measurement or analyses. The principles are designed so that they are not onerous to

*Corresponding author. E-mail: sn2121@columbia.edu
†The views and opinions expressed in this paper are those of the authors and not necessarily the views and opinions of USAID or U.S. EPA. See full list of affiliations online.

Natural-science principles and guidelines for PES interventions

For an intervention to be successful, basic guidelines (blue) must be followed. Desirable guidelines (orange) should be followed. See the supplementary materials for further details.

PRINCIPLE: Dynamics

OBJECTIVE: Ensure project capacity to adapt to dynamic natural and anthropogenic processes.

SCIENTIFIC GUIDELINES:

- Identify key services for each service type beyond target services.
- Identify spatiotemporal scales of targeted services.
- Identify data needs, resources, and gaps.
- Identify stressors and their spatiotemporal variability.
- Identify and forecast trends in endogenous and exogenous threats.
- Identify services' production functions and sensitivities.
- Determine trade-offs and synergies among services.
- Determine how functional diversity influences resilience.

PRINCIPLE: Baseline

OBJECTIVE: Document initial conditions.

SCIENTIFIC GUIDELINES:

- Measure influences of interventions on services.
- Measure status and trends of non-target services.
- Ensure that measurements are feasible given resources.
- Assess initial state of exogenous and endogenous threats to services.
- Measure factors important for forecasting service trends.

PRINCIPLE: Multiple Services

OBJECTIVE: Recognize trade-offs and synergies among services.

SCIENTIFIC GUIDELINES:

- Assess how intervention influences the other services.
- Avoid "double counting."
- Assess impacts of intervention on non-target services.

PRINCIPLE: Monitoring

OBJECTIVE: Track factors necessary for management, trade, forecasting, and assessment.

SCIENTIFIC GUIDELINES:

- Quantify deliverables associated with target services.
- Identify spatiotemporal scales in advance of implementation.
- Use established methods/protocols and best practices for monitoring.
- Estimate uncertainties.
- Monitoring should inform decision-making.
- Monitoring should detect potential changes in baseline conditions.
- Monitor non-target services that influence target services.

PRINCIPLE: Metrics

OBJECTIVE: Robust, efficient, and versatile methods for procuring data.

SCIENTIFIC GUIDELINES:

- Must be relevant, reliable, and appropriate in scale.
- Should comply with voluntary standards, certification and regulations.
- Should reflect spatiotemporal scales as identified in Dynamics.
- Optimize balance between precision and simplicity.
- Assess progress (in conjunction with Baseline and Monitoring).
- Establish benchmarks (in conjunction with Baseline and Monitoring).
- Should measure both absolute changes and changes in trends.
- Preferentially selected to allow comparisons across service types.
- Assess how services influence each other.

PRINCIPLE: Ecological Sustainability

OBJECTIVE: Insure project durability and sustainability.

SCIENTIFIC GUIDELINES:

- Estimate short-term and long-term project or program performance.

address but, if considered to whatever degree possible, can improve the likelihood of project success, support adaptive management, help identify important knowledge gaps and potential areas of concern, and increase investor confidence. The guidelines thus serve as a reference for evaluating project design and means for comparisons with other projects. There are also benefits to including traditional knowledge (*17*) that further iterations of these guidelines could accommodate.

ESTABLISHING STANDARDS. Given the increasing importance placed on PES mechanisms to address environmental externalities and resolve conservation and development trade-offs (*1*, *4*, *18*), international commitment is needed from donors, researchers, and practitioners to test, refine, disseminate, and improve upon scientific guidelines and further develop tools, metrics, and methods. An international neutral body, such as the IPBES, would be an ideal coordinator for regular review and assessment of science guidelines for PES and could establish an expert review board to oversee guidelines for improving PES design and implementation. In the interim, those developing PES or similar projects can follow our guidelines and report on their utility and areas for improvement. Through this process, PES project standards that provide technical guidance to project developers, assurance to investors, and templates for reporting will emerge as they have for other environmental programs, such as the Verified Carbon Standard; the Climate, Community, and Biodiversity Alliance; the Business and Biodiversity Offsets Program; and voluntary standards maintained by the International Organization for Standardization.

Challenges will remain for PES, such as pressure for simplicity and quick fixes, contending with competing goals and multiple objectives, and dealing with policy- and decision-makers who often work at scales and time frames different from those of importance to scientists. Too often, science and practice are poorly linked in environmental interventions. An inclusive process in developing, testing, and refining basic science principles will ensure greater success of promising new approaches. ■

SUPPLEMENTARY MATERIALS

www.sciencemag.org/content/347/6227/1206/suppl/DC

REFERENCES AND NOTES

1. G. C. Daily, P. A. Matson, *Proc. Natl. Acad. Sci. U.S.A.* **105**, 9455 (2008).
2. S. Wunder, S. Engel, S. Pagiola, *Ecol. Econ.* **65**, 834 (2008).
3. J. C. Ingram *et al.*, *Ecosystem Services* **7**, 10 (2014).
4. P. J. Ferraro, S. K. Pattanayak, *PLOS Biol.* **4**, e105 (2006).
5. S. K. Pattanayak, S. Wunder, P. J. Ferraro, *Rev. Environ. Econ. Policy* **4**, 254 (2010).
6. R. Pirard, R. Lapeyre, *Ecosystem Services* **9**, 106 (2014).
7. P. Ina, Payments for environmental services: Lessons from the Costa Rican PES programme. IIED (2013). http://pubs.iied.org/pdfs/G03561.pdf
8. G. Grolleau, L. M. J. McCann, *Ecol. Econ.* **76**, 87 (2012).
9. T. Clements *et al.*, *Ecol. Econ.* **69**, 1283 (2010).
10. R. Muradian *et al.*, *Conserv. Lett.* **6**, 274 (2013).
11. S. Wunder, *Conserv. Lett.* **6**, 230 (2013).
12. R. Yin, T. Liu, S. Yao, M. Zhao, *For. Policy Econ.* **35**, 66 (2013).
13. A. P. Kinzig *et al.*, *Science* **334**, 603 (2011).
14. P. Kareiva, A. Chang, M. Marvier, *Science* **321**, 1638 (2008).
15. K. Ellison, *Front. Ecol. Environ* **7**, 60 (2009).
16. R. Muradian, E. Corbera, U. Pascual, N. Kosoy, P. H. May, *Ecol. Econ.* **69**, 1202 (2010).
17. W. J. Sutherland, T. A. Gardner, L. J. Haider, L. V. Dicks, *Oryx* **48**, 1 (2014).
18. J. Farley, R. Costanza, *Ecol. Econ.* **69**, 2060 (2010).

ACKNOWLEDGMENTS

This work has been supported by the U.S. Agency for International Development TRANSLINKS program (EPP-A-00-06-00014-00) and the National Academies Keck Futures Initiative.

10.1126/science.aaa1403

ENVIRONMENTAL TOXICOLOGY

Pick your poison

How getting rid of DDT opened the door for more dangerous pesticides

By **Jacob Darwin Hamblin**

Rachel Carson urges Congress to control the sale of chemical pesticides and reduce aerial spraying at a Senate subcommittee hearing on 4 June 1963.

The sacred success story in environmental literature is that of Rachel Carson, who awakened America to the dangers of indiscriminate pesticide use and led the charge to ban the sale of DDT and other chlorinated hydrocarbons in the United States. In her best-selling 1962 book *Silent Spring*, Carson introduced many readers to the concept of ecology, warning that persistent pesticides might accumulate and magnify at unexpected intersections of the web of life. Those opposed to this legislation typically argue that DDT saved more lives by preventing mosquito-borne illnesses than it harmed, but there is another reason to be wary of the vilification of DDT. In *Banned*, historian of science Frederick Rowe Davis argues that doing so actually diverted attention away from the most toxic pesticides.

The science of toxicology itself was born from crises in consumer confidence. It began to pull away from pharmacology in the early 20th century, maturing in the 1930s after a wave of deaths from Elixir Sulfanilamide, an improperly prepared medicine that had been provided to consumers without first being tested for safety. Recognizing the need for standardized safety studies, the Food and Drug Administration devised statistical approaches and benchmarks (such as identifying the lethal dose to 50% of animal test subjects) that shaped the science for years to come. Toxicological studies expanded during World War II. With its high toxicity to insects and seemingly low toxicity to mammals, DDT seemed an ideal means to control mosquito-borne malaria among American troops.

When the Environmental Protection Agency ultimately banned DDT in 1972, the nightmare scenario of leading toxicologists became reality. Farmers turned to alternative pesticides that would-be regulators had already failed to keep from consumers, including cast-offs from chemical weapons laboratories. Ironically, Rachel Carson had done such a good job of drawing attention to hidden dangers, such as chronic exposure to small quantities and persistence in the environment, that chemicals with acute, direct effects went relatively unnoticed.

When Rachel Carson criticized indiscriminate use of pesticides, she identified not only DDT but also organophosphates as potentially dangerous. However, her readers focused on the troubling ecological implications of persistent pesticides. Organophosphates appeared to break down within days, acquitting them of long-term environmental impact.

Among toxicologists, however, organophosphates were considered far more troubling. Organophosphates are especially dangerous because they inhibit cholinesterase, an enzyme crucial for neural communication, leading to muscle spasms, defecation, drooling, and asphyxiation. As weapons, these compounds were called "nerve gas," but in the hands of farmers and household gardeners, they were dubbed pesticides. In 1971, during the height of the DDT debate, one of the scientists studying these compounds, Kenneth DuBois, expressed concern that if DDT were banned, the market would be flooded with these dangerous neurotoxins.

One might ask: If organophosphates were so terrible, why weren't they banned along with DDT? Davis reveals that under pressure from pesticide corporations, Congress took the path of least resistance and simply required labeling. Thus, organophosphate insecticides "passed through the screen" or "slipped through the cracks," as Davis variously puts it, despite the fact that everyone from Rachel Carson to Monsanto acknowledged that they were the worst of the bunch. In fact, their use did not diminish at all but instead expanded to "a degree that would have shocked and disappointed Carson." By 1989, only three of the heaviest-use pesticides (more than half a million pounds applied) were not organophosphates.

Many organophosphates were banned eventually, some as recently as 2006, but not because of their acute toxicity. The EPA found that, like other pesticides before them, they, too, could be banned based on environmental persistence and links to cancer. This took a very long time, however, and in the meantime, neurotoxins once imagined for wartime use filled the agricultural and gardening void left by the departure of DDT.

Although Davis is an admirer of Rachel Carson, *Banned* offers a provocative counternarrative to the triumphal story of *Silent Spring*. Reading it should convince anyone to be wary of such success stories and, above all, to read labels carefully.

The reviewer is at Oregon State University, Corvallis, OR 97331, USA. E-mail: jacob.hamblin@oregonstate.edu

Banned
A History of Pesticides and the Science of Toxicology
Frederick Rowe Davis
Yale University Press, 2014. 284 pp.

10.1126/science.aaa3383

PHOTO: ASSOCIATED PRESS

MATERIALS SCIENCE

Precious metals

Balancing the growing demand for rare earth minerals with sustainable mining practices

By **Saleem H. Ali**

Modern technology is highly dependent on a complex array of materials that have increasingly become more distant from the consumer. In particular, the more esoteric elements of the periodic table remain obscure and underappreciated by even many scientifically informed citizens. In this context, a book such as Keith Veronese's *Rare*, which seeks to connect rare earth minerals to the supply chain of our computers, cars, and myriad other technologies, is a welcome addition to the genre of popular chemistry narratives that have gained traction in recent years.

Praseodymium, in water.

The lanthanides and actinides have been literal and figurative outcasts from the periodic table, occupying two separate rows outside the main expanse of the elemental matrix. Veronese, a chemist by training, capitalizes on their oddity with fast-paced episodic prose, which includes topics ranging from the methods that researchers employed to estimate the prevalence of promethium in the Earth's crust to Cold War stories of the chemical synthesis of unstable, ephemeral elements. In this regard, his book is reminiscent of Sam Kean's bestseller *The Disappearing Spoon* (*1*), but with less detail and a more staccato style of writing.

Perhaps this difference can be attributed to the fact that Veronese is trying to capture so many facets of a highly complex topic within a relatively short textual frame. His coverage is ultimately more superficial than other recent books devoted to specific elements, such as uranium (*2*) or plutonium (*3*).

Given the panoramic view that *Rare* attempts to provide, it would also have been an opportunity to link to a broader theme of sustainability within the narrative. For example, all too often, the key argument from environmentalists regarding the sustainability of mineral extraction is linked to the ostensible "nonrenewability" of these materials on human time scales. Yet from a chemical perspective, elements are renewable if we are able to use energy to restore them to lower states of entropy. Mining itself extracts minerals from higher states of entropy in geological environments, but then manufactured uses of these elements raise their entropy again. Veronese does delve into "dirty recycling" but spends more time describing the pitfalls of amateur recyclers using sodium cyanide to extract gold than on making broad connections to sustainability. More analysis of social and environmental trade-offs is needed to clarify the optimal ratio of recycling versus mining of materials. Moving forward, rare earth mining companies will need to reinvent themselves as material service providers that incorporate recycling practices into their business models in addition to mining from the earth itself.

The use of rare materials, particularly rare earth minerals, in green technologies could ultimately help us to achieve cleaner energy production (*4*). *Rare* indicates the use of neodymium magnets in wind power generation and lanthanum in hybrid cars, but Veronese's citations neglect broad demand scenario studies that could have added weight to his arguments. Similarly, the photographic insert depicting mining operations and close-ups of rare minerals is visually appealing, but diagrams from the primary literature (*5*) that attempt to make connections about the life cycles of rare earth minerals would have added analytical weight for the informed reader.

Despite these criticisms, Veronese has provided a useful introduction to rare elements that will likely spark the interest of a general reader. As the public and policy-makers engage with emerging powers such as China on metal supply concerns and technologies become more complex, such books should be in high demand.

The reviewer is at the Sustainable Minerals Institute, University of Queensland, Brisbane, QLD 4072, Australia.
E-mail: saleem@alum.mit.edu

REFERENCES

1. S. Kean, *The Disappearing Spoon: And Other True Tales of Madness, Love, and the History of the World from the Periodic Table of the Elements* (Back Bay Books, New York, 2011).
2. T. Zoellner, *Uranium: War, Energy, and the Rock That Shaped the World* (Penguin Books, New York, 2010).
3. J. Bernstein, *Plutonium: A History of the World's Most Dangerous Element* (Cornell Univ. Press, Ithaca, NY, 2009).
4. E. Alonso, A. M. Sherman, T. J. Wallington, M. P. Everson, F. R. Field, R. Roth, R. E. Kirchain, *Environ. Sci. Technol.* **46**, 3406 (2012).
5. X. Du, T. E. Graedel, *Sci. Rep.* **1**, 145 (2011).

10.1126/science.aaa4546

Rare
The High-Stakes Race to Satisfy Our Need for the Scarcest Metals on Earth
Keith Veronese
Prometheus Books, 2015. 278 pp.

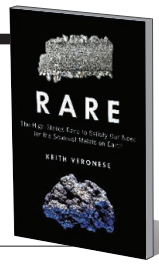

IN BRIEF

Cancer: The Emperor of All Maladies
Barak Goodman
Ken Burns, Executive Producer
airing on PBS on 30 March, 31 March, and 1 April 2015; check local listings

Based on the 2010 book by Siddhartha Mukherjee [see *Science* **332**, 423 (2011)], this three-part documentary weaves together a sweeping history of cancer with intimate stories of contemporary patients. Told largely through interviews with researchers and oncologists, the series highlights Sidney Farber's efforts to galvanize a national "war on cancer" in the 1940s, delves into the development of targeted drug compounds in the late 20th century, and explores the promise of personalized immunotherapies.

10.1126/science.aaa9764

Sidney Farber (left) with colleagues, c. 1950.

PHOTOS: (MIDDLE LEFT) W. OELEN/WIKICOMMONS; (BOTTOM RIGHT) COURTESY DANA-FARBER CANCER INSTITUTE

LETTERS

Edited by **Jennifer Sills**

Emergency response for marine diseases

MARINE DISEASES CAN decimate populations and can have substantial ecological, economic, and social impacts. Recent disease outbreaks in marine mammals, shellfish, sponges, seagrasses, crustaceans, corals, and fishes demonstrate the potential for catastrophic effects, including reduced biodiversity, community shifts, local extirpation of species, disruption of ecosystem services, and loss of fisheries (*1*, *2*). Currently, seastar wasting syndrome threatens marine populations by impairing ecological integrity through shifts in populations of foundation species and declines in ecosystem services. In the past year, over 20 seastar species on both coasts of the United States have declined to the point of local extirpation (*3*).

At this point, very limited funding is available to identify, monitor, forecast, and mitigate marine diseases. The Marine Disease Emergency Act (H.R. 5546), reintroduced by Rep. Dennis Heck (D-Wash.) to the House of Representatives in February 2015, would provide immediate resources to mount a rapid response when marine infectious diseases are first detected. If the legislation passes, the funding would enable (i) a basic research program to increase diagnostic tools, understand pathogenesis, and quantify epidemiological processes; (ii) a surveillance program to identify marine disease outbreaks; (iii) a marine disease forecasting program; and (iv) directed mitigation programs to reduce the intensity of disease outbreaks and their downstream impacts [e.g., (*4*)]. These activities were only possible to a very limited extent during the recent seastar wasting syndrome outbreaks.

As our global reliance on oceans for food, ecosystem services, and cultural activities rises, anthropogenic stresses to the oceans are increasing, creating new opportunities for disease. This past year (2014) was also the warmest on record, and continually rising temperatures under climate change are predicted to increase seagrass wasting disease, seastar wasting, abalone withering syndrome, coral bleaching, infectious coral diseases, and risk for human infection by zoonotic vibrio species (*5*–*8*). If passed, the Marine Disease Emergency Act will greatly enhance capacity for rapid responses to marine disease outbreaks, maximizing opportunities for research and management of these diseases and their downstream impacts.

Maya Groner,[1]* Rachel Breyta,[2] Andy Dobson,[3] Carolyn S. Friedman,[2] Brett Froelich,[4] Melissa Garren,[5] Frances Gulland,[6] Jeffrey Maynard,[7] Ernesto Weil,[8] Sandy Wyllie-Echeverria,[9] Drew Harvell[7]

[1]Centre for Veterinary and Epidemiological Research, Department of Health Management, Atlantic Veterinary College, University of Prince Edward Island, Charlottetown, PE, C1A 4P3, Canada. [2]School of Aquatic and Fishery Sciences, University of Washington, Seattle, WA 98195, USA. [3]Department of Ecology and Evolutionary Biology, Princeton, NJ 08544, USA. [4]Department of Marine Science, University of North Carolina, Chapel Hill, NC 27599, USA. [5]Department of Civil and Environmental Engineering, Massachusetts Institute of Technology, Cambridge, MA 02139, USA. [6]The Marine Mammal Center, Sausalito, CA 94965, USA. [7]Department of Ecology and Evolutionary Biology, Cornell University, Ithaca, NY 14853, USA. [8]Department of Marine Sciences, University of Puerto Rico, Mayaguez, Mayaguez, PR 00680, USA. [9]Friday Harbor Laboratories, University of Washington, Friday Harbor, WA 98250, USA.

*Corresponding author. E-mail: mgroner@upei.ca

Ochre star losing its second arm to wasting disease.

PHOTO: DREW HARVELL

REFERENCES

1. C. A. Burge *et al.*, *Annu. Rev. Mar. Sci.* **6**, 249 (2014).
2. K. D. Lafferty *et al.*, *Annu. Rev. Mar. Sci.* **7**, 471 (2015).
3. I. Hewson et al., *Proc. Natl. Acad. Sci. U.S.A.* **111**, 17278 (2014).
4. J. A. Maynard *et al.*, *Coral Reefs* **30**, 485 (2011).
5. L. M. Crosson *et al.*, *Dis. Aquat. Org.* **108**, 261 (2014).
6. J. W. Turner *et al.*, *Environ. Microbiol.* **16**, 1019 (2014).
7. J. C. Bull, E. J. Kenyon, K. J. Cook, *Oecologia* **169**, 135 (2012).
8. D. Ruiz-Morenol *et al.*, *Dis. Aquat. Org.* **100**, 249 (2012).

Sparing grasslands: Map misinterpreted

J. W. VELDMAN *et al.* argue that the world's ancient (old-growth) grasslands should be spared from restoration-motivated tree planting ("Tyranny of trees in grassy biomes," Letters, 30 January, p. 484). We strongly agree. However, they also claim that the global Atlas of Forest Landscape Restoration Opportunities (*1*–*3*)—created by the World Resources Institute, International Union for Conservation of Nature, and University of Maryland—calls for such afforestation. It does not.

Forest Landscape Restoration (FLR) is a process to regain ecological integrity and enhance human well-being in deforested or degraded forest landscapes (*4*). Its goal is to enhance native ecosystem functions and biodiversity, not to increase forest cover per se. FLR does not call for increasing tree cover beyond what would be ecologically appropriate for a particular location, and should not cause any loss or conversion of natural forests, grasslands, or other ecosystems.

We created the Atlas to estimate the global potential for FLR, thereby underpinning the formulation of the Bonn Challenge ("to restore 150 million hectares of deforested and degraded forest lands by 2020") (*5*), and to identify areas where a more refined analysis is warranted.

It is important to note that the map is coarse. We used only globally consistent geospatial data sets at a 1-km resolution. We defined forest landscapes broadly, considering climate, soils, and ecoregions. All lands biophysically capable of supporting a tree canopy cover of at least 10% were included.

Given its coarseness, the Atlas was not intended or designed as a tool to guide precisely where restoration should occur, or to decide what interventions may be suitable for a particular location. Rather, national and subnational assessments are needed to determine what is ecologically, socially, and economically appropriate in a particular context. These assessments should consider local ecological conditions, engage local experts and stakeholders, use local definitions, and incorporate richer, higher-resolution data. To help with this, we developed a Restoration Opportunities Assessment Methodology (*6*).

To our knowledge, no global map of old-growth grasslands has yet been published. Mapping these areas is difficult, as they form gradients in the landscape, have shifted over time, and depend heavily on the periodicity of fires (*7*), which may or may not have been subject to human influence. We invite researchers, including Veldman *et al.*, to collaborate on a more in-depth mapping of ecosystem restoration opportunities, which can incorporate new information on the world's old-growth grasslands and other important biomes as it becomes available.

Lars Laestadius,[1]* Stewart Maginnis,[2] Susan Minnemeyer,[1] Peter V. Potapov,[3] Katie Reytar,[1] Carole Saint-Laurent[2]

[1]World Resources Institute, Washington, DC 20002, USA. [2]International Union for Conservation of Nature, 1196, Gland, Switzerland. [3]Department of Geographical Sciences, University of Maryland, College Park, MD 20742, USA.

*Corresponding author. E-mail: larsl@wri.org

REFERENCES

1. S. Minnemeyer, L. Laestadius, N. Sizer, C. Saint-Laurent, P. Potapov, "A world of opportunity" (World Resources Institute, Washington, DC, 2011).
2. L. Laestadius *et al.*, *Unasylva 238*, **62**, 47 (2011/2).
3. World Resources Institute, "Atlas of forest landscape restoration opportunities" (World Resources Institute, Washington, DC, 2014); www.wri.org/applications/maps/flr-atlas/#.
4. ITTO, IUCN, "Restoring Forest Landscapes" (ITTO/IUCN, *ITTO Technical Series No. 23*, 2005).
5. Global Partnership on Forest Landscape Restoration, "The Bonn Challenge" (GPFLR, 2013); www.forestlandscaperestoration.org/topic/bonn-challenge).
6. IUCN, World Resources Institute, "A guide to the Restoration Opportunities Assessment Methodology (ROAM)" (IUCN and WRI, Gland, Switzerland, 2014); http://cmsdata.iucn.org/downloads/roam_handbook_lowres_web.pdf.
7. W. A. Hoffman *et al.*, *Ecol. Lett.* **15**, 759 (2012).

Sparing grasslands: FAO's active role

WE AGREE WITH much of the Letter "Tyranny of trees in grassy biomes" (30 January, p. 484), in which J. W. Veldman *et al.* caution against indiscriminate afforestation in general and especially in grassland areas, as well as acknowledge grasslands' substantial contribution to carbon sequestration (*1*, *2*). We consider it misleading, however, to claim that because grasslands are not "formally" recognized, they are not actively studied and considered in ongoing activities of the U.N. Food and Agriculture Organization (FAO).

The FAO has been working on grasslands activities for more than 30 years (*3*) and recognizes that even within grasslands, there are many categories. The FAO's 2005 publication *Grasslands of the World* explicitly includes grassland biomes (*4*). We estimate that 26% of the world land area and 70% of the world agricultural area are covered by grasslands, which contribute to the livelihoods of over 800 million people (*5*). We have also developed a grassland database with descriptions of more than 300 grassland species from different grassland ecosystems. The FAO has many grassland-related projects and case studies (*6*), including rehabilitation of degraded areas through protected areas and promoting native grassland species. Two relevant projects are the completed "Range rehabilitation and establishment of a wildlife reserve in the Syrian steppe" and the ongoing, globally focused, "Participatory assessment of land degradation and sustainable land management in grassland and pastoral systems" (*7*). We do acknowledge that the definitions of grasslands need to be harmonized and that more research is needed into understanding these areas.

Eduardo Rojas-Briales

Assistant Director-General for Forestry, Food and Agriculture Organization of the United Nations, 00153, Rome, Italy. E-mail: fo-adg@fao.org

REFERENCES

1. FAO, Grasslands Carbon Working Group (www.fao.org/agriculture/crops/thematic-sitemap/theme/spi/gcwg/en).
2. FAO, Knowledge Base (www.fao.org/agriculture/crops/thematic-sitemap/theme/spi/gcwg/gcwg-docs/en).
3. FAO, Publications (www.fao.org/ag/AGP/AGPC/doc/pasture/publ_year.htm).
4. FAO, Grasslands of the World, J. M. Suttie, S. G. Reynolds, C. Batello, Eds. (FAO, Rome, 2005); ftp://ftp.fao.org/docrep/fao/008/y8344e/y8344e00.pdf.
5. FAO, Are grasslands under threat? (www.fao.org/ag/agp/agpc/doc/grass_stats/grass-stats.htm).
6. FAO, Case studies on grassland and rangeland management (www.fao.org/agriculture/crops/thematic-sitemap/theme/spi/scpi-home/managing-ecosystems/management-of-grasslands-and-rangelands/grasslands-cases/en).
7. FAO, Participatory assessment of land degradation and sustainable land management in grassland and pastoral systems (www.fao.org/agriculture/crops/intranet/projects-database/detail/en/c/234274).

RESEARCH

Human TREK-2 potassium channel binds Prozac

Dong et al., *p. 1256*

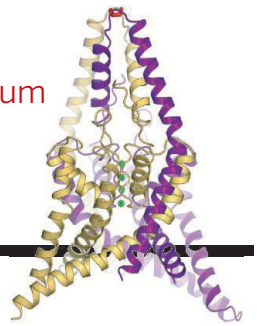

IN *SCIENCE* JOURNALS

Edited by **Stella Hurtley**

Tanzanian mothers awaiting vaccinations

EPIDEMIOLOGY

Vaccinate children despite Ebola

During the medical emergency caused by the Ebola virus outbreak in West Africa, routine childhood vaccination programs have been suspended. If vaccination is not resumed soon, there could be even more deaths. Measles is highly infectious, and outbreaks are a sign of health care systems in trouble. Using mathematical modelling, Takahashi *et al*. estimate that about a million children across Liberia, Sierra Leone, and Guinea are vulnerable to measles. Aggressive public health programs are vital for this region to minimize harm, not only from measles but also from polio, malaria, tuberculosis, and other childhood infections. — CA

Science, this issue p. 1240

ORGANIC SYNTHESIS

A block-by-block way to manufacture molecules

Carbon-based small molecules involved in biochemistry and drug design exhibit extraordinary structural diversity. But can we come up with a general set of building blocks from which a machine could put most of them together, in assembly-line fashion? Li *et al.* present progress toward this goal by showcasing the range of structures available via coupling reactions of fragments bearing a specific type of boronate group. They successfully made complex polycyclic structures by stringing together a linear precursor and then coaxing it to fold back on itself. They also developed a purification method that facilitates automation of the reaction and product isolation. — JSY

Science, this issue p. 1221

METABOLIC DISEASE

Special delivery for fatty liver disease

Nonalcoholic fatty liver disease is one of many unwelcome consequences of the global rise in obesity rates. Fat accumulation within the liver can lead to inflammation and cirrhosis, a predisposing factor for liver cancer. Treatment options are limited. Perry *et al.* revisit a mitochondrial uncoupling agent (2,4-dinitrophenol) that was used as a drug for weight loss in the 1930s but was discontinued because of serious toxicities. Encouragingly, an altered formulation of the drug that ensures its controlled release at low levels ameliorated fatty liver and diabetes in rodent models, without side effects. — PAK

Science, this issue p. 1253

LUNG INJURY

Exercising away the effects of lung injury

We all know that healthy people benefit from exercise, but recent evidence suggests that it also helps the sickest patients in the ICU. Files *et al.* studied mice with acute lung injury to understand why exercise is beneficial and confirmed their findings in human respiratory failure patients receiving therapeutic exercise. Exercise prevented muscle wasting and limited the number of immune cells infiltrating the lung by decreasing levels of a growth factor called G-CSF. — YN

Sci. Transl. Med. **7**, 278ra32 (2015).

LUNAR GEOLOGY

Onsite radar shows what lies beneath

In more active periods of the Moon's history, volcanic eruptions created lava plains that formed layers of dark basalt. Without subsurface probing,

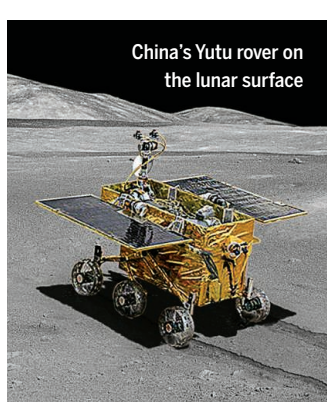

China's Yutu rover on the lunar surface

IMAGES: (CLOCKWISE FROM TOP) DONG *ET AL.*; CNSA; STEVE RINGMAN/MCT/NEWSCOM

Published by AAAS

we can only examine the most recent flows. After the soft landing of the Chang'E-3 spacecraft, Xiao *et al.* made penetrating radar measurements of the lunar crust with the Yutu rover. Several subsurface layers suggest multiple geologic processes at play throughout the crustal history, including multiple lava flows and the weathering-induced creation of dust and rocky debris. — MMM

Science, this issue p. 1226

POLITICAL PSYCHOLOGY

Be mindful of a self-reported gap

Happiness is a notoriously hard to pin down quantity possibly best described by the phrase, "I know it when I see it." Self-reported ratings of happiness are generally higher for political conservatives in the United States than for those with more liberal leanings. Wojcik *et al.* examined three data sets based on behavioral measures, such as tweets and smiles. Despite self-reported claims to the contrary, liberals exhibited more happiness than their more conservative counterparts. For instance, as judged from their photographs on a business-oriented social network, more employees of the *New York Times* smiled genuinely than did those of the *Wall Street Journal*. — GJC

Science, this issue p. 1243

CIRCADIAN RHYTHMS

Midnight snacks are bad for the heart

Circadian clocks help animals coordinate their active and rest periods with the daily cycles of light and darkness. As anyone who has suffered jet lag or worked night shifts knows, losing this coordination can have deleterious effects. Gill *et al.* compared fruit flies that were allowed to eat at any time with flies that were only allowed to eat during the day (when they are active). The flies with restricted feeding times slept better and had a slower decline in heart function as they aged. They also showed less weight gain, even though both groups of flies consumed about the same amount. — LBR

Science, this issue p. 1265

BEHAVIORAL NEUROSCIENCE

Crickets say NO to fight or flight

In crickets, to flee or not to flee is a life-and-death decision weighed on the scales of nitric oxide (NO) signaling. Stevenson and Rillich found that the making of this critical decision in the heat of battle sums the impact of the opponent's attacks. At a threshold level, the NO signaling pathway is activated. This depresses aggression and promotes flight of the loser from the scene. Activation of the NO pathway has an aftermath. Losers avoid further battles, at least for a time. — PLY

Sci. Adv. 10.1126/sciadv.150060 (2015).

QUANTUM WALKS

Quantum walkers under a microscope

Generations of physics students have been taught to think of one-dimensional random walks in terms of a drunken sailor taking random steps to the right or to the left. But that doesn't compare with the complexity of a quantum walker, who can propagate down multiple paths at the same time. Preiss *et al.* detected particles in single sites of an optical lattice to study the dynamics of two interacting atoms of ^{87}Rb performing a quantum walk (see the Perspective by Widera). Depending on the initial conditions and the interaction strength between the atoms, the atoms either ignored each other, stuck to each other, or tried to get as far away from each other as possible. — JS

Science, this issue p. 1229; see also p. 1200

IN OTHER JOURNALS

Edited by **Kristen Mueller** *and* **Jesse Smith**

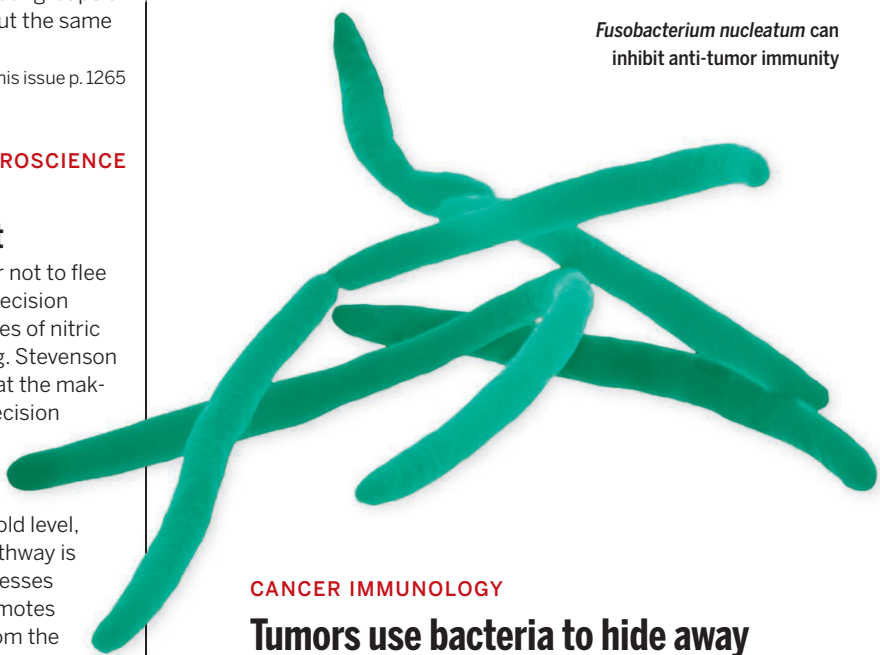

Fusobacterium nucleatum can inhibit anti-tumor immunity

CANCER IMMUNOLOGY

Tumors use bacteria to hide away

Although bacteria can help the immune system wage war against cancer, they can play for the other side, too. Gur *et al.* reveal one such example for the bacterium *Fusobacterium nucleatum*, which is found in human tumors such as colon adenocarcinomas. A protein on the bacteria (Fap2) binds to an inhibitory receptor called TIGIT expressed on the surface of natural killer cells and T cells, reducing their ability to kill bacteria-associated tumor cells in culture. Whether *F. nucleatum* plays a similar role in people with colon adenocarcinomas remains to be determined. — KLM

Immunity **42**, 344 (2015).

STRUCTURAL IMMUNOLOGY

Disarming a cellular defense system

Macrophages are cells that engulf and destroy foreign substances in a process called phagocytosis. Lee *et al.* now show how a bacterium from the *Yersinia* family, which includes the bacteria that causes bubonic plague, acts to disable phagocytosis. *Yersinia enterocolitica* injects a protein called YopO into macrophages. A crystal structure shows that YopO binds to single host actin proteins in a way that prevents them from adding to actin filaments that form the skeleton of the cell. Moreover, the complex sequesters and phosphorylates proteins required for remodeling the actin skeleton, probably preventing the remodeling required for phagocytosis. — VV

Nat. Struct. Mol. Biol. 10.1038/nsmb.2964 (2015).

MATERIALS SCIENCE

Patterned pockets for preparing particles

The functional properties of multiphasic micro- and nanoparticles are critically dependent on their geometry and chemistry.

PHOTO: DENNIS KUNKEL MICROSCOPY, INC./VISUALS UNLIMITED, INC.

ALSO IN *SCIENCE* JOURNALS

Edited by **Stella Hurtley**

EPIDEMIOLOGY

Mathematical modeling of infectious diseases

The spread of infectious diseases can be unpredictable. With the emergence of antibiotic resistance and worrying new viruses, and with ambitious plans for global eradication of polio and the elimination of malaria, the stakes have never been higher. Anticipation and measurement of the multiple factors involved in infectious disease can be greatly assisted by mathematical methods. In particular, modeling techniques can help to compensate for imperfect knowledge, gathered from large populations and under difficult prevailing circumstances. Heesterbeek *et al.* review the development of mathematical models used in epidemiology and how these can be harnessed to develop successful control strategies and inform public health policy. — CA

Science, this issue p. 1216

INNATE IMMUNITY

Innate immune receptor signaling, united

Innate immune receptors such as RIG-I, cGAS, and Toll-like receptors bind microbial fragments and alert the immune system to an infection. Each receptor type signals through a different adapter protein. These signals activate the protein kinase TBK1 and the transcription factor IRF3, which tells cells to secrete interferon proteins (IFNs) important for host defense. Liu *et al.* now report a common signaling mechanism used by all three types of innate immune receptor-adaptor protein pairs to activate IRF3 and generate IFNs. This is important because cells must regulate their IFN production carefully to avoid inflammation and autoimmunity. — KLM

Science, this issue p. 1217

ORGANOMETALLICS

Taking advantage of four for a nickel

Metal atoms change their oxidation state—i.e., lose or gain electrons—relatively easily. This is a major reason why metal compounds accelerate so many chemical reactions. Camasso and Sanford now report a straightforward way to prepare complexes of nickel in the +4 oxidation state, based on careful tuning of the coordination environment around the metal center (see the Perspective by Riordan). These complexes could prove useful in coupling carbon to oxygen, nitrogen, or sulfur, and complement more traditional nickel catalysts that operate in lower oxidation states. — JSY

Science, this issue p. 1218; see also p. 1203

CHEMISTRY

Using chemical design to avoid regrets

In response to public health concerns, the chemical bisphenol A (BPA) has been widely replaced with the related compound bisphenol S (BPS) in consumer products such as baby bottles. Yet recent studies have shown that BPS may also be harmful to human health. In a Perspective, Zimmerman and Anastas discuss how such "regrettable substitutions" may be avoided. They chart a progression via informed chemical substitutions designed to avoid toxicity and other hazards. — JFU

Science, this issue p. 1198

SYMPATHETIC COOLING

Highly charged ions in cold confines

High-energy irradiation can strip many electrons away from individual atoms, producing ions with charges of +10 or more. However, many of the interesting properties of such highly charged ions are hard to study or exploit under the extreme conditions needed to prepare them. Schmöger *et al.* cooled down argon ions with +14 charges from the megakelvin temperatures needed for their generation to millikelvin temperatures appropriate for high-precision spectroscopy. The method relies on sympathetic cooling by a cold sample of singly charged beryllium ions and is likely to be applicable to a broad range of other elements. — JSY

Science, this issue p. 1233

OCEANOGRAPHY

Connecting orbit to the ocean floor

The amount of magma erupted at mid-ocean ridges can be modified by periodic ice ages that alter sea level. Crowley *et al.* analyzed high-resolution ocean depth data across the Australian-Antarctic ocean ridge (see the Perspective by Conrad). The results revealed 23-, 41-, and 100-thousand-year periodicity. These periods are similar to the well-known Milankovitch cycles associated with ice ages that are triggered by changes in Earth's orbit. Decreasing sea levels decrease the overlying pressure, thereby increasing the amount of erupted magma. The cyclic nature of glaciations and sea level creates a series of spaced topographic highs along the sea floor. Thus, Earth's atmosphere and mantle are coupled on a glacial time scale. — BG

Science, this issue p. 1237; see also p. 1204

HUMAN PALEOECOLOGY

Pleistocene humans in tropical rainforest

The tropical rainforest environment is nutritionally poor and tricky to navigate as compared to open habitats. This poses challenges for human subsistence. There has been little evidence to suggest that human populations relied on rainforest resources before the start of the Holocene, 10,000 years ago. Roberts *et al.* analyzed earlier fossil human and animal tooth enamel from Sri Lanka. The diet of these humans suggests rainforest rather than open-habitat foraging. Thus, humans were effectively exploiting rainforests in Sri Lanka since at least 20,000 years ago throughout periods of considerable climatic and environmental flux. — AMS

Science, this issue p. 1246

PROTEIN STABILITY

The N-end rule finds a physiological function

The N-end–rule pathway for protein degradation is a canonical degradation pathway discovered in the 1980s. In recent years, studies have focused on finding novel variant pathways of N-end recognition. The "classical" pathway is blocked by N-terminal acetylation of the substrate. However, in yeast, N-terminal acetylation need not block degradation, because a second pathway can act on acetylated N-termini. But is this alternate pathway a major player in the physiology of mammals? Park *et al.* now confirm the existence of the alternate pathway in mammalian cells. Most notably, patient-derived point mutations thought to confer hypertension in humans affect susceptibility to this pathway for the encoded protein substrate, Rgs2. — SMH

Science, this issue p. 1249

ION CHANNELS

A sensitive regulator of cellular potassium

A class of potassium channels called K2P channels modulates resting membrane potential in most cells. The channels are

regulated by multiple ligands, including the antidepressant drug Prozac, as well as factors such as mechanical stretch and voltage. Dong *et al.* determined the structure of the human K2P channel, TREK-2, in two conformations and bound to a metabolite of Prozac. The structures show how ligand binding or mechanical stretch might induce switching between the states. Although both states have open channels, one appears primed for gating. A Prozac metabolite binds to the primed state and prevents conformational switching. K2P channels are not a target of Prozac, but their inhibition may contribute to side effects. — VV

Science, this issue p. 1256

SEPSIS

A new therapeutic target for sepsis

Infections can sometimes unleash powerful immune responses that careen out of control, leading to sepsis, organ failure, and death. Although antibiotics can help to quash the infection, sepsis patients also need therapies that will rein in the immune response. Weber *et al.* now identify one potential target, the secreted protein interleukin-3 (IL-3) (see the Perspective by Hotchkiss). In sepsis patients, higher serum concentrations of IL-3 were correlated with higher rates of mortality. In septic mice, IL-3 caused the immune system to produce large amounts of cells called monocytes and neutrophils, which secrete highly inflammatory proteins. Blocking IL-3 protected mice from sepsis-induced death. — KLM

Science, this issue p. 1260; see also p. 1201

STRUCTURAL BIOLOGY

Lighting up rhodopsin movement

One of the fastest signaling events is the eye's response to light, which is detected by the G protein–coupled receptor rhodopsin. In contrast to the majority of structural analyses that have been done with this and other G protein–coupled receptors, Malmerberg *et al.* determined light-induced conformational changes in rhodopsin in its native membrane environment. Within a few milliseconds, rhodopsin adopted a stable active conformation that was associated with the movement of portions of two adjacent transmembrane domains. These movements were considerably larger and implied a more extended conformational change in the light activation of rhodopsin than was suggested by crystal structures of activated rhodopsin. — NRG

Sci. Signal. **8**, ra26 (2015).

REVIEW SUMMARY

EPIDEMIOLOGY

Modeling infectious disease dynamics in the complex landscape of global health

Hans Heesterbeek,* Roy M. Anderson, Viggo Andreasen, Shweta Bansal, Daniela De Angelis, Chris Dye, Ken T. D. Eames, W. John Edmunds, Simon D. W. Frost, Sebastian Funk, T. Deirdre Hollingsworth, Thomas House, Valerie Isham, Petra Klepac, Justin Lessler, James O. Lloyd-Smith, C. Jessica E. Metcalf, Denis Mollison, Lorenzo Pellis, Juliet R. C. Pulliam, Mick G. Roberts, Cecile Viboud, Isaac Newton Institute IDD Collaboration

BACKGROUND: Despite many notable successes in prevention and control, infectious diseases remain an enormous threat to human and animal health. The ecological and evolutionary dynamics of pathogens play out on a wide range of interconnected temporal, organizational, and spatial scales that span hours to months, cells to ecosystems, and local to global spread. Some pathogens are directly transmitted between individuals of a single species, whereas others circulate among multiple hosts, need arthropod vectors, or persist in environmental reservoirs. Many factors, including increasing antimicrobial resistance, human connectivity, population growth, urbanization, environmental and land-use change, as well as changing human behavior, present global challenges for prevention and control. Faced with this complexity, mathematical models offer valuable tools for understanding epidemiological patterns and for developing and evaluating evidence for decision-making in global health.

ADVANCES: During the past 50 years, the study of infectious disease dynamics has matured into a rich interdisciplinary field at the intersection of mathematics, epidemiology, ecology, evolutionary biology, immunology, sociology, and public health. The practical challenges range from establishing appropriate data collection to managing increasingly large volumes of information. The theoretical challenges require fundamental study of many-layered, nonlinear systems in which infections evolve and spread and where key events can be governed by unpredictable pathogen biology or human behavior. In this Review, we start with an examination of real-time outbreak response using the West African Ebola epidemic as an example. Here, the challenges range from underreporting of cases and deaths, and missing information on the impact of control measures to understanding human responses. The possibility of future zoonoses tests our ability to detect anomalous outbreaks and to estimate human-to-human transmissibility against a backdrop of ongoing zoonotic spillover while also assessing the risk of more dangerous strains evolving. Increased understanding of the dynamics of infections in food webs and ecosystems where host and nonhost species interact is key. Simultaneous multispecies infections are increasingly recognized as a notable public health burden, yet our understanding of how different species of pathogens interact within hosts is rudimentary. Pathogen genomics has become an essential tool for drawing inferences about evolution and transmission and, here but also in general, heterogeneity is the major challenge. Methods that depart from simplistic assumptions about random mixing are yielding new insights into the dynamics of transmission and control. There is rapid growth in estimation of model parameters from mismatched or incomplete data, and in contrasting model output with real-world observations. New data streams on social connectivity and behavior are being used, and combining data collected from very different sources and scales presents important challenges.

All these mathematical endeavors have the potential to feed into public health policy and, indeed, an increasingly wide range of models is being used to support infectious disease control, elimination, and eradication efforts.

OUTLOOK: Mathematical modeling has the potential to probe the apparently intractable complexity of infectious disease dynamics. Coupled to continuous dialogue between decision-makers and the multidisciplinary infectious disease community, and by drawing on new data streams, mathematical models can lay bare mechanisms of transmission and indicate new approaches to prevention and control that help to shape national and international public health policy. ■

ON OUR WEB SITE

Read the full article at http://dx.doi.org/10.1126/science.aaa4339

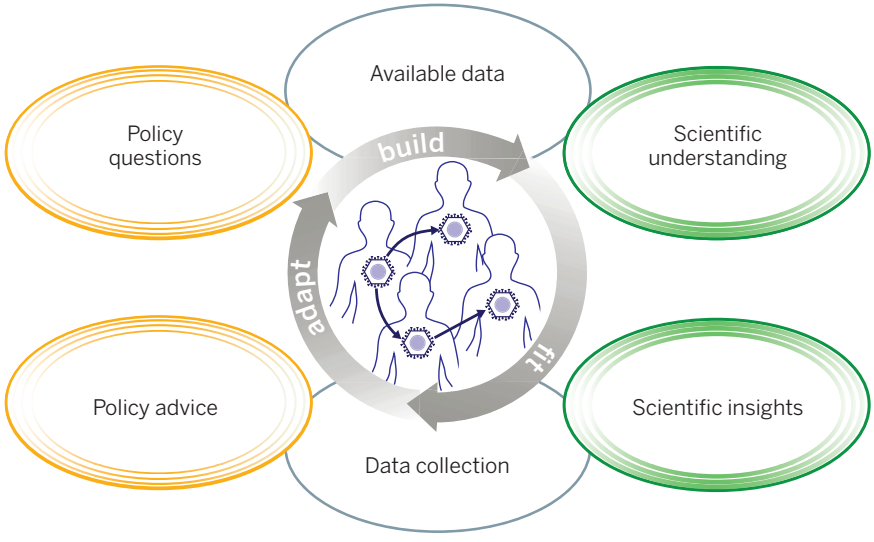

Modeling for public health. Policy questions define the model's purpose. Initial model design is based on current scientific understanding and the available relevant data. Model validation and fit to disease data may require further adaptation; sensitivity and uncertainty analysis can point to requirements for collection of additional specific data. Cycles of model testing and analysis thus lead to policy advice and improved scientific understanding.

The list of author affiliations is available in the full article online.
*Corresponding author. E-mail: j.a.p.heesterbeek@uu.nl
Cite this article as H. Heesterbeek *et al.*, *Science* **347**, aaa4339 (2015). DOI: 10.1126/science.aaa4339

REVIEW

EPIDEMIOLOGY

Modeling infectious disease dynamics in the complex landscape of global health

Hans Heesterbeek,[1*†] Roy M. Anderson,[2] Viggo Andreasen,[3] Shweta Bansal,[4] Daniela De Angelis,[5] Chris Dye,[6] Ken T. D. Eames,[7] W. John Edmunds,[7] Simon D. W. Frost,[8] Sebastian Funk,[4] T. Deirdre Hollingsworth,[9,10] Thomas House,[11] Valerie Isham,[12] Petra Klepac,[8] Justin Lessler,[13] James O. Lloyd-Smith,[14] C. Jessica E. Metcalf,[15] Denis Mollison,[16] Lorenzo Pellis,[11] Juliet R. C. Pulliam,[17,18] Mick G. Roberts,[19] Cecile Viboud,[18] Isaac Newton Institute IDD Collaboration[‡§]

Despite some notable successes in the control of infectious diseases, transmissible pathogens still pose an enormous threat to human and animal health. The ecological and evolutionary dynamics of infections play out on a wide range of interconnected temporal, organizational, and spatial scales, which span hours to months, cells to ecosystems, and local to global spread. Moreover, some pathogens are directly transmitted between individuals of a single species, whereas others circulate among multiple hosts, need arthropod vectors, or can survive in environmental reservoirs. Many factors, including increasing antimicrobial resistance, increased human connectivity and changeable human behavior, elevate prevention and control from matters of national policy to international challenge. In the face of this complexity, mathematical models offer valuable tools for synthesizing information to understand epidemiological patterns, and for developing quantitative evidence for decision-making in global health.

Thirty-five years ago, it was believed that the health burden of infectious diseases was close to becoming insignificant as hygiene, improved nutrition, drugs, and vaccines brought about a steady decline in overall mortality (*1*). In recent decades, however, it has become clear that the threat from serious infectious diseases will persist, and human mortality attributed to infection is projected to remain at current levels of 13 to 15 million deaths annually until at least 2030 (*2*). Successes in eradicating smallpox and rinderpest have been isolated events in a landscape of endemic and epidemic infections (*3*). Newly emerging infectious agents represent a continuing challenge—for example, HIV in the 20th century; more recently, severe acute respiratory syndrome (SARS) and Middle Eastern respiratory syndrome (MERS) coronaviruses; West Nile Virus; Nipah virus; drug-resistant pathogens; novel influenza A strains; and a major Ebola virus outbreak in 2014–2015. Most new infections enter the human population from wildlife or livestock, and the possibilities for emergence and spread in the coming decades are likely to increase as a result of population growth, increased urbanization and land changes, greater travel, and increased livestock production to meet demands from the world's expanding population (*4*–*8*). In our modern world of instant communication, the changing behavior of individuals in response to publicity about epidemics can have profound effects on the course of an outbreak (*9*, *10*). Phylogenetic data shed light on an additional layer of complexity (*11*), as will increased understanding of the human genome in relation to susceptibility, infectiousness, and its duration. At the same time, the development of effective new vaccines remains a difficult challenge, especially for antigenically very variable pathogens (e.g., HIV or falciparum malaria) and for pathogens that stimulate immunity that is only partly protective (e.g., *Mycobacterium tuberculosis*) or temporary (e.g., *Vibrio cholerae*).

In the face of this complexity, computational tools (Box 1) are essential for synthesizing information to understand epidemiological patterns and for developing and weighing the evidence base for decision-making. Here, we review the contribution of these tools to our understanding of infectious disease dynamics for public health by using representative examples and by ranging into current developments. We argue that to improve decision-making for human health and for sustaining the health of our food systems, experts on infectious disease dynamics and experts on prevention and control need to collaborate on a global scale. To succeed, quantitative analysis needs to lie at the heart of public health policy formulation.

Models and public health policy formulation

The value of mathematical models to investigate public health policy questions was recognized at least 250 years ago when, in 1766, Daniel Bernoulli published a mathematical analysis of the benefits of smallpox inoculation (then called variolation) (*12*). In the past 50 years, the study of infectious disease dynamics has grown into a rich interdisciplinary field. For example, decision-making for vaccination strategies increasingly depends on model analyses in which infection dynamics are combined with cost data (Box 2, Influenza: prevention and control). In recent decades, responses to major infectious disease outbreaks, including HIV, bovine spongiform encephalopathy (BSE), foot-and-mouth disease (FMD), SARS, and pandemic and avian influenza, have shown both the need for and capabilities of models (Box 3, HIV: Test and treat strategy). Model-based analysis of such outbreaks also continually brings improvements in methodology and data, emerging from the comparison of model prediction with observed patterns.

For infectious agents important to public health, a series of principles has emerged for modeling infection dynamics (Table 1 and Box 4). The basic reproduction number R_0, for example, is a central concept characterizing the average number of secondary cases generated by one primary case in a susceptible population. This concept highlights what must be measured to interpret observed disease patterns and to quantify the impact of selected control strategies (Fig. 1).

Two fundamental properties of the world that shape infectious disease dynamics make computational tools key for understanding reality. The world is essentially a stochastic and highly

[1]Faculty of Veterinary Medicine, University of Utrecht, Utrecht, Netherlands. [2]School of Public Health, Imperial College, London, UK. [3]Roskilde University, Roskilde, Denmark. [4]Georgetown University, Washington, DC, USA. [5]MRC Biostatistics Unit, Cambridge, UK. [6]WHO, Geneva, Switzerland. [7]Centre for the Mathematical Modelling of Infectious Diseases, London School of Hygiene Tropical Medicine, London, UK. [8]University of Cambridge, Cambridge, UK. [9]School of Life Sciences, University of Warwick, UK. [10]School of Tropical Medicine, University of Liverpool, UK. [11]Warwick Mathematics Institute, University of Warwick, Coventry, UK. [12]Department of Statistical Science, University College London, London, UK. [13]Department of Epidemiology, Johns Hopkins Bloomberg School of Public Health, Baltimore, MD, USA. [14]Department of Ecology and Evolutionary Biology, University of California, Los Angeles, CA, USA. [15]Department of Zoology, University of Oxford, Oxford, UK, and Department of Ecology and Evolutionary Biology, Princeton University, Princeton, NJ, USA. [16]Heriot-Watt University, Edinburgh, UK. [17]Department of Biology–Emerging Pathogens Institute, University of Florida, Gainesville, FL, USA. [18]Division of International Epidemiology and Population Studies, Fogarty International Center, NIH, Bethesda, MD, USA. [19]Institute of Natural and Mathematical Sciences, Massey University, Auckland, New Zealand.
***Corresponding author. E-mail: j.a.p.heesterbeek@uu.nl**
†Authors, apart from first and last author, are in alphabetical order. ‡All authors are members of this collaboration. §In addition to the authors listed above, this collaboration includes: Nimalan Arinaminpathy,[1] Frank Ball,[2] Tiffany Bogich,[3] Julia Gog,[4] Bryan Grenfell,[3] Alun L. Lloyd,[5] Angela Mclean,[6] Philip O'Neill,[2] Carl Pearson,[11] Steven Riley,[1] Gianpaolo Scalia Tomba,[12] Pieter Trapman,[13] James Wood[7]. Affiliations: [1]Imperial College, London, UK. [2]University of Nottingham, Nottingham, UK. [3]Princeton University, Princeton, NJ, USA. [4]University of Cambridge, Cambridge, UK. [5]North Carolina State University, Raleigh, NC, USA. [6]University of Oxford, Oxford, UK. [11]University of Florida, Gainesville, FL, USA. [12]University of Rome "La Sapienza," Rome, Italy. [13]University of Stockholm, Stockholm, Sweden.

nonlinear system. The nonlinearity derives not only from the complex interaction between factors involved in transmission, but also from the influence that the infection process has on the distribution of important characteristics at various temporal and spatial scales. This effect is seen in the age-related nature of infection and mortality in HIV changing the age distribution of the population, and in previous exposure to strains of influenza altering the distribution of influenza susceptibility. Such feedback mechanisms contribute to the nonlinearity of infection processes. Nonlinearity also leads to counterintuitive phenomena (Fig. 2) and prevents simple extrapolation of experience from one situation to another, such as when deciding whether to implement a vaccination policy in different countries (Fig. 1). Mathematical tools, relating to data and processes on a large range of interacting scales, have become essential to explore, anticipate, understand, and predict the effects of feedbacks within such complex systems, including changes caused by intervention.

Current and future opportunities for models in public health

Over the past decade, key public health questions, ranging from emergence to elimination, have posed a range of challenges for modeling infectious disease dynamics, many of which rely on leveraging disparate data sources and integrating data from a range of scales from genomics to global circulation. Given commonalities in processes across pathogens, progress made in one area can lead to advances in another. Progress in the areas described above all build on and inform each other, making this a dynamic time for research in the discipline (*13*). A few themes are chosen to illustrate current trends in model development and public health application.

Real-time outbreak modeling: The Ebola 2014–2015 outbreak

The 2014–2015 outbreak of Ebola in West Africa serves to highlight both opportunities and challenges in modeling for public health. In the initial phase of this outbreak, real-time estimates of the reproduction number or simple exponential extrapolation (*14*) allowed short-term predictions of epidemic growth that were used, for example, to plan for necessary bed capacity. Quantitative phylogenetic tools applied to samples from initial victims provided important estimates of the origin of the outbreak (*15*). Early mechanistic models that explicitly took into account the roles played by different transmission routes or settings were informed by analysis of earlier outbreaks (*16*, *17*). When the failure to contain the epidemic with methods successful in previous outbreaks led to a scale-up of capacity driven by international aid, such models were used to assess the impact of, for example, reducing transmission at funerals (17) and whether the construction of novel types of treatment centers could end up doing more harm than good. Ensuring that the most effective combinations of interventions were implemented required close and fast interaction between modelers and policymakers (*18*). Looking forward, models are now used to help clinical trial design and inform a debate on the optimal deployment of initially scarce Ebola vaccines, once such vaccines become available.

With the opportunities of real-time modeling for public health come specific challenges. The imperative to produce reliable and meaningful analysis for those treating infected people has to be balanced against the pressures and delays of scientific publication. In an ongoing outbreak, data can be patchy and reporting delayed, and different data sources are not always synthesized. When the Ebola outbreak expanded explosively in the summer of 2014, data were often lacking on the effect on transmission dynamics of the various control measures that operated simultaneously in the hectic circumstances of the most severely hit areas. In any emerging epidemic, underreporting is a critical challenge for ongoing assessment of this epidemic and has had enormous impact on predictions of outbreak size, but also of outbreak impact—for example, in terms of the case-fatality ratio (the proportion of cases that lead to death). Early in any outbreak, this estimate of severity can suffer from imprecise information on both the numerator (if not all deaths due to the infection are identified as such; for example, because health services are overwhelmed caring for the sick) and the denominator (if cases are not reported or, conversely, noncases get reported as cases if they are not laboratory-confirmed). This caused problems early in the H1N1 influenza outbreak first reported in in Mexico in 2009, as well as in the current Ebola outbreak. Although level of underreporting can be estimated from retrospective serological studies, it is usually not identifiable in real-time data.

These limitations make it almost impossible to make reliable long-term predictions. Thus, modeling results are often based on scenarios in which a pathogen spreads unaltered by behavioral changes or the public health response. This rarely reflects reality, especially in such a devastating outbreak as Ebola, where the situation constantly changes owing to growing awareness in the community, as well as national and international intervention. Careful communication of findings is key, and data and methods of analysis (including code) must be made freely available to the wider research community. Only in this way can reproducibility of analyses and an open exchange of methods and results be ensured for maximal transparency and benefit to public health.

Emergence of novel human pathogens

There is an ever-present hazard that novel human pathogens emerge from livestock and wild

Box 1. Quantitative tools in infectious disease dynamics.

Here, we use the words "computational tools" loosely. In infectious disease dynamics, there is a broad range of relevant quantitative tools, and we refer to the entire collection. It comprises statistical methods for inference directly from data, including methods to analyze sequencing and other genetic data. This leads to estimates of important epidemiological information such as length of latency, incubation and infectious periods and their statistical distributions, inferred transmission chains and trees early in outbreaks, the risks related to various transmission routes, or estimates of rates of evolution. Mathematical models in the strict sense refer to mathematical descriptions of processes thought to be associated with the dynamics of infection—for example, in a population or within an individual. Such models take many forms, depending on the level of biological knowledge of processes involved and data available, and depending on the purpose.

Several classes of model are used, spanning the spectrum of information available. At one end of the range are detailed individual-based simulation models, where large numbers of distinct individual entities (with their own characteristic traits such as age, spatial location, sex, immune status, risk profile, or behavior pattern) are described in interaction with each other, possibly in a contact network, and with the infectious agent. At the other end are compartmental models where no individuals are recognized, but only states for individuals (for example: susceptible, infectious, immune) aggregated into compartments where everyone has the same average characteristics and where interaction is typically uniform (everybody interacts with everybody else). Such models do not describe the disease history of single individuals, but rather the time evolution of aggregated variables, such as the number of individuals that are currently susceptible.

Mathematical models can have both mechanistic parts in their description, based on assumptions about biological mechanisms involved, and more phenomenological parts, where there is a statistical or presumed relation between variables, without clear assumptions from which this relation can be derived. An example of the former is the assumption of mass action to describe interaction between individual hosts; an example of the latter is an empirical relation between the length of an infectious period in a mosquito and environmental temperature.

For infectious disease dynamics, our world is clearly stochastic, in that chance events play a role in many of the processes involved. Certainly at lower levels of biological aggregation, chance dominates—for example, in infection of individual cells or in contacts individual hosts make. At higher aggregation levels, many cells or individuals interact, and chance effects may average out to allow deterministic descriptions. There are purely stochastic models, purely deterministic models, and models that are mixed. It is important to point out that, even though the world is stochastic, stochastic descriptions are not by definition better than deterministic descriptions. Both are still models of reality, and the fact that chance plays a role may have a far less significant influence on model outcome and prediction than choices made in the relations between ingredients and variables.

Areas of rapid growth are statistical and numerical methods and tools to estimate model parameters from, often scarce, mismatched or incomplete data, and to contrast model output with real-world observations.

mammal and bird reservoirs. Research on potential emerging zoonoses draws on concepts from across the spectrum of infectious disease dynamics, disease ecology, microbiology, and phylogenetic analysis. Particular challenges include estimating human-to-human transmissibility against a backdrop of ongoing zoonotic spillover, detecting anomalous outbreaks, and assessing the risk that more dangerous strains may arise through pathogen evolution.

The recently identified gap in methodology for zoonoses with weak human-to-human transmission (*6*) is being filled with new approaches for estimating R_0 and other transmission-related quantities from subcritical outbreak data (*19*–*21*). These studies address key public health concerns, but rely on strong assumptions regarding the quality and completeness of case observations. Better information on surveillance program efficacy could be gained through serological surveys (where blood and saliva samples reveal evidence of past and present infections) or sociological study, and modeling studies can help to design and characterize efficient surveillance programs (*22*). Given the predominance of zoonotic pathogens among emerging infections, models for transmission dynamics and evolution in multispecies ecosystems and food webs (consisting of host species and nonhost species interacting ecologically and epidemiologically) are a crucial area for future development (*6*, *23*). The greatest challenge—and the greatest prize—in modeling emerging zoonoses is to assess which diseases pose the most risk to humans and how these might change over time and in different localities (*24*). Such tasks, which will join molecular studies to experimental infections to epidemiological and ecological surveys, will drive empirical and theoretical efforts for decades to come.

The rising availability of pathogen genome sequence data, coupled with new computational methods, presents opportunities to identify with precision "who infects whom" and the networks of infection between humans and reservoirs (*25*). Full realization of this potential, though, will require denser and more systematic whole-genome sampling of pathogens coupled with associated epidemiological data, as well as baseline information on genetic diversity and evolutionary rates, especially in animal hosts (*26*).

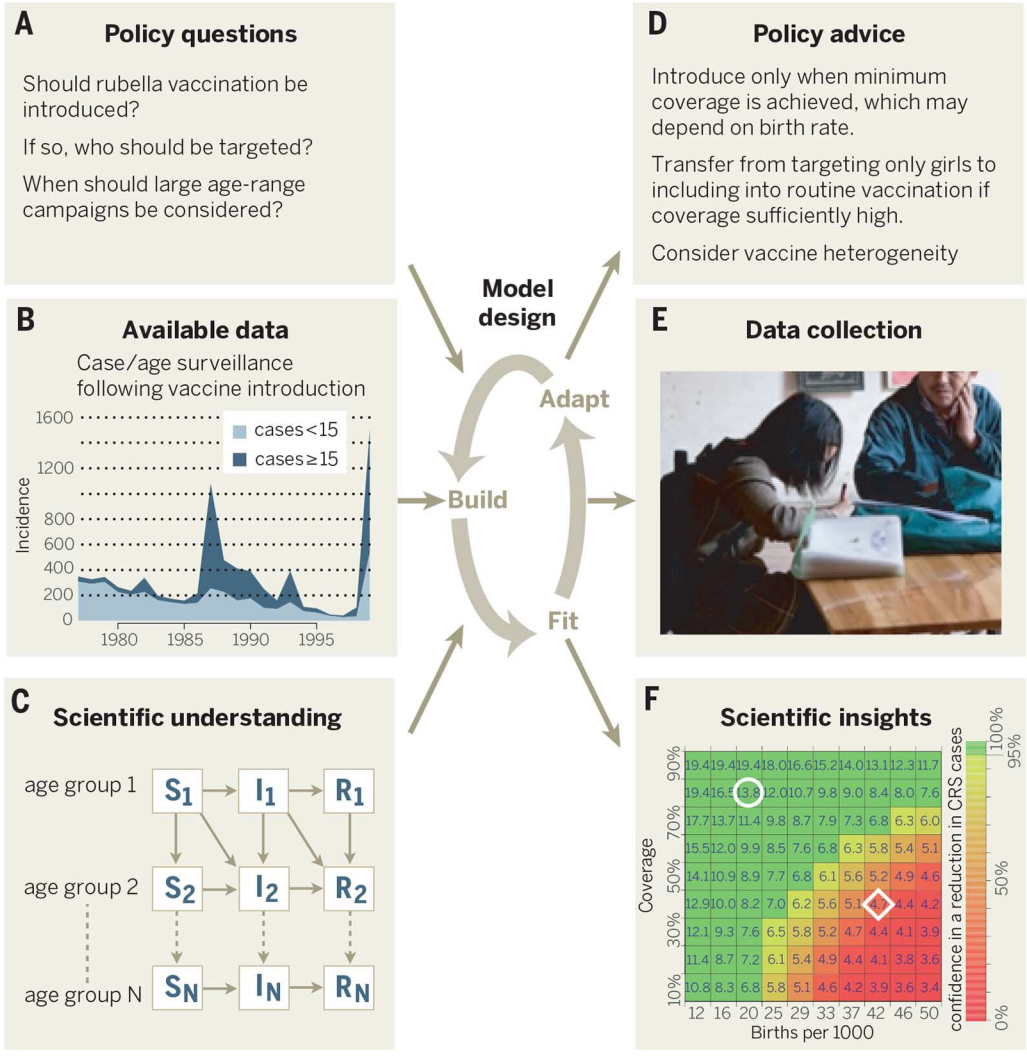

Fig. 1. Modeling for public health exemplified by rubella. (**A** to **F**) Policy questions are formulated; available data are brought to bear on the question. In this example, the incidence of rubella is shown following the introduction of vaccination in individuals under 15 or 15+ years of age in Costa Rica (*127*). Application of a nonlinear age-structured SIR model (see Box 4) to these circumstances led to the collection of key missing data. In the bottom right-hand plot, each square depicts a combination of birth rate and infant vaccine coverage reflecting different countries (e.g., Somalia depicted by a diamond and Nepal by a circle), colored by expected effect on congenital rubella syndrome (CRS) in newborns, related to local R_0 (*128*). This translates into confidence that routine vaccination is likely to reduce the public health burden caused by CRS in Nepal (green), but not in Somalia (red).

Pathogen evolution and phylodynamics

As pathogen genetic data become increasingly available, modelers are finding ways to synthesize these new data streams with more traditional epidemiological information in phylodynamic tools (*27*, *28*). However, current frameworks employ compartmental epidemiological models, which do not make efficient use of individual-level epidemiological data. Although sampling theory is well developed for standard surveillance data, the relationship between a set of pathogen sequences and the phylogeny inferred from a population sample is more complex (*11*). Many-to-one mapping possibilities between, on the one hand, combinations of epidemiological, immunological, and evolutionary processes shaping sequences and, on the other hand, the inferred phylogeny, demand the integration of diverse data sources and an increased focus on systematic sampling.

Phylodynamic studies to date have largely focused on fast-evolving RNA viruses, driven by the large amount of data generated for clinical [e.g., hepatitis C virus (HCV) or HIV)] or surveillance (e.g., influenza) purposes (*11*). Replicating these efforts on an expanded array of pathogens, including DNA viruses, bacteria, fungi, protozoa (e.g., malaria), and helminths, is a promising avenue for future research (*29*). It is of particular importance in the context of the evolution and spread of drug-resistant variants and vaccine escape mutants. However, genome-wide pathogen data also present challenges, in particular in relation to accommodating recombination, reassortment, and mobile genetic elements. Analysis of bacterial genomes usually considers only those genes that are shared across taxa, but there are good reasons to believe that noncore

genes play an important role in bacterial evolution, including the evolution of antibiotic resistance (30).

Although sequence data are extremely valuable, to link these data fully to disease dynamics, it will be important to determine how sequence changes affect functions related to pathogen fitness, such as replication rate, transmissibility, and immune recognition. Molecular epidemiological studies often treat pathogen genetic variation as simply reflecting the underlying transmission process, whereas in reality such variation may play an important role in determining transmission dynamics, as exemplified by escape from herd immunity by influenza A virus (31).

"Deep" sequencing of pathogens within individual hosts generates information on within-host diversity, resulting from evolution within the host (often in response to drug treatment), or multiple infections. To tackle within-host diversity, models that embed pathogen evolution within a transmission tree are needed. Such models, which cross the within- and between-host scales, are only just becoming analytically and computationally feasible despite being proposed several years ago (32). Similarly, although progress has been made in scaling inference from genes to genomes (33), scaling inference to large numbers of sequences is lagging far behind.

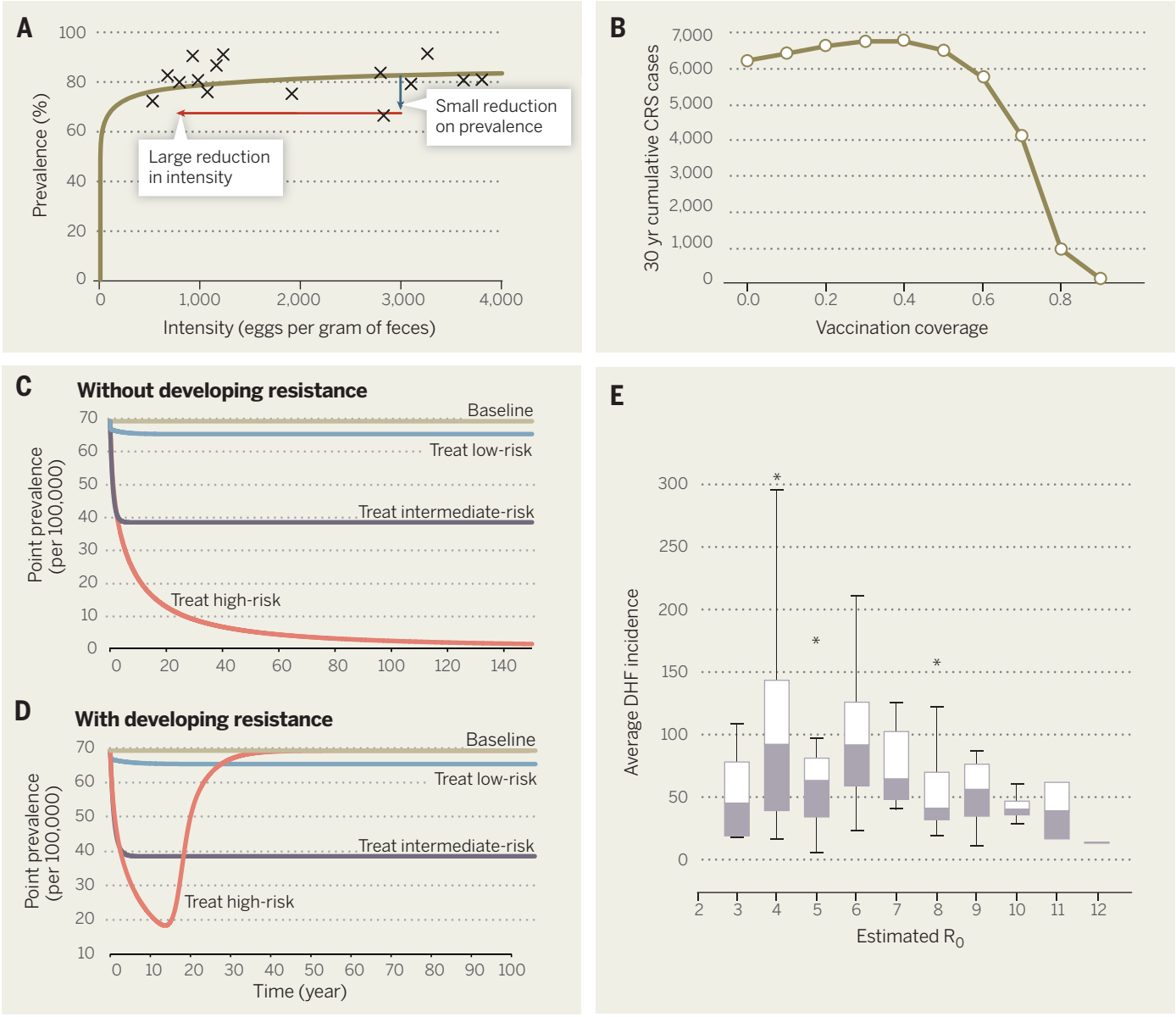

Fig. 2. Examples of counterintuitive effects of nonlinear infection dynamics. (**A**) Nonlinear interaction between prevalence of a helminth infection and infection pressure (as measured by the mean intensity of existing infections) means that control measures must have a disproportionately large impact on intensity before prevalence is reduced. This effect is predicted by a mathematical model (solid line) and corroborated by field data (crosses) (129). (**B**) Nonlinear relation between total number of cases of congenital rubella syndrome (CRS) and rubella vaccine coverage, showing that suboptimal levels of vaccine coverage cause worse health outcomes than no vaccination [adapted from (130)]. The line shows model predictions; similar effects have been documented for real rubella control situations (131). (**C** and **D**) Modeling results of rebound of gonorrhea transmission with different treatment strategies without (C) and with (D) antimicrobial resistance developing [adapted from (132)]. In the presence of resistance, focusing treatment on the high-risk core group leads to an increase in prevalence approaching that of untreated baseline prevalence, after an initially strong decline for more than a decade. (**E**) Box plot from field data of a nonlinear relation between R_0 for dengue transmission and average dengue hemorrhagic fever (DHF) incidence across Thailand, showing that control measures that reduce R_0 may paradoxically increase cases of DHF [adapted from (133)].

Multiple infections

Infectious disease epidemiology evolved by focusing on interactions between a single host species and a single infectious agent. It is becoming increasingly clear that multiple agents simultaneously infecting the same host populations and individuals appreciably add to the public health burden and complicate prevention and control. Coinfections in relation to HIV— for example, tuberculosis and HCV—or coinfection of different strains of influenza A virus raise important public health and evolutionary issues. Multiple agents infecting the same host individual have been shown to influence each other by increasing or decreasing susceptibility and/or infectivity of that individual, thereby influencing the population dynamics of these agents in ways that we have yet to explore and understand (*34*, *35*).

Multiple infections of the same individual with closely related pathogens occur when infection elicits no immunity, or only a partial immune response. Macroparasites, including many of the important human helminth infections, are good examples of pathogens that evade human immune responses and cause repeated infection of the same host (*36*). Biological mechanisms giving rise to such multiple infections include sequential reinfections caused by antigenic drift in influenza, antigenic variation in respiratory syncytial virus (RSV), and waning (slow loss of) immunity in pertussis, while lack of cross-protection in many colonizing microparasites— for example, pneumococcus and human papilloma virus (HPV)—allows for multiple concurrent infections. Although the existence of reinfections is a clinical fact, population-level data are scarce as reinfections are often subclinical and individual-based longitudinal infection histories are often only anecdotal. Results from new analytical approaches relating to deep sequencing and neutralization tests covering multiple antigens are being utilized (*37*).

The immunodynamics of influenza have clear policy implications for the identification of high-risk groups in connection with pandemic planning (*38*), while the dynamics of waning immunity are key to the current concerns about immunization level for pertussis (*39*). Multivalent vaccines covering only a targeted subset from the circulating strains of pneumococcus and HPV pose important new applied problems (*40*). The spread of recombinant viruses implies the existence of multiple infections. One example is the Sydney 2012 strain of norovirus, but how this can occur in such an acute infection remains to be understood, as the time window for multiple exposures is limited, unless subclinical or environmental reservoirs of infection are important. Mathematical models could help to explore how, for example, such subpopulations may contribute to the dynamics of multiple infections.

Behavior of hosts

Human behavior is a fundamental determinant of infectious disease dynamics, whether by affecting how people come in contact with each other, vaccination coverage, reporting biases, or adherence to treatment. Traditional epidemic models have tended to ignore heterogeneity in contact behavior [although early HIV models addressed heterogeneity in sexual behavior by necessity (*41*)]. Increasing sophistication of contact network models (*42*), together with data on epidemiological contacts, creates opportunities for understanding and controlling transmission at a fundamental level (*43*) and opens up the possibility of independent study of relevant social factors (*10*). Recent years have seen exciting developments in the measurement of contact patterns and "who might infect whom" through advances in individual electronic identification technology. This is a promising avenue for linking pathogen genetic data and human behavior.

Contact patterns are not static and can shift during outbreaks as individuals change their behavior in response to perceived risk and public health interventions (*44*). Modeling has illuminated this process—for example, by the incorporation of peer influence on vaccination behavior into models of infectious disease dynamics (*45*, *46*). Analysis of data from online social networks has also created promising opportunities to validate such approaches with empirical observations (*47*, *48*).

Movement and travel are tightly linked to the spread of infection and have been explored through models to highlight commuting and agricultural migration driving local disease transmission (*49*) and global disease patterns through air travel (*50*). These processes are now being investigated to gain insights into the more complex case of vector-borne diseases, such as malaria and dengue, where both host and vector movement

Box 2. Influenza: prevention and control.

Human influenza—pandemic and seasonal—remains a major issue in public health owing to the continued emergence of novel genetic strains, and one where models have successfully addressed questions from basic biology to epidemiology and health policy. In recent years, modeling and other quantitative analysis has been used to study at least three major issues: pandemic preparedness and mitigation strategies (*84*–*89*), rethinking vaccination strategies for seasonal influenza (*70*), and improved methods in phylodynamics and influenza strain evolution (*11*). Recent models of influenza fitness have also been developed to predict viral evolution from one year to the next, providing a principled and more precise method for the vaccine selection required every year (*90*).

For seasonal influenza, models have played a key role in providing the scientific evidence base for vaccination policy, making use of the information in multiple, often unavoidably biased, data sources such as syndromic time series, vaccine coverage and efficacy, economic costs, and contact patterns in the population. For example, a combined epidemic and economic model was fitted to fine-grained data from many sources to describe the dynamics of influenza in the United Kingdom, and the influence of previous vaccination programs (*70*). With confidence in the model's predictions based on its ability to capture past patterns, it was used to look at alternative vaccination strategies and led to a new national policy to vaccinate school-age children (*91*). Targeting those individuals most likely to spread the virus, rather than only those most likely to suffer the largest morbidity, is a marked departure from established practice in the UK and is currently under consideration elsewhere (*92*).

Box 3. HIV: test and treat.

Mathematical modeling has played a central role in our understanding of the HIV epidemic, and in informing policy from the outset of our recognition of the pandemic (*93*). Some of the many insights include a model-based analysis of viral load data from inhibition experiments, which revealed the rapid and ongoing turnover of the within-host viral population (*94*), and the use of phylogenetic models to show that the HIV pandemic did not emerge in the 1980s, but had its roots in the early 20th century (*95*).

A key contribution of mathematical modeling has been to identify when viral transmission occurs over the course of infection, which determines the potential to halt spread by various measures. Models have shown that transmission of HIV depends on the epidemic phase and the sexual behavior of the population, and a large proportion of transmissions may occur late in infection (*96*). Model-based inference in the Netherlands also suggested that the effective reproduction number (Box 4) had fallen below 1 due to a combination of low-risk behavior and a very effective diagnosis and treatment program (*97*). The debate was transformed in the mid-2000s, when eradication of HIV through a "test and treat" strategy was hypothesized (*98*, *99*). Subsequent trial results showing that antiretroviral treatment (ART) of HIV-positive individuals could practically eliminate transmission within sexual partnerships when the index case is treated (*100*) have further supported the role of treatment as prevention. Although these findings have not dispelled concerns about transmission early in infection (*93*), or about extra-couple transmission (*101*), it is suggested that high population coverage of ART may have reduced the incidence of HIV infection in rural KwaZulu-Natal, South Africa (*102*).

These findings, combined with the prospect of cheaper, more effective drugs and delivery structures, underpin UNAIDS' goal of "zero new infections" for HIV and the initiation of a multi-million dollar cluster-randomized trial (*103*), which will have its outcome assessed against model predictions. In the meantime, the scientific discussion of the effectiveness of ART in preventing transmission continues, sparked by studies that fail to show a decline in incidence after increased treatment (*104*). Such debates are essential to elucidate areas for improvement of the models used and data needs for such improvement, and to highlight methodological limitations (*105*).

can interact to drive local (51) and large-scale dynamics (52).

Elimination and eradication

Modeling has long provided support for elimination efforts: Vector control (53), critical community size (54), herd immunity, and critical vaccination threshold (55, 56) were all powerful insights from models framed in relatively simple and homogeneous terms. Subtleties and complexities in many current eradication programs, as well as the availability of novel data sources, have called for a range of extensions in the theory. As we approach elimination targets, disease dynamics have changed in ways that were largely predicted by models, but also in unanticipated ways as a result of ignorance about key epidemiological processes (3).

Incentives for control efforts also change, both at the individual level [passive or active refusal to participate can develop (57)] and at the country level (58). This reinforces the call for development of models of human behavior and its interaction with infectious disease dynamics (9)

Table 1. Principles for modeling infection dynamics. As different infections have become the focus of public health attention, the modeling community has responded by developing improved concepts and methods. The table concentrates on the period since 1950. The first column lists the classes of infection, and the second column lists factors whose importance to infection dynamics became particularly clear in relation to those infections; the third and fourth columns highlight concepts and methods that were developed in response. For each row, only a few typical references are given. Many factors, concepts, and methods are relevant, in current use, and in continual development for much larger classes of infectious agents.

Motivating studies	Important factors	Concepts	Methods
Malaria [1910s, 1950s onwards, (53, 106, 107)]	Transmission via insect vectors; nonlinear dependence of transmission on mosquito biting rate; influence of environmental and climatic variables.	Threshold for control, basic reproduction number.	Models with two host species (host-vector models); using models to support and guide field campaigns; relating models to field data.
Childhood infectious diseases, e.g., measles. [1950s onwards, (54, 108)]	Immunizing infections; spatial and temporal heterogeneity; demography; age structure; household structure.	Critical community size and herd immunity; periodic outbreaks; fade out; vaccine efficacy.	*SIR* models; age-structured models; models with periodic forcing; spatial and stochastic models; metapopulation models; time-series models.
Macroparasites. [1970s onwards, (108)]	Clumped infections, multistrain and multispecies infections, cross immunity, concurrent infections.	Consequences of overdispersed distribution of parasite load (Fig. 1)	Stochastic models, approximations including hybrid models and moment closure.
Sexually transmitted infections, e.g., HIV. [1980s onwards, (108, 109)]	High/low risk groups; nonrandom contact structure; partnerships; within-host strain diversity and evolution; time scale.	Incubation and infectious period distribution; core group; next-generation matrix and operator; partnership dynamics.	Statistical methods (e.g., back calculation); models with (dis)assortative mixing; pair-formation models; within-host dynamic models.
Veterinary outbreaks, e.g. BSE and FMD. [1990s onwards, (110, 111)]	Fixed spatial locations with changing contact networks.	Local versus long-range transmission; spatial intervention (ring vaccination/culling); conflict of priorities at different scales.	Individual-based models and spatial simulations (FMD); data-driven real-time modeling; inference of transmission trees.
Novel emerging infections, e.g., SARS, Nipah virus, MERS. [2000 onwards, (6, 19, 112–115)]	Behavior change; global interconnectedness and international cooperation in control; responses in absence of biomedical measures; animal reservoirs.	Zoonotic spillover; stuttering chains; importance of index case; superspreaders; unobserved dynamics in an animal reservoir; supershedding	Contact tracing; modeling international spread and control; quarantine and case isolation; individual heterogeneity in infectiousness, incubation, and latency period.
Influenza, including avian influenza. [Present, (27, 28, 116–118)]	Distribution of prior immunity; within-population and species strain differences, virus evolution and interaction; role of wildlife and farm animals.	Pandemics; spillover between wild birds and farmed birds; phylodynamics.	Interaction between immunological and epidemiological dynamics; integrating phylogenetic and epidemic methods and models.
Vector-borne diseases, e.g., dengue, malaria. [Present, (119-122)]	The influence of climate and environment on vector and pathogen development; animal reservoirs; interaction between strains within-host and between-host.	Dilution effect and role of biodiversity in infectious disease dynamics; reemerging infections.	Evolutionary impact of vaccines/other interventions; synthesis of data from ecology and epidemiology; elimination modeling; statistical modeling of environmental vector suitability.
Bacterial infections, e.g., pneumococcal disease, MRSA, and tuberculosis. [Present, (39, 123–126)]	Antibiotic/drug resistance; adaptive dynamics.	Vaccine effectiveness; interacting natural immunity and vaccine boosting.	Modeling interacting and emerging strains; stochastic models in small populations.

potentially drawing on new data sources from social media (59, 60), as well as for models that can capture national and nongovernmental motivations, interactions, and competition, economical or otherwise. Long-term control puts pathogens under strong selection for resistance, calling for evolution-proof control methods (61) and novel vaccine technologies and their optimized delivery (62).

Finally, since the era of smallpox eradication, patterns of global disease circulation have changed radically. Human mobility and migration are increasing global connectivity, strengthening the need for cooperation and international synchronization of efforts (as illustrated by polio). Techniques for analysis of novel data sources are again key here; e.g., mobile phone records provide unique opportunities to understand disease source-sink dynamics (52).

Computational statistics, model fitting, and big data

By definition and design, models are not reality. The properties of stochasticity and nonlinearity strongly influence the accuracy of absolute predictions over long time horizons. Even if the mechanisms involved are broadly understood and relevant data are available, predicting the exact future course of an outbreak is impossible owing to changes in conditions in response to the outbreak itself, and because of the many chance effects in play. These stochastic effects dominate developments in situations with relatively few infected individuals that occur at emergence, approaching the threshold for sustained host-host spread, or approaching elimination and eradication. This makes it virtually impossible to predict which infectious disease agent is going to emerge and evolve next and where, or to predict when and where the next or last case in an outbreak will occur. There is, typically in complex systems, a fundamental horizon beyond which accurate prediction is impossible. The field has yet to explore where that horizon is and whether computational tools and additional data (and if so which data) can stretch predictions to this limit. In contrast, "what-if" scenarios for public health intervention can provide qualitative (and increasingly semiquantitative) insight into their population consequences.

With growing applications in public health, there is an increasing demand to validate models by making model predictions consistent with observed data. The development of ever-more-powerful computers is accompanied by new techniques utilizing this power, notably for statistically rigorous parameter estimation and model comparison. Techniques such as Markov chain Monte Carlo (MCMC) have become firmly established tools for parameter estimation from data in infectious disease models [e.g., (63)], and Monte Carlo based methods will play a pivotal role in addressing the challenges that lie in reconciling predictions and observations (64, 65). Other techniques, such as so-called particle filters, approximate Bayesian computation, emulation, and their combinations with MCMC [e.g., (66)], are rapidly developing and allow stochastic models that explicitly account for incomplete observations to be matched to time series of cases, giving insights into scenarios as diverse as cholera in Bangladesh (67) and influenza (68, 69). The need to integrate multiple data sources (70, 71), as well as to include uncertainty in model parameters and/or structure, has driven the use of Bayesian approaches.

Although the rapid expansion of infectious disease models and their application over the past decade has coincided with an increase in open access data sets available from a variety of sources, progress in data capture needs to be accelerated. Although some of these technologically advanced data streams have been incorporated into models—for example, to track the incidence of influenza in the United States (72), to elucidate the spatial dynamics of measles and malaria in Africa (53, 73), and to chart the spread of dengue globally (74)—much more remains to be done to leverage data collected from different sources (e.g., demographic, genetic, epidemiological, treatment, and travel patterns) and at different temporal and spatial scales.

Concluding remarks

Infectious diseases are an important frontier in public health, and their prevention and control call for global, rather than national or regional, coordinated efforts (75–78). The success of smallpox and rinderpest eradication campaigns shows the possibilities; the global spread of newly emerged pathogens (recently avian influenza strains and MERS coronavirus), the difficulties in curbing the spread of antibiotic resistance, the upsurge of polio toward the "end-phase" of its eradication, and the recent unprecedented spread of Ebola virus, are examples that show the need for international coordination and collaboration. Nonlinearity in infectious disease dynamics and global connectivity cause suboptimal national decisions on control and prevention to have regional and even global repercussions.

Given the mismatch with regions where most expertise on infectious disease dynamics is concentrated, it is important to empower local scientists and policy-makers, in regions where the burden of disease is heaviest, about the problems facing their own countries and the consequences of local actions. It is essential to make expertise, data, models, statistical methods, and software widely available by open access. There are several initiatives (e.g., Thiswormyworld.org, Garkiproject.nd.edu, EDENextdata.com, the Humanitarian Data Exchange (HDX), and the Malaria Atlas Project), but more needs to be done. Modeling tools and software for data analysis are beginning to become open source, such that findings can be replicated, additional scenarios can be evaluated, and others can incorporate methods for data analysis or simulation. Ultimately, sharing models guarantees more

Box 4. Some fundamental terms and concepts.

- **susceptible**: individual who is at risk of becoming infected if exposed to an infectious agent.
- **basic reproduction number, R_0**: average number of infections caused by a typical infected individual in a population consisting only of susceptibles; if $R_0 > 1$, the infectious agent can start to spread.
- **effective reproduction number, R_e**: average number of infections caused by a typical infected individual when only part of the population is susceptible; as long as $R_e > 1$, the agent can continue to spread.
- **herd immunity**: state of the population where the fraction protected is just sufficient to prevent outbreaks ($R_e < 1$).
- **critical elimination threshold, p_c**: proportion of the susceptible population that needs to be successfully protected—for example, by vaccination—to achieve herd immunity; $p_c = 1 - 1/R_0$ is a rule of thumb from models when hosts are assumed to mix randomly.
- **force of infection**: per capita rate at which susceptible individuals acquire infection.
- **final size**: fraction of the initial susceptible population that eventually becomes infected during an outbreak.
- **prevalence**: proportion of the population with infection or disease at a given time point.
- **superspreader/supershedder**: infected individual that produces substantially more new cases than the average because of greater infectiousness, longer duration of infectiousness, many more transmission opportunities and contacts, or combinations of these. Even when the average R_0 is relatively small, these individuals have large effects on outbreaks.
- **metapopulation**: collection of populations, separated in space, but connected through movement of individuals.
- **critical community size**: minimum number of individuals in a population that allow an infectious agent to persist without importation of cases.
- **case fatality ratio**: proportion of symptomatic infections that result in death.
- **SIR model**: most basic model metaphor for immunizing infections where each living individual is assumed to be in one of three epidemiological states at any given time: susceptible, infected and infectious, and recovered and immune. The model specifies the rates at which individuals change their state. Individuals progress from S to I when infected, then from I to R upon recovery. Many variants exist—for example, recognizing different classes of S, I, and R individuals, depending on individual traits such as age.

reproducible results, while maximizing model transparency.

Making data sets widely available is also crucial, for example, to support replication of findings and broader comparative analyses (*79*). As models become open access, so should much of the data collected by governments, international agencies, and epidemiology research groups. Two outbreaks never occur in exactly matching circumstances, even for the same infectious agent, so there is potential to study many outbreaks in parallel to gain insight into the determinants of outbreak pattern and severity. Looking forward, there is a major opportunity to design experiments, clinical trials [for example for vaccines (*80*)], and surveillance protocols to test model predictions or assumptions, and to help reduce or better target the enormous costs involved. By integrating modeling approaches throughout the full life cycle of infectious disease policies, including economic considerations (*58*, *70*, *81*), health outcomes can be improved and scientific understanding can be advanced.

At present, the evidence provided by infectious disease models is not considered by the Grading of Recommendations Assessment, Development and Evaluation (GRADE) working group (www.gradeworkinggroup.org) alongside that of conventional studies such as clinical trials. Regardless, models are essential when diverse sources of data (including GRADE-scale evidence) need to be combined and weighed to assess quality of evidence and recommendations made in health care scenarios. In many cases, the definitive trial cannot be performed, and in such circumstances models can offer insight and extract maximum value from data that are available. In recent years, uniformity of practice and quality control for models has received more attention, resulting in initial attempts to characterize good modeling practice for infectious diseases (*82*, *83*).

The optimal use of models to inform policy decisions requires a continuous dialogue between the multidisciplinary infectious disease dynamics community and decision-makers. This is increasingly understood by governments in developed countries, in nongovernmental agencies and by large funding bodies. This dialogue will help to reduce the burden from infectious diseases by providing better-informed control strategies. Mathematical models will allow us to capitalize on new data streams and lead to an ever-greater ability to generate robust insight and collectively shape successful local and global public health policy.

REFERENCES AND NOTES

1. World Health Organization, Global strategy for health for all by the year 2000 (WHO, Geneva, 1981, http://whqlibdoc.who.int/publications/9241800038.pdf).
2. World Health Organization, Mortality and global health estimates 2013 (WHO, 2013, http://apps.who.int/gho/data/node.main.686?lang=en.).
3. P. Klepac, C. J. Metcalf, A. R. McLean, K. Hampson, Towards the endgame and beyond: Complexities and challenges for the elimination of infectious diseases. *Philos. Trans. R. Soc. Lond. B* **368**, 20120137 (2013). doi: 10.1098/rstb.2012.0137; pmid: 23798686
4. P. Daszak, A. A. Cunningham, A. D. Hyatt, Emerging infectious diseases of wildlife—threats to biodiversity and human health. *Science* **287**, 443–449 (2000). doi: 10.1126/science.287.5452.443; pmid: 10642539
5. K. E. Jones *et al*., Global trends in emerging infectious diseases. *Nature* **451**, 990–993 (2008). doi: 10.1038/nature06536; pmid: 18288193
6. J. O. Lloyd-Smith *et al*., Epidemic dynamics at the human-animal interface. *Science* **326**, 1362–1367 (2009). doi: 10.1126/science.1177345; pmid: 19965751
7. F. Keesing *et al*., Impacts of biodiversity on the emergence and transmission of infectious diseases. *Nature* **468**, 647–652 (2010). doi: 10.1038/nature09575; pmid: 21124449
8. K. F. Smith *et al*., Global rise in human infectious disease outbreaks. *J. R. Soc. Interface* **11**, 20140950 (2014). doi: 10.1098/rsif.2014.0950; pmid: 25401184
9. S. Funk, M. Salathé, V. A. A. Jansen, Modelling the influence of human behaviour on the spread of infectious diseases: A review. *J. R. Soc. Interface* **7**, 1247–1256 (2010). doi: 10.1098/rsif.2010.0142; pmid: 20504800
10. C. T. Bauch, A. P. Galvani, Epidemiology. Social factors in epidemiology. *Science* **342**, 47–49 (2013). doi: 10.1126/science.1244492; pmid: 24092718
11. E. M. Volz, K. Koelle, T. Bedford, Viral phylodynamics. *PLOS Comput. Biol.* **9**, e1002947 (2013). doi: 10.1371/journal.pcbi.1002947; pmid: 23555203
12. D. Bernoulli, S. Blower, An attempt at a new analysis of the mortality caused by smallpox and of the advantages of inoculation to prevent it. *Rev. Med. Virol.* **14**, 275–288 (2004). Reprinted translation by L. Bradley with review by S. Blower; original in French 1766). doi: 10.1002/rmv.443; pmid: 15334536
13. J. O. Lloyd-Smith, D. Mollison, J. E. Metcalf, P. Klepac, J. A. P. Heesterbeek, Eds., *Challenges in Modelling Infectious Disease Dynamics. Epidemics* **10** (special issue, March 2015).
14. WHO Ebola Response Team, Ebola virus disease in West Africa—the first 9 months of the epidemic and forward projections. *N. Engl. J. Med.* **371**, 1481–1495 (2014). doi: 10.1056/NEJMoa1411100; pmid: 25244186
15. S. K. Gire *et al*., Genomic surveillance elucidates Ebola virus origin and transmission during the 2014 outbreak. *Science* **345**, 1369–1372 (2014). doi: 10.1126/science.1259657; pmid: 25214632
16. A. Camacho *et al*., Potential for large outbreaks of Ebola virus disease. *Epidemics* **9**, 70–78 (2014). doi: 10.1016/j.epidem.2014.09.003; pmid: 25480136
17. A. Pandey *et al*., Strategies for containing Ebola in West Africa. *Science* **346**, 991–995 (2014). doi: 10.1126/science.1260612; pmid: 25414312
18. C. J. M. Whitty *et al*., Infectious disease: Tough choices to reduce Ebola transmission. *Nature* **515**, 192–194 (2014). doi: 10.1038/515192a; pmid: 25391946
19. S. Blumberg, J. O. Lloyd-Smith, Inference of R_0 and transmission heterogeneity from the size distribution of stuttering chains. *PLOS Comput. Biol.* **9**, e1002993 (2013). doi: 10.1371/journal.pcbi.1002993; pmid: 23658504
20. S. Cauchemez *et al*., Using routine surveillance data to estimate the epidemic potential of emerging zoonoses: Application to the emergence of US swine origin influenza A H3N2v virus. *PLOS Med.* **10**, e1001399 (2013). doi: 10.1371/journal.pmed.1001399; pmid: 23472057
21. A. Kucharski, H. Mills, A. Pinsent, C. Fraser, M. Van Kerkhove, C. A. Donnelly, S. Riley, Distinguishing between reservoir exposure and human-to-human transmission for emerging pathogens using case onset data. *PLOS Curr.* (2014). pmid: 24619563
22. O. Restif *et al*., Model-guided fieldwork: Practical guidelines for multidisciplinary research on wildlife ecological and epidemiological dynamics. *Ecol. Lett.* **15**, 1083–1094 (2012). doi: 10.1111/j.1461-0248.2012.01836.x; pmid: 22809422
23. S. Selakovic, P. C. de Ruiter, H. Heesterbeek, Infectious disease agents mediate interaction in food webs and ecosystems. *Proc. Biol. Sci.* **281**, 20132709 (2014). doi: 10.1098/rspb.2013.2709; pmid: 24403336
24. R. K. Plowright *et al*., Ecological dynamics of emerging bat virus spillover. *Proc. Biol. Sci.* **282**, 20142124 (2015). doi: 10.1098/rspb.2014.2124; pmid: 25392474
25. M. Cotten *et al*., Spread, circulation, and evolution of the Middle East respiratory syndrome coronavirus. *MBio* **5**, e01062 (2014). doi: 10.1128/mBio.01062-13; pmid: 24549846
26. K. M. Pepin, S. Lass, J. R. Pulliam, A. F. Read, J. O. Lloyd-Smith, Identifying genetic markers of adaptation for surveillance of viral host jumps. *Nat. Rev. Microbiol.* **8**, 802–813 (2010). doi: 10.1038/nrmicro2440; pmid: 20938453
27. B. T. Grenfell *et al*., Unifying the epidemiological and evolutionary dynamics of pathogens. *Science* **303**, 327–332 (2004). doi: 10.1126/science.1090727; pmid: 14726583
28. A. Rambaut *et al*., The genomic and epidemiological dynamics of human influenza A virus. *Nature* **453**, 615–619 (2008). doi: 10.1038/nature06945; pmid: 18418375
29. J. L. Gardy *et al*., Whole-genome sequencing and social-network analysis of a tuberculosis outbreak. *N. Engl. J. Med.* **364**, 730–739 (2011). doi: 10.1056/NEJMoa1003176; pmid: 21345102
30. H. W. Stokes, M. R. Gillings, Gene flow, mobile genetic elements and the recruitment of antibiotic resistance genes into Gram-negative pathogens. *FEMS Microbiol. Rev.* **35**, 790–819 (2011). doi: 10.1111/j.1574-6976.2011.00273.x; pmid: 21517914
31. B. F. Koel *et al*., Substitutions near the receptor binding site determine major antigenic change during influenza virus evolution. *Science* **342**, 976–979 (2013). doi: 10.1126/science.1244730; pmid: 24264991
32. B. Vrancken *et al*., The genealogical population dynamics of HIV-1 in a large transmission chain: Bridging within and among host evolutionary rates. *PLOS Comput. Biol.* **10**, e1003505 (2014). pmid: 24699231
33. D. L. Ayres *et al*., BEAGLE: An application programming interface and high-performance computing library for statistical phylogenetics. *Syst. Biol.* **61**, 170–173 (2012). doi: 10.1093/sysbio/syr100; pmid: 21963610
34. S. Telfer *et al*., Species interactions in a parasite community drive infection risk in a wildlife population. *Science* **330**, 243–246 (2010). doi: 10.1126/science.1190333; pmid: 20929776
35. I. M. Cattadori *et al*., Infections do not predict shedding in co-infections with two helminths from a natural system. *Ecology* **95**, 1684–1692 (2014). doi: 10.1890/13-1538.1; pmid: 25039232
36. R. Anderson, J. Truscott, T. D. Hollingsworth, The coverage and frequency of mass drug administration required to eliminate persistent transmission of soil-transmitted helminths. *Phil. Trans. R. Soc. B* **369**, 20130435 (2014). doi: 10.1098/rstb.2013.0435; pmid: 24821921
37. J. Lessler *et al*., Evidence for antigenic seniority in influenza A (H3N2) antibody responses in southern China. *PLOS Pathog.* **8**, e1002802 (2012). doi: 10.1371/journal.ppat.1002802; pmid: 22829765
38. M. A. Miller, C. Viboud, M. Balinska, L. Simonsen, The signature features of influenza pandemics—implications for policy. *N. Engl. J. Med.* **360**, 2595–2598 (2009). doi: 10.1056/NEJMp0903906; pmid: 19423872
39. J. S. Lavine, A. A. King, O. N. Bjørnstad, Natural immune boosting in pertussis dynamics and the potential for long-term vaccine failure. *Proc. Natl. Acad. Sci. U.S.A.* **108**, 7259–7264 (2011). doi: 10.1073/pnas.1014394108; pmid: 21422281
40. S. Cobey, M. Lipsitch, Niche and neutral effects of acquired immunity permit coexistence of pneumococcal serotypes. *Science* **335**, 1376–1380 (2012). doi: 10.1126/science.1215947; pmid: 22383809
41. S. Gupta, R. M. Anderson, R. M. May, Networks of sexual contacts: Implications for the pattern of spread of HIV. *AIDS* **3**, 807–817 (1989). doi: 10.1097/00002030-198912000-00005; pmid: 2517202
42. L. Danon *et al*., Networks and the epidemiology of infectious disease. *Interdiscip. Perspect. Infect. Dis.* **2011**, 284909 (2011). doi: 10.1155/2011/284909; pmid: 21437001
43. S. Bansal, B. T. Grenfell, L. A. Meyers, When individual behaviour matters: Homogeneous and network models in epidemiology. *J. R. Soc. Interface* **4**, 879–891 (2007). doi: 10.1098/rsif.2007.1100; pmid: 17640863
44. S. Bansal, J. Read, B. Pourbohloul, L. A. Meyers, The dynamic nature of contact networks in infectious disease epidemiology. *J. Biol. Dyn.* **4**, 478–489 (2010). doi: 10.1080/17513758.2010.503376; pmid: 22877143
45. S. Funk, E. Gilad, C. Watkins, V. A. A. Jansen, The spread of awareness and its impact on epidemic outbreaks. *Proc. Natl. Acad. Sci. U.S.A.* **106**, 6872–6877 (2009). doi: 10.1073/pnas.0810762106; pmid: 19332788
46. T. Oraby, V. Thampi, C. T. Bauch, The influence of social norms on the dynamics of vaccinating behaviour for paediatric infectious diseases. *Proc. Biol. Sci.* **281**, 20133172 (2014). doi: 10.1098/rspb.2013.3172; pmid: 24523276
47. D. Centola, The spread of behavior in an online social network experiment. *Science* **329**, 1194–1197 (2010). pmid: 20813952

48. M. Salathé, S. Khandelwal, Assessing vaccination sentiments with online social media: Implications for infectious disease dynamics and control. *PLOS Comput. Biol.* **7**, e1002199 (2011). doi: 10.1371/journal.pcbi.1002199; pmid: 22022249
49. M. J. Ferrari *et al*., The dynamics of measles in sub-Saharan Africa. *Nature* **451**, 679–684 (2008). doi: 10.1038/nature06509; pmid: 18256664
50. T. D. Hollingsworth, N. M. Ferguson, R. M. Anderson, Will travel restrictions control the international spread of pandemic influenza? *Nat. Med.* **12**, 497–499 (2006). doi: 10.1038/nm0506-497; pmid: 16675989
51. T. A. Perkins, T. W. Scott, A. Le Menach, D. L. Smith, Heterogeneity, mixing, and the spatial scales of mosquito-borne pathogen transmission. *PLOS Comput. Biol.* **9**, e1003327 (2013). pmid: 24348223
52. A. Wesolowski *et al*., Quantifying the impact of human mobility on malaria. *Science* **338**, 267–270 (2012). doi: 10.1126/science.1223467; pmid: 23066082
53. R. Ross, *The Prevention of Malaria* (John Murray, London, ed. 2, 1911).
54. M. S. Bartlett, Measles periodicity and community size. *J. R. Stat. Soc. Ser A* **120**, 48–70 (1957). doi: 10.2307/2342553
55. R. M. Anderson, R. M. May, Directly transmitted infections diseases: Control by vaccination. *Science* **215**, 1053–1060 (1982). doi: 10.1126/science.7063839; pmid: 7063839
56. A. R. McLean, R. M. Anderson, Measles in developing countries. Part II. The predicted impact of mass vaccination. *Epidemiol. Infect.* **100**, 419–442 (1988). doi: 10.1017/S0950268800067170; pmid: 3378585
57. D. S. Saint-Victor, S. B. Omer, Vaccine refusal and the endgame: Walking the last mile first. *Phil. Trans. R. Soc. B* **368**, 20120148 (2013). doi: 10.1098/rstb.2012.0148; pmid: 23798696
58. P. Klepac, R. Laxminarayan, B. T. Grenfell, Synthesizing epidemiological and economic optima for control of immunizing infections. *Proc. Natl. Acad. Sci. U.S.A.* **108**, 14366–14370 (2011). doi: 10.1073/pnas.1101694108; pmid: 21825129
59. M. Salathé *et al*., Digital epidemiology. *PLOS Comput. Biol.* **8**, e1002616 (2012). doi: 10.1371/journal.pcbi.1002616; pmid: 22844241
60. M. Salathé, C. C. Freifeld, S. R. Mekaru, A. F. Tomasulo, J. S. Brownstein, Influenza A (H7N9) and the importance of digital epidemiology. *N. Engl. J. Med.* **369**, 401–404 (2013). doi: 10.1056/NEJMp1307752; pmid: 23822655
61. A. F. Read, P. A. Lynch, M. B. Thomas, How to make evolution-proof insecticides for malaria control. *PLOS Biol.* **7**, e1000058 (2009). doi: 10.1371/journal.pbio.1000058; pmid: 19355786
62. N. Arinaminpathy, J. S. Lavine, B. T. Grenfell, Self-boosting vaccines and their implications for herd immunity. *Proc. Natl. Acad. Sci. U.S.A.* **109**, 20154–20159 (2012). doi: 10.1073/pnas.1209683109; pmid: 23169630
63. O. Diekmann, J. A. P. Heesterbeek, T. Britton, *Mathematical Tools for Understanding Infectious Disease Dynamics* (Princeton Univ. Press, Princeton, 2013).
64. C. P. Jewell, G. O. Roberts, Enhancing Bayesian risk prediction for epidemics using contact tracing. *Biostatistics* **13**, 567–579 (2012). doi: 10.1093/biostatistics/kxs012; pmid: 22674466
65. E. S. Knock, P. D. O'Neill, Bayesian model choice for epidemic models with two levels of mixing. *Biostatistics* **15**, 46–59 (2014). doi: 10.1093/biostatistics/kxt023; pmid: 23887980
66. J. Dureau, K. Kalogeropoulos, M. Baguelin, Capturing the time-varying drivers of an epidemic using stochastic dynamical systems. *Biostatistics* **14**, 541–555 (2013). doi: 10.1093/biostatistics/kxs052; pmid: 23292757
67. A. A. King, E. L. Ionides, M. Pascual, M. J. Bouma, Inapparent infections and cholera dynamics. *Nature* **454**, 877–880 (2008). doi: 10.1038/nature07084; pmid: 18704085
68. O. Ratmann, G. Donker, A. Meijer, C. Fraser, K. Koelle, Phylodynamic inference and model assessment with approximate bayesian computation: Influenza as a case study. *PLOS Comput. Biol.* **8**, e1002835 (2012). doi: 10.1371/journal.pcbi.1002835; pmid: 23300420
69. M. Farah, P. J. Birrell, S. Conti, D. De Angelis, Bayesian Emulation and Calibration of a Dynamic Epidemic Model for A/H1N1 Influenza. *J. Am. Stat. Assoc.* **109**, 1398–1411 (2014). doi: 10.1080/01621459.2014.934453
70. M. Baguelin *et al*., Assessing optimal target populations for influenza vaccination programmes: An evidence synthesis and modelling study. *PLOS Med.* **10**, e1001527 (2013). doi: 10.1371/journal.pmed.1001527; pmid: 24115913
71. D. De Angelis, A. M. Presanis, S. Conti, A. E. Ades, Estimation of HIV Burden through Bayesian Evidence Synthesis. *Stat. Sci.* **29**, 9–17 (2014). doi: 10.1214/13-STS428
72. J. Ginsberg *et al*., Detecting influenza epidemics using search engine query data. *Nature* **457**, 1012–1014 (2009). doi: 10.1038/nature07634; pmid: 19020500
73. N. Bharti *et al*., Explaining seasonal fluctuations of measles in Niger using nighttime lights imagery. *Science* **334**, 1424–1427 (2011). doi: 10.1126/science.1210554; pmid: 22158822
74. J. P. Messina *et al*., Global spread of dengue virus types: Mapping the 70 year history. *Trends Microbiol.* **22**, 138–146 (2014). doi: 10.1016/j.tim.2013.12.011; pmid: 24468533
75. C. Dye *et al*., WHO and the future of disease control programmes. *Lancet* **381**, 413–418 (2013). doi: 10.1016/S0140-6736(12)61812-1; pmid: 23374479
76. C. Dye, After 2015: Infectious diseases in a new era of health and development. *Philos. Trans. R. Soc. Lond. B* **369**, 20130426 (2014). doi: 10.1098/rstb.2013.0426; pmid: 24821913
77. M. Woolhouse, J. Farrar, Policy: An intergovernmental panel on antimicrobial resistance. *Nature* **509**, 555–557 (2014). doi: 10.1038/509555a; pmid: 24877180
78. R. F. Terry, J. F. Salm Jr., C. Nannei, C. Dye, Creating a global observatory for health R&D. *Science* **345**, 1302–1304 (2014). doi: 10.1126/science.1258737; pmid: 25214621
79. P. Rohani, A. A. King, Never mind the length, feel the quality: The impact of long-term epidemiological data sets on theory, application and policy. *Trends Ecol. Evol.* **25**, 611–618 (2010). doi: 10.1016/j.tree.2010.07.010; pmid: 20800928
80. M. E. Halloran, I. M. Longini, C. J. Struchiner, *Design and Analysis of Vaccine studies* (Springer, Berlin, 2010).
81. M. L. Ndeffo Mbah *et al*., Cost-effectiveness of a community-based intervention for reducing the transmission of *Schistosoma haematobium* and HIV in Africa. *Proc. Natl. Acad. Sci. U.S.A.* **110**, 7952–7957 (2013). doi: 10.1073/pnas.1221396110; pmid: 23589884
82. R. Pitman *et al*., Dynamic transmission modeling: A report of the ISPOR-SMDM modeling good research practices task force-5. *Value Health* **15**, 828–834 (2012). doi: 10.1016/j.jval.2012.06.011; pmid: 22999132
83. M. E. J. Woolhouse *et al*., Guide to good practice for quantitative veterinary epidemiology. www.qve-goodpracticeguide.org.uk/ (2011).
84. T. D. Hollingsworth, D. Klinkenberg, H. Heesterbeek, R. M. Anderson, Mitigation strategies for pandemic influenza A: Balancing conflicting policy objectives. *PLOS Comput. Biol.* **7**, e1001076 (2011). doi: 10.1371/journal.pcbi.1001076; pmid: 21347316
85. J. T. Wu, B. J. Cowling, The use of mathematical models to inform influenza pandemic preparedness and response. *Exp. Biol. Med.* **236**, 955–961 (2011). doi: 10.1258/ebm.2010.010271; pmid: 21727183
86. B. Y. Lee, A. E. Wiringa, The 2009 H1N1 influenza pandemic: A case study of how modeling can assist all stages of vaccine decision-making. *Hum. Vaccin.* **7**, 115–119 (2011). doi: 10.4161/hv.7.1.13740; pmid: 21263227
87. M. Lipsitch, L. Finelli, R. T. Heffernan, G. M. Leung, S. C. Redd; 2009 H1n1 Surveillance Group, Improving the evidence base for decision making during a pandemic: The example of 2009 influenza A/H1N1. *Biosecur. Bioterror.* **9**, 89–115 (2011). pmid: 21612363
88. T. House *et al*., Modelling the impact of local reactive school closures on critical care provision during an influenza pandemic. *Proc. Biol. Sci.* **278**, 2753–2760 (2011). doi: 10.1098/rspb.2010.2688; pmid: 21288945
89. M. D. Van Kerkhove, N. M. Ferguson, Epidemic and intervention modelling—a scientific rationale for policy decisions? Lessons from the 2009 influenza pandemic. *Bull. World Health Organ.* **90**, 306–310 (2012). pmid: 22511828
90. M. Luksza, M. Lässig, A predictive fitness model for influenza. *Nature* **507**, 57–61 (2014). doi: 10.1038/nature13087; pmid: 24572367
91. UK Government, (2012, https://www.gov.uk/government/uploads/system/uploads/attachment_data/file/224775/JCVI-statement-on-the-annual-influenza-vaccination-programme-25-July-2012.pdf).
92. M. A. Rose *et al*., The epidemiological impact of childhood influenza vaccination using live-attenuated influenza vaccine (LAIV) in Germany: Predictions of a simulation study. *BMC Infect. Dis.* **14**, 40 (2014). doi: 10.1186/1471-2334-14-40; pmid: 24450996
93. HIV Modelling Consortium Treatment as Prevention Editorial Writing Group, HIV treatment as prevention: Models, data, and questions—towards evidence-based decision-making. *PLOS Med.* **9**, e1001259 (2012). doi: 10.1371/journal.pmed.1001259; pmid: 22802739
94. A. S. Perelson, A. U. Neumann, M. Markowitz, J. M. Leonard, D. D. Ho, HIV-1 dynamics in vivo: Virion clearance rate, infected cell life-span, and viral generation time. *Science* **271**, 1582–1586 (1996). doi: 10.1126/science.271.5255.1582; pmid: 8599114
95. N. R. Faria *et al*., The early spread and epidemic ignition of HIV-1 in human populations. *Science* **346**, 56–61 (2014). doi: 10.1126/science.1256739; pmid: 25278604
96. T. D. Hollingsworth, R. M. Anderson, C. Fraser, HIV-1 transmission, by stage of infection. *J. Infect. Dis.* **198**, 687–693 (2008). doi: 10.1086/590501; pmid: 18662132
97. D. Bezemer *et al*., A resurgent HIV-1 epidemic among men who have sex with men in the era of potent antiretroviral therapy. *AIDS* **22**, 1071–1077 (2008). doi: 10.1097/QAD.0b013e3282fd167c; pmid: 18520351
98. J. S. Montaner *et al*., The case for expanding access to highly active antiretroviral therapy to curb the growth of the HIV epidemic. *Lancet* **368**, 531–536 (2006). doi: 10.1016/S0140-6736(06)69162-9; pmid: 16890841
99. R. M. Granich, C. F. Gilks, C. Dye, K. M. De Cock, B. G. Williams, Universal voluntary HIV testing with immediate antiretroviral therapy as a strategy for elimination of HIV transmission: A mathematical model. *Lancet* **373**, 48–57 (2009). doi: 10.1016/S0140-6736(08)61697-9; pmid: 19038438
100. M. S. Cohen *et al*., Prevention of HIV-1 infection with early antiretroviral therapy. *N. Engl. J. Med.* **365**, 493–505 (2011). doi: 10.1056/NEJMoa1105243; pmid: 21767103
101. S. E. Bellan *et al*., Extra-couple HIV transmission in sub-Saharan Africa: A mathematical modelling study of survey data. *Lancet* **381**, 1561–1569 (2013). doi: 10.1016/S0140-6736(12)61960-6; pmid: 23391466
102. F. Tanser, T. Bärnighausen, E. Grapsa, J. Zaidi, M. L. Newell, High coverage of ART associated with decline in risk of HIV acquisition in rural KwaZulu-Natal, South Africa. *Science* **339**, 966–971 (2013). doi: 10.1126/science.1228160; pmid: 23430656
103. S. H. Vermund, S. J. Fidler, H. Ayles, N. Beyers, R. J. Hayes, Can combination prevention strategies reduce HIV transmission in generalized epidemic settings in Africa? The HPTN 071 (PopART) study plan in South Africa and Zambia. *J. Acquir. Immune Defic. Syndr.* **63** (suppl. 2), S221–S227 (2013). doi: 10.1097/QAI.0b013e318299c3f4; pmid: 23764639
104. M. K. Smith, K. A. Powers, K. E. Muessig, W. C. Miller, M. S. Cohen, HIV treatment as prevention: The utility and limitations of ecological observation. *PLOS Med.* **9**, e1001260 (2012). doi: 10.1371/journal.pmed.1001260; pmid: 22802740
105. M. S. Cohen *et al*., Antiretroviral treatment of HIV-1 prevents transmission of HIV-1: Where do we go from here? *Lancet* **382**, 1515–1524 (2013). doi: 10.1016/S0140-6736(13)61998-4; pmid: 24152938
106. G. MacDonald, The analysis of equilibrium in malaria. *Trop. Dis. Bull.* **49**, 813–829 (1952). pmid: 12995455
107. K. Dietz, L. Molineaux, A. Thomas, A malaria model tested in the African savannah. *Bull. World Health Organ.* **50**, 347–357 (1974). pmid: 4613512
108. R. M. Anderson, R. M. May, *Infectious Diseases of Humans: Dynamics and Control* (Oxford Univ. Press, Oxford, 1992).
109. A. S. Perelson, R. M. Ribeiro, Modeling the within-host dynamics of HIV infection. *BMC Biol.* **11**, 96 (2013). doi: 10.1186/1741-7007-11-96; pmid: 24020860
110. C. A. Donnelly, N. M. Ferguson, 2000, *Statistical Aspects of BSE and vCJD: Models for Epidemics* (Chapman & Hall/CRC, Boca Raton, FL, 2000).
111. M. J. Keeling, Models of foot-and-mouth disease. *Proc. Biol. Sci.* **272**, 1195–1202 (2005). doi: 10.1098/rspb.2004.3046; pmid: 16024382
112. R. M. Anderson *et al*., Epidemiology, transmission dynamics and control of SARS: The 2002-2003 epidemic. *Phil. Trans. R. Soc. B* **359**, 1091–1105 (2004). doi: 10.1098/rstb.2004.1490; pmid: 15306395
113. S. Blumberg, J. O. Lloyd-Smith, Comparing methods for estimating R_0 from the size distribution of subcritical transmission chains. *Epidemics* **5**, 131–145 (2013). doi: 10.1016/j.epidem.2013.05.002; pmid: 24021520
114. J. O. Lloyd-Smith, S. J. Schreiber, P. E. Kopp, W. M. Getz, Superspreading and the effect of individual variation on

disease emergence. *Nature* **438**, 355–359 (2005). doi: 10.1038/nature04153; pmid: 16292310
115. L. Matthews *et al*., Heterogeneous shedding of *Escherichia coli* O157 in cattle and its implications for control. *Proc. Natl. Acad. Sci. U.S.A.* **103**, 547–552 (2006). doi: 10.1073/pnas.0503776103; pmid: 16407143
116. N. M. Ferguson, A. P. Galvani, R. M. Bush, Ecological and immunological determinants of influenza evolution. *Nature* **422**, 428–433 (2003). doi: 10.1038/nature01509; pmid: 12660783
117. K. Koelle, S. Cobey, B. Grenfell, M. Pascual, Epochal evolution shapes the phylodynamics of interpandemic influenza A (H3N2) in humans. *Science* **314**, 1898–1903 (2006). doi: 10.1126/science.1132745; pmid: 17185596
118. M. Recker, O. G. Pybus, S. Nee, S. Gupta, The generation of influenza outbreaks by a network of host immune responses against a limited set of antigenic types. *Proc. Natl. Acad. Sci. U.S.A.* **104**, 7711–7716 (2007). doi: 10.1073/pnas.0702154104; pmid: 17460037
119. S. Funk, H. Nishiura, H. Heesterbeek, W. J. Edmunds, F. Checchi, Identifying transmission cycles at the human-animal interface: The role of animal reservoirs in maintaining gambiense human african trypanosomiasis. *PLOS Comput. Biol.* **9**, e1002855 (2013). doi: 10.1371/journal.pcbi.1002855; pmid: 23341760
120. R. C. Reiner Jr. *et al*., A systematic review of mathematical models of mosquito-borne pathogen transmission: 1970-2010. *J. R. Soc. Interface* **10**, 20120921 (2013). doi: 10.1098/rsif.2012.0921; pmid: 23407571
121. E. M. Stuckey, T. A. Smith, N. Chitnis, Estimating malaria transmission through mathematical models. *Trends Parasitol.* **29**, 477–482 (2013). doi: 10.1016/j.pt.2013.08.001; pmid: 24001452
122. N. G. Reich *et al*., Interactions between serotypes of dengue highlight epidemiological impact of cross-immunity. *J. R. Soc. Interface* **10**, 20130414 (2013). doi: 10.1098/rsif.2013.0414; pmid: 23825116
123. B. S. Cooper *et al*., Methicillin-resistant *Staphylococcus aureus* in hospitals and the community: Stealth dynamics and control catastrophes. *Proc. Natl. Acad. Sci. U.S.A.* **101**, 10223–10228 (2004). doi: 10.1073/pnas.0401324101; pmid: 15220470
124. C. Dye, B. G. Williams, The population dynamics and control of tuberculosis. *Science* **328**, 856–861 (2010). doi: 10.1126/science.1185449; pmid: 20466923
125. A. F. Read, T. Day, S. Huijben, The evolution of drug resistance and the curious orthodoxy of aggressive chemotherapy. *Proc. Natl. Acad. Sci. U.S.A.* **108** (suppl. 2), 10871–10877 (2011). doi: 10.1073/pnas.1100299108; pmid: 21690376
126. S. Cobey, M. Lipsitch, Pathogen diversity and hidden regimes of apparent competition. *Am. Nat.* **181**, 12–24 (2013). doi: 10.1086/668598; pmid: 23234842
127. C. J. E. Metcalf *et al*., Structured models of infectious disease: Inference with discrete data. *Theor. Popul. Biol.* **82**, 275–282 (2012). doi: 10.1016/j.tpb.2011.12.001; pmid: 22178687
128. J. Lessler, C. J. E. Metcalf, Balancing evidence and uncertainty when considering rubella vaccine introduction. *PLOS ONE* **8**, e67639 (2013). doi: 10.1371/journal.pone.0067639; pmid: 23861777
129. R. Anderson, T. D. Hollingsworth, J. Truscott, S. Brooker, Optimisation of mass chemotherapy to control soil-transmitted helminth infection. *Lancet* **379**, 289–290 (2012). doi: 10.1016/S0140-6736(12)60120-2; pmid: 22284644
130. C. J. E. Metcalf *et al*., Implications of spatially heterogeneous vaccination coverage for the risk of congenital rubella syndrome in South Africa. *J. R. Soc. Interface* **10**, 20120756 (2013). doi: 10.1098/rsif.2012.0756; pmid: 23152104
131. T. Panagiotopoulos, I. Antoniadou, E. Valassi-Adam, A. Berger, Increase in congenital rubella occurrence after immunisation in Greece: Retrospective survey and systematic review. *BMJ* **319**, 1462–1467 (1999). doi: 10.1136/bmj.319.7223.1462; pmid: 10582926
132. C. H. Chan, C. J. McCabe, D. N. Fisman, Core groups, antimicrobial resistance and rebound in gonorrhoea in North America. *Sex. Transm. Infect.* **88**, 200–204 (2012). doi: 10.1136/sextrans-2011-050049; pmid: 22169277
133. Y. Nagao, K. Koelle, Decreases in dengue transmission may act to increase the incidence of dengue hemorrhagic fever. *Proc. Natl. Acad. Sci. U.S.A.* **105**, 2238–2243 (2008). doi: 10.1073/pnas.0709029105; pmid: 18250338

ACKNOWLEDGMENTS

H.H. conceived and wrote the paper; R.M.A., V.A., S.B., D.D.A., C.D., K.T.D.E., W.J.E., S.D.W.F., S.F., T.D.H., T.H., V.I., P.K., J.L., J.O.L.-S., C.J.E.M., D.M., J.R.C.P., L.P., M.G.R., and C.V. provided text and edited the manuscript; J.L., C.J.E.M. and T.D.H. produced figures; the Isaac Newton Institute IDD Collaboration jointly produced and discussed ideas for the outline and content (all of the above plus N.A., F.B., T.B., J.G., B.G., A.L.L., A.M., P.O.N., C.P., S.R., G.S.T., P.T., and J.W.). We gratefully acknowledge help by K. Koelle and D. Fisman in producing adapted versions of their figures for Fig. 2 (panels C, D, and E). This paper was conceived and developed at a program on Infectious Disease Dynamics at the Isaac Newton Institute for Mathematical Sciences, Cambridge, UK, 19 August to 13 September 2013 and 19 May to 6 June 2014 (www.newton.ac.uk). We gratefully acknowledge financial and infrastructural support from the Isaac Newton Institute for Mathematical Sciences which is fundamental to the success of this program. We are also grateful for the financial support the program received from the Research and Policy for Infectious Disease Dynamics (RAPIDD) program of the Science and Technology Directorate, U.S. Department of Homeland Security, and the Fogarty International Center, NIH. R.M.A. is a non–executive director of GlaxoSmithKline. C.D. acts as an advisor for the Wellcome Trust, for which he receives financial remuneration.

10.1126/science.aaa4339

RESEARCH ARTICLE SUMMARY

INNATE IMMUNITY

Phosphorylation of innate immune adaptor proteins MAVS, STING, and TRIF induces IRF3 activation

Siqi Liu, Xin Cai, Jiaxi Wu, Qian Cong, Xiang Chen, Tuo Li, Fenghe Du, Junyao Ren, You-Tong Wu, Nick V. Grishin, Zhijian J. Chen*

INTRODUCTION: Sensing of pathogenic microbes and tissue damage by the innate immune system triggers immune cells to secrete cytokines that promote host defense. Viral RNA, cytosolic DNA, and the bacterial cell wall component lipopolysaccharide activate signaling cascades through a number of pattern recognition receptor (PRR)–adaptor protein pairs, including RIG-I–MAVS, cGAS-STING, and TLR3/4-TRIF (TLR3/4, Toll-like receptors 3 and 4). Activation of these signaling modules results in the production of type I interferons (IFNs), a family of cytokines that are essential for host protection. The adaptor proteins MAVS, STING, and TRIF each activate the downstream protein kinase TBK1, which then phosphorylates the transcription factor interferon regulatory factor 3 (IRF3), which drives type I IFN production. Although much progress has been made in our understanding of PRR and adaptor protein activation, the mechanism by which the adaptor proteins activate TBK1 and IRF3 remains unclear.

RATIONALE: Other signaling pathways besides the RIG-I–MAVS, cGAS-STING, and TLR3/4-TRIF pathways activate TBK1. However, IRF3 phosphorylation by TBK1 is observed only in the IFN-producing pathways that use MAVS, STING, or TRIF as the adaptor protein. The discrepant activation of TBK1 and IRF3 implies the existence of a kinase-substrate specification mechanism exclusive to the IFN-producing pathways. Specification of TBK1-mediated IRF3 activation is essential for the tight regulation of IFN production, which would otherwise lead to autoimmune diseases.

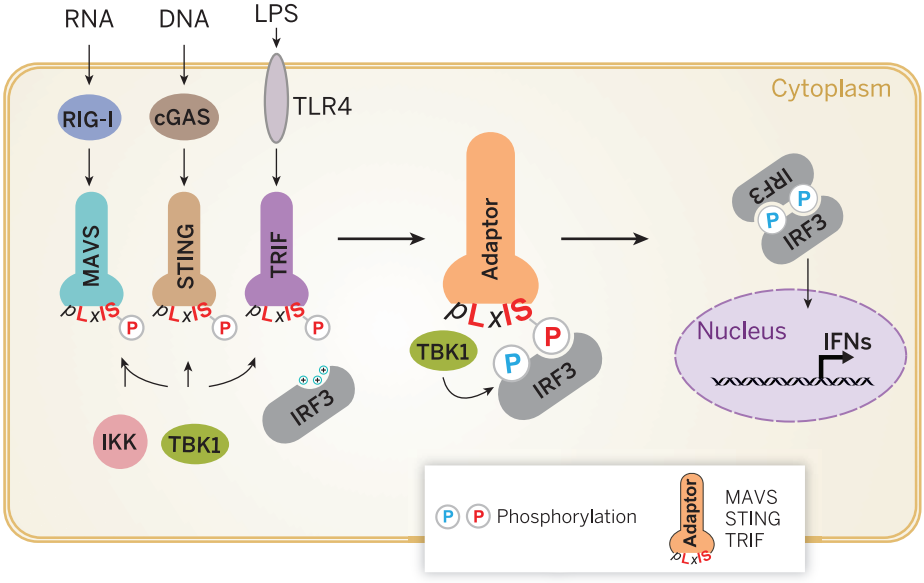

Phosphorylation of innate immune adaptor proteins licenses IRF3 activation. MAVS, STING, and TRIF—which are activated by viral RNA, cytosolic DNA, and bacterial lipopolysaccharide (LPS), respectively—activate the kinases IKK and TBK1. These kinases then phosphorylate the adaptor proteins, which in turn recruit IRF3, thereby licensing IRF3 for phosphorylation (P) by TBK1. Phosphorylated IRF3 dissociates from the adaptor proteins, dimerizes, and then enters the nucleus to induce IFNs.

RESULTS: Using biochemical and mouse cell– and human cell–based assays, we found that both MAVS and STING interacted with IRF3 in a phosphorylation-dependent manner. We show that both MAVS and STING are phosphorylated in response to stimulation at their respective C-terminal consensus motif, *p*L*x*IS (*p*, hydrophilic residue; *x*, any residue; S, phosphorylation site). This phosphorylation event then recruits IRF3 to the active adaptor protein and is essential for IRF3 activation. Point mutations that impair the phosphorylation of MAVS or STING at their consensus motif abrogated IRF3 binding and subsequent IFN induction.

We found that MAVS is phosphorylated by the kinases TBK1 and IKK, whereas STING is phosphorylated by TBK1. Phosphorylated MAVS and STING subsequently bind to conserved, positively charged surfaces of IRF3, thereby recruiting IRF3 for its phosphorylation and activation by TBK1. Point mutations at IRF3's positively charged surfaces abrogated IRF3 binding to MAVS and STING and subsequent IRF3 phosphorylation and activation. We further show that TRIF-mediated activation of IRF3 depends on TRIF phosphorylation at the *p*L*x*IS motif commonly found in MAVS, STING, and IRF3. These results reveal that phosphorylation of innate immune adaptor proteins is an essential and conserved mechanism that selectively recruits IRF3 to activate type I IFN production.

ON OUR WEB SITE

Read the full article at http://dx.doi.org/10.1126/science.aaa2630

CONCLUSION: We uncovered a general mechanism of IRF3 activation by the innate immune adaptor proteins MAVS, STING, and TRIF, which functions in three distinct pattern recognition pathways. Following its activation, each adaptor protein recruits and activates downstream kinase TBK1, which phosphorylates the cognate upstream adaptor protein at a consensus motif. Phosphorylated MAVS, STING, or TRIF in turn recruits IRF3 through its conserved, positively charged phospho-binding domain, allowing IRF3 phosphorylation by TBK1. Phosphorylated IRF3 subsequently dissociates from the adaptor protein and dimerizes though the same phospho-binding domain before translocating into the nucleus to induce IFN. These results elucidate how IRF3 activation and IFN production are tightly controlled and explain why TBK1 is necessary but not sufficient to phosphorylate IRF3: Phosphorylation of IRF3 by TBK1 occurs only with the assistance of an adaptor protein such as MAVS, STING, or TRIF, which also must be phosphorylated. ■

The list of author affiliations is available in the full article online.
*Corresponding author. E-mail: zhijian.chen@utsouthwestern.edu
Cite this article as S. Liu *et al.*, *Science* **347**, aaa2630 (2015). DOI: 10.1126/science.aaa2630

RESEARCH ARTICLE

INNATE IMMUNITY

Phosphorylation of innate immune adaptor proteins MAVS, STING, and TRIF induces IRF3 activation

Siqi Liu,[1] Xin Cai,[1] Jiaxi Wu,[1] Qian Cong,[2] Xiang Chen,[1,3] Tuo Li,[1] Fenghe Du,[1,3] Junyao Ren,[1] You-Tong Wu,[1] Nick V. Grishin,[2,3] Zhijian J. Chen[1,3]*

During virus infection, the adaptor proteins MAVS and STING transduce signals from the cytosolic nucleic acid sensors RIG-I and cGAS, respectively, to induce type I interferons (IFNs) and other antiviral molecules. Here we show that MAVS and STING harbor two conserved serine and threonine clusters that are phosphorylated by the kinases IKK and/or TBK1 in response to stimulation. Phosphorylated MAVS and STING then bind to a positively charged surface of interferon regulatory factor 3 (IRF3) and thereby recruit IRF3 for its phosphorylation and activation by TBK1. We further show that TRIF, an adaptor protein in Toll-like receptor signaling, activates IRF3 through a similar phosphorylation-dependent mechanism. These results reveal that phosphorylation of innate adaptor proteins is an essential and conserved mechanism that selectively recruits IRF3 to activate the type I IFN pathway.

The innate immune system employs germline-encoded pattern recognition receptors to detect common pathogenic molecular features (*1*). Cytosolic DNA and viral RNA are detected by cGAS and RIG-I–like receptors, respectively, to activate several convergent signaling pathways to produce type I interferons (IFNs) (*2*–*6*). After ligand binding, cGAS and RIG-I signal through respective adaptor proteins STING and MAVS to recruit the kinases IKK and TBK1, which then activate the transcription factors NF-κB and interferon regulatory factor 3 (IRF3), respectively. Recent studies on the RIG-I pathway have provided mechanistic insights into innate immune signaling. Specifically, activated RIG-I forms oligomers to convert MAVS into prion-like polymers, which then recruit ubiquitin E3 ligases TRAF2, TRAF5, and TRAF6 to synthesize polyubiquitin chains (*7*–*10*); in turn, these ubiquitin chains recruit and activate IKK and TBK1 to trigger IFN production (*9*, *11*).

The critical role of TRAF2, TRAF5, and TRAF6 in MAVS downstream signaling closely resembles that of TRAF recruitment in other NF-κB activating pathways such as those emanating from interleukin-1β (IL-1β), tumor necrosis factor–α (TNF-α), T cell receptor, and CD40 (*12*). However, stimulation of cells with IL-1β or TNF-α activates only IKK and TBK1, but not IRF3 (fig. S1A, lanes 1 to 5) (*13*). In contrast, activation of the RIG-I–MAVS and cGAS-STING pathways through vesicular stomatitis virus (VSV) infection and herring testis DNA (HT-DNA) transfection, respectively, leads to activation of IKK and TBK1, as well as IRF3 (fig. S1A, lanes 6 to 8). Similarly, Toll-like receptors 3 and 4 (TLR3 and TLR4) signal through the adaptor protein TRIF to active TBK1 and IRF3 (*1*). However, other TLRs that do not signal through TRIF can activate TBK1 but are unable to activate IRF3. How MAVS, STING, and TRIF possess the ability to activate both TBK1 and IRF3 is unknown.

MAVS and IRF3 form a ubiquitination- and phosphorylation-dependent complex

To understand how MAVS activates IRF3, we used cell-free assays that recapitulate IRF3 and IκBα activation by different upstream activators (*8*, *11*, *14*). We have previously shown that a recombinant MAVS protein, MAVSΔTM (MAVS lacking the C-terminal transmembrane domain) (*8*), spontaneously forms prion-like fibers to activate IKK, TBK1, and IRF3 in HeLa cytosolic extracts (S100), which could be detected by immunoblotting with phospho-specific antibodies or by native gel electrophoresis that reveals IRF3 dimerization (Fig. 1A, top). However, recombinant TRAF6 protein led to the activation of IKK and TBK1, but not IRF3 (Fig. 1A, bottom), suggesting that TBK1 activation alone is insufficient to activate IRF3.

Next, to examine potential interactions between downstream effectors (IRF3 or IκBα) and upstream activators (MAVSΔTM or TRAF6), HeLa S100 was incubated with MAVSΔTM or TRAF6 at 0°C (control) or 30°C. Flag-tagged IRF3 (Flag-IRF3) or IκBα (Flag-IκBα) was then added to the reaction mixtures for immunoprecipitation (IP) (Fig. 1B). After an in vitro assay with MAVSΔTM, a smear of protein bands in complex with Flag-IRF3 was detected with a MAVS antibody. TBK1 was also present in the MAVS-IRF3 complex (Fig. 1B, lane 3). In contrast, in cell extracts incubated with TRAF6, Flag-IRF3 was unable to pull down TBK1 (Fig. 1B, lane 9), suggesting that MAVS, but not TRAF6, induced interaction between IRF3 and TBK1.

To determine if IRF3 and MAVS form a complex in virus-infected cells, we expressed IRF3 Ser^{385}→Ala^{385} (S385A)/S386A (*15*) (Flag-IRF3 2A), which is unable to form a homodimer and may therefore associate with TBK1 or MAVS more tightly, in human embryonic kidney 293T (HEK293T) cells. Infection of these cells with Sendai virus led to the association of Flag-IRF3 2A with endogenous MAVS, TRAF2, TRAF6, and TBK1 (Fig. 1C, lane 12). These results suggest that MAVS may serve as a scaffold to bring IRF3 and TBK1 into proximity, thereby facilitating IRF3 phosphorylation by TBK1.

Because multiple E3 ubiquitin ligases are involved in MAVS downstream signaling (*9*), we next examined the role of ubiquitination in MAVS-IRF3 interaction. A deubiquitination enzyme containing the ovarian tumor type domain of the Crimean Congo hemorrhagic fever virus (vOTU) completely blocked MAVS-IRF3 interaction when it was added to the cell-free reaction (Fig. 1D, lane 3). However, vOTU no longer affected MAVS-IRF3 complex formation when added after the reaction, suggesting that ubiquitination is required only for initiating but not maintaining MAVS-IRF3 interaction (Fig. 1D, lane 4). In contrast, treatment with lambda protein phosphatase after the reaction abolished MAVS-IRF3 interaction, suggesting that MAVS-IRF3 interaction is dependent on phosphorylation (Fig. 1D, lane 5). Consistently, MAVS bound to IRF3 appeared on SDS–polyacrylamide gel electrophoresis (PAGE) as a slower-migrating smear, which was sensitive to phosphatase but not vOTU treatment (fig. S1B). These results suggest that the initial ubiquitination and subsequent phosphorylation on MAVS are necessary for MAVS-IRF3 interaction.

MAVS serine-rich clusters containing Ser^{442} are essential for IRF3 binding and activation

To map the MAVS phosphorylation site(s) essential for downstream signaling, we tested a panel of MAVS truncation mutants for their ability to bind and activate IRF3 (fig. S1C). We have previously shown that whereas the MAVS polymerization domain CARD is essential, the middle proline-rich (residues 94 to 153) and C-terminal transmembrane (510 to 540) regions of MAVS are dispensable for recombinant MAVS to activate IRF3 in the cell-free assay (*8*). Through a series of deletion analyses, we found that a truncated MAVS harboring the first 130 amino acids (containing CARD) and a C-terminal 61–amino

[1]Department of Molecular Biology, University of Texas Southwestern Medical Center, Dallas, TX 75390-9148, USA. [2]Departments of Biophysics and Biochemistry, University of Texas Southwestern Medical Center, Dallas, TX 75390-9148, USA. [3]Howard Hughes Medical Institute (HHMI), University of Texas Southwestern Medical Center, Dallas, TX 75390-9148, USA.
*Corresponding author. E-mail: zhijian.chen@utsouthwestern.edu

acid fragment (MAVS-N460 Δ131-398) was sufficient for both IRF3 binding and activation (fig. S1, C to E). Further mutagenesis revealed two MAVS C-terminal serine/threonine clusters, S426/S430/S433 (3S) and S442/S444/T445/S446 (4T/S), to be essential for IRF3 activation (fig. S1, F to H, and fig. S2, A and B). An unbiased structure-guided alignment of full-length IRF3, MAVS, and STING across species revealed sequence similarity among the MAVS 4T/S cluster, STING C terminus and the IRF3 5T/S cluster (396 to 405), whose phosphorylation is known to be essential for IRF3 dimerization (Fig. 2, A and B). Specifically, not only are MAVS S442/S444 aligned with IRF3 S396/S398, the essential IRF3 phosphorylation sites, but the charged and hydrophobic residues surrounding MAVS 4T/S (such as D438, L439, and I441) also aligned well with those around IRF3 S396/S398, suggesting that these two regions take on a similar structural fold by sharing a DL*x*IS (where *x* is any amino acid) consensus motif. Mutagenesis of the hydrophobic resides L439 and I441 to Asp or Ala abolished the ability of MAVS to activate IRF3 (fig. S2C). Furthermore, the location of MAVS S426/S430/S433 (3S) relative to MAVS S442 resembles the position of IRF3 S385/S386 with respect to IRF3 S396 (fig. S2A); phosphorylation of both IRF3 serine clusters is essential for its dimerization and activation (*16*, *17*).

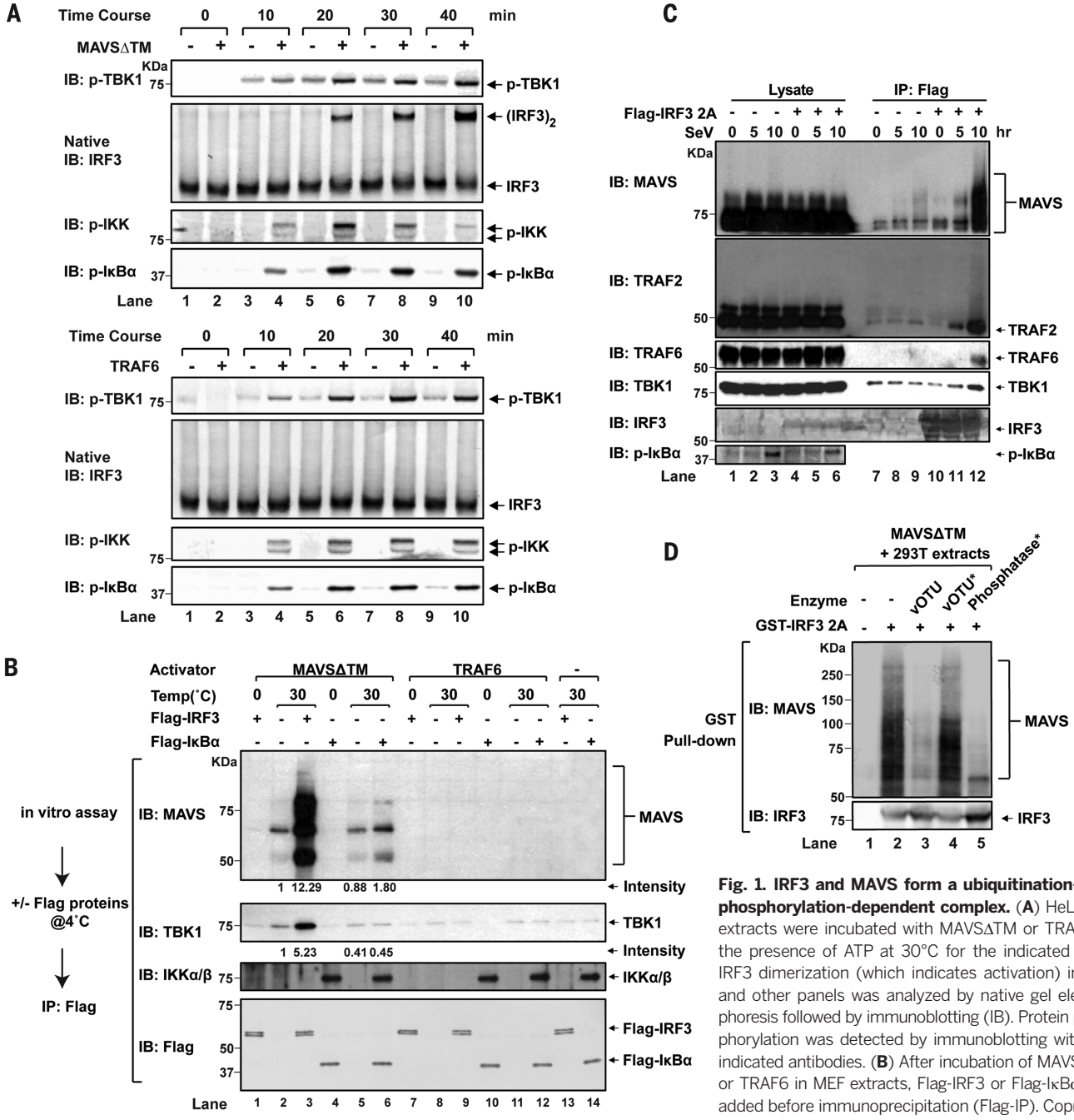

Fig. 1. IRF3 and MAVS form a ubiquitination- and phosphorylation-dependent complex. (**A**) HeLa cell extracts were incubated with MAVSΔTM or TRAF6 in the presence of ATP at 30°C for the indicated time. IRF3 dimerization (which indicates activation) in this and other panels was analyzed by native gel electrophoresis followed by immunoblotting (IB). Protein phosphorylation was detected by immunoblotting with the indicated antibodies. (**B**) After incubation of MAVSΔTM or TRAF6 in MEF extracts, Flag-IRF3 or Flag-IκBα was added before immunoprecipitation (Flag-IP). Coprecipitated proteins were detected by immunoblotting. (**C**) Twelve hours after Flag-IRF3-S385A/S386A (2A) transfection, HEK293T cells were infected with Sendai virus as indicated. Flag-IP was carried out in whole-cell lysates, and coprecipitated proteins were detected by immunoblotting. (**D**) Indicated enzymes (vOTU and phosphatase) were added during or after (indicated by asterisks) incubation of recombinant MAVSΔTM in HEK293T extracts. GST-IRF3 2A was then added as indicated, followed by GST-pull down. MAVS-IRF3 interaction was examined by immunoblotting. The data presented in this and all subsequent figures were reproduced in at least two independent experiments.

To examine whether phosphorylation of the MAVS 4T/S cluster is important for IRF3 activation, we mutated the residues to alanine (4T/S→4A) or to aspartic acid (4T/S→4D). Recombinant MAVS 4T/S→4A with the transmembrane domain deletion (MAVS-N460 4T/S→4A) failed to bind or activate IRF3 (fig. S2, B and D). MAVS-N460 4T/S→4D, however, resulted in weak IRF3 interaction and activation, probably due to incomplete phosphate mimic by aspartic acid, analogous to the loss of function of IRF3 S385D/S386D (*18*, *19*). Similar to the MAVS wild type (WT), the MAVS 4A mutant still triggered phosphorylation of TBK1 and IκBα, and it also directly interacted with TRAF2 and TRAF6 (fig. S2, B and E), indicating that the observed defect in IRF3 binding and activation is specific and not due to misfolding of MAVS.

Subsequent mutation of each T/S residue revealed that MAVS S422A alone abolished IRF3 dimerization (Fig. 2C). To examine the possibility that S442 may be important structurally (e.g., for hydrogen bonding or polarity), we mutated S442 into other amino acids. Mutating S442 into cysteine (S442C) or asparagine (S442N), which retains serine's hydrogen bonding ability or polarity but can no longer be phosphorylated, abolished MAVS' ability to activate IRF3 (fig. S2F). In contrast, serine-to-threonine (S442T) or serine–to–glutamic acid (S442E) mutants largely retained the activity, suggesting that MAVS S442 phosphorylation is essential for IRF3 activation in vitro.

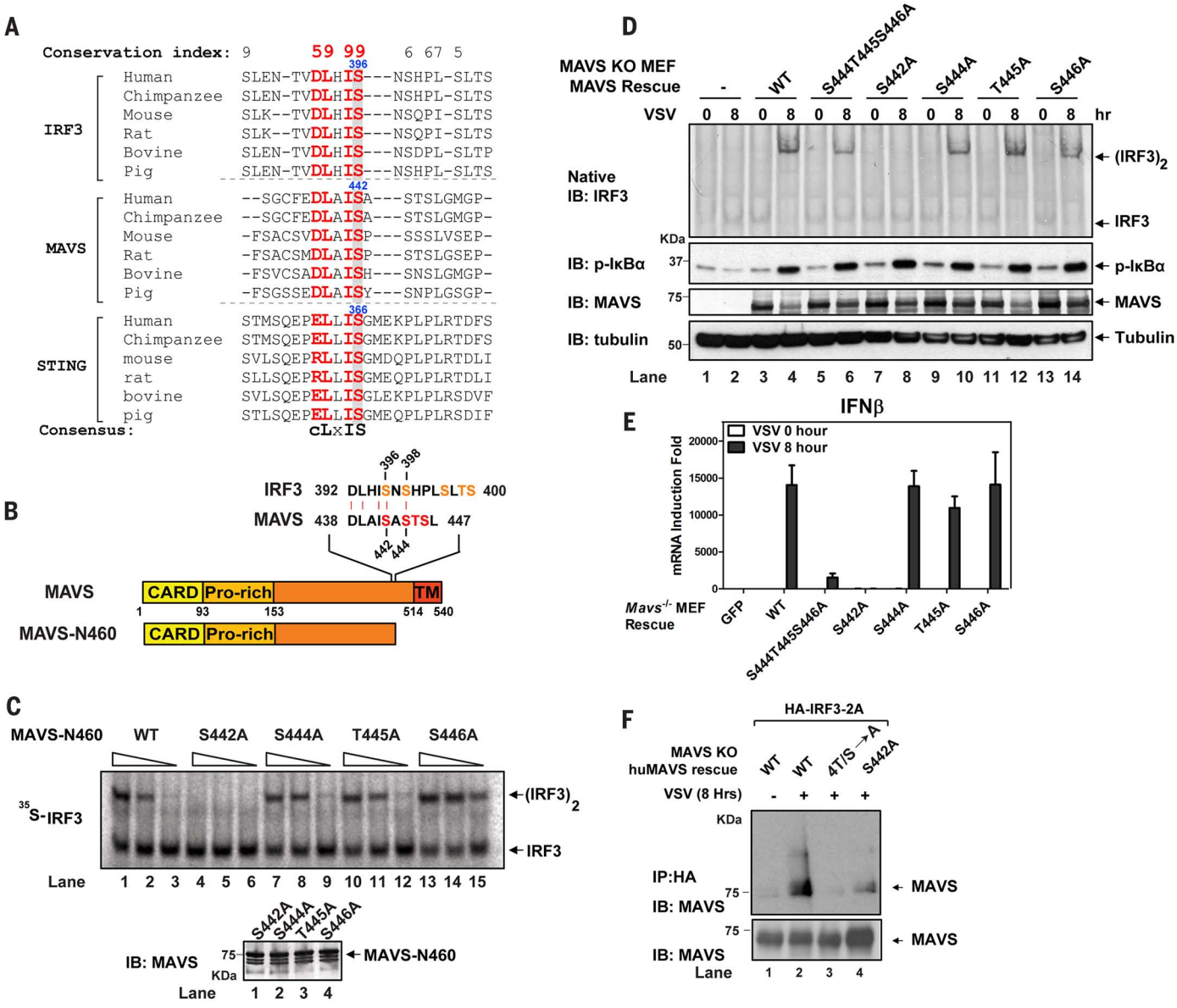

Fig. 2. MAVS C terminus harbors a conserved serine-rich region containing Ser^{442} essential for IRF3 binding and activation. (**A**) A structure-guided cross-species sequence alignment of full-length IRF3, STING, and MAVS using PROMALS3D (*32*) revealed a cLxIS (*c*, charged residues; *x*, any amino acid) consensus motif in the C-terminal regions. Conservation index score: 9 is the highest, ≥5 is significant (*46*). IRF3 structures were used to assist alignment by the software. (**B**) Diagrams of MAVS domains and its 4T/S site compared to IRF3 5T/S site. TM, transmembrane domain. (**C**) Recombinant MAVS WT and point mutants at the 4T/S site were tested for their ability to activate IRF3 in the cell-free assay. MAVS protein level was analyzed by immunoblotting. (**D** and **E**) *Mavs*$^{-/-}$ MEFs reconstituted with MAVS WT or 4T/S mutants were infected with VSV for the indicated time. IRF3 dimerization, IκBα phosphorylation, and protein expression were analyzed by immunoblotting. IFN-β mRNA levels were measured by q-RT-PCR. Error bars in this and other figures represent SDs of triplicates. (**F**) HA-tagged IRF3 2A was further stably expressed in the reconstituted cells described in (D) and (E). After VSV infection, HA-IP was carried out using a HA antibody to examine the interaction between IRF3 2A and the MAVS proteins.

To investigate the role of MAVS S442 during virus infection, we reconstituted MAVS WT or mutants into *Mavs*$^{-/-}$ mouse embryonic fibroblasts (MEFs). *Mavs*$^{-/-}$ MEFs expressing MAVS S442A failed to activate IRF3 or produce IFN-α or -β in response to VSV, whereas IκBα phosphorylation was unaffected (Fig. 2, D and E, and fig. S3A). Virus infection, however, induced comparable TBK1 phosphorylation at serine 172 in both MAVS WT and S442A-expressing cells, indicative of normal TBK1 activation (fig. S3B). Point mutation of S442 to Cys or Asn, but not Thr or Asp, abolished MAVS' ability to induce IRF3 dimerization in cells upon virus infection, suggesting that MAVS S442 is essential due to its phosphorylation, but not the serine's other structural roles (fig. S3, D to F). Both MAVS 4A and S442A mutations also diminished the ability of MAVS to interact with IRF3 2A in response to VSV infection (Fig. 2F and fig S3C). Altogether, these results indicate that MAVS phosphorylation at S442 is critical for IRF3 activation but dispensable for TBK1 and IKK activation.

In contrast to the S442 point mutants, individual mutation of the other three Ser/Thr at the 4T/S site (S444A, T445A, or S446A) did not impair IRF3 dimerization or IFN-α or -β induction (Fig. 2, D and E, and fig. S3A). However, simultaneous mutations of these residues (S444A/T445A/S446A) strongly diminished IRF3 dimerization and IFN-α or -β induction, indicating that residues in the 4T/S site function cooperatively in IRF3 activation.

To examine the role of the first serine cluster (3S) of MAVS in IRF3 activation, we reconstituted *Mavs*$^{-/-}$ MEFs with MAVS harboring simultaneous (S426A/S430A/S433A, or 3S→3A) or single mutations. MAVS 3S→3A, but not individual mutants, abolished virus induction of IFN-β (fig. S3G). Additionally, similar to MAVS 4T/S→4A, the MAVS 3S→3A mutation also completely abolished MAVS' ability to interact with IRF3 upon VSV infection (fig. S3C). Hence, the MAVS 3S site, in addition to the 4T/S site, is also important for virus-induced IRF3 activation. This pattern of two key serine/threonine clusters on MAVS is reminiscent of those on IRF3, where phosphorylation at S385 and S386, in addition to S396/S398-containing 5T/S phosphorylation, is required for IRF3 dimerization.

MAVS 4T/S site, including Ser^{442}, is phosphorylated redundantly by TBK1 and IKK

To monitor Ser^{442} phosphorylation, we generated a polyclonal antibody specific for human MAVS phospho-serine 442 (p-S442). After IRF3 activation in the cell-free assay, the MAVS p-S442 antibody recognized only MAVS-N460 WT, but not S442A (fig. S4A). MAVS S442 phosphorylation was not observed in assays with MAVS E26A, a polymerization-defective mutant unable to activate downstream kinases (fig. S4B, lane 3) (*9*). MAVS was also not phosphorylated in cell extracts treated with vOTU or deficient in TRAF2/5 or NEMO, which were unable to support IRF3 activation (fig. S4B, lanes 2, 6, and 7). However, S442-phosphorylated MAVS was strongly enriched in the IRF3 immunoprecipitates after the cell-free assay (fig. S4A, lane 3, top). Hence, MAVS S442 phosphorylation depends on MAVS polymerization and TRAF-mediated polyubiquitin synthesis and correlates with MAVS-IRF3 complex formation.

We then examined whether MAVS S442 phosphorylation could be detected in virus-infected cells. The p-S442 antibody was unable to detect a clear MAVS signal in whole-cell lysates before or after Sendai virus infection. However, IP with the p-S442 antibody revealed a MAVS smear that appeared only after virus infection, indicating that MAVS S442 phosphorylation was induced by the virus (Fig. 3A). Using targeted quantification by mass spectrometry, we observed a robust induction of phosphorylated peptides containing the MAVS 4T/S site, including S442 after virus infection (Fig. 3B and fig. S4, D to F; see also Materials and methods section on Mass spectrometry). Our mass spectrometry results also revealed that MAVS became phosphorylated at many other Ser/Thr residues after virus infection (table S2), which may explain its formation of a smear on SDS-PAGE (Fig. 3A, lane 4).

Virus infection recruits TBK1 to MAVS. However, in *Tbk1*$^{-/-}$ extracts, MAVS S442 phosphorylation and interaction with IRF3 were unaffected, whereas *Ikkα/Ikk*β-deficient extracts showed reduced IRF3 activation and binding to MAVS (fig. S4B and fig. S5A). MAVS S442 phosphorylation in *Tbk1*$^{-/-}$ extracts was completely blocked by an IKK inhibitor, TPCA-1, but not by a TBK1 inhibitor BX795 (fig. S5B). Subsequent analysis indicated that the combination of IKK and TBK1 inhibitors, but not each alone, blocked MAVS-IRF3 interaction and MAVS S442 phosphorylation in WT cell extracts (fig. S5, C and D).

In U2OS cells infected with Sendai virus, the combination of IKK and TBK1 inhibitors, but not each alone, abolished MAVS phosphorylation, as revealed by IP with the p-S442 antibody (Fig. 3C). Mass spectrometry analysis indicated that the abundance of singly phosphorylated MAVS 4T/S peptide (including p-S442) was severely diminished only when both inhibitors were added to virus-infected HEK293T cells (Fig. 3D, and fig. S5E).

In vitro kinase assays revealed that recombinant TBK1 and IKKβ directly phosphorylated MAVS S442 (Fig. 3E). TBK1 also induced MAVS-IRF3 interaction, which was abolished by phosphatase treatments (fig. S5F). Altogether, these results indicate that TBK1 and IKK are capable of directly phosphorylating MAVS C terminus upon virus infection. Phosphorylated MAVS may then recruit IRF3 for its phosphorylation by TBK1 (see below).

IRF3 C terminus harbors positively charged surfaces important for MAVS-IRF3 interaction and IRF3 dimerization

To map the IRF3 region responsible for binding to phosphorylated MAVS, we made a series of recombinant IRF3 truncation mutants and tested their MAVS binding ability (fig. S6, A and B). In vitro IRF3 IP revealed that the entire IRF3 C terminus (190 to 427, IRF3-C), containing the IRF3 association domain and the serine-rich region, is necessary and sufficient for MAVS binding (fig. S6, A and B). IRF3-C crystal structures revealed a similar fold to the Mad homology 2 (MH2) domain of the SMAD family of proteins (*20*, *21*). As a well-known phospho-binding domain, the MH2 domain contains positively charged surfaces composed of conserved basic residues that are important for both phosphorylated transforming growth factor–β (TGF-β) receptor binding and subsequent dimerization of the phosphorylated SMADs (*22*). Similarly, IRF3-C contains positively charged patches composed of conserved basic resides (Fig. 4A, and fig. S7), mutations of which were shown to abolish phosphorylation and dimerization of IRF3 in virus-infected cells (*21*).

To determine whether the observed IRF3 phosphorylation defect was due to impaired MAVS binding, we tested IRF3 2A proteins containing positively charged surface mutations for their ability to bind MAVS. Compared to IRF3 2A, all of the positively charged surface mutants had reduced interaction with MAVS and TBK1 in our cell-free assay (Fig. 4B). Additionally, when reconstituted into *Irf3*$^{-/-}$*Irf7*$^{-/-}$ MEF cells, only IRF3 2A but not 2A proteins containing positively charged surface mutations interacted with endogenous MAVS in response to VSV infection (Fig. 4C and fig. S6C). These results indicate that the positively charged surfaces on IRF3-C are important for two interactions: the binding to phosphorylated MAVS and to a second phosphorylated IRF3 molecule (i.e., dimerization of phosphorylated IRF3).

To uncouple the steps of MAVS-IRF3 binding and IRF3 dimerization, Flag-IRF3 WT or 2A (S385A/S386A, which cannot dimerize) was added to cell extracts with active MAVS either before the 30°C incubation, so that the reaction could go to completion, or afterward at 4°C where MAVS had been phosphorylated but IRF3 remained unphosphorylated (Fig. 4D). When added to the reaction at 30°C, IRF3 WT dimerized exclusively, whereas IRF3 2A stably interacted with MAVS (Fig. 4D, lane 5 and 6). However, when added at 4°C after the 30°C assay, both IRF3 WT and 2A interacted with MAVS comparably (lanes 7 and 8), suggesting that IRF3 first binds to phosphorylated MAVS (lane 7) before dissociating to form a dimer (lane 5). To further validate this model, Flag-IRF3 WT or 2A was added to *Tbk1*$^{-/-}$ cell extracts before the 30°C incubation, in which MAVS was still phosphorylated at S442 by IKK but IRF3 could not be phosphorylated (fig. S4B and fig. S6D, bottom). Here, unphosphorylated IRF3 exclusively interacted with MAVS without forming a dimer (fig. S6D, lane 2). This is in contrast to IRF3 WT in WT cell extracts, which was phosphorylated and formed a dimer (fig. S6D, lane 1). The phosphorylation-defective IRF3 2A mutant, however, exclusively interacted with MAVS (fig. S6D, lane 3). Hence, IRF3 phosphorylation causes its dissociation from MAVS. Consistently, compared with IRF3 2A, IRF3 WT pulled down less MAVS in response to VSV infection

from cells, suggesting that the majority of IRF3 WT proteins had dissociated from MAVS and undergone phosphorylation-induced dimerization (Fig. 4C, lanes 2 and 7). Taken together, these results indicate that IRF3 directly binds to phosphorylated MAVS through conserved, positively charged surfaces within the IRF3-C domain, which also mediate interaction with another phosphorylated IRF3 monomer after its dissociation from MAVS.

Both MAVS polymerization and phosphorylation are required for MAVS-IRF3 interaction

In vitro kinase assay revealed that recombinant MAVS 361-460 could be directly phosphorylated by recombinant TBK1 and IKK, but the phosphorylated fragment failed to interact with IRF3, suggesting that phosphorylation alone is insufficient for IRF3 recruitment. Given that recombinant MAVS containing CARD and a C-terminal fragment (399 to 460) interacted with IRF3 in the cell-free assay (fig. S1E), we tested whether MAVS-CARD–mediated polymerization is important for IRF3 binding. Active recombinant TBK1 induced S442 phosphorylation in both MAVS-N460 WT and polymerization-defective mutants (Fig. 4E). However, only MAVS WT, but not the CARD polymerization mutants, interacted with IRF3 in a MAVS phosphorylation–dependent manner (Fig. 4E). These results indicate that MAVS-CARD polymerization is not only important for TRAF and kinase recruitment (*9*) but also required for subsequent IRF3 binding and activation.

STING phosphorylation at Ser^{366} is required for IRF3 binding and activation in the DNA-sensing pathway

STING is an essential adaptor protein in the cytosolic DNA sensing pathway that also activates IRF3 (*23*). Recently, STING Ser^{366} was shown to be important in IRF3 binding and activation because a mutation to alanine (S366A) abolished DNA induced IRF3 activation (*24*). In contrast, another study suggested that Ser^{366} phosphorylation by ULK1 negatively regulates STING because an aspartic acid (S366D) mutation renders the protein inactive (*25*). Thus, the

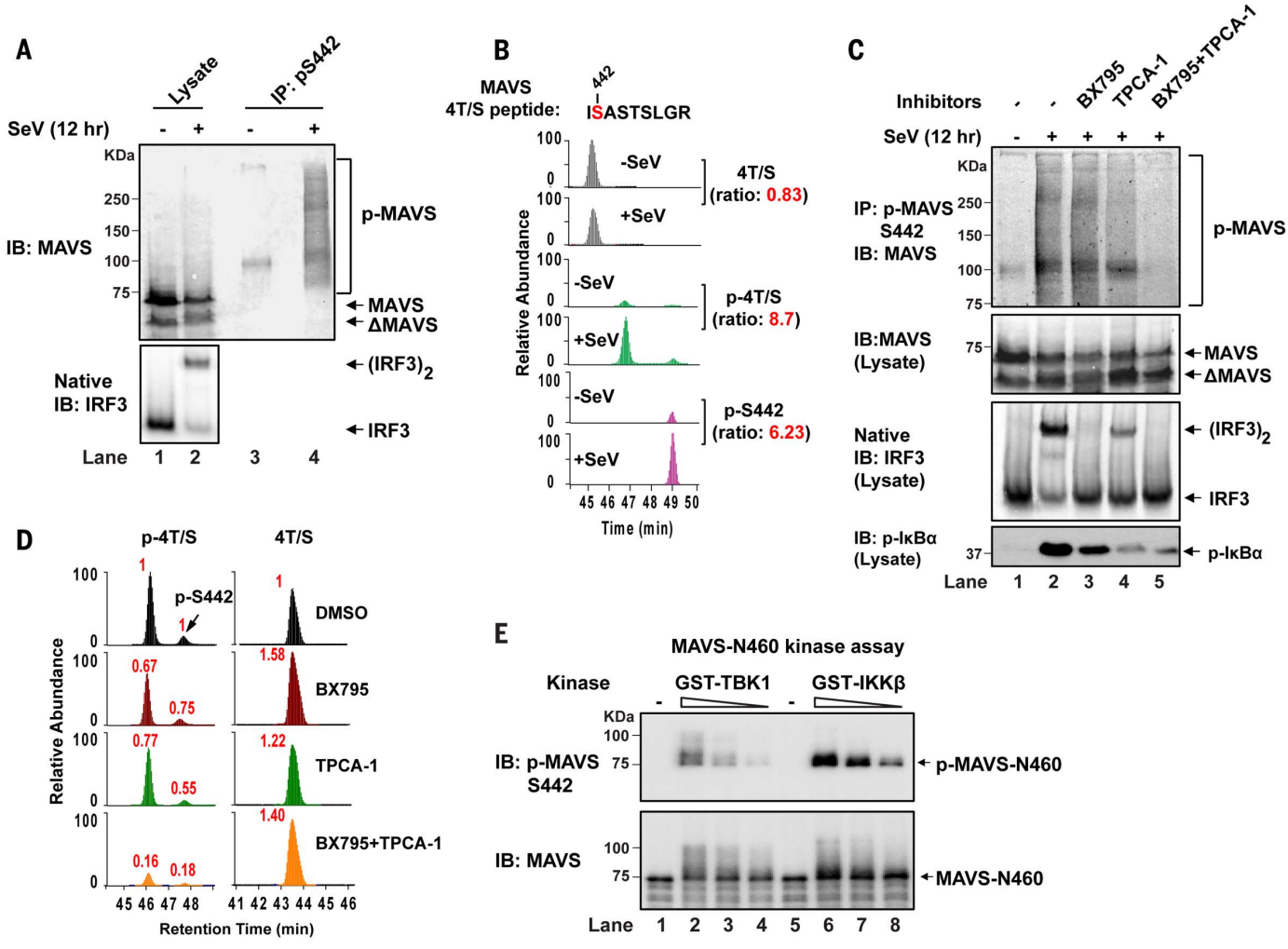

Fig. 3. The MAVS 4T/S cluster including Ser^{442} is redundantly phosphorylated by TBK1 and IKK. (**A**) U2OS cells were infected with Sendai virus (SeV) for 12 hours, then whole-cell extracts were immunoprecipitated with a MAVS p-S442 specific antibody under denaturing conditions. The whole-cell extracts and IP products were then immunoblotted with a MAVS antibody. IRF3 dimerization was monitored by native gel electrophoresis and immunoblotting. (**B**) Targeted MS2 quantification of the IS^{442}ASTSLGR peptide containing MAVS 4T/S site before or after SeV infection. The relative abundance of nonphosphorylated 4T/S (4T/S), singly phosphorylated 4T/S (p-4T/S), or phosphorylated S442 (p-S442) peptides were selectively monitored using ions specific for each species (also see table S1 and Materials and methods). The intensity ratio (in red) = MA_{+SeV}/MA_{-SeV} (MA, mass area). (**C** and **D**) Similar to (A) and (B), except that the cells were treated with a TBK1 inhibitor (BX795), an IKK inhibitor (TPCA-1), or both 1 hour before virus infection. In (D), the relative intensity of each peak is shown in red (normalized with peptide MA of DMSO-treated samples). (**E**) Recombinant TBK1 or IKKβ was incubated with purified MAVS N460 in the presence of ATP at 30°C. The reaction products were analyzed by immunoblotting with an antibody specific for p-S442 MAVS or total MAVS.

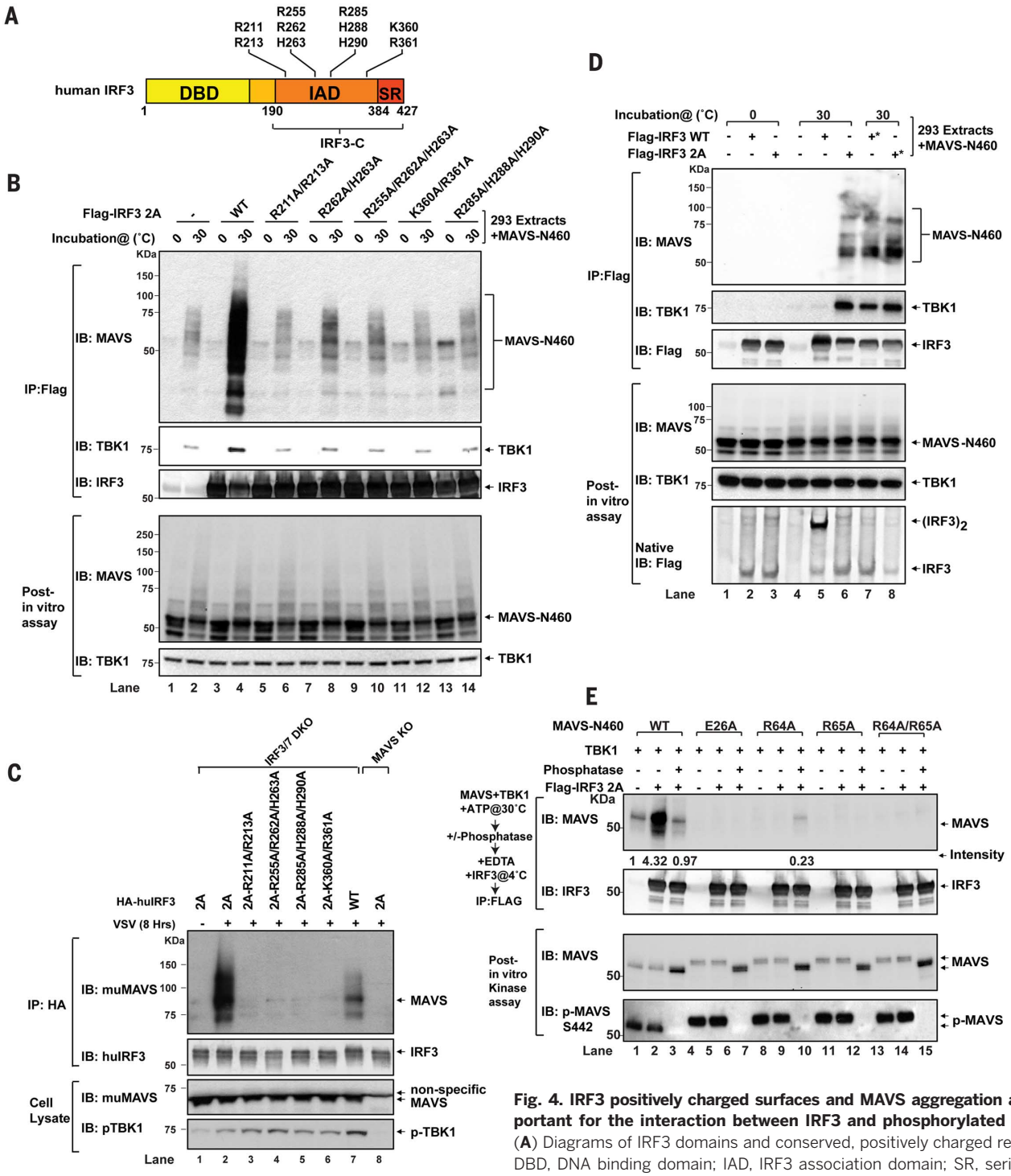

Fig. 4. IRF3 positively charged surfaces and MAVS aggregation are important for the interaction between IRF3 and phosphorylated MAVS. (**A**) Diagrams of IRF3 domains and conserved, positively charged residues. DBD, DNA binding domain; IAD, IRF3 association domain; SR, serine-rich region. (**B**) Purified Flag-IRF3 2A or 2A containing positively charged surface mutations was examined for the ability to form a complex with MAVS and TBK1 in cell extracts. (**C**) *Irf3*$^{-/-}$*Irf7*$^{-/-}$ (IRF DKO) or *Mavs*$^{-/-}$ MEF cells stably expressing HA-tagged IRF3 WT, 2A, or 2A containing mutations at the positively charged surfaces were infected with VSV, then HA-IP was carried out to examine the interaction between MAVS and IRF3 WT or mutants. (**D**) Flag-IRF3 WT and 2A proteins were either incubated with active recombinant MAVS in HEK293T extracts at 30°C (lanes 5 and 6) or added after the reaction and then incubated at 4°C (lanes 7 and 8; indicated by asterisks). Flag-IP was then carried out to examine IRF3-MAVS-TBK1 complex formation. IRF3 dimerization after the reactions was monitored by immunoblotting. (**E**) MAVS WT and CARD mutants were incubated with recombinant TBK1 in the presence of ATP followed by the addition of phosphatase (CIP) when indicated. Flag-IRF3 2A was then added followed by Flag-IP to examine the interaction between MAVS and IRF3. MAVS proteins and their phosphorylation at S442 after the reaction were analyzed by immunoblotting.

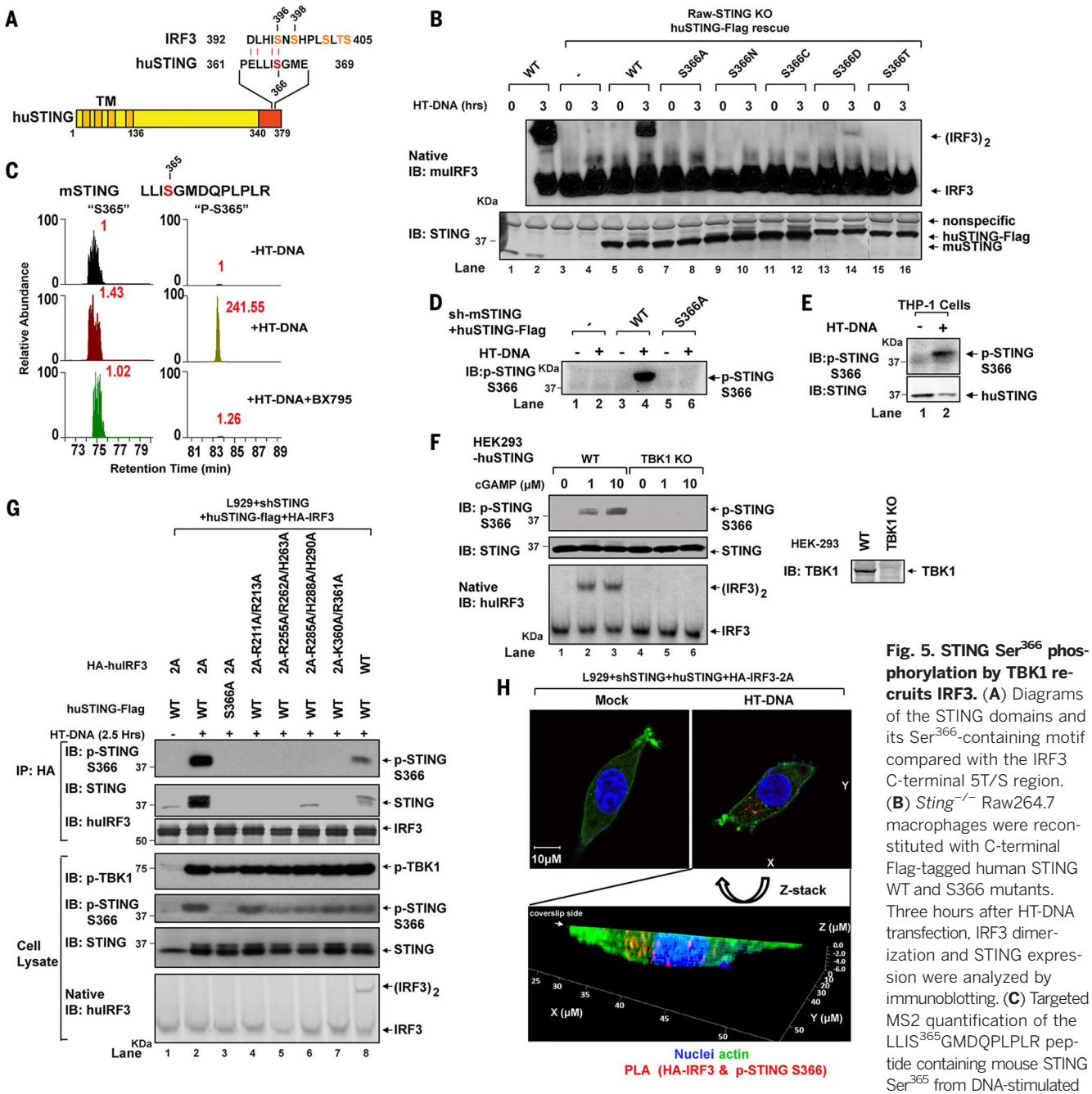

Fig. 5. STING Ser^{366} phosphorylation by TBK1 recruits IRF3. (**A**) Diagrams of the STING domains and its Ser^{366}-containing motif compared with the IRF3 C-terminal 5T/S region. (**B**) *Sting*$^{-/-}$ Raw264.7 macrophages were reconstituted with C-terminal Flag-tagged human STING WT and S366 mutants. Three hours after HT-DNA transfection, IRF3 dimerization and STING expression were analyzed by immunoblotting. (**C**) Targeted MS2 quantification of the LLIS^{365}GMDQPLPLR peptide containing mouse STING Ser^{365} from DNA-stimulated (+HT-DNA), unstimulated (-HT-DNA), or DNA-stimulated cells treated with the TBK1 inhibitor (+HT-DNA+BX795). Phosphorylated (p-S365) or non-phosphorylated peptides (S365) were calculated by selectively using ions specific for each species (also see table S1 and Materials and methods). (**D**) L929 cells depleted of endogenous STING were reconstituted with hSTING WT or S366A. STING S366 phosphorylation after HT-DNA transfection was detected with the p-S366 antibody (fig. S8E). (**E**) S366 phosphorylation of endogenous STING in THP-1 cells after HT-DNA transfection was examined by immunoblotting with the p-S366 antibody. (**F**) WT or *Tbk1*$^{-/-}$ HEK293T cells stably expressing hSTING were stimulated by cytosolic delivery of cGAMP, then IRF3 dimerization and STING phosphorylation at Ser^{366} were analyzed by immunoblotting. (**G**) HA-tagged IRF3 WT, 2A, or 2A proteins containing mutations at the positively charged surfaces were stably expressed in the L929 STING-reconstituted cells, as described in (D). After HT-DNA transfection, HA-IP was carried out to examine the interaction between IRF3 and phosphorylated STING. (**H**) L929 cells stably expressing hSTING-Flag and HA-IRF3 2A as described in (G) were transfected with HT-DNA for 2 hours or mock transfected. Interaction between IRF3 2A and p-S366-STING was visualized under confocal microscopy, using PLA with an anti-HA monoclonal antibody for IRF3 and an anti–p-S366 rabbit polyclonal antibody (top). The cell in the top right was further subjected to a *z*-stack collection, which obtains and combines multiple images at different focal distances along the *z* axis (bottom). The image was shown as three-dimensional, maximum projection mode in the Zen software. No PLA-positive cells were observed without DNA transfection, and ~50% of the HT-DNA–stimulated cells are PLA-positive (red). Blue, DAPI; green, phalloidin labeled actin filaments. The images are representative of >100 cells examined.

mechanism of STING-mediated IRF3 activation and the role of Ser^{366} need to be clarified.

Structure-guided sequence alignment of IRF3, MAVS, and STING revealed that STING S366 is positioned within the *c*L*x*IS (*c*, charged residue; *x*, any residue) consensus motif that is also found around MAVS S442 and IRF3 S396 (Figs. 2A and 5A). Moreover, STING also harbors another serine cluster (S353/S358 in human STING; S354/S357 in mouse STING) upstream of S366, positioned similarly to IRF3 S385/S386 and MAVS 3S with respect to IRF3 S396 and MAVS S442 (fig. S8A). These observations suggest that STING and MAVS may activate IRF3 through similar mechanisms. Consistently, L929 cells in which endogenous STING was depleted by short hairpin RNA (shRNA) and replaced with mouse STING (mSTING) S365A (corresponding to hSTING S366A) failed to activate IRF3 after HT-DNA transfection (fig. S8, B and C). mSTING S357A (corresponding to hSTING S358A) also had diminished ability to activate IRF3, whereas mutations of other Ser or Thr residues had little effect. mSTING S365A and S357A mutations did not affect DNA-induced activation of TBK1 and IKK (fig. S8C). Contrary to a previous report (*25*), the S365A mutation of mSTING also did not inhibit DNA-induced degradation of STING (fig. S8D). When reconstituted in *Sting*$^{-/-}$ Raw264.7 macrophages or L929 cells depleted of endogenous STING, hSTING S366A, S366C, or S366N failed to activate IRF3 in response to DNA, whereas S366D retained weak activity (Fig. 5B and fig. S8E). These results suggest that, like MAVS S442, STING S366 is important because of its phosphorylation rather than other structural roles. Similar to the MAVS 4T/S→4D and IRF3 S385D/S386D mutants, the weak activity of S366D may be due to incomplete phosphate mimic by aspartic acid.

Quantitative mass spectrometry analysis confirmed that phosphorylation of mSTING S365 was induced by more than 200-fold after HT-DNA transfection and that this phosphorylation was abolished by the TBK1 inhibitor BX795 (Fig. 5C and fig. S8F; see also Materials and methods section on Mass spectrometry). We also generated a rabbit polyclonal antibody specific for S366-phosphorylated hSTING (p-S366); this antibody detected phosphorylated hSTING in HT-DNA–transfected cells but not in unstimulated cells (Fig. 5, D and E). The S366A hSTING mutant was not detected by the antibody. Additionally, the hSTING p-S366 antibody detected a perinuclear punctate structure only in DNA-stimulated cells (fig. S8G, top), similar to the previously observed STING foci (fig. S8G, bottom) (*26*). To rule out any nonspecific staining by the phospho-specific antibody, we used proximity ligation assay (PLA) in L929-hSTING-Flag cells (Fig. S8H), where positive signals (red immunofluorescence) occur only when the hSTING p-S366 antibody is in close proximity to the Flag-antibody. We observed peri-nuclear signals only in cells after DNA transfection but not after poly(I:C) or mock transfection, indicating that our antibody specifically recognizes hSTING p-S366. After reconstitution of hSTING into WT and *Tbk1*$^{-/-}$ HEK293T cells (which lack endogenous STING), cGAMP stimulation induced STING p-S366 and IRF3 dimerization in WT but not *Tbk1*$^{-/-}$ cells, suggesting that TBK1 is essential for STING S366 phosphorylation in cells (Fig. 5F). These results indicate that STING undergoes TBK1-dependent phosphorylation at Ser^{366} only in DNA-stimulated cells.

We have previously shown that a STING C-terminal fragment (residues 281 to 379) could activate IRF3 in cytosolic cell extracts (*24*). This STING fragment was phosphorylated at S366 in the cell extracts, as revealed by immunoblotting with the p-S366 antibody (fig. S9A). Phosphorylation of STING depended on TBK1 but not on NEMO (fig. S9A). To test whether STING phosphorylation by TBK1 is important for IRF3 association with TBK1, we incubated recombinant TBK1 with WT or S366A mutant STING (281 to 379) and then added Flag-IRF3 for IP (fig. S9B). WT but not S366A STING formed a complex with IRF3 and TBK1; the formation of this complex was abolished by phosphatase treatment (fig. S9B, lanes 5, 6, and 11). Similar results were obtained after incubating the recombinant STING (281 to 379) with crude cell extracts (fig. S9C). These results demonstrate that TBK1 directly phosphorylates STING at Ser^{366} and phosphorylated STING recruits IRF3, thereby facilitating IRF3 phosphorylation by TBK1.

We next examined whether full-length STING interacts with IRF3 in response to DNA stimulation in cells. Upon DNA transfection, IRF3 2A interacted with hSTING WT but not S366A, suggesting that hSTING S366 is essential for DNA-induced interaction between STING and IRF3 (Fig. 5G, lane 2 and 3). Additionally, IRF3 WT and IRF3 2A, but not IRF3 2A bearing positively charged surface mutations, interacted with S366-phosphorylated STING, suggesting that the phospho-binding domain of IRF3 is crucial for binding to phosphorylated STING. Notably, compared with IRF3 2A, IRF3 WT pulled down substantially less STING. This suggests that analogous to MAVS-IRF3 interaction, phosphorylated IRF3 dissociates from STING and forms a dimer (Fig. 5G, lane 8).

Using the PLA assay, we examined the interaction between phosphorylated STING and IRF3 in L929 cells in which endogenous STING was depleted by shRNA and replaced by hSTING. These cells also stably expressed HA-IRF3 2A. The PLA assay using the HA antibody and the p-S366 STING antibody revealed positive signals (red immunofluorescent dots) in the perinuclear regions only after DNA stimulation (Fig. 5H; also see Materials and methods). In contrast, no PLA-positive signals were observed in DNA-stimulated cells expressing STING S366A or IRF3 2A R211/R213A (a positively charged surface mutant) (fig. S9D). Altogether, these results indicate that analogous to the role of MAVS S442 phosphorylation, STING phosphorylation at S366 is critical for direct IRF3 recruitment and activation through IRF3's phospho-binding domain.

Phosphorylation of TRIF recruits and activates IRF3

Besides the cytosolic nucleic acid–sensing pathways, stimulation of certain TLRs (namely TLR3 and TLR4) also activates IRF3 and induces type I IFNs. TLR3 and TLR4 can each activate the adaptor protein TRIF, which in turn activates IRF3 (*27*). TRIF contains an N-terminal domain that includes the TIR domain important for interaction with TLRs and a C-terminal RIP homotypic interaction motif, which can activate cell death pathways (fig. S10A). The N-terminal fragment containing ~540 amino acids of TRIF (TRIF-N540) has been shown to bind IRF3 and activate the interferon promoter when transiently expressed in HEK293T cells (*28*, *29*). To avoid triggering cell death, we chose TRIF-N540 to investigate the mechanism by which IRF3 is activated in the TLR3/4 pathways.

To examine whether TRIF interacts with IRF3 in a phosphorylation-dependent manner, we transiently expressed Flag-tagged IRF3 2A and TRIF-N540 in HEK293T cells. IP of IRF3 revealed an interaction between IRF3 2A and TRIF-N540 that was greatly diminished after pretreatment of cells with the TBK1 inhibitor BX795, suggesting that TBK1 is important for inducing TRIF-IRF3 interaction (Fig. 6A, lane 2 and 3). Moreover, phosphatase treatment of cell lysates using calf intestinal phosphatase (CIP) or Lambda phosphatase (Lambda PP) before Flag-IRF3 IP completely abolished TRIF binding to IRF3-2A, suggesting that a phosphorylation event induced the TRIF-IRF3 interaction (Fig. 6A, lanes 4 and 5). IRF3 WT and IRF3 2A containing mutations in the positively charged surface (described above) all failed to pull down TRIF-N540 (Fig. 6B). Collectively, these data indicate that, similar to MAVS and STING, TRIF also recruits IRF3 through a mechanism that depends on the kinase TBK1, its phosphorylation, and the phospho-binding domain of IRF3.

Through examination of the TRIF-N540 sequence, we found a conserved Ser/Thr cluster (S210/S212/T214) whose surrounding sequence *p*LEIS (*p*, hydrophilic amino acid) shares marked similarity to the consensus *c*L*x*IS motif (*c*, charged; *x*, any) found in IRF3, MAVS, and STING (Fig. 6C). TRIF S210 is positioned similarly to IRF3 S396, MAVS S442, and STING S366 (Fig. 6C). On the basis of this sequence analysis, we expressed a panel of TRIF mutants, including S210A/S212A/T214A (TRIF 3A), in HEK293T cells and tested their ability to interact with IRF3 2A. Only TRIF 3A, but not other TRIF mutants, failed to interact with IRF3 2A (Fig. 6D). These results suggest that the TRIF S210/S212/T214 cluster probably functions similarly to MAVS 4T/S and STING S366 in IRF3 binding and activation.

Quantitative mass spectrometry analysis identified phosphorylated peptides containing S210 in TRIF protein that was transiently expressed in HEK293T cells (fig. S10B). The intensity of phosphorylated peptides containing S210 increased by >11-fold after TBK1 coexpression (fig. S10B), suggesting that TBK1 mediates TRIF phosphorylation at the S210/S212/T214 cluster. Overexpression of WT, but not kinase-dead mutant of TBK1 (TBK1 Mut), induced a robust and phosphatase-sensitive interaction between TRIF-N540 and HA-IRF3 2A (Fig. 6E, lanes 3 to 6). In contrast, TBK1 failed to induce interaction between TRIF 3A and HA-IRF3 2A, suggesting that TRIF phosphorylation

at S210/S212/T214 by TBK1 probably induced the interaction between TRIF and IRF3 (Fig. 6E, lane 7). Taken together, these data indicate that TRIF is phosphorylated at its consensus motif S210/S212/T214 by the kinase TBK1, which leads to IRF3 recruitment.

When transiently expressed in HEK293T cells, only TRIF 3A, but not other TRIF mutants, failed to induce IRF3 dimerization (Fig. 6F). TRIF 3A

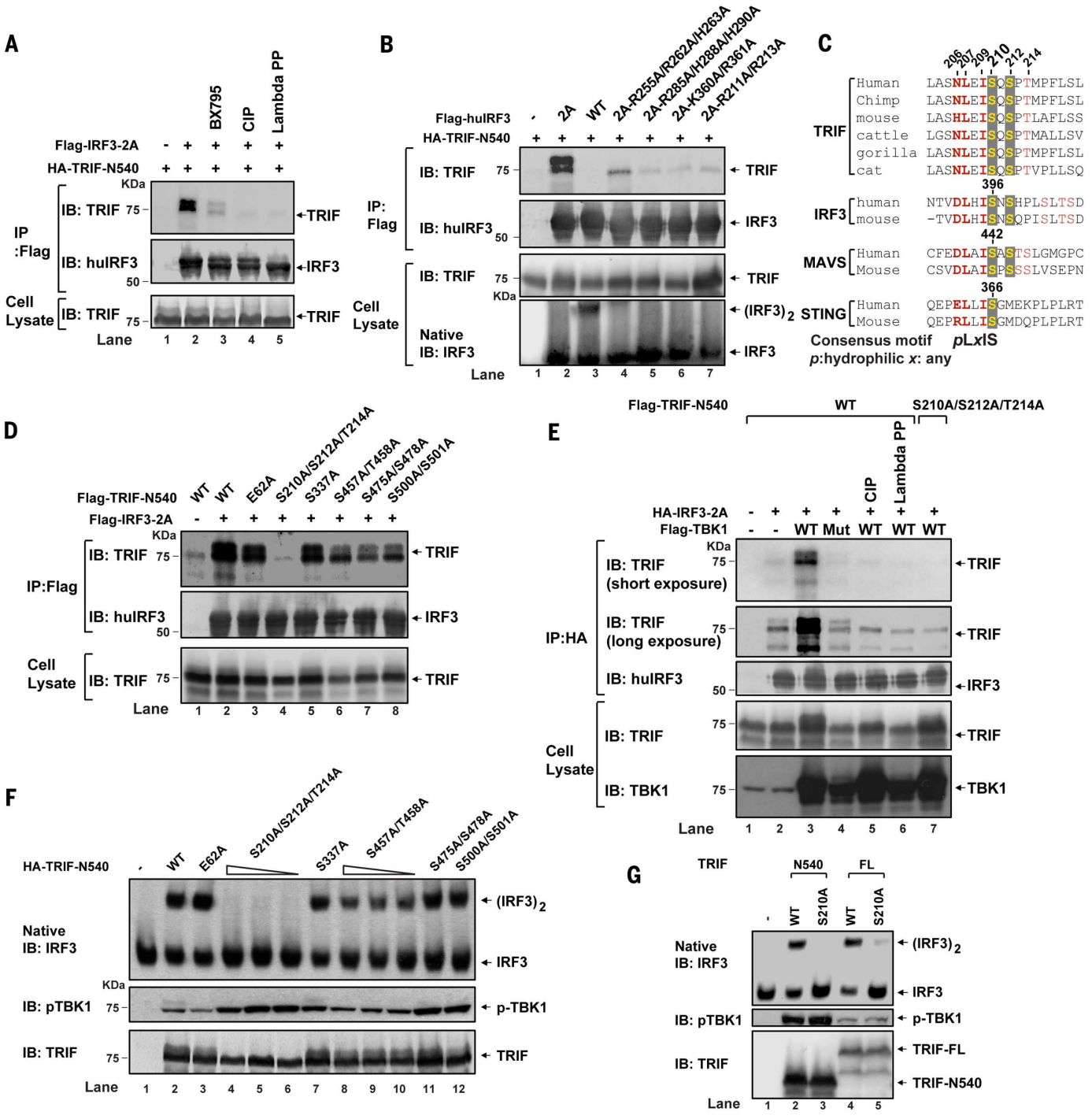

Fig. 6. TRIF recruits and activates IRF3 through phosphorylation at the *p*LxIS motif. (**A**) TRIF-N540 and Flag-tagged IRF3 2A were transiently expressed in HEK293T cells or cells that were treated with or without the TBK1 inhibitor BX795. Cell extracts were treated with different phosphatases, as indicated, before they were subjected to Flag-IP to examine the interaction between TRIF and IRF3 2A. (**B**) Similar to (A), except that IRF3 WT or IRF3 2A proteins containing mutations at the positively charged surfaces were examined for their ability to bind TRIF. (**C**) A cross-species sequence alignment between TRIF, IRF3, MAVS, and STING showing the consensus phosphorylation motif in TRIF. (**D**) Similar to A, except that different TRIF mutants were examined for their ability to bind IRF3 2A. (**E**) Similar to (A), except that Flag-tagged TRIF WT or mutant, HA-IRF3 2A, and Flag-TBK1 WT or kinase-dead mutant (Mut) were transiently expressed in HEK293T cells. HA-IP was carried out to examine the TRIF-IRF3 interaction. (**F** and **G**) After transient expression of TRIF mutants in HEK293T cells, IRF3 dimerization, TBK1 phosphorylation, and TRIF expression were analyzed by immunoblotting.

led to normal TBK1 phosphorylation at S172, indicating that the observed IRF3 dimerization defect is specific and not due to misfolding of TRIF (Fig. 6F). Moreover, mutagenesis of S210 to alanine alone in TRIF-N540 or full-length TRIF abolished its ability to induce IRF3 dimerization, suggesting that, like MAVS S442 and STING S366, TRIF S210 is the critical phosphorylation site that mediates IRF3 activation (Fig. 6G). Altogether, our data indicate that TRIF binds and activates IRF3 through a phosphorylation-dependent mechanism that is similar to that of MAVS and STING.

Discussion

Through in vitro reconstitution and cell-based assays, we reveal that phosphorylation of a consensus motif in MAVS, STING, and TRIF is essential for IRF3 recruitment and subsequent phosphorylation by TBK1. Based on previously published results and those presented here, we propose the following model for MAVS/STING/TRIF-mediated IRF3 activation (Fig. 7): (i) Adaptor protein activation: after ligand binding, RIG-I, cGAS, and TLR3/4 activate downstream adaptor proteins MAVS, STING, and TRIF, respectively. (ii) Kinase activation: active MAVS polymers or TRIF proteins recruit TRAF family ubiquitin E3 ligases (i.e., TRAF2, 5 and 6) to synthesize polyubiquitin chains to activate IKK and TBK1, whereas active STING directly recruits and activates TBK1. (iii) Adaptor protein phosphorylation: the recruited kinases then phosphorylate MAVS, STING, or TRIF at their conserved *p*L*x*IS motif. (iv) IRF3 recruitment: IRF3 binds to phosphorylated MAVS, STING, or TRIF through IRF3's conserved, positively charged surface. (v) IRF3 phosphorylation: IRF3 is efficiently phosphorylated by TBK1 once they are in close proximity. (vi) IRF3 self-association: phosphorylated IRF3 dissociates from the adaptors and dimerizes though the same positively charged surfaces. IRF3 dimer then enters the nucleus, where it functions together with NF-κB to turn on type I interferons and other cytokines.

The recruitment of IRF3 to phosphorylated MAVS, STING, and TRIF for its subsequent activation by TBK1 is markedly similar to the mechanism of SMAD activation by the TGF-β receptor (*22*). Analogous to TGF-β receptor I (TβR-I) phosphorylation by recruited TβR-II, MAVS, STING, and TRIF are phosphorylated at their conserved consensus serine-rich clusters by recruited TBK1 and/or IKK. Phosphorylated TβR-I and MAVS/STING/TRIF then recruit SMAD and IRF3, respectively, through structurally similar phospho-binding domains on SMAD and IRF3 that also mediate their respective homodimerization. This allows phosphorylated IRF3 or SMAD to dimerize and then enter the nucleus (*30*). In contrast, IL-1β, TNF-α, and other TLRs (e.g, TLR2) only activate IKK and TBK1, but not IRF3, due to the lack of a phosphorylated adaptor protein that can recruit IRF3.

Sequence profiles of IRF3, MAVS, STING, and TRIF across mammalian species revealed a consensus IRF3 binding motif: *p*L*x*IS (*p*, hydrophilic; *x*, nonaromatic) (fig. S11), which is always located in a disordered region of the respective protein. In addition, the presence of another conserved serine(s) can be found within 15 amino acids upstream of the *p*L*x*IS motif and serves as a second phosphorylation site (i.e., S385/S386 in IRF3 and S426/S430/S433 in MAVS) for IKK-related kinases. By taking these features into account, we performed a mammalian proteome-wide bioinformatic search to identify other proteins that harbor a similar motif (*31*, *32*). Twenty-one mammalian gene candidates were found to contain such a motif, and they were grouped based on their functional similarity (fig. S12, and table S3, B and C; also see Materials and methods section on Computational biology). Among these 21 candidates, proteins related to innate immunity form the largest cluster, suggesting that the consensus motif found in MAVS, STING, TRIF,

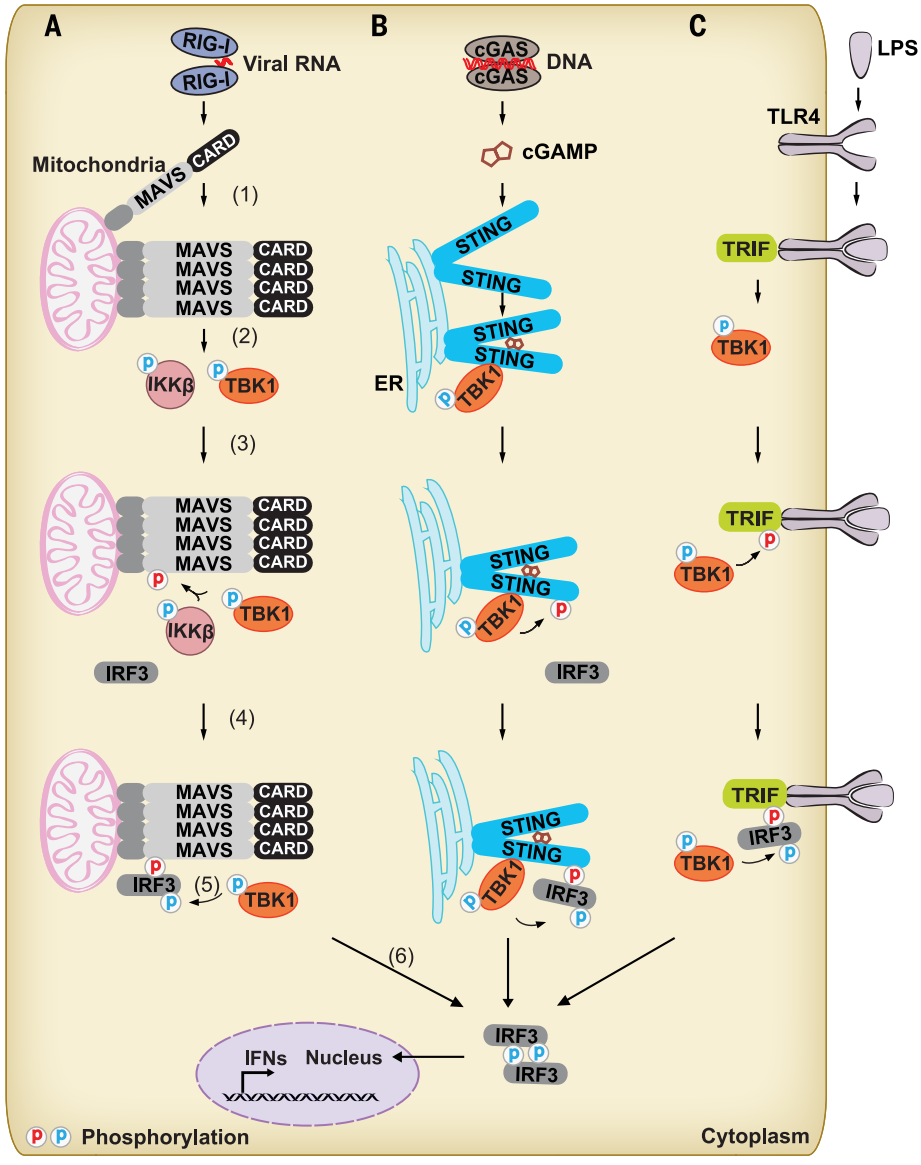

Fig. 7. A model of kinase-substrate specification by phosphorylated adaptors. (**A**) After its binding to viral RNA, RIG-I induces the polymerization of MAVS on the mitochondrial outer membrane. MAVS then recruits TRAF proteins to activate IKK and TBK1, which in turn phosphorylate MAVS at the consensus *p*L*x*IS motif. Phosphorylated MAVS binds to the C-terminal positively charged region of IRF3, thereby recruiting IRF3 for phosphorylation (P) by TBK1 through induced proximity. Phosphorylated IRF3 then forms a homodimer that enters the nucleus to turn on transcription. See the Discussion section for a more detailed description of the steps in the pathway. (**B**) Similar to (A), except that STING is phosphorylated by TBK1 in response to stimulation by DNA. DNA in the cytosol activates cGAS to produce the second messenger cGAMP, which then binds and activates STING. (**C**) lipopolysaccharide (LPS) stimulation activates TLR4, which in turn activates the adaptor proteins MyD88 and TRIF. TRIF activates TBK1, which in turn phosphorylates TRIF at the consensus motif. Phosphorylated TRIF then recruits IRF3 to facilitate IRF3 phosphorylation by TBK1.

and IRF3 is mostly related to innate immune responses, possibly as a conserved mechanism to regulate the IRF family of transcription factors. In this regard, it is interesting to note that IRF5, a key transcription factor that regulates inflammation, also contains the *pLx*IS motif. The serine residue within this motif (S445 in mouse IRF5 and S446 in human IRF5) has recently been shown to be phosphorylated by IKKβ for IRF5 activation (*33*, *34*). In summary, phosphorylation of innate immune adaptor proteins (e.g, MAVS, STING, and TRIF) and their recruitment of kinase substrates (e.g, IRF3) may be a general and conserved mechanism that provides signaling specificity in innate immunity.

Materials and methods

Antibodies

Rabbit antibodies against human IRF3, TRAF2, TRAF6, and IKKα/β and mouse antibody against human MAVS (residues 1 to 130) were obtained from Santa Cruz Biotechnology; Flag antibody (M2), M2-conjugated agarose, and tubulin antibody were purchased from Sigma; HA antibody and anti-HA–conjugated agarose were from Covance; antibodies against p-IRF3 Ser^{396}, p-TBK1 Ser^{172}, p-IκBα $Ser^{32/36}$, and p-IKKα Ser^{176}/p-IKKβ Ser^{177} were from Cell Signaling; and mouse IRF3 antibody was from Invitrogen. Anti-TBK1 monoclonal antibody was from IMGENEX. Polyclonal antibody against human TRIF was from Cell Signaling. Mouse immunoglobulin G TrueBlot ULTRA was from Rockland. The rabbit antibodies against human MAVS and STING were generated as described before (*24*, *35*). Rabbit antibodies against MAVS p-Ser^{442} and STING p-Ser^{366} were generated by immunizing rabbits with KLH-conjugated, chemically synthesized peptides "acetyl-EDLAIS(phospho)ASTSC" and "acetyl-PELLIS (phospho)GMEKC," respectively. The antibodies were affinity purified with corresponding phosphopeptide columns.

Expression constructs, recombinant proteins, and RNAi

For expression in mammalian cells, human cDNAs encoding N-terminal Flag-tagged IRF3 and IκBα were cloned into pcDNA3. After overexpression of these constructs in HEK293T cells, the encoded Flag-tagged proteins were further purified with M2 agarose, followed by Flag peptide elution. Human cDNA encoding MAVS WT and mutants were cloned into pTY-EF1A-puroR-2a lentiviral vector. Flag- or HA-tagged human IRF3-S385AS386A (2A) and other mutants were cloned into pTY-EF1A-HygromycinR-2a lentiviral vector. A human MAVS shRNA sequence (5′-GGAGAGAATTCAGAGCAAG-3′) containing U6 promoter, along with Flag-tagged human MAVS A440RM449R (2R), was cloned into pTY-U6-shRNA-EF1A-puroR-2a. STING lentiviral vectors pTY-U6-sh-mSTING-EF1A-puroR-2a-STING were cloned as described previously (*24*). These lentiviruses were transduced into $Mavs^{-/-}$ MEF cells, HEK293T cells, or L929 cells as described previously (*24*). HA- or Flag-tagged TRIF-N540 and mutants were cloned into pcDNA3. Flag-tagged TRIF-FL was in pEF-BOS vector. Mutants were constructed with the QuikChange Site-Directed Mutagenesis Kit (Stratagene; also see table S4 for the primer information). For expression in *Escherichia coli*, pET23a-His_6-MAVS ΔTM [amino acids (aa) 1 to 510] and pET28a-His_6-SUMO-MAVS-N460 (aa 1 to 460; WT and mutants) were transformed and expressed in *E. coli* BL21(DE3)-pLysS strain. These His-tagged proteins were purified as described previously (*8*). Sumo protease was subsequently used to cut off His_6-SUMO tag, yielding nontagged proteins. In addition, His_8-IRF3 (from *E. coli*), His_6-TRAF6 (from insect Sf9 cells), GST-TBK1 (Sf9 cells; GST, glutathione *S*-transferase), and GST-IKKβ (Sf9 cells) were purified as described previously (*8*, *11*, *14*).

Viruses, cell culture, and transfection

Sendai virus (Cantell strain, Charles River Laboratories) was used at a final concentration of 100 hemagglutinating units/ml. VSV (ΔM51)-GFP virus was from J. Bell (Univ. of Ottawa) and was propagated in Vero cells. Plasmids and HT-DNA were transfected into cells using lipofectamine 2000 (Life Technologies). Digitonin permeabilization was used to deliver cGAMP into cultured cells as previously described (*36*). A lentiviral system for stable gene expression and shRNA knockdown were used as described before (*24*). All cells were cultured at 37°C in an atmosphere of 5% (v/v) CO_2. HEK293T and Raw264.7 macrophages were cultured in Dulbecco's modified Eagle's medium (DMEM) supplemented with 10% (v/v) cosmic calf serum (Hyclone), penicillin (100 U/ml), and streptomycin (100 μg/ml). HeLa, MEF, U2OS, L929, and BJ cells were cultured in DMEM supplemented with 10% (v/v) fetal bovine serum (Atlanta) and antibiotics. THP1 cells were cultured in RPMI 1640 supplemented with 10% fetal bovine serum, 2 mM β-mercaptoethanol, and antibiotics. $Sting^{-/-}$ Raw264.7 macrophages were purchased from InvivoGen.

Generation of TBK1 knockout HEK293T cells by CRISPR/Cas9

Single-guide RNA (sgRNA) with the sequence 5′-CATAAGCTTCCTTCGTCCAG-3′ was designed for targeting exon 2 of the human TBK1 genomic locus. The sgRNA sequence driven by a U6 promoter was cloned into a lentiCRISPR vector that also expresses Cas9 as previously described (*37*). The lentiviral plasmid DNA was then packaged into a lentivirus for infection in HEK293T cells. Infected cells were selected in puromycin (2 μg/ml) for 2 weeks before single colonies were selected and tested for TBK1 expression by immunoblotting.

Biochemical assays for IRF3 activation and MAVS-IRF3 complex formation

Cell-free assays for IRF3 activation and phosphorylation of IκBα, IKKα/β, and TBK1 were preformed as described previously (*8*, *9*, *11*). Similarly, MAVS S442 and STING S366 phosphorylation was detected by immunoblotting with the p-S442 and p-S366 antibodies, respectively, after the cell-free assay. For a better MAVS p-S442 detection, His_6-tagged MAVS-N460 in 100-μl reaction mixtures was pulled down with the Ni-NTA agarose in 8 M urea. After washing the agarose with buffer A [20 mM Tris-HCl (pH 7.0), 1 M NaCl, and 0.5% NP-40], MAVS phosphorylation was detected by immunoblotting with the p-S442 antibody.

To determine MAVS-IRF3 or STING-IRF3 complex formation in the cell-free assay, a reaction mixture (100 μl) containing buffer B [20 mM HEPES-KOH (pH 7.0), 2 mM adenosine triphosphate (ATP), 5 mM $MgCl_2$, and 0.5 mM dithiothreitol (DTT)], 200 ng recombinant MAVSΔTM or MAVS-N460 or His_6-STING (281 to 379), 200 μg cytosolic extracts (S5 or S100), and 200 ng Flag-IRF3 2A or GST-Flag-IRF3 2A was incubated at 30°C for 1 hour. In some experiments, Flag-IRF3 WT or 2A was added into the reaction mixture at 4°C right before IP as indicated. Flag-IP was then carried out using Flag antibody (M2) agarose at 4°C for 2 hours in the presence of buffer C [20mM Tris-HCl (PH 7.5), 150 mM NaCl, 0.5% NP-40] and the protease inhibitor cocktail (Roche). The agarose beads were washed three times with buffer C, and coprecipitated proteins were detected by immunoblotting.

For MAVS or STING phosphorylation by purified kinases TBK1 or IKKβ, a reaction mixture (10 μl) containing buffer A, 25 ng recombinant MAVS protein, and 40 ng GST-TBK1 or GST-IKKβ was incubated at 30°C for 40 min. Phosphorylation of MAVS and STING were detected by immunoblotting with the p-S442 and p-S366 antibodies, respectively.

To determine MAVS-IRF3 or STING-IRF3 complex formation in the purified kinase assay, a reaction mixture (100 μl) containing buffer A, 250 ng recombinant MAVS or STING protein, and 400 ng GST-TBK1 or GST-IKKβ was incubated at 30°C for 40 min. After stopping the reaction with 5 mM EDTA, Flag-IRF3 2A was added into the reaction mix at 4°C before IP. Flag-IP was then carried out using M2-agarose at 4°C for 1 hour in the presence of buffer C and 0.2 μg/μl bovine serum albumin. The agarose beads were washed three times with buffer C, and coprecipitated proteins were detected by immunoblotting.

IP assay for adaptor-IRF3 interactions in cells

To determine MAVS-IRF3 complex formation in cells, tagged IRF3 WT or 2A was stably expressed in the indicated cells. After virus infection, whole-cell lysates were prepared in the presence of buffer D [20 mM Tris-HCl (PH 7.5), 100 mM NaCl, 10% glycerol, 0.5% NP-40, and 0.5% DDM] and the protease inhibitor cocktail (Roche). Anti-Flag (M2) agarose or anti-HA agarose was added into the whole-cell lysate and incubated at 4°C for 2 hours. The agarose beads were washed three times with buffer D, and coprecipitated proteins were detected by immunoblotting.

To determine STING-IRF3 complex formation in cells, HA-tagged IRF3 WT or 2A was stably expressed in the indicated cells. After HT-DNA transfection, cells were homogenized in hypotonic buffer (10 mM Tris-Cl [pH 7.5], 10 mM KCl, 0.5 mM EGTA, 1.5 mM MgCl2, and Roche

EDTA-free protease inhibitor cocktail). The homogenates were centrifuged at 1000 × g for 5 min to pellet nuclei and unbroken cells (P1). The supernatant (S1) was subjected to centrifugation at 5000 × g for 10 min to separate crude mitochondrial pellet from cytosolic supernatant (S5). Anti-HA agarose beads were added into the S5 and incubated at 4°C for 2 hours. The agarose beads were washed three times with buffer C, and coprecipitated proteins were detected by immunoblotting.

To determine TRIF-IRF3 complex formation in cells, tagged IRF3 and TRIF-N540 were transiently expressed in HEK293T cells. 24 hours after transfection, whole-cell lysates were prepared in the presence of buffer E [20 mM Tris-HCl (PH 7.5), 150 mM NaCl, 10% glycerol, 0.5% CHAPS] and the protease inhibitor cocktail (Roche). Anti-Flag (M2) agarose or anti-HA agarose beads were added into the whole-cell lysates and incubated at 4°C for 2 hours. The agarose beads were washed three times with buffer E, and coprecipitated proteins were detected by immunoblotting.

Quantitative reverse transcription polymerase chain reaction (q-RT-PCR)

Total RNA was isolated using TRIzol (Invitrogen). 0.1 μg total RNA was reverse-transcribed into cDNA using iScript Kit (Bio-Rad). The resulting cDNA served as the template for quantitative PCR analysis using iTaq Universal SYBR Green Supermix (Bio-Rad) and Real-Time PCR System (ABI). Primers for specific genes are listed as follows: mouse β-actin, 5′-TGACGTTGACATCCGTAAAGACC-3′ and 5′-AAGGGTGTAAAACGCAGCTCA-3′; mouse IFN-β, 5′CCCTATGGAGATGACGGAGA-3′ and 5′-CTGTCTGCTGGTGGAGTTCA-3′; mouse IFN-α, 5′-ATTTTGGATTCCCCTTGGAG-3′ and 5′-TATGTCCTCACAGCCAGCAG-3′.

Purification of MAVS, STING, and TRIF for phosphorylation site identification by mass spectrometry

For human MAVS, HEK293T cells were stably infected with a lentiviral vector, pTY-U6-shMAVS-EF1A-Flag-MAVS-2R, which depleted endogenous MAVS by shRNA and replaced it with a Flag-tagged MAVS containing two amino acids substitution (A440R/M449R or MAVS-2R), which permits trypsin digestion and therefore facilitates phosphorylation site mapping by mass spectrometry (see below). The cells were infected with Sendai virus to activate the RIG-I–MAVS pathway. For STING, HT-DNA was transfected into L929 cells with endogenous STING depleted by shRNA and replaced with mouse STING-Flag (pTY-U6-shSTING-EF1A-mSTING-flag). For TRIF, HA-TRIF-N540 was transfected alone or cotransfected with Flag-TBK1 in HEK293T cells. Cells were then harvested in PBS containing 3 mM EDTA, followed by addition of 1% SDS to denature proteins. The denatured cell lysates were sonicated to shear DNA and boiled at 95°C for 10 minutes. Excess SDS was removed with SDS-OUT precipitation kit from Pierce and Flag-IP for MAVS and STING or HA-IP for TRIF was carried out in the presence of buffer A [20 mM Tris-HCl (pH 7.0), 1M NaCl, 0.5% NP-40] at 4°C overnight. The anti-Flag M2 agarose beads were then washed three times with buffer A and buffer C. Bound STING or MAVS proteins were eluted with the Flag peptide. Eluted proteins were buffer-exchanged into 50 mM NH_4HCO_3, reduced in 5 mM DTT, and alkylated in 2.7 mM iodoacetamide. After trypsin digestion (1:20) at 30°C overnight, the peptide mixture was acidified with 1% formic acid, purified with C_{18} Zip-tip (Millipore), and then analyzed by nano–liquid chromatography–mass spectrometry (nano-LC-MS). For HA-TRIF, anti-HA agarose beads with bound proteins were directly boiled in SDS sample buffer containing 2% SDS and subjected to SDS-PAGE and Coomassie-blue staining. Gel slices near 75 kD were subsequently subjected to trypsin digestion and C_{18} Zip-tip purification, followed by nano-LC-MS analysis.

Mass spectrometry

Mass spectrometry analyses and targeted quantification of tryptic MAVS, STING, or TRIF peptides were conducted on a Dionex Ultimate 3000 nanoLC system coupled to a Q-Exactive mass spectrometer (Thermo Scientific). The LC conditions and ion source parameters have been described before (*4*, *9*). For tandem MS/MS analyses, full-scan mass spectra were acquired in the range of mass/charge ratio (m/z) = 300 to 1500, with a resolution of 70,000 at m/z = 200 in the Orbitrap. MS/MS spectra (resolution: 17,500 at m/z = 200) were acquired in a data-dependent mode whereby the top 15 most abundant parent ions were subjected to further fragmentation by higher-energy collision dissociation (HCD). Phosphorylated and nonphosphorylated TRIF S210–containing peptides were directly analyzed and quantified with Xcalibar 2.2 (Thermo Scientific), according to the specific ions indicated in table S1.

To quantify phosphorylated and nonphosphorylated MAVS and STING peptides, targeted SIM and targeted MS2 assays were developed on the Q-Exactive mass spectrometer. The precursor ions in the inclusion list for both of the assays are shown in table S1. Settings for targeted SIM were: resolution, 70,000; AGC target, 5E4; maximum injection time, 250 ms; isolation window, 0.5 m/z. The targeted MS2 settings were as follows: resolution, 35,000; AGC target, 2E4; maximum injection time, 120 ms; isolation window, 0.5 m/z; and normalized collision energy, 30. Data acquisition and analyses were performed with Xcalibar 2.2. The relative abundance of each peptide or site-specific phosphorylation on the same peptide was represented by the intensity of product ions that are specific to each phosphorylation site (see table S1).

Targeted mass spectrometry identifies MAVS phosphorylation sites in virus-infected cells

The MAVS C-terminal region containing the 3S and 4T/S sites (aa 420 to 460) lacks lysine and arginine (fig. S2A). To facilitate trypsin digestion and mass spectrometry analysis, a Flag-tagged MAVS mutant (A440R/M449R or MAVS-2R) was introduced into a HEK293T cell line that was depleted of endogenous MAVS by shRNA. The MAVS-2R mutant robustly rescued IRF3 dimerization after viral infection (fig. S4C), indicating that the substitutions do not alter the function of MAVS. Trypsin digestion of purified Flag-MAVS-2R from cells created a short peptide ("ISASTSLGR") including the 4T/S site (4T/S peptide), which was identified by nano-LC-MS. Following viral infection, we observed substantially increased abundance of an ion with m/z of 486.23 ($z = 2^+$), the fragmentation pattern of which matched to singly phosphorylated 4T/S peptides (fig. S4D). Furthermore, by using targeted quantification, we observed robust induction of singly phosphorylated 4T/S peptides from the virus-infected sample (Fig. 3B and fig. S4D). The singly phosphorylated peptides eluted as two peaks (peak a and b). By examining site-localizing fragment ions specific to each phospho-serine in the MS^2 spectra, we found that peak a contains mainly p-S446 peptides, whereas peak b is a mixture of p-S442 and p-S444 peptides (fig. S4, E and F). Both phospho-S442 and total phospho-4T/S signals were induced by virus infection (Fig. 3B).

Targeted mass spectrometry reveals phosphorylation of mouse STING at Ser^{365} in DNA-stimulated cells

We generated L929 cells stably expressing a C-terminal Flag-tagged mouse STING (human STING C-terminus lacks arginine or lysine that can be cleaved by trypsin) in place of endogenous STING, which was depleted by shRNA. In these cells, HT-DNA transfection resulted in strong IRF3 activation, which was completely blocked by treatment with the TBK1 inhibitor, BX795 (fig. S8F). Tryptic digestion of purified mSTING-Flag from the DNA-transfected cells led to the identification of a peptide ("LLIS^{365}GMDQPLPLR") covering the S365 site (S366 in human STING) by nano-LC-MS. Following virus infection, we observed substantially increased abundance of an ion with m/z of 766.90 ($z = 2^+$), which was confirmed to be phosphorylated S365 peptides by HCD fragmentation. Furthermore, by using targeted quantification (table S1), we observed robust induction of the phosphorylated S365 peptide only from the DNA-transfected sample (Fig. 5C).

Kinase inhibitors for cell-free assay or cell-based experiments

The kinase inhibitors were dissolved in dimethyl sulfoxide (DMSO) and used both in vitro and in cells at the following final concentrations: TBK1 inhibitor (BX795, Selleckchem), 4 μM; IKK inhibitor (TPCA-1, Sigma), 20 μM; and PLK1 inhibitor (BI2356, Selleckchem), 20 μM. For cell-free assays, the kinase inhibitors were incubated with the reaction mixtures at 30°C, and the final DMSO concentration was kept below 5% of total reaction volume. In cell-based experiments, the inhibitors were added 1 hour before viral infection, HT-DNA, or TRIF transfection.

Immunofluorescence

BJ cells with or without HT-DNA transfection were fixed and incubated with the STING p-S366–specific antibody, followed by a secondary antibody

conjugated with Alexa Fluor 488. Green fluorescent signals were imaged by a Zeiss LSM710 confocal microscope (Carl Zeiss). Nuclei were stained with 4′,6-diamidino-2-phenylindole (DAPI) in the mounting medium (Vector Labs).

Proximity ligation assay (PLA)

Proximity ligation assays to detect STING phosphorylation and STING-IRF3 interaction were conducted using the Duolink In Situ Red Kit Mouse/Rabbit (Sigma-Aldrich). L929 cells stably expressing huSTING-Flag and HA-IRF3 2A with or without HT-DNA transfection were fixed and incubated with primary antibodies against two proteins as indicated; secondary antibodies conjugated with plus and minus PLA probes were then added. After ligation, rolling circle amplification, and hybridization with fluorescently labeled oligonucleotides, red fluorescent dots (indicating close proximity of proteins recognized by two different primary antibodies) were imaged by a Zeiss LSM710 confocal microscope. Cell shapes were indicated by phalloidin-labeled actin filaments, and nuclei were stained with DAPI in the mounting medium.

Computational biology

Combining the experimental data and sequence profiles of IRF3, MAVS, STING, and TRIF (fig. S11), we derived that an IRF3 binding motif harbors the following sequence features: *p*L*x*IS (*p*, hydrophilic; *x*, nonaromatic; S, phosphorylated) and another serine surrounded by a hydrophobic residue within the upstream 15 amino acids. Starting from all of the 99,459 alternatively spliced isoforms of human proteins in the Ensembl database (*38*), we identified 4229 motifs with this pattern. Requiring this motif to be conserved among the 43 mammalian species (table S3A), we narrowed this list down to 403 motifs from 399 isoforms. We required 90% of sequences to follow the sequence pattern for the most conserved positions (the second and the last two positions), whereas for those more variable positions, we allowed 20% of sequences to be amino acids that were not suggested as permissible in experimental data and sequence alignments of IRF3, MAVS, STING, and TRIF.

The observation that this motif tends to be in the flexible linkers (usually predicted to be disordered) between domains helped us to further reduce the number of candidates. We detected domains in these proteins using HMMER (*39*) against Pfam domains (*40*) and predicted the disordered regions using the Espritz Web server (*41*) with parameters trained on disordered proteins in the Disprot database (*42*). We identified 72 candidate motifs from 72 protein isoforms that were largely in the linkers between domains and that were predicted to be largely disordered. All of these candidate protein isoforms were further mapped to the Uniprot entries (*43*), resulting in the final candidate list of 21 protein-coding genes (table S3B).

We extracted the gene ontology (GO) terms (*44*) in the category of "biological process" associated with these candidate proteins from Uniprot. The enriched GO terms associated with these proteins were detected with a binomial test, and the most significantly enriched GO terms are listed in table S3C. In addition, we used the number of shared GO terms to represent the functional similarity between proteins and clustered all of the candidates in CLANS (*45*) based on similarity in function; the result is shown in fig. S12. We further assigned a confidence level of these motifs based on: (i) how well they overlap with domain linkers and disordered regions and (ii) additional sequence features we observed in IRF3, MAVS, STING, and TRIF (i.e., the presence of multiple serine residues upstream of the motif and the preference of negatively charged versus positively charged residues in the motif). The confidence level of these motifs is reflected by the color code in fig. S12.

The largest cluster of proteins containing the consensus motif and other features described above is that related to innate immune responses (fig. S12). Statistical tests also support significant enrichment in several GO terms related to innate immune response. In addition to MAVS, STING, TRIF, and IRF3, the proteins identified from this analysis include IRF5, which is important for proinflammatory cytokine induction by multiple pathways; brain-specific angiogenesis inhibitor 1–associated protein 2 (BAIP2_HUMAN in Uniprot); and dual-specificity mitogen-activated protein kinase kinase 4 (MP2K4_HUMAN in Uniprot). The roles and regulations of these and other proteins identified from our computational analysis require further studies.

REFERENCES AND NOTES

1. S. Akira, S. Uematsu, O. Takeuchi, Pathogen recognition and innate immunity. *Cell* **124**, 783–801 (2006). doi: 10.1016/j.cell.2006.02.015; pmid: 16497588
2. M. Yoneyama, T. Fujita, RNA recognition and signal transduction by RIG-I-like receptors. *Immunol. Rev.* **227**, 54–65 (2009). doi: 10.1111/j.1600-065X.2008.00727.x; pmid: 19120475
3. J. Wu *et al.*, Cyclic GMP-AMP is an endogenous second messenger in innate immune signaling by cytosolic DNA. *Science* **339**, 826–830 (2013). doi: 10.1126/science.1229963; pmid: 23258412
4. L. Sun, J. Wu, F. Du, X. Chen, Z. J. Chen, Cyclic GMP-AMP synthase is a cytosolic DNA sensor that activates the type I interferon pathway. *Science* **339**, 786–791 (2013). pmid: 23258413
5. A. Pichlmair, C. Reis e Sousa, Innate recognition of viruses. *Immunity* **27**, 370–383 (2007). doi: 10.1016/j.immuni.2007.08.012; pmid: 17892846
6. D. B. Stetson, R. Medzhitov, Recognition of cytosolic DNA activates an IRF3-dependent innate immune response. *Immunity* **24**, 93–103 (2006). doi: 10.1016/j.immuni.2005.12.003; pmid: 16413926
7. X. Jiang *et al.*, Ubiquitin-induced oligomerization of the RNA sensors RIG-I and MDA5 activates antiviral innate immune response. *Immunity* **36**, 959–973 (2012). doi: 10.1016/j.immuni.2012.03.022; pmid: 22705106
8. F. Hou *et al.*, MAVS forms functional prion-like aggregates to activate and propagate antiviral innate immune response. *Cell* **146**, 448–461 (2011). doi: 10.1016/j.cell.2011.06.041; pmid: 21782231
9. S. Liu *et al.*, MAVS recruits multiple ubiquitin E3 ligases to activate antiviral signaling cascades. *eLife* **2**, e00785 (2013). doi: 10.7554/eLife.00785; pmid: 23951545
10. W. Zeng *et al.*, Reconstitution of the RIG-I pathway reveals a signaling role of unanchored polyubiquitin chains in innate immunity. *Cell* **141**, 315–330 (2010). doi: 10.1016/j.cell.2010.03.029; pmid: 20403326
11. W. Zeng, M. Xu, S. Liu, L. Sun, Z. J. J. Chen, Key role of Ubc5 and lysine-63 polyubiquitination in viral activation of IRF3. *Mol. Cell* **36**, 315–325 (2009). doi: 10.1016/j.molcel.2009.09.037; pmid: 19854139
12. S. Liu, Z. J. Chen, Expanding role of ubiquitination in NF-κB signaling. *Cell Res.* **21**, 6–21 (2011). doi: 10.1038/cr.2010.170; pmid: 21135871
13. K. Clark, L. Plater, M. Peggie, P. Cohen, Use of the pharmacological inhibitor BX795 to study the regulation and physiological roles of TBK1 and IkappaB kinase epsilon: A distinct upstream kinase mediates Ser-172 phosphorylation and activation. *J. Biol. Chem.* **284**, 14136–14146 (2009). doi: 10.1074/jbc.M109.000414; pmid: 19307177
14. L. Deng *et al.*, Activation of the IkappaB kinase complex by TRAF6 requires a dimeric ubiquitin-conjugating enzyme complex and a unique polyubiquitin chain. *Cell* **103**, 351–361 (2000). doi: 10.1016/S0092-8674(00)00126-4; pmid: 11057907
15. Single-letter abbreviations for the amino acid residues are as follows: A, Ala; C, Cys; D, Asp; E, Glu; F, Phe; G, Gly; H, His; I, Ile; K, Lys; L, Leu; M, Met; N, Asn; P, Pro; Q, Gln; R, Arg; S, Ser; T, Thr; V, Val; W, Trp; and Y, Tyr.
16. R. Lin, C. Heylbroeck, P. M. Pitha, J. Hiscott, Virus-dependent phosphorylation of the IRF-3 transcription factor regulates nuclear translocation, transactivation potential, and proteasome-mediated degradation. *Mol. Cell. Biol.* **18**, 2986–2996 (1998). pmid: 9566918
17. M. Yoneyama *et al.*, Direct triggering of the type I interferon system by virus infection: Activation of a transcription factor complex containing IRF-3 and CBP/p300. *EMBO J.* **17**, 1087–1095 (1998). doi: 10.1093/emboj/17.4.1087; pmid: 9463386
18. W. Suhara *et al.*, Analyses of virus-induced homomeric and heteromeric protein associations between IRF-3 and coactivator CBP/p300. *J. Biochem.* **128**, 301–307 (2000). doi: 10.1093/oxfordjournals.jbchem.a022753; pmid: 10920266
19. R. Lin, Y. Mamane, J. Hiscott, Structural and functional analysis of interferon regulatory factor 3: Localization of the transactivation and autoinhibitory domains. *Mol. Cell. Biol.* **19**, 2465–2474 (1999). pmid: 10082512
20. B. Y. Qin *et al.*, Crystal structure of IRF-3 reveals mechanism of autoinhibition and virus-induced phosphoactivation. *Nat. Struct. Biol.* **10**, 913–921 (2003). doi: 10.1038/nsb1002; pmid: 14555996
21. K. Takahasi *et al.*, X-ray crystal structure of IRF-3 and its functional implications. *Nat. Struct. Biol.* **10**, 922–927 (2003). doi: 10.1038/nsb1001; pmid: 14555995
22. Y. Shi, J. Massagué, Mechanisms of TGF-beta signaling from cell membrane to the nucleus. *Cell* **113**, 685–700 (2003). doi: 10.1016/S0092-8674(03)00432-X; pmid: 12809600
23. H. Ishikawa, G. N. Barber, STING is an endoplasmic reticulum adaptor that facilitates innate immune signalling. *Nature* **455**, 674–678 (2008). doi: 10.1038/nature07317; pmid: 18724357
24. Y. Tanaka, Z. J. Chen, STING specifies IRF3 phosphorylation by TBK1 in the cytosolic DNA signaling pathway. *Sci. Signal.* **5**, ra20 (2012). doi: 10.1126/scisignal.2002521; pmid: 22394562
25. H. Konno, K. Konno, G. N. Barber, Cyclic dinucleotides trigger ULK1 (ATG1) phosphorylation of STING to prevent sustained innate immune signaling. *Cell* **155**, 688–698 (2013). doi: 10.1016/j.cell.2013.09.049; pmid: 24119841
26. H. Ishikawa, Z. Ma, G. N. Barber, STING regulates intracellular DNA-mediated, type I interferon-dependent innate immunity. *Nature* **461**, 788–792 (2009). doi: 10.1038/nature08476; pmid: 19776740
27. M. Yamamoto *et al.*, Role of adaptor TRIF in the MyD88-independent toll-like receptor signaling pathway. *Science* **301**, 640–643 (2003). doi: 10.1126/science.1087262; pmid: 12855817
28. K. J. Han *et al.*, Mechanisms of the TRIF-induced interferon-stimulated response element and NF-kappaB activation and apoptosis pathways. *J. Biol. Chem.* **279**, 15652–15661 (2004). doi: 10.1074/jbc.M311629200; pmid: 14739303
29. M. Yamamoto *et al.*, Cutting edge: A novel Toll/IL-1 receptor domain-containing adapter that preferentially activates the IFN-beta promoter in the Toll-like receptor signaling. *J. Immunol.* **169**, 6668–6672 (2002). doi: 10.4049/jimmunol.169.12.6668; pmid: 12471095
30. J. W. Wu *et al.*, Crystal structure of a phosphorylated Smad2. Recognition of phosphoserine by the MH2 domain and insights on Smad function in TGF-beta signaling. *Mol. Cell* **8**, 1277–1289 (2001). doi: 10.1016/S1097-2765(01)00421-X; pmid: 11779503
31. B. Chen *et al.*, The WAVE regulatory complex links diverse receptors to the actin cytoskeleton. *Cell* **156**, 195–207 (2014). doi: 10.1016/j.cell.2013.11.048; pmid: 24439376

32. J. Pei, B. H. Kim, N. V. Grishin, PROMALS3D: A tool for multiple protein sequence and structure alignments. *Nucleic Acids Res.* **36**, 2295–2300 (2008). doi: 10.1093/nar/gkn072; pmid: 18287115
33. M. Lopez-Pelaez *et al*., Protein kinase IKKβ-catalyzed phosphorylation of IRF5 at Ser462 induces its dimerization and nuclear translocation in myeloid cells. *Proc. Natl. Acad. Sci. U.S.A.* **111**, 17432–17437 (2014). doi: 10.1073/pnas.1418399111; pmid: 25326418
34. J. Ren, X. Chen, Z. J. Chen, IKKβ is an IRF5 kinase that instigates inflammation. *Proc. Natl. Acad. Sci. U.S.A.* **111**, 17438–17443 (2014). doi: 10.1073/pnas.1418516111; pmid: 25326420
35. R. B. Seth, L. Sun, C. K. Ea, Z. J. Chen, Identification and characterization of MAVS, a mitochondrial antiviral signaling protein that activates NF-kappaB and IRF 3. *Cell* **122**, 669–682 (2005). doi: 10.1016/j.cell.2005.08.012; pmid: 16125763
36. J. J. Woodward, A. T. Iavarone, D. A. Portnoy, c-di-AMP secreted by intracellular *Listeria monocytogenes* activates a host type I interferon response. *Science* **328**, 1703–1705 (2010). doi: 10.1126/science.1189801; pmid: 20508090
37. O. Shalem *et al*., Genome-scale CRISPR-Cas9 knockout screening in human cells. *Science* **343**, 84–87 (2014). doi: 10.1126/science.1247005; pmid: 24336571
38. P. Flicek *et al*., Ensembl 2014. *Nucleic Acids Res.* **42**, D749–D755 (2014). pmid: 24316576
39. R. D. Finn, J. Clements, S. R. Eddy, HMMER web server: Interactive sequence similarity searching. *Nucleic Acids Res.* **39** (suppl. 2), W29–W37 (2011). doi: 10.1093/nar/gkr367; pmid: 21593126
40. R. D. Finn *et al*., Pfam: The protein families database. *Nucleic Acids Res.* **42**, D222–D230 (2014). doi: 10.1093/nar/gkt1223; pmid: 24288371
41. I. Walsh, A. J. Martin, T. Di Domenico, S. C. Tosatto, ESpritz: Accurate and fast prediction of protein disorder. *Bioinformatics* **28**, 503–509 (2012). doi: 10.1093/bioinformatics/btr682; pmid: 22190692
42. M. Sickmeier *et al*., DisProt: The database of disordered proteins. *Nucleic Acids Res.* **35** (suppl. 1), D786–D793 (2007). doi: 10.1093/nar/gkl893; pmid: 17145717
43. UniProt Consortium, Activities at the Universal Protein Resource (UniProt). *Nucleic Acids Res.* **42**, D191–D198 (2014). doi: 10.1093/nar/gkt1140; pmid: 24253303
44. Gene Ontology Consortium, Gene Ontology annotations and resources. *Nucleic Acids Res.* **41**, D530–D535 (2013). doi: 10.1093/nar/gks1050; pmid: 23161678
45. T. Frickey, A. Lupas, CLANS: A Java application for visualizing protein families based on pairwise similarity. *Bioinformatics* **20**, 3702–3704 (2004). doi: 10.1093/bioinformatics/bth444; pmid: 15284097
46. J. Pei, N. V. Grishin, AL2CO: Calculation of positional conservation in a protein sequence alignment. *Bioinformatics* **17**, 700–712 (2001). doi: 10.1093/bioinformatics/17.8.700; pmid: 11524371

ACKNOWLEDGMENTS

We thank Y. Yu, H. Mirzae, and C. Long for advice on mass spectrometry; L. Jia for advice on generating phospho-specific antibodies; and L. Sun, N. Varnado, and M. Xu for critically reading our manuscript. The data presented in this manuscript are tabulated in the main paper and in the supplementary materials. This work was supported by grants from the NIH (AI-93967 and GM-63692 to Z.J.C. and GM-094575 to N.G.) and the Welch Foundation (I-1389 to Z.J.C. and I-1505 to N.G.). X.Cai, J.W., and Q.C. were supported by International Student Fellowships from HHMI. Z.J.C. is an HHMI Investigator.

SUPPLEMENTARY MATERIALS

www.sciencemag.org/content/347/6227/aaa2630/suppl/DC1
Figs. S1 to S12
Tables S1 to S4
References (*47*–*49*)

9 November 2014; accepted 16 January 2015
Published online 29 January 2015;
10.1126/science.aaa2630

REPORTS

ORGANOMETALLICS

Design, synthesis, and carbon-heteroatom coupling reactions of organometallic nickel(IV) complexes

Nicole M. Camasso and Melanie S. Sanford*

Homogeneous nickel catalysis is used for the synthesis of pharmaceuticals, natural products, and polymers. These reactions generally proceed via nickel intermediates in the Ni^0, Ni^I, Ni^{II}, and/or Ni^{III} oxidation states. In contrast, Ni^{IV} intermediates are rarely accessible. We report herein the design, synthesis, and characterization of a series of organometallic Ni^{IV} complexes, accessed by the reaction of Ni^{II} precursors with the widely used oxidant *S*-(trifluoromethyl)dibenzothiophenium triflate. These Ni^{IV} complexes undergo highly selective carbon(sp^3)-oxygen, carbon(sp^3)-nitrogen, and carbon(sp^3)-sulfur coupling reactions with exogenous nucleophiles. The observed reactivity has the potential for direct applications in the development of nickel-catalyzed carbon-heteroatom coupling reactions.

Transition metal–catalyzed cross-coupling reactions are widely used synthetic methods for the construction of carbon-carbon and carbon-heteroatom bonds, the importance of which was recognized with the Nobel Prize in chemistry in 2010. While the vast majority of these transformations use palladium-based catalysts, over the past decade there has been a resurgence in the development of nickel-catalyzed cross-coupling reactions (*1*, *2*). Nickel catalysts offer the advantage of being more sustainable and economical than their palladium analogs (*1*). In addition, the intrinsic properties of nickel can enable transformations that are challenging with palladium catalysts. For example, nickel catalysts can promote cross-coupling reactions that use tertiary alkyl halides (*3*) or phenol derivatives (*4*) as electrophiles.

Mechanistic studies have shown that Ni-catalyzed reactions can occur via organometallic Ni^0, Ni^I, Ni^{II}, and Ni^{III} intermediates (*2*, *5*). In marked contrast, the accessibility of Ni^{IV} in catalysis has not been definitively established. A few reports have proposed the intermediacy of Ni^{IV} (*1*, *2*, *6*, *7*) [for example, in Ni-catalyzed C–H bond functionalization (*7*)]. However, the transient nature of these putative intermediates has hindered definitive characterization and confirmation of their role. Overall, examples of well-characterized Ni^{IV} complexes are exceedingly rare (*8*–*12*), and the reactivity of these species in carbon-carbon and carbon-heteroatom bond-forming reactions has not been thoroughly investigated (*8*–*10*).

Our interest in the design and synthesis of organometallic Ni^{IV} complexes stems from the hypothesis that such complexes could possess distinct reactivity from the more common oxidation states of Ni. This hypothesis is predicated on analogous chemistry of Pd^{IV}. Until recently, Pd^{IV} was also considered an unusual oxidation state that was rarely relevant in catalysis. However, over the past two decades, fundamental organometallic studies have revealed that Pd^{IV} complexes can be accessed with many common oxidants (e.g., alkyl halides, hypervalent iodine reagents, electrophilic halogenating reagents) (*13*–*15*). Furthermore, these Pd^{IV} complexes often display complementary reactivity and selectivity relative to their Pd^{II}, Pd^{I}, and Pd^0 analogs (*13*–*15*). In particular, the reactivity of Pd^{IV} in mediating couplings between carbon and heteroatoms (O, N, S) has led to the development of numerous $Pd^{II/IV}$-catalyzed C-H oxidation and alkene difunctionalization reactions (*16*, *17*).

Inspired by this emergence of high-valent palladium chemistry, we sought to unveil similar organometallic chemistry of Ni^{IV}. We report herein that isolable Ni^{IV} complexes can be prepared by the oxidation of Ni^{II} precursors with *S*-(trifluoromethyl)dibenzothiophenium triflate (TDTT). Furthermore, we demonstrate that these Ni^{IV} complexes participate in highly selective C(sp^3)-oxygen, C(sp^3)-nitrogen, and C(sp^3)-sulfur bond-forming reactions with exogenous nucleophiles.

We initially hypothesized that a Ni^{IV} complex could be accessed via the $2e^-$ oxidation of the Ni^{II} starting material [(bpy)Ni^{II}(CH_2CMe_2-*o*-C_6H_4)] (**1**). This hypothesis was based on literature investigations of the reactivity of Ni^{II} (*18*–*20*) and Pd^{II} (*21*, *22*) analogs of **1**, as well as on cyclic voltammetry studies carried out in our lab. As shown in Fig. 1A, the cyclic voltammogram of **1** in CH_3CN shows two oxidative waves at –0.61 V and +0.27 V versus Fc/Fc^+ (Fc, ferrocene). We assign these features to the Ni^{II}/Ni^{III} and the Ni^{III}/Ni^{IV} couples, respectively. These waves are both quasi-reversible and at relatively low potentials, suggesting that Ni^{IV} could be accessible with this ligand system.

The chemical oxidation of **1** was first examined with three different inner sphere oxidants that are known to promote the $2e^-$ oxidation of other group 10 metal complexes: *N*-fluoro-2,4,6-trimethylpyridinium triflate (NFTPT), iodobenzene diacetate [$PhI(OAc)_2$], and iodobenzene dichloride ($PhICl_2$) (*16*, *21*, *22*). We anticipated that these oxidants would react with **1** to generate coordinatively saturated, diamagnetic Ni^{IV} intermediates of general structure **2** (X is F/OTf, OAc, or Cl). If intermediate **2** were sufficiently long-lived, it should be detectable by nuclear magnetic resonance (NMR) spectroscopy. The treatment of **1** with any of the three oxidants in CD_3CN resulted in near-quantitative formation of benzocyclobutane **3** within minutes at room temperature (Fig. 1B, pathway a) (*23*). Organic product **3** is likely generated via C(sp^2)–C(sp^3) bond-forming reductive elimination from Ni^{IV} intermediate **2**. However, **2** could not be detected by ^1H NMR spectroscopy at room temperature or at –40°C with any of these oxidants, suggesting that this putative intermediate is highly reactive.

We reasoned that the Ni^{IV} intermediate could be stabilized by replacing one of the X-type ligands with trifluoromethyl (CF_3) (*24*). Indeed, the reaction of **1** with the "CF_3^+" oxidant *S*-TDTT in CD_3CN at room temperature resulted in transfer of a CF_3 ligand to Ni to form a detectable, diamagnetic Ni–CF_3 complex. This intermediate persists in solution for several hours, and in situ ^1H and ^{19}F NMR spectroscopic characterization implicates the formation of Ni^{IV} complex **4** (Fig. 1B, pathway b). Complex **4** undergoes C(sp^2)-C(sp^3) coupling to form benzocyclobutane **3** over the course of 15 hours at 25°C. The detection of **4** in this reaction provided the first evidence that Ni^{IV} can be formed under these conditions and suggested that modification of the ligand scaffold could yield an isolable Ni^{IV} complex.

To further enhance the stability of the proposed Ni^{IV} intermediate, we replaced the bidentate bipyridine ligand with a facial tridentate ligand, tris(2-pyridyl)methane (Py_3CH) (*25*). The oxidation of [(Py_3CH)Ni^{II}(CH_2CMe_2-*o*-C_6H_4)] (**5**) with TDTT in CH_3CN at 25°C led to an immediate color change from dark red to yellow, with concomitant formation of the diamagnetic Ni^{IV}–CF_3 complex **6** (Fig. 2A) as determined by NMR spectroscopy. Notably, this complex was stable in CH_3CN solution at room temperature for at least 3 days. Complex **6** was isolated in 92% yield by recrystallization from benzene, and x-ray–quality crystals were obtained via slow evaporation of a concentrated acetone solution (Fig. 2B). The solid-state structure of this Ni^{IV} complex displays the expected octahedral geometry, with tridentate facial coordination of the Py_3CH ligand. This is only the second example of an organometallic Ni^{IV} complex with an octahedral geometry (*8*, *9*).

Department of Chemistry, University of Michigan, 930 North University Avenue, Ann Arbor, MI 48109, USA.
*Corresponding author. E-mail: mssanfor@umich.edu

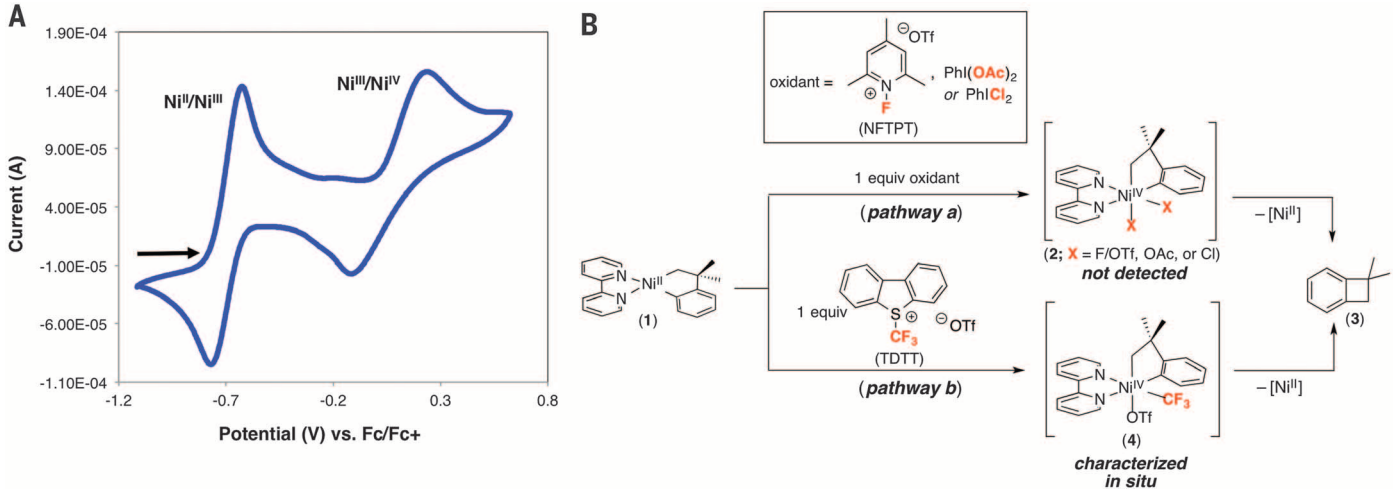

Fig. 1. Initial studies with Ni^{II} complex 1. (**A**) Cyclic voltammogram of (bpy)$Ni^{II}(CH_2CMe_2$-*o*-$C_6H_4)$ (**1**). (**B**) Reaction of **1** (a) with 1 equiv. of NFTPT, $PhI(OAc)_2$, or $PhICl_2$; (b) with 1 equiv of *S*-(trifluoromethyl)dibenzothiophenium triflate (TDTT).

Moreover, TDTT is frequently used as an oxidant in transition-metal catalysis (*26*, *27*); as such, the isolation and characterization of **6** suggest the potential feasibility of $Ni^{II/IV}$ catalysis manifolds with this reagent.

We next investigated the reactivity of this isolated Ni^{IV} complex toward both carbon-carbon and carbon-heteroatom bond formation. Upon heating at 95°C for 7 hours, complex **6** underwent $C(sp^2)$-$C(sp^3)$ bond-forming reductive elimination to produce benzocyclobutane ***3*** in quantitative yield (Fig. 2C, a). Furthermore, the treatment of **6** with exogenous acetate (1.2 equiv. of NMe_4OAc) in CH_3CN at room temperature resulted in selective $C(sp^3)$–O coupling to afford Ni^{II} product **7** in >98% yield, as determined by ^{19}F NMR spectroscopy. Complex **7** was isolated in 78% yield (Fig. 2C, b).

Whereas **6** reacted cleanly with NMe_4OAc, other exogenous nucleophiles (NMe_4X; X is OPh, SPh) afforded complicated mixtures of products. We hypothesized that this might be due, at least in part, to the overall +1 charge on **6**, which would render the complex highly electrophilic and thus susceptible to side reactions with nucleophiles (*25*, *28*). As a result, we prepared a closely analogous neutral Ni^{IV} complex (**8**) in which the Py_3CH ligand was replaced with a trispyrazolylborate (Tp) ligand (Fig. 3A) (*29*). Notably, $TpNi^{IV}$ complex **8** was found to react with a diverse set of exogenous nucleophiles [NMe_4X; X is OAc, OPh, SPh, and N(Me)(Ms), where Ms is $MeSO_2^-$] to yield the products of $C(sp^3)$–oxygen, $C(sp^3)$–sulfur, and $C(sp^3)$–nitrogen coupling (Fig. 3B, products **9a** to **9d**). The $C(sp^3)$–heteroatom coupling reactions to form **9a** to **9d** were extremely selective and high-yielding (>98% conversion as determined by ^1H and ^{19}F NMR spectroscopy; 78 to 94% isolated yields). Products derived from competing $C(sp^2)$–$C(sp^3)$ coupling or $C(sp^2)$–heteroatom coupling were not detected in the ^1H NMR spectra of the crude reaction mixtures. Notably, $C(sp^3)$-heteroatom coupling reactions of this type are rare in organometallic chemistry (*20*–*22*, *30*–*34*), and most previously reported examples involve second- or third-row metal centers. In addition, the observation of selective $C(sp^3)$-heteroatom coupling is complementary to the reactivity of other oxidation states of Ni, where $C(sp^2)$-heteroatom bond formation has notable precedent (*35*–*37*).

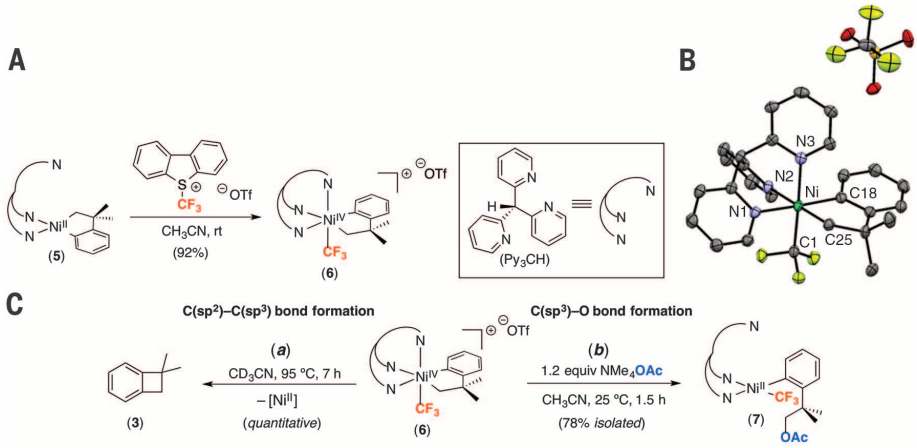

Fig. 2. Synthesis, characterization, and reactivity of complex 6. (**A**) Synthesis of the stable Ni^{IV} complex $[(Py_3CH)Ni^{IV}(CH_2CMe_2$-*o*-$C_6H_4)(CF_3)]OTf$ (**6**). (**B**) Oak Ridge Thermal Ellipsoid Plot (ORTEP) of cationic complex **6**. Thermal ellipsoids are drawn at 50% probability. Hydrogen atoms are omitted for clarity. Selected bond lengths (Å): Ni-N1 2.057(2), Ni-N2 2.073(2), Ni-N3 2.018(2), Ni-C1 1.956(2), Ni-C18 1.953(2), Ni-C25 2.006(2). Selected bond angles (°): N1-Ni-N2 88.04(7), N1-Ni-N3 88.09(7), N1-Ni-C18 174.75(8), C18-Ni-C25 82.27(9), C1-Ni-C25 89.00(9), C1-Ni-C18 92.63(9). (**C**) Reactivity of complex **6**: (a) $C(sp^2)$-$C(sp^3)$ reductive elimination and (b) $C(sp^3)$-O coupling.

Whereas Ni^{II} complexes **9a** to **9d** were stable toward isolation, the treatment of Ni^{IV} complex **8** with 1 equiv. of NBu_4N_3 led to intermediate **9e**, which was observed in situ but was unstable in CH_3CN solution (Fig. 3C). Azide intermediate **9e** slowly converted to 3,3′-dimethylindoline (**11**; quantitative conversion) over 15 hours at room temperature. This transformation likely proceeds via the pathway shown in Fig. 3C. Here, the pendant alkyl azide that results from C-N coupling inserts into the $C(sp^2)$–Ni bond to generate Ni^{II} intermediate **10**. Related intermolecular azide insertions into Ni^{II}–C bonds have been reported by Koo and Hillhouse (*19*). Protonation of the Ni–N bond by adventitious water then releases the indoline product **11**.

Finally, we sought to gain preliminary insights into the mechanism of these $C(sp^3)$–heteroatom coupling reactions. Related transformations at octahedral Pd^{IV} and Pt^{IV} centers are believed to proceed via S_N2-type attack on the metal–C bond by the nucleophile (*21*, *22*, *30*–*32*). In the current system, an S_N2 mechanism would be expected to show a first-order kinetic dependence on both [Ni] and NMe_4X. Indeed, rate studies of the reaction between **8** and NMe_4OAc showed that this transformation is first-order in [Ni] and first-order in NMe_4OAc, consistent with an S_N2 pathway (fig. S7). Another common feature of S_N2 reactions is that the reaction rates show a correlation

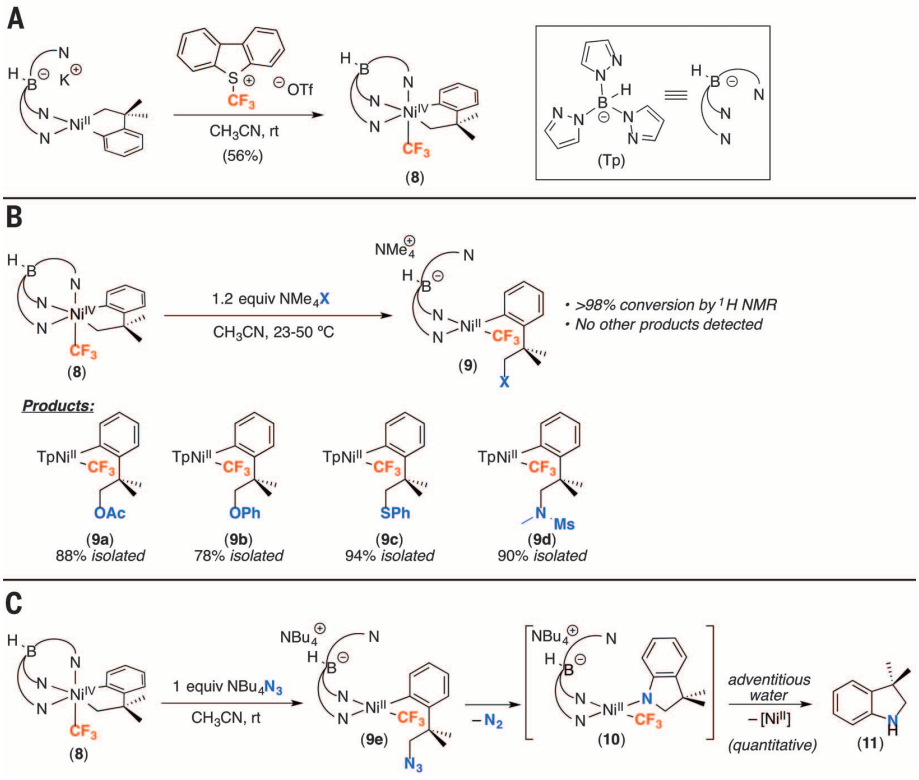

Fig. 3. Synthesis and reactivity of Ni^{IV} complex 8. (**A**) Synthesis of [(Tp)Ni^{IV}(CH_2CMe_2-*o*-C_6H_4)(CF_3)] (**8**); (**B**) selective C(sp^3)–O, C(sp^3)–S, and C(sp^3)–N bond formation; (**C**) formation of indoline **11** from alkyl azide intermediate **9e**.

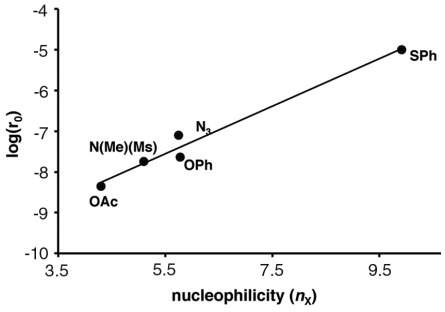

Fig. 4. Evidence for an S_N2 mechanism. Correlation between experimental initial rates (r_0) of C-X coupling from complex **8** and Swain-Scott nucleophilicity values (n_X). $y = 0.58x - 10$, $R^2 = 0.97$. The nucleophilicity value for $^-$N(Me)(Ms) is an estimation based on the available value for a related sulfonamide, $^-NHSO_2Ph$ (*39*).

with the Swain-Scott nucleophilicity parameters (*38*). These nucleophilicity parameters (n_X, where X is a series of different nucleophiles) are derived from a prototypical S_N2 reaction (that of a nucleophile with CH_3I) (*39*). The initial rate (r_0) of C–heteroatom coupling at **8** with AcO^-, PhO^-, PhS^-, $^-N(Me)(Ms)$, and N_3^- was determined at 23°C in CD_3CN. A plot of log(r_0) versus n_X is shown in Fig. 4. The excellent linear correlation (R^2 = 0.97) provides further support for an S_N2 type C–X coupling pathway in this system.

We anticipate that the ability of Ni^{IV} complexes to engage in selective C(sp^3)-heteroatom coupling reactions can ultimately be exploited in catalysis. A key challenge for achieving this objective will be to delineate the classes of oxidants and supporting ligands that enable selective access to Ni^{IV} (rather than more common Ni^{III}) intermediates. This should enable the design of catalytic sequences in which a Ni-carbon bond-forming step (e.g., transmetallation, C-H activation at Ni^{II}) is coupled with oxidation and C–heteroatom coupling via $Ni^{II/IV}$ catalysis.

REFERENCES AND NOTES

1. S. Z. Tasker, E. A. Standley, T. F. Jamison, *Nature* **509**, 299–309 (2014).
2. J. Montgomery, in *Organometallics in Synthesis: Fourth Manual*, B. H. Lipschutz, Ed. (Wiley, Hoboken, NJ, 2013), pp. 319–428.
3. S. L. Zultanski, G. C. Fu, *J. Am. Chem. Soc.* **135**, 624–627 (2013).
4. B. M. Rosen *et al.*, *Chem. Rev.* **111**, 1346–1416 (2011).
5. X. Hu, *Chem. Sci.* **2**, 1867–1886 (2011).
6. J. Terao, N. Kambe, *Acc. Chem. Res.* **41**, 1545–1554 (2008).
7. Y. Aihara, N. Chatani, *J. Am. Chem. Soc.* **136**, 898–901 (2014).
8. H.-F. Klein, A. Bickelhaupt, T. Jung, G. Cordier, *Organometallics* **13**, 2557–2559 (1994).
9. H.-F. Klein *et al.*, *Organometallics* **16**, 668–676 (1997).
10. V. Dimitrov, A. Linden, *Angew. Chem. Int. Ed.* **42**, 2631–2633 (2003).
11. S. Shimada, M. L. N. Rao, M. Tanaka, *Organometallics* **18**, 291–293 (1999).
12. M. Carnes *et al.*, *Angew. Chem. Int. Ed.* **48**, 290–294 (2009).
13. P. Sehnal, R. J. K. Taylor, I. J. S. Fairlamb, *Chem. Rev.* **110**, 824–889 (2010).
14. A. J. Hickman, M. S. Sanford, *Nature* **484**, 177–185 (2012).
15. A. J. Canty, *Dalton Trans.* (47): 10409–10417 (2009).
16. T. W. Lyons, M. S. Sanford, *Chem. Rev.* **110**, 1147–1169 (2010).
17. K. Muñiz, *Angew. Chem. Int. Ed.* **48**, 9412–9423 (2009).
18. J. Campora *et al.*, *Organometallics* **13**, 1728–1745 (1994).
19. K. Koo, G. L. Hillhouse, *Organometallics* **14**, 4421–4423 (1995).
20. K. Koo, G. L. Hillhouse, *Organometallics* **17**, 2924–2925 (1998).
21. M. H. Pérez-Temprano, J. M. Racowski, J. W. Kampf, M. S. Sanford, *J. Am. Chem. Soc.* **136**, 4097–4100 (2014).
22. N. M. Camasso, M. H. Pérez-Temprano, M. S. Sanford, *J. Am. Chem. Soc.* **136**, 12771–12775 (2014).
23. R. H. Grubbs, A. Miyashita, M. Liu, P. Burk, *J. Am. Chem. Soc.* **100**, 2418–2425 (1978).
24. Y. Ye, N. D. Ball, J. W. Kampf, M. S. Sanford, *J. Am. Chem. Soc.* **132**, 14682–14687 (2010).
25. A. Maleckis, J. W. Kampf, M. S. Sanford, *J. Am. Chem. Soc.* **135**, 6618–6625 (2013).
26. X. Wang, L. Truesdale, J.-Q. Yu, *J. Am. Chem. Soc.* **132**, 3648–3649 (2010).
27. C. Zhang, *Org. Biomol. Chem.* **12**, 6580–6589 (2014).
28. H. Martínez-García, D. Morales, J. Pérez, M. Puerto, I. del Río, *Chemistry* **20**, 5821–5834 (2014).
29. S. Reinartz, P. S. White, M. Brookhart, J. L. Templeton, *J. Am. Chem. Soc.* **123**, 6425–6426 (2001).
30. G. A. Luinstra, J. A. Labinger, J. E. Bercaw, *J. Am. Chem. Soc.* **115**, 3004–3005 (1993).
31. A. V. Pawlikowski, A. D. Getty, K. I. Goldberg, *J. Am. Chem. Soc.* **129**, 10382–10393 (2007).
32. A. N. Vedernikov, *Top. Organomet. Chem.* **31**, 101–121 (2010).
33. S. L. Marquard, J. F. Hartwig, *Angew. Chem. Int. Ed.* **50**, 7119–7123 (2011).
34. M. Feller, Y. Diskin-Posner, G. Leitus, L. J. W. Shimon, D. Milstein, *J. Am. Chem. Soc.* **135**, 11040–11047 (2013).
35. A. T. Higgs, P. J. Zinn, S. J. Simmons, M. S. Sanford, *Organometallics* **28**, 6142–6144 (2009).
36. B. Zheng *et al.*, *J. Am. Chem. Soc.* **136**, 6499–6504 (2014).
37. J.-P. Cloutier, B. Vabre, B. Moungang-Soumé, D. Zargarian, *Organometallics* **34**, 133–145 (2015).
38. C. G. Swain, C. B. Scott, *J. Am. Chem. Soc.* **75**, 141–147 (1953).
39. R. G. Pearson, H. R. Sobel, J. Songstad, *J. Am. Chem. Soc.* **90**, 319–326 (1968).

ACKNOWLEDGMENTS

This work was supported by NSF grant CHE-1361542. We acknowledge J. W. Kampf for x-ray crystallographic analyses of **6** and **S2**, as well as funding from NSF grant CHE-0840456 for x-ray instrumentation. Metrical parameters for the structures are available free of charge from the Cambridge Crystallographic Data Centre under reference numbers CCDC-1038703 and 1038702, respectively. R. E. M. Brooner is acknowledged for assistance with electrochemical studies of **1**. The supplementary materials contain complete experimental and spectral details for all new compounds and all reactions reported herein. This paper is dedicated to the memory of Prof. Gregory Hillhouse for his seminal contributions to the organometallic chemistry of nickel.

SUPPLEMENTARY MATERIALS

www.sciencemag.org/content/347/6227/1218/suppl/DC1
Materials and Methods
Supplementary Text
NMR Spectral Data
Figs. S1 to S12
Tables S1 to S13
References (*40*–*43*)

8 December 2014; accepted 21 January 2015
Published online 5 February 2015;
10.1126/science.aaa4526

ORGANIC SYNTHESIS

Synthesis of many different types of organic small molecules using one automated process

Junqi Li,* Steven G. Ballmer,* Eric P. Gillis, Seiko Fujii, Michael J. Schmidt, Andrea M. E. Palazzolo, Jonathan W. Lehmann, Greg F. Morehouse, Martin D. Burke†

Small-molecule synthesis usually relies on procedures that are highly customized for each target. A broadly applicable automated process could greatly increase the accessibility of this class of compounds to enable investigations of their practical potential. Here we report the synthesis of 14 distinct classes of small molecules using the same fully automated process. This was achieved by strategically expanding the scope of a building block–based synthesis platform to include even C_{sp3}-rich polycyclic natural product frameworks and discovering a catch-and-release chromatographic purification protocol applicable to all of the corresponding intermediates. With thousands of compatible building blocks already commercially available, many small molecules are now accessible with this platform. More broadly, these findings illuminate an actionable roadmap to a more general and automated approach for small-molecule synthesis.

Small molecules perform many important functions in nature, medicine, and technology. However, efforts to discover and optimize new small-molecule function are often impeded by limitations in synthetic access to this class of compounds. For peptides (*1*) and oligonucleotides (*2*), the development of automated synthesis platforms removed this bottleneck. The resulting expanded access to these molecules permitted widespread exploration and applications of their functional potential. Substantial progress has also been made toward automating the synthesis of oligosaccharides (*3*). In each of these cases, automation was enabled by the development of a general building block–based synthesis strategy and a common purification process for the corresponding intermediates. Such standardization reduced the number of processes employed and thus decreased the number of challenges involved in automating the synthesis platform. In contrast, despite tremendous progress in the field, small-molecule syntheses typically employ strategies and purification methods that are highly customized for each target, thus requiring automation solutions to be developed on an ad hoc basis (*4*–*7*). To enable the more generalized automation of small-molecule synthesis, we asked whether many different types of small molecules could be prepared using a common building block–based strategy and a common purification process.

Small molecules can be very diverse in structure, as illustrated by representative compounds **1** to **14** in Fig. 1A. Synthesis of this entire set of targets using a common approach thus represents a major challenge. However, like peptides, oligonucleotides, and oligosaccharides, most natural products (such as **1** to **4**) are biosynthesized via the iterative assembly of a small set of building blocks, such as malonyl coenzyme A, isopentenyl pyrophosphate, and pyruvic acid (*8*). Many materials and pharmaceuticals (such as **5** to **9**) comprise collections of aryl and/or heteroaryl components (*9*). Even topologically complex natural products containing macrocyclic or polycyclic frameworks (such as **10** to **14**) are usually biosynthesized via an iterative building block–based assembly of linear precursors, which are then (poly)cyclized to yield more complex molecular architectures (*10*–*12*). This analysis suggests that many small molecules might be accessible via a common, biosynthesis-inspired strategy involving the iterative assembly of building blocks. Supporting this notion, we recently demonstrated that more than 75% of all polyene natural product motifs can be prepared using just 12 building blocks and one coupling reaction (*13*).

That study employed a synthesis platform analogous to iterative peptide coupling that sequentially assembles bifunctional *N*-methyliminodiacetic acid (MIDA) boronates (Fig. 1B) (*14*). Iterative cycles of coupling and deprotection are enabled by the MIDA ligand, which attenuates the reactivity of boronic acids and thus prevents undesired oligomerization. This approach is both efficient and flexible because all of the required functional groups, oxidation states, and stereochemical elements are preinstalled into the building blocks. These features are then faithfully translated into the products using the same mild and stereospecific coupling chemistry (*15*). Hundreds of MIDA boronates and thousands of additional halide and boronic acid building blocks are now commercially available, and natural products from most major biosynthetic pathways, including **1** to **4**, have been manually synthesized in prior studies using this strategy (*16*–*19*).

With this promising starting point, we set out to expand the scope of this platform to include all of the structures shown in Fig. 1A. C_{sp3}-rich cyclic and polycyclic natural product frameworks such as **10** to **14** represent especially challenging targets and thus required a strategic advance. Because many of these molecules are biosynthesized via cyclization of modular linear precursors derived from iterative building block assembly (*10*–*12*), we hypothesized that an analogous linear-to-cyclized strategy might enable this platform to access many such structures. In this approach, the same building block assembly process is used to generate a linear precursor, which is then (poly)cyclized into the topologically complex product. The stereochemical information in the building blocks is first translated into linear precursors via stereospecific couplings and then into the targeted products via stereospecific and/or stereoselective (poly)cyclization reactions. To enable such cyclizations, such linear precursors must be suitably flexible and, therefore, rich in sp^3 hybridized carbons. Building block–based assembly of these precursors thus requires many C_{sp3} couplings, which can be challenging.

To test this linear-to-cyclized strategy, we targeted the manual synthesis of the highly complex pentacyclic secodaphnane alkaloid core **14**. This core can, in theory, be derived from a much simpler linear precursor **15** via a bioinspired cyclization cascade involving amine condensation and intramolecular Diels-Alder and Prins cyclizations (*20*). In turn, **15** was targeted via the iterative assembly of building blocks **16** to **18** in which all of the required double bond stereochemistry is preinstalled. C_{sp3} coupling of **16** and **17** generates MIDA boronate intermediate **19**. Deprotection of **19** yields a free boronic acid, which is engaged in another C_{sp3} coupling with **18** to complete the iterative assembly of linear precursor **15**. The aforementioned diastereoselective cyclization cascade is then used to transform **15** into the pentacyclic alkaloid (±)-**14**.

Having established a strategy to access even topologically complex small molecules using the same building block–based approach, we next questioned whether a common purification protocol could also be developed and thereby enable this platform to be automated. Small-molecule synthesis typically involves purifications customized for each intermediate, such as chromatography with eluents optimized for each compound. Such customization is incompatible with generalized automated purification. Solid-phase synthesis can address this problem for peptides (*1*), oligonucleotides (*2*), oligosaccharides (*3*), and some organic polymers (*21*). In some cases, syntheses of natural products and pharmaceuticals have also been aided by solid-phase methods (*22*). This approach is well established, is compatible with a wide range of chemistries, and has been employed in industry (*23*). However, small molecules do not possess a common functional group handle for attachment to solid support, which precludes generalized application of this approach. Thus, we needed a different solution.

Howard Hughes Medical Institute (HHMI), Department of Chemistry, University of Illinois at Urbana-Champaign, Urbana, IL 61801, USA.
*†These authors contributed equally to this work. †Corresponding author. E-mail: mdburke@illinois.edu

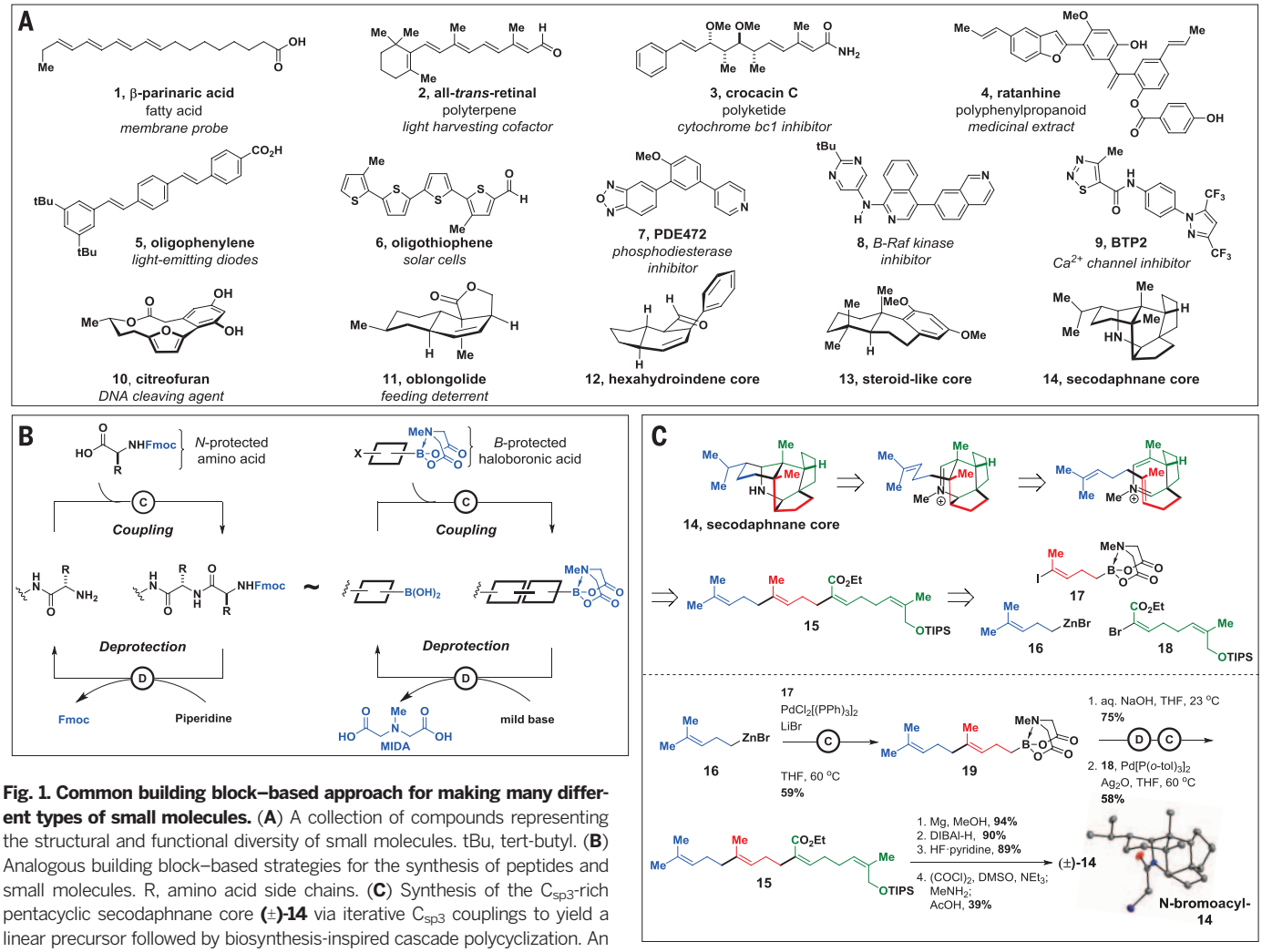

Fig. 1. Common building block–based approach for making many different types of small molecules. (**A**) A collection of compounds representing the structural and functional diversity of small molecules. tBu, tert-butyl. (**B**) Analogous building block–based strategies for the synthesis of peptides and small molecules. R, amino acid side chains. (**C**) Synthesis of the C_{sp3}-rich pentacyclic secodaphnane core **(±)-14** via iterative C_{sp3} couplings to yield a linear precursor followed by biosynthesis-inspired cascade polycyclization. An x-ray crystallographic study of the *N*-bromoacyl derivative of **14** unambiguously confirmed the structure of **14**. TIPS, triisopropylsilyl; Ph, phenyl; DMSO, dimethyl sulfoxide.

We recognized that each iteration of building block assembly in our platform generates a MIDA boronate as the key intermediate (Fig. 1, B and C). This led us to question whether the MIDA boronate motif could serve as a surrogate common handle for purification. In this vein, we discovered that MIDA boronates uniformly possess highly unusual binary affinity for silica gel with certain pairs of eluents (Fig. 2A). Specifically, all MIDA boronates **20** to **39**, with appended fragments representing a wide range of sizes, polarities, and functional group content, show minimal mobility on thin-layer silica gel chromatography when eluting with MeOH:Et_2O (Me, methyl; Et, ethyl) (Fig. 2A, left). However, all of the same MIDA boronates are rapidly eluted with tetrahydrofuran (THF) (Fig. 2A, right). This phenomenon enabled us to develop a new type of catch-and-release purification protocol applicable to any intermediate that contains a MIDA boronate. A crude reaction mixture is passed over silica gel, and the MIDA boronate is temporarily caught while excess reagents and by-products are removed via washing with MeOH:Et_2O. The MIDA boronate is then cleanly released by switching the eluent to THF. The MIDA boronate motif can thus serve as both a latent reactive functional group for iterative coupling and a traceless common functional group handle for generalized purification.

With both a common building block–based synthesis platform and a common purification method, we designed and built a synthesizer that iteratively assembles MIDA boronate building blocks in a fully automated fashion (Fig. 2B) (*24*). This device comprises three modules that sequentially execute the deprotection, coupling, and purification steps required for each cycle. All solutions are automatically transferred via computer-controlled syringe pumps running custom-designed software. Thus, each automated synthesis simply requires placing prepacked cartridges onto the synthesizer and pressing "start."

The fully automated synthesis commences at the deprotection module, where THF and water are syringed into a cartridge containing the MIDA boronate and NaOH. After deprotection, the reaction is quenched and the resulting THF solution of the freshly prepared boronic acid is separated from the water-soluble MIDA ligand. The coupling module then heats and stirs a solution of the next building block and the coupling reagents. The synthesizer then adds the freshly prepared solution of boronic acid to the coupling reaction. At the end of the reaction, the synthesizer filters and transfers the crude reaction mixture to the purification module, which executes the catch-and-release purification protocol with MeOH:Et_2O followed by THF. The THF solution of the purified product is then transferred directly into the deprotection module to start the next iteration of the synthesis.

To first test the capacity of this synthesizer to execute one cycle of deprotection, coupling, and purification, we subjected a series of commercially available aryl, heteroaryl, and vinyl MIDA boronates to automated deprotection and coupling with a model bifunctional building block, 4-bromophenyl MIDA boronate (*24*) (table S2). Using a standard set of hydrolysis conditions (NaOH, THF:H_2O, 23°C, 20 min) and coupling conditions ($PdXPhos$, K_3PO_4) (*25*), we obtained the desired cross-coupling products in good yields and purities in all cases (table S2, entries 1 to 3). The synthesizer was also capable of executing a

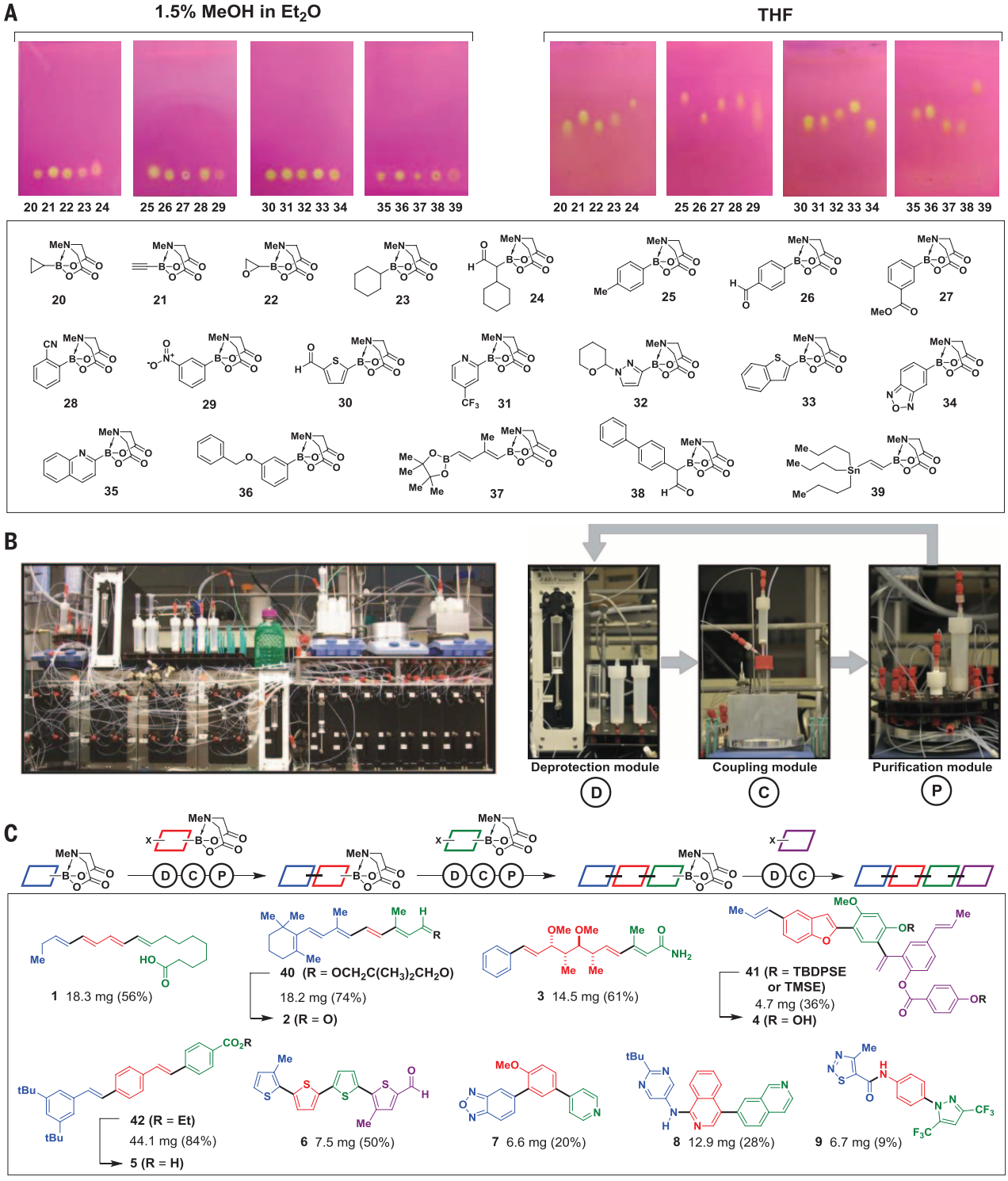

Fig. 2. General purification process to enable automation. (**A**) MIDA boronates uniformly show binary elution properties on silica gel thin-layer chromatography. (**B**) Photograph of the small-molecule synthesizer, which comprises three modules that execute the deprotection, coupling, and purification steps. (**C**) Automated synthesis of natural products, materials, pharmaceuticals, and biological probes via iterative coupling of building blocks indicated by different colors (*24*). TBDPSE, tert-butyldiphenylsilylethyl; TMSE, trimethylsilylethyl.

C_{sp3} coupling using Pd[P(*o*-tol$_3$)]$_2$ (tol, tolyl) and Ag_2O/K_2CO_3 (table S2, entry 4).

Accessing many pharmaceuticals and materials represented by structures **5** to **9** requires the flexibility to link building blocks via carbon-heteroatom and/or carbon-carbon bonds. The stability of MIDA boronates toward many reaction conditions (*26*, *27*) and the synthetic versatility of boronic acids (*28*) allowed us to add carbon-heteroatom bond formations to the same platform. The synthesizer successfully executed a series of automated carbon-heteroatom bond formations, including a Buchwald-Hartwig amination, O-alkylation, and amide bond formations (table S3). Despite the different reagents

and by-products, the same catch-and-release process purified all of the corresponding MIDA boronate products.

Having confirmed the capacity to reliably execute single cycles of deprotection, coupling, and purification, we next targeted the automated synthesis of a wide range of linear small molecules (**1** to **9**) via multiple carbon-carbon and/or carbon-heteroatom bond formations (Fig. 2C). These include natural products from major biosynthetic pathways (**1** to **4**), materials components (**5**, **6**), and pharmaceuticals and biological probes (**7** to **9**). Most of the corresponding building blocks are commercially available. Similar to automated peptide, oligonucleotide, and oligosaccharide syntheses, all of the synthesizer-generated final products were purified using standard chromatographic techniques, and any protecting groups other than MIDA were easily removed in a separate step (*24*). In each case, a single automated run successfully delivered the targeted small molecule in multi-milligram quantities, fulfilling the requirements of most functional discovery assays.

The development of small molecules with optimized functions often requires efficient access to many structural derivatives of a parent compound. To test if this platform could enable such access, we targeted the automated preparation of many derivatives of the complex neolignan natural product ratanhine **4**. In this experiment, we did not optimize any of the deprotection, coupling, or purification conditions used to construct **41** (Fig. 2C). We input four sets of building blocks representing common substructural elements found throughout the neolignan family and/or other pharmaceutically relevant motifs (Fig. 3). These building blocks included variations in oxidation states, methylation patterns, fluorine content, aromatic ring identity, and size. They also represent preprogrammed oligomer lengths of 3 to 4 units, based on whether the third building block was a bifunctional halo-MIDA boronate or a capping halide. In the event, the synthesizer successfully generated 20 out of 20 of the targeted derivatives, collectively representing all possible combinations of this four-component matrix of building blocks (Fig. 3).

Finally, we tested whether a wide range of macro- and polycyclic natural products and natural product–like cores (**10** to **14** in Fig. 1A) could be generated using the same automated building

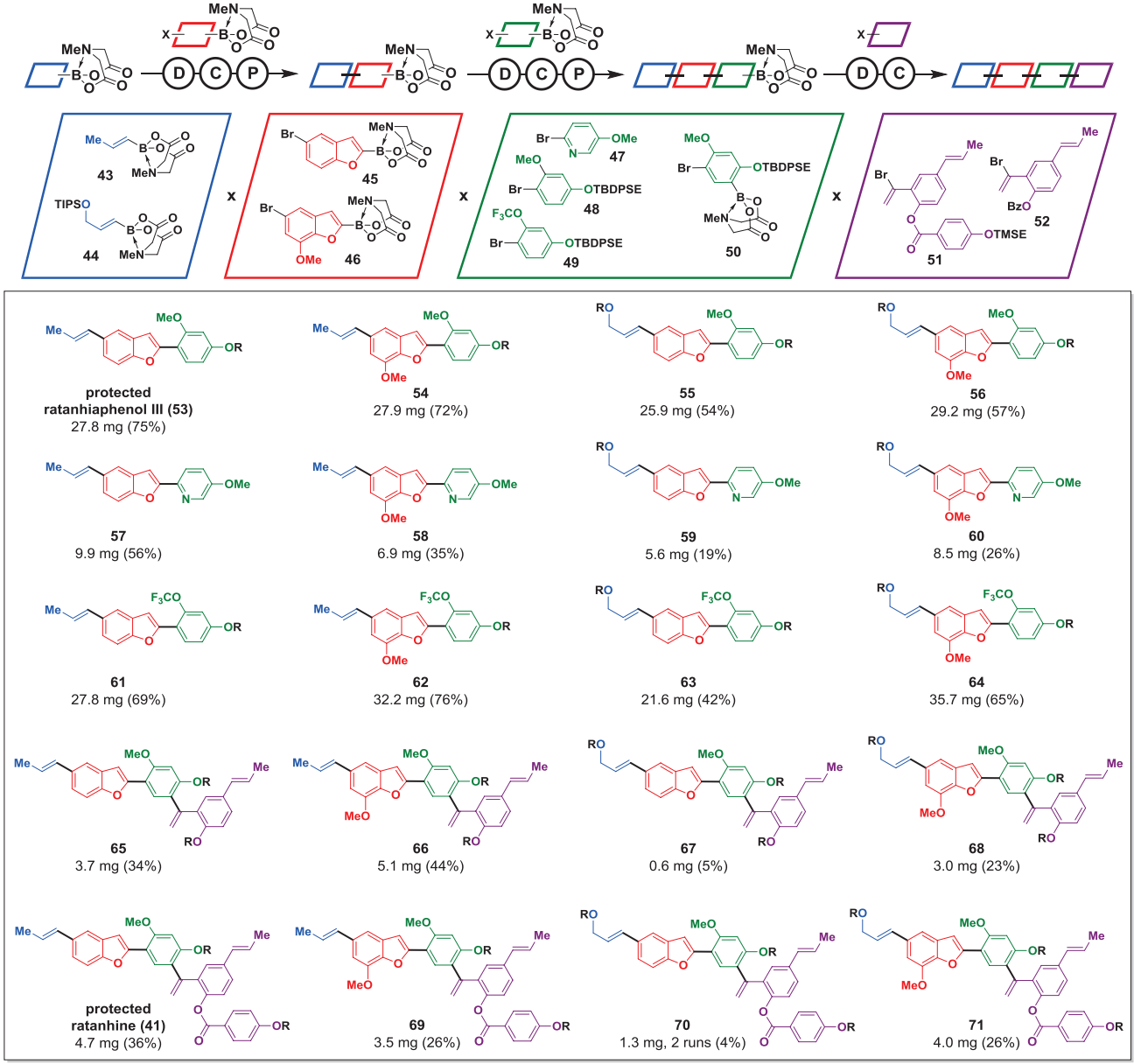

Fig. 3. Automated synthesis of ratanhine derivatives. Conditions: Deprotection – NaOH, THF:H_2O. Coupling – cycle 1: $Pd(OAc)_2$, SPhos, K_2CO_3, THF, 55°C, 16 hours; cycle 2: $Pd(OAc)_2$, XPhos, K_3PO_4, THF, 55°C, 14 hours; cycle 3: $Pd(OAc)_2$, SPhos, K_3PO_4, THF, 55°C, 24 hours. Purification – SiO_2, MeOH:Et_2O; THF. All protecting groups other than MIDA [R: TIPS, TBDPSE, TMSE, or Bz (benzoyl)] were successfully removed in a separate step (*24*). OAc, acetate.

block assembly process and the linear-to-cyclized strategy. The macrocyclic natural product citreofuran possesses both C_{sp3} and atropisomerism stereochemical elements (Fig. 4, entry 1). This complex target can be derived from linear precursor **76** (*29*), which can, in theory, be assembled from building blocks **72** to **74**. All of the required stereochemical information for citreofuran is preencoded in the chiral nonracemic MIDA boronate building block **72**. On the synthesizer, fully automated deprotection of **72**, C_{sp3} coupling with **73**, and purification yielded intermediate **75**. A second round of deprotection and coupling of the resulting 2-furanyl boronic acid with **74** produced linear precursor **76**. This linear precursor was then deprotected and atropdiastereoselectively macrocyclized to generate citreofuran.

Oblongolide is a norsesquiterpene γ-lactone natural product containing a 6,6,5-tricyclic core with five C_{sp3} stereogenic centers, one of which is quaternary (Fig. 4, entry 2). The three building blocks **44**, **77**, and **78** were automatically assembled via iterative C_{sp2} and C_{sp3} couplings to produce linear precursor **80**. After deprotection, the linear precursor was subjected to a cascade intramolecular substrate-controlled diastereoselective Diels-Alder reaction and lactonization process (*30*), which defined the four contiguous stereogenic centers in oblongolide.

In cases where no C_{sp3} stereogenic centers are present in the linear precursors, the enantioselectivity of cyclizations can be controlled using a rapidly expanding toolbox of chiral catalysts (*31*). This approach allows the stereoselective construction of the natural product–like hexahydroindene and steroid-like core structures **12** and **13** using the same linear-to-cyclized strategy (Fig. 4, entries 3 and 4). Specifically, building blocks **81** to **83**, all possessing olefins with predefined geometries required for cyclization, were assembled on the synthesizer to produce linear precursor **85**. This precursor was then subjected to deprotection and a chiral imidazolidinone-promoted organocatalytic enantio- and diastereoselective Diels-Alder reaction to generate **12** (Fig. 4, entry 3) (*32*). Similarly, iterative C_{sp3} coupling of building blocks **16, 17**, and **86** generated linear precursor **87**, which then underwent catalyst-promoted enantio- and diastereoselective cation-π cyclization (*33*) followed by reduction to generate **13** (Fig. 4, entry 4). Finally, by simply replacing building block **86** with **18** and using the same automated platform, even the highly complex pentacyclic secodaphnane core (±)-**14** was readily prepared (Fig. 4, entry 5).

Thus, many different types of small molecules (**1** to **14** in Fig. 1A) can be synthesized using one automated building block assembly platform. This advance was enabled by standardizing the synthesis and purification processes used to assemble these structures. Importantly, a majority of the building blocks employed herein are already commercially available.

Further expanding the scope of this automated synthesis platform represents an actionable roadmap toward a general and broadly accessible solution to the small-molecule synthesis problem. This roadmap includes creating building blocks representing the highly redundant

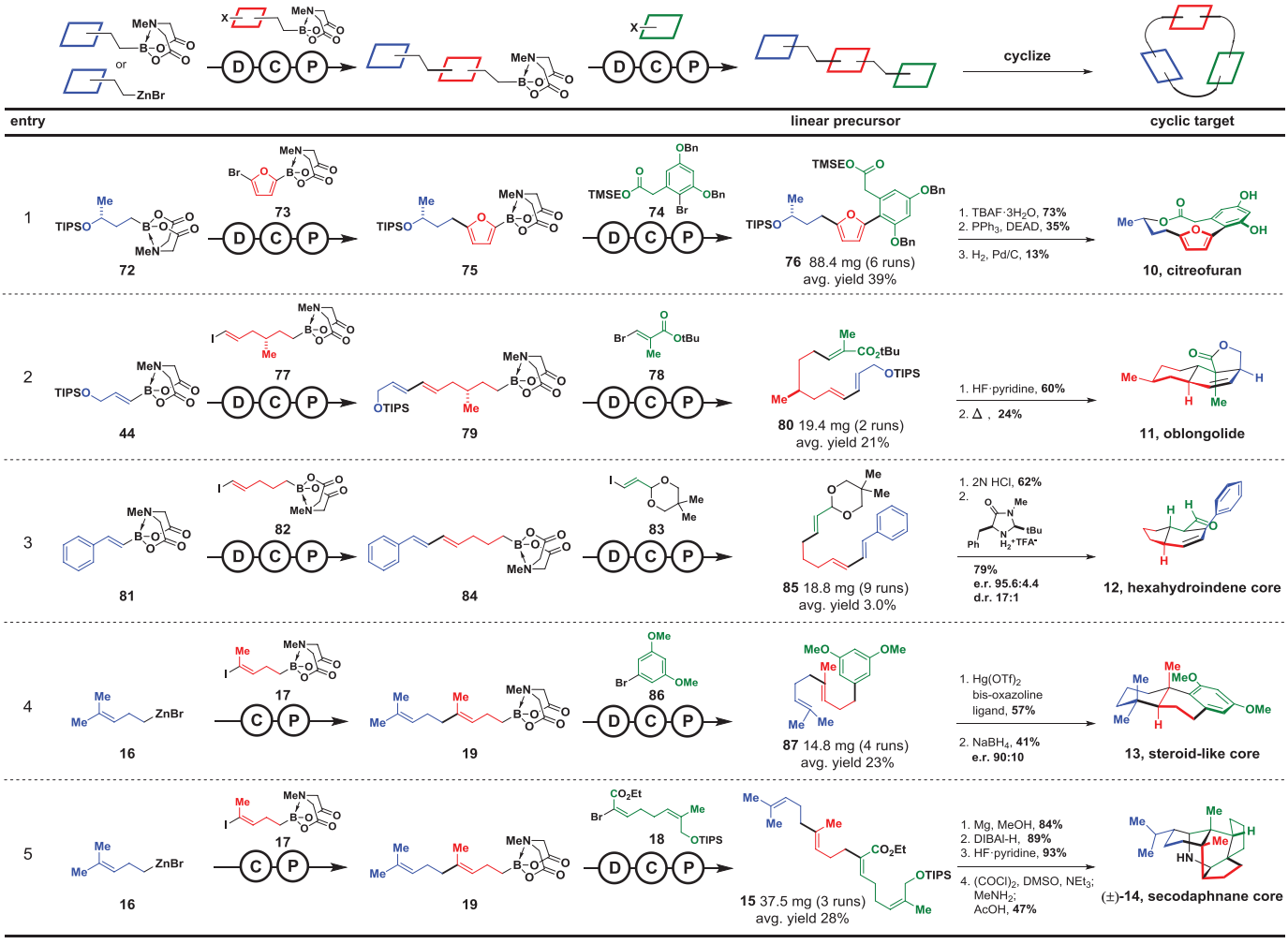

Fig. 4. Synthesis of C_{sp3}-rich macro- and polycyclic natural products and natural product–like cores. Modular linear precursors assembled via automated C_{sp2} and C_{sp3} couplings are diastereo- and/or enantioselectively cyclized. TBAF, tetra-*n*-butylammonium fluoride; DEAD, diethyl azodicarboxylate; OTf, trifluoromethanesulfonate; DIBAl-H, diisobutylaluminum hydride. e.r., enantiomeric ratio; d.r., diastereomeric ratio.

substructural elements found in many small molecules (*13*), developing better methods for iteratively coupling those building blocks together, and advancing the capacity for biosynthesis-inspired cyclizations of linear precursors to yield complex natural product frameworks. Achieving these objectives stands to better enable the scientific community to bring the substantial power of small-molecule synthesis to bear upon many important unsolved problems in society.

REFERENCES AND NOTES

1. R. B. Merrifield, *Science* **150**, 178–185 (1965).
2. M. H. Caruthers, *Science* **230**, 281–285 (1985).
3. O. J. Plante, E. R. Palmacci, P. H. Seeberger, *Science* **291**, 1523–1527 (2001).
4. S. V. Ley, D. E. Fitzpatrick, R. J. Ingham, R. M. Myers, *Angew. Chem. Int. Ed.* **54**, 10.1002/anie.201410744 (2015).
5. S. Fuse, K. Machida, T. Takahashi, in *New Strategies in Chemical Synthesis and Catalysis*, B. Pignataro, Ed. (Wiley, Weinheim, Germany, 2012), chap. 2.
6. A. G. Godfrey, T. Masquelin, H. Hemmerle, *Drug Discov. Today* **18**, 795–802 (2013).
7. S. Newton *et al.*, *Angew. Chem. Int. Ed.* **53**, 4915–4920 (2014).
8. P. M. Dewick, *Medicinal Natural Products: A Biosynthetic Approach* (Wiley, West Sussex, UK, 2009).
9. E. Vitaku, D. T. Smith, J. T. Njardarson, *J. Med. Chem.* **57**, 10257–10274 (2014).
10. R. A. Yoder, J. N. Johnston, *Chem. Rev.* **105**, 4730–4756 (2005).
11. E. M. Stocking, R. M. Williams, *Angew. Chem. Int. Ed.* **42**, 3078–3115 (2003).
12. F. Kopp, M. A. Marahiel, *Nat. Prod. Rep.* **24**, 735–749 (2007).
13. E. M. Woerly, J. Roy, M. D. Burke, *Nat. Chem.* **6**, 484–491 (2014).
14. E. P. Gillis, M. D. Burke, *J. Am. Chem. Soc.* **129**, 6716–6717 (2007).
15. N. Miyaura, A. Suzuki, *Chem. Rev.* **95**, 2457–2483 (1995).
16. E. P. Gillis, M. D. Burke, *Aldrichim Acta* **42**, 17–27 (2009).
17. E. M. Woerly, A. H. Cherney, E. K. Davis, M. D. Burke, *J. Am. Chem. Soc.* **132**, 6941–6943 (2010).
18. K. C. Gray *et al.*, *Proc. Natl. Acad. Sci. U.S.A.* **109**, 2234–2239 (2012).
19. K. Fujita, R. Matsui, T. Suzuki, S. Kobayashi, *Angew. Chem. Int. Ed.* **51**, 7271–7274 (2012).
20. C. H. Heathcock, S. Piettre, R. B. Ruggeri, J. A. Ragan, J. C. Kath, *J. Org. Chem.* **57**, 2554–2566 (1992).
21. E. L. Elliott, C. R. Ray, S. Kraft, J. R. Atkins, J. S. Moore, *J. Org. Chem.* **71**, 5282–5290 (2006).
22. M. Mentel, R. Breinbauer, *Top. Curr. Chem.* **278**, 209–241 (2007).
23. S. Maechling, J. Good, S. D. Lindell, *J. Comb. Chem.* **12**, 818–821 (2010).
24. Materials and methods are available as supplementary materials on *Science* Online.
25. T. Kinzel, Y. Zhang, S. L. Buchwald, *J. Am. Chem. Soc.* **132**, 14073–14075 (2010).
26. E. P. Gillis, M. D. Burke, *J. Am. Chem. Soc.* **130**, 14084–14085 (2008).
27. J. E. Grob *et al.*, *Org. Lett.* **14**, 5578–5581 (2012).
28. D. G. Hall, Ed., *Boronic Acids: Preparation and Applications in Organic Synthesis, Medicine and Materials* (Wiley, Weinheim, Germany, 2011).
29. F. Bracher, B. Schulte, *Nat. Prod. Res.* **17**, 293–299 (2003).
30. T. K. M. Shing, J. Yang, *J. Org. Chem.* **60**, 5785–5789 (1995).
31. E. J. Corey, L. Kürti, in *Enantioselective Chemical Synthesis: Methods, Logic, and Practice* (Direct Book Publishing, Dallas, TX, 2010), pp. 121–151.
32. R. M. Wilson, W. S. Jen, D. W. C. Macmillan, *J. Am. Chem. Soc.* **127**, 11616–11617 (2005).
33. S. A. Snyder, D. S. Treitler, A. Schall, *Tetrahedron* **66**, 4796–4804 (2010).

ACKNOWLEDGMENTS

We acknowledge the NIH (grants GM080436 and GM090153), the NSF (grant 0747778), HHMI, and Bristol-Myers Squibb for funding. M.D.B. is an HHMI Early Career Scientist, J.L. was an HHMI International Student Research Fellow, and J.L. and E.P.G. were Bristol-Myers Squibb Graduate Fellows. We thank D. Gray for performing the x-ray analysis on **N-bromoacyl-14**. The University of Illinois has filed patent applications on MIDA boronate chemistry and the automated synthesis platform reported herein. These inventions have been licensed to REVOLUTION Medicines, a company for which M.D.B. is a founder. Metrical parameters for the structure of **N-bromoacyl-14** are available free of charge from the Cambridge Cyrstallographic Data Centre under reference CCDC-1045844.

SUPPLEMENTARY MATERIALS

www.sciencemag.org/content/347/6227/1221/suppl/DC1
Materials and Methods
Supplementary Text
Figs. S1 to S14
Tables S1 to S3
References (*34*–*52*)

22 December 2014; accepted 12 February 2015
10.1126/science.aaa5414

LUNAR GEOLOGY

A young multilayered terrane of the northern Mare Imbrium revealed by Chang'E-3 mission

Long Xiao,[1,2]* Peimin Zhu,[1]* Guangyou Fang,[3]* Zhiyong Xiao,[1,4] Yongliao Zou,[5] Jiannan Zhao,[1] Na Zhao,[1] Yuefeng Yuan,[1] Le Qiao,[1] Xiaoping Zhang,[2] Hao Zhang,[1] Jiang Wang,[1] Jun Huang,[1] Qian Huang,[1] Qi He,[1] Bin Zhou,[3] Yicai Ji,[3] Qunying Zhang,[3] Shaoxiang Shen,[3] Yuxi Li,[3] Yunze Gao[3]

China's Chang'E-3 (CE-3) spacecraft touched down on the northern Mare Imbrium of the lunar nearside (340.49°E, 44.12°N), a region not directly sampled before. We report preliminary results with data from the CE-3 lander descent camera and from the Yutu rover's camera and penetrating radar. After the landing at a young 450-meter crater rim, the Yutu rover drove 114 meters on the ejecta blanket and photographed the rough surface and the excavated boulders. The boulder contains a substantial amount of crystals, which are most likely plagioclase and/or other mafic silicate mineral aggregates similar to terrestrial dolerite. The Lunar Penetrating Radar detection and integrated geological interpretation have identified more than nine subsurface layers, suggesting that this region has experienced complex geological processes since the Imbrian and is compositionally distinct from the Apollo and Luna landing sites.

Chang'E-3 (CE-3) landed at 340.49°E, 44.12°N on the Moon on 14 December 2013, and it released the Yutu (Jade Rabbit) rover the next morning (*1*). This was the first soft landing on the Moon since the Soviet Union's Luna 24 mission in 1976 and is a new landing site in the north part of the Mare Imbrium (fig. S1). Yutu is China's first lunar geologic mission and traveled in total ~114 m on the lunar surface. Following a zigzagging route, Yutu came to a halt about 20 m to the southwest of the landing site (Fig. 1). Yutu explored the lunar surface and subsurface near a young crater (fig. S2) using its four main instruments: Panoramic Camera, Lunar Penetrating Radar (LPR), Visible–Near Infrared Spectrometer (VNIS), and Active Particle-Induced X-ray Spectrometer (APXS). In this study, we report the preliminary results obtained from the cameras and LPR.

[1]China University of Geosciences, Wuhan 430074, China. [2]Macau University of Science and Technology, Macau, China. [3]Institute of Electronics, China Academy of Science, Beijing 100190, China. [4]The Centre for Earth Evolution and Dynamics, University of Oslo, Sem Sælandsvei 24, 0371 Oslo, Norway. [5]National Astronomical Observatories, China Academy of Science, Beijing 100012, China.
***Corresponding author. E-mail: longxiao@cug.edu.cn (L.X.); zhupm@cug.edu.cn (P.Z.); gyfang@mail.ie.ac.cn (G.F.)**

High-resolution images returned by both Yutu and the lander show that the landing site features thin regolith and numerous small craters that are centimeters to tens of meters in diameter (Fig. 1 and figs. S3 to S6). Although at the regional scale the mare surface at the landing site appears relatively flat, the landing site is located ~50 m from the eastern rim of the ~450-m crater (C_1) (*2*). The traversed area of the Yutu rover was wholly restricted within the continuous ejecta deposits (fig. S2). Crater size-frequency distribution measurements (*2*) for the continuous ejecta deposits of the C_1 crater yield a minimum model age of ~27 million years (My) and a maximum model age of ~80 My, which is late Copernican (*3*), consistent with the estimation made from the preservation state of the crater and from the meter-sized boulders observed on the crater rim (*2*).

Yutu drove very close to the rim of the C_1 crater, and its panoramic cameras photographed the shape and interior features of the crater. A full image of the crater was also acquired (fig. S4A) when Yutu stood behind the Loong rock (position number 13 in Fig. 1) (*1*). This circular-rimmed crater has distinct rocky walls and rims, except on the northern side. The ejected boulders are

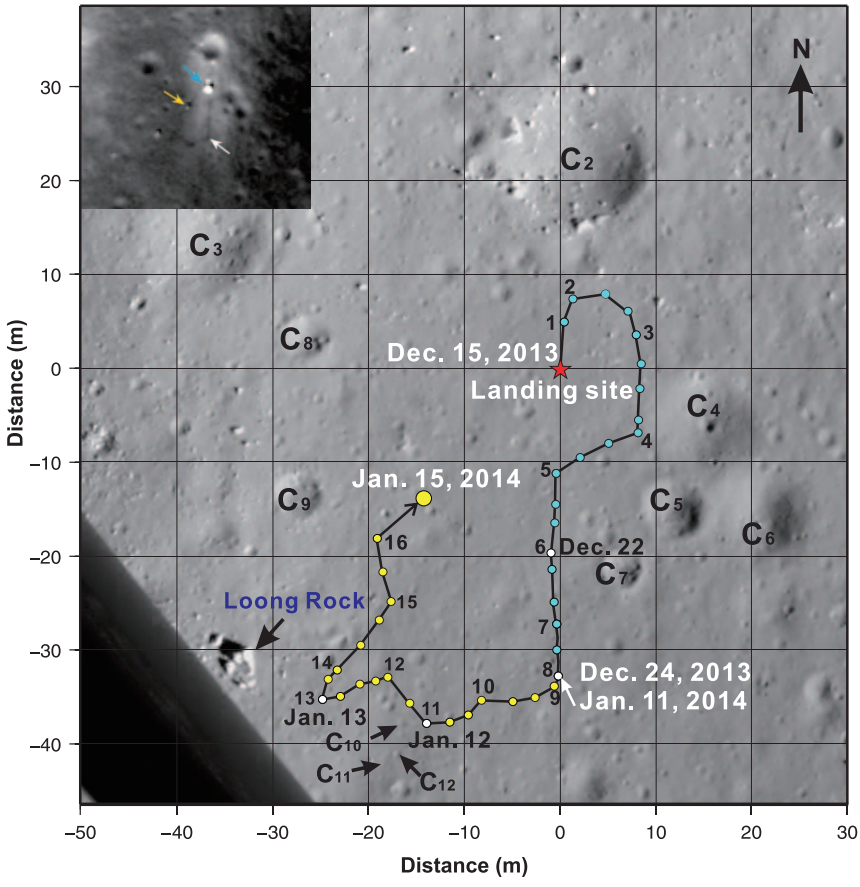

Fig. 1. Yutu's path on the Moon. The cyan and yellow dots mark the first and second lunar daytime stops, which ended on 24 December 2013 and 15 January 2014, respectively. The numbers aligned to the dots denote the positions where the LPR was rebooted. The white dots indicate positions where the APXS, VNIS, and panoramic camera gathered data. The context image was taken by the descent camera at an elevation of ~120 m, and the lower left corner was blocked by the lander. The inset image shows the positions of the CE-3 lander (blue arrow), the Yutu rover (yellow arrow), and its track (dark gray line) (the white arrow points to the spot where Yutu rested for the first lunar night). The inset image was taken by the Lunar Reconnaissance Orbiter Camera Narrow Angle Camera (LROC NAC; NASA/Goddard/Arizona State University).

irregular in shape and of various sizes, which are up to several meters tall and wide—e.g., the Loong rock (~4 m long by ~1.5 m high).

Small craters on the ejecta blanket of the C_1 crater vary in shape, roughness, and albedo (fig. S4). Regolith exhumed by Yutu's wheels has a lower reflectance compared with regolith on the surface, which is probably due to larger grain sizes of regolith at depths (fig. S5). Extensive shallow and linear features are visible around the landing site (figs. S5 and S6). Most of them occur in two preferential directions and are intersected and/or cross-cut with each other (figs. S5 and S6). Although this region was affected by the recoil rockets during the landing process, as evident from the inset image shown in Fig. 1, any rocket jets would have formed continuous, multidirectional and/or radial features on the surface, which are not observed along the track of the Yutu rover. Furthermore, newly created surface features on the Moon should have a rougher appearance and display distinctively lower albedos compared with the surroundings, which are not observed at the landing site either. Nearby impact craters may also distribute radial ejecta rays to the surroundings, but their potential in forming such multigroup subparallel linear features is low. Alternatively, linear features with comparable scales and similar appearances were widely observed at the Apollo 11, 12, and 15 landing sites, which were interpreted to be caused by a combination of obliquely incident sunlight and small surface topographic irregularities (*4*, *5*). The linear features observed at the CE-3 landing site, therefore, could simply be illumination features caused by the undulated surface.

Orbital chemical composition measurements from the gamma ray spectrometer onboard Lunar Prospector revealed that this area may be covered by intermediate Ti mare basalts [$TiO_2 = 5 \pm 1$ weight percent (wt %) and FeO = 20 ± 2 wt %] (*6*). The Loong rock appears to be homogeneous in high-resolution images obtained by the Yutu rover (fig. S7). Coarse granular or porphyritic textures are visible within the boulder. The light-colored crystals are ~1.5 to 2 cm in length and exhibit diffuse margins (fig. S7B). Image comparisons between this outcrop and the Lunar Sample Compendium (http://curator.jsc.nasa.gov/lunar/lsc) indicate that the Loong rock is distinct in texture from the other lunar basalts or breccias. The light-colored crystals are most likely plagioclases or aggregates of plagioclase (*7*) and other mafic silicate minerals—e.g., pyroxene and olivine (*8*)—indicating that this boulder may be coarse-crystalline basalt or dolerite excavated by the impact that formed the C_1 crater.

The LPR onboard Yutu consists of two types of antennas that have different frequencies, allowing subsurface structures at the landing site to be resolved at different depths and vertical resolutions (*2*, *9*, *10*). The dominant frequencies of these two channels are 60 MHz (Channel 1) and 500 MHz (Channel 2). The LPR has obtained radar echoes along the whole traverse of Yutu. Here, we report the preliminary interpretations on the radar data returned from the two antennas.

The LPR data have been processed using a standard calibration method (*2*, *9*, *10*). The Channel 1 radar reveals subsurface structures to depths of ~400 m and resolves several interfaces that have clear reflection characteristics (Fig. 2B). Subsurface structures less than ~20 m deep are not well resolved by the Channel 1 radar because of both the lower resolution and signal-to-noise ratio caused by signal saturation at such small depths (*2*, *10*). The Channel 2B data, however, reveal structures at depths less than 12 m but with greater detail compared with the Channel 1 data (Fig. 2A).

The Yutu rover surveyed a small area over the Eratosthenian basalts within the Imbrium basin. These mare basalts are believed to be among the youngest [~2.5 billion years (Gy) old] (*11*), compared with the landing sites of Apollo and Luna missions (*3*). The uppermost and also the youngest stratigraphic unit at the landing site is a regolith layer formed from the ejecta deposits excavated in the formation of the C_1 crater (layer a in Fig. 2A). This layer is ~1 m thick, as inferred from the morphology of small craters at the landing site [(*2*) and fig. S3]. At different locations along Yutu's track, small

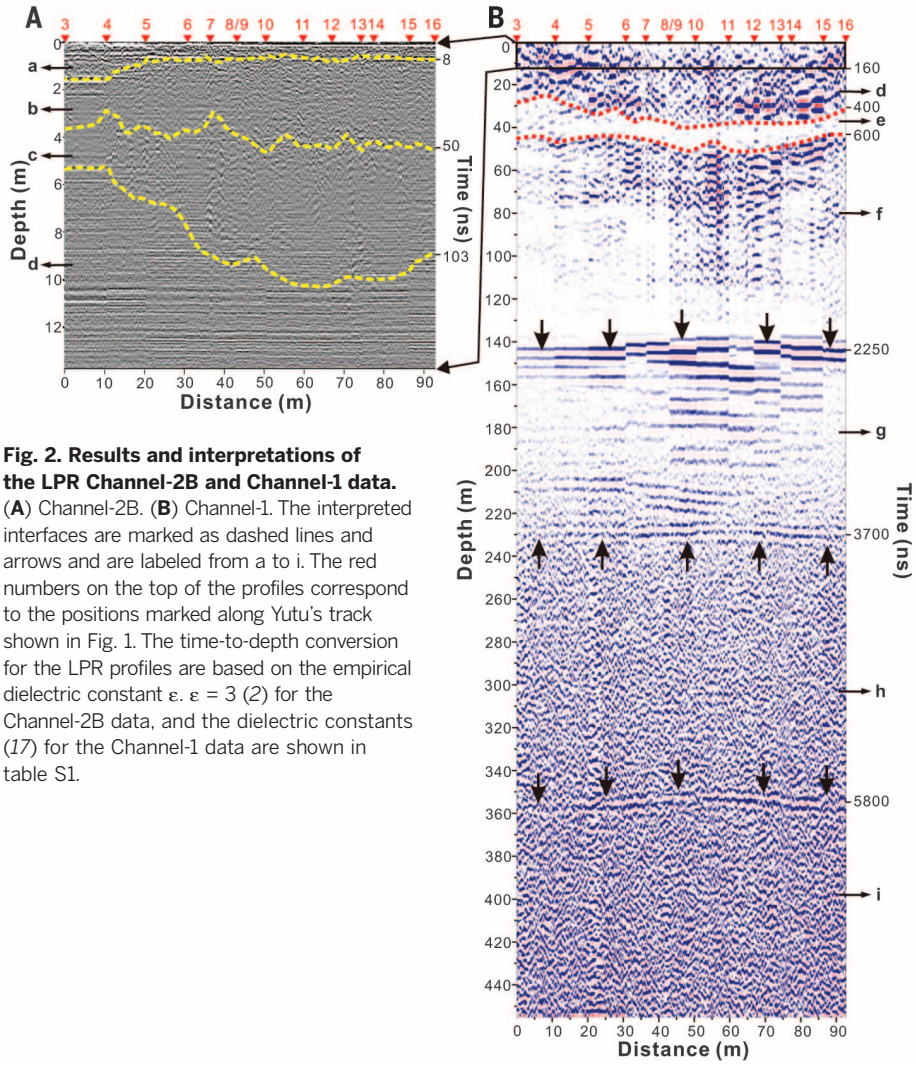

Fig. 2. Results and interpretations of the LPR Channel-2B and Channel-1 data. (**A**) Channel-2B. (**B**) Channel-1. The interpreted interfaces are marked as dashed lines and arrows and are labeled from a to i. The red numbers on the top of the profiles correspond to the positions marked along Yutu's track shown in Fig. 1. The time-to-depth conversion for the LPR profiles are based on the empirical dielectric constant ε. ε = 3 (*2*) for the Channel-2B data, and the dielectric constants (*17*) for the Channel-1 data are shown in table S1.

craters postdating the C_1 crater, such as the C_2 and C_4 craters (Fig. 1), have modified the local regolith thickness by impact excavation and deposition. This thickness variation is also resolved in the interpreted layer a from the Channel 2B data, which is ~2 m thick between positions 3 and 4 and ~1 m thick at the rest area along Yutu's track (Fig. 2A). Below the surface regolith layer are the remnant ejecta deposits from the C_1 crater, which are generally thicker near the crater rim and then thin outwardly (*12*). This layer of ~1 to ~4 m is recognized in the Channel 2B data (layer b in Fig. 2A), which is thicker from positions 4 to 16 (Fig. 1). Also, there may be many rocks with the size of about 0.3 to 1 m within the ejecta deposits, based on the presence of diffraction events of radar wave (see fig. S14).

Before the C_1 crater formed ~27 to 80 million years ago (Ma), a boulder-bearing paleoregolith layer (c in Fig. 2A) had accumulated at the base of the Eratosthenian basalts [~2.5 billion years ago (Ga)] by space weathering and impact gardening. Continuous ejecta from the C_1 crater was then deposited (layer b in Fig. 2A) over this paleoregolith layer. This layer is consistent with the third layer recognized at depths from ~4 to ~10 m from the Channel 2B (layer c in Fig. 2A). It exhibits a wide range of thickness from ~2 to ~6 m, which is consistent with the large variety of regolith depth over small distances on the Moon (*13*). It may be a record of the nonuniform production rate of regolith over the lunar surface and/or the disturbance by later impacts, such as the C_1 crater. Materials at depths larger than ~6 to 10 m (layer d in Fig. 2A) show regular layering and the radar echoes indicating larger density compared with shallower regolith or fractured ejecta deposits. These radar features suggest that layer d is made of thick competent rocks, most likely

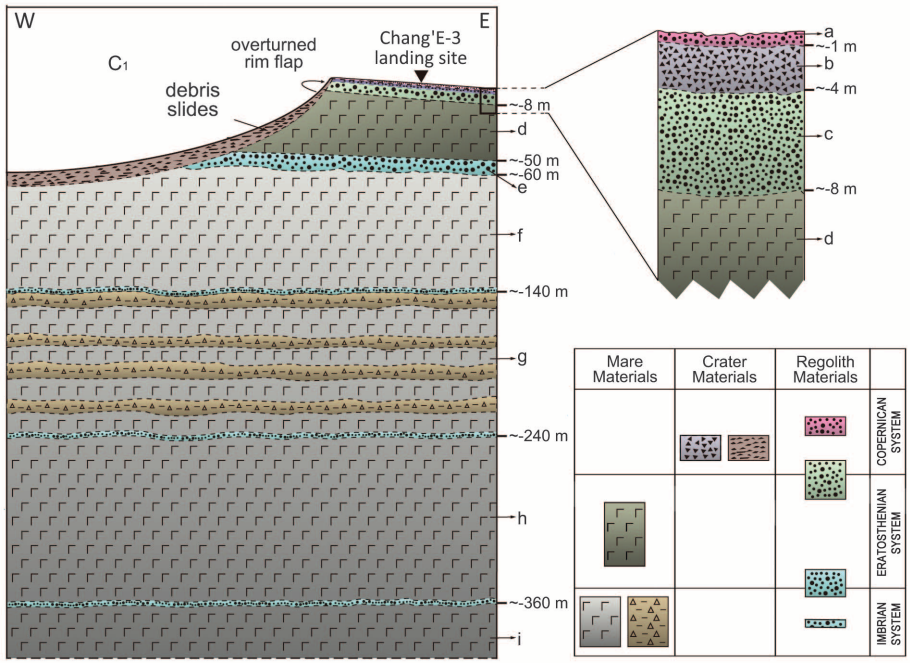

Fig. 3. Sketched geological cross section and an inferred profile of the CE-3 landing site. Yutu has detected seven subsurface interfaces, which formed from Imbrian to Copernican. Letters a to i indicate interpreted subsurface layers based on LPR data (Fig. 2).

similar to the Eratosthenian basalts beneath the paleoregolith layer.

The Channel 1 data reveal that the Eratosthenian basalts at the landing site extend to a depth of ~35 m (layer d in Fig. 2, A and B), which is consistent with the depth estimated from nearby impact craters that have excavated deeper Imbrian materials (*14*). Two clear interfaces that feature higher radar reflection strengths are shown at depths ~35 m and ~50 m (layer e in Fig. 2B), respectively. This fifth layer (layer e), is interpreted to be the paleoregolith formed on top of the Imbrian lava flows (>~3.3 Ga) (*11*), over which the Eratosthenian basalts were emplaced subsequently. A deeper layer between ~50 and 140 m has similar radar reflections to the Eratosthenian basalts resolved in layer d, suggesting that this layer probably represents the latest Imbrian basalts that filled in the Imbrium basin around 3.3 Ga (layer f in Fig. 2B). Other subhorizontal interfaces are visible at depths larger than ~140 m, such as those at depths of ~240 and ~360 m (layers g, h, and i in Fig. 2B). Interestingly, layer g shows different reflection texture compared with layers f and h. The reflection wave is comparable to those of bedded rocks—e.g., sedimentary or pyroclastic rocks on Earth. Considering the geological history of the lunar mare area (*15*), we propose that this layer is probably bedded or interlayered lava flow and/or pyroclastic rocks or thin and multilayered basaltic lavas.

Current regional geologic studies suggest that at least five episodes of lava eruptions filled the northeast region of the Imbrium basin, forming about 1-km-thick basaltic layers (*16*). Yutu's LPR has revealed five distinct episodes of pyroclastic/lava filling events within the upper ~400 m depth, although it is very likely that more episodes of volcanic eruptions have filled the Imbrium basin at greater depths (*8*).

Integrated geologic and geophysical explorations using the scientific payloads onboard the Yutu rover have revealed the detailed subsurface geological structures and the geological history of this area. Compared with previous Apollo and Luna landing sites, this area has the youngest mare basalts that appear to have unusual petrofabric characteristics. The LPR data have revealed complex subsurface structures of shallow crust within the mare, providing valuable information to reveal the lava eruption extents, style, and filling history within the Imbrium basin and the production history of regolith since ~3.3 Ga (Fig. 3). The available data suggest that the diversity of geological characteristics and thermal history of different lunar mare areas indicates there is more complex geological history than we had thought.

REFERENCES AND NOTES

1. L. Xiao, *Nat. Geosci.* **7**, 391–392 (2014).
2. Materials and methods are available as supplementary materials on *Science* Online.
3. H. Hiesinger, J. Head, U. Wolf, R. Jaumann, G. Neukum, *Spec. Pap. Geol. Soc. Am.* **477**, 1–51 (2011).
4. G. G. Schaber, G. A. Swann, *Proc. Lunar Planet. Sci. Conf.* **1**, 27–38 (1971).
5. E. W. Wolfe, N. G. Bailey, *Proc. Lunar Planet. Sci. Conf.* **1**, 15–25 (1972).
6. T. H. Prettyman *et al.*, *J. Geophys. Res.* **111** (E12), E12007 (2006).
7. E. M. Shoemaker *et al.*, *J. Geophys. Res.* **74**, 6081–6119 (1969).
8. F. Thiessen, S. Besse, M. I. Staid, H. Hiesinger, *Planet. Space Sci.* **104**, 244–252 (2014).
9. G. Y. Fang *et al.*, *Research in Astronomy and Astrophysics* **14**, 1607–1622 (2014).
10. N. Zhao, P. Zhu, K. Yang, Y. Yuan, S. Guo, *Sci. China-Phys. Mech. Astron.* **57**, 2346–2353 (2014).
11. J. Zhao *et al.*, *Sci. China-Phys. Mech. Astron.* **57**, 569–576 (2014).
12. T. R. McGetchin, M. Settle, J. Head, *Earth Planet. Sci. Lett.* **20**, 226–236 (1973).
13. B. B. Wilcox, M. S. Robinson, P. C. Thomas, B. R. Hawke, *Meteorit. Planet. Sci.* **40**, 695–710 (2005).
14. L. Qiao, L. Xiao, J. Zhao, Q. Huang, J. Haruyama, *Planet. Space Sci.* **101**, 37–52 (2014).
15. B. L. Jolliff, M. A. Wieczorek, C. K. Shearer, C. R. Neal, Eds., *New Views of the Moon* (Mineralogical Society of America, Chantilly, VA, 2006).
16. B. J. Thomson, E. B. Grosfils, D. B. J. Bussey, P. D. Spudis, *Geophys. Res. Lett.* **36**, L12201 (2009).
17. Z. Wang, Y. Li, J. Jiang, D. Li, *Sci. China Earth Sci.* **53**, 1365–1378 (2010).

ACKNOWLEDGMENTS

All the authors acknowledge support from the Key Research Program of the Chinese Academy of Sciences (grant KGZD-EW-603). L.X., Z.Y.X., J.N.Z., L.Q., and J.H. acknowledge support of the Natural Science Foundation of China (grant 41373066). X.P.Z. acknowledges support from the Science and Technology Development Fund (FDCT) of Macau (grants 068/2011/A, 048/2012/A2, and 091/2013/A3). We thank C. L. Li and the Ground Application System of Lunar Exploration, National Astronomical Observatories, Chinese Academy of Sciences, for their valuable and efficient help on data calibration and supplying. Author contributions: L.X., Z.Y.X., J.N.Z., L.Q., Y.L.Z., J.H., H.Z., X.P.Z., J.W., Q. Huang, and Q. He processed the imagery data and conducted image and radar data interpretation and geological analysis. P.M.Z., G.Y.F., N.Z., and Y.F.Y processed LPR data and did interpretation. B.Z, Y.C.J., Q.Y.Z., S.X.S., Y.X.L., and Y.Z.G. are team members of the LPR instrument. All authors contributed to the writing of the paper. The imagery data obtained by the Panoramic Camera onboard Yutu are the level 2C data. The imagery data obtained by the Descent Camera onboard the Chang'E-3 lander are the level 2A data. The IDs for the images used in the figures are listed in table S2 in the supplementary materials. Data presented in this paper are hosted at http://moon.bao.ac.cn.

SUPPLEMENTARY MATERIALS

www.sciencemag.org/content/347/6227/1226/suppl/DC1
Materials and Methods
Figs. S1 to S14
Tables S1 and S2
References (*18*–*30*)

11 August 2014; accepted 5 February 2015
10.1126/science.1259866

QUANTUM WALKS

Strongly correlated quantum walks in optical lattices

Philipp M. Preiss,[1] Ruichao Ma,[1] M. Eric Tai,[1] Alexander Lukin,[1] Matthew Rispoli,[1] Philip Zupancic,[1]* Yoav Lahini,[2] Rajibul Islam,[1] Markus Greiner[1]†

Full control over the dynamics of interacting, indistinguishable quantum particles is an important prerequisite for the experimental study of strongly correlated quantum matter and the implementation of high-fidelity quantum information processing. We demonstrate such control over the quantum walk—the quantum mechanical analog of the classical random walk—in the regime where dynamics are dominated by interparticle interactions. Using interacting bosonic atoms in an optical lattice, we directly observed fundamental effects such as the emergence of correlations in two-particle quantum walks, as well as strongly correlated Bloch oscillations in tilted optical lattices. Our approach can be scaled to larger systems, greatly extending the class of problems accessible via quantum walks.

Quantum walks are the quantum mechanical analogs of the classical random walk process, describing the propagation of quantum particles on periodic potentials (*1*, *2*). Unlike classical objects, particles performing a quantum walk can be in a superposition state and take all possible paths through their environment simultaneously, leading to faster propagation and enhanced sensitivity to initial conditions. These properties have generated considerable interest in using quantum walks for the study of position-space quantum dynamics and for quantum information processing (*3*). Two distinct models of quantum walk with similar physical behavior were devised: (i) the discrete-time quantum walk (*1*), in which the particle propagates in discrete steps determined by a dynamic internal degree of freedom, and (ii) the continuous-time quantum walk (*2*), in which the dynamics is described by a time-independent lattice Hamiltonian.

Experimentally, quantum walks have been implemented for photons (*4*), trapped ions (*5*, *6*), and neutral atoms (*7*–*9*), among other platforms (*4*). Until recently, most experiments were aimed at observing the quantum walks of a single quantum particle, which are described by classical wave equations.

[1]Department of Physics, Harvard University, Cambridge, MA 02138, USA. [2]Department of Physics, Massachusetts Institute of Technology, Cambridge, MA 02139, USA.
*Present address: Institute for Quantum Electronics, ETH Zürich, 8093 Zürich, Switzerland. †Corresponding author. E-mail: greiner@physics.harvard.edu

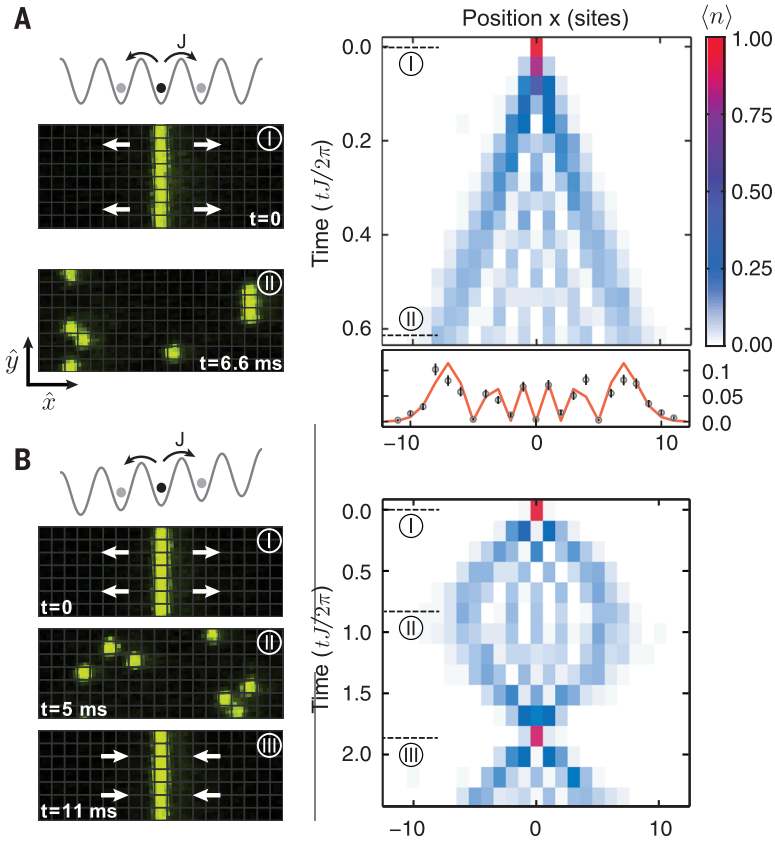

Fig. 1. Coherent single-particle quantum walks. (**A**) Left: Starting from a localized initial state (I), individual atoms perform independent quantum walks in an optical lattice (II). Right: The single-particle density distribution expands linearly in time, and atoms coherently delocalize over 20 sites (lower panel shows the averaged density distribution at the end of the quantum walk and a fit to Eq. 2 with the tunneling rate J as a free parameter). Error bars indicate SEM. (**B**) In the presence of a gradient, a single particle undergoes Bloch oscillations. The atom initially delocalizes (II) but maintains excellent coherence and reconverges to its initial position after one period (III). Densities are averages over ~700 and ~200 realizations for (A) and (B), respectively.

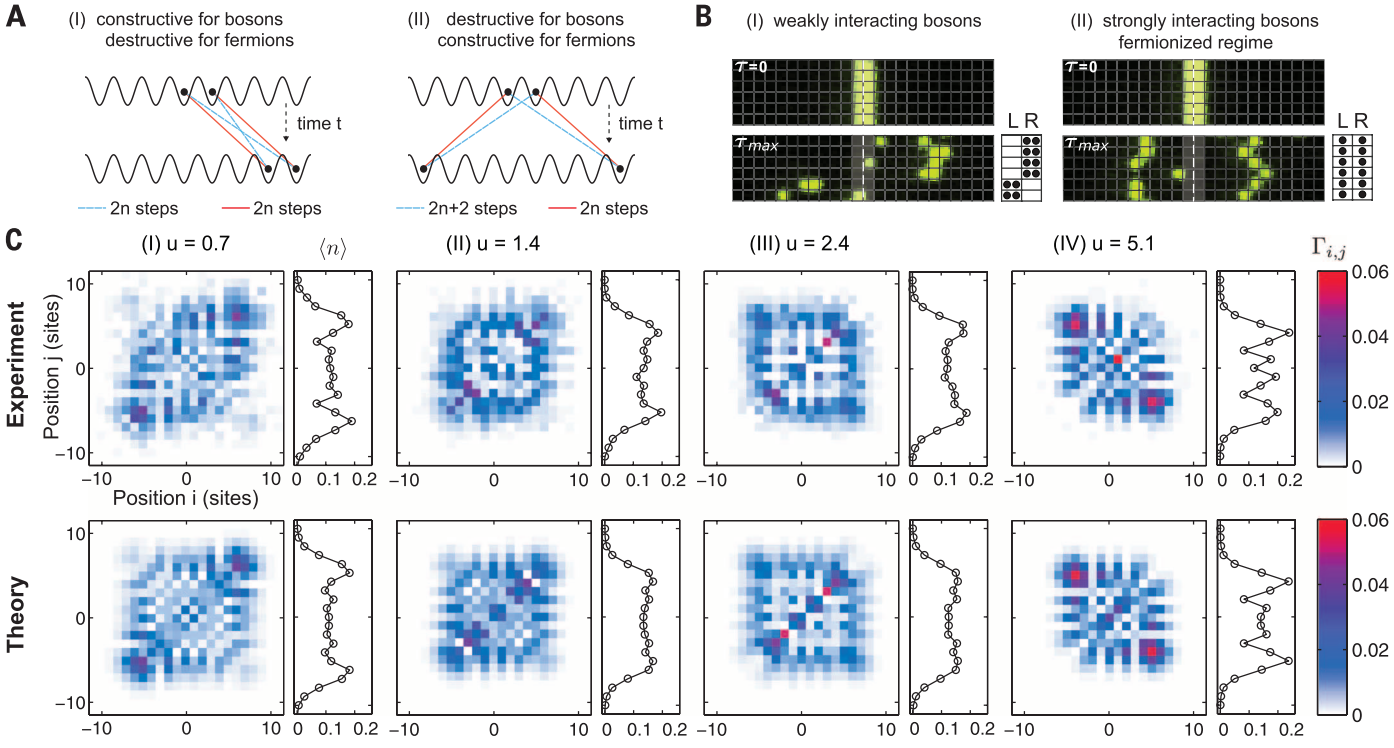

Fig. 2. Hanbury-Brown-Twiss interference and fermionization. (**A**) Processes connecting the initial and final two-particle states interfere coherently. Each tunneling step contributes a phase i. For noninteracting bosons, processes of the same length add constructively (I), whereas processes differing in length by two steps interfere destructively (II). (**B**) Weakly interacting bosons display strong bunching (I). Strong, repulsive on-site interactions cause bosons in one dimension to fermionize and develop long-range anticorrelations (II). (**C**) Measured correlator $\Gamma_{i,j}$ at time $\tau_{max} \approx 2\pi \times 0.5$, averaged over ~3200 realizations. The interactions are tuned from weak ($u < 1$) to strong ($u \gg 1$) by choosing $V_x = 1E_r$, $2.5E_r$, $4E_r$, and $6.5E_r$.

An enhancement of quantum effects emerges when more than one indistinguishable particle participates in the quantum walk simultaneously. In such cases, quantum correlations can develop as a consequence of Hanbury-Brown-Twiss (HBT) interference and quantum statistics, as was investigated theoretically (*10*, *11*) and experimentally (*12*–*17*). In the absence of interactions or auxiliary feedforward measurements of the Knill-Laflamme-Milburn type (*18*), this problem is believed to lack full quantum complexity, although it can still become intractable by classical computing (*11*).

The inclusion of interaction between indistinguishable quantum walkers (*19*, *20*) may grant access to a much wider class of computationally hard problems, such as many-body localization and the dynamics of interacting quantum disordered systems (*21*). Similarly, in the presence of interactions, the quantum walk can yield universal and efficient quantum computation (*22*).

The classical simulation of such correlated quantum dynamics has been achieved with single-particle quantum walks in photonic systems, where effective interactions may be engineered through conditional phase shifts in fiber networks (*23*) or waveguide arrays (*24*). Here, we used bosonic atoms in an optical lattice to directly implement continuous two-particle quantum walks with strong, tunable interactions and direct scalability to larger particle numbers. Our system realizes the fundamental building block of interacting many-body systems with atom-resolved access to the strongly correlated dynamics in a quantum gas microscope (*25*).

In our experiment, ultracold atoms of bosonic ^{87}Rb perform quantum walks in decoupled one-dimensional tubes of an optical lattice with spacing d = 680 nm. The atoms may tunnel in the x direction with amplitude J and experience a repulsive on-site interaction U, realizing the Bose-Hubbard Hamiltonian

$$H_{\mathrm{BH}} = \sum_{\langle i,j \rangle} J a_i^\dagger a_j + \sum_i \frac{U}{2} n_i(n_i - 1) + \sum_i i E n_i \quad (1)$$

where $a_i^\dagger$ and a_i are the bosonic creation and annihilation operators, respectively, and $n_i = a_i^\dagger a_i$ gives the atom number on site i. The values of J and U are tunable via the depth V_x of the optical lattice, specified in units of the recoil energy $E_\mathrm{r} = 2\pi \times (h/8md^2) \approx 2\pi \times 1240$ Hz, where h is Planck's constant and m is the atomic mass of ^{87}Rb. The energy shift per lattice site E is set by a magnetic field gradient. We measure time in units of inverse tunneling rates, $\tau = tJ$, and define the dimensionless interaction $u = U/J$ and gradient $\Delta = E/J$.

We set the initial motional state of the atoms through an adaptable single-site addressing scheme, enabling the deterministic preparation of a wide range of few-body states: Using a digital micromirror device (DMD) as an amplitude hologram in a Fourier plane, we generate arbitrary diffraction-limited potentials in the plane of the atoms. Starting from a low-entropy two-dimensional Mott insulator with a fixed number of atoms per site, we project a repulsive Hermite-Gauss profile to isolate atoms in selected rows while a short reduction of the optical lattice depth ejects all other atoms from the system (*26*). For the quantum walk, we prepare one or two rows of atoms along the y direction of a deep optical lattice with $V_x = V_y = 45E_\mathrm{r}$ (Fig. 1A). The quantum walk is performed at a reduced lattice depth V_x while the y lattice and the out-of-plane confinement are fixed at $V_y = 45E_\mathrm{r}$ and $\omega_z = 2\pi \times 7.2$ kHz, respectively. The atom positions are recorded with single-site resolution using fluorescence imaging in a deep optical lattice (*25*). Pairs of atoms residing on the same site are lost during imaging because of light-assisted collisions and cannot be detected directly. Using a magnetic field gradient, we separate pairs of atoms along the direction of the quantum walk prior to imaging (*26*) and obtain the full two-particle correlator $\Gamma_{i,j} = \langle a_i^\dagger a_j^\dagger a_i a_j \rangle$ and the density distribution. Only outcomes with the correct number of atoms per row are included in the data analysis (*26*).

We first consider quantum walks of individual atoms (Fig. 1A). A single particle is initialized at a chosen site in each horizontal tube and propagates in the absence of an external force. For each individual realization, the particle is detected on a single lattice site, while the average over many experiments yields the single-particle probability distribution. In contrast to a classical random walk, for which slow, diffusive expansion of the Gaussian density distribution is expected, coherent interference of all single-particle paths leads to ballistic transport with well-defined wavefronts (*4*). The measured probability density ρ expands linearly in time (Fig. 1A, right panel), in good agreement with the theoretical expectation

$$\rho_i(t) = |\mathcal{J}_i(2Jt)|^2 \quad (2)$$

(*27*), where $\mathcal{J}_i$ is a Bessel function of the first kind on lattice site i. If a potential gradient is applied to ultracold atoms in an optical lattice, net transport does not occur because of the absence of dissipation and the separation of the

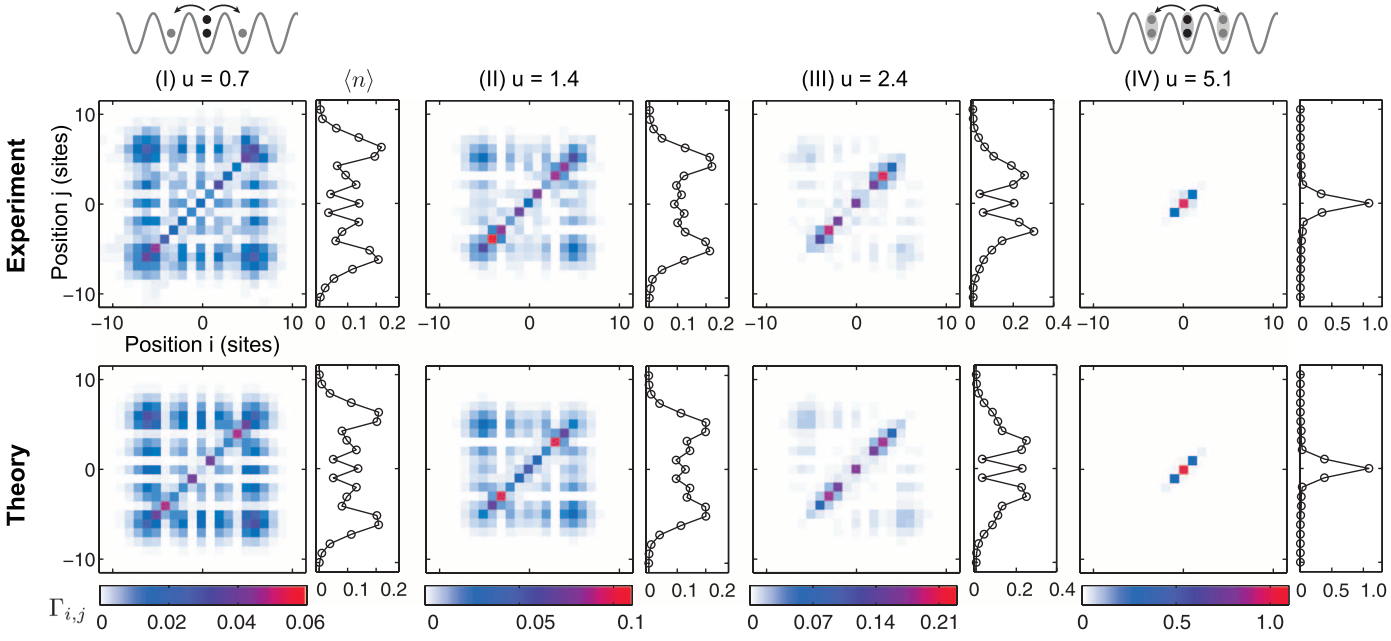

Fig. 3. Formation of repulsively bound pairs. Two-particle correlations at $\tau_{\mathrm{max}} \approx 2\pi \times 0.5$ for two particles starting on site 0 in state $(1/\sqrt{2})a_0^\dagger a_0^\dagger|0\rangle$. For weak interactions (u = 0.7), the atoms perform independent single-particle quantum walks. As the interaction strength is increased, repulsively bound pairs form and undergo an effective single-particle quantum walk along the diagonal of the two-particle correlator. Experimental parameters are identical to those in Fig. 2.

spectrum into discrete bands. Instead, the gradient induces a position-dependent phase shift and causes atoms to undergo Bloch oscillations (*28*). For a fully coherent single-particle quantum walk with gradient Δ, the atom remains localized to a small volume and undergoes a periodic breathing motion in position space (*27*, *29*–*31*) with a maximal half width $L_B = 4/\Delta$ and temporal period $T_B = 2\pi/\Delta$ in units of the inverse tunneling.

Figure 1B shows a single-particle quantum walk with $\Delta = 0.56$, resulting in Bloch oscillations over ~14 lattice sites. We observed a high-quality revival after one Bloch period and detected the particle back at the origin with a probability of up to 0.96 ± 0.03 at $\tau = T_B$ in individual tubes. The average over six adjacent rows in Fig. 1B displays a revival probability of 0.88 ± 0.02, limited by the temporal resolution of the measurements and inhomogeneous broadening across different rows. The fidelity

$$F(t) = \sum_x \sqrt{p_x(t) q_x(t)} \qquad (3)$$

for the measured and expected probability distributions $p_x(t)$ and $q_x(t)$, averaged over ~1.5 Bloch oscillations, is $98.1 \pm 0.1\%$, indicating that a high level of coherence is maintained while the particle delocalizes over ~10 μm in the optical lattice.

If two particles perform a quantum walk simultaneously, they undergo HBT interference (*12*, *32*) and their dynamics are sensitive to the underlying particle statistics. All two-particle processes in the system add coherently, leading to quantum correlations between the particles (Fig. 2A): For bosons, the processes bringing both particles into close proximity of each other add constructively, leading to bosonic bunching, as observed in tunnel-coupled optical tweezers (*33*), expanding atomic clouds (*32*, *34*), and photonic implementations of quantum walks (*12*, *13*). For fermionic particles, on the other hand, particle exchange leads to an additional phase shift of π, causing a reversal of the HBT logic and characteristic antibunching of free fermions (*13*, *32*).

In our experiment, the bunching of free bosonic atoms is apparent in single-shot images of quantum walks with two particles starting from adjacent sites in the state $a_0^\dagger a_1^\dagger|0\rangle$. For weak interactions, the two atoms are very likely to be detected close to each other because of HBT interference, as shown in raw images in Fig. 2B. To characterize the degree of bunching, we used the density-density correlator $\Gamma_{i,j}$ (Fig. 2C), measured at time $\tau_{max} \approx 2\pi \times 0.5$. Panel I of Fig. 2C shows the two-particle correlator for a quantum walk with weak interactions ($u = 0.7$). Sharp features are caused by quantum interference and demonstrate the good coherence of the two-particle dynamics. The concentration of probability on and near the diagonal of the correlator $\Gamma_{i,j}$ indicates HBT interference of nearly free bosonic particles.

We used the quantum walk's sensitivity to quantum statistics to probe the "fermionization" of bosonic particles caused by repulsive interactions in one-dimensional systems. When such interactions are strong, double occupancies are suppressed by the large energy cost U, which takes the role of an effective Pauli exclusion principle for bosonic particles. In the limiting case of infinite, "hard-core" repulsive interactions, one-dimensional bosonic systems "fermionize" and display densities and spatial correlations that are identical to those of noninteracting spinless fermions (*35*). This behavior has been observed in equilibrium in the pair correlations and momentum distributions of large one-dimensional Bose-Einstein condensates (*36*, *37*). These systems are characterized by the dimensionless ratio of interaction to kinetic energy γ, and the fermionized Tonks-Girardeau regime is entered when γ is large. For Bose-Hubbard systems below unity filling, such as ours, the corresponding parameter is the ratio $u = U/J$.

We studied the process of fermionization in the fundamental unit of two interacting particles by repeating the quantum walk from initial state $a_0^\dagger a_1^\dagger|0\rangle$ at increasing interaction strengths (*19*). Figure 2C shows $\Gamma_{i,j}$ for several values of u. At intermediate values of the interaction, $u = 1.4$ and $u = 2.4$, the correlation distribution is relatively uniform, as repulsive interactions compete with HBT interference. For the strongest interaction strength, $u = 5.1$, most of the weight is concentrated on the antidiagonal of $\Gamma_{i,j}$, corresponding to pronounced antibunching. The anticorrelations are strong enough to be visible in raw images of the quantum walk (Fig. 2B, panel II), and $\Gamma_{i,j}$ is almost identical to the expected outcome for noninteracting fermions. Note that although the correlations change markedly with increasing interaction, the densities remain largely unchanged. At all interaction strengths, the observed densities and correlations are in excellent agreement with a numerical integration of the Schrödinger equation with the Bose-Hubbard Hamiltonian in Eq. 1 (*26*). Interactions in two-particle scattering events, which we observed on a lattice, take on a central role in closely related models that may be solved via the Bethe ansatz (*35*), such as Heisenberg spin chains (*9*) and bosonic continuum systems (*37*): Within integrable models, scattering between arbitrary numbers of particles may be decomposed into two-particle scattering events, and the phase shift acquired in such processes determines the microscopic and thermodynamic properties of the system.

The precise control over the initial state in our system enables the study of strongly interacting bosons in scenarios not described by fermionization, such as the quantum walks of two atoms prepared in the same state. Figure 3 shows the correlations and densities for the initial state $(1/\sqrt{2})a_0^\dagger a_0^\dagger|0\rangle$. Because both atoms originate from the same site, HBT interference terms are not present. In the weakly interacting regime ($u = 0.7$), both particles undergo independent free dynamics and the correlator is the direct product of the single-particle densities. As the interaction increases, separation of the individual atoms onto different lattice sites becomes

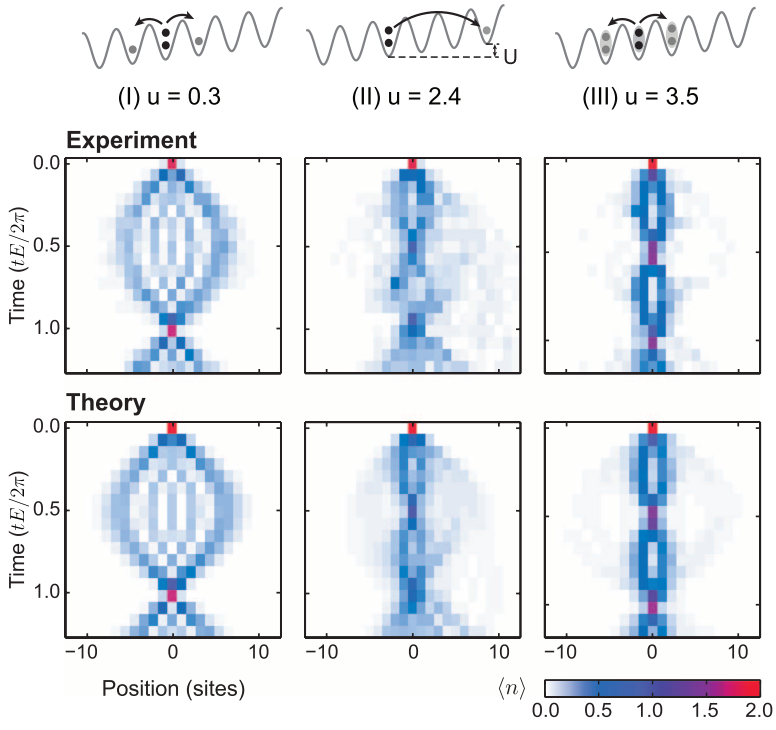

Fig. 4. Bloch oscillations of repulsively bound pairs. In the weakly interacting regime (I), two particles initialized on the same site undergo clean, independent Bloch oscillations. Increasing the interaction strength (II) leads to complex dynamics: Pairs of atoms remain bound near the origin or they separate, breaking left-right symmetry via long-range tunneling. For the largest interactions (III), repulsively bound pairs perform coherent, frequency-doubled Bloch oscillations. Densities are averages over ~220 independent quantum walks.

energetically forbidden. The two atoms preferentially propagate through the lattice together, as reflected in increasing weights on the diagonal of the correlation matrix. For the strongest interactions, the particles form a repulsively bound pair with effective single-particle behavior (*38*). The two-particle dynamics may be described as a quantum walk of the bound pair (*19*, *20*) at a decreased tunneling rate J_{pair}, which reduces to the second-order tunneling (*39*) $J_{pair} = (2J^2/U) << J$ for large values of u.

The formation of repulsively bound pairs and their coherent dynamics can be observed in two-particle Bloch oscillations. We focused on the dynamics of two particles initially prepared on the same site with a gradient $\Delta \approx 0.5$ (Fig. 4). In the weakly interacting regime ($u = 0.3$), both particles undergo symmetric Bloch oscillations as in the single-particle case, and we observed a high-quality revival after one Bloch period. For intermediate interactions ($u = 2.4$), the density evolution is very complex: In this regime where J, U, and E are similar in magnitude, states both with and without double occupancy are energetically allowed and contribute to the dynamics. The skew to the right against the applied force is caused by resonant long-range tunneling of single particles over several sites (*40*, *41*) and agrees with numerical simulation. When the interactions are sufficiently strong ($u = 3.5$), the pairs of atoms are tightly bound by the repulsive interaction and behave like a single composite particle. However, the effective gradient has doubled with respect to the single-particle case, and the pairs perform Bloch oscillations at twice the fundamental frequency and reduced spatial amplitude. The frequency doubling of Bloch oscillations was predicted for electron systems (*42*) and cold atoms (*20*, *40*) and has recently been simulated with photons in a waveguide array (*24*). Throughout the breathing motion, the repulsively bound pairs themselves undergo coherent dynamics and delocalize without unbinding. The clean revival after half a Bloch period directly demonstrates the entanglement of atom pairs during the oscillation.

Quantum walks of ultracold atoms in optical lattices offer an ideal starting point for the "bottom-up" study of many-body quantum dynamics. The present two-particle implementation provides intuitive access to essential features of many-body systems, such as localization caused by interactions or fermionization of bosons. Such microscopic features, when scaled to larger system sizes, manifest in emergent phenomena—for example, quantum phase transitions, quasi-particles, or superfluidity—as observed in other cold atom experiments. The particle-by-particle assembly of interacting systems may give access to the crossover from few- to many-body physics and may reveal the microscopic details of disordered quantum systems (*21*) and many-body quench dynamics (*43*).

REFERENCES AND NOTES

1. Y. Aharonov, L. Davidovich, N. Zagury, *Phys. Rev. A* **48**, 1687–1690 (1993).
2. E. Farhi, S. Gutmann, *Phys. Rev. A* **58**, 915–928 (1998).
3. S. E. Venegas-Andraca, *Quantum Inf. Process.* **11**, 1015–1106 (2012).
4. K. Manouchehri, J. Wang, *Physical Implementation of Quantum Walks* (Springer-Verlag, Berlin, 2014).
5. H. Schmitz *et al.*, *Phys. Rev. Lett.* **103**, 090504 (2009).
6. F. Zähringer *et al.*, *Phys. Rev. Lett.* **104**, 100503 (2010).
7. M. Karski *et al.*, *Science* **325**, 174–177 (2009).
8. C. Weitenberg *et al.*, *Nature* **471**, 319–324 (2011).
9. T. Fukuhara *et al.*, *Nature* **502**, 76–79 (2013).
10. Y. Bromberg, Y. Lahini, R. Morandotti, Y. Silberberg, *Phys. Rev. Lett.* **102**, 253904 (2009).
11. S. Aaronson, A. Arkhipov, *Proceedings of the 43rd Annual ACM Symposium on Theory of Computing* (ACM Press, New York, 2011), pp. 333–342.
12. A. Peruzzo *et al.*, *Science* **329**, 1500–1503 (2010).
13. L. Sansoni *et al.*, *Phys. Rev. Lett.* **108**, 010502 (2012).
14. M. A. Broome *et al.*, *Science* **339**, 794–798 (2013).
15. J. B. Spring *et al.*, *Science* **339**, 798–801 (2013).
16. M. Tillmann *et al.*, *Nat. Photonics* **7**, 540–544 (2013).
17. A. Crespi *et al.*, *Nat. Photonics* **7**, 545–549 (2013).
18. E. Knill, R. Laflamme, G. J. Milburn, *Nature* **409**, 46–52 (2001).
19. Y. Lahini *et al.*, *Phys. Rev. A* **86**, 011603 (2012).
20. A. Ahlbrecht *et al.*, *New J. Phys.* **14**, 073050 (2012).
21. D. L. Shepelyansky, *Phys. Rev. Lett.* **73**, 2607–2610 (1994).
22. A. M. Childs, D. Gosset, Z. Webb, *Science* **339**, 791–794 (2013).
23. A. Schreiber *et al.*, *Science* **336**, 55–58 (2012).
24. G. Corrielli, A. Crespi, G. Della Valle, S. Longhi, R. Osellame, *Nat. Commun.* **4**, 1555 (2013).
25. W. S. Bakr, J. I. Gillen, A. Peng, S. Fölling, M. Greiner, *Nature* **462**, 74–77 (2009).
26. See supplementary materials on *Science* Online.
27. T. Hartmann, F. Keck, H. J. Korsch, S. Mossmann, *New J. Phys.* **6**, 2 (2004).
28. M. Ben Dahan, E. Peik, J. Reichel, Y. Castin, C. Salomon, *Phys. Rev. Lett.* **76**, 4508–4511 (1996).
29. A. Alberti, V. V. Ivanov, G. M. Tino, G. Ferrari, *Nat. Phys.* **5**, 547–550 (2009).
30. E. Haller *et al.*, *Phys. Rev. Lett.* **104**, 200403 (2010).
31. M. Genske *et al.*, *Phys. Rev. Lett.* **110**, 190601 (2013).
32. T. Jeltes *et al.*, *Nature* **445**, 402–405 (2007).
33. A. M. Kaufman *et al.*, *Science* **345**, 306–309 (2014).
34. S. Fölling *et al.*, *Nature* **434**, 481–484 (2005).
35. M. A. Cazalilla, R. Citro, T. Giamarchi, E. Orignac, M. Rigol, *Rev. Mod. Phys.* **83**, 1405–1466 (2011).
36. B. Paredes *et al.*, *Nature* **429**, 277–281 (2004).
37. T. Kinoshita, T. Wenger, D. S. Weiss, *Science* **305**, 1125–1128 (2004).
38. K. Winkler *et al.*, *Nature* **441**, 853–856 (2006).
39. S. Fölling *et al.*, *Nature* **448**, 1029–1032 (2007).
40. R. Khomeriki, D. O. Krimer, M. Haque, S. Flach, *Phys. Rev. A* **81**, 065601 (2010).
41. F. Meinert *et al.*, *Science* **344**, 1259–1262 (2014).
42. W. S. Dias, E. M. Nascimento, M. L. Lyra, F. A. B. F. de Moura, *Phys. Rev. B* **76**, 155124 (2007).
43. J. P. Ronzheimer *et al.*, *Phys. Rev. Lett.* **110**, 205301 (2013).

ACKNOWLEDGMENTS

We thank S. Aaronson, M. Endres, and M. Knap for helpful discussions. Supported by grants from NSF through the Center for Ultracold Atoms, the Army Research Office with funding from the DARPA OLE program and a MURI program, an Air Force Office of Scientific Research MURI program, the Gordon and Betty Moore Foundation's EPiQS Initiative, the U.S. Department of Defense through the NDSEG program (M.E.T.), a NSF Graduate Research Fellowship (M.R.), and the Pappalardo Fellowship in Physics (Y.L.).

SUPPLEMENTARY MATERIALS

www.sciencemag.org/content/347/6227/1229/suppl/DC1
Materials and Methods
Table S1
References (*44*, *45*)

25 August 2014; accepted 4 February 2015
10.1126/science.1260364

SYMPATHETIC COOLING

Coulomb crystallization of highly charged ions

L. Schmöger,[1,2] O. O. Versolato,[1,2]* M. Schwarz,[1,2] M. Kohnen,[2] A. Windberger,[1] B. Piest,[1] S. Feuchtenbeiner,[1] J. Pedregosa-Gutierrez,[3] T. Leopold,[2] P. Micke,[1,2] A. K. Hansen,[4]† T. M. Baumann,[5] M. Drewsen,[4] J. Ullrich,[2] P. O. Schmidt,[2,6] J. R. Crespo López-Urrutia[1]‡

Control over the motional degrees of freedom of atoms, ions, and molecules in a field-free environment enables unrivalled measurement accuracies but has yet to be applied to highly charged ions (HCIs), which are of particular interest to future atomic clock designs and searches for physics beyond the Standard Model. Here, we report on the Coulomb crystallization of HCIs (specifically $^{40}Ar^{13+}$) produced in an electron beam ion trap and retrapped in a cryogenic linear radiofrequency trap by means of sympathetic motional cooling through Coulomb interaction with a directly laser-cooled ensemble of Be^+ ions. We also demonstrate cooling of a single Ar^{13+} ion by a single Be^+ ion—the prerequisite for quantum logic spectroscopy with a potential 10^{-19} accuracy level. Achieving a seven-orders-of-magnitude decrease in HCI temperature starting at megakelvin down to the millikelvin range removes the major obstacle for HCI investigation with high-precision laser spectroscopy.

Methods to simultaneously control both internal electronic and motional degrees of freedom of individual atoms, molecules, and low-charge-state ions in traps (*1*) have enabled unparalleled measurement accuracies. Prime examples include optical atomic clocks operating at an accuracy level of a few parts per 10^{-18} (*2*, *3*), which is sufficient to measure subtle effects of relativity (*4*), achieve sensitivity to geodesic gravitational potential differences of Earth, and set upper limits on possible temporal or spatial variations of fundamental constants (*5*, *6*). Most laser spectroscopy work on trapped samples has explored a small class of atoms and atomic ions—namely, the hydrogen atom, the alkali/alkaline-earth atoms/ions, and a

few other species. These species offer electronic transitions well suited to efficient laser cooling, which achieves the low kinetic energies and strong localization required for precision spectroscopy. A signature of this regime for trapped ions is the formation of Coulomb crystals, which are spatially ordered ensembles of mutually repelling ions, confined in a common external trapping potential. Such crystals form when the thermal kinetic energy becomes much smaller than the ion-ion electrostatic energy. For species lacking a direct transition for laser cooling, sympathetic cooling by use of co-trapped ions has been a successful strategy in the past for singly and doubly charged atoms and molecules (*7*, *8*).

Highly charged ions (HCIs) constitute another, much larger class of atomic systems that offer a wealth of physics opportunities (*9*) in precision metrology (*10*), astrophysics (*11*, *12*), and searches for new physics beyond the Standard Model of particle physics (*13*). HCIs provide many electric-dipole–forbidden—thus narrow—transitions, which offer excellent properties for future optical atomic clocks, such as strongly reduced systematic effects compared with those of neutral or singly charged atoms (*10*, *13*). Binding energies of valence electrons strongly increase with ion charge state, leading to electronic wave function penetration of the nucleus, which provides access to fundamental electron-nucleon interactions such as the weak interaction (*14*). Effects of quantum electrodynamics (QED) are strongly enhanced and readily measured in HCIs, offering an opportunity to test this most accurate theory in physics in the nonperturbative regime (*15*). Such studies usually have to deal with x-ray photon energies, which are beyond the reach of narrow-bandwidth lasers. However, subtle level-crossing effects (*16*) in which huge contributions to the binding energy nearly cancel result in an electronic structure that features transitions in the optical regime, readily accessible with narrow-linewidth lasers. High ionization potentials are accompanied by strong relativistic effects, rendering HCIs among the most sensitive candidates for studying a possible variation of the fine structure constant α at the 10^{-20}/year level (*16*, *17*).

In order to exploit these opportunities, efficient techniques enabling the motional control of HCIs are indispensable. Direct laser cooling of HCIs is precluded by their lack of appropriate allowed transitions in the optical regime. Unfortunately, all sources of HCIs—whether based on accelerators, high-power lasers, electron cyclotron resonance (ECR), or electron beam ion sources (EBIS) and traps (EBIT)—produce them at high temperatures, typically in the megakelvin regime, far from the millikelvin scale at which high-precision measurements are typically performed (*1*). Cooling to such low temperatures has been a long and elusive target of various studies that chiefly aimed to retrap HCIs magnetically after an initial hot production phase in another device. Although major progress was achieved in Penning traps during the 1990s (*18*), followed by recent efforts using the same technique (*19*, *20*), to date no millikelvin-range HCI temperatures below 1 K (18) have been demonstrated. Efforts to cool HCI

[1]Max-Planck-Institut für Kernphysik, Saupfercheckweg 1, 69117 Heidelberg, Germany. [2]Physikalisch-Technische Bundesanstalt, Bundesallee 100, 38116 Braunschweig, Germany. [3]Physique des Interactions Ioniques et Moléculaires, Aix-Marseille Université, 13397 Marseille, France. [4]Department of Physics and Astronomy, Aarhus University, 8000 Aarhus C, Denmark. [5]National Superconducting Cyclotron Laboratory (NSCL), Michigan State University, 640 S. Shaw Lane, East Lansing, MI 48824, USA. [6]Institut für Quantenoptik, Leibniz Universität Hannover, Welfengarten 1, 30167 Hannover, Germany.
*Present address: Advanced Research Center for Nanolithography, Science Park 104, 1098 XG Amsterdam, Netherlands. †Present address: Danmarks Tekniske Universitet (DTU) Fotonik, Frederiksborgvej 399, 4000 Roskilde, Denmark. **‡Corresponding author. E-mail: jose.crespo@mpi-hd.mpg.de**

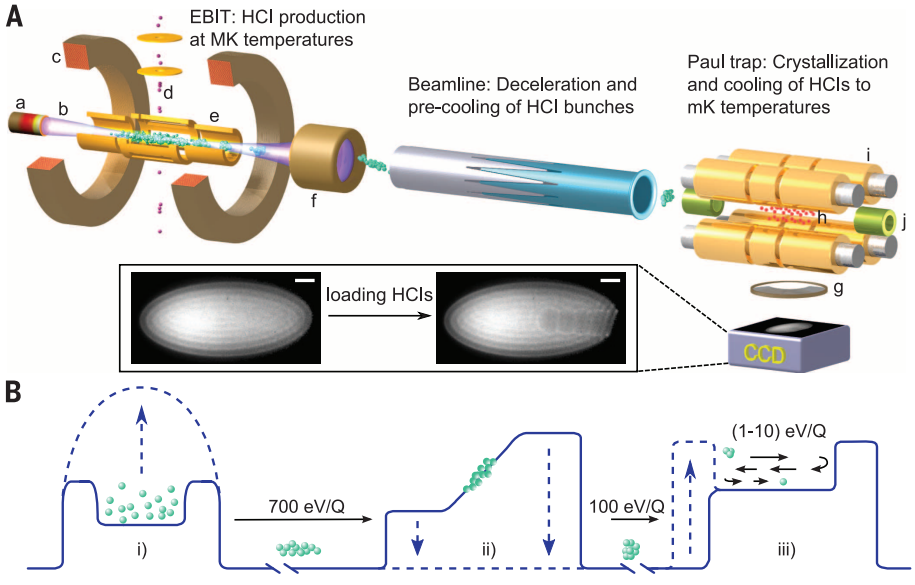

Fig. 1. Retrapping process and crystallization of HCIs. (**A**) Illustration of experimental setup consisting of an EBIT as HCI production site, a beamline for deceleration and reduction of energy spread of HCI bunches, a cryogenic Paul trap with external ion injection capabilities for HCI storage and sympathetic cooling to the millikelvin regime, and an imaging system for laser-induced fluorescence detection of the Be^+ coolant ions at 313 nm. (Inset) CCD image of the Be^+ Coulomb crystal before and after implantation of five Ar^{13+} ions. Be^+ trap frequencies are measured to be $\omega_x = 2\pi \times 115.0$ kHz in axial and $\omega_y = 2\pi \times 187.5$ kHz, $\omega_z = 2\pi \times 200.0$ kHz in radial directions, respectively. Scale bars, 100 μm. For better visibility of all image regions, we have applied a modulation of the contrast along the horizontal axis. The components are (a) electron gun, (b) electron beam, (c) superconducting Helmholtz coils, (d) atomic beam, (e) electrodes for axial trapping, (f) collector, (g) imaging lens, (h) Be^+ Coulomb crystal, (i) segmented electrodes of linear Paul trap, and (j) switchable electrostatic mirrors for HCI retrapping designed as hollow cylinders to allow cooling laser access along the Paul trap axis. (**B**) Schematic of time-varying electrode voltages used in our retrapping method, aligned with the corresponding elements of (A). Blue solid and dashed curves denote initial and final electrode potentials, respectively. Dashed arrows indicate rapid switching of voltages. Black arrows indicate ion motion, and their length encodes HCI axial velocity amplitude.

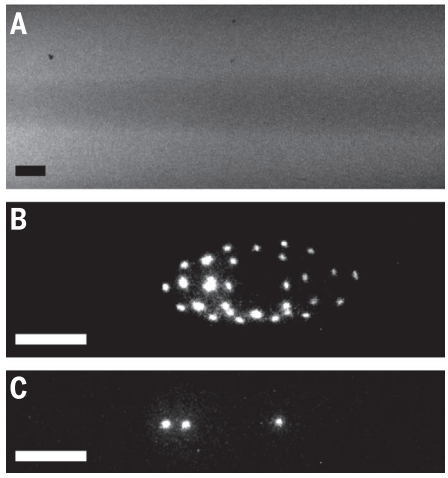

Fig. 2. Various cooling configurations. (**A**) Approximately 20 crystallized highly charged Ar ions are cooled by a Be^+ ion ensemble in a noncrystallized liquid phase after successive loading from the EBIT. The trap is operated at trap frequencies of $(\omega_x, \omega_y, \omega_z) = 2\pi \times (91.0, 193.0, 204.0)$ kHz for the Be^+ species. (**B**) One highly charged ion is cooled by 29 crystallized Be^+ ions. Axial and radial confinement is provided at Be^+ trap frequencies of $(\omega_x, \omega_y, \omega_z) = 2\pi \times (105.0, 166.0, 180.0)$ kHz. (**C**) One Ar^{13+} ion is cooled by three Be^+ ions in a linear string configuration at an axial Be^+ trap frequency of $\omega_x = 2\pi \times 112.0$ kHz. Scale bars, 100 μm. For better visibility of all image regions of (A) and (B), we suppress the stronger fluorescence on the left side (because of axial excess micromotion effects) with a modulation of the contrast along the horizontal axis.

in radiofrequency (RF) traps, the most suitable platform for precision laser spectroscopy experiments, have so far been lacking.

Here, we present a versatile approach to reduce the kinetic energy of HCIs by more than seven orders of magnitude through slowing and stopping highly charged $^{40}Ar^{13+}$ ions after extraction from an EBIT, facilitating unambiguous charge state determination. The HCIs are stopped through Coulomb interaction with a Be^+ ion Coulomb crystal in a cryogenic linear RF trap. At the end of the stopping process, the HCIs become part of mixed-species ordered crystalline structures at millikelvin temperatures (*21*, *22*). Ar^{13+} has been chosen as a test case because it has an experimentally investigated optical transition with large QED contributions to the transition energy (*23*) and the upper-state lifetime (*24*) and also offers the prospect of measuring relativistic many-body nuclear recoil effects (*25*). The method presented in this work, however, is likely to be general and readily applicable to almost all HCIs.

We used the recently commissioned cryogenic setup CryPTEx (*26*, *27*), consisting of a RF Paul trap and ion optics for external ion injection. The apparatus operates at a temperature of 7 K to provide the ultrahigh-vacuum environment required for long trap lifetimes of HCIs exceeding 15 min in our setup. Beyond electrodynamical trap losses, the HCI lifetime is limited by charge exchange collisions with residual gas, mainly H_2 at estimated densities below 6×10^4 cm^{-3} (H_2 partial pressure below 6×10^{-14} mbar in the 7 K environment). CryPTEx is operated in line with Hyper-EBIT, which delivers the HCIs through an electrodynamic deceleration setup with precooling properties (Fig 1A) (*28*).

HCIs—in this case, Ar^{13+}—are extracted in a pulsed mode from Hyper-EBIT by applying a fast high-voltage pulse at the central trap electrode (Fig. 1, A and B, i). The HCI bunches leave their production site with a kinetic energy in the kilo–electron volt range and with an energy spread of a few hundred electron volts because of the ion temperature within the EBIT. Slowing down of the fast HCI bunches is performed by means of the pulsed drift tube principle. Additional cooling is provided by biasing two interlaced serrated electrodes at different voltages, resulting in a linear deceleration potential that is quickly pulsed to ground when the HCI bunch is inside the interlaced region (Fig. 1B, ii). Precooling reduces the longitudinal kinetic energy spread, increasing the phase space density of the HCI bunch. This step improves matching the EBIT emittance to the Paul trap acceptance, thus increasing the stopping efficiency in the laser-cooled Be^+ ensemble. The slowed-down ion bunch leaks into the trap center by barely overcoming an adjustable electrostatic potential barrier (Fig. 1B, iii). A mirror electrode downstream stops and reverses the HCIs' motion, while another one upstream is quickly set to a voltage that closes the trap (Fig. 1B, iii). The captured HCIs execute an oscillatory motion between the two switchable mirror electrodes, providing axial confinement. Hence, they are forced to interact multiple times with the millimeter-sized laser-cooled Be^+ Coulomb crystal (ranging between 1500 Be^+ ions in the case of Fig. 1 to hundreds of Be^+ ions). Its stopping power performs the final deceleration steps until the HCIs become crystallized (Fig. 1A, inset). They are located near the trap axis as a result of their charge-to-mass ratio, which enforces an effective pseudopotential that is stronger than for the Be^+ ions.

Once the HCIs are crystallized, a large variety of cooling configurations is possible. These range from large numbers of crystallized HCIs—more suitable, for example, for laser-induced fluorescence spectroscopy (Fig. 2 A)—to small numbers of HCIs sympathetically cooled by medium-sized or small Be^+ Coulomb crystals, to ion string configurations (Figs. 2C, 3, and 4). Dark circular regions appear as general features in the charge-coupled device (CCD) images in Figs. 1 and 2B, suggesting a spherical shape near the trap axis with a diameter a few times larger than that of

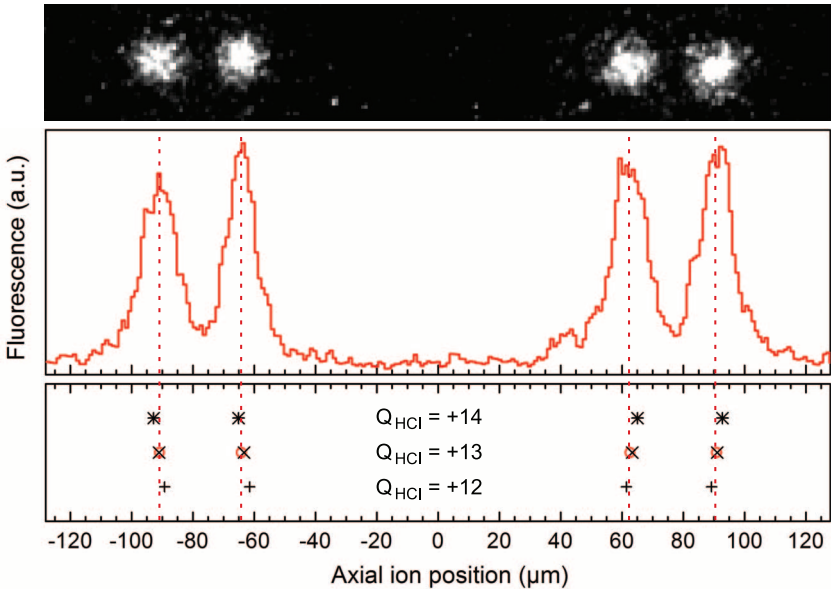

Fig. 3. Determination of HCI charge state in ion string configurations. (**Top**) CCD image of four Be^+ ions cooling one dark HCI in the middle at an axial Be^+ trap frequency of $\omega_x = 2\pi \times 112.3(3)$ kHz. (**Middle**) Region of interest projected onto Paul trap axis, which allows the determination of the large gap of 126.8(6) μm between the two Be^+ pairs. (**Bottom**) Comparison of experimental peak positions (red circles) and red dashed vertical lines (multiple Gaussian fit) with theoretically calculated (+, x, *) Be^+ ion positions for adjacent charge states of the HCI around $Q_{HCI} = +13\ e$. Small systematic deviations between measured and calculated positions of the two inner Be^+ ions originate from neglecting light-pressure effects that stem from the presence of only one cooling laser beam along the axis. Error bars are within symbols and thus not shown here.

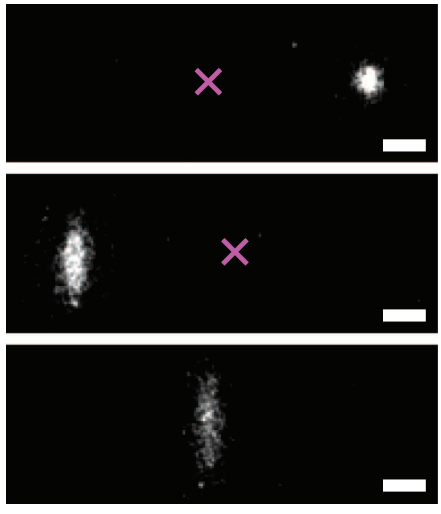

Fig. 4. One HCI sympathetically cooled by one laser-cooled Be^+ ion. (**Top**) CCD image series starting with one Be^+ ion on the right side cooling one nonfluorescing Ar^{13+} ion on the left side. (**Middle**) CCD image after a voltage-induced configuration change. (**Bottom**) One Be^+ ion remaining after the HCI was lost from the trap. The purple "x" marks the theoretically predicted position of dark Ar^{13+} ion for an axial single Be^+ ion trap frequency of: $\omega_x = 2\pi \times 112.0$ kHz. Scale bars, 20 μm. Differing secular temperatures (because of configuration-dependent heating and cooling rates) result in vertical smearing of the Be^+ fluorescence of different magnitudes for the three CCD images. The Be^+ ion position at bottom is not exactly in the middle between the two magenta crosses of the top and middle but is shifted slightly to the left. This effect is due to the asymmetric light pressure on the Be^+ ion, which stems from only one cooling laser beam along the axis being used (coming from the right). The light pressure displaces a single Be^+ ion more than a Be^+ ion co-trapped with a HCI on either side.

the typical ion-ion separation of the Be^+ cooling species.

Ellipsoidal crystals, with all their appeal for trapping large numbers of HCIs along the trap axis, are more difficult to analyze than are simpler ion strings. Therefore, we induced further crystal melting and evaporation steps by reducing the RF voltage and thus the radial Mathieu stability parameter q, sharply and simultaneously blocking the cooling laser. Implementing this method, we were able to set Be^+ ions loose while keeping the HCIs in a controlled manner. Subsequently, recrystallization of the remaining ions was performed by raising q to its initial value so as to reproducibly generate few-ion strings with a HCI candidate in their midst (Figs. 2C and 3). From the measured Be^+ trap frequencies (discerned by using parametric heating of the Be^+ ion motion) (*29*), we could numerically calculate the equilibrium ion positions for all possible charge states of the cocrystallized HCI in absolute numbers by considering the mutual Coulomb repulsion between all ions in the string in a one-dimensional axial harmonic potential (*30*, *31*). These ion positions are distinct regarding the number and ionic charge state of cotrapped dark ions and do not depend on their masses (*31*). The gap induced by the dark ion in the $2Be^+/1HCI/2Be^+$ configuration of Fig. 3 is consistent with a charge state of 12.96(28) positive charges (standard deviation in parentheses), which is in accord with that of Ar^{13+}. Further, we have observed that small electric pulses can induce reversible jumps of the Ar^{13+} ion position in a given string. This excludes the presence of more than one dark ion, as does the fact that all instances of few- and single-ion strings with an HCI end with just the Be^+ ions after a single loss event.

Furthermore, parametric heating of the ion reveals additional resonances that are consistent with radial excitation of the motion of a single highly charged Ar ion co-trapped with the Be^+ partners and axial common mode excitation of the whole mixed-species ion string. However, the resonances obtained this way are not sufficiently resolved to allow discrimination between neighboring argon charge states around +13 e. This is why the charge-state identification of the sympathetically cooled HCI is preferably done by comparing theoretically calculated ion positions with experimentally obtained CCD images, as presented in Fig. 3.

Analysis of the images of the trapped ions (Fig. 3) by means of spatial thermometry allowed us to determine the axial temperature of the Be^+ coolant ions by measuring their spatial width depending on their motional energy (*32*). Correcting for the limited resolution of the imaging system, whose root mean square point spread function is between 2 and 8 μm, we arrive at a conservative upper temperature limit for Be^+ of 17(2) mK. This in turn directly leads to a conservative upper limit for the axial temperature of the cotrapped Ar^{13+} ion of 221(26) mK. Our molecular dynamics simulations show that radial HCI temperatures above 300 mK would be noticeable owing to an associated decrease in separation of the two closest Be^+ ions. Thus, the above given temperature is also an upper limit for the radial temperature of the sympathetically cooled Ar^{13+} ion. This is consistent with the value obtained for the larger mixed-species crystals of Fig. 1A (~1500 Be^+ ions) by a different method. It relies on a lower bound for the so-called plasma coupling parameter as a measure for the onset of crystallization (*22*, *33*, *34*). The plasma coupling parameter Γ is given by the ratio of the Coulomb energy of neighboring ions to the thermal ion energy (Eq. 1)

$$\Gamma = \frac{Q^2 e^2}{4\pi\varepsilon_0 a_{WS} k_B T} \quad (1)$$

where Q is the ion charge state, k_B is the Boltzmann constant, T is the temperature of the plasma, and a_{WS} is the Wigner-Seitz radius, which is for a certain ion species fully determined by the knowledge of the corresponding trap frequencies. Γ is directly related to the thermodynamic state of the confined finite one-component plasma. Here, molecular dynamics simulations of harmonically confined ion plasmas have shown that the continuous transition from the liquid-like state (Γ = 2) to the fully crystallized state (Γ > 300) starts with the formation of ellipsoidal shell structures at Γ = 20 (*33*). This gives an upper limit of 35 mK for the temperature of the Be^+ plasma in Fig. 1, at which the shell structure is already quite pronounced. At the same time, the co-trapped Ar^{13+} ions are clearly fully crystallized, giving a value greater than 300 for the plasma coupling parameter (*35*). Thus, even assuming nonthermalization of the HCI with the Be+ ion ensemble (at 35 mK), the temperature of the Ar^{13+} ions would be below 235 mK (Eq. 1).

Toward our exploration of the application of precision spectroscopy schemes to HCI, we expelled more Be^+ ions until a single coolant ion was left in the trap, with its location clearly displaced from the potential minimum by a repelling dark ion that again possessed a charge state of Q_{HCI} = +13 e (Fig. 4). This is the prerequisite needed for application of quantum logic spectroscopy (*36*). Within this framework, a single Be^+ ion can serve as the logic ion for sympathetic cooling, state preparation, and internal state detection of a HCI, enabling ultraprecise laser spectroscopy of HCIs. Our demonstration of such a two-ion crystal paves the way for exciting spectroscopic applications of HCIs, ranging from competitive optical clocks working at a projected 10^{-19} fractional accuracy level (*10*, *13*) to tests of fundamental physics and varying constants, to development of qubit systems for ion trap–based quantum computing. Last, in this configuration, highest-resolution vacuum ultraviolet and x-ray spectroscopy of HCIs should become feasible at latest-generation light sources.

REFERENCES AND NOTES

1. D. J. Wineland, *Rev. Mod. Phys.* **85**, 1103–1114 (2013).
2. C. W. Chou, D. B. Hume, J. C. J. Koelemeij, D. J. Wineland, T. Rosenband, *Phys. Rev. Lett.* **104**, 070802 (2010).
3. B. J. Bloom *et al.*, *Nature* **506**, 71–75 (2014).
4. C. W. Chou, D. B. Hume, T. Rosenband, D. J. Wineland, *Science* **329**, 1630–1633 (2010).
5. T. Rosenband *et al.*, *Science* **319**, 1808–1812 (2008).
6. N. Huntemann *et al.*, arXiv:1407.4408 [physics.atom-ph] (2014).
7. D. J. Larson, J. C. Bergquist, J. J. Bollinger, W. M. Itano, D. J. Wineland, *Phys. Rev. Lett.* **57**, 70–73 (1986).
8. M. Drewsen *et al.*, *Int. J. Mass Spectrom.* **229**, 83–91 (2003).
9. J. R. Crespo López-Urrutia, Z. Harman, in *Fundamental Physics in Particle Traps*, W. Quint, M. Vogel, Eds. (Springer, Heidelberg, Germany, 2014), pp. 315–373.
10. A. Derevianko, V. A. Dzuba, V. V. Flambaum, *Phys. Rev. Lett.* **109**, 180801 (2012).
11. S. Bernitt *et al.*, *Nature* **492**, 225–228 (2012).
12. K. Schnorr *et al.*, *Astrophys. J.* **776**, 121 (2013).
13. M. S. Safronova *et al.*, *Phys. Rev. Lett.* **113**, 030801 (2014).
14. M. Zolotorev, D. Budker, *Phys. Rev. Lett.* **78**, 4717–4720 (1997).
15. S. Sturm *et al.*, *Phys. Rev. Lett.* **107**, 023002 (2011).
16. J. C. Berengut, V. A. Dzuba, V. V. Flambaum, *Phys. Rev. Lett.* **105**, 120801 (2010).
17. J. C. Berengut, V. A. Dzuba, V. V. Flambaum, A. Ong, *Phys. Rev. Lett.* **106**, 210802 (2011).
18. L. Gruber *et al.*, *Phys. Rev. Lett.* **86**, 636–639 (2001).
19. Z. Andelkovic *et al.*, *Phys. Rev. A* **87**, 033423 (2013).
20. S. Brewer, N. Guise, J. Tan, *Phys. Rev. A* **88**, 063403 (2013).
21. P. Blythe, B. Roth, U. Fröhlich, H. Wenz, S. Schiller, *Phys. Rev. Lett.* **95**, 183002 (2005).
22. L. Hornekaer, N. Kjaergaard, A. M. Thommesen, M. Drewsen, *Phys. Rev. Lett.* **86**, 1994–1997 (2001).
23. V. Mäckel, R. Klawitter, G. Brenner, J. R. Crespo López-Urrutia, J. Ullrich, *Phys. Rev. Lett.* **107**, 143002 (2011).
24. A. Lapierre *et al.*, *Phys. Rev. Lett.* **95**, 183001 (2005).
25. R. S. Orts *et al.*, *Phys. Rev. Lett.* **97**, 103002 (2006).
26. M. Schwarz *et al.*, *Rev. Sci. Instrum.* **83**, 083115 (2012).
27. A. K. Hansen *et al.*, *Nature* **508**, 76–79 (2014).
28. L. Schmöger, thesis, Heidelberg University (2013).
29. M. Drewsen, A. Mortensen, R. Martinussen, P. Staanum, J. L. Sørensen, *Phys. Rev. Lett.* **93**, 243201 (2004).
30. H. C. Nägerl, W. Bechter, J. Eschner, F. Schmidt-Kaler, R. Blatt, *Appl. Phys. B* **66**, 603–608 (1998).
31. T. P. Meyrath, D. F. V. James, *Phys. Lett. A* **240**, 37–42 (1998).
32. S. Knünz *et al.*, *Phys. Rev. A* **85**, 023427 (2012).
33. D. H. Dubin, T. M. O'Neil, *Phys. Rev. Lett.* **60**, 511–514 (1988).
34. H. Thomas *et al.*, *Phys. Rev. Lett.* **73**, 652–655 (1994).
35. L. Hornekær, M. Drewsen, *Phys. Rev. A* **66**, 013412 (2002).
36. P. O. Schmidt *et al.*, *Science* **309**, 749–752 (2005).

ACKNOWLEDGMENTS

The project was supported by the Max-Planck Society and the Physikalisch-Technische Bundesanstalt. P.O.S. acknowledges the support of Deutsche Forschungsgemeinschaft through the Cluster of Excellence Quantum Engineering and Space-Time Research (QUEST). M.D. appreciates generous support through the Danish National Research Foundation Center for Quantum Optics (QUANTOP); The Danish Agency for Science, Technology and Innovation; the Carlsberg Foundation; the Lundbeck Foundation; and the European Commission under the Seventh Framework Programme FP7 GA 607491 COMIQ. J.P.-G., O.O.V., and M.S. acknowledge funding from Short-Term Scientific Missions travel grants from COST-Action IOTA. Last, the Max-Planck-Institut für Kernphysik mechanical workshops have been of crucial importance for the construction of the cryogenic traps.

SUPPLEMENTARY MATERIALS

www.sciencemag.org/content/347/6227/1233/suppl/DC1
Materials and Methods
Figs. S1 to S3
Reference (*37*)

13 November 2014; accepted 2 February 2015
10.1126/science.aaa2960

OCEANOGRAPHY

Glacial cycles drive variations in the production of oceanic crust

John W. Crowley,[1,2]* Richard F. Katz,[1]† Peter Huybers,[2]
Charles H. Langmuir,[2] Sung-Hyun Park[3]†

Glacial cycles redistribute water between oceans and continents, causing pressure changes in the upper mantle, with consequences for the melting of Earth's interior. Using Plio-Pleistocene sea-level variations as a forcing function, theoretical models of mid-ocean ridge dynamics that include melt transport predict temporal variations in crustal thickness of hundreds of meters. New bathymetry from the Australian-Antarctic ridge shows statistically significant spectral energy near the Milankovitch periods of 23, 41, and 100 thousand years, which is consistent with model predictions. These results suggest that abyssal hills, one of the most common bathymetric features on Earth, record the magmatic response to changes in sea level. The models and data support a link between glacial cycles at the surface and mantle melting at depth, recorded in the bathymetric fabric of the sea floor.

The bathymetry of the sea floor has strikingly regular variations around intermediate and fast-spreading ocean ridges. Parallel to the ridge are long, linear features with quasi-regular spacing called abyssal hills (*1*). High-resolution mapping of the sea floor over the past few decades (*2*–*4*) has shown that these hills are among the most common topographic features of the planet, populating the sea floor over ~50,000 km of ridge length. Hypothesized models for these features include extensional faulting parallel to the ridge (*3*), variations in the magmatic budget of ridge volcanoes (*5*), and variation in mantle melting under ridges owing to sea-level change associated with glacial cycles (*6*). This latter model stems from the fact that glacial-interglacial variations transfer ~5 × 10^{19} kg of water between the oceans and the continents. This mass redistribution translates to sea-level variations of ~100 m and modifies the lithostatic pressure beneath the entire ocean. Because mantle melting beneath ridges is driven by depressurization, ocean ridge volcanism should respond to sea-level changes, potentially leading to changes in the thickness and elevation of ocean crust.

Plate spreading at mid-ocean ridges draws mantle flow upward beneath the ridge; rising parcels of mantle experience decreasing pressure and hence decreasing melting point, causing partial melting. Mantle upwelling rates are ~3 cm/year on average, whereas sea-level change during the last deglaciation was at a mean rate of 1 cm/year over 10 thousand years (ky). Because water has one third the density of rock, sea-level changes would modify the depressurization rate associated with upwelling by ±10%, with corresponding effects on the rate of melt production. Mantle upwelling rate scales with the mid-ocean ridge spreading rate, but the rate of sea-level change over the global mid-ocean ridge system is roughly uniform. On this basis, previous workers inferred that the relative effect of sea-level change should scale inversely with spreading rate, reaching a maximum at the slowest rates (*6*). An elaboration of this model with parameterized melt transport gave a similar scaling (*7*).

To test these qualitative inferences, we investigated the crustal response to sea-level change using a model that computes mantle flow, thermal structure, melting, and pathways of melt transport. The model is based on canonical statements of conservation of mass, momentum, and energy for partially molten mantle (*8*, *9*) and has previously been used to simulate mid-ocean ridge dynamics with homogeneous (*10*) and heterogeneous (*11*) mantle composition. It predicts time scales of melt transport that are consistent with those estimated from ^{230}Th disequilibrium in young lavas (*12*). In the present work, the model is used to predict crustal thickness time series arising from changes in sea level (Fig. 1) (*13*).

A suite of nine model runs for three permeability scales and three spreading rates was driven over a 5-million-year period by using a Plio-Pleistocene sea-level reconstruction (*14*). Crustal curves from simulations with larger permeability and faster spreading rate contain relatively more high-frequency content than those of lower permeability and slower-spreading-rate runs (Fig. 1). Our model results contradict the previous scaling arguments (*6*, *7*) in not showing a simple decrease in the sea-level effect on ridge magmatism with increasing spreading rate.

To better understand these numerical results, we carried out an analysis of leading-order processes using a reduced complexity model. This model provides a solution for crustal thickness response to changes in sea level, approximating the results of the full numerical model, but with greater transparency. Assuming that all melt produced by sea-level change is focused to the

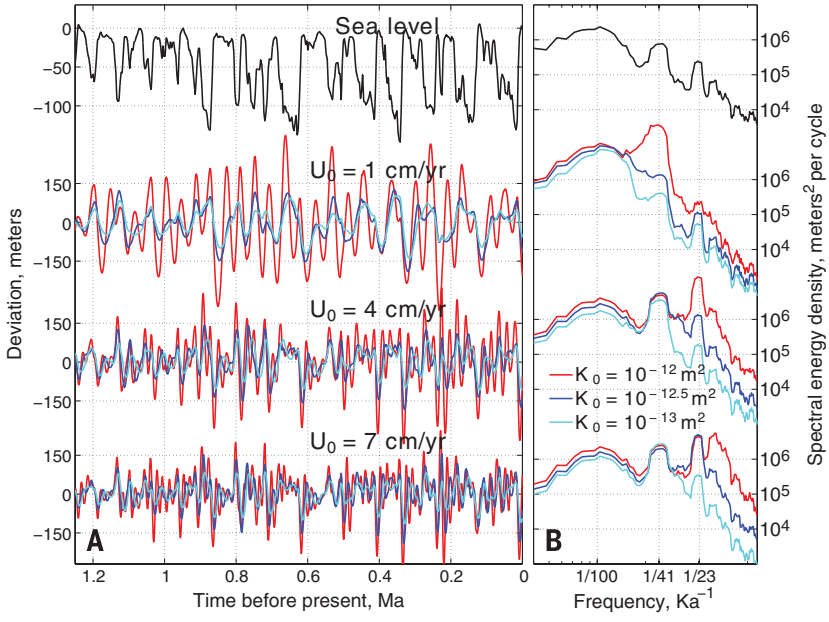

Fig. 1. Simulated bathymetric relief driven by Plio-Pleistocene sea-level variation. (**A**) Imposed sea-level variation [black, from (*14*)] and predicted bathymetric relief (color) for the past 1.25 million years from simulations at three half-spreading rates U_0 and three permeability levels K_0. Isostatic compensation is assumed to scale the amplitude of crustal thickness variation by 6/23 to give bathymetric relief. Permeability in the simulations is computed by applying $K(x,z) = K_0(\phi/\phi_0)^3$ m^2 to the porosity field $\phi(x,z)$, where $\phi_0 = 0.01$ is a reference porosity. Light blue, dark blue, and red lines correspond to $\log_{10}K_0 = -(13, 12.5, 12)$, respectively. (**B**) Power spectral density estimates for each time series, made by using the multitaper method with seven tapers. Axes are logarithmic.

[1]Department of Earth Sciences, University of Oxford, Oxford, UK. [2]Department of Earth and Planetary Sciences, Harvard University, Cambridge, USA. [3]Division of Polar Earth-System Sciences, Korea Polar Research Institute, Incheon, Korea. *Present address: Engineering Seismology Group Canada, Kingston, Canada. †Corresponding author. E-mail: richard.katz@earth.ox.ac.uk (R.F.K.); shpark314@kopri.re.kr (S.-H. P.)

ridge axis, we obtain a magmatic flux in units of kilograms per year per meter along the ridge of

$$M_{SL}(t) = \int_{z_m}^{0} x_l(z) \frac{\rho_w}{\rho_m} \Pi \dot{S}[t - \tau(z)] dz \quad (1)$$

where ρ_w/ρ_m is the density ratio of sea water to mantle rock, Π is the adiabatic productivity of upwelling mantle (in kilograms of melt per cubic meter of mantle per meter of upwelling), $x_l(z)$ is the half-width of the partially molten region beneath the mid-ocean ridge at a depth z, z_m is the maximum depth of silicate melting beneath the ridge, and $\dot{S}[t - \tau(z)]$ is the rate of sea-level change τ years before time t (*13*).

This formulation reveals why our numerical model results (Fig. 1) contradict earlier work (*6*, *7*). Whereas earlier work noted that variations in crustal thickness are inversely proportional to spreading rate, $C_{SL} = M_{SL}/(U_0\rho_c)$, our model shows that mass flux is proportional to the width of the partially molten region beneath the ridge. This width can be expressed as $x_l(z) = U_0 R(z)/(4\kappa)$, where U_0 is the half-spreading rate, κ is the thermal diffusivity, and $R(z)$ accounts for depth-dependent influences on melting that are independent of spreading rate (fig. S1). The competing influences associated with the volume of mantle from which melt is extracted and the rate at which new crust is formed means that sensitivity to sea-level variation does not simply decrease with increasing spreading rate.

Instead, the magnitude of the crustal response depends on the time scale of sea-level forcing relative to the time required to deliver melt from depth to the surface. Melt delivery times τ are computed in the reduced model by using a one-dimensional melt column formulation and decrease with higher pemeability and faster spreading rate (*13*, *15*). The same response occurs in the numerical model; in both cases, τ decreases with increasing spreading rate because the background melting rate, dynamic melt fraction, and permeability of the melting region all increase.

To quantify crustal response as a function of time scale, we use the amplitude ratio of crustal to sea-level variation, called admittance, computed at discrete frequencies by applying sinusoidal forcing. Admittance curves for both the numerical (Fig. 2A) and reduced (Fig. 2B) models show a distinct maximum that shifts toward higher frequencies and larger magnitudes with shorter τ. When the period of sea-level forcing is short relative to the characteristic transport time $\tau_m = \tau(z_m)$, additional melt produced at depth (falling sea-level phase) does not have time to reach the surface before a negative perturbation to melt production occurs (rising sea-level phase); positive and negative perturbations cancel, and crustal variation is small. When forcing periods are long relative to τ_m, melt perturbations reach the surface but are again small because melt production scales with the rate-of-change of sea level. Forcing periods near τ_m give maximum admittance because of a combination of large perturbation of melting rates and sufficient time to reach the surface (Fig. 2C). These results suggest that ridges are tuned according to melt-transport rates to respond most strongly to certain frequencies of sea-level variability.

The correspondence of the results from the numerical and reduced models provides a sound basis for investigating the potential effects of sea-level change on sea-floor bathymetry. Variations in melt production lead to variations in crustal thickness, and through isostatic compensation, such thickness variations should produce changes in bathymetry identifiable in high-resolution surveys. The prominent spectral peaks of late Pleistocene sea-level variation at the approximately 1/100 ky^{-1} ice age, 1/41 ky^{-1} obliquity, and 1/23 ky^{-1} precession frequencies (*16*) therefore translate into a prediction for a bathymetric response that depends on permeability and spreading rate.

Our model results suggest that the best chance to detect a sea-level response between 1/100 ky^{-1} to 1/20 ky^{-1} frequencies is at intermediate spreading ridges. Slow spreading ridges show little precession response, an obliquity response that is sensitive to uncertainties in permeability, and the effects of intense normal faulting. Such faulting causes rift valleys with larger relief than expected from sea level–induced melting variations. The sea-level signal should be less polluted by tectonic effects at fast spreading ridges but may have peak admittances at frequencies higher than 1/20 ky^{-1} that would obscure the responses at predicted frequencies. For example, the numerical simulation with the fastest spreading and highest pemeability has peak spectral energy at frequencies above precession (Fig. 1B).

At intermediate half-spreading rates of 3 cm/year, 40-ky periods lead to predicted bathymetric variations with a wavelength of 1200 m on each side of the ridge. Such fine-scale variations can be obscured in global topographic databases that grid data from multiple cruises and may have offsets in navigation or depth. To investigate the model predictions, a modern data set with uniform navigation and data reduction from a single survey is preferred. Such data are available for two areas of the Australian-Antarctica ridge that were surveyed by the icebreaker Araon of the Korean Polar Research Institute in 2011 and 2013 (Fig. 3).

Analysis was undertaken by identifying a region whose abyssal hill variability is relatively undisturbed by localized anomalies, averaging off-axis variability into a single bathymetric line and converting off-axis distance into an estimate of elapsed time by using a plate motion solution (*17*). Spectral analysis of the associated bathymetry time series is performed by using the multitaper procedure (*18*) and shows spectral peaks that are significant at an ~95% confidence level

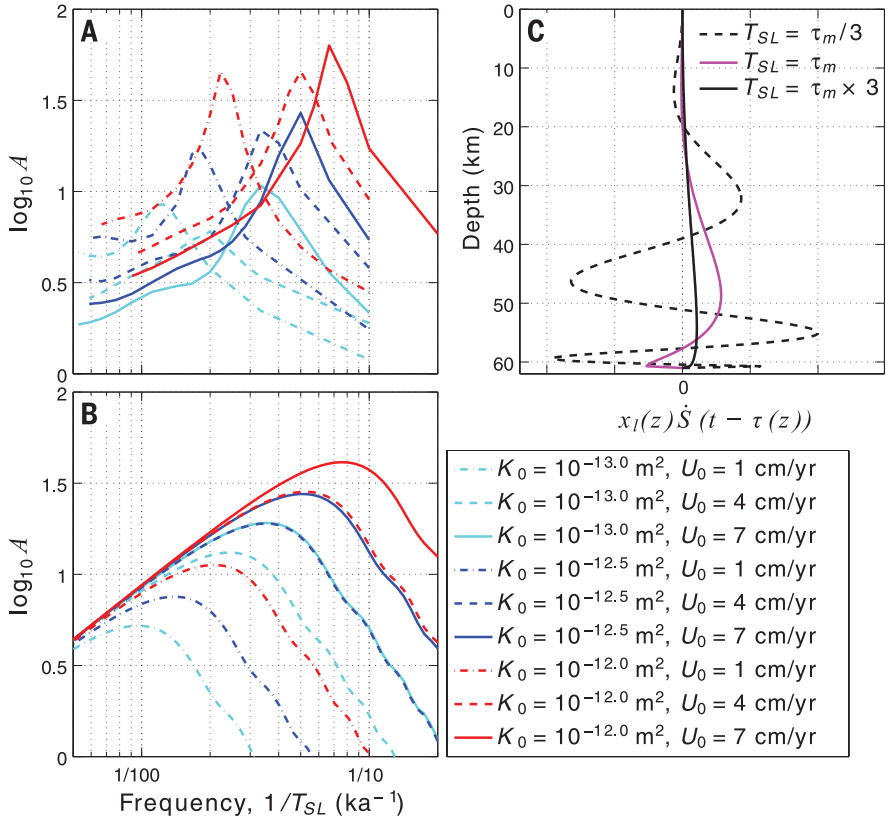

Fig. 2. Crustal thickness admittance, computed for a sinusoidal variation in sea level with period T_{SL}. (**A** and **B**) Admittance curves derived from (A) numerical simulations and (B) the reduced model (*13*). (**C**) A plot of depth z versus the integrand from the reduced model of magma production owing to sea-level variation, $M_{SL}(t) \propto \int_{Zm}^{0} x_l(z)\dot{S}[t - \tau(z)]dz$ (Eq. 1 and text following). The model is evaluated for U_0 = 4 cm/year, $K_0 = 10^{-13}$ m^2, and three values of sea-level oscillation period T_{SL}.

near the predicted ice age, obliquity, and precession frequencies (Fig. 3). Although absolute ages are uncertain because we lack sea-floor magnetic reversal data, spectral analysis only requires constraining the relative passage of time. The 2σ uncertainties associated with relative Australian-Antarctic plate motion are ±4% (*17*), implying, for example, that the 1/41 ky^{-1} obliquity signal resides in a band from 1/39 ky^{-1} to 1/43 ky^{-1}, a width that is smaller than our spectral resolution.

Another check on model-data consistency is to compare magnitudes of variability. Surface bathymetry will be roughly 6/23rds of the total variation in crustal thickness because of the relative density differences of crust-water and crust-mantle, assuming conditions of crustal isostasy. The closest match between simulation results and observations, in terms of the distribution of spectral energy, is achieved by specifying a permeability at 1% porosity of $K_0 = 10^{-13}$ m^2 (Fig. 3). The standard deviation of the simulated bathymetry is 36 m, after multiplying crustal thickness by 6/23 and filtering (*13*). To minimize the contribution from non-sea-level–induced variations in the observed bathymetry, it is useful to filter frequencies outside of those between 1/150 ky^{-1} and 1/10 ky^{-1}. The standard deviation of the filtered observations is 44 m, where the slightly larger value is consistent with changes in sea level being an important but not exclusive driver of changes in crustal thickness.

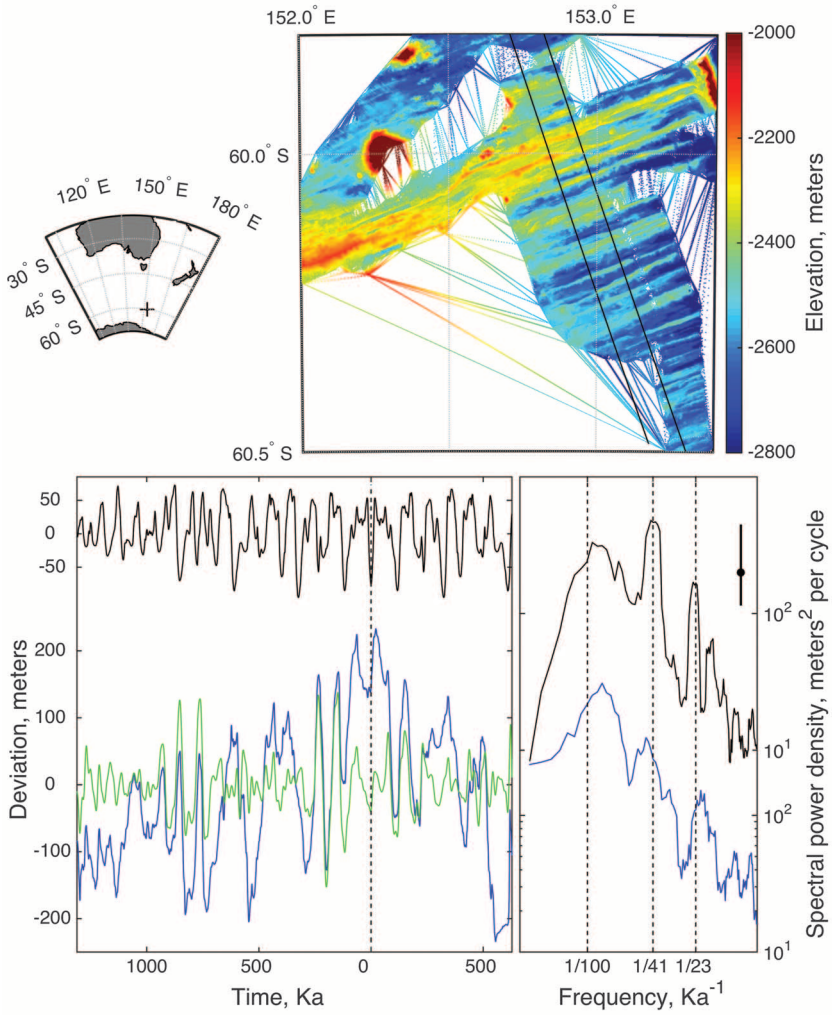

Fig. 3. Bathymetry at a section of the Australian-Antarctic Ridge. A region of consistent bathymetry is indicated between the black lines (**top right**) and is shown in profile (**bottom left**, blue) after converting off-axis distance to an estimate of time. Time is zero at the approximate ridge center. Also shown is bathymetry after filtering frequencies outside of 1/150 ky and 1/10 ky (green), and simulated bathymetry (black, for U_0 = 3.3 cm/year and $K_0 = 10^{-13}$ m^2). Spectral estimates (**bottom right**) are shown for the unfiltered bathymetry (blue) and model results (black), where the latter are offset upward by an order of magnitude for visual clarity. Data availability is uneven across the ridge, and spectral estimates are for the longer, southern flank. Unlike in Fig. 1B, spectral estimates are prewhitened in order to improve the detectability of spectral peaks (supplementary materials). Vertical dashed lines indicate frequencies associated with 100-ky late-Pleistocene ice ages, obliquity, and precession. Axes are logarithmic. Statistical significance is indicated by the black bar at the top right; spectral peaks rising further than the distance between the mean background continuum (corresponding to the black dot) and 95th percentile (top of black bar) are significant.

Analysis of bathymetry in another area of the Australian-Antarctic ridge 400 km to the southeast (fig. S2) shows a significant spectral peak at the obliquity frequency and indication of a peak near 1/100 ky^{-1}, but no peak near the precession frequencies. Predicted and observed bathymetry is also similar, with standard deviations of 33 and 34 m, respectively, after accounting for fractional surface expression and filtering. Absence of a precession peak may result from spectral estimates being more sensitive to elapsed time errors at higher frequencies (*19*), where such errors may be introduced through extensional faulting or asymmetric spreading. Detection could also be obscured by the previously noted influence of faulting (*3*, *20*) as well as off-axis volcanism or sediment infilling of abyssal troughs. Detection of significant spectral peaks at predicted frequencies at two locations of the Australian-Antarctic ridge nonetheless constitutes strong evidence for modulation of crustal production by variations in sea level.

Our numerical and analytical results show a complex relationship between spreading rate and amplitudes of crustal thickness variations associated with changes in sea level. Perturbations to the background melt production and delivery depend on the frequency content of the sea-level signal, as a result of the dynamics of magma transport. Reference mantle permeability and ridge-spreading rate are key controls on this frequency dependence. This result could be useful: The spreading rate can be accurately determined for a ridge, but parameters associated with magma dynamics are far less certain, such as the amplitude and scaling of permeability. Uncertainty associated with spectral estimates of bathymetry and sea-level estimates need to be better characterized, but together, these may provide a constraint on the admittance and hence dynamical parameters of a ridge.

Although results from the high-resolution bathymetry are promising, much remains to be done to further test the hypothesis advanced here. Crustal thickness is not an instantaneous response to melt delivery from the mantle but also reflects crustal processes that may introduce temporal and spatial averaging. Where long-lived magma chambers are present, for example, there may also be a crustal time-averaging that depends on spreading rate. In addition, faulting at all spreading rates is an observed and important phenomenon, and sea-floor bathymetry reflects the combined effects of magma output and crustal faulting (*3*, *20*). Deconvolving the relative roles of such processes will be important. High-resolution surveys in targeted regions will provide the opportunity for a more complete and rigorous analysis than is presently possible.

REFERENCES AND NOTES

1. H. Menard, J. Mammerickz, *Earth Planet. Sci. Lett.* **2**, 465–472 (1967).
2. D. Scheirer *et al.*, *Mar. Geophys. Res.* **18**, 1–12 (1996).

3. K. Macdonald, P. Fox, R. Alexander, R. Pockalny, P. Gente, *Nature* **380**, 125–129 (1996).
4. J. Goff, Y. Ma, A. Shah, J. Cochran, J. Sempere, *J. Geophys. Res.* **102** (B7), 15521 (1997).
5. E. Kappel, W. Ryan, *J. Geophys. Res.* **91** (B14), 13925 (1986).
6. P. Huybers, C. Langmuir, *Earth Planet. Sci. Lett.* **286**, 479–491 (2009).
7. D. C. Lund, P. D. Asimow, *Geochem. Geophys. Geosyst.* **12**, 12009 (2011).
8. D. McKenzie, *J. Petrol.* **25**, 713–765 (1984).
9. R. Katz, *J. Petrol.* **49**, 2099 (2008).
10. R. Katz, *Geochem. Geophys. Geosys.* **10**, Q0AC07 (2010).
11. R. Katz, S. Weatherley, *Earth Planet. Sci. Lett.* **335-336**, 226–237 (2012).
12. A. Stracke, B. Bourdon, D. McKenzie, *Earth Planet. Sci. Lett.* **244**, 97–112 (2006).
13. Materials and methods are available as supplementary materials on *Science* Online.
14. M. Siddall, B. Hönisch, C. Waelbroeck, P. Huybers, *Quat. Sci. Rev.* **29**, 170–181 (2010).
15. I. Hewitt, *Earth Planet. Sci. Lett.* **300**, 264–274 (2010).
16. J. D. Hays, J. Imbrie, N. J. Shackleton, *Science* **194**, 1121–1132 (1976).
17. C. DeMets, R. G. Gordon, D. F. Argus, *Geophys. J. Int.* **181**, 1–80 (2010).
18. D. Percival, A. Walden, *Spectral Analysis for Physical Applications: Multitaper and Conventional Univariate Techniques* (Cambridge Univ. Press, Cambridge, UK, 1993).
19. P. Huybers, C. Wunsch, *Paleoceanography* **19**, PA1028 (2004).
20. W. R. Buck, L. L. Lavier, A. N. Poliakov, *Nature* **434**, 719–723 (2005).

ACKNOWLEDGMENTS

The research leading to these results has received funding from the European Research Council (ERC) under the European Union's Seventh Framework Programme (FP7/2007–2013)/ERC grant agreement 279925 and from the U.S. National Science Foundation under grant 1338832. It is a part of project PP13040 and PE14050 funded by the Korea Polar Research Institute. J.W.C. thanks J. Mitrovica, and R.F.K. thanks the Leverhulme Trust for additional support. Numerical models were run at Oxford's Advanced Research Computing facility. Bathymetry data are included in the supplementary materials.

SUPPLEMENTARY MATERIALS

www.sciencemag.org/content/347/6227/1237/suppl/DC1
Figs. S1 to S3
Table S1
References (*21*–*29*)
Data Files KR1 and KR2

22 September 2014; accepted 28 January 2015
10.1126/science.1261508

EPIDEMIOLOGY

Reduced vaccination and the risk of measles and other childhood infections post-Ebola

Saki Takahashi,[1] C. Jessica E. Metcalf,[1,2] Matthew J. Ferrari,[3] William J. Moss,[4] Shaun A. Truelove,[4] Andrew J. Tatem,[5,6,7] Bryan T. Grenfell,[1,6] Justin Lessler[4]*

The Ebola epidemic in West Africa has caused substantial morbidity and mortality. The outbreak has also disrupted health care services, including childhood vaccinations, creating a second public health crisis. We project that after 6 to 18 months of disruptions, a large connected cluster of children unvaccinated for measles will accumulate across Guinea, Liberia, and Sierra Leone. This pool of susceptibility increases the expected size of a regional measles outbreak from 127,000 to 227,000 cases after 18 months, resulting in 2000 to 16,000 additional deaths (comparable to the numbers of Ebola deaths reported thus far). There is a clear path to avoiding outbreaks of childhood vaccine-preventable diseases once the threat of Ebola begins to recede: an aggressive regional vaccination campaign aimed at age groups left unprotected because of health care disruptions.

The current Ebola crisis in West Africa is one of the worst public health disasters in recent memory, having caused more than 21,000 cases and 8400 deaths as of January 2015 and raising the specter of a broader international crisis (*1*). However, there are signs of hope. Evidence shows that the number of cases is declining in Liberia (*2*), and sustained transmission has been confined to Guinea, Liberia, and Sierra Leone, despite several transnational introductions including recent transmission in Mali. Stopping Ebola would be a triumph for the global health community and the public health agencies of the affected countries. But even after the last Ebola case recovers, the disruptions of local health systems caused by the outbreak could lead to a second infectious disease crisis that could kill as many as, if not more than, the original outbreak.

Through the combination of the World Health Organization (WHO) Expanded Programme on Immunization (EPI) and periodic supplemental immunization campaigns, annual childhood deaths from vaccine-preventable diseases have dropped from an estimated 900,000 in 2000 to 400,000 in 2010 (*3*). Measles is emblematic of this success; globally, estimated annual measles mortality has decreased from 499,000 to 102,000 since 2000 (*4*, *5*). The Ebola-affected countries have been an important part of this achievement: The three countries reported nearly 93,685 cases of measles in the decade between 1994 and 2003 (despite Sierra Leone not reporting in 4 years), and only 6937 between 2004 and 2013 (in both periods it is likely that only a fraction of measles cases were reported to the WHO) (*6*). Despite this success, measles susceptibility has been growing in all three countries in recent years, and each had planned a measles vaccination campaign prior to the Ebola outbreak.

Measles epidemics often follow humanitarian crises. Measles is one of the most transmissible infections, and immunization rates tend to be lower than for other EPI vaccines, in part because of the older age at which measles vaccine must be administered [9 months, versus 6 weeks or younger for the first dose of other vaccines (*7*)]. For this reason, explosive measles outbreaks are often an early result of health system failure. Outbreaks have followed disruptions due to war [e.g., the current conflict in Syria (*8*)], natural disasters [e.g., the eruptions of Mt. Pinatubo in 1991 (*9*)], and political crises [e.g., Haiti in the early 1990s (*10*)]. The effects are most acute when measles epidemics are associated with famine or long-term national instability: A survey of 595 households displaced as a result of the Ethiopian famine in 2000 found measles to be a contributing cause in 35 of 159 deaths (*11*), and after years of instability in the Democratic Republic of Congo, the country experienced a measles outbreak of 294,455 cases and 5045 deaths between 2010 and 2013 (*12*).

To understand how Ebola-related health care disruptions are increasing the risk from measles, we estimated the spatial distribution of unvaccinated children and the measles susceptibility profile for each country before and after these disruptions. Geolocated cross-sectional data from Demographic and Health Surveys (DHS) in Guinea, Liberia, Sierra Leone, and surrounding countries were used to estimate vaccine coverage in each 5 km × 5 km grid cell by means of a hierarchical Bayesian model and spatial smoothing techniques. These rates were applied to spatially explicit data on population and birth cohort size to map the number of children between 9 months and 5 years of age who were unvaccinated against measles before Ebola-related health care disruptions (Fig. 1A) (*13*, *14*). Forward projections of the number of unvaccinated children after 6, 12, and 18 months were generated by reducing the rate of routine vaccination by 75% for the specified duration (reductions of 25, 50, and 100% were also considered as a sensitivity analysis). Full population susceptibility on a national level at baseline and after 18 months of disruptions were then estimated by combining these estimates with the results of models that estimate the immune profile in each age cohort on the basis of their

[1]Department of Ecology and Evolutionary Biology, Princeton University, Princeton, NJ 08544, USA. [2]Woodrow Wilson School, Princeton University, Princeton, NJ 08544, USA. [3]Centre for Infectious Disease Dynamics, Pennsylvania State University, State College, PA 16801, USA. [4]Department of Epidemiology, Johns Hopkins Bloomberg School of Public Health, Baltimore, MD 21205, USA. [5]Department of Geography and Environment, University of Southampton, Southampton SO17 1BJ, UK. [6]Fogarty International Center, National Institutes of Health, Bethesda, MD 20892, USA. [7]Flowminder Foundation, 17177 Stockholm, Sweden.
***Corresponding author. E-mail: justin@jhu.edu**

experience of routine immunization, supplemental immunization activities (SIAs), and natural infection [using techniques from Simons *et al.* (*5*) and data reported to the WHO (*6*)]. The expected size of any regional post-disruption measles outbreak was then calculated using a phenomenological model of the previously observed relationship between population susceptibility and the percentage of susceptibles infected in an outbreak (i.e., the attack rate) in the region. Finally, we estimated the number of resulting deaths by applying estimates of the case fatality ratio (CFR) for outbreak settings to the overall attack rates (*15*). Full methodological details are available in the supplement.

We estimate that at the start of the Ebola crisis, there were 778,000 [95% credible interval (CrI): 715,000 to 915,000] unvaccinated children in the three countries (Fig. 1A). These children reside in a large contiguous cluster that crosses national boundaries. With every month of health care disruptions, we estimate that the number of children between 9 months and 5 years of age who are not vaccinated against measles increases by an average of 19,514 (assuming a 75% reduction in vaccination rates nationally), reaching 964,346 (95% CrI: 862,682 to 1,129,026) after 6 months (Fig. 1B), 1,068,833 (95% CrI: 914,108 to 1,288,857) after 12 months (Fig. 1C), and 1,129,376 (95% CrI: 934,926 to 1,409,052) after 18 months (Fig. 1D). The results of variations in the spatial distribution and magnitude of disruptions in vaccination are shown in the supplement. This growing cluster of measles susceptibility abuts non–Ebola-affected countries (e.g., Cote d'Ivoire) and regional cross-border migration is frequent (*16*, *17*), thus placing their populations at risk (Fig. 1D).

This increase in unvaccinated children occurs on top of an already growing pool of measles susceptibility in the three countries (Fig. 2) resulting from years of suboptimal routine vaccination (*6*). After 18 months of disruptions, a large cohort of susceptible children will have entered the population. This growth in susceptibility increases the risk and projected size of regional measles outbreaks. If vaccination had continued at pre-Ebola rates, a generalized measles outbreak would have caused 126,868 (plausible range: 84,833 to 181,769) cases. However, the projected outbreak size increases to 227,484 (153,458 to 321,702) cases after 18 months of disruptions, resulting in a projected 5209 (1757 to 16,173) additional deaths from measles (*15*). Measles mortality could be at the high end of this range because of the limited health care services and increased prevalence of malnutrition and vitamin A deficiency associated with the Ebola outbreak (*18*).

The uncertain and rapidly changing Ebola situation in West Africa limits data availability and necessitates numerous analytic assumptions. Our assumption of a 75% reduction in routine vaccination rates is consistent with surveys of health care providers (*19*, *20*) and the qualitative assessment of those who have been involved in the response; however, as there is no reliable information on current vaccination rates, we have considered reductions of 25%, 50%, and 100% in sensitivity analyses. An unusual age distribution of measles cases, poor- or high-quality medical care, and other factors may lead to CFRs that are higher or lower than the range used here, although our estimates are based on a comprehensive assessment of measles CFRs in outbreaks (*15*). There may be preexisting pockets of susceptibility in older individuals not detected by our analysis for a variety of reasons (e.g., overreporting of vaccination); hence, campaign planning should not be solely based on the effects of the Ebola epidemic. The choice to project no further than 24 months into the future, and to focus on 18 months as the primary analysis, is necessarily somewhat arbitrary; however, it is unlikely that the region will remain measles-free if disruptions continue much beyond 2 years, and there is some evidence that the Ebola situation is beginning to improve (*2*).

Measles vaccine is just one of several childhood vaccines for which distribution may be limited by the Ebola outbreak. Similar reductions in the rate of vaccination would increase the number of children not receiving a pentavalent vaccine, Bacillus-Calmette-Guérin (BCG), and oral polio vaccine (OPV) by about 600,000 to 700,000. These setbacks have the potential to erode the substantial gains in the control of these diseases over recent decades, and a large population of children susceptible to poliovirus infection could threaten the Global Polio Eradication Initiative, should wild poliovirus be reintroduced.

Epidemics of measles are often an early result of interruptions in the delivery of public health services. However, childhood infections are not the only, or even the worst, potential health consequences of disruptions in the health care system. Malaria is the biggest infectious killer in sub-Saharan Africa, and lack of vector control interventions and proper diagnosis and treatment can increase malaria morbidity and mortality [these concerns have prompted Médecins Sans Frontières to conduct mass drug administration of antimalarial drugs in some areas (*21*)]. Provision of care to individuals with chronic infections, such as HIV and tuberculosis, is negatively affected by the Ebola outbreak. Noninfectious causes of death increase substantially when medical care is not available (e.g., if maternal mortality rates rose to year 2000 levels, there would be an additional 4454 deaths for each year of health care disruptions).

However, childhood vaccine-preventable diseases are an area where there is a clear, relatively inexpensive, and one-time intervention that could erase the impact of Ebola-related health care disruptions. Coordinated campaigns across the three Ebola-affected countries (and possibly neighboring countries) targeting those children who likely missed critical routine vaccinations during the Ebola epidemic with measles and polio vaccines, and potentially other life-saving childhood vaccines, could thwart a second public health disaster and avoid nearly 12,000 deaths from measles alone. Such a campaign should not only target those age groups likely missed during the Ebola crisis (children from birth to an age equal to the length of health care disruptions plus 1 year of age; see Fig. 2), but also those groups where measles susceptibility was already suspected to be

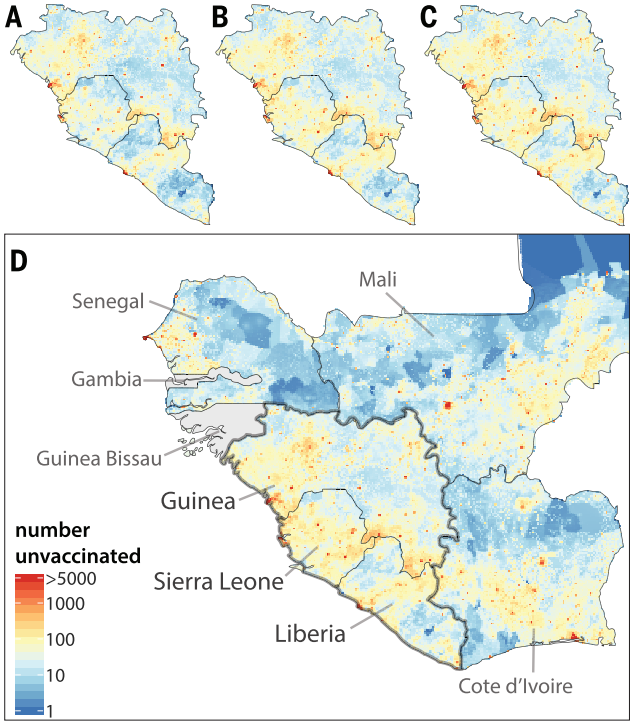

Fig. 1. Geographic distribution of measles susceptibility (**A** to **D**) Number of children 9 to 59 months of age not vaccinated against measles in Guinea, Liberia, and Sierra Leone before disruptions in vaccination due to Ebola (A), after 6 months of a 75% reduction in measles vaccination rates due to Ebola-related health care disruptions (B), after 12 months of disruptions (C), and after 18 months of disruptions (D), with numbers of unvaccinated children (without disruptions) in neighboring countries shown.

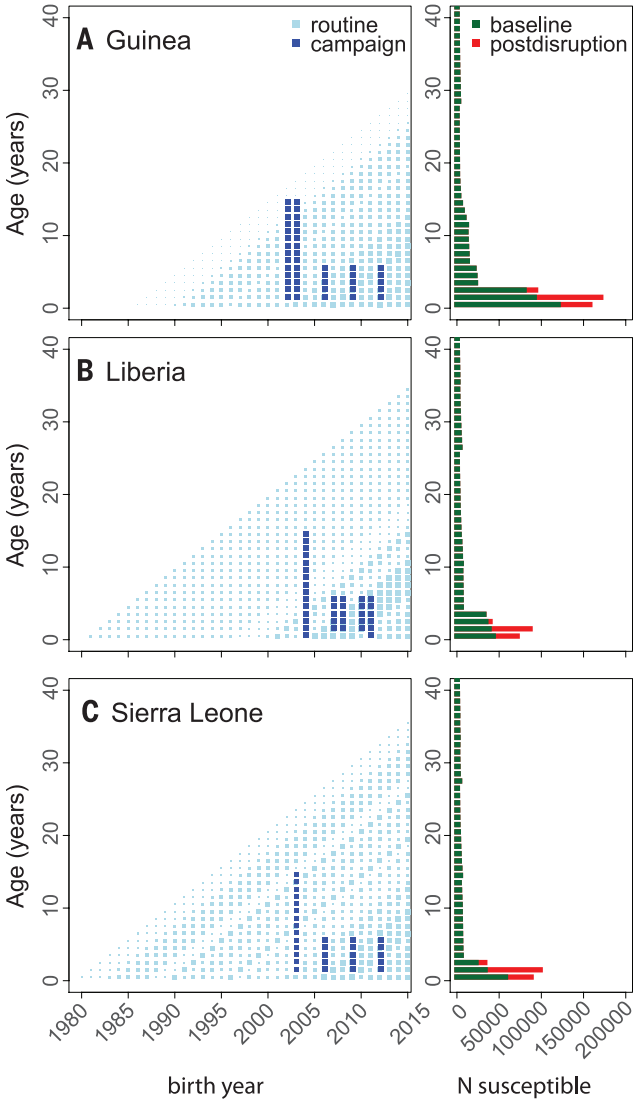

Fig. 2. Age distribution of measles susceptibility (**A** to **C**) Left: History of routine vaccination (light blue squares; size indicates coverage) and SIA campaigns (dark blue squares) for each age cohort by year in Guinea (A), Liberia (B), and Sierra Leone (C). Right: Projected number susceptible to measles in each age cohort from 0 to 40 years of age. Green denotes projected 2015 age distribution of measles susceptibility if no Ebola-related disruptions to vaccination occurred; red denotes distribution after 18 months of Ebola-related health care disruptions.

on the rise. Hence, at the very least, a campaign should target children 6 months to 5 years of age (typical of the age range targeted by follow-up SIAs), perhaps extending the lower age range and administering childhood vaccines other than measles vaccine to the youngest children (e.g., those younger than the length of health care disruptions). The need for and logistics of simultaneous deployment of additional key public health interventions, such as vitamin A supplementation and insecticide-treated bed nets, should also be considered. Planning for such a vaccine campaign should begin now so that we can respond quickly when the situation stabilizes and minimize the time at risk for disease outbreaks. The growing pool of susceptible individuals in Guinea, Liberia, and Sierra Leone may place bordering countries at increased risk for a measles outbreak; they too may have suffered disruptions to their health care systems due to a focus on the threat from Ebola. These countries should carefully assess the performance of their vaccination programs and consider instituting campaigns to shore up any gaps.

REFERENCES AND NOTES

1. World Health Organization, "Ebola situation report" (2015); www.who.int/csr/disease/ebola/situation-reports/en/.
2. T.G. Nyenswah *et al.*, Evidence for declining numbers of Ebola cases—Montserrado County, Liberia, June–October 2014. *Morbid. Mortal. Wkly. Rep.* 63 (early release), 1–5; www.cdc.gov/mmwr/preview/mmwrhtml/mm63e1114a2.htm.
3. World Health Organization, "Global vaccine action plan 2011–2020" (2013); www.who.int/immunization/global_vaccine_action_plan/GVAP_doc_2011_2020/en/.
4. L. Liu *et al.*, *Lancet* **385**, 430–440 (2015).
5. E. Simons *et al.*, *Lancet* **379**, 2173–2178 (2012).
6. World Health Organization, "Immunization, vaccines and biologicals: Data, statistics and graphics" (2015); www.who.int/immunization/monitoring_surveillance/data/en/.
7. World Health Organization, "WHO recommendations for routine immunization—summary tables"; www.who.int/immunization/policy/immunization_tables/en/.
8. S. L. Sharara, S. S. Kanj, *PLOS Pathog.* **10**, e1004438 (2014).
9. M. R. Surmieda *et al.*, *MMWR CDC Surveill. Summ.* **41**, 9–12 (1992).
10. UNICEF, "Sanctions: Children hard hit in Haiti"; www.unicef.org/sowc96/dsanctns.htm.
11. P. Salama *et al.*, *JAMA* **286**, 563–571 (2001).
12. S. Mancini *et al.*, *Confl. Health* **8**, 9 (2014).
13. C. Linard, M. Gilbert, R. W. Snow, A. M. Noor, A. J. Tatem, *PLOS ONE* **7**, e31743 (2012).
14. A. J. Tatem *et al.*, *Int. J. Health Geogr.* **13**, 2 (2014).
15. L. J. Wolfson, R. F. Grais, F. J. Luquero, M. E. Birmingham, P. M. Strebel, *Int. J. Epidemiol.* **38**, 192–205 (2009).
16. A. Wesolowski *et al.*, *PLOS Curr.* **6**, (2014).
17. A. J. Garcia, D. K. Pindolia, K. K. Lopiano, A. J. Tatem, Modeling internal migration flows in sub-Saharan Africa using census microdata. *Migrat. Stud.* 10.1093/migration/mnu036 (2014).
18. W. McFerron, "Ebola stokes Liberian food shortage as farmers eat seeds," Bloomberg News (2014); www.bloomberg.com/news/2014-11-20/ebola-stokes-liberian-food-shortage-as-farmers-eat-seeds.html.
19. Epicentre, "Cross-sectional survey on health care capacity and utilization, safety and hygiene measures available in health structures, and attack rate among health facility staff during the Ebola outbreak, Monrovia, Liberia, August 2014" (Médecins Sans Frontières document, 2014).
20. H. A. Bolkan, D. A. Bash-Taqi, M. Samai, M. Gerdin, J. von Schreeb, Ebola and indirect effects on health service function in Sierra Leone. *PLOS Curr. Outbreaks* 10.1371/currents.outbreaks.0307d588df619f9c9447f8ead5b72b2d (2014).
21. Médecins Sans Frontières, "MSF begins malaria program in Ebola-ravaged Monrovia, Liberia" (2015); www.doctorswithoutborders.org/article/msf-begins-malaria-program-ebola-ravaged-monrovia-liberia.
22. ICF International, Demographic and Health Surveys (various); http://dhsprogram.com/data/.
23. Ambassade de France à Conakry, "Ebola: Point de situation au 16 janvier 2015"; www.ambafrance-gn.org/Ebola-point-de-situation-au-16-1040.
24. Liberian Ministry of Health, "Liberia Ebola Daily Sitrep no. 242 for 12th January 2015"; www.mohsw.gov.lr/documents/Sitrep 242 Jan 12th 2015.pdf.
25. Sierra Leone National Ebola Response Centre (NERC), "Ebola outbreak updates—January 16, 2015"; http://health.gov.sl/wp-content/uploads/2015/01/Ebola-Update-January-16-2015.pdf.

ACKNOWLEDGMENTS

Supported by Bill & Melinda Gates Foundation grant OPP1094793 and U.S. Department of Homeland Security Science & Technology Directorate contract HSHQDC-12-C-00058 (B.T.G., C.J.E.M.); the RAPIDD program of the Department of Homeland Security Science & Technology Directorate and the NIH Fogarty International Center (C.J.E.M., B.T.G., A.J.T.); National Institute of Allergy and Infectious Diseases (NIAID) grant R01 AI102939 (J.L.); and NIAID grant U19AI089674 and Bill & Melinda Gates Foundation grants OPP1106427 and 1032350 (A.J.T.). We thank M. Hanson for helping to organize the assessment of the impact of Ebola on measles vaccination and for motivating this work, and W. Hao for helpful discussion in preparation of the manuscript. Demographic and Health Surveys data are made freely available to those filing a request (*22*). WorldPop project demographic data may be obtained from www.worldpop.org.uk. Data on measles incidence, routine vaccination coverage, and SIAs are available at www.who.int/immunization/monitoring_surveillance/data/en/. Ebola incidence data were extracted from publicly available situation reports (*23*–*25*).

SUPPLEMENTARY MATERIALS

www.sciencemag.org/content/347/6227/1240/suppl/DC1
Materials and Methods
Figs. S1 to S7
Tables S1 and S2
References (*26*–*31*)

22 November 2014; accepted 5 February 2015
10.1126/science.aaa3438

POLITICAL PSYCHOLOGY

Conservatives report, but liberals display, greater happiness

Sean P. Wojcik,[1]* Arpine Hovasapian,[1] Jesse Graham,[2] Matt Motyl,[3] Peter H. Ditto[1]*

Research suggesting that political conservatives are happier than political liberals has relied exclusively on self-report measures of subjective well-being. We show that this finding is fully mediated by conservatives' self-enhancing style of self-report (study 1; *N* = 1433) and then describe three studies drawing from "big data" sources to assess liberal-conservative differences in happiness-related behavior (studies 2 to 4; *N* = 4936). Relative to conservatives, liberals more frequently used positive emotional language in their speech and smiled more intensely and genuinely in photographs. Our results were consistent across large samples of online survey takers, U.S. politicians, Twitter users, and LinkedIn users. Our findings illustrate the nuanced relationship between political ideology, self-enhancement, and happiness and illuminate the contradictory ways that happiness differences can manifest across behavior and self-reports.

Are political conservatives happier than political liberals? Several recent studies have found that greater political conservatism predicts higher levels of self-reported happiness and life satisfaction in the United States (*1*–*4*). This "ideological happiness gap" has been attributed to a number of different psychological factors. Some explanations posit that conservatives' greater happiness is due to a suite of adaptive personal, social, and cultural values (*1*), such as high levels of personal agency, optimism, and transcendent moral beliefs (*2*). Others portray conservatism as a protective or even defensive mechanism that serves the palliative function of justifying troubling societal inequalities (*3*). Although researchers disagree over the mechanism underlying the happiness gap, meta-analytic review has confirmed that it is a small but reliable effect (r = 0.12) (*4*).

All of the data supporting the relation between political conservatism and subjective well-being rely on self-report measures (e.g., stated agreement with face-valid items such as "In most ways my life is close to ideal") (*4*, *5*). This is not surprising given that self-reports are the foundation of subjective well-being research (*6*, *7*), but reliance on any single methodology within an area of research can result in systematic methodological artifacts due to common method variance (*8*). There are many challenges involved in self-report research (*9*–*11*), including the influence of self-enhancement motives, which commonly lead to unrealistically favorable self-assessments (*12*). Self-reports of happiness and life satisfaction, much like self-assessments of other valued characteristics, are susceptible to self-enhancing distortions (*13*). Both individual differences in, and experimental manipulations of, self-enhancement motivation predict the tendency to report happiness and life satisfaction at unrealistically positive levels (i.e., the "happier-than-average effect") (*13*).

Self-enhancing tendencies are not evenly distributed across populations (*14*–*16*), and there are reasons to suspect that liberals and conservatives may self-enhance to differing degrees. Conservatism (*17*) has been characterized as an ideology grounded in ego defensiveness (*18*), enhanced sensitivity to negativity (*19*), and personality dimensions related to defensive forms of motivated social cognition (*20*, *21*). Self-enhancement is also associated with a number of factors related to politically conservative ideologies: It is more pronounced among individualistic cultures (*14*), religious people (*15*), and competitive, hierarchically oriented groups (*16*). Given that self-reported happiness is related to political conservatism (*4*) and self-enhancement (r = 0.10) (*13*) at comparable magnitudes, it is possible that ideological happiness differences may simply be an example of conservatives' stronger tendency to evaluate the self favorably.

In study 1, we examined whether conservatives' reports of greater subjective well-being, relative to liberals, could be attributed to self-enhancing tendencies. Visitors to YourMorals.org, a psychological research Website, reported their political ideology and completed the Satisfaction With Life Scale, the most frequently used measure of subjective well-being (*5*), as well as the Balanced Inventory of Desirable Responding, a well-validated measure of the tendency to engage in self-deceptive enhancement (*22*). As expected, increasing political conservatism predicted greater reported life satisfaction [r(1433) = 0.10, P < 0.001; adjusting for demographic characteristics: β = 0.09, P = 0.002]. This happiness gap was similar in magnitude to that found in past research (*4*). Importantly, we also found that self-deceptive enhancement was higher among conservatives than liberals [r(1433) = 0.16, P < 0.001; adjusting for demographics: β = 0.18, P < 0.001]. A bootstrapped mediation analysis revealed that, as hypothesized, self-deceptive enhancement fully mediated the ideology–life satisfaction association [indirect effect: b = 0.05, P < 0.001, 95% confidence interval (CI) = (0.03, 0.07)] (see Table 1).

These results indicate that conservatives' greater reports of life satisfaction were attributable to their stronger tendency to engage in self-enhancement. But there are two possible interpretations of these findings. First, conservative participants may be experiencing greater happiness and life satisfaction than liberals as a beneficial consequence of their self-enhancing predispositions (*23*). Alternatively, conservatives' elevated reports may simply be an example of their stronger tendency to provide unrealistically favorable self-assessments. This interpretative ambiguity highlights a major limitation of relying on self-reports alone: They do not distinguish between genuine and superficial presentations of happiness.

Behavioral indicators of happiness provide important information that can clarify this ambiguity. If we take self-reports of well-being at face value, rather than as examples of self-enhanced assessments, we would expect to observe conservatives' greater happiness in unobtrusive measures of happiness-related behavior—for example, in the emotional content of liberals' and conservatives' speech, or in the frequency and intensity of their smiling behavior. Assessing smiling behavior also allows us to distinguish between genuine and superficial expressions of happiness. Intense, genuine smiling, known as Duchenne smiling, involves the muscles lifting the corner of the mouth as well as those orbiting the eye (*24*). Non-Duchenne (also known as social, deceptive, or standard) smiling involves only the muscles lifting the corners of the mouth and is less often related to genuine feelings of happiness or enjoyment. Non-Duchenne smiling is also less predictive than Duchenne smiling of beneficial long-term psychological and physical health outcomes (*24*, *25*).

In study 2, we examined happiness-related behavior among the United States' most salient liberals and conservatives: members of the U.S. Congress. We assessed two behavioral indicators of happiness within this group: the use of positive and negative emotional language from a text analysis of the 2013 U.S. *Congressional Record* and the smiling behavior exhibited in their publicly available photographs. For our linguistic analysis, we recorded word-use frequencies for members of the 113th U.S. Congress using relevant terms from one of the most frequently used emotion scales in the psychological literature, the Positive and Negative Affect Schedule: Expanded Form (PANAS-X) (*26*). We assessed political ideology using continuous liberalism-conservatism scores based on analysis of each politician's voting record (*27*) and controlled for each member's legislative chamber, status as a political minority/majority member in their chamber, overall word usage, and demographic characteristics. Greater conservatism was associated with a small but significant decrease in positive affect word use (β = −0.16, P < 0.001). Conservatism was not significantly associated with the use of negative affect words, joviality-related words, or sadness-related

[1]Department of Psychology and Social Behavior, University of California, Irvine, CA 92697, USA. [2]Department of Psychology, University of Southern California, CA 90089, USA. [3]University of Illinois, Chicago, IL 60607, USA.
*Corresponding author. E-mail: swojcik@uci.edu (S.P.W.); phditto@uci.edu (P.H.D.)

words (Table 2). We replicated this analysis with political ideology defined by party identification instead of voting record and found a similar pattern of results.

We also tested the reliability of the relationship over time by assessing emotional language at the party level across 18 years of *Congressional Record* data, including more than 432 million words. Members of the liberal-leaning Democratic Party used a higher ratio of positive to negative affect words (M = 13.65:1) than members of the conservative-leaning Republican Party (M = 11.50:1), including a higher frequency of positive affect word usage in 17 of 18 years.

This pattern of emotional expression was not limited to linguistic analyses. We next analyzed smiling behavior in photos from the *Congressional Pictorial Directory* of the 113th U. S. Congress (*28*) using the Facial Action Coding System (FACS) (*29*). A FACS-certified coder assessed the intensity of two action units (AUs) associated with genuine smiling behavior: activity in the orbicularis oculi (AU6) and the zygomatic major (AU12). We found that increasing political conservatism predicted

Table 1. Unstandardized coefficients from mediation analyses of self-reported life satisfaction (study 1). Standard errors are given in parentheses. Indirect effect for bootstrapped mediation analysis with 5000 resamples for model 1: b = 0.05, SE = 0.01, z = 5.57, P < 0.001, and 95% CI = (.03, 0.07); for model 2: b = 0.05, SE = 0.01, z = 5.47, P < 0.001, and 95% CI = (0.03, 0.07).

Predictor	Model 1		Model 2	
	Step 1	Step 2	Step 1	Step 2
Political conservatism	0.09 (0.02)***	0.04 (0.02)$^{+}$	0.07 (0.01)***	0.03 (0.02) ns
Self-deceptive enhancement		0.73 (0.05)***		0.69 (0.05)***
Socioeconomic status			0.02 (0.01)**	0.07 (0.01)***
Education			−0.02 (0.02) ns	0.21 (0.03)***
Sex (1 = female)			−0.03 (0.04) ns	0.32 (0.07)***
Age			0.00 (0.00) ns	0.00 (0.00) ns
Age squared			0.00 (0.00) ns	0.00 (0.00)***
Religious attendance			−0.03 (0.02)*	0.07 (0.02)**
Constant	4.13 (0.08)***	1.35 (0.22)***	3.87 (0.10)***	−0.42 (0.29) ns
F(df)	F(1, 1431) = 14.45***	F(2, 1430) = 95.63***	F(7, 1373) = 10.15***	F(8, 1372) = 46.15***
R^2	0.01	0.12	0.05	0.21

ns, P > 0.10; ^{+}P < 0.10; *P < 0.05; **P < 0.01; ***P < 0.001

Table 2. Unstandardized regression coefficients for linguistic analyses and smile analyses for politicians in 2013 U.S. *Congressional Record* (study 2). Standard errors are given in parentheses.

Predictor	Linguistic analyses				Smile analyses		
	Positive affect	Negative affect	Joviality	Sadness	Overall smile	Zygomatic major (AU12)	Orbicularis oculi (AU6)
Political conservatism	−0.88 (0.19)***	0.04 (0.05) ns	−0.04 (0.07) ns	−0.09 (0.05)$^{+}$	−0.03 (0.01)*	−0.02 (0.01)$^{+}$	−0.03 (0.02)*
Chamber (1 = House)	2.79 (2.28) ns	1.07 (0.58)$^{+}$	0.08 (0.91) ns	2.18 (0.61)***	0.11 (0.13) ns	0.02 (0.12) ns	0.24 (0.17) ns
Party majority status (1 = Majority)	7.06 (1.93)***	−0.60 (0.49) ns	−0.21 (0.77) ns	0.73 (0.52) ns	0.13 (0.13) ns	0.13 (0.12) ns	0.13 (0.16) ns
Age	−0.02 (0.07) ns	0.00 (0.02) ns	−0.06 (0.03)$^{+}$	0.00 (0.02) ns	0.00 (0.00) ns	0.00 (0.00) ns	0.00 (0.01) ns
Ethnicity: African American	−0.38 (3.07) ns	−0.23 (0.79) ns	−0.62 (1.23) ns	−0.43 (0.83) ns	−0.58 (0.20)**	−0.28 (0.19) ns	−0.88 (0.26)**
Ethnicity: Hispanic American	−2.38 (3.01) ns	−0.44 (0.77) ns	3.32 (1.21)**	−0.46 (0.81) ns	−0.16 (0.20) ns	0.00 (0.18) ns	−0.33 (0.25) ns
Ethnicity: Asian American	−2.17 (5.58) ns	0.26 (1.43) ns	−0.50 (2.24) ns	−0.47 (1.50) ns	−0.05 (0.37) ns	0.13 (0.34) ns	−0.22 (0.47) ns
Ethnicity: Other	−5.61 (7.66) ns	−0.95 (1.97) ns	−1.47 (3.08) ns	0.35 (2.06) ns	−0.52 (0.50) ns	0.06 (0.47) ns	−1.11 (0.64)$^{+}$
Sex (1 = male)	−2.38 (2.04) ns	−0.36 (0.52) ns	−0.84 (0.82) ns	−1.05 (0.55)$^{+}$	−0.38 (0.13)**	−0.63 (0.12)***	−0.13 (0.17) ns
Wordiness	3.5×10^{-3} (10^{-4})***	3×10^{-4} (3×10^{-5})***	8×10^{-4} (5×10^{-5})***	9×10^{-4} (3×10^{-5})***			
Constant	2.91 (5.29) ns	−0.01 (1.36) ns	4.29 (2.12)*	−1.34 (1.42) ns	2.38 (0.34)***	3.15 (0.32)***	1.60 (0.44)***
F(df)	F(10, 516) = 115.69***	F(10, 516) = 10.01***	F(10, 516) = 38.64***	F(10, 516) = 92.04***	F(9, 517) = 2.44**	F(9, 517) = 4.08***	F(9, 517) = 2.12**
R^2	0.69	0.16	0.43	0.64	0.04	0.07	0.04

ns, P > 0.10, ^{+}P < 0.10, *P < 0.05, **P < 0.01, ***P < 0.001.

less intense overall smiling (β = −0.12, P = 0.032), controlling for the same variables as the linguistic analysis above (Table 2). We observed only marginally significant differences in the intensity of smiling behavior in the muscles lifting the corners of the mouth (AU12: β = −0.10, P = 0.096), but conservatism predicted significantly less intense facial action in the muscles around the eyes that indicate genuine happiness (AU6: β = −0.13, P = 0.031). The odds of displaying non-Duchenne smiles (i.e., action in AU12 but not AU6) were slightly higher for conservatives than for liberals, but this did not reach statistical significance [controlling for demographics: odds ratio (OR) = 1.04, P = 0.206].

Study 2 revealed no evidence of greater emotionally positive behavior among conservative elected officials. Instead, it was liberal politicians who tended to more frequently express positive emotional language, smile more intensely, and smile more genuinely. These effects were modest in size, but in the opposite direction of the previously observed self-report–based happiness gap (*4*). Of course, elected political leaders are not representative of liberal and conservative individuals more generally, and it is unclear how well speech and facial expressions occurring within the confines of Capitol Hill reflect similar happiness-related behaviors in less overtly political contexts.

Accordingly, study 3 assessed the linguistic content of 47,257 Twitter status updates ("tweets") from liberal and conservative members of the general public. We analyzed the statuses of individuals who subscribed to ("followed") the official Twitter pages of either the Democratic or Republican Party, excluding those following both, under the assumption that users who followed one party exclusively were likely to share that party's political views. We assessed the emotional content of each tweet using word lists from the PANAS-X, the Linguistic Inquiry Word Count software (LIWC) (*30*), and lists of "happy" and "sad" emoticons. Logistic regressions predicting the presence or absence of emotion words/emoticons at the tweet level were conducted, with political party followed as the independent variable. Relative to Democratic Party subscribers' updates, Republican Party subscribers' updates were significantly less likely to contain positive emotion words, joviality words, and happy emoticons, and significantly more likely to contain negative emotion words (all Ps < 0.05) (Table 3). Marginal effects also revealed similar patterns on the PANAS-X negative affect and sadness subscales.

In study 4, we analyzed 457 publicly available photographs of individuals from LinkedIn, a business-oriented social networking Web site. We selected participants who publicly self-identified as employees at organizations strongly associated with ideologically liberal or conservative values (e.g., Planned Parenthood versus the Family Research Council), under the assumption that the majority of employees at these organizations were likely to share the organizations' ideological views. As we found among Democratic and Republican Congress members in study 2, smiles were marginally more intense among employees at ideologically liberal organizations (M = 1.98, SD = 1.35) than among employees of ideologically conservative organizations [M = 1.75, SD = 1.24 ; t(455) = 1.91, d = 0.18, P = 0.057; controlling for gender and ethnicity: β = −0.07, P = 0.143]. We again did not observe ideological differences in the intensity of smiling behavior in the muscles lifting the corners of the mouth [AU12; liberals: M = 2.18, SD = 1.45; conservatives: M = 1.99, SD = 1.32; t(455) = 1.42, d = 0.13, P = 0.157; controlling for gender and ethnicity: β = −0.03, P = 0.458]. However, individuals at conservative organizations expressed significantly less intense facial action in the muscles around the eyes that indicate genuine feelings of happiness [AU6; liberals: M = 1.78, SD = 1.43; conservatives: M = 1.50, SD = 1.38; t(455) = 2.14, d = 0.20, P = 0.033; controlling for gender and ethnicity: β = −0.09, P = 0.051]. We also found that the proportion of individuals displaying non-Duchenne smiles was significantly higher at conservative organizations (n = 41 of 217, or 18.89%) than at liberal organizations (n = 24 of 240, or 10.00%; χ^2 = 7.39, P = 0.007; controlling for demographics: OR = 2.35, P = 0.003).

Together, our studies found that political liberals exhibited more frequent and intense happiness-related behavior than political conservatives. Contrary to the pattern found in self-reports of happiness and life satisfaction (*1*–*4*), linguistic analyses of massive archives of text from both elected politicians and the general public revealed a modest but consistent tendency for liberals to use more positive emotional language than conservatives. In addition, we found that liberal politicians and employees at organizations promoting liberal values smiled more intensely and genuinely than their conservative counterparts. Although the effects in these studies were small, they consistently revealed greater happiness-related behavior among liberals, rather than conservatives. These behavioral data support our finding from study 1 that differences in liberals' and conservatives' reports of happiness can be attributed to conservatives' stronger tendency to provide flattering self-assessments.

These findings add nuance to past research suggesting that subjective well-being is a multifaceted construct composed of both hedonic or experiential aspects (e.g., reports of current affect and observed behavior) and eudaimonic or evaluative ones (e.g., global assessments of happiness or life satisfaction) (*31*, *32*). What does it mean when self-reports and behavioral indicators provide contradictory data? Happiness lacks an objective "gold standard" validation criterion, and both self-report (*6*) and behavioral (*25*, *33*) measures of happiness have been linked to beneficial short- and long-term outcomes. For this reason, it would be a mistake to infer from our data that liberals are "objectively" happier than conservatives or that conservatives' self-enhancing tendencies are necessarily maladaptive. It is not currently known whether claims of happiness bolstered by self-enhancement motivation are any less advantageous than more "genuine" reports of positive well-being. In fact, there is evidence that self-enhancement tendencies can often facilitate psychological adjustment, including the capacity for productive work, satisfying relationships, and resilience to psychological threat (*23*). This possibility raises important questions for future research, including the potential existence of "defensive" forms of happiness similar to other forms of defensive self-evaluation, such as those uncovered in research on self-esteem (*34*).

Our studies did not directly test previously proposed mechanisms for the ideological happiness gap, such as differences in ideological values (*1*), system justification motivation (*3*), or judgments about personal agency, optimism, and transcendent moral beliefs (*2*). However, it seems plausible that these explanations share common motivational mechanisms with self-enhancement (*21*, *23*). A key difference is that these previous accounts would predict happiness-related behavior to correspond with self-report evidence of greater conservative happiness. Our self-enhancement-based account explains this discrepancy. Future research should continue to examine whether these motivational mechanisms truly lead to genuinely positive emotional experiences and greater

Table 3. Odds of emotion-related words appearing in tweets of Republican party subscribers relative to Democratic party subscribers (study 3). ORs above 1.00 indicate that conservative tweets contained a higher percentage than liberal tweets; values below 1.00 indicate the opposite. *N* of tweets for PANAS-X and LIWC analyses = 37,857; *N* for emoticon analyses = 47,257.

	Positive emotion word lists				Negative emotion word lists			
	PANAS-X Positive affect	PANAS-X Joviality	LIWC Positive emotion	Happy emoticons	PANAS-X Negative affect	PANAS-X Sadness	LIWC Negative emotion	Sad emoticons
OR	0.88	0.80	0.95	0.83	1.44	1.32	1.07	0.77
SE	0.08	0.06	0.02	0.07	0.20	0.22	0.03	0.17
P	0.159	0.007	0.018	0.030	0.051	0.093	0.015	0.229

psychological adjustment or if they primarily motivate the superficial report of one's positive qualities.

The questions raised by this research are important because of a growing interest in using self-report measures of happiness to inform public policy (*1*, *6*). Our research supports those recommending caution about promoting any particular ideology or policy as a road to happiness (*32*). Research investigating self-report–based happiness differences between nonrandomized groups (e.g., cultures, nations, and religious groups) may inadvertently capture differences in self-reporting styles rather than actual differences in emotional experience. Both behavioral measures and self-reports of subjective well-being are valuable tools, but any comprehensive assessment of subjective well-being should involve multiple methodological approaches (*6*, *8*). Reliance on any single methodology is likely to lead to an oversimplified account of not only who is happier than whom but also what it means to be happy at all.

REFERENCES AND NOTES

1. A. C. Brooks, *Gross National Happiness: Why Happiness Matters for America—and How We Can Get More of It* (Basic Books, New York, 2008).
2. B. R. Schlenker, J. R. Chambers, B. M. Le, *J. Res. Pers.* **46**, 127–146 (2012).
3. J. L. Napier, J. T. Jost, *Psychol. Sci.* **19**, 565–572 (2008).
4. E. Onraet, A. Van Hiel, K. Dhont, *Pers. Soc. Psychol. Bull.* **39**, 509–522 (2013).
5. E. Diener, R. A. Emmons, R. J. Larsen, S. Griffin, *J. Pers. Assess.* **49**, 71–75 (1985).
6. The term "subjective well-being" is used interchangeably with "happiness" and consists of life satisfaction, positive and negative affect, and domain satisfaction (*7*).
7. E. Diener, *Am. Psychol.* **55**, 34–43 (2000).
8. D. T. Campbell, D. W. Fiske, *Psychol. Bull.* **56**, 81–105 (1959).
9. C. Zou, U. Schimmack, J. Gere, *Psychol. Assess.* **25**, 1247–1254 (2013).
10. R. E. Nisbett, T. D. Wilson, *Psychol. Rev.* **84**, 231–259 (1977).
11. B. Gawronski, B. K. Payne, Eds., *Handbook of Implicit Social Cognition: Measurement, Theory, and Applications* (Guilford Press, New York, 2010).
12. J. D. Brown, *Pers. Soc. Psychol. Bull.* **38**, 209–219 (2012).
13. S. P. Wojcik, P. H. Ditto, *Soc. Psychol. Personal. Sci.* **5**, 825–834 (2014).
14. S. J. Heine, S. Kitayama, T. Hamamura, *Asian J. Soc. Psychol.* **10**, 198–200 (2007).
15. K. Eriksson, A. Funcke, *Soc. Psychol. Personal. Sci.* **5**, 76–83 (2014).
16. S. Loughnan *et al.*, *Psychol. Sci.* **22**, 1254–1258 (2011).
17. Political ideology is a complex and nebulous construct that is most frequently operationalized in this literature using self-report measures of ideology, party affiliation, or scores on psychological constructs associated with self-reported conservatism such as authoritarianism and social dominance orientation (*4*, *20*). The meaning ascribed to terms like "liberal," "progressive," and "conservative" also varies over time and across national contexts. Given this conceptual complexity, we have restricted our analyses to U.S. samples where possible and tested our effects across multiple operationalizations of liberalism-conservatism, including self-identified ideology (study 1) and party affiliation (study 2), but also using behavioral measures such as congressional voting records (study 2), social media subscriptions (study 3), and involvement with liberal and conservative organizations (study 4).
18. G. D. Wilson, Ed., *The Psychology of Conservatism* (Academic Press, London, 1973).
19. J. R. Hibbing, K. B. Smith, J. R. Alford, *Behav. Brain Sci.* **37**, 297–307 (2014).
20. J. T. Jost, J. Glaser, A. W. Kruglanski, F. J. Sulloway, *Psychol. Bull.* **129**, 339–375 (2003).
21. J. T. Jost *et al.*, in A. C. Kay *et al.*, Eds., *The Psychology of Justice and Legitimacy: The Ontario Symposium* (Erlbaum, Hillsdale, NJ, 2010), pp. 173–203.
22. D. L. Paulhus, *Balanced Inventory of Desirable Responding: Reference Manual for BIDR Version 6* (University of British Columbia, Vancouver, Canada, 1994).
23. S. E. Taylor, J. D. Brown, *Psychol. Bull.* **103**, 193–210 (1988).
24. P. Ekman, R. J. Davidson, W. V. Friesen, *J. Pers. Soc. Psychol.* **58**, 342–353 (1990).
25. L. Harker, D. Keltner, *J. Pers. Soc. Psychol.* **80**, 112–124 (2001).
26. D. Watson, L. A. Clark, *The PANAS-X: Manual for the Positive and Negative Affect Schedule-Expanded Form* (University of Iowa, Ames, Iowa, IA, 1994).
27. That's My Congress, Legislative Scorecards; http://thatsmycongress.com/index.php/legislative-scorecards
28. United States Congress Joint Committee on Printing, Ed., *Congressional Pictorial Directory: One Hundred Thirteenth Congress* (Government Printing Office, Washington, DC, 2013).
29. P. Ekman, W. V. Friesen, *Facial Action Coding System: Investigator's Guide* (Consulting Psychologists Press, Washington, DC, 1978).
30. J. W. Pennebaker, M. F. Francis, R. J. Booth, *Linguistic Inquiry and Word Count: LIWC-2001 Operations Manual* (LIWC.net, Austin, TX, 2001).
31. E. L. Deci, R. M. Ryan, *J. Happiness Stud.* **9**, 1–11 (2008).
32. A. B. Krueger, A. A. Stone, *Science* **346**, 42–43 (2014).
33. S. D. Pressman, S. Cohen, *Health Psychol.* **31**, 297–305 (2012).
34. M. H. Kernis, *Psychol. Inq.* **14**, 1–26 (2003).

ACKNOWLEDGMENTS

The authors received no financial support for the research, authorship, and/or publication of this article and declared no potential conflicts of interest. We thank J. Haidt and A. Stone for their feedback on an earlier draft of the manuscript and R. Idrogo-Lam and J. Larsen for their assistance in data collection. The data used in this paper are available from Open ICPSR: http://doi.org/10.3886/E26078V1.

SUPPLEMENTARY MATERIALS

www.sciencemag.org/content/347/6227/1243/suppl/DC1
Materials and Methods
References

4 September 2014; accepted 5 February 2015
10.1126/science.1260817

HUMAN PALEOECOLOGY

Direct evidence for human reliance on rainforest resources in late Pleistocene Sri Lanka

Patrick Roberts,[1]* Nimal Perera,[2] Oshan Wedage,[3] Siran Deraniyagala,[3] Jude Perera,[3] Saman Eregama,[3] Andrew Gledhill,[4] Michael D. Petraglia,[1] Julia A. Lee-Thorp[1]

Human occupation of tropical rainforest habitats is thought to be a mainly Holocene phenomenon. Although archaeological and paleoenvironmental data have hinted at pre-Holocene rainforest foraging, earlier human reliance on rainforest resources has not been shown directly. We applied stable carbon and oxygen isotope analysis to human and faunal tooth enamel from four late Pleistocene–to–Holocene archaeological sites in Sri Lanka. The results show that human foragers relied primarily on rainforest resources from at least ~20,000 years ago, with a distinct preference for semi-open rainforest and rain forest edges. *Homo sapiens*' relationship with the tropical rainforests of South Asia is therefore long-standing, a conclusion that indicates the time-depth of anthropogenic reliance and influence on these habitats.

The expansion of *Homo sapiens* beyond Africa in the late Pleistocene [125 to 12 thousand years ago (ka)] required a capacity to adapt successfully to a diversity of environments (*1*, *2*). One environment in particular, tropical rainforest, has been widely considered an unattractive prospect for long-term foraging because it is difficult to navigate, lacks abundant carbohydrate and protein resources, and requires significant subsistence and technological developments for occupation to be feasible (*3*, *4*). Ethnographic observations of existing and historical rainforest foragers, and those foragers' typical nutrient intake, however, have called this view into question (*5*, *6*). Furthermore, discoveries and reappraisal of early human archaeological sites in Africa (*7*), Southeast Asia (*8*), and Melanesia (*9*) have associated environmental indications from pollen, archaeobotanical, and archaeozoological remains with human material to demonstrate that human rainforest resource use may have occurred as early as ~46 ka. The association of stone tool assemblages with offsite pollen records for forest conditions of unknown catchment have been more controversially argued to show human forest foraging back to ~200 ka in Africa (*7*). However, archaeological evidence against the contention that prehistoric humans avoided rainforest environments as long-term ecologies for

[1]School of Archaeology, Research Laboratory for Archaeology and the History of Art, Dyson Perrins Building, University of Oxford, South Parks Road, Oxford OX1 3QY, UK. [2]Postgraduate Institute of Archaeology, 407 Bauddhaloka Mawatha, Colombo 00700, Sri Lanka. [3]Department of Archaeology, Sir Marcus Fernando Mawatha, Colombo, Sri Lanka. [4]Division of Geographic, Archaeological and Environmental Sciences, University of Bradford, Bradford BD7 1DP, UK.
*Corresponding author. E-mail: patrick.roberts@rlaha.ox.ac.uk

habitation has been sparse, meaning that the question has remained open.

We studied prehistoric human use of rainforest resources directly by means of isotopic analysis of archaeological human tooth enamel from Sri Lanka, based on the well-established ^{13}C depletion of plants and animals in canopied tropical forests (*10*). Sri Lanka has yielded some of the earliest dated material and fossil evidence for *H. sapiens* occupation, ~36,000 calibrated years before the present (cal yr B.P.), in a modern rainforest context beyond Africa (*11*, *12*), with the exception of the Niah Caves, Borneo, dated to ~46 ka (*8*). The well-preserved rockshelter sequences in Sri Lanka's tropical forest have yielded some of the earliest microlithic toolkits, bone technologies, evidence for personal ornamentation, and human remains anywhere in South Asia, in direct association with well-preserved floral, faunal, and micromorphological sequences (*12*). The records span from 36 ka through the climatic oscillations of the Last Glacial Maximum (20 ka) and the terminal Pleistocene/Holocene boundary (12 to 8 ka), making them useful for the study of long-term human adaptations to rainforest ecologies. Moreover, the presence on this relatively small island of just three climatic zones, with corresponding vegetation divisions (Fig. 1) (*13*–*15*), makes the assessment of human rainforest specialization an attainable goal.

We applied stable carbon and oxygen isotope analysis to human and faunal tooth enamel from four late Pleistocene/Holocene archaeological sequences (Fig. 1) (*16*) in Sri Lanka to test the extent of prehistoric human reliance on rainforest resources. Stable isotope analysis of faunal tissues in tropical or subtropical regions has frequently been used to assess the proportion of C_3 or C_4 biomass in the diets of early hominins and fauna, based on the distinction between the C_3 or C_4 photosynthetic pathways at the base of tropical food webs (*17*–*20*). In the context of tropical forest ecologies, this distinction can be used to assess the degree of faunal reliance on C_3 forest resources as opposed to C_4 plant resources available in open habitats, with C_4 plants being enriched in ^{13}C relative to C_3 plants (*17*–*19*). This distinction is further enhanced by the "canopy effect," whereby vegetation growing under a closed dense forest canopy is strongly depleted in ^{13}C, due to low light and the presence of large amounts of respired CO_2 (*10*, *21*–*23*). Therefore, the tissues of forest-dwelling animals have more negative $\delta^{13}C$ values than those that spend some or all of their time consuming open-habitat foodstuffs (*22*, *24*, *25*). For instance, Levin *et al.* found a range of −26.0 to −14.1 per mil (‰) for modern faunal enamel in the closed-canopy C_3 Ituri Forest of the Democratic Republic of Congo and a range of −12.0 to 0.2 ‰ for herbivores in open C_3/C_4 grasslands of East Africa (*26*). Stable oxygen isotope measurements from faunal enamel provide additional paleoecological information about water and food (*27*, *28*). It has also been shown that both $\delta^{13}C$ and $\delta^{18}O$ measurements of CO_2, plant tissues, and faunal tissues can track vertical differentiation in forest canopy eco-niches (*10*, *28*). Flora and fauna living on the forest floor, including humans, are exposed to the greatest ^{13}C and ^{18}O canopy depletion (*10*, *28*, *29*).

Tooth enamel samples of a variety of fauna (table S2) and humans (table S3) from the terminal Pleistocene/Holocene deposits (~12,000 to 3000 cal yr B.P.) of Fa Hien-lena, Balangoda Kuragala, and Bellan-bandi Palassa (*16*) (figs. S1 to S3 and table S1) provided a suite of samples that encompass the full climatic and environmental spectrum of the island's modern climate and vegetation zones [Fig. 1; full methods in (*16*)]. Human specimens ~20,000 to 17,000 cal yr B.P. from Batadomba-lena, in association with fauna spanning 20,000 to 12,000 cal yr B.P., provide an earlier record of human rainforest foraging (fig. S4 and tables S1 to S3).

Faunal $\delta^{13}C$ and $\delta^{18}O$ data from the archaeological sequences of Fa Hien-lena (fig. S5), Balangoda Kuragala (fig. S6), and Bellan-bandi Palassa (fig. S7) show that a climatic division of Sri Lanka into a wet zone, intermediate zone, and dry zone, and associated vegetation distributions of closed rainforest, more open intermediate tropical forest, and open grassland conditions (Fig. 1 and table S4), persisted through the terminal Pleistocene and Holocene (Fig. 2A). It is possible that changes in rainforest extent and the exact positions of these boundaries may have occurred during this time (*30*, *31*) but are not visible in our data (table S4). Fauna known to occur in the wet zone rainforests of Sri Lanka today from the deposits of Fa Hien-lena (table S2) have $\delta^{13}C$ values from −17.8 to −13.2 ‰, whereas the mixture of forest-adapted and open-adapted fauna of Balangoda Kuragala and Bellan-bandi Palassa (table S2) have $\delta^{13}C$ ranges of −15.7 to −3.3 ‰ and −14.8 to −9.5 ‰, respectively, indicative of more open forest and open plain conditions. Analysis of variance (ANOVA) testing, followed by post-hoc Tukey HSD-corrected pairwise comparison, indicate that $\delta^{13}C$ from these sites does not form a single population [$F(3, 291) = 48.72$, $P < 0.05$] (table S6), with both Bellan-bandi Palassa and Balangoda Kuragala being statistically different from Fa Hien-lena ($P < 0.05$).

At Balangoda Kuragala, two $\delta^{13}C$ groups are apparent, with ranges of −15.7 to −11.4 ‰ and −9.6 to −3.3 ‰, respectively (Fig. 2 and fig. S6). Whereas the first group, predominantly made up of semiarboreal and ground-dwelling forest mammals [including porcupine (*Hystrix indica*), giant squirrel (*Ratufa macroura*), mouse deer (*Moschiola meminna*), and two monkey species (*Macaca sinica* and *Semnopithecus entellus priam*)] is representative of modern intermediate rainforest fauna, *Elephas* sp., cervids, suids, and hare (*Lepus nigricollis*) from the latter group have $\delta^{13}C$ associated with open conditions (table S4).

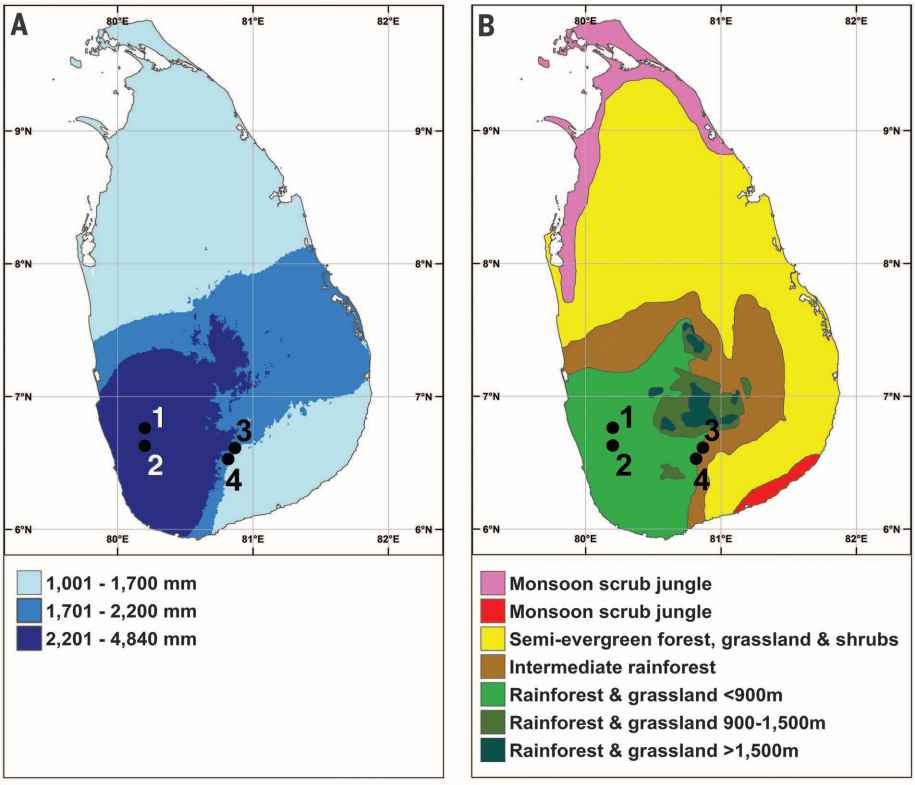

Fig. 1. Archaeological sites sampled. 1, Batadomba-lena; 2, Fa Hien-lena; 3, Balangoda Kuragala; and 4, Bellan-bandi Palassa, located on precipitation and vegetation maps of Sri Lanka. (**A**) Annual precipitation data from Worldclim 1.3. (*37*) divided into three categories on the basis of natural breaks (Jenks natural breaks optimization), showing the division of Sri Lanka into wet, intermediate, and dry zones. (**B**) Vegetation zones are based on Ashton and Gunatilleke (*13*) and Erdelen (*14*).

Past conditions at Balangoda Kuragala were therefore similar to the division of intermediate rainforest and open grassland that is visible at the site today (*11*) (Fig. 1). The $\delta^{13}C$ of Bellan-bandi Palassa fauna is indistinguishable from that of the forest faunal group of Balangoda Kuragala, which is demonstrative of intermediate forest at this locality in the past (table S6). Our data show that $\delta^{13}C$ provides the best indicator of forest coverage experienced by human and faunal populations, although the open Balangoda Kuragala fauna also have $\delta^{18}O$ values toward the top of that site's range of –7.8 to –3.3 ‰, indicative of open evaporative sources of drinking water (Fig. 2A and fig S6).

Faunal isotopic differences between sites and their inferred ecologies were used to determine the long-term ecological niches of terminal Pleistocene/Holocene human foragers in Sri Lanka. $\delta^{13}C$ and $\delta^{18}O$ of human tooth enamel from Fa Hien-lena and Balangoda Kuragala plot directly over the forest faunal isotopic niches at these sites (Fig. 2B, figs. S5 and S6, and table S5). *t* tests show the $\delta^{13}C$ and $\delta^{18}O$ of human and faunal enamel to be indistinguishable at both sites ($P < 0.05$, tables S8 and S9). On the basis of faunal isotope data (Fig. 2A), the Fa Hien-lena human ($\delta^{13}C$ = –14.9 ‰, $\delta^{18}O$ = –5.8 ‰), dated to ~12,000 cal yr B.P., occupied either closed wet zone rainforest environments or more open intermediate rainforest. The same is true of the Balangoda Kuragala human specimens dated to between 12,000 and 4000 cal yr B.P., although there is a distinct preference for intermediate tropical forest (Fig. 2B). The group of open grassland fauna at Balangoda Kuragala did not contribute significantly to terminal Pleistocene/early Holocene human subsistence at either site. Two Balangoda Kuragala human individuals with $\delta^{13}C$ values of –5.0 and –4.3 ‰, respectively, are from layers dated to ~3000 cal yr B.P., a point by which forests are likely to have opened in the region as a result of agricultural clearance (*32*), and are included here to show that humans occupied more-open habitats in later periods.

$\delta^{13}C$ and $\delta^{18}O$ values from characteristic forest fauna (tables S2 and S4 and fig. S8) at the wet zone site of Batadomba-lena, spanning the earlier period of 20,000 to 12,000 cal yr B.P., plot between the closed wet zone rainforest and intermediate rainforest fauna of Fa Hien-lena and Balangoda Kuragala (Fig. 2C), suggesting that wet zone rainforest was more open during the Last Glacial Maximum than during the terminal Pleistocene/early Holocene. This is supported by ANOVA and pairwise comparison of faunal $\delta^{13}C$ values demonstrating that Batadomba-lena differs from both Fa Hien-lena and Balangoda Kuragala [$F(3, 291) = 48.72$, $P < 0.05$] (table S6). Faunal $\delta^{18}O$ from Batadomba-lena is indistinguishable from faunal $\delta^{18}O$ at Fa Hien-lena and Balangoda Kuragala [$F(3, 291) = 9.95$, $P < 0.05$] (table S7). Human $\delta^{13}C$ and $\delta^{18}O$ values from Batadomba-lena deposits dated to ~20,000 to 17,000 cal yr B.P. (Fig. 2C and table S5) are indistinguishable from those of humans from Balangoda Kuragala and Fa Hien-lena [$F(2, 23) = 0.66$, $P < 0.05$] [$F(2, 23) = 0.85$, $P < 0.05$, tables S11 and S12]. These observations indicate that preferential foraging in the intermediate rainforest extended back into the late Pleistocene.

Our data from stable carbon and oxygen isotopes allow us to directly assess the degree and longevity of prehistoric human reliance on rainforest resources. Although terminal Pleistocene/Holocene human specimens from Fa Hien-lena and Balangoda Kuragala could have occupied closed wet zone rainforest, the majority of humans from this period, and those dated to ~20,000 cal yr B.P. at Batadomba-lena, have $\delta^{13}C$ and $\delta^{18}O$ values indicative of long-term subsistence concentration and habitation in more-open intermediate tropical forests and forest fringe environments (Fig. 1). No late Pleistocene or early Holocene human specimen has an isotopic composition resembling that of the open group found at Balangoda Kuragala. This suggests that, contrary to earlier arguments (*3*, *4*), Sri Lankan human foragers concentrated on the exploitation of forest environments rather than using them as part of more-diverse seasonal subsistence strategies, which would have resulted in much greater $\delta^{13}C$ enrichment, akin to that in two Iron Age human specimens from Balangoda Kuragala.

The stability of Sri Lankan tropical forest environments for human foragers is indicated by the early and ongoing presence of microlithic toolkits, bone technologies, and personal ornamentation evidenced at sites in Sri Lanka's wet zone and intermediate zone forests from 36,000 cal yr B.P. through the Last Glacial Maximum and terminal Pleistocene/Holocene transition, until the Iron Age, ~3000 cal yr B.P. (*11*, *12*, *33*). Faunal isotopic data from Batadomba-lena indicate that wet zone tropical forest was more similar to that of the modern-day intermediate zone during the Last Glacial Maximum. The opening

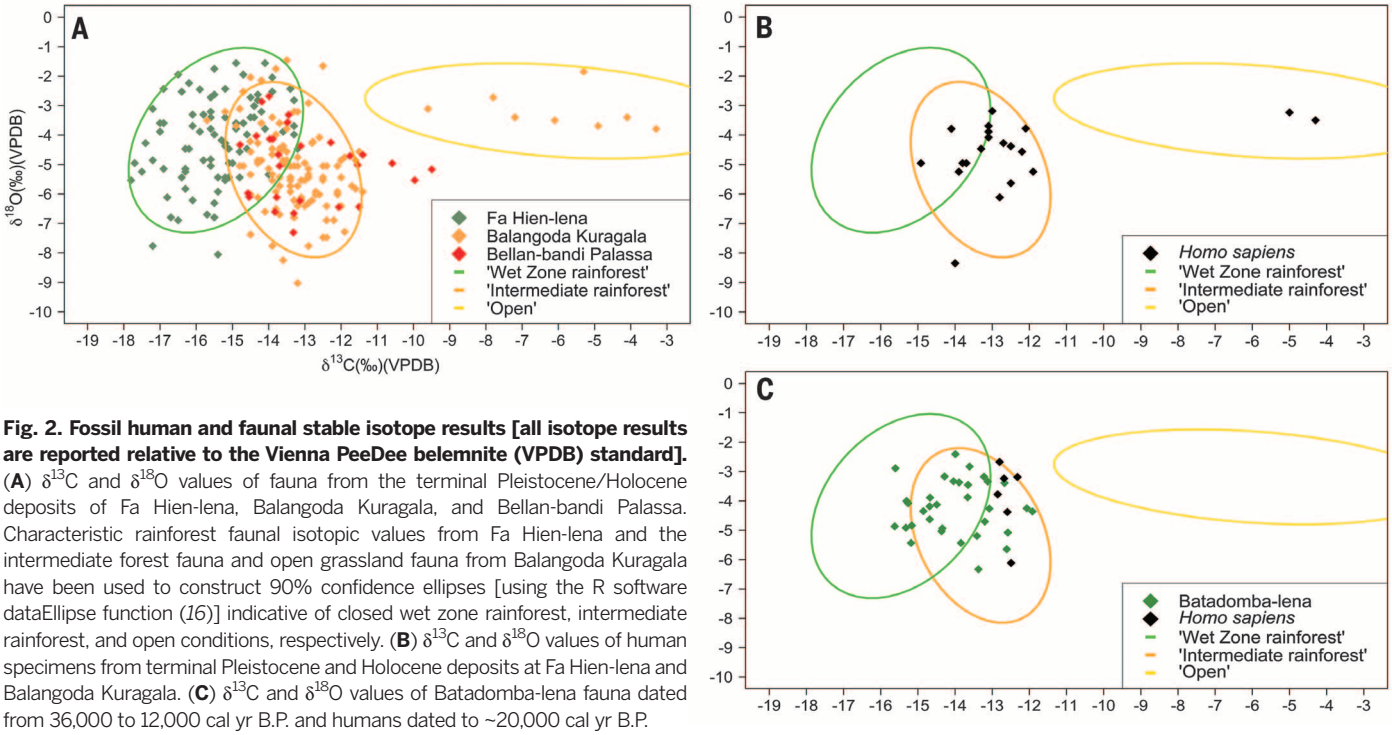

Fig. 2. Fossil human and faunal stable isotope results [all isotope results are reported relative to the Vienna PeeDee belemnite (VPDB) standard]. (**A**) $\delta^{13}C$ and $\delta^{18}O$ values of fauna from the terminal Pleistocene/Holocene deposits of Fa Hien-lena, Balangoda Kuragala, and Bellan-bandi Palassa. Characteristic rainforest faunal isotopic values from Fa Hien-lena and the intermediate forest fauna and open grassland fauna from Balangoda Kuragala have been used to construct 90% confidence ellipses [using the R software dataEllipse function (*16*)] indicative of closed wet zone rainforest, intermediate rainforest, and open conditions, respectively. (**B**) $\delta^{13}C$ and $\delta^{18}O$ values of human specimens from terminal Pleistocene and Holocene deposits at Fa Hien-lena and Balangoda Kuragala. (**C**) $\delta^{13}C$ and $\delta^{18}O$ values of Batadomba-lena fauna dated from 36,000 to 12,000 cal yr B.P. and humans dated to ~20,000 cal yr B.P.

of tropical forests has also been documented elsewhere at this time (*34*–*36*). However, despite potential fluctuations in the extent and productivity of Sri Lankan tropical forests associated with these climatic changes, late Pleistocene human foragers maintained a reliance on intermediate rainforest and tropical forest fringes. Therefore, rainforests in South Asia have clearly long provided diverse and stable resources relied upon by humans for at least the past 20,000 years.

REFERENCES AND NOTES

1. N. Boivin, D. Q. Fuller, R. Dennell, R. Allaby, M. D. Petraglia, *Quat. Int.* **300**, 32–47 (2013).
2. P. R. Nigst *et al.*, *Proc. Natl. Acad. Sci. U.S.A.* **111**, 14394–14399 (2014).
3. K. L. Hutterer, *Anthropos* **78**, 169 (1983).
4. R. Bailey *et al.*, *Am. Anthropol.* **91**, 59–82 (1989).
5. S. Bahuchet, D. McKey, I. de Garine, *Hum. Ecol.* **19**, 213–243 (1991).
6. P. A. Colinvaux, M. B. Bush, *Am. Anthropol.* **93**, 153–160 (1991).
7. J. Mercader, *Evol. Anthropol.* **11**, 117–124 (2002).
8. G. Barker *et al.*, *J. Hum. Evol.* **52**, 243–261 (2007).
9. G. R. Summerhayes *et al.*, *Science* **330**, 78–81 (2010).
10. N. J. van der Merwe, E. Medina, *J. Archaeol. Sci.* **18**, 249–259 (1991).
11. S. U. Deraniyagala, *The Prehistory of Sri Lanka: An Ecological Perspective* (Department of Archaeological Survey, Colombo, Sri Lanka, ed. 2, 1992).
12. N. Perera *et al.*, *J. Hum. Evol.* **61**, 254–269 (2011).
13. P. S. Ashton, C. V. S. Gunatilleke, *J. Biogeogr.* **14**, 249 (1987).
14. W. Erdelen, *Biol. Conserv.* **43**, 115–135 (1988).
15. K. M. Puvaneswaran, P. A. Smithson, *Theor. Appl. Climatol.* **47**, 105–115 (1993).
16. Materials and methods are available as supplementary materials on *Science* Online.
17. J. Lee-Thorp, J. F. Thackeray, N. van der Merwe, *J. Hum. Evol.* **39**, 565–576 (2000).
18. T. D. White *et al.*, *Science* **326**, 75–86 (2009).
19. T. E. Cerling *et al.*, *Proc. Natl. Acad. Sci. U.S.A.* **108**, 9337–9341 (2011).
20. M. Sponheimer *et al.*, *Proc. Natl. Acad. Sci. U.S.A.* **110**, 10513–10518 (2013).
21. N. J. van der Merwe, E. Medina, *Geochim. Cosmochim. Acta* **53**, 1091–1094 (1989).
22. T. E. Cerling, J. A. Hart, T. B. Hart, *Oecologia* **138**, 5–12 (2004).
23. G. D. Farquhar, J. R. Ehleringer, K. T. Hubick, *Annu. Rev. Plant Physiol.* **40**, 503–537 (1989).
24. V. M. Oelze, J. S. Head, M. M. Robbins, M. Richards, C. Boesch, *J. Hum. Evol.* **66**, 95–106 (2014).
25. G. A. Macho, J. A. Lee-Thorp, *PLOS ONE* **9**, e102794 (2014).
26. N. E. Levin *et al.*, in *The Geology of Early Humans in the Horn of Africa, Geological Society of America Special Paper 446*, J. Quade, J. G. Wynn, Eds., (Geological Society of America, Boulder, CO, 2008), pp. 215–234.
27. P. L. Koch, in *Stable Isotopes in Ecological and Environmental Science*, B. Michener, K. Lajtha, Eds. (Blackwell, Boston, MA, 2007), pp. 99–154.
28. J. Krigbaum, M. H. Berger, D. J. Daegling, W. S. McGraw, *Biol. Lett.* **9**, 20130466 (2013).
29. J. Krigbaum, *J. Anthropol. Archaeol.* **22**, 292–304 (2003).
30. M. Servant *et al.*, *Global Planet. Change* **7**, 25–40 (1993).
31. J. Mercader *et al.*, *Quat. Res.* **54**, 102–112 (2000).
32. S. U. Deraniyagala, in *The Art and Archaeology of Sri Lanka, 1*, P. L. Prematilleke, S. Bandaranayake, S. U. Deraniyagala, R. Silva, Eds. (Central Cultural Fund, Colombo, Sri Lanka, 2007), pp. 1–96.
33. N. Perera, *Prehistoric Sri Lanka: Late Pleistocene Rockshelters and an Open Air Site* (BAR International Series, Archaeopress, Oxford, 2010).
34. S. Levis, J. A. Foley, D. Pollard, *J. Geophys. Res. Atmos.* **104**, 31191 (1999).
35. L. G. Thompson, E. Mosley-Thompson, K. A. Henderson, *J. Quat. Sci.* **15**, 377–394 (2000).
36. G. Yu *et al.*, *J. Biogeogr.* **27**, 635–664 (2000).
37. R. J. Hijmans, S. E. Cameron, J. L. Parra, P. G. Jones, A. Jarvis, *Int. J. Climatol.* **25**, 1965–1978 (2005).

ACKNOWLEDGMENTS

The authors declare no conflicts of interest. This project was funded by grants from the Natural Environmental Research Council; the European Research Council (grant no. 295719 to M.D.P.); and the Boise Fund, University of Oxford. We thank the members of Excavation Branch of the Department of Archeology, Government of Sri Lanka, for their assistance with faunal, stratigraphic, and chronological information. We also thank P. Mitchell for his comments on an earlier draft of this paper as well as E. Nitsch and J. Pouncett for their help with the R statistical package and GIS software, respectively. Fossil faunal and human samples are stored by the Department of Archeology, Government of Sri Lanka. Stable carbon and oxygen isotope data, site stratigraphies, and site chronologies are all available in the supplementary materials.

SUPPLEMENTARY MATERIALS

www.sciencemag.org/content/347/6227/1246/suppl/DC1
Text S1 to S3
Figs. S1 to S8
Tables S1 to S12
References (*38*–*55*)

28 October 2014; accepted 6 February 2015
10.1126/science.aaa1230

PROTEIN STABILITY

Control of mammalian G protein signaling by N-terminal acetylation and the N-end rule pathway

Sang-Eun Park,[1]* Jeong-Mok Kim,[1]* Ok-Hee Seok,[1] Hanna Cho,[1] Brandon Wadas,[2] Seon-Young Kim,[3,4] Alexander Varshavsky,[2]† Cheol-Sang Hwang[1]†

Rgs2, a regulator of G proteins, lowers blood pressure by decreasing signaling through $G\alpha_q$. Human patients expressing Met-Leu-Rgs2 (ML-Rgs2) or Met-Arg-Rgs2 (MR-Rgs2) are hypertensive relative to people expressing wild-type Met-Gln-Rgs2 (MQ-Rgs2). We found that wild-type MQ-Rgs2 and its mutant, MR-Rgs2, were destroyed by the Ac/N-end rule pathway, which recognizes N^{α}-terminally acetylated (Nt-acetylated) proteins. The shortest-lived mutant, ML-Rgs2, was targeted by both the Ac/N-end rule and Arg/N-end rule pathways. The latter pathway recognizes unacetylated N-terminal residues. Thus, the Nt-acetylated Ac-MX-Rgs2 (X = Arg, Gln, Leu) proteins are specific substrates of the mammalian Ac/N-end rule pathway. Furthermore, the Ac/N-degron of Ac-MQ-Rgs2 was conditional, and Teb4, an endoplasmic reticulum (ER) membrane-embedded ubiquitin ligase, was able to regulate G protein signaling by targeting Ac-MX-Rgs2 proteins for degradation through their N^{α}-terminal acetyl group.

Regulators of G protein signaling (RGSs) bind to specific Gα subunits of heterotrimeric G proteins (Gαβγ) and accelerate the hydrolysis of Gα-bound guanosine triphosphate, thereby abrogating the signaling by G proteins (*1*–*4*). The mammalian Rgs2 protein regulates stress responses, translation, circadian rhythms, Ca^{2+} channels, specific hormones, and cardiovascular homeostasis (*3*–*10*). Blood pressure–increasing vasoconstrictors such as norepinephrine and angiotensin II are up-regulated by activated $G\alpha_q$ proteins, which are deactivated by Rgs2 (*7*). Both *Rgs2*$^{-/-}$ and heterozygous *Rgs2*$^{+/-}$ mice are strongly hypertensive (*8*, *9*). Human patients with decreased Rgs2 signaling are hypertensive as well (*10*).

In some hypertensive patients, one of two *Rgs2* genes encodes Met-Leu-Rgs2 (ML-Rgs2), in which Gln at position 2 of wild-type Met-Gln-Rgs2 (MQ-Rgs2) is replaced by Leu. Another hypertension-associated Rgs2 mutant is Met-Arg-Rgs2 (MR-Rgs2) (*10*). The Gln → Leu and Gln → Arg mutations are not detected in the general population (*10*). All three Rgs2 proteins are up-regulated by a proteasome inhibitor, which suggests that they may be targeted by a proteasome-dependent proteolytic system (*11*).

The N-end rule pathway recognizes proteins containing N-terminal (Nt) degradation signals called N-degrons, polyubiquitylates these proteins, and thereby causes their degradation by the proteasome (fig. S1) (*12*–*20*). The main determinant of an N-degron is a destabilizing Nt residue of a protein. Recognition components of the N-end rule pathway, called N-recognins, are E3 ubiquitin ligases that can target N-degrons. Regulated degradation of proteins by the N-end rule

[1]Department of Life Sciences, Pohang University of Science and Technology, Pohang, Gyeongbuk 790-784, South Korea. [2]Division of Biology and Biological Engineering, California Institute of Technology, Pasadena, CA 91125, USA. [3]Medical Genomics Research Center, KRIBB, Daejeon, South Korea. [4]Department of Functional Genomics, University of Science and Technology, Daejeon, South Korea.
*These authors contributed equally to this work. **†Corresponding author. E-mail: cshwang@postech.ac.kr (C.-S.H.); avarsh@caltech.edu (A.V.)**

pathway mediates a broad range of biological functions (fig. S1) (*12*–*20*).

The N-end rule pathway consists of two branches. One branch, the Arg/N-end rule pathway, targets unacetylated destabilizing Nt residues (*12*, *14*, *16*). The Nt residues Arg, Lys, His, Leu, Phe, Tyr, Trp, and Ile, as well as Nt-Met [if it is followed by a bulky hydrophobic (Φ) residue], are directly recognized by N-recognins (*16*). In contrast, the unacetylated Asn, Gln, Asp, and Glu (as well as Cys, under some conditions) Nt residues are destabilizing, owing to their preliminary enzymatic modifications (fig. S1D).

The pathway's other branch, called the Ac/N-end rule pathway, targets proteins through their N^{α}-terminally acetylated (Nt-acetylated) residues (fig. S1, A and C) (*13*, *15*, *16*). Degrons and E3 ubiquitin ligases of the Ac/N-end rule pathway are called Ac/N-degrons and Ac/N-recognins, respectively. Approximately 90% of human proteins are cotranslationally and irreversibly Nt-acetylated by ribosome-associated Nt-acetylases (*21*, *22*). (In contrast, acetylation of internal Lys residues is reversible and largely posttranslational.) Doa10, an ER membrane-embedded E3 ubiquitin ligase of the yeast *Saccharomyces cerevisiae* (*23*, *24*), functions as an Ac/N-recognin (*13*). Not4, a cytosolic and nuclear E3, is another yeast Ac/N-recognin (*15*).

The Arg/N-end rule pathway is present in all examined eukaryotes, from fungi to mammals and plants (fig. S1D) (*12*, *18*, *19*). In contrast, the Ac/N-end rule pathway (fig. S1C) has been identified in *S. cerevisiae* (*13*, *15*, *16*), but its presence in mammals and other multicellular eukaryotes has been conjectural so far.

We began by subjecting wild-type human MQ-Rgs2 and its ML-Rgs2 mutant to cycloheximide (CHX) chases in yeast (*13*, *15*, *16*). The C-terminally HA (hemagglutinin)–tagged MQ-$Rgs2_{ha}$ was short-lived ($t_{1/2} \approx 30$ min) in wild-type yeast and was stabilized in both *naa20*Δ and *doa10*Δ cells, which lacked, respectively, the cognate NatB Nt-acetylase and the Doa10 Ac/N-recognin (*13*) (Fig. 1, A and C, and figs. S1C and S2). Thus, in yeast, wild-type MQ-$Rgs2_{ha}$ was degraded largely by the Ac/N-end rule pathway (*13*, *15*, *16*).

The mutant human ML-$Rgs2_{ha}$ was also short-lived in wild-type *S. cerevisiae* ($t_{1/2} < 15$ min) and was partially stabilized in both *naa30*Δ and *ubr1*Δ cells, which lacked, respectively, the cognate NatC Nt-acetylase and the Ubr1 N-recognin of the Arg/N-end rule pathway (Fig. 1, B and D, and figs. S1C, S2, and S3, A and D). ML-$Rgs2_{ha}$ was nearly completely stabilized in double-mutant *naa30*Δ *ubr1*Δ cells, including strongly elevated time-zero (pre-chase) levels of ML-$Rgs2_{ha}$ (Fig. 1, B and D, and fig. S3, A and D).

Many cellular proteins are partially Nt-acetylated (*21*). Non–Nt-acetylated yeast MΦ-type proteins are eliminated by the Arg/N-end rule pathway, whereas the Nt-acetylated counterparts of these proteins are destroyed by the Ac/N-end rule pathway (*15*, *16*). This dual-targeting pattern was also observed with human ML-$Rgs2_{ha}$ (Fig. 1, B and D, and fig. S3, A and D). The contribution of the Ubr1 N-recognin to the degradation of ML-$Rgs2_{ha}$ (Fig. 1B and fig. S3A) indicated its incomplete Nt-acetylation in *S. cerevisiae*, similarly to results with natural MΦ-type yeast proteins (*15*, *16*). Both wild-type MQ-Rgs2 and the second hypertension-associated mutant MR-Rgs2 were targeted (after their Nt-acetylation) solely by the Ac/N-end rule pathway, because the unacetylated Nt-Met followed by a non-Φ residue such as Gln or Arg is not recognized by the Arg/N-end rule pathway (in contrast to an MΦ-type protein such as ML-$Rgs2_{ha}$) (fig. S1D) (*16*).

Wild-type MQ-Rgs2 is a predicted substrate of the NatB Nt-acetylase (fig. S2), in agreement with stabilization of MQ-$Rgs2_{ha}$ in *naa20*Δ *S. cerevisiae*, which lack NatB (Fig. 1, A and C). Using mass spectrometry (*13*), we analyzed the MQ-Rgs2 protein from human embryonic kidney (HEK) 293 cells, confirming its Nt-acetylation (fig. S5A).

Considerably unequal levels of transiently expressed MQ-$Rgs2_{ha}$, MR-$Rgs2_{ha}$, and ML-$Rgs2_{ha}$ in human HeLa cells suggested their different stabilities (MQ > MR > ML) in these cells—an interpretation consistent with near-equal levels of the corresponding *MX-Rgs2* mRNAs (fig. S4, C, F, and G). Indeed, CHX chases in HeLa

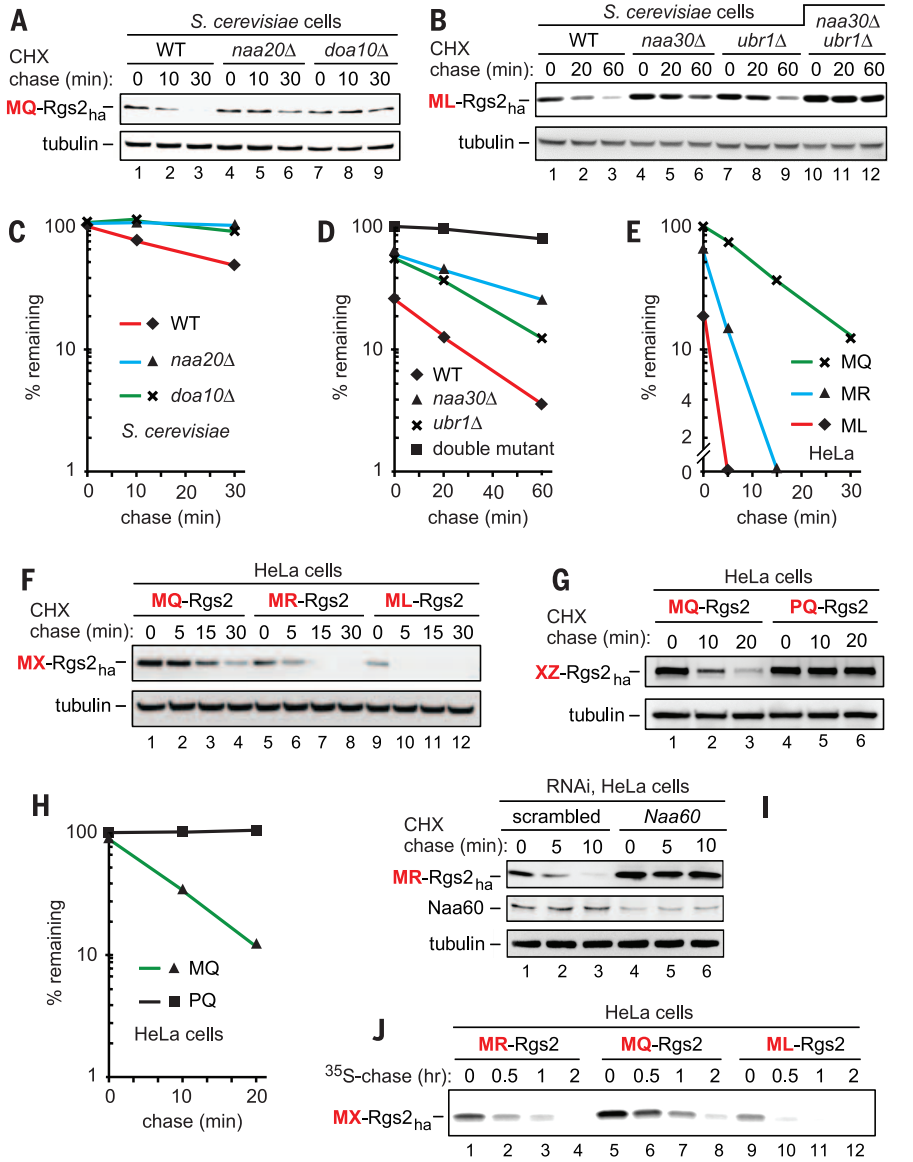

Fig. 1. Rgs2 as an N-end rule substrate. (**A**) CHX chases with wild-type human MQ-$Rgs2_{ha}$ in wild-type, *naa20*Δ, and *doa10*Δ *S. cerevisiae*. (**B**) As in (A) but with ML-$Rgs2_{ha}$ in wild-type, *naa30*Δ, *ubr1*Δ, and *naa30*Δ *ubr1*Δ strains. (**C** to **E**) Quantification of data in (A), (B), and (F), respectively. See the legend to fig. S3 for definitions of "100%" levels at zero time. (**F**) CHX chases with exogenously expressed MX-$Rgs2_{ha}$ (X = Arg, Gln, Leu) in HeLa cells. (**G**) As in (F) but with MQ-$Rgs2_{ha}$ versus PQ-$Rgs2_{ha}$. (**H**) Quantification of data in (G). (**I**) CHX chases with exogenously expressed MR-Rgs2 in HeLa cells subjected to RNAi for a either a "scrambled" target or Naa60. (**J**) ^{35}S-pulse chases with MX-$Rgs2_{ha}$ (X = Arg, Gln, Leu) in HeLa cells.

cells showed that MR-Rgs2$_{ha}$ ($t_{1/2}$ < 8 min) and ML-Rgs2$_{ha}$ ($t_{1/2}$ < 5 min) were shorter-lived than the also unstable wild-type MQ-Rgs2$_{ha}$ ($t_{1/2}$ ≈ 15 min) (Fig. 1, E and F, and fig. S3, B and E). The same (MQ > MR > ML) order of degradation rates was observed in ^{35}S pulse chases of MQ-Rgs2$_{ha}$, MR-Rgs2$_{ha}$, and ML-Rgs2$_{ha}$ (Fig. 1J and fig. S4J).

In contrast to Nt-acetylatable (and therefore short-lived) wild-type MQ-Rgs2$_{ha}$, the otherwise identical PQ-Rgs2$_{ha}$ (Pro-Gln-Rgs2$_{ha}$), generated cotranslationally from MPQ-Rgs2$_{ha}$, was neither Nt-acetylated nor recognized by the Arg/N-end rule pathway (figs. S1 and S2). PQ-Rgs2$_{ha}$ was long-lived in HeLa cells (Fig. 1, G and H). This result was an additional, conceptually independent piece of evidence for the targeting of Ac-MQ-Rgs2$_{ha}$ by the Ac/N-end rule pathway (fig. S1C).

Remarkably, the exogenous (overexpressed) wild-type MQ-Rgs2$_{ha}$ was much shorter-lived ($t_{1/2}$ ≈ 15 min) than the endogenous MQ-Rgs2 ($t_{1/2}$ ≈ 3 hours) in HeLa cells that did not overexpress MQ-Rgs2$_{ha}$ (Fig. 1, E and F, Fig. 2B, and figs. S3, B and E, and S4, A and B). These results, with human cells, agreed with the recent demonstration of the biologically relevant conditionality of *S. cerevisiae* Ac/N-degrons (through their steric shielding in cognate protein complexes) (*15*). Given this understanding with natural Ac/N-end rule substrates in yeast (*15*, *16*, *25*), the present results (fig. S4, A and B) are what one would expect if Ac-MQ-Rgs2, in human cells that do not overexpress it, can be (reversibly) shielded from the Ac/N-end rule pathway soon after Nt-acetylation of MQ-Rgs2. This shielding would occur through formation of one or more physiologically relevant protective complexes between Ac-MQ-Rgs2 and its protein ligand(s). In contrast to the long half-life of the endogenous, "stoichiometrically" expressed MQ-Rgs2, its overexpression in HeLa cells would make the resulting "unprotectable" excess of Ac-MQ-Rgs2$_{ha}$ molecules vulnerable to destruction by the Ac/N-end rule pathway, thereby accounting for the large difference between the slowly degraded endogenous MQ-Rgs2 (in cells that do not overexpress MQ-Rgs2) and the short half-life of overexpressed MQ-Rgs2$_{ha}$ (fig. S4, A and B). Indeed, the short-lived MQ-Rgs2 was strongly stabilized by co-overexpression of one of its binding partners, the Gα_q protein (Fig. 3, A and B).

A candidate Ac/N-recognin of the mammalian Ac/N-end rule pathway was Teb4, an ER membrane–embedded E3 ubiquitin ligase that polyubiquitylates proteins retrotranslocated from the ER. Teb4 is similar to the *S. cerevisiae* Doa10 Ac/N-recognin (*13*, *23*, *24*). We found that human Teb4 was indeed an Ac/N-recognin:

1) Transiently expressed MQ-Rgs2$_{ha}$ was upregulated by a proteasome inhibitor, whereas coexpression of human Teb4 (Teb4$_{3f}$) and MQ-Rgs2$_{ha}$ in HeLa cells down-regulated MQ-Rgs2$_{ha}$ (Fig. 2, A and F). In addition, incrementally higher levels of Teb4$_{3f}$ resulted in incrementally lower levels of endogenous MQ-Rgs2 (Fig. 2G).

2) The level of MQ-Rgs2$_{ha}$ in HeLa cells was not decreased when MQ-Rgs2$_{ha}$ was coexpressed with Teb4$^{C9A}_{3f}$, a missense mutant that is inactive as a ubiquitin ligase (*24*) (Fig. 2F). Analogous assays with MR-Rgs2$_{ha}$ and ML-Rgs2$_{ha}$ gave similar results (fig. S4, D and E).

3) The in vivo polyubiquitylation of MQ-Rgs2$_{ha}$ in HeLa cells was increased by coexpression of Teb4$_{3f}$, but not by coexpression of the mutant Teb4$^{C9A}_{3f}$ (fig. S3F).

4) In CHX chases, endogenous MQ-Rgs2 was stabilized by RNA interference (RNAi)–mediated knockdowns of either endogenous Teb4 E3 or endogenous cognate NatB Nt-acetylase (Fig. 2B and fig. S4A). Similar results were obtained with exogenous (overexpressed) MQ-Rgs2$_{ha}$, confirming the targeting of MQ-Rgs2 by Teb4 and indicating that this targeting required Nt-acetylation of MQ-Rgs2 by the NatB Nt-acetylase (Fig. 2B and fig. S4, A and B). In addition, overexpressed (hypertension-associated) MR-Rgs2$_{ha}$ as well as the engineered MK-Rgs2$_{ha}$ (which has a different basic residue at position 2) were stabilized by RNAi-based knockdown of Naa60, the catalytic subunit of cognate NatF Nt-acetylase (*21*, *22*), but these MX-Rgs2$_{ha}$ proteins were not stabilized by knockdown of the noncognate NatB (Naa20) Nt-acetylase (Fig. 1I and fig. S4, H and I).

5) Cross-linking and coimmunoprecipitation experiments indicated that Teb4 interacted with MQ-Rgs2 (more accurately, with Nt-acetylated Ac-MQ-Rgs2$_{ha}$, as shown below) (Fig. 2, H and I).

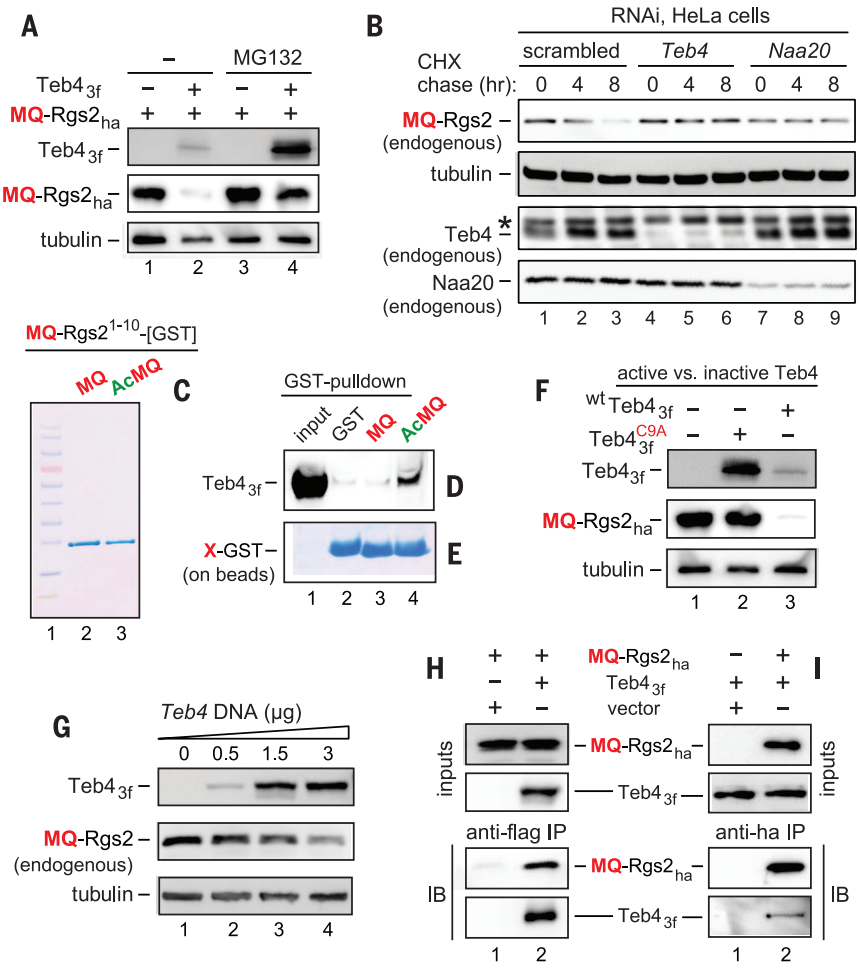

Fig. 2. Teb4 as an Ac/N-recognin. (**A**) MQ-Rgs2$_{ha}$ in HeLa cells with or without Teb4$_{3f}$ or the MG132 proteasome inhibitor. (**B**) CHX chases with endogenous MQ-Rgs2, Teb4, and Naa20 subjected to RNAi for a "scrambled" target, Teb4, or Naa20. The asterisk indicates a protein cross-reacting with anti-Teb4. (**C**) Molecular weight standards, purified MQ-Rgs2$^{1-10}$-GST, and purified Ac-MQ-Rgs2$^{1-10}$-GST, respectively. (**D**) Lane 1, Teb4$_{3f}$ input; lanes 2 to 4, GST pull-downs with GST alone, MQ-Rgs2$^{1-10}$-GST, and Ac-MQ-Rgs2$^{1-10}$-GST, respectively. (**E**) As in (D) but Coomassie-stained GST fusions released from beads. (**F**) MQ-Rgs2$_{ha}$ in HeLa cells overexpressing wild-type Teb4$_{3f}$ or Teb4$^{C9A}_{3f}$. (**G**) Increases in Teb4$_{3f}$ led to decreases in MQ-Rgs2$_{ha}$. (**H**) HeLa cells expressing MQ-Rgs2$_{ha}$ alone (lane 1) or together with Teb4$_{3f}$ (lane 2) were treated with a cell-penetrating cross-linker, followed by immunoprecipitations with anti-FLAG, reversal of cross-links, SDS–polyacrylamide gel electrophoresis (PAGE), and immunoblotting with anti-HA and anti-FLAG. (**I**) As in (H) but Teb4$_{3f}$ alone in lane 1, and immunoprecipitations with anti-HA.

6) PQ-Rgs2$_{ha}$ was neither Nt-acetylated nor recognized by the Arg/N-end rule pathway and was a long-lived protein, in contrast to short-lived MQ-Rgs2$_{ha}$ (Fig. 1, G and H, and fig. S1C). In agreement with these in vivo results, Teb4$_{sf}$ coimmunoprecipitated with MQ-Rgs2$_{ha}$ (Ac-MQ-Rgs2$_{ha}$) but not with PQ-Rgs2$_{ha}$ (Fig. 2, H and I, and fig. S3C).

7) Glutathione *S*-transferase (GST) pull-down assays showed that Teb4$_f$ interacted with Ac-MQ-Rgs2$^{1-10}$-GST (containing the first 10 residues of wild-type human Rgs2) but not with MQ-Rgs2$^{1-10}$-GST or GST alone, indicating that the binding of Teb4 to Ac-MQ-Rgs2$^{1-10}$-GST required its Nt-acetyl group (Fig. 2, C to E, and fig. S5B).

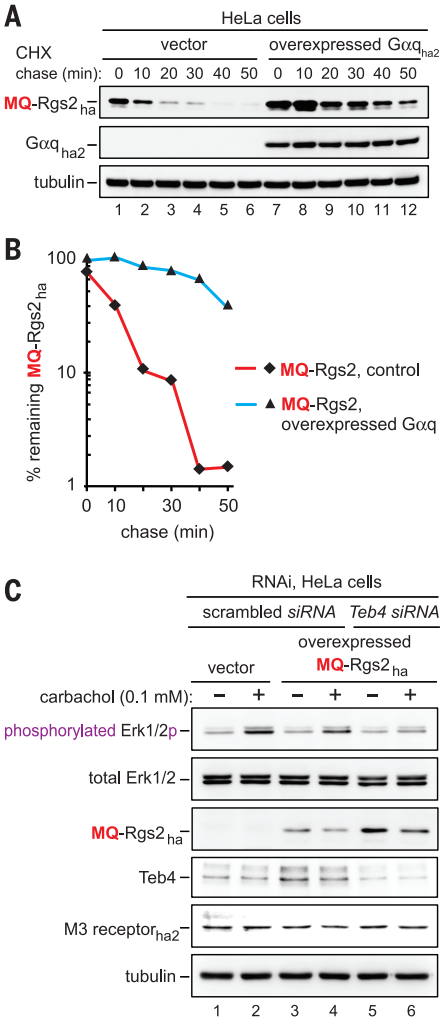

Fig. 3. Gα$_q$ stabilizes Rgs2 while the Teb4-mediated degradation of Rgs2 increases signaling by Gα$_q$. (**A**) CHX chase of MQ-Rgs2$_{ha}$ in HeLa cells that did not express or overexpressed the HA-tagged Gα$_q$. (**B**) Quantification of data in (A). See the legend to fig. S3 for definitions of "100%" levels at zero time. (**C**) HeLa cells were subjected to RNAi either for a "scrambled" target or for Teb4. The M3 receptor was transiently expressed either alone or together with MQ-Rgs2$_{ha}$. The levels of indicated proteins, including the levels of either total Erk1/2 or the activated (specifically phosphorylated) Erk1/2p, were determined by SDS-PAGE and immunoblotting of cell extracts that had been prepared 10 min after treatment of cells with carbachol.

By increasing the rate of deactivation of Gα$_q$, Rgs2 can down-regulate Gα$_q$-activated protein kinases, including the growth-promoting kinase Erk1/2 (*3*, *4*). We asked whether the Teb4 Ac/N-recognin could regulate the activation of Erk1/2 through the degradation of Nt-acetylated Ac-MQ-Rgs2. The Gα$_q$-coupled M3 acetylcholine receptor was expressed in HeLa cells either alone or together with MQ-Rgs2$_{ha}$. By activating the M3 receptor–coupled Gα$_q$, the agonist carbachol strongly increased the level of activated Erk1/2 [measured by detecting its phosphorylation by the "upstream" Mek1/Mek2 kinases (*3*, *4*)]. As predicted by the model in which the Teb4-Rgs2 circuit regulates the activation of Erk1/2, this effect of carbachol on Erk1/2 was decreased in cells that also expressed MQ-Rgs2$_{ha}$ and was further diminished upon RNAi-mediated knockdown of Teb4—a change that stabilized MQ-Rgs2$_{ha}$ and thereby further elevated its level (Fig. 3C).

Thus, wild-type human Ac-MQ-Rgs2, its hypertension-associated natural mutants Ac-ML-Rgs2 and Ac-MR-Rgs2, and its engineered mutant Ac-MK-Rgs2 are conditionally short-lived physiological substrates of the mammalian Ac/N-end rule pathway, and the Teb4 ubiquitin ligase acts as an Ac/N-recognin of this pathway. Teb4 promotes G protein signaling by destroying the Ac-MX-Rgs2 proteins (X = Arg, Gln, Leu), which are targeted for degradation through their N$^{\alpha}$-terminal acetyl group. The faster degradation of ML-Rgs2 and MR-Rgs2 (relative to wild-type MQ-Rgs2) and their consequently lower levels can account, at least in part, for the hypertensive phenotypes of these mutants. The resulting understanding of Rgs2 with respect to the N-end rule pathway is summarized in fig. S6.

Identification of Teb4 as an Ac/N-recognin of the mammalian Ac/N-end rule pathway suggests that some previously characterized substrates of Teb4, including specific transmembrane proteins [(*23*, *24*, *26*) and references therein], may be recognized by Teb4 at least in part though their Nt-acetylated Nt residues (Ac/N-degrons)—a testable proposition.

More than 30 human proteins contain an RGS-type domain (fig. S7) (*3*, *4*). The N-terminal Cys residue, a common feature of Rgs4, Rgs5, and Rgs16, can be oxidized in vivo by nitric oxide (NO) and oxygen. The resulting Nt-arginylation of oxidized Cys and the ensuing degradation of these RGSs by the Arg/N-end rule pathway mediate its previously described function as a sensor of NO and oxygen (fig. S1D) [reviewed in (*12*, *18*, *19*)]. Our study identified Rgs2 (MQ-Rgs2) as a different kind of N-end rule substrate, an Nt-acetylated one. Given their inferred N-terminal sequences, it is possible, indeed likely, that a number of other mammalian RGS proteins (in addition to Rgs2, Rgs4, Rgs5, and Rgs16) may also prove to be substrates of either the Ac/N-end rule pathway or the Arg/N-end rule pathway, or both of these proteolytic systems (fig. S7).

Many cellular proteins contain Ac/N-degrons, having acquired them during synthesis (*13*). These degradation signals, recognized by the Ac/N-end rule pathway, tend to be conditional, owing to their shielding in cognate protein complexes (*15*). In addition, the Ac/N-end rule pathway and the Arg/N-end rule pathway are functionally complementary (*16*). It could therefore be possible to control the levels (and thus the activities) of many different proteins therapeutically, including Rgs2 and other RGSs, by modulating their Ac/N-degrons or specific components of the Ac/N-end rule pathway.

REFERENCES AND NOTES

1. R. J. Lefkowitz, *Angew. Chem. Int. Ed.* **52**, 6366–6378 (2013).
2. B. Kobilka, *Angew. Chem. Int. Ed.* **52**, 6380–6388 (2013).
3. B. Sjögren, L. L. Blazer, R. R. Neubig, *Prog. Mol. Biol. Transl. Sci.* **91**, 81–119 (2010).
4. A. J. Kimple, D. E. Bosch, P. M. Giguère, D. P. Siderovski, *Pharmacol. Rev.* **63**, 728–749 (2011).
5. P. Chidiac, A. J. Sobiesiak, K. N. Lee, R. Gros, C. H. Nguyen, *Cell. Signal.* **26**, 1226–1234 (2014).
6. M. Matsuo, S. L. Coon, D. C. Klein, *FEBS Lett.* **587**, 1392–1398 (2013).
7. M. R. Nance *et al.*, *Structure* **21**, 438–448 (2013).
8. K. M. Tang *et al.*, *Nat. Med.* **9**, 1506–1512 (2003).
9. S. P. Heximer *et al.*, *J. Clin. Invest.* **111**, 445–452 (2003).
10. J. Yang *et al.*, *J. Hypertens.* **23**, 1497–1505 (2005).
11. J. Bodenstein, R. K. Sunahara, R. R. Neubig, *Mol. Pharmacol.* **71**, 1040–1050 (2007).
12. A. Varshavsky, *Protein Sci.* **20**, 1298–1345 (2011).
13. C.-S. Hwang, A. Shemorry, A. Varshavsky, *Science* **327**, 973–977 (2010).
14. C.-S. Hwang, A. Shemorry, D. Auerbach, A. Varshavsky, *Nat. Cell Biol.* **12**, 1177–1185 (2010).
15. A. Shemorry, C.-S. Hwang, A. Varshavsky, *Mol. Cell* **50**, 540–551 (2013).
16. H.-K. Kim *et al.*, *Cell* **156**, 158–169 (2014).
17. J. M. Kim, C. S. Hwang, *Cell Cycle* **13**, 1366–1367 (2014).
18. T. Tasaki, S. M. Sriram, K. S. Park, Y. T. Kwon, *Annu. Rev. Biochem.* **81**, 261–289 (2012).
19. D. J. Gibbs, J. Bacardit, A. Bachmair, M. J. Holdsworth, *Trends Cell Biol.* **24**, 603–611 (2014).
20. A. Mogk, R. Schmidt, B. Bukau, *Trends Cell Biol.* **17**, 165–172 (2007).
21. K. K. Starheim, K. Gevaert, T. Arnesen, *Trends Biochem. Sci.* **37**, 152–161 (2012).
22. P. Van Damme *et al.*, *PLOS Genet.* **7**, e1002169 (2011).
23. S. G. Kreft, L. Wang, M. Hochstrasser, *J. Biol. Chem.* **281**, 4646–4653 (2006).
24. G. Hassink *et al.*, *Biochem. J.* **388**, 647–655 (2005).
25. J. K. Monda *et al.*, *Structure* **21**, 42–53 (2013).
26. N. Zelcer *et al.*, *Mol. Cell. Biol.* **34**, 1262–1270 (2014).

ACKNOWLEDGMENTS

We thank R. Neubig, M. Mulvihill, and E. Wiertz for gifts of plasmids, and K. Piatkov for helpful suggestions. Supported by grants from the National Research Foundation of the Korea government (MSIP) (NRF-2011-0021975, NRF-2012R1A4A1028200, NRF-2013R1A1A2012529) and BK21 Plus Program (C.-S.H.), and by NIH grants DK039520 and GM031530 (A.V.).

SUPPLEMENTARY MATERIALS

www.sciencemag.org/content/347/6227/1249/suppl/DC1
Materials and Methods
Figs. S1 to S7
Tables S1 to S3
References (*27*–*110*)

27 November 2014; accepted 6 February 2015
10.1126/science.aaa3844

METABOLIC DISEASE

Controlled-release mitochondrial protonophore reverses diabetes and steatohepatitis in rats

Rachel J. Perry,[1,2,3] Dongyan Zhang,[1] Xian-Man Zhang,[2] James L. Boyer,[2,4] Gerald I. Shulman[1,2,3]*

Nonalcoholic fatty liver disease (NAFLD) is a major factor in the pathogenesis of type 2 diabetes (T2D) and nonalcoholic steatohepatitis (NASH). The mitochondrial protonophore 2,4 dinitrophenol (DNP) has beneficial effects on NAFLD, insulin resistance, and obesity in preclinical models but is too toxic for clinical use. We developed a controlled-release oral formulation of DNP, called CRMP (controlled-release mitochondrial protonophore), that produces mild hepatic mitochondrial uncoupling. In rat models, CRMP reduced hypertriglyceridemia, insulin resistance, hepatic steatosis, and diabetes. It also normalized plasma transaminase concentrations, ameliorated liver fibrosis, and improved hepatic protein synthetic function in a methionine/choline–deficient rat model of NASH. Chronic treatment with CRMP was not associated with any systemic toxicity. These data offer proof of concept that mild hepatic mitochondrial uncoupling may be a safe and effective therapy for the related epidemics of metabolic syndrome, T2D, and NASH.

Nonalcoholic fatty liver disease (NAFLD) affects 15 to 30% of the world's population (*1*) and is a key predisposing factor for nonalcoholic steatohepatitis (NASH), cirrhosis, and hepatocellular carcinoma. The role of hepatic steatosis in the pathogenesis of NASH and liver fibrosis remains undefined, and thus far, no therapeutic agents improve liver histology or hepatic protein synthetic function in animal models of NASH. In addition, NAFLD is strongly associated with hepatic insulin resistance and type 2 diabetes (T2D); however, efforts to ameliorate NAFLD or diabetes with pharmacologic agents have met with limited success.

The mitochondrial protonophore 2,4-dinitrophenol (DNP) has been investigated since the early 20th century for its ability to promote weight loss; however, after numerous reports of deaths in individuals taking DNP, production of the drug ceased in the United States in the late 1930s. Nevertheless, given its ability to promote insulin sensitivity in the rat (*2*), we investigated whether DNP could be pharmacologically manipulated to improve its safety margin. In a previous study (*3*), we showed that promoting subtle increases in hepatic mitochondrial uncoupling with a liver-targeted derivative of DNP ameliorates NAFLD and T2D in the rat. Although liver-targeted DNP was well tolerated, we hypothesized that we could further improve the safety and efficacy of DNP by developing a version of the drug with lower peak plasma concentrations and sustained-release pharmacokinetics.

To test this hypothesis, we first examined whether a 5-day continuous, low-dose intragastric infusion of DNP to achieve sustained plasma DNP concentrations in the 1 to 5 μM range would lead to reductions in hepatic steatosis and improve whole-body insulin sensitivity in high-fat–fed rats. This intragastric infusion of DNP resulted in steady-state plasma and liver DNP concentrations of ~3 and ~1 μM, respectively (fig. S1A). Nevertheless, these very low concentrations of DNP resulted in lower fasting plasma glucose and insulin concentrations as well as 80% reductions in plasma, liver, and skeletal muscle triacylglycerol (TAG) content (fig. S1, B to F).

Given the encouraging results of the intragastric infusion studies, we synthesized an orally available, controlled-release formulation of DNP, which is described in the supplemental materials, materials and methods. This formulation, called CRMP (controlled-release mitochondrial protonophore), was fed to rats in a small amount of peanut butter. In contrast to DNP, which caused a dose-dependent increase in body temperature at doses above 25 mg/kg, CRMP had a negligible effect on temperature at doses less than 100 mg/kg (fig. S2, A and B). To compare the safety and efficacy of CRMP and DNP, we performed 5-day parallel group dosing studies in high-fat–fed rats and found that the minimum effective dose of CRMP to decrease liver TAG was 0.5 mg/kg, whereas that of DNP was 5 mg/kg (fig. S2, C and D). In concert with this, the median lethal dose (LD_{50}) of CRMP was more than 10-fold higher than that of DNP (fig. S2E). No changes to alanine aminotransferase (ALT), aspartate aminotransferase (AST), blood urea nitrogen (BUN), or creatinine were observed with any of the doses of CRMP below 125 mg/kg, whereas DNP treatment at doses above 0.5 mg/kg raised AST concentrations (fig. S3, A to H). Thus, the 5-day no observed adverse effect level (NOAEL) of CRMP was 100 mg/kg, as compared with 0.5 mg/kg for DNP.

We next examined whether the improved safety of CRMP might be related to differences in pharmacokinetic properties (fig. S4, A to F). Peak plasma DNP concentrations at each toxic dose of DNP were significantly higher than equimolar doses of CRMP, whereas the area under the curve of DNP concentration was higher after treatment with CRMP, likely accounting for CRMP's improved efficacy and reduced toxicity (fig. S4, E and F). Detailed pharmacologic data can be found in the supplementary materials (fig. S5, A to H).

To further evaluate the safety margins of CRMP as compared with DNP, we treated rats for 6 weeks with oral DNP or CRMP. Six weeks of CRMP treatment at 1 mg/kg was well tolerated and did not result in any alterations in behavior, food intake, body weight, body temperature, liver or kidney histology, or induction of neuropathy (fig. S6, A to I). In addition, no toxic effects were seen with doses up to 100 mg/kg CRMP, whereas increases in AST were seen at 1 mg/kg DNP treatment (fig. S6, D to G). Thus, the 6-week NOAEL for CRMP is at least 100-fold greater for CRMP (more than 100 mg/kg) than for DNP (less than 1 mg/kg). Taken together, our data indicate that the toxicity of a DNP derivative is predicted by the maximum concentration of DNP (fig. S4F), whereas its efficacy is predicted by the area under the curve of plasma DNP concentrations (fig. S4E).

To examine the impact of CRMP on rates of hepatic mitochondrial glucose and fat oxidation, we assessed these rates using a combined liquid chromatography–mass spectrometry (MS)/MS–nuclear magnetic resonance method (*4*). We observed a 60% increase in rates of hepatic mitochondrial tricarboxylic acid cycle flux (V_{TCA}) flux in CRMP-treated rats, which could be attributed to a 65% increase in rates of fat oxidation (Fig. 1A). In contrast, there were no differences in fat oxidation relative to V_{TCA} in kidney, brain, heart, or skeletal muscle, indicating that the uncoupling effect of CRMP is confined to the liver (fig. S7A). To examine whether uncoupling with CRMP reduces tissue lipid content and improves insulin sensitivity, we treated a high-fat–fed rat model of NAFLD and insulin resistance with daily CRMP (1 mg/kg) or vehicle for 5 days. Despite identical body weight and fat content at the time of study, CRMP-treated rats exhibited 30 to 40% reductions in fasting plasma glucose, fatty acid, and triglyceride concentrations; a 30% increase in high-density lipoprotein concentration; and a 50% reduction in plasma insulin concentration, without any difference in hepatic gluconeogenic protein expression (Fig. 1, B to D, and fig. S7, B to H).

Rats treated with CRMP manifested improved glucose tolerance, with lower plasma glucose and insulin concentrations throughout an intraperitoneal glucose tolerance test (Fig. 1, E and F, and fig. S7, I and J). To evaluate the effect of CRMP on whole-body insulin sensitivity, we performed hyperinsulinemic-euglycemic clamps with

[1]Howard Hughes Medical Institute, Yale University School of Medicine, New Haven, CT, USA. [2]Departments of Internal Medicine, Yale University School of Medicine, New Haven, CT, USA. [3]Department of Cellular and Molecular Physiology, Yale University School of Medicine, New Haven, CT, USA. [4]Yale Liver Center, Yale University School of Medicine, New Haven, CT, USA.
*Corresponding author. E-mail: gerald.shulman@yale.edu

radiolabeled glucose (fig. S8, A and B). Consistent with improved whole-body insulin sensitivity, the CRMP-treated rats required twofold more glucose to maintain euglycemia (Fig. 1G and fig. S8C). This improvement in insulin-stimulated whole-body glucose metabolism in the CRMP-treated animals could be attributed to increases in both liver and muscle insulin sensitivity, as reflected by a 2.5-fold increase in insulin-stimulated

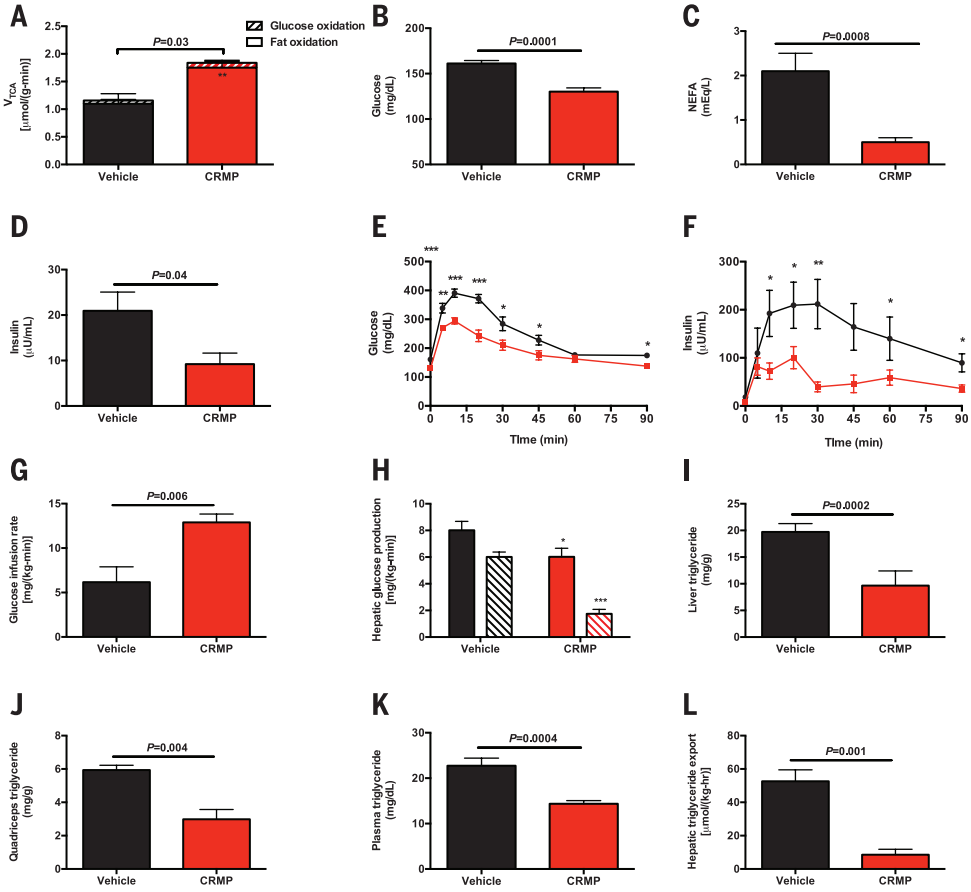

Fig. 1. CRMP improves insulin sensitivity in high-fat–fed rats. (**A**) Hepatic V_{TCA} from fat oxidation (solid bars) and glucose oxidation (striped bars) in chow fed rats. (**B** to **D**) Fasting plasma glucose, NEFA, and insulin concentrations. (**E** and **F**) Plasma glucose and insulin concentrations during an intraperitoneal glucose tolerance test. *P < 0.05, **P < 0.01, ***P < 0.001 by means of Student's t test. (**G**) Glucose infusion rate during a hyperinsulinemic-euglycemic clamp. (**H**) Basal (solid bars) and clamped (striped bars) rates of hepatic glucose production. (**I** to **K**) Liver, quadriceps, and plasma triglyceride concentrations. (**L**) Liver VLDL export. In (A) to (L), data are mean ± SEM of n = 6 to 8 rats per group.

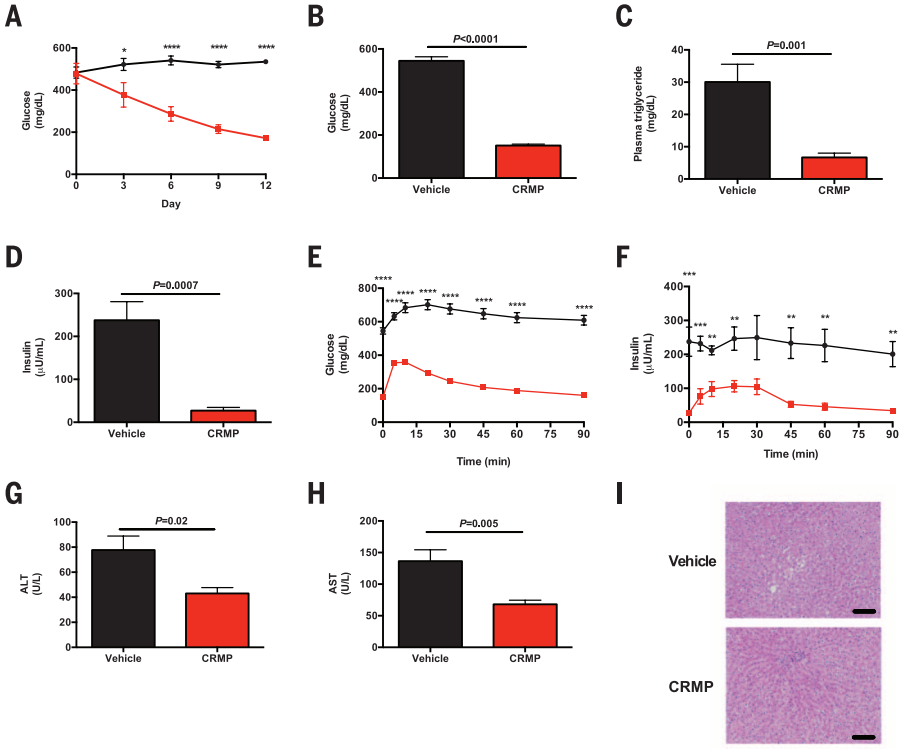

Fig. 2. CRMP improves glucose tolerance in diabetic rats. (**A**) Random plasma glucose concentrations in vehicle-treated (black circles) and CRMP-treated rats (red squares). (**B** to **D**) Fasting plasma glucose, triglyceride, and insulin concentrations. (**E** and **F**) Glucose and insulin concentrations during an intraperitoneal glucose tolerance test. (**G** and **H**) Plasma ALT and AST concentrations. (**I**) Liver histology (hematoxylin and eosin stain). Scale bars, 100 μm. In (A) to (I), *P < 0.05, **P < 0.01, ***P < 0.001, ****P < 0.0001 by means of Student's t test. Data are mean ± SEM of n = 6 to 7 rats per group.

peripheral muscle glucose uptake and a threefold greater suppression of hepatic glucose production in CRMP-treated rats during the hyperinsulinemic-euglycemic clamp (Fig. 1H and fig. S8D).

Previous studies have shown a strong causal relationship between ectopic diacylglycerol (DAG) accumulation and insulin resistance in liver and skeletal muscle. Consistent with this, we found that CRMP-treated rats had lower TAG and DAG content and decreased protein kinase Cε (PKCε) and PKCθ translocation in liver and skeletal muscle, respectively (Fig. 1, I and J and fig. S8, E to J). The reduction in skeletal muscle triglycerides was associated with 40% lower plasma triglyceride concentrations and an 80% reduction in liver very-low-density lipoprotein (VLDL) export (Fig. 1, K and L), explaining the reduced muscle lipid content as a result of liver-specific mitochondrial uncoupling. However, these reductions in TAG and DAG content were dissociated from any changes in liver or muscle acylcarnitine or ceramide content, liver glycogen, plasma inflammatory markers, FGF-21, or adiponectin concentration, or markers of uncoupling in brown fat (fig. S9, A to O).

CRMP also prevented the development of NAFLD: Rats fed a high-fat diet for 2 weeks and concurrently fed CRMP had lower fasting plasma glucose and nonesterified fatty acid (NEFA) and insulin concentrations associated with 50 to 90% reductions in triglyceride concentrations in plasma, liver, and skeletal muscle (fig. S10, A to F). To examine the effect of CRMP treatment on whole-body energy metabolism, we performed Comprehensive Lab Animal Monitoring System (CLAMS) metabolic cage studies in mice and observed no differences in any parameter examined (fig. S11, A to H). These data demonstrate that low levels of mitochondrial uncoupling confined to the liver are sufficient to reduce liver fat content and improve whole-body insulin resistance, without affecting food intake or whole-body energy expenditure.

We next examined whether CRMP could reverse diabetes in the Zucker Diabetic Fatty (ZDF) rat. We treated high-fat–fed ZDF rats with CRMP daily for 14 days. CRMP treatment was associated with a progressive reduction in random plasma glucose concentrations and a 400 mg/dL decrease in fasting plasma glucose concentrations after 2 weeks of treatment along with marked decrements in fasting plasma insulin and triglyceride concentrations, despite identical body weight before and after treatment (Fig. 2, A to D, and fig. S12A). CRMP-treated rats also displayed a 60% reduction in hepatic acetyl coenzyme A (acetyl CoA), a key allosteric activator of hepatic gluconeogenesis (fig. S12B) (*4*). The improved glycemia in CRMP-treated rats was associated with improved glucose tolerance during an intraperitoneal glucose tolerance test (Fig. 2, E and F, and fig. S12, C and D). These increments in insulin sensitivity and glucose tolerance were associated with 65 and 55% reductions in liver and quadriceps TAG, respectively (fig. S12, E and F). There was no detectable renal toxicity with this 2-week treatment (fig. S12, G and H). In addition to reducing ectopic fat content in liver and skeletal muscle, CRMP also reversed liver inflammation in ZDF rats, as reflected by normalization of liver enzymes (Fig. 2, G and H). Histologic analysis confirmed the resolution of NAFLD with CRMP treatment in this model of poorly controlled diabetes (Fig. 2I).

To investigate whether CRMP could ameliorate NAFLD-induced NASH and liver fibrosis, we fed rats a methionine/choline–deficient diet (MCD) for 8 weeks so as to induce NASH (*5*, *6*) and subsequently treated the animals with CRMP for 6 weeks. CRMP reduced liver triglyceride concentrations by 90% and normalized plasma transaminase concentrations (Fig. 3, A to C). Consistent with this reduction in liver inflammation, CRMP-treated rats displayed lower concentrations of five inflammatory cytokines in the liver and reduced hepatic CD69 protein (Fig. 3D and fig. S13, A and B). Histological analysis confirmed the resolution of NAFLD and liver fibrosis in CRMP-treated rats, with a 90% reduction in the liver fibrosis score and accompanying reductions in collagen mRNA, smooth muscle actin, hydroxyproline, and caspase concentrations and unchanged terminal deoxynucleotidyl transferase–mediated deoxyuridine triphosphate nick end labeling (TUNEL) staining (Fig. 3, F to K, and fig. S13C). Because patients with liver cirrhosis manifest reduced hepatic glycogen content (*7*), we measured hepatic glycogen content in MCD-fed rat livers and found an 80% increase in glycogen content in CRMP-treated rats associated with reversal of fasting hypoglycemia (fig. S13, D and E). Additionally, CRMP improved liver protein synthetic function, indicated by increases in plasma albumin concentrations (Fig. 3L). By demonstrating an improvement in hepatic protein and carbohydrate synthetic function in addition to reversal of liver fibrosis in a NASH model, these data emphasize the potential efficacy of mitochondrial protonophores as a therapeutic agent for NAFLD-associated NASH to prevent liver cirrhosis and potentially hepatocellular carcinoma.

We have shown that altering the pharmacokinetics of DNP to promote a low sustained systemic release can increase the therapeutic window of this agent by more than 500-fold. Daily CRMP administration reversed NAFLD, insulin resistance, T2D, NASH, and liver fibrosis in rats without detectable toxicity. Altering the pharmacokinetics of DNP by increasing the DNP

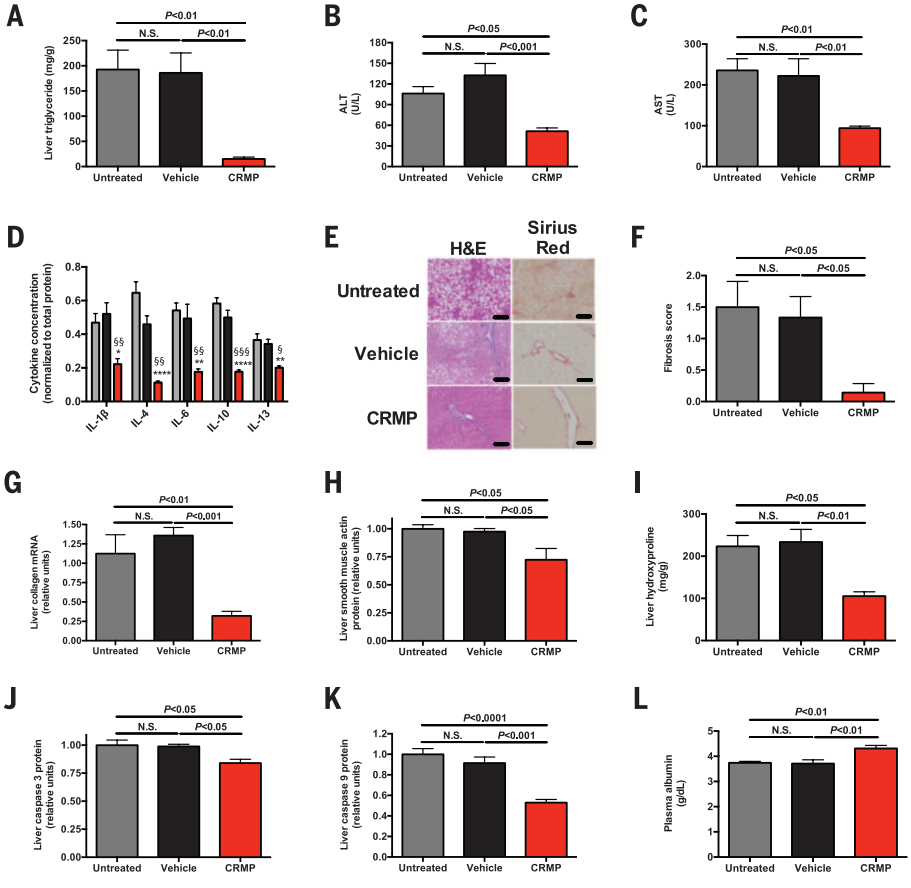

Fig. 3. CRMP ameliorates liver disease in a rat model of NASH. (**A**) Liver triglyceride content. (**B** and **C**) Plasma ALT and AST. (**D**) Liver inflammatory cytokine concentrations, normalized to total protein. $n = 4$ rats per group. (**E**) Liver histology. Scale bars, 100 μm. (**F**) Fibrosis score. (**G**) Liver collagen mRNA. (**H**) Liver smooth muscle actin protein. (**I**) Hepatic hydroxyproline content. (**J** and **K**) Liver caspase 3 and caspase 9 protein. (**L**) Plasma albumin. Unless otherwise specified, $n = 6$ to 8 rats per group. Data are mean ± SEM, with comparisons by means of analysis of variance.

area under the curve while reducing the peak plasma DNP concentrations with a sustained-release coating increased the ratio of toxic to effective dose 25-fold over liver-targeted DNP and 1250-fold over unaltered DNP. These data support the potential utility of mitochondrial protonophores and other mitochondrial uncoupling agents for the treatment of the related epidemics of NASH, metabolic syndrome, and T2D.

REFERENCES AND NOTES

1. V. Ratziu, S. Bellentani, H. Cortez-Pinto, C. Day, G. Marchesini, *J. Hepatol.* **53**, 372–384 (2010).
2. V. T. Samuel *et al.*, *J. Biol. Chem.* **279**, 32345–32353 (2004).
3. R. J. Perry *et al.*, *Cell Metab.* **18**, 740–748 (2013).
4. R. J. Perry *et al.*, *Nat. Med.* **20**, 759–763 (2014).
5. I. A. Leclercq *et al.*, *J. Clin. Invest.* **105**, 1067–1075 (2000).
6. E. Ip, G. Farrell, P. Hall, G. Robertson, I. Leclercq, *Hepatology* **39**, 1286–1296 (2004).
7. K. F. Petersen *et al.*, *Am. J. Physiol.* **276**, E529–E535 (1999).

ACKNOWLEDGMENTS

We thank J. Dong, C. Soroka, J. P. Camporez, M. Jurczak, J. Stack, M. Kahn, C. Borders, Y. Kosover, A. Nasiri, G. Butrico, M. Batsu, and W. Zhu for their invaluable technical assistance; C. Frassetto and A. Barkley for their work to formulate the CRMP; B. Ehrlich for assistance with the thermal algesia studies; M. Kashgarian for expert analysis of renal histology; and A. Ray and C. Tay for toxicology advice. Yale University has applied for a patent (provisional patent application 61/919, 003) related to the use of CRMP and similar protonophores for the treatment of metabolic diseases, including NAFLD/NASH and T2D. This research was funded by grants from the United States National Institutes of Health (R01 DK-40936, R24 DK-085638, U24 DK-059635, T32 DK-101019, P30 DK-45735, P30 DK-34989, and UL1 TR-000142) and the Novo Nordisk Foundation Center for Basic Metabolic Research, University of Copenhagen, Copenhagen, Denmark.

SUPPLEMENTARY MATERIALS

www.sciencemag.org/content/347/6227/1253/suppl/DC1
Materials and Methods
Figs. S1 to S13
References (*8*–*17*)

11 October 2014; accepted 5 February 2015
Published online 26 February 2015;
10.1126/science.aaa0672

ION CHANNELS

K2P channel gating mechanisms revealed by structures of TREK-2 and a complex with Prozac

Yin Yao Dong,[1]* Ashley C. W. Pike,[1]* Alexandra Mackenzie,[1,2] Conor McClenaghan,[2,3] Prafulla Aryal,[2,3,4] Liang Dong,[1]† Andrew Quigley,[1] Mariana Grieben,[1] Solenne Goubin,[1]‡ Shubhashish Mukhopadhyay,[1] Gian Filippo Ruda,[1,5] Michael V. Clausen,[2] Lishuang Cao,[6] Paul E. Brennan,[1,5] Nicola A. Burgess-Brown,[1] Mark S. P. Sansom,[3,4] Stephen J. Tucker,[2,3]§ Elisabeth P. Carpenter[1,3]§

TREK-2 (KCNK10/K2P10), a two-pore domain potassium (K2P) channel, is gated by multiple stimuli such as stretch, fatty acids, and pH and by several drugs. However, the mechanisms that control channel gating are unclear. Here we present crystal structures of the human TREK-2 channel (up to 3.4 angstrom resolution) in two conformations and in complex with norfluoxetine, the active metabolite of fluoxetine (Prozac) and a state-dependent blocker of TREK channels. Norfluoxetine binds within intramembrane fenestrations found in only one of these two conformations. Channel activation by arachidonic acid and mechanical stretch involves conversion between these states through movement of the pore-lining helices. These results provide an explanation for TREK channel mechanosensitivity, regulation by diverse stimuli, and possible off-target effects of the serotonin reuptake inhibitor Prozac.

Two-pore domain potassium (K2P) channels contribute to the background leak potassium currents in nearly all cells and exhibit versatile, polymodal patterns of regulation. This functional diversity contributes to regulation of the resting membrane potential in many excitable and nonexcitable tissues. K2P channels represent important clinical targets for the treatment of cardiovascular disease and several neurological disorders, including pain and depression (*1*).

The archetypal polymodal K2P channels TREK-1 and TREK-2 are regulated by physical factors such as mechanical stretch, voltage, and temperature; by natural ligands including polyunsaturated fatty acids such as arachidonic acid (AA); and by intra- and extracellular pH (pH_{int} and pH_{ext}) (*1*–*3*). Their activity can also be modulated by diverse pharmacological agents such as volatile anesthetics, neuroprotective drugs, and antidepressants such as fluoxetine (Prozac) (*1*–*6*). Such diverse regulation allows these channels to couple cellular electrical activity to a variety of signaling pathways; consequently, they represent important pharmacological targets (*6*). In particular, TREK channels are inhibited in vitro by fluoxetine and its active metabolite norfluoxetine at physiologically relevant concentrations (*4*, *5*, *7*). This selective serotonin reuptake inhibitor is used in the treatment of a range of depressive and anxiety disorders. In addition to its principal effect of directly inhibiting serotonin transporters, fluoxetine also inhibits several G protein–coupled receptors and ion channels (*4*, *8*). TREK-1 knockout mice appear resistant to depression, suggesting that TREK channel inhibition by fluoxetine may contribute to its antidepressant effects (*5*, *8*). Inhibition of TREK channels in the cardiovascular system may also contribute to some of the drug's known side effects (*9*). Norfluoxetine is a state-dependent blocker of TREK channels (*4*) and is used here as a tool compound to probe the structural basis of TREK channel inhibition.

The molecular and structural mechanisms that allow K2P channels to sense such diverse stimuli are poorly understood. Structures of two members of the K2P channel family (TRAAK and TWIK-1) reveal that they share many basic structural features with classical tetrameric K^+ channels but assemble as dimers with a pseudotetrameric pore (*10*–*12*). Also, they do not appear to gate via constriction of the cytoplasmic entrance to the pore. Instead, this lower part of the conduction pathway remains open even when the channel is closed, and gating occurs primarily within the selectivity filter (*2*, *13*, *14*). However, the mechanisms that relay regulatory stimuli to the pore, and how drugs modulate this process, remain unclear.

To understand the mechanisms of polymodal K2P channel gating and inhibition by drugs, we solved the crystal structure of human TREK-2 in two conformations at 3.4 and 3.9 Å resolution (*15*) (figs. S1 and S2 and table S1). The truncated protein used for crystallization retains many functional properties exhibited by wild-type TREK-2, including activation by stretch and AA and inhibition by norfluoxetine (fig. S3). The two TREK-2 structures show the classic K2P channel fold (*10*–*12*), with four transmembrane helices (M1 to M4), two pore-forming regions per chain (P1 and P2), and an extracellular cap domain (Fig. 1, A and B). TREK-2 exhibits the domain swap seen in TRAAK (*10*) (fig. S4).

Differences between the two conformations are centered around the lower sections of the M2, M3, and M4 helices (Fig. 1, C and D; fig. S5; and movie S1). In the 3.9 Å structure, these

[1]Structural Genomics Consortium, University of Oxford, Oxford OX3 7DQ, UK. [2]Clarendon Laboratory, Department of Physics, University of Oxford, Oxford OX1 3PU, UK. [3]OXION Initiative in Ion Channels and Disease, University of Oxford, Oxford OX1 3PN, UK. [4]Department of Biochemistry, University of Oxford, Oxford OX1 3QU, UK. [5]Target Discovery Institute, Nuffield Department of Medicine, University of Oxford, Oxford OX3 7FZ, UK. [6]Pfizer Neusentis, Granta Park, Cambridge CB21 6GS, UK. *These authors contributed equally to this work. †Present address: Department of Clinical Neurosciences, Cambridge Institute for Medical Research, University of Cambridge, Cambridge CB2 0XY, UK. ‡Present address: Solenne Goubin, School of Veterinary Medicine and Science, University of Nottingham, Sutton Bonington Campus, Sutton Bonington, Leicestershire LE12 5RD, UK.
§Corresponding author. E-mail: liz.carpenter@sgc.ox.ac.uk (E.P.C.); stephen.tucker@physics.ox.ac.uk (S.J.T.)

regions project further into the cytoplasm (the "down state"), whereas in the 3.4 Å structure, they move further up into the membrane (the "up state"). In both structures there are two copies of the dimer in the asymmetric unit, and each of the four chains adopts a similar conformation, despite different crystal-packing arrangements (fig. S6), suggesting that the two conformations are not imposed by crystal packing. Profiles of the inner pore show that the cytoplasmic entrance to the vestibule remains open in both conformations (Fig. 1D and fig. S5, D to F). In the up state, M4 is kinked, with a hinge around a conserved glycine (Gly^{312}). In addition, there are hinges in M2 at Gly^{201}/Gly^{206}

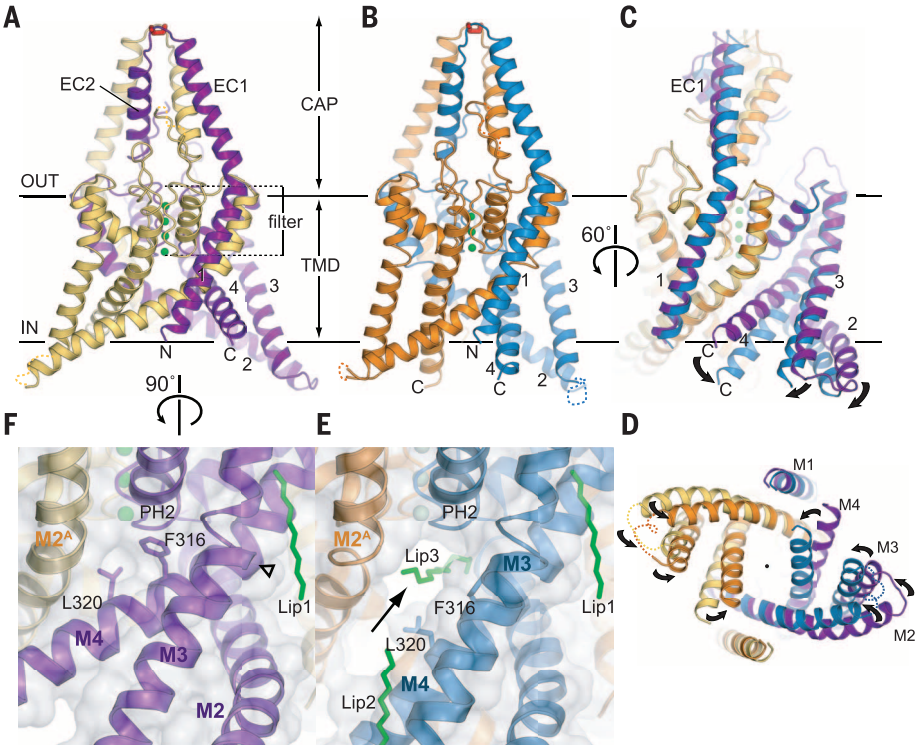

Fig. 1. Crystal structures of two conformations of TREK-2. TREK-2 overall fold viewed parallel to the plane of the membrane, with views of (**A**) the up-state 3.4 Å structure, with chains A and B in yellow and purple; (**B**) the down-state 3.9 Å structure, with chains A and B in orange and blue; (**C**) a superposition of the states; and (**D**) the superposition viewed from the cytoplasmic side of the membrane. Potassium ions are colored green and the cap disulfide bond in red. (**E**) Fenestration (indicated with an arrow) in the down state, with the aliphatic chain that binds in the vestibule and the fenestration (Lip3) and lipids (Lip1, Lip2) on the channel surface (green sticks). (**F**) View of the up state, in the same orientation as in (E), showing absence of the fenestration due to elevation of M4 and insertion of the side chains of Phe^{316} and Leu^{320} into the fenestration. The hinge point around Gly^{312} in M4 is indicated by an open triangle. N, N terminus; C, C terminus; CAP, extracellular CAP domain; TMD. transmembrane domain.

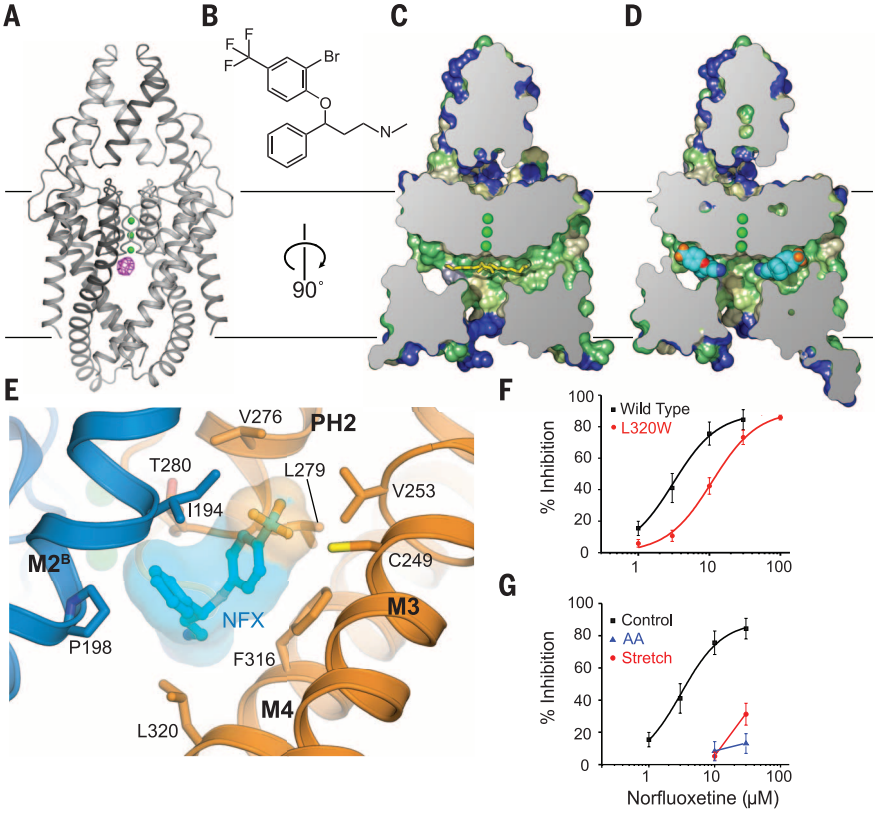

Fig. 2. Norfluoxetine and Br-fluoxetine bind to TREK-2 in the down-state fenestration adjacent to the pore filter entrance. (**A**) Overall fold of the TREK-2 down state shown with the 5 Å anomalous difference map for the Br-fluoxetine/TREK-2 complex shown in pink (contoured at 4.5σ), indicating the location of Br-fluoxetine in the fenestration. (**B**) Chemical structure of Br-fluoxetine. Norfluoxetine lacks the methyl group on the nitrogen. (**C**) Cross section of a surface view of TREK-2 in the down state, colored by hydrophobicity [green (most hydrophobic) through yellow to blue (least hydrophobic)]. Yellow sticks represent Lip3. (**D**) Complex of TREK-2 with norfluoxetine. Norfluoxetine is shown in light blue, dark blue, red, and orange for carbon, nitrogen, oxygen, and fluorine atoms, respectively. For clarity, only one enantiomer of norfluoxetine is shown in (D) and (E). (**E**) Norfluoxetine binding site, with chains A and B in gold and blue, respectively, and norfluoxetine colored as in (D). (**F**) Disruption of the binding site by the L320W mutation reduces norfluoxetine inhibition. (**G**) Stretch activation (−11 mmHg, red) at pH_{int} 7.3 dramatically reduces the efficacy of norfluoxetine inhibition, as does activation by 10 μM AA (blue). Error bars in (F) and (G) denote ± SEM.

and in M3 at Gly^{248}, allowing movement of all three helices (Fig. 1F). The down state is similar to that previously observed in the K2P channels TRAAK and TWIK-1 (*10*–*12*). We observe substantial movement of all three helices (M2, M3, and M4) between the two conformations (movie S1 and fig. S5). While this manuscript was under review, two studies of TRAAK also observed movement of M4 in both chains (*16*, *17*) or of M2 in one of the chains (*17*), and these movements were associated with the regulation of channel activity. In TREK-2, we observe movement of all three helices (M2, M3, and M4) in both chains. This coordinated movement of all three helices is supported by molecular dynamics (MD) simulations of the structures within a bilayer. These simulations exhibit downward movement of M2, M3, and M4 in the up state to adopt a conformation similar to the down state, thus indicating that movement between states can occur (fig. S7).

A key feature of K2P channel structures is the intramembrane-side fenestrations just below the selectivity filter (*11*, *12*). These are present only in the down state (Fig. 1E). In the up state, the fenestration is closed by the upward movement and rotation of M4, which places the side chains of Phe^{316} and Leu^{320} in the fenestration (Fig. 1F). In the TREK-2 and TWIK-1 down states, there is density for lipid-like molecules extending across the top of the inner vestibule below the filter (Fig. 1E and fig. S5, A and B), which may represent copurified lipids or polyethylene glycol molecules.

To form a fully conductive channel, all four K^+ binding sites within the filter must be occupied (*18*, *19*). The TREK-2 up state has electron density for four K^+ ions in the filter, suggesting that this state is conductive. By contrast, the down state has density for only three ions (Fig. 1, A and B, and fig. S8), implying that it may represent a nonconductive state, even though the inner pore is open. However, the available TRAAK and TWIK-1 structures (*10*–*12*, *16*, *17*) have similar occupancy for all four sites within the filter in both states.

To probe the functional importance of these two states, we examined TREK-2 inhibition by fluoxetine and norfluoxetine because both exhibit state-dependent inhibition of TREK channel activity via a selective interaction with the closed state (*4*). We solved the structure of TREK-2 in complex with norfluoxetine and brominated fluoxetine {3-[2-bromo-4-(trifluoromethyl) phenoxy]-*N*-methyl-3-phenylpropan-1-amine (hereafter referred to as Br-fluoxetine)} at 3.7 and 3.64 Å resolution (Fig. 2 and fig. S9). These structures were in the down state with clear peaks in anomalous difference maps for bromine in Br-fluoxetine in the fenestrations (Fig. 2A and fig. S9), unequivocally identifying the binding site for Br-fluoxetine. Norfluoxetine was also found bound within the fenestration (Fig. 2, C to E, and movie S1), but neither ligand extended into the vestibule to block the ion path directly (Fig. 2, D and E). The fenestration provides a hydrophobic environment close to the selectivity filter in which both Br-fluoxetine and norfluoxetine interact with residues Ile^{194} and Pro^{198} on M2 of chain B, Cys^{249} and Val^{253} on M3, Phe^{316} and Leu^{320} on M4, and Val^{276}, Leu^{279}, and Thr^{280} on pore helix 2 (Fig. 2E). There is some flexibility in positioning of fluoxetine derivatives (fig. S9), but this is not

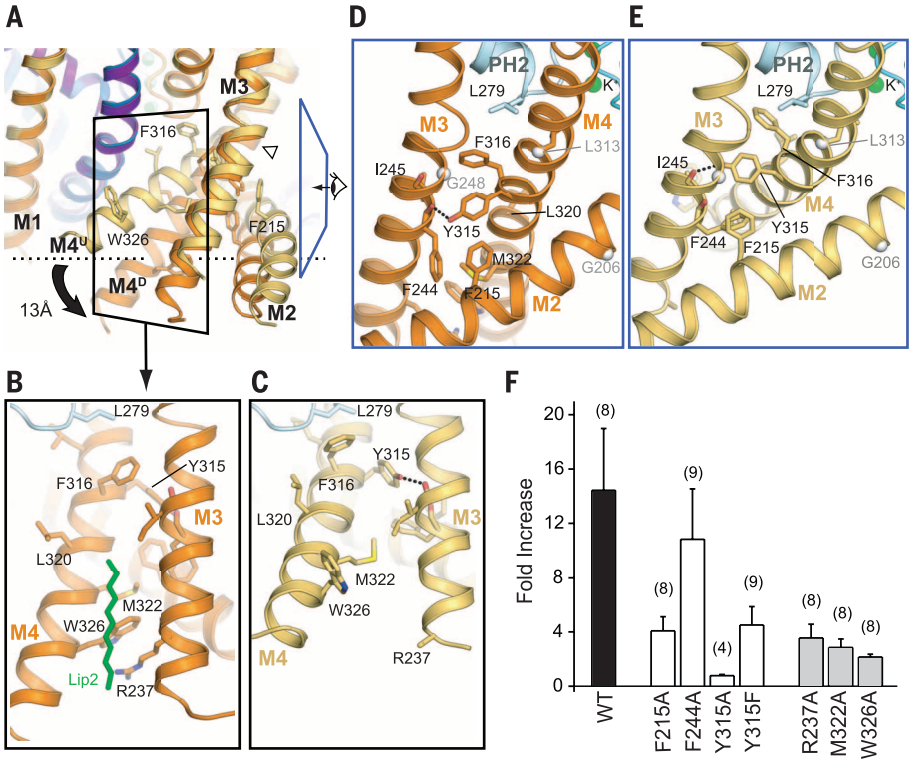

Fig. 3. Concerted motion of transmembrane helices M2, M3, and M4. (**A**) Superposition of the up and down states highlighting movement of M2 to M4. (**B**) Interactions between helices M2, M3, and M4 in the down state, involving Trp^{326}, Arg^{237}, and Met^{322}. View shown is indicated by black boxed region in (A). The lipid chain that overlays this interface is shown in green. (**C**) View of corresponding region in the up state, showing disruption of the distal M3-M4 interface due to a shift in M4 orientation. (**D** and **E**) Interactions at the top of the M2, M3, and M4 helices, proximal to the pore in the down (D) and up (E) states viewed from the direction indicated by blue boxed region in (A). Transmembrane helix hinge points are indicated by gray spheres. (**F**) Mutations at the interface between M2, M3, and M4 reduce activation by membrane stretch (–11 mmHg). Error bars denote ± SEM; numbers in parentheses indicate the number of repeats. WT, wild type.

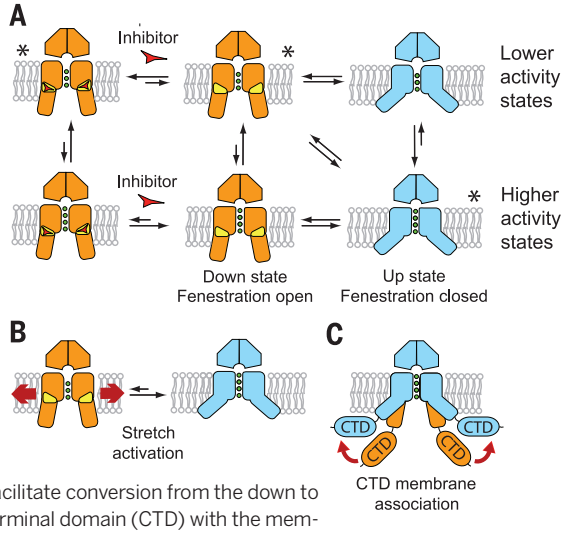

Fig. 4. Model of K2P channel gating and inhibition by norfluoxetine. The down state is shown in orange, fenestrations in yellow, and the up state in blue. Inhibitors such as norfluoxetine are represented by a red triangle-like symbol. (**A**) Overall scheme for K2P channel gating. Higher- and lower-activity states are shown for both conformations, as the filter may gate independently of these larger changes, though with a different probability. Conformations seen in crystal structures are indicated by asterisks. (**B**) Schematic of activation of TREK channels by mechanical stretch. The direct interaction of TREK-2 with lipids in the membrane may allow lateral forces to facilitate conversion from the down to the up state. (**C**) Association of the C-terminal domain (CTD) with the membrane. The diverse cytoplasmic C-terminal extensions of K2P channels provide an additional site for modulation of channel activity. Posttranslational modification of the CTD or protonation due to pH changes could favor association of the CTD with the membrane, thus stabilizing the more active up state.

unexpected for a relatively low-affinity ligand. Furthermore, a mutation within the binding site [Leu^{320}→Trp^{320} (L320W) on M4] (*20*) reduces the inhibition of TREK-2 by norfluoxetine (Fig. 2F).

The fenestration is present only in the down state; transition to the up state closes the fenestration, thus removing the norfluoxetine binding site. This is consistent with a state-dependent block of the closed channel by norfluoxetine (*4*) and with the observation that in the down state there are only three K^+ ions in the filter, suggesting a nonconductive state. It also predicts that the up state represents a more activated state, which does not bind norfluoxetine. To test this hypothesis, we examined the effect of channel activation on norfluoxetine inhibition. We found that activation either by membrane stretch or AA reduced subsequent norfluoxetine inhibition (Fig. 2G). The mechanisms underlying both stretch and AA activation are thought to be similar (*21*, *22*), suggesting that the up state may represent a conformation activated by stretch and AA. Furthermore, we found that norfluoxetine markedly slows the rate of stretch activation (fig. S10A). These effects are consistent with fluoxetine preventing conversion between the two states. In addition, norfluoxetine's binding site close to the filter gate may also help to stabilize the nonconductive state.

Movement between these two conformations provides a structural mechanism for coupling regulatory signals to the filter gate. In particular, it allows movement of M4 to be coupled to the cytoplasmic domain, which moves on and off the membrane surface in response to various regulatory signals (*8*, *13*, *21*, *23*). Movement of the helices between states is also associated with reorientation of side chains between M2, M3, and M4. At the cytoplasmic end of M4, Trp^{326} is packed between the side chains of Met^{322} on M4 and Arg^{237} on M3 in the down state (Fig. 3, A and B). However, in the up state, a kinking and 30° rotation of M4 allows the Trp^{326} side chain to insert into the bilayer, moving the three helices further into the membrane (Fig. 3, A and C). Disruption of these interactions should therefore preferentially destabilize the down state, and we found that mutation of these residues (W326A, M322A, and R237A) reduced stretch activation. (Fig. 3F and fig. S10C).

Immediately above Trp^{326}, a set of hydrophobic residues (Phe^{215}, Phe^{244}, Ile^{245}, and Tyr^{315}) form another core of interactions between M2, M3, and M4 (Fig. 3, D and E). These side chains all rearrange between conformations (Fig. 3A). Mutations within this region also reduced stretch activation (Fig. 3F and fig. S10C). In particular, Tyr^{315} on M4 hydrogen bonds with the backbone carbonyl of Phe^{244} on M3 in the up state but shifts to Ile^{245} in the down state. Both the Y315A and Y315F mutations reduced stretch activation, supporting a functional role for this interaction (Fig. 3, D and E).

TREK channels are regulated by many natural lipids in addition to AA (*24*). We observe lipid-like density on the channel surface in grooves at the top and bottom of M3 and M4: The lower site is found only in the down state, packed against Trp^{326}, potentially stabilizing the down state, whereas the upper site is found in both conformations (Fig. 3B). MD simulations confirm that both of these sites can accommodate lipids (fig. S11).

TREK-2 is also sensitive to changes in both intracellular and extracellular pH. Lower external pH (pH_{ext}) affects the filter gate through protonation of a conserved histidine (His^{156}) and also the external P2-M4 linker (*25*). Our structures reveal that His^{156} is located within a solvent-accessible extracellular cavity adjacent to both the P1-M2 and P2-M4 linkers (fig. S12, A to C). It is also at the center of an extensive hydrogen bond network. Mutations within either this network or the linkers affected the response to pH_{ext} (fig. S12D), which suggests that the structural dynamics of this network may couple external stimuli to the filter gate. Intracellular acidification (pH_{int}) also activates TREK-2, and a glutamate residue within the proximal C terminus (Glu^{337}) is critical for this process (*21*). However, this region is not resolved in our structures. Furthermore, pH_{int} activation does not reduce norfluoxetine inhibition (fig. S10B), suggesting that the mechanism underlying pH_{int} activation may be different from that of stretch and AA activation. Nevertheless, this distal segment of M4 is still well positioned to affect movement between the up and down states, thereby integrating many regulatory pathways (*8*, *21*).

These studies allow us to propose a gating mechanism (Fig. 4) in which movement of the pore-lining helices converts TREK-2 between two functional states. The down state represents a closed or "low-activity" state stabilized by inhibitors such as norfluoxetine binding within the fenestrations. By contrast, activation by membrane stretch or AA stabilizes a "higher-activity" up state that is insensitive to norfluoxetine (Fig. 4). It is possible that these two conformations represent the only open and closed states, but differences in filter-ion occupancy in the down state compared with TRAAK (*16*, *17*) suggest that the filter may be able to gate independently in both conformations, perhaps with a higher open probability in the up state (Fig. 4). Our results provide a mechanism for coupling mechanical forces within the membrane to channel activity through movement of the transmembrane helices (Fig. 4), supporting recent evidence that mechanosensitive K2P channels sense force directly through interactions with lipids (*26*–*28*). A related mechanism of mechanosensitivity has been proposed for the TRAAK channel (*16*), but precisely how such conformational changes influence the selectivity filter gate (*14*, *23*), the relative hydration status of the inner pore (*29*), and whether physiological lipids can sterically occlude the pore in the down state (*30*) remain to be determined. Nevertheless, our results clearly demonstrate how movement of the pore-lining helices creates a mechanism for regulation of K2P channel gating by diverse stimuli and illustrate how state-dependent inhibition of TREK channels by Prozac may contribute to possible off-target effects of the drug.

REFERENCES AND NOTES

1. P. Enyedi, G. Czirják, *Physiol. Rev.* **90**, 559–605 (2010).
2. A. Cohen, Y. Ben-Abu, N. Zilberberg, *Eur. Biophys. J.* **39**, 61–73 (2009).
3. J. Noël, G. Sandoz, F. Lesage, *Channels* **5**, 402–409 (2011).
4. L. E. Kennard *et al*., *Br. J. Pharmacol.* **144**, 821–829 (2005).
5. C. Heurteaux *et al*., *Nat. Neurosci.* **9**, 1134–1141 (2006).
6. Z. Es-Salah-Lamoureux, D. F. Steele, D. Fedida, *Trends Pharmacol. Sci.* **31**, 587–595 (2010).
7. M. E. Henry *et al*., *Neuropsychopharmacology* **30**, 1576–1583 (2005).
8. E. Honoré, *Nat. Rev. Neurosci.* **8**, 251–261 (2007).
9. A. Gurney, B. Manoury, *Eur. Biophys. J.* **38**, 305–318 (2009).
10. S. G. Brohawn, E. B. Campbell, R. MacKinnon, *Proc. Natl. Acad. Sci. U.S.A.* **110**, 2129–2134 (2013).
11. S. G. Brohawn, J. del Mármol, R. MacKinnon, *Science* **335**, 436–441 (2012).
12. A. N. Miller, S. B. Long, *Science* **335**, 432–436 (2012).
13. S. N. Bagriantsev, R. Peyronnet, K. A. Clark, E. Honoré, D. L. Minor Jr., *EMBO J.* **30**, 3594–3606 (2011).
14. P. L. Piechotta *et al*., *EMBO J.* **30**, 3607–3619 (2011).
15. Materials and methods are available as supplementary materials on *Science* Online.
16. S. G. Brohawn, E. B. Campbell, R. MacKinnon, *Nature* **516**, 126–130 (2014).
17. M. Lolicato, P. M. Riegelhaupt, C. Arrigoni, K. A. Clark, D. L. Minor Jr., *Neuron* **84**, 1198–1212 (2014).
18. M. Zhou, J. H. Morais-Cabral, S. Mann, R. MacKinnon, *Nature* **411**, 657–661 (2001).
19. D. A. Köpfer *et al*., *Science* **346**, 352–355 (2014).
20. Single-letter abbreviations for the amino acid residues are as follows: A, Ala; C, Cys; D, Asp; E, Glu; F, Phe; G, Gly; H, His; I, Ile; K, Lys; L, Leu; M, Met; N, Asn; P, Pro; Q, Gln; R, Arg; S, Ser; T, Thr; V, Val; W, Trp; and Y, Tyr.
21. E. Honoré, F. Maingret, M. Lazdunski, A. J. Patel, *EMBO J.* **21**, 2968–2976 (2002).
22. F. Maingret, A. J. Patel, F. Lesage, M. Lazdunski, E. Honoré, *J. Biol. Chem.* **274**, 26691–26696 (1999).
23. S. N. Bagriantsev, K. A. Clark, D. L. Minor Jr., *EMBO J.* **31**, 3297–3308 (2012).
24. J. Chemin *et al*., *Pflugers Arch.* **455**, 97–103 (2007).
25. G. Sandoz, D. Douguet, F. Chatelain, M. Lazdunski, F. Lesage, *Proc. Natl. Acad. Sci. U.S.A.* **106**, 14628–14633 (2009).
26. A. Anishkin, S. H. Loukin, J. Teng, C. Kung, *Proc. Natl. Acad. Sci. U.S.A.* **111**, 7898–7905 (2014).
27. S. G. Brohawn, Z. Su, R. MacKinnon, *Proc. Natl. Acad. Sci. U.S.A.* **111**, 3614–3619 (2014).
28. J. Teng, S. Loukin, A. Anishkin, C. Kung, *Pflugers Arch.* **467**, 27–37 (2015).
29. P. Aryal, F. Abd-Wahab, G. Bucci, M. S. Sansom, S. J. Tucker, *Nat. Commun.* **5**, 4377 (2014).
30. P. Aryal, F. Abd-Wahab, G. Bucci, M. S. Sansom, S. J. Tucker, *Channels* **9**, 44–49 (2015).

ACKNOWLEDGMENTS

The Structural Genomics Consortium is a registered charity (no. 1097737) that receives funds from AbbVie, Bayer, Boehringer Ingelheim, Genome Canada through Ontario Genomics Institute grant OGI-055, GlaxoSmithKline, Janssen, Lilly Canada, the Novartis Research Foundation, the Ontario Ministry of Economic Development and Innovation, Pfizer, Takeda, and Wellcome Trust grant 092809/Z/10/Z. M.S.P.S. and S.J.T. are supported by the UK Biotechnology and Biological Sciences Research Council and the Wellcome Trust. Atomic coordinates and structure factors have been deposited with the Protein Data Bank under accession codes 4XDJ (down state), 4BW5 (up state), 4XDL (Br-fluoxetine complex), and 4XDK (norfluoxetine complex). We declare no competing financial interests.

SUPPLEMENTARY MATERIALS

www.sciencemag.org/content/347/6227/1256/suppl/DC1
Materials and Methods
Supplementary Text
Figs. S1 to S13
Table S1
References (*31*–*49*)
Movie S1

22 September 2014; accepted 5 February 2015
10.1126/science.1261512

SEPSIS

Interleukin-3 amplifies acute inflammation and is a potential therapeutic target in sepsis

Georg F. Weber,[1,2]*† Benjamin G. Chousterman,[1]* Shun He,[1]* Ashley M. Fenn,[1] Manfred Nairz,[1] Atsushi Anzai,[1] Thorsten Brenner,[3] Florian Uhle,[3] Yoshiko Iwamoto,[1] Clinton S. Robbins,[1] Lorette Noiret,[1] Sarah L. Maier,[2] Tina Zönnchen,[2] Nuh N. Rahbari,[2] Sebastian Schölch,[2] Anne Klotzsche-von Ameln,[4] Triantafyllos Chavakis,[4] Jürgen Weitz,[2] Stefan Hofer,[3] Markus A. Weigand,[3] Matthias Nahrendorf,[1] Ralph Weissleder,[1,5] Filip K. Swirski[1]*†

Sepsis is a frequently fatal condition characterized by an uncontrolled and harmful host reaction to microbial infection. Despite the prevalence and severity of sepsis, we lack a fundamental grasp of its pathophysiology. Here we report that the cytokine interleukin-3 (IL-3) potentiates inflammation in sepsis. Using a mouse model of abdominal sepsis, we showed that innate response activator B cells produce IL-3, which induces myelopoiesis of Ly-6C^{high} monocytes and neutrophils and fuels a cytokine storm. IL-3 deficiency protects mice against sepsis. In humans with sepsis, high plasma IL-3 levels are associated with high mortality even after adjusting for prognostic indicators. This study deepens our understanding of immune activation, identifies IL-3 as an orchestrator of emergency myelopoiesis, and reveals a new therapeutic target for treating sepsis.

Interleukin-3 (IL-3) contributes to leukocyte production, proliferation, and survival (*1*–*4*). Myeloid cells such as monocytes and neutrophils produce IL-1β, IL-6, and tumor necrosis factor–α (TNF-α), the three inflammatory hallmark cytokines constituting the cytokine storm during septic shock (*5*–*7*). Yet despite these links, IL-3's role in sepsis remains unknown. *Il3*$^{-/-}$ mice have normal blood monocyte and neutrophil profiles (fig. S1, A to G) (*8*) and thus do not require IL-3 for myelopoiesis in the steady state. To test whether IL-3 is important in sepsis, we subjected *Il3*$^{-/-}$ and control wild-type (WT) mice to cecal ligation and puncture (CLP), a model of polymicrobial sepsis (*9*). Compared to WT mice, *Il3*$^{-/-}$ mice were protected from sepsis, as seen in their lower mortality rates, even after antibiotic treatment (Fig. 1A). *Il3*$^{-/-}$ mice had better clinical scores, body temperatures (Fig. 1B), and blood pressure (Fig. 1C), and their recovery was associated with efficient microbial clearance, indicating that the absence of IL-3 did not compromise bactericidal activity or recognition (Fig. 1D and fig. S2).

To characterize the host response more completely, we performed time-course tissue, cellular, and molecular experiments. At 1 day after CLP, WT mice developed neutrophilia and inflammatory Ly-6C^{high} monocytosis (Fig. 1E), whereas in *Il3*$^{-/-}$ mice, monocyte and neutrophil numbers remained relatively unchanged. The increased cell numbers in WT mice were associated with higher serum levels of IL-1β, IL-6, and TNF-α (Fig. 1F). Phagocytic leukocytes were major sources of IL-1β, IL-6, and TN-Fα, because phagocyte depletion with clodronate liposomes and anti–Ly-6G before CLP abolished the cytokine storm (fig. S3A). However, IL-3–mediated cytokine induction was indirect: Both WT and *Il3*$^{-/-}$ neutrophils and monocytes contained similar intracellular reservoirs of the three cytokines (fig. S3B). Analyzing other leukocytes showed IL-3–dependent differences in T and B cell numbers after CLP (fig. S4A), but no differences in basophils, mast cells (*10*–*12*) (fig. S4, B and C), or histamine (fig. S4D), which suggests that IL-3 had little to no effect on basophil and mast cell production and function during the initial inflammation-dominant phase. Consequently, WT but not *Il3*$^{-/-}$ mice accumulated monocytes and neutrophils in the lung (Fig. 1G) and liver (Fig. 1H); developed lung pathology (fig. S5A) with increased protein in bronchoalveolar lavage (fig. S5B); and evolved abnormal liver morphology (fig. S5C) with increased markers of cytolysis in serum (fig. S5D). These data show that IL-3 contributed to septic shock, the most severe form of sepsis (*13*, *14*).

IL-3 promotes hematopoiesis by acting on its receptor, a heterodimer that consists of the IL-3–specific α chain (CD123) and the common β chain (CD131) (*4*). In the steady state, Lin$^-$ c-kit$^+$ hematopoietic stem and progenitor cells (HSPCs), including megakaryocyte and erythrocyte progenitors (MEPs), common myeloid progenitors (CMPs), granulocyte and macrophage progenitors (GMPs), and macrophage and dendritic progenitors (MDPs), expressed CD123 at the same level in both WT and *Il3*$^{-/-}$ mice (Fig. 2A and S6). One day after CLP, the numbers of medullary HSPCs, CMPs, MEPs, and GMPs/MDPs increased over the steady state in WT but not *Il3*$^{-/-}$ mice (Fig. 2B). GMPs are committed to differentiate into monocytes and neutrophils (*15*). We therefore pursued fate-mapping experiments involving adoptively transferring green fluorescent protein–positive (GFP$^+$) GMPs into WT or *Il3*$^{-/-}$ mice. In response to CLP, the bone marrow of WT mice contained a larger population of GFP$^+$ cells than the bone marrow of *Il3*$^{-/-}$ mice, indicating IL-3–dependent progenitor expansion (Fig. 2C). To bolster this observation, we placed Lin$^-$ bone marrow cells (containing predominantly HSPCs) in vitro in medium either alone or supplemented with IL-3, lipopolysaccharide (LPS), or both. We found that IL-3, but not LPS, increased cell expansion and generated myeloid cells well above the numbers initially placed into culture (Fig. 2D). Although IL-3 alone modestly affected IL-1β, IL-6, and TNF-α production, combined IL-3 and LPS exacerbated the response (Fig. 2E). These data suggest that IL-3 is responsible for the cytokine storm, albeit indirectly, by generating a large pool of cells that, upon recognizing bacterial components, produce cytokines in larger quantities.

To determine whether IL-3 can trigger severe sepsis in vivo, whether it can do so alone or in combination with infection, and whether it relies on its specific receptor, we injected (i) recombinant IL-3 (rIL-3) into otherwise healthy WT mice; (ii) anti-CD123 into WT mice subjected to CLP; and (iii) rIL-3 into *Il3*$^{-/-}$ mice subjected to CLP. rIL-3 augmented GMPs in the bone marrow and leukocyte numbers in the blood of healthy WT mice to levels akin to those in WT mice subjected to CLP (Fig. 2F). Despite this increase, rIL-3 per se did not induce a cytokine storm in the absence of infection (Fig. 2G), thus confirming our in vitro observations. Conversely, anti-CD123 attenuated cell numbers in WT CLP mice (Fig. 2F) and tended to decrease serum cytokines (although the differences were not statistically significant) (Fig. 2G) without depleting HSPCs (fig. S7). *Il3*$^{-/-}$ mice receiving rIL-3 in the context of CLP augmented medullary GMP, circulating neutrophil, and Ly-6C^{high} monocyte numbers (Fig. 2F). These increases corresponded to higher cytokine levels in serum (Fig. 2G). Ultimately, WT mice treated with anti-CD123 had a modest but significant improvement in survival (Fig. 2H), whereas *Il3*$^{-/-}$ mice receiving rIL-3 succumbed to infection and died as often as WT mice (Fig. 2I). These data confirm the effects of IL-3 on cell production and survival and identify the IL-3–CD123 axis as a potential new therapeutic target for treating sepsis.

Activated T cells (*16*) and thymic epithelial cells (*17*) produce IL-3 in the steady state, but the

[1]Center for Systems Biology, Massachusetts General Hospital, Harvard Medical School, Boston, MA, USA. [2]Department of Visceral, Thoracic and Vascular Surgery, Technische Universität Dresden, Dresden, Germany. [3]Department of Anesthesiology, University of Heidelberg, Heidelberg, Germany. [4]Department of Clinical Pathobiochemistry and Institute for Clinical Chemistry and Laboratory Medicine, Technische Universität Dresden, Dresden, Germany. [5]Department of Systems Biology, Harvard Medical School, Boston, MA 02115, USA.
*These authors contributed equally to this work.
†Corresponding author. E-mail: fswirski@mgh.harvard.edu (F.K.S.); georg.weber@uniklinikum-dresden.de (G.F.W.)

cytokine's source in sepsis is unknown. mRNA profiling identified the spleen, thymus, and lymph nodes as hubs of basal *Il3* expression. After CLP, *Il3* mRNA progressively increased in the spleen, followed by the thymus and lymph nodes, with no signal in the bone marrow, lung, liver, peritoneum, or duodenum (Fig. 3A). As indicated by flow cytometry (Fig. 3, B and C) and Western blots (Fig. 3D), IL-3$^+$ cells were CD19$^+$ B cells. According to enzyme-linked immunosorbent assay, IL-3 levels increased in serum after CLP (Fig. 3E) but to a lesser extent in splenectomized mice (Fig. 3E).

Identifying B cells as sources of IL-3 prompted testing of whether IL-3–producing B cells resemble innate response activator (IRA) B cells (fig. S8A), whose GM-CSF (granulocyte-macrophage colony-stimulating factor) product protects against sepsis and pneumonia via polyreactive immunoglobulin M (IgM) (*18*, *19*). Phenotypic profiling showed that splenic IL-3 producers were IgM^{high} CD23^{low} CD19$^+$ CD138^{high} CD43$^+$ VLA4$^+$ (Fig. 3F and fig. S8B), as well as CD5^{int} LFA1$^+$ CD284$^+$ CD11b$^{low/-}$ (fig. S8C). This phenotype matches that of IRA

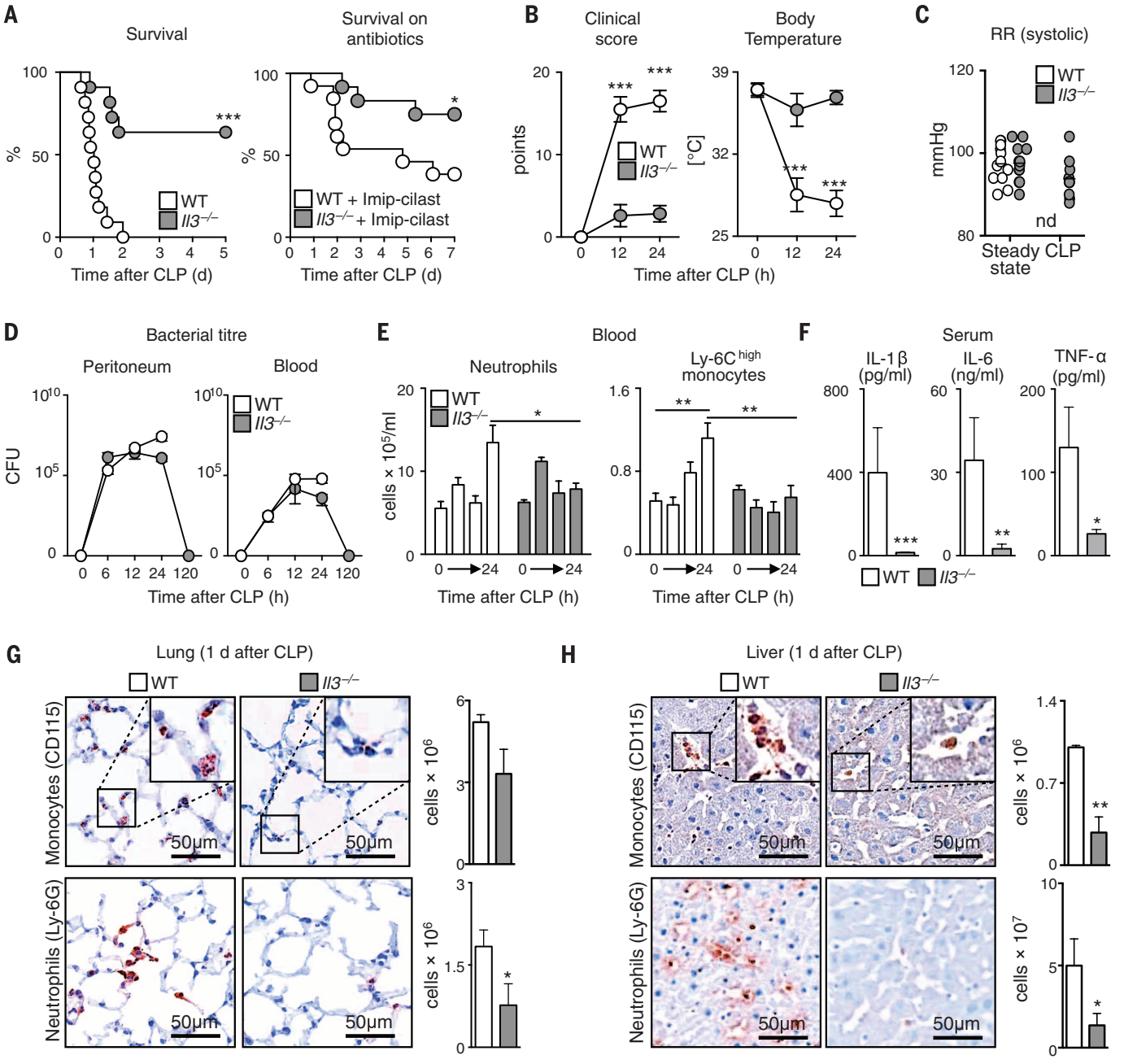

Fig. 1. IL-3 is detrimental in experimental sepsis. Comparison of *Il3*$^{-/-}$ and Balb/c (WT) mice during experimental sepsis using the CLP model. (**A**) Kaplan-Meier survival curve in mice not receiving antibiotics (n = 10 mice per group) and in mice receiving antibiotics (Imipenem) (n = 12 or 13 per group). d, days. (**B**) Clinical score and body temperature (n = 6 to 10 per group). h, hours. (**C**) Blood pressure. The blood pressure in WT mice was below the detection limit (n = 6 to 10 per group). (**D**) Bacterial titer of peritoneal cavity and blood (n = 3 to 10 per group). (**E**) Enumeration of neutrophils and Ly-6C^{high} monocytes in 1 ml of blood at 0, 6, 12, and 24 hours after CLP (n = 3 to 12 per group). (**F**) Levels of IL-1β, IL-6, and TNF-α in serum 1 day after CLP (n = 8 or 9 per group). (**G** and **H**) Immunohistochemical staining and flow cytometric enumeration of monocytes (CD115) and neutrophils (Ly-6G) in entire lung (G) and liver (H) tissue 1 day after CLP (n = 6; *P < 0.05, **P < 0.01, ***P < 0.001). Error bars indicate means ± SEM. Significance was assessed by log rank test (A) or Mann-Whitney test [(B) to (H)]. Data are the result of $N \geq 2$ independent experiments and are grouped.

B cells (*18*–*20*). The remaining, non-B IL-3–positive cells in the spleen and thymus were $CD4^+$ T cells, $CD8^+$ T cells, and non-T, non-B cells (fig. S8D).

By comparing IL-3 and GM-CSF, which are two IRA B cell products, we determined that the growth factors are not interdependent: In response to CLP, the spleens of *Csf2*$^{-/-}$ mice accumulated IL-3–producing IRA B cells, whereas *Il3*$^{-/-}$ mice accumulated GM-CSF–producing IRA B cells (fig. S9A). On the one hand, in contrast to GM-CSF (*19*), IL-3 was not essential to IgM production (fig. S9, B and C). On the other hand, unlike IL-3, GM-CSF was dispensable for emergency myelopoiesis (fig. S9D, E). The IL-3–producing IRA B cells were readily visualized by immunofluorescence and increased in frequency after CLP (Fig. 3, G and H, and fig. S10). Thus, IRA B cells can both protect against and aggravate sepsis, depending on the particular growth factor they produce.

Peritoneal B1 cells relocate to the spleen after peritoneal LPS challenge (*21*) and differentiate to IRA B cells (*18*). To determine whether IL-3$^+$ B cells arise similarly, we transferred B1 cells from the peritoneum of naïve GFP$^+$ mice into the peritoneum of WT mice. Two days after CLP, IL-3$^+$ (Fig. 3I) and GM-CSF$^+$ B cells (fig. S11) accumulated in the spleen, indicating peritoneal B cell relocation, splenic accumulation, and IRA B cell differentiation. To test whether IL-3–producing B cells are important in sepsis, we transferred peritoneal B1 B cells from WT or *Il3*$^{-/-}$ mice into *Il3*$^{-/-}$ mice subjected to CLP and found increased monocyte levels, cytokine levels, and morbidity in WT B cell recipients (Fig. 3J). Overall, the data show that IL-3–producing IRA B cells induce emergency myelopoiesis and potentiate septic shock in a mouse sepsis model.

Because the validity of mouse sepsis models as mirrors of human disease has been challenged (*22*, *23*), we sought to determine whether our experimental findings correlate with the pathogenesis of human sepsis. First, we retrospectively analyzed plasma from a cohort of septic patients [RAMMSES cohort, $n = 60$ (table S1)] (*24*) and found that IL-3 levels during the first 24 hours after the onset of sepsis predicted death: Patients

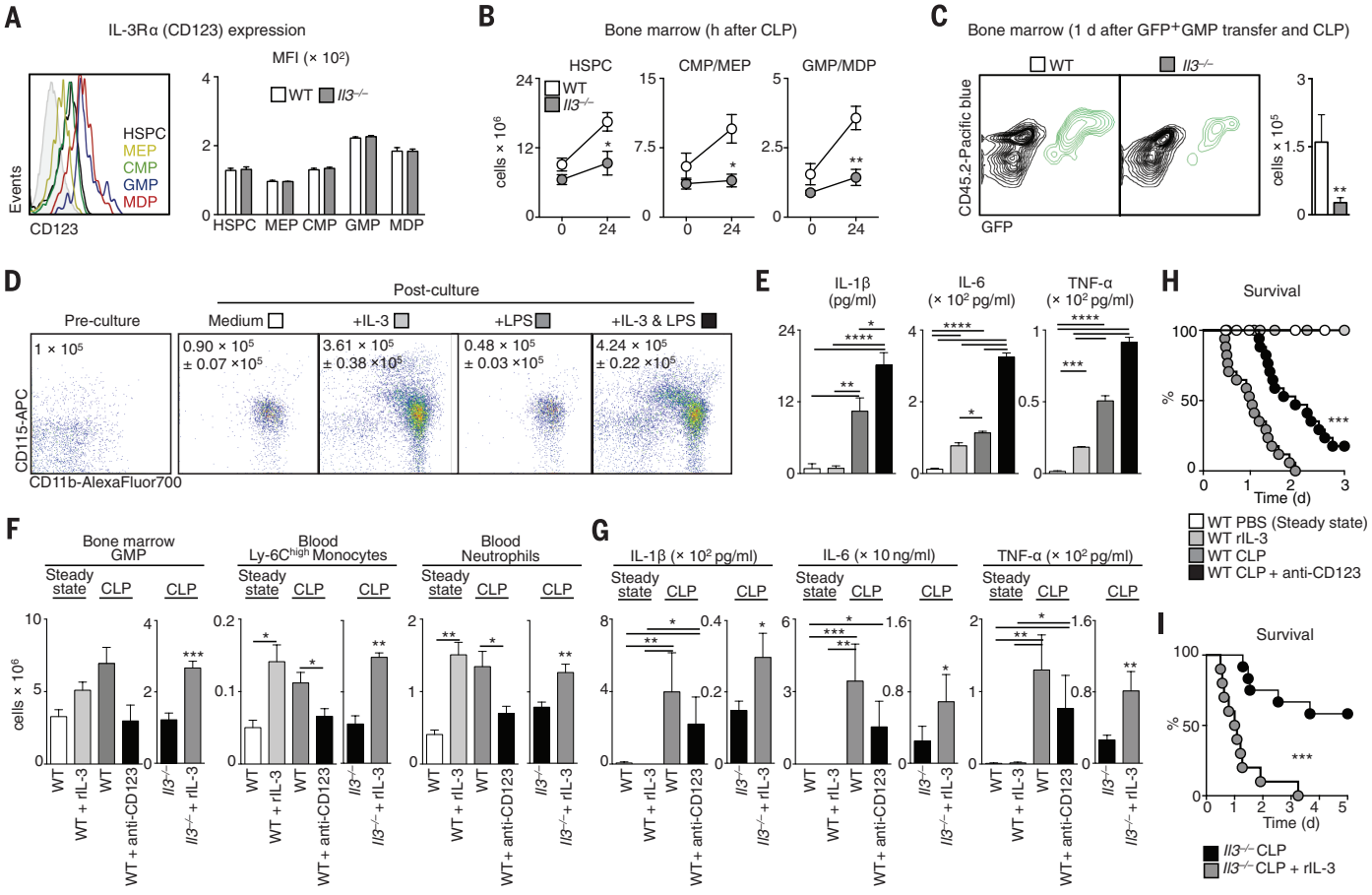

Fig. 2. IL-3 induces emergency hematopoiesis and potentiates the cytokine storm in sepsis. (**A**) Surface expression of IL-3Rα (CD123) on HSPCs, MEPs, CMPs, GMPs, and MDPs in bone marrow of WT and *Il3*$^{-/-}$ mice ($n = 3$ per group). A representative plot of $n = 3$ is shown. (**B**) Enumeration of HSPCs, CMPs/MEPs, and GMPs/MDPs in bone marrow in a steady state and 1 day after CLP in WT and *Il3*$^{-/-}$ mice ($n = 3$ per group). (**C**) Analysis and enumeration of GFP$^+$ cells retrieved from the bone marrow 1 day after CLP from WT and *Il3*$^{-/-}$ mice that received 2×10^5 GFP$^+$ GMP intravenously before CLP ($n = 3$ per group). (**D**) Bone marrow cells were sorted for Lin$^-$ cells (i.e., enriched in HSPCs). Shown are representative CD11b versus CD115 flow cytometry plots showing cell phenotype just before placement into culture and 4 days after in vitro culture in the indicated conditions. The numbers inside the plots denote cells plated and retrieved ($n = 4$ per group). (**E**) Supernatant levels of IL-1β, IL-6, and TNF-α in the four post-culture groups shown in (D). Values are the result of technical triplicates from $n = 2$ experiments. (**F**) Enumeration of indicated cell types in (i) WT mice at a steady state; (ii) WT mice receiving rIL-3 alone; (iii) WT mice subjected to CLP; (iv) WT mice subjected to CLP and receiving antibody to CD123; (v) *Il3*$^{-/-}$ mice subjected to CLP; and (vi) *Il3*$^{-/-}$ mice subjected to CLP and receiving rIL-3 ($n = 4$ to 10). (**G**) Serum levels of IL-1β, IL-6, and TNF-α in the six groups shown in (F) ($n = 4$ to 10). (**H**) Kaplan-Meier survival curves showing the four WT mouse groups ($n = 6$ to 17 per group). (**I**) Kaplan-Meier survival curves showing the two *Il3*$^{-/-}$ mouse groups ($n = 10$ per group) (*$P < 0.05$, **$P < 0.01$, ***$P < 0.001$). Error bars indicate means ± SEM. Significance was assessed by Mann-Whitney test [(B), (C), (F), and (G)]; one-way analysis of variance (ANOVA) with Tukey's multiple comparison test (E); Kruskal-Wallis test with Dunn's multiple comparison test [(F) and (G)]; and log rank [(H) and (I)]. Data are the result of $N = 2$ independent experiments acquired in triplicates (in vitro) and $n \geq 2$ independent experiments (in vivo), and are grouped.

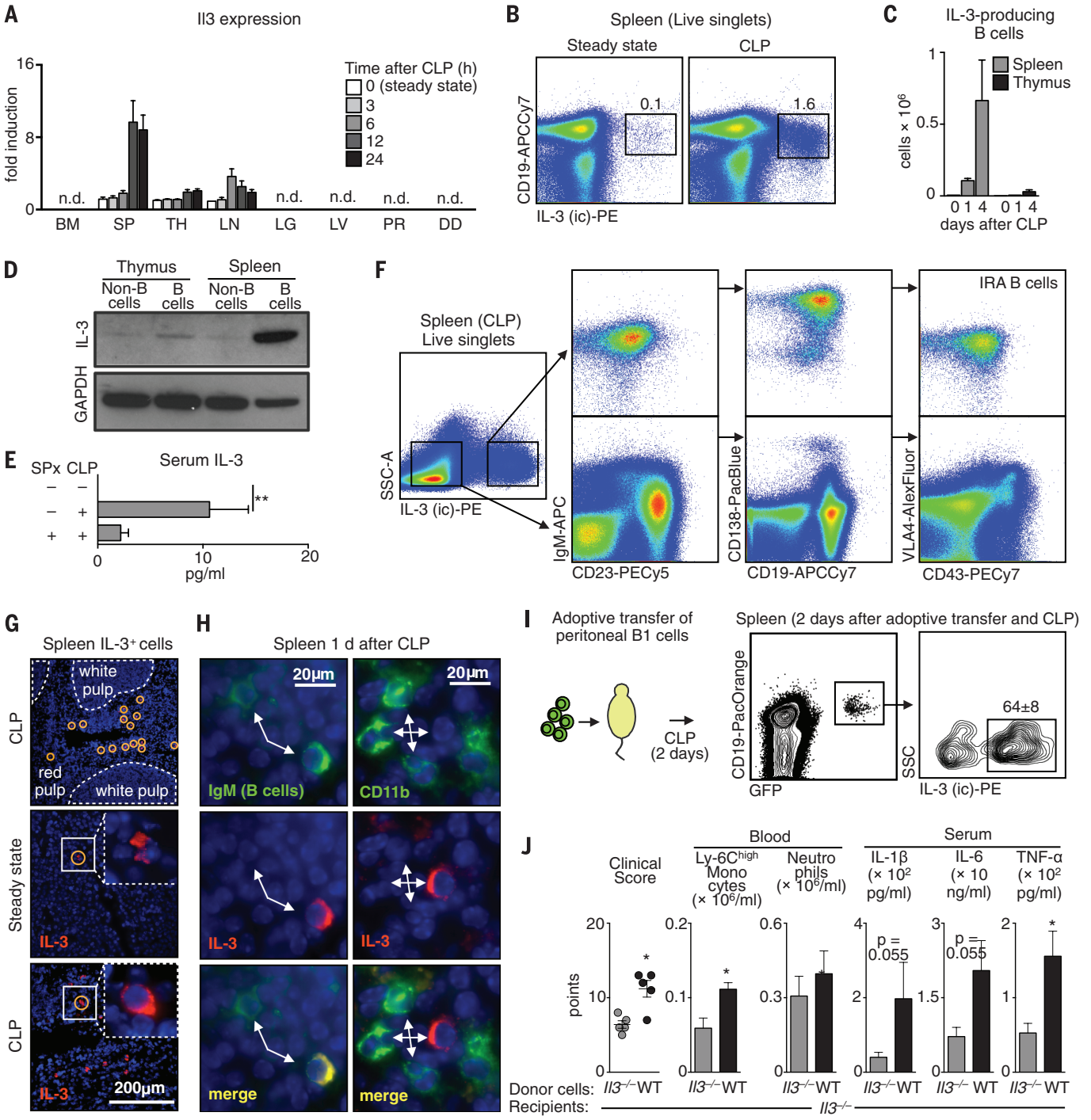

Fig. 3. IRA B cells are major sources of IL-3 in sepsis. (**A**) *Il3* mRNA expression in the indicated organs during a steady state and 3, 6, 12, and 24 hours after CLP (n = 6 to 8). (**B**) Identification of IL-3–producing cells in the spleen 4 days after CLP. (**C**) Enumeration of IL-3–producing B cells in spleen and thymus in a steady state and 1 and 4 days after CLP (n = 5). (**D**) Western blot showing IL-3 expression by B cells and non-B cells sorted from the spleen and thymus 1 day after CLP. (**E**) IL-3 serum levels in a steady state and 1 day after CLP with and without splenectomy (SPx) (n = 3 to 6). (**F**) Flow cytometric plots show the phenotype of IL-3$^+$ and IL-3$^-$ cells retrieved from the spleen after CLP. A representative plot of n = 5 is shown. (**G**) Immunofluorescence microscopy of spleen tissue in the steady state and 1 day after CLP. (**H**) Co-staining of representative IL-3$^+$ cells with IgM. (**I**) Adoptive transfer of 1.5 × 10^6 peritoneal B1 B cells from GFP$^+$ mice into WT mice subjected to CLP at the time of cell transfer. Representative plots from flow cytometric analysis of n = 3 mice are shown. (**J**) Adoptive transfer of 3 × 10^6 peritoneal B1 B cells from WT or *Il3*$^{-/-}$ mice to the peritoneum of *Il3*$^{-/-}$ recipients subjected to CLP. Data show the clinical score, number of Ly-6C^{high} monocytes, neutrophils, and serum cytokines 1 day after CLP (n = 5). (*P < 0.05, **P < 0.01). Error bars indicate means ± SEM. Significance was assessed by a Kruskal-Wallis test with Dunn's multiple comparison test (E) and a Mann-Whitney test (J).

with IL-3 plasma levels >87.4 pg/ml at admission had a poor prognosis (fig. S12, A and B, and table S2). We therefore decided to test, in a new prospective cohort [SEPIL-3 cohort, n = 37 (table S3)], whether IL-3 and blood monocytes correlate. In septic patients monitored over 28 days, blood leukocyte numbers peaked at the onset of sepsis and decreased slowly thereafter (Fig. 4A). The increase was associated with a sharp spike of plasma cytokines (Fig. 4B). Compared to healthy volunteers, mean IL-3 in septic patient plasma did not differ (Fig. 4C). Nevertheless, the detectable levels of IL-3 correlated with circulating monocyte levels in septic patients (Fig. 4D). Kaplan-Meier survival analysis showed that patients with plasma levels of >89.4 pg/ml had a poor prognosis (fig. S13 and table S4), thus confirming the results from the RAMMSES cohort. Pooling the cohorts showed the impact of IL-3 on survival to be even more striking (odds ratio: 4.979; confidence interval: 1.680 to 14.738 and P = 0.001 for the Kaplan-Meier survival curve) (Fig. 4E). The association remained significant after adjusting for prognostic parameters in multivariate analyses (table S5), whereas multivariate logistic regression analyses consistently showed improvement in the death prediction when IL-3 was included, as shown by a reduction of the Aikake information criterion and an increase of McFadden's pseudo R^2 (table S6). We also conducted flow cytometry and immunofluorescence on human spleens from patients undergoing splenectomy. By flow cytometry, we found CD20$^+$ HLADR^{int} CD19^{high} IgM$^{int/high}$ B and CD3$^+$ T cells to be producers of IL-3 (Fig. 4F and fig. S14A). In tissue sections, human spleens contained IL-3–producing CD19$^+$ and IgM$^+$ B cells (Fig. 4G and fig. S14, B and C), suggesting that IL-3–producing IRA B cells

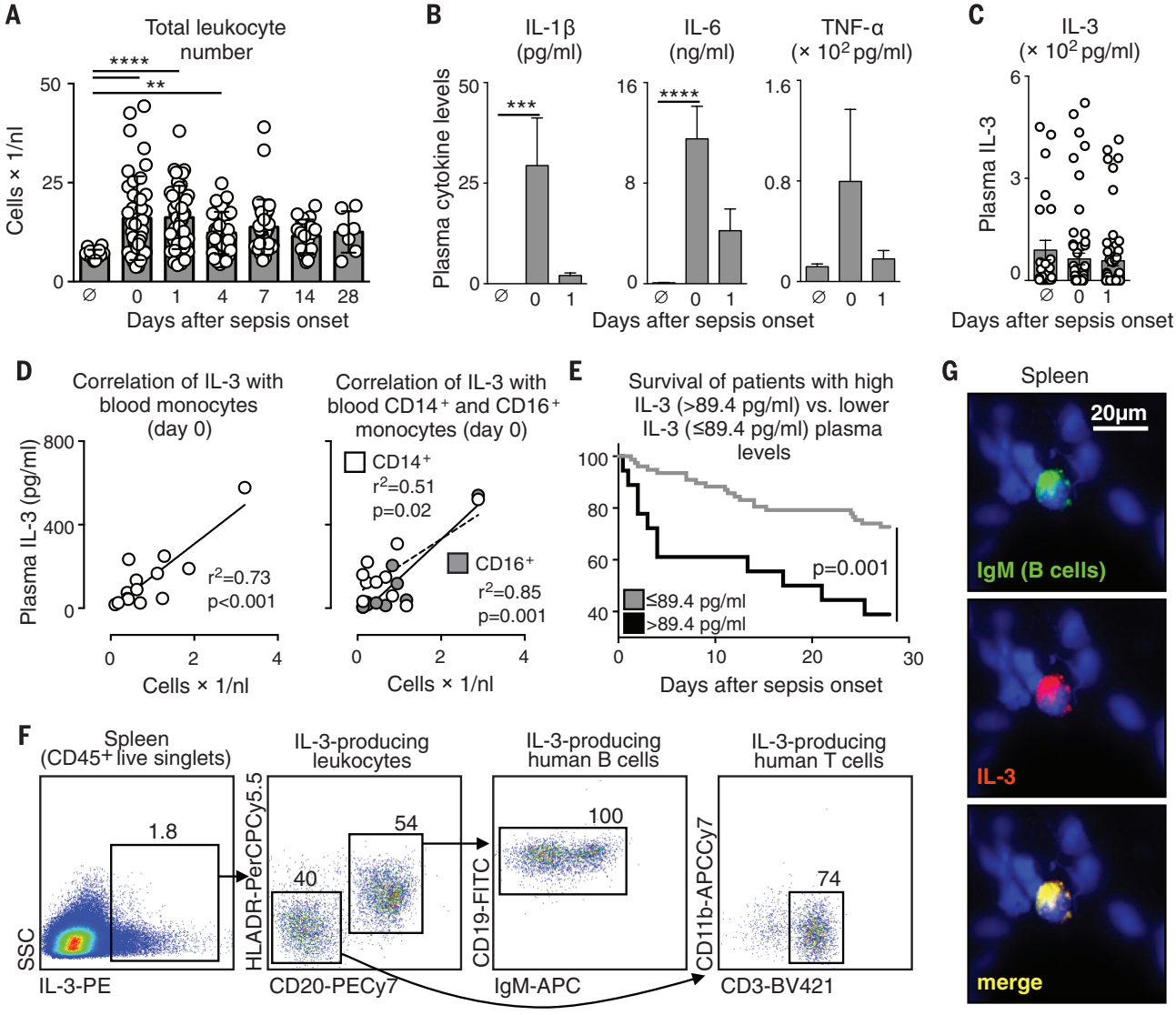

Fig. 4. IL-3 is an independent early predictor for outcome in human sepsis. (**A**) Total leukocyte number in nonseptic people and in septic patients at the time of sepsis onset (0) and 1, 4, 7, 14, and 28 days later. (**B**) Plasma levels of IL-1β, IL-6, and TNF-α in nonseptic people (n = 18) and in septic patients at the time of sepsis onset (n = 37) and 1 day later (n = 17). (**C**) IL-3 plasma levels in healthy people and in patients at sepsis onset and 1 day later. (**D**) Correlation of IL-3 plasma levels with total blood monocytes and with CD14$^+$ and CD16$^+$ blood monocytes in septic patients with measurable IL-3 plasma levels. (**E**) Kaplan-Meier analysis showing the survival of patients in the RAMMSES and SEPIL-3 studies with IL-3 at >89.4 pg/ml (top quintile, measured within 1 day after sepsis onset) versus the survival of patients with IL-3 ≤ 89.4 pg/ml. (**F**) Representative flow cytometry plot of n = 2 patients showing the identity of IL-3–producing human splenocytes. (**G**) Immunofluorescence of human spleen showing IL-3–producing B cells in high magnification (×60). A representative immunofluorescence section of n = 6 spleens is shown (*P < 0.05, ****P < 0.0001). Error bars indicate means ± SEM. Significance was assessed by one-way ANOVA with Tukey's multiple comparison test [(A) and (C)], a Pearson correlation test (D), and log rank (E). Data in (A) to (D) are from the SEPIL-3 cohort; data in (E) are pooled from the RAMMSES and SEPIL-3 cohorts.

amplify inflammation in humans as well as mice (fig. S15).

Mortality from sepsis ranges between 30 and 50% and is rising because of drug-resistant organisms, a growing elderly population, and an increased incidence of immunosuppression (*25*–*28*). The failures of anti–Toll-like receptor 4, recombinant activated protein C, and anti–TNF-α therapies in clinical trials necessitate a rethinking of sepsis' pathophysiology (*6*, *29*–*33*). Because many early-phase inflammatory cytokines operate concurrently and redundantly, identifying upstream triggers may generate therapies with broad downstream benefits. Altogether, the evidence shown here supports the hypothesis that IL-3 mediates experimental and human sepsis, is a major upstream orchestrator of the septic inflammatory phase, and can be harnessed for therapeutic intervention.

REFERENCES AND NOTES

1. Y. C. Yang *et al.*, *Cell* **47**, 3–10 (1986).
2. A. J. Hapel, J. C. Lee, W. L. Farrar, J. N. Ihle, *Cell* **25**, 179–186 (1981).
3. J. N. Ihle, L. Pepersack, L. Rebar, *J. Immunol.* **126**, 2184–2189 (1981).
4. G. T. Williams, C. A. Smith, E. Spooncer, T. M. Dexter, D. R. Taylor, *Nature* **343**, 76–79 (1990).
5. D. C. Angus, T. van der Poll, *N. Engl. J. Med.* **369**, 840–851 (2013).
6. R. S. Hotchkiss, G. Monneret, D. Payen, *Nat. Rev. Immunol.* **13**, 862–874 (2013).
7. C. S. Deutschman, K. J. Tracey, *Immunity* **40**, 463–475 (2014).
8. Materials and methods are available as supplementary materials on *Science* Online.
9. D. Rittirsch, M. S. Huber-Lang, M. A. Flierl, P. A. Ward, *Nat. Protoc.* **4**, 31–36 (2009).
10. M. C. Jamur, C. Oliver, *Front. Biosci. (Schol. Ed.)* **S3**, 1390–1406 (2011).
11. D. Voehringer, *Eur. J. Immunol.* **42**, 2544–2550 (2012).
12. E. Rönnberg *et al.*, *Immunology* **143**, 155–163 (2014).
13. D. Annane, E. Bellissant, J. M. Cavaillon, *Lancet* **365**, 63–78 (2005).
14. P. A. Ward, *EMBO Mol. Med.* **4**, 1234–1243 (2012).
15. M. Kondo *et al.*, *Annu. Rev. Immunol.* **21**, 759–806 (2003).
16. J. E. Groopman, J. M. Molina, D. T. Scadden, *N. Engl. J. Med.* **321**, 1449–1459 (1989).
17. A. H. Dalloul *et al.*, *Blood* **77**, 69–74 (1991).
18. P. J. Rauch *et al.*, *Science* **335**, 597–601 (2012).
19. G. F. Weber *et al.*, *J. Exp. Med.* **211**, 1243–1256 (2014).
20. I. Hilgendorf *et al.*, *Circulation* **129**, 1677–1687 (2014).
21. S. A. Ha *et al.*, *J. Exp. Med.* **203**, 2541–2550 (2006).
22. J. Seok *et al.*, *Proc. Natl. Acad. Sci. U.S.A.* **110**, 3507–3512 (2013).
23. K. Takao, T. Miyakawa, *Proc. Natl. Acad. Sci. U.S.A.* **112**, 1167–1172 (2015).
24. T. Brenner *et al.*, *Crit. Care* **18**, 683 (2014).
25. G. S. Martin, D. M. Mannino, S. Eaton, M. Moss, *N. Engl. J. Med.* **348**, 1546–1554 (2003).
26. K. A. Wood, D. C. Angus, *Pharmacoeconomics* **22**, 895–906 (2004).
27. M. Bosmann, P. A. Ward, *Trends Immunol.* **34**, 129–136 (2013).
28. C. M. Coopersmith *et al.*, *Crit. Care Med.* **40**, 1072–1079 (2012).
29. E. Dolgin, *Nat. Med.* **18**, 1000 (2012).
30. S. M. Opal *et al.*, *Crit. Care Med.* **25**, 1115–1124 (1997).
31. J. S. Boomer *et al.*, *JAMA* **306**, 2594–2605 (2011).
32. R. S. Hotchkiss, C. M. Coopersmith, J. E. McDunn, T. A. Ferguson, *Nat. Med.* **15**, 496–497 (2009).
33. P. A. Ward, *JAMA* **306**, 2618–2619 (2011).

ACKNOWLEDGMENTS

We thank M. Greene for secretarial assistance, M. Waring and A. Chicoine for sorting cells, and K. Joyes for editing the manuscript. The data presented in this manuscript are tabulated in the main paper and in the supplementary materials. The General Hospital Corporation has filed a patent application (61/973,458) with the U.S. Patent and Trademark Office entitled "Agents and Methods for Diagnosing and Treating Sepsis," which names F.K.S. and G.F.W. as inventors. *Il3*$^{-/-}$ mice are available from Riken, Japan, under a materials transfer agreement. This work was supported by NIH grants 5R01HL095612 and R56-AI104695 and the Massachusetts General Hospital Howard M. Goodman Fellowship (F.K.S.). G.F.W. was supported by the German Research Foundation (WE4892/1-2 and 3-1). B.G.C. was supported by the Société Française d'Anesthésie-Réanimation (SFAR), Institut Servier, Fondation Groupe Pasteur Mutualité, and Fulbright Scholarships (Monahan Foundation and Harvard French Scholarship Fund). M.N. was supported by an Erwin Schrödinger Fellowship of the Austrian Science Fund FWF (J3486-B13). The authors declare no conflicts of interest.

SUPPLEMENTARY MATERIALS

www.sciencemag.org/content/347/6227/1260/suppl/DC1
Materials and Methods
Figs. S1 to S15
Tables S1 to S6
References (*34*–*36*)

4 December 2014; accepted 21 January 2015
10.1126/science.aaa4268

CIRCADIAN RHYTHMS

Time-restricted feeding attenuates age-related cardiac decline in *Drosophila*

Shubhroz Gill,[1,2] Hiep D. Le,[1] Girish C. Melkani,[3]* Satchidananda Panda[1]*

Circadian clocks orchestrate periods of rest or activity and feeding or fasting over the course of a 24-hour day and maintain homeostasis. To assess whether a consolidated 24-hour cycle of feeding and fasting can sustain health, we explored the effect of time-restricted feeding (TRF; food access limited to daytime 12 hours every day) on neural, peripheral, and cardiovascular physiology in *Drosophila melanogaster*. We detected improved sleep, prevention of body weight gain, and deceleration of cardiac aging under TRF, even when caloric intake and activity were unchanged. We used temporal gene expression profiling and validation through classical genetics to identify the TCP-1 ring complex (TRiC) chaperonin, the mitochondrial electron transport chain complexes, and the circadian clock as pathways mediating the benefits of TRF.

To determine whether a daily rhythm of feeding and fasting without reducing caloric intake can improve health metrics, we subjected a 2-week-old wild-type (WT) Oregon-R strain (table S1) of *Drosophila melanogaster* adults to ad libitum feeding (ALF) or 12-hour time-restricted feeding (TRF) of a standard cornmeal diet exclusively during daytime. At nighttime, the TRF cohorts were placed in vials with 1.1% agar to prevent desiccation (fig. S1A). The daily food intake was equivalent in both groups, although ALF flies consumed some of their food during nighttime (Fig. 1A). Unlike ALF flies, the TRF group did not gain body weight at 5 and 7 weeks of age (Fig. 1B). The ability to fly (flight index) was slightly improved in the TRF group (Fig. 1C). Although the total daily activity was equivalent between both groups of flies (Fig. 1D), the TRF flies were more active during daytime. Sleep (defined as five consecutive minutes of inactivity) (*1*) assessment revealed that flies on TRF had less daytime sleep, but more nighttime and more total sleep, than the ALF flies (Fig. 1E and fig. S1).

Increase in sleep duration correlates with improved cardiac function (*2*). Therefore, by high-speed video imaging of ex vivo denervated hearts bathed in artificial hemolymph (*3*), we measured the diameter of the beating *Drosophila* heart at full relaxation and contraction and the time interval between successive contractions to calculate cardiac function parameters (Fig. 2A). At 3 weeks of age, the performance of both ALF and TRF hearts was indistinguishable with equivalent heart period (HP), systolic diameter (SD), systolic interval (SI), diastolic diameter (DD), diastolic interval (DI), arrhythmia index (AI), and heart contractility, measured as fractional shortening (FS) (Fig. 2, B to F; fig. S2; and movie S1). In the next 2 weeks, the cardiac performance in ALF flies exhibited characteristic age-dependent deterioration (*4*), with increased SI, DI, HP, and AI and reduced DD, SD, and FS. TRF flies showed smaller changes in these cardiac performance parameters in both genders (fig. S2).

We investigated whether a limited period of TRF early or late in life could attenuate age-dependent

[1]Regulatory Biology Laboratory, The Salk Institute for Biological Studies, La Jolla, CA 92037, USA. [2]Division of Biological Sciences, University of California San Diego, La Jolla, CA 92037, USA. [3]Departments of Biology and Molecular Biology, and Heart Institutes, San Diego State University, San Diego, CA 92182, USA.
***Corresponding author. E-mail: gmelkani@mail.sdsu.edu (G.C.M.); satchin@salk.edu (S.P.)**

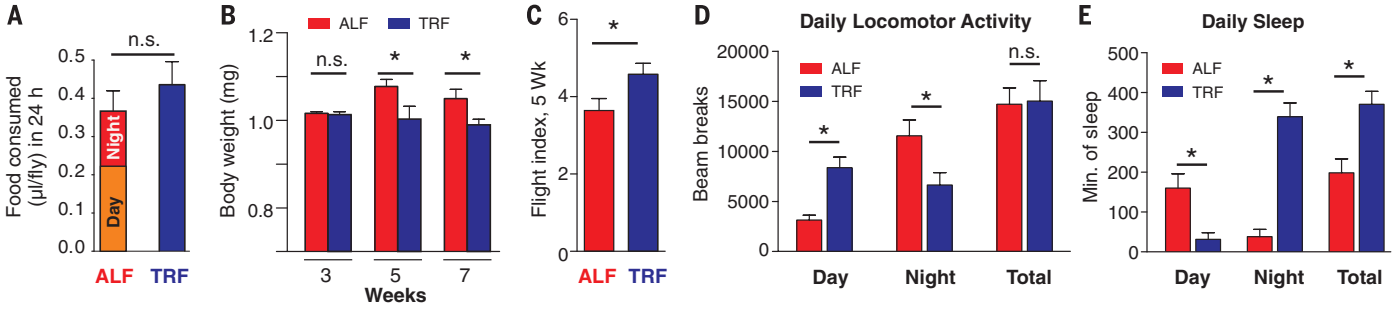

Fig. 1. TRF improves sleep and prevents body weight gain without reducing caloric intake. (**A**) Food consumption (Capillary Feeder or CAFÉ assay) over a 24-hour period in 5-week-old WT Oregon-R flies. (**B**) Body weight of 3-, 5-, and 7-week-old flies. (**C**) Flight index of 5-week-old flies ($n > 30$ flies). (**D**) Activity counts and (**E**) sleep duration of 5-week-old flies averaged from at least 7 days of recording. Values are mean + SEM, $^*P < 0.05$, not significant (n.s.): $P > 0.05$, Student's t test.

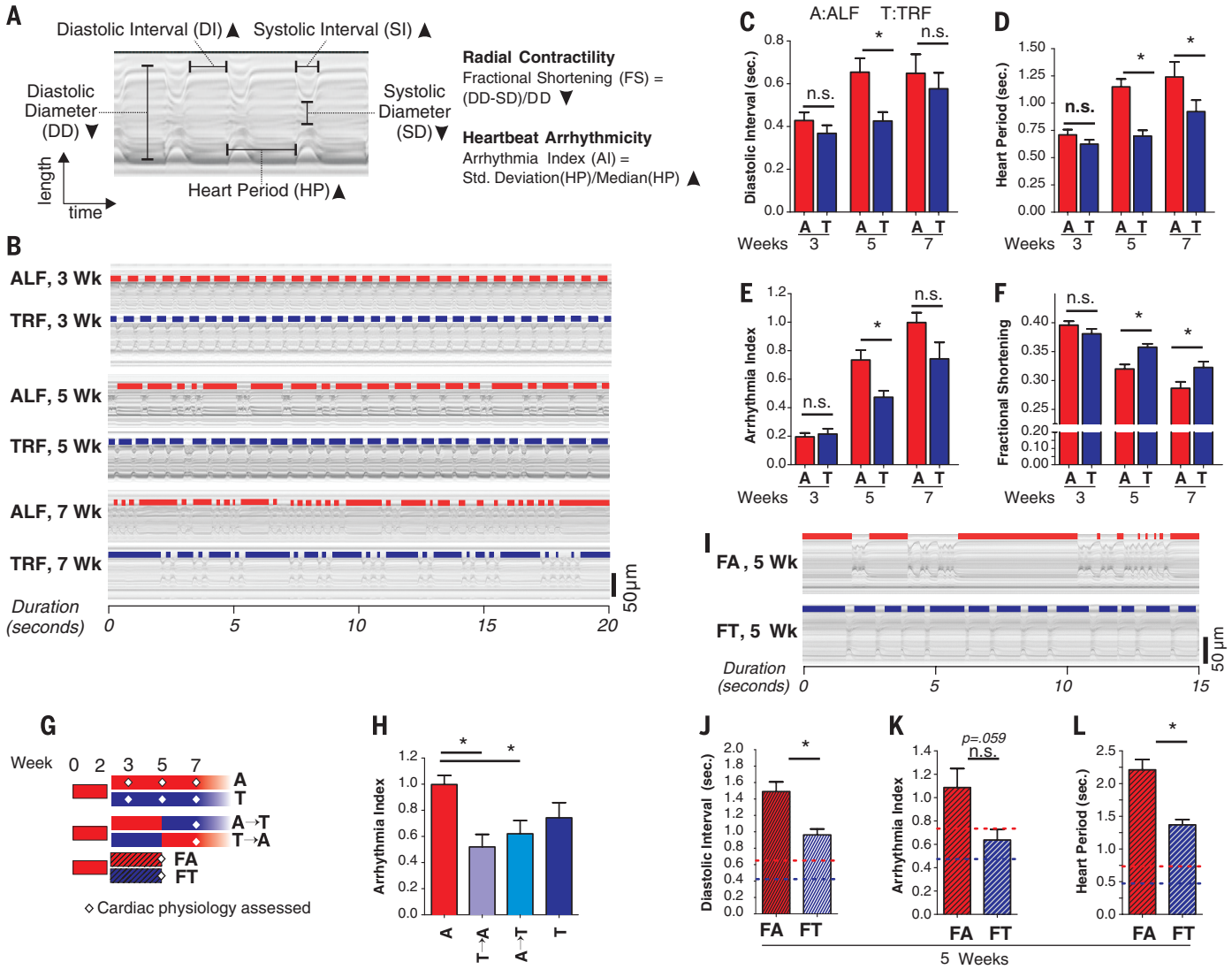

Fig. 2. TRF protects against age- and diet-induced decline in cardiac function. (**A**) M-mode (mechanical mode) traces showing the movement of the heart tube edge (y axis) over time (x axis) were generated from videos of the heart beneath the third thoracic segment by digitally excising and aligning a 1-pixel-wide vertical strip spanning the heart tube from a fixed location in successive frames. From the M-mode, cardiac parameters are calculated. Arrowheads indicate the direction of age- or high-fat diet–induced changes. (**B**) Example 20-s M-mode traces of ALF and TRF flies with superimposed orange (ALF) or blue (TRF) bar indicating diastolic intervals. Average (**C**) DI, (**D**) HP, (**E**) AI, and (**F**) FS show protection from age-dependent deterioration in the TRF flies. (**G**) Feeding regimens used to test the effect of TRF at an early or late age revealed improvement in (**H**) AI. (**I**) Representative M-modes of 5-week-old flies subjected to fat diet ALF (FA) or TRF (FT). Average (**J**) DI, (**K**) AI, and (**L**) HP improved under TRF. Average values for ALF and TRF flies fed normal cornmeal diets are shown as broken lines for reference. Averages ($n > 30$) are shown. $^*P < 0.05$, Mann Whitney test. Error bars: SEM.

decline in cardiac performance. Flies on ALF or TRF at 5 weeks of age were switched to the TRF or ALF condition, respectively (Fig. 2G). In both groups, 7-week-old flies showed improvement in some (but not all; see fig. S3) parameters, including reduced HP and AI, as well as increased FS relative to that of flies maintained in ALF for 7 weeks (Fig. 2H).

Because fat-containing diets deteriorate cardiac performance (*5*, *6*), we tested the effect of TRF on flies fed a standard cornmeal diet supplemented with 2% w/v coconut oil. Flies on this fat diet ad libitum (FA) for 3 weeks showed severe deterioration of cardiac performance relative to standard cornmeal-fed counterparts, including long HP, increased AI, and reduced FS. Yet flies fed the same fat-supplemented diet under TRF condition (FT; access to fat diet for 12 hours of daytime) showed smaller declines in cardiac performance (Fig. 2, I to L; fig. S4; and movie S2) relative to the FA cohort.

The improved cardiac function under TRF could result from systemic changes, local changes in the heart, or both. We measured RNA concentrations in the head and periphery (i.e., entire fly except the head) of 3-, 5-, and 7-week-old ALF and TRF (standard diet) flies collected every 6 hours over 24 hours (ZT or zeitgeber time 0, 6, 12, and 18). In TRF flies, the gene expression signature had no resemblance to that of flies exposed to starvation (*7*) or dietary restriction (DR) (*8*) (figs. S5 and S6 and tables S2 and S3). No transcript showed a large change (fold change > 2 between ALF and TRF group, $P < 0.05$) at both 5 and 7 weeks of age, indicating that either the diurnal expression pattern or a small but concerted change in the expression level of multiple, functionally related genes might account for the health benefits of TRF.

To assess diurnal gene expression, we examined transcripts from the head and the periphery of 5-week-old flies (on normal diet; ALF or TRF) at eight different time points spanning 24 hours. A total of 868 transcripts in the head and 1233 transcripts in the periphery were defined as rhythmic under both ALF and TRF conditions ($P < 0.05$, 22 hours < period < 26 hours) (Fig. 3, A and B, and tables S4 and S5). There were differences in the amplitude and synchrony of these oscillating transcripts in ALF and TRF flies. The amplitude (peak-to-trough difference)

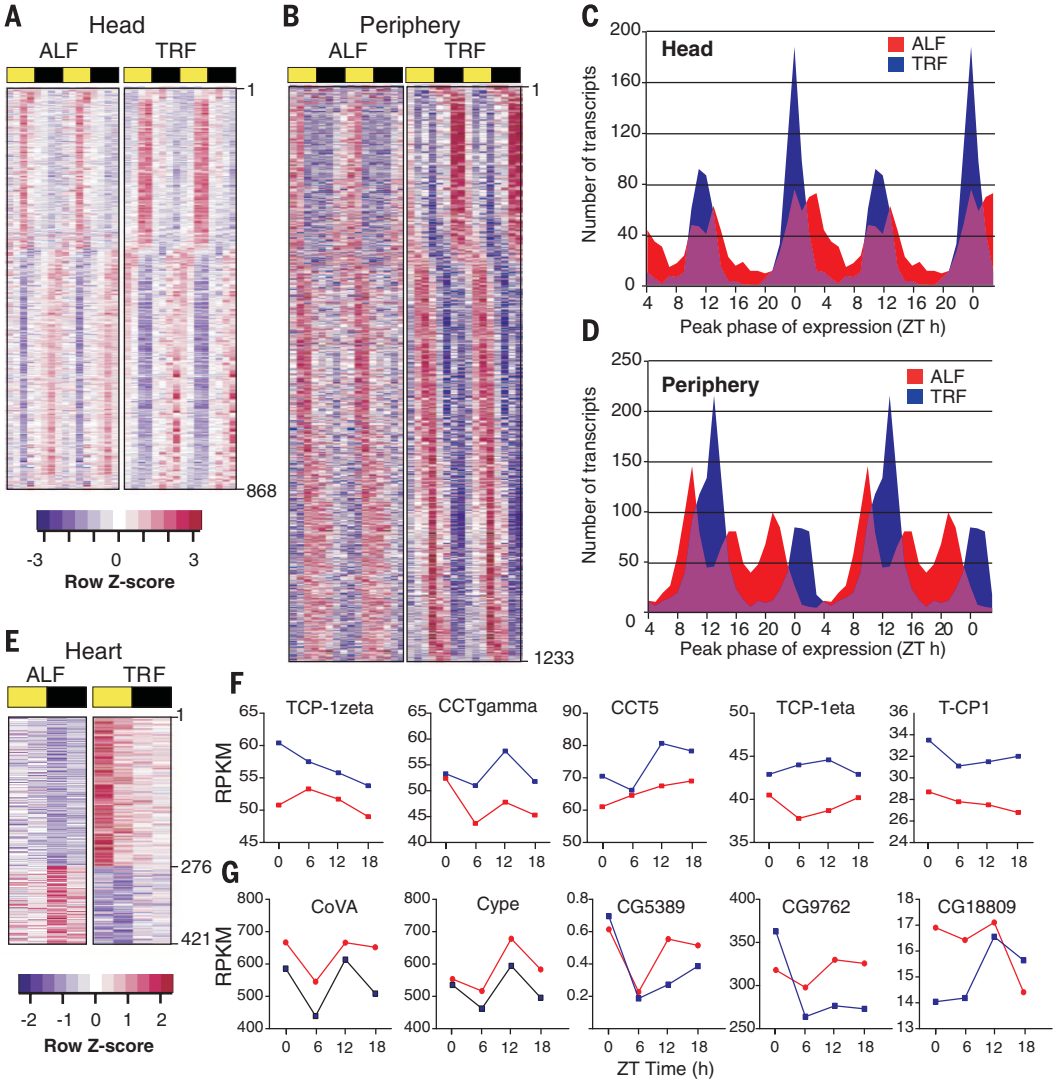

Fig. 3. Transcriptional correlates of improved health in TRF. Heat-map representation of transcripts scored rhythmic under both ALF and TRF conditions in (**A**) head and (**B**) periphery of 5-week-old flies. Normalized and color-coded transcript levels at eight different Zeitgeber times (ZT) spanning day (yellow bar) and night (dark bar) are shown. Area plots showing the peak phase of expression of rhythmic transcripts in ALF (red) or TRF (blue) fly (**C**) head or (**D**) periphery binned into 1-hour intervals. For clarity, data in (A) to (D) are double plotted over two 24-hour periods. (**E**) Heat-map representation of transcripts that are up- (purple) or down- (blue) regulated in TRF flies. Transcript levels in fly hearts collected at 6-hour intervals over 24 hours are shown. (**F**) Expression level (RPKMs; reads per kilobase of gene model per million reads uniquely aligned to the genome) of example TRiC chaperonin subunits and (**G**) ETC components in ALF and TRF hearts at 5 weeks age.

of oscillation of 876 transcripts (71%) from the periphery and 516 transcripts from the head (59%) increased under the TRF condition. Furthermore, the peak phases of expression of rhythmic transcripts in ALF flies were distributed over 24 hours, whereas TRF consolidated the peak phases to two principal times of the day corresponding to the ends of the feeding and fasting periods (Fig. 3, C and D). These synchronous transcript oscillations may coordinate fasting- or feeding-related metabolism to the appropriate time. As seen in mice (*9*), the combined action of the molecular circadian clock and the imposed rhythm of feeding and fasting may improve gene expression rhythms under TRF and offer systemic metabolic benefit.

To identify the transcriptomic correlates of improved cardiac physiology, we measured cardiac gene expression in 5-week-old ALF and TRF flies every 6 hours over a 24-hour period. Heart-enriched transcripts including *Hand*, *Tinman*, *He*, and *H15* (*10*) were confirmed to be more abundant in the heart than in the head and the periphery. Comparisons between ALF and TRF yielded 145 and 276 transcripts that showed decreased or increased expression, respectively, at all four time points in the TRF hearts (Fig. 3, E to G, and table S6). Functional annotation of these transcripts identified the adenosine 5′-triphosphate (ATP)–dependent TCP-1 ring complex (TRiC) (also known as chaperonin-containing TCP-1; CCT) chaperonin (*11*) and mitochondrial electron transport chain (ETC) as the top functional clusters with increased or decreased expression in the TRF heart, respectively. Seven out of eight TRiC subunit RNAs were more abundant at all four time points (fig. S7 and table S8). Concurrently, mRNAs encoding 52 components of the ETC were decreased in abundance at three out of four time points and 27 at all four time points in TRF hearts (fig. S8 and table S7). Thus, we considered the circadian clock, TRiC chaperonin, and mitochondrial ETC as potentially mediating the beneficial cardioprotective effects of TRF.

The *Drosophila* circadian oscillator is based on a transcriptional negative feedback loop generated by the activators clock (CLK) and cycle (CYC) and the repressors period (PER) and timeless (TIM) (*12*). To test the role of the molecular clock in TRF-dependent improvement of cardiac physiology, we examined flies carrying loss-of-function mutations in oscillator components: *clk*, *cyc*, *per*, or *tim*. These fly strains lacking both molecular and behavioral circadian rhythms are born without major morphological defects of the heart. Although these mutants all lacked a functional circadian oscillator, cardiac performance in 5-week-old flies was variably affected under ALF (Fig. 4A and fig. S9). For example, the heart period of per^{01} and clk^{ar} mutants was comparable to that of WT, whereas cyc^{01} and tim^{01} mutants showed slower heart rate (Fig. 4A). The WT flies on TRF showed improved relaxation-contraction function relative to their ALF counterparts, as reflected in decreased heart period and arrhythmicity. However, the heart period increased in clk^{ar} mutant flies and did not change significantly in per^{01} and cyc^{01} mutants. TRF increased arrhythmia in cyc^{01} flies and had smaller or no significant effect in per^{01}, tim^{01}, or clk^{ar} flies (Fig. 4, A and B, and movie S3). Thus, imposition of a diurnal feeding rhythm was insufficient for protecting against cardiac aging unless endogenous circadian oscillations were intact (figs. S9 and S10).

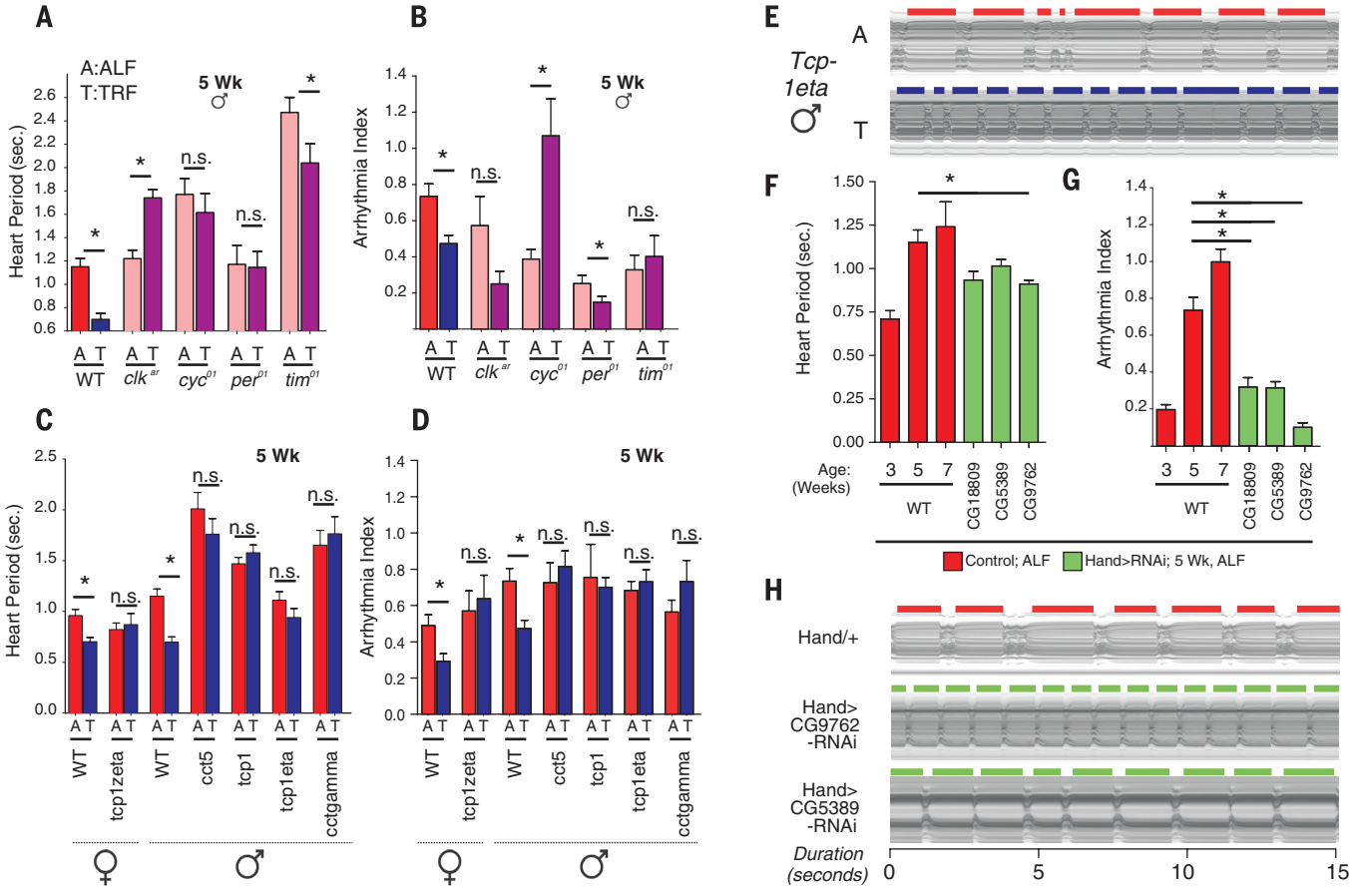

Fig. 4. Genetic basis for the beneficial effects of TRF. Five-week-old flies carrying loss-of-function mutations in (**A** and **B**) clock components or heterozygous for P-element insertions in (**C** and **D**) TRiC chaperonin components fail to improve (A and C) HP and (B and D) AI under TRF ($n \geq 12$ circadian mutants, $n \geq 17$ TRiC mutants). WT (Oregon-R) data are included for reference. (**E**) Representative M-modes of *Tcp-1eta* mutant flies exhibiting lack of TRF-driven cardioprotection. (**F**) HP, (**G**) AI, and (**H**) representative M-modes show improved cardiac function in 5-week-old ALF flies with heart-specific knockdown of genes encoding mitochondrial ETC proteins relative to 5-week-old male WT flies ($n \geq 24$). Three- and 7-week-old male WT data are included for reference. *$P < 0.05$, Mann Whitney test. Error bars: SEM.

We tested whether the TRiC chaperonin complex contributes to the beneficial cardioprotective effect of TRF. We investigated heterozygous P-element insertional mutants for five TRiC chaperonin subunits (*cct5*, *cct-gamma*, *tcp1*, *tcp-1eta*, *tcp-1zeta*) under ALF and TRF. No gross morphological heart defect was seen in ALF TRiC flies (fig. S11). For the TRiC mutants, TRF failed to improve cardiac contractility relative to genotype- and age-matched ALF flies as measured by heart period and arrhythmicity (Fig. 4, C to E; figs. S11 and S12; and movie S4). A potential dominant-negative effect of the P-element insertion or the reduced expression of some TRiC components (fig. S12) might affect normal function of the TRiC complex in these mutants. The lack of cardioprotective benefits of TRF by multiple mutants for different TRiC subunits provides genetic evidence that the integrity of the entire TRiC complex supports TRF-driven deceleration of cardiac aging.

To determine whether the cardiac tissue–restricted reduction of mitochondrial ETC transcripts contributes to TRF-dependent cardioprotection, we tested flies with heart-specific RNA interference (RNAi)–mediated reduction of ETC complex components. Heart-specific RNAi of complex I component CG9762 led to improved cardiac physiology in 5-week-old ALF flies (Fig. 4, F to H, and movie S5), reminiscent of TRF benefits in WT flies. Heart-specific RNAi of two additional components, CG5389 and CG18809, also led to reduced arrhythmia in 5-week-old ALF flies, although improvement in HP was not significant (Fig. 4, F to H, and fig. S13). Thus, lowering of ETC function may account for at least a part of the beneficial effect of TRF.

Genetic, dietary, and lifestyle (shiftwork) perturbation of circadian rhythms predisposes organisms to chronic diseases, including cardiovascular diseases. In rodents, the daily cycle of feeding-fasting under TRF reinforces diurnal rhythms in multiple organs and prevents metabolic diseases when the animals are administered a high-fat diet (*13*). Here we show that TRF protects against cardiac tissue aging in flies on either a normal or a fat-supplemented diet. This benefit appears to be mediated by the circadian clock, the TRiC chaperonin, and mitochondrial ETC components.

REFERENCES

1. P. J. Shaw, C. Cirelli, R. J. Greenspan, G. Tononi, *Science* **287**, 1834–1837 (2000).
2. F. P. Cappuccio, D. Cooper, L. D'Elia, P. Strazzullo, M. A. Miller, *Eur. Heart J.* **32**, 1484–1492 (2011).
3. M. Fink *et al.*, *Biotechniques* **46**, 101–113 (2009).
4. R. J. Wessells, E. Fitzgerald, J. R. Cypser, M. Tatar, R. Bodmer, *Nat. Genet.* **36**, 1275–1281 (2004).
5. R. T. Birse *et al.*, *Cell Metab.* **12**, 533–544 (2010).
6. R. T. Birse, R. Bodmer, *Crit. Rev. Biochem. Mol. Biol.* **46**, 376–385 (2011).
7. S. F. Farhadian, M. Suárez-Fariñas, C. E. Cho, M. Pellegrino, L. B. Vosshall, *Physiol. Behav.* **105**, 544–553 (2012).
8. M. Antosh *et al.*, *Cell Cycle* **10**, 904–911 (2011).
9. C. Vollmers *et al.*, *Proc. Natl. Acad. Sci. U.S.A.* **106**, 21453–21458 (2009).
10. K. Ocorr *et al.*, *Trends Cardiovasc. Med.* **17**, 177–182 (2007).
11. A. Y. Dunn, M. W. Melville, J. Frydman, *J. Struct. Biol.* **135**, 176–184 (2001).
12. P. E. Hardin, S. Panda, *Curr. Opin. Neurobiol.* **23**, 724–731 (2013).
13. M. Hatori *et al.*, *Cell Metab.* **15**, 848–860 (2012).

ACKNOWLEDGMENTS

We thank Vienna Drosophila RNAi Center, Bloomington Stock Center, and P. Hardin for fly strains; R. Bodmer and K. Ocorr for use of *Drosophila* heart analysis setup; S. Bernstein for use of the lab facility; and M. Ku and C. Benner for RNA sequencing and bioinformatics. This work was partially supported by NIH grants DK091618, EY016807, and NS066457 and American Federation for Aging Research grant M14322 to S.P. and by NIH grant RR032100 and American Heart Association grant 13BGIA17260057 to G.C.M. S.G. was supported by the H. A. and Mary K. Chapman Trust, an Aginsky Research Scholar Award, and Leona M. and Harry B. Helmsley Charitable Trust grant 2012-PG-MED002. Additional support came from NIH P30 CA014195, P30 EY019005, and the Glenn Center for Aging. We declare no conflicting interests.

SUPPLEMENTARY MATERIALS

www.sciencemag.org/content/347/6227/1265/suppl/DC1
Materials and methods
Figs. S1 to S14
Tables S1 to S9
Movies S1 to S5
References (*14*–*23*)

29 May 2014; accepted 12 February 2015
10.1126/science.1256682

TRANSLATE DISCOVERIES INTO INNOVATIONS

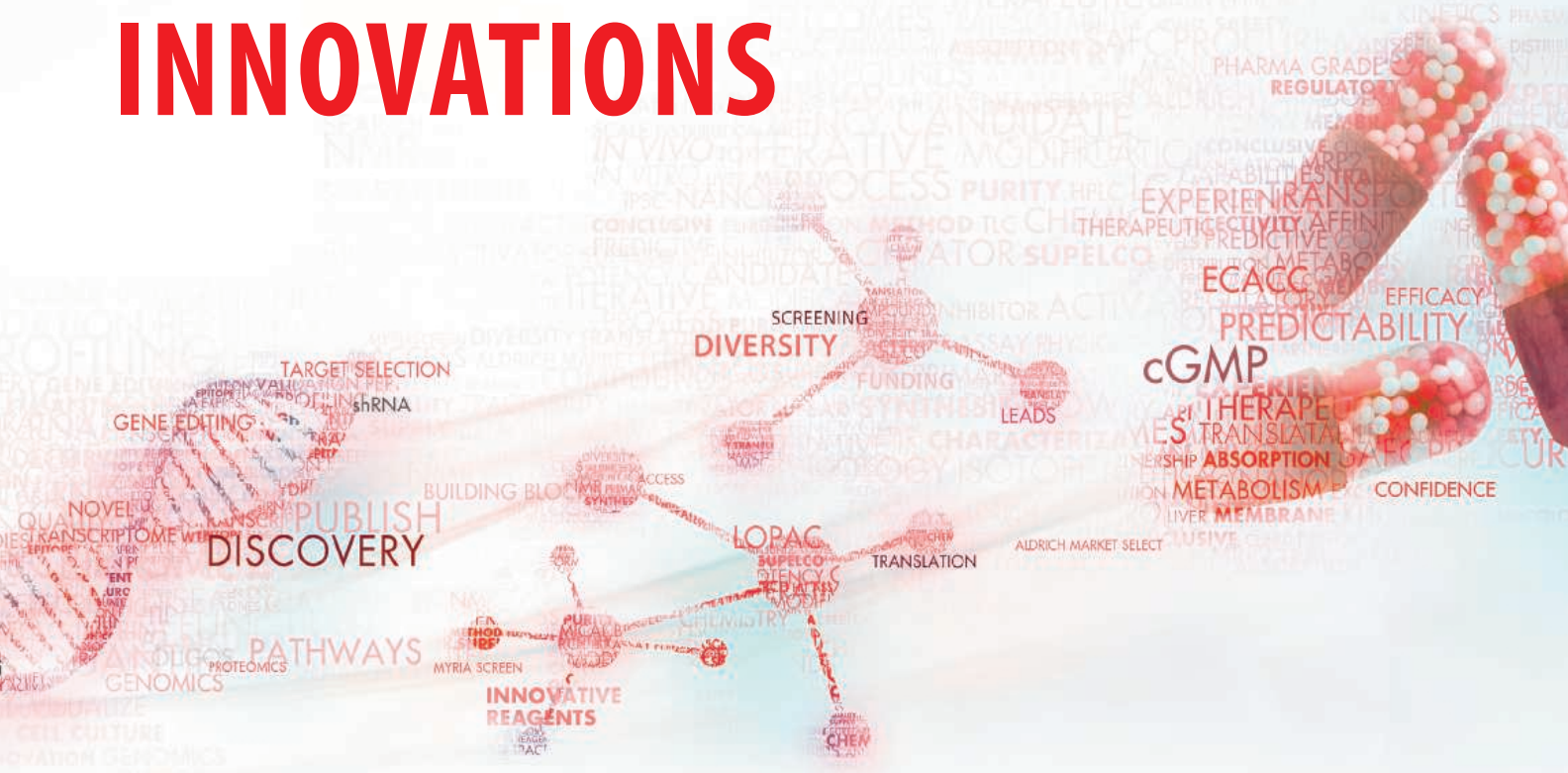

Improve accuracy, reproducibility and confidence in your discovery process

- **Late Stage Functionalization** – fueled by academic collaborations
- **Lab Essentials** – optimized portfolio to accelerate discovery
- **Innovative Catalysts and Reagents** – a market leading pipeline for creating diverse compounds

TRANSLATIONAL RESEARCH SOLUTIONS

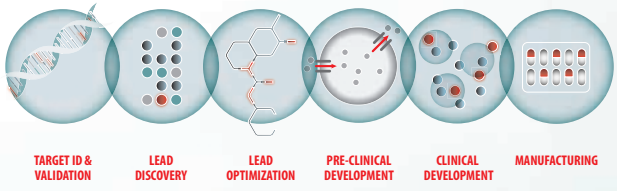

Rediscover the power of your research
sigma-aldrich.com/translational

#sigmaaldrich

Learn more at ACS Spring, Booth #1216

83320

SIGMA® | ALDRICH® | SUPELCO® | SAFC®

SIGMA-ALDRICH®

EMD MILLIPORE

Take Control
with dynamic cell culture.

Biology is so much more than DMEM/FBS, 37 °C, 5% CO_2.
It's easy to program automated changes to culture media, gas and temperature, while tracking cell responses, with the flexible, intuitive CellASIC® ONIX Microfluidic Platform. By taking control of this truly *in vivo*-like environment, you'll be able to perform dynamic, time-lapse experiments never before possible.

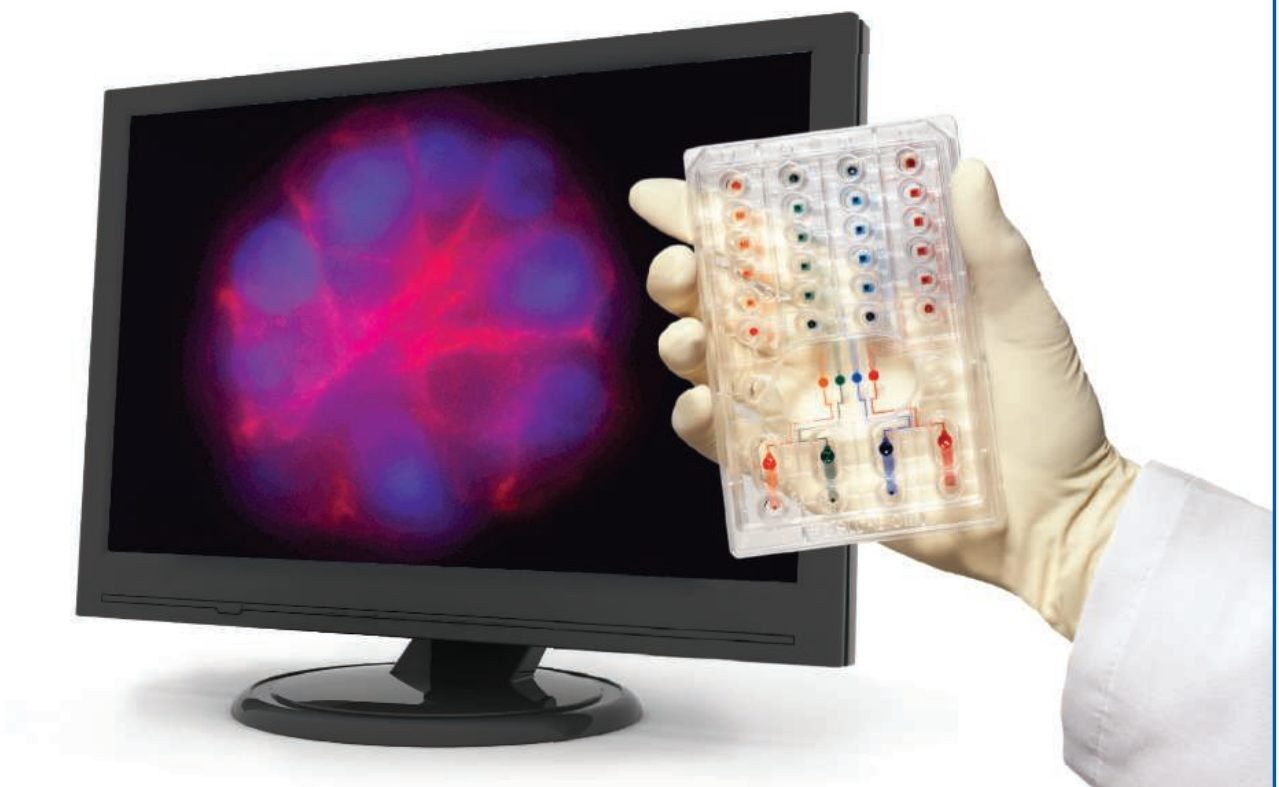

Watch live cells respond in real time:
www.emdmillipore.com/CellASIC

EMD Millipore is a division of Merck KGaA, Darmstadt, Germany

VECTOR

PIONEERS in State of the Art

Labeling & Detection

Cellular Imaging
Immunofluorescence
Immunohistochemistry
Multiple Antigen Labeling
In Situ Hybridization
DNA/RNA Applications
Western Blot Detection
Enzyme Immunoassays
Neuronal Tracing
Glycobiology


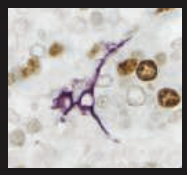
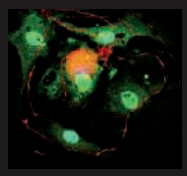
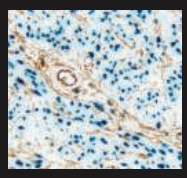

Since 1976

As a U.S. based primary manufacturer of the highest quality detection reagents, Vector Laboratories is able to provide our products to customers in standard, bulk and OEM formats, at low cost directly from our facilities.

Producers of innovative products including: VECTASTAIN® ABC Kits • ImmPRESS™ Enzyme Polymer Reagents • Mouse on Mouse (M.O.M.™) Kits • ImmPACT™ Substrates Avidin/Biotin Systems • Secondary Antibodies • NEUROBIOTIN™ Tracers • Lectins VECTASHIELD® Mounting Media

www.vectorlabs.com

UNITED STATES UNITED KINGDOM CANADA

An open letter to the American research community:

For 102 years Research Corporation for Science Advancement (RCSA) has supported unique, impactful basic research in the physical sciences at our nation's universities and colleges. Today the level of real federal dollars devoted to basic research is projected to contract, even as the cost of research grows. Within this context RCSA, a private philanthropy, seeks to continue to make a difference. Therefore, during the decade ahead the Foundation and its partners will focus on expanding and improving RCSA's two major programs:

RESEARCH CORPORATION
for SCIENCE ADVANCEMENT

Cottrell Scholars This program is expanded to include opportunities for early career Chemistry, Physics and Astronomy faculty at primarily undergraduate institutions (PUIs) as well as the traditional Cottrell Scholar beneficiaries from research universities. Cottrell Scholars are provided with unique opportunities to help them launch and establish truly outstanding careers. The size of the award is increased 33 percent to $100,000.

In addition to receiving financial support for research, Cottrell Scholars belong to a community whose members help each other to develop the skills and relationships necessary to become academic leaders. To strengthen this aspect of the program, RCSA announces two new awards:

Innovation
Community
Leadership

Competitive Career Advancement Awards of $25,000 will be presented at the Cottrell Scholars Conference held annually in Tucson, Arizona.

Cottrell Fellows Award, $250,000. This is an annual competition for Cottrell Scholars who achieve tenure. It is meant to celebrate outstanding, forward-looking, creative ideas in basic research.

Since the inception of the program in 1994, RCSA has maintained its commitment to Cottrell Scholars throughout their careers. The Foundation continues to draw on senior members of the Cottrell Scholar family to serve as mentors for the next generation.

Scialog Supporting high-risk basic research on complex problems challenging society, Scialog seeks to stimulate real progress. Over the past five years, the Scialog (science+dialog) approach has proven highly effective at encouraging early career researchers to forge new collaborations across varied disciplines. Subsequently many of these collaborations, which have been focused on increasing efficiencies in solar energy conversion, have attracted federal support.

A second Scialog round, Molecules Come to Life, co-sponsored by the Gordon and Betty Moore Foundation, begins in March. It is projected to be a two-year initiative involving early career scientists from physics, biology and related disciplines interested in pursuing collaborative, high-risk discovery research on untested ideas in physical cell biology. This initiative aims to catalyze the development of a community in which theory informs experiment, with both working together to achieve understanding of fundamental cellular processes.

The challenge for Scialog is to identify timely and scientifically critical topics for future rounds. RCSA is asking all members of its 35,000-strong community of researchers, academic and science administrators to propose and discuss Scialog topics for the coming decade. Begin the conversation by contacting us at email@scialog.org.

As it has for the past century, Research Corporation for Science Advancement continues to fund innovative research as well as to nurture collaboration, community and superb leadership skills among America's physical scientists.

Sincerely,

Robert N. Shelton
President
Research Corporation for Science Advancement

Visit us online at **www.rcsa.org**

Mirus | The Transfection Experts

X2 X3

DNA

siRNA

AACR Annual Meeting

Visit us at Booth #2440

A Transfection Breakthrough

NEW! *Trans*IT-X2® Dynamic Delivery System

Achieve superior transfections with an advanced non-liposomal, polymeric system that efficiently delivers both DNA *and/or* RNA out of the endosome and into the cytoplasm, overcoming a critical barrier to nucleic acid delivery.

The *Trans*IT-X2® Dynamic Delivery System gives researchers:

- **Efficiency**–superior broad spectrum transfection
- **Delivery**–independent *or* simultaneous delivery of plasmid DNA and siRNA
- **Technology**–novel, non-liposomal, polymeric technology

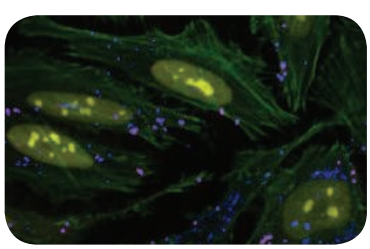

Functional Co-delivery of Plasmid DNA and siRNA. *Trans*IT-X2® Dynamic Delivery System was used to *simultaneously* transfect Cy™5-labeled plasmid DNA (blue) encoding nuclear YFP (yellow) and Cy™3-labeled siRNA (red) into HeLa cells. Actin cytoskeleton is stained green.

Visit www.mirusbio.com for full experimental details.

ADVANCE YOUR TRANSFECTIONS.
Request a FREE SAMPLE of *Trans*IT-X2® Dynamic Delivery System.
Visit www.mirusbio.com,
call 888.530.0801 (U.S. only) or +1.608.441.2852 (outside the U.S.)

VISION Celebrating 20 YEARS PASSION LOYALTY

www.mirusbio.com

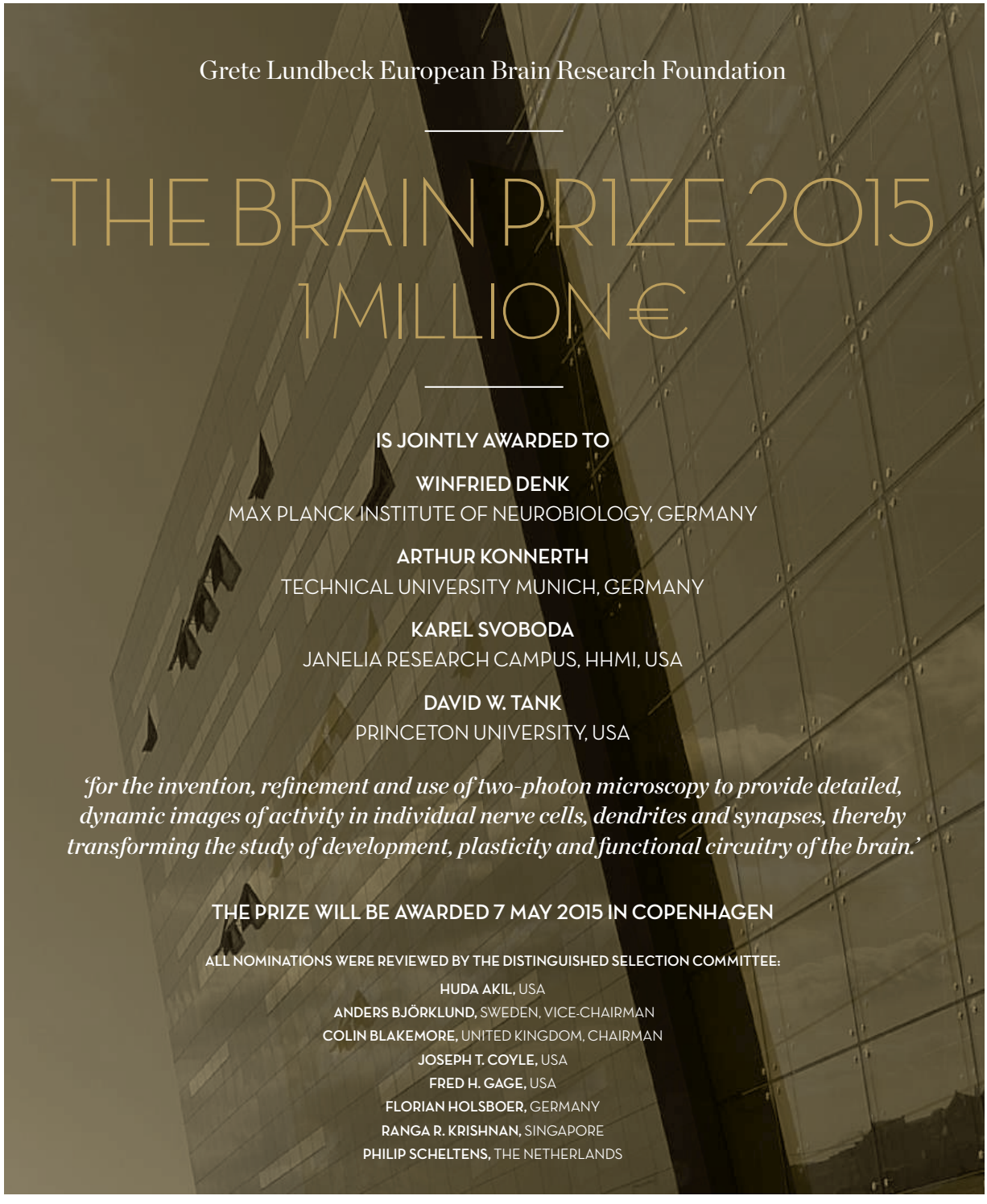

Grete Lundbeck European Brain Research Foundation

THE BRAIN PRIZE 2015

1 MILLION €

IS JOINTLY AWARDED TO

WINFRIED DENK
MAX PLANCK INSTITUTE OF NEUROBIOLOGY, GERMANY

ARTHUR KONNERTH
TECHNICAL UNIVERSITY MUNICH, GERMANY

KAREL SVOBODA
JANELIA RESEARCH CAMPUS, HHMI, USA

DAVID W. TANK
PRINCETON UNIVERSITY, USA

'for the invention, refinement and use of two-photon microscopy to provide detailed, dynamic images of activity in individual nerve cells, dendrites and synapses, thereby transforming the study of development, plasticity and functional circuitry of the brain.'

THE PRIZE WILL BE AWARDED 7 MAY 2015 IN COPENHAGEN

ALL NOMINATIONS WERE REVIEWED BY THE DISTINGUISHED SELECTION COMMITTEE:

HUDA AKIL, USA
ANDERS BJÖRKLUND, SWEDEN, VICE-CHAIRMAN
COLIN BLAKEMORE, UNITED KINGDOM, CHAIRMAN
JOSEPH T. COYLE, USA
FRED H. GAGE, USA
FLORIAN HOLSBOER, GERMANY
RANGA R. KRISHNAN, SINGAPORE
PHILIP SCHELTENS, THE NETHERLANDS

GRETE LUNDBECK EUROPEAN BRAIN RESEARCH FOUNDATION

THE BRAIN PRIZE

The Brain Prize recognizes and rewards outstanding contributions to European neuroscience, from basic to clinical

eppendorf & Science

PRIZE FOR NEURO BIOLOGY

2014 Winner
Eiman Azim, Ph.D.
Columbia University
For research on skilled limb movement

Application Deadline
June 15, 2015

Call for Entries

Eppendorf & Science Prize for Neurobiology
The annual Eppendorf & Science Prize for Neurobiology is an international award which honors young scientists for their outstanding contributions to neurobiological research based on methods of molecular and cell biology. The winner and finalists are selected by a committee of independent scientists, chaired by Science's Senior Editor, Dr. Peter Stern. To be eligible, you must be 35 years of age or younger.

You could be next to win this prize and to receive
> Prize money of US$25,000
> Publication of your work in Science
> Full support to attend the Prize Ceremony held in conjunction with the Annual Meeting of the Society for Neuroscience in the USA
> An invitation to visit Eppendorf in Hamburg, Germany

It's easy to apply!

Learn more at: www.eppendorf.com/prize

eppendorf Science AAAS

eppendorf

Impress Yourself

The new Eppendorf Cell Culture Consumables

The all new product line of Eppendorf Cell Culture Consumables will truly delight your cells. Its outstanding design, reliability and purity is based on more than 50 years of experience.
Products created by experts, developed for perfectionists. Impress yourself!

> Unsurpassed quality, clarity, purity and sterility, providing reliable cell culture conditions
> Significantly improved design for more safety and consistency
> Maximum safety and confidence during storage and transportation

www.eppendorf.com/ccc

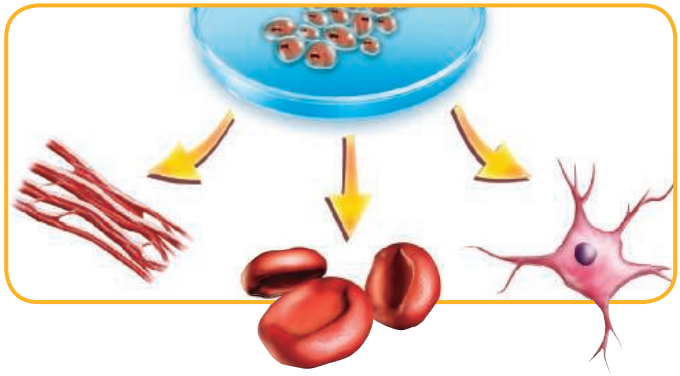

Disease Modeling with Patient-Specific iPS Cells

Whether in mice or macaques, disease modeling traditionally has been a tedious and expensive affair, not to mention unreliable, as mutations that are crippling in humans could have negligible impacts in animals, and vice versa. As drug development often requires preclinical animal studies, that disconnect has had real implications for the pharmaceuticals industry, both in money and missed opportunities. Today, researchers increasingly are migrating their models from the mouse house to the culture room. Armed with induced pluripotent stem cells made from patient cells, these investigators are probing everything from basic biology and disease etiology to drug discovery and cell therapeutics. **By Jeffrey M. Perkel**

In the nine years since Shinya Yamanaka first described them, induced pluripotent stem (iPS) cells have proven to be extraordinarily powerful research tools. Most obviously, they provide an ethically attractive alternative to embryonic stem (ES) cells, from which researchers theoretically can derive any cell type in the body. "An iPS cell and an ES cell are functionally equivalent," says Emile Nuwaysir, chief operations officer at **Cellular Dynamics International** (CDI). But they are so much more than that.

For one thing, says Nuwaysir, they provide much-needed genetic diversity. Traditionally, researchers have little opportunity to test their models or therapeutics before initiating clinical trials, at which point projects all too often fall apart. Using iPS cells, however, researchers are limited only by their ability to acquire some noninvasive tissue samples, like a blood draw or skin punch, or the lines derived therefrom.

But it's the iPS cells made from patient samples that truly expose the technology's power. By recapitulating the growth and differentiation of those patient cells in a dish, researchers can investigate how mutations impact development, identify critical signaling pathways, and test potential pharmaceuticals—all without biopsy or animal models. "You can take a patient, … take their skin, [reprogram the cells in it], and then attempt to replay the disease," says Clive Svendsen, director of the Regenerative Medicine Institute at **Cedars Sinai Medical Center** in Los Angeles. Researchers can even replay those diseases in cell types that otherwise are difficult if not impossible to obtain, simply by growing them from scratch. Svendsen notes, for instance, that "neurons are almost impossible to get from human tissues." By using patient-specific iPS cells, "for the very first time, we're able to interrogate neurons from Huntington's disease … [and] Lou Gehrig's disease, in the dish."

Columbia University Medical Center ophthalmologist Stephen Tsang calls patient-specific iPS cells "a patient-in-a-dish." In one study, Tsang generated them from two individuals with retinitis pigmentosa (RP), a form of inherited blindness affecting 1.5 million people worldwide. RP has multiple genetic sources, including a gene of unknown function called membrane frizzled-related protein (MFRP). Tsang's study demonstrated that MFRP mutations lead to defects in actin organization, apical microvilli, and "leaky" cell-cell junctions—effects that could be reversed, both in patient cells and in mice, by delivering a wild-type copy of the gene via gene-therapy vectors. In effect, says Tsang, the study provided his team a budget-conscious way to test-drive its vectors. "It's more cost-efficient to do testing of your viral vectors in culture than doing it in vivo," he explains.

Cell therapeutics

Researchers use patient-specific iPS cells to drive three primary applications: basic biology, drug discovery, and cellular therapeutics. The former two applications are most widespread to date, but cell therapeutics are advancing, too. In 2013, Japanese researchers launched the world's first clinical trial of a cellular therapeutic derived from iPS cells. Led by Masayo Takahashi at the **RIKEN Center for Developmental Biology**, the trial targets age-related macular degeneration (AMD), differentiating iPS cells from patients into retinal pigment epithelium (RPE), the cell layer underneath the retina that dies in the disease. Six patients are enrolled in the trial, the first of which underwent transplantation in September 2014.

The advantage of iPS cells for cell therapeutics is immune compatibility. Because the transplanted cells are derived from the patient's own cells, no immunosuppression should be required—at least theoretically. "We don't know that for sure yet," says Dennis Clegg, codirector of the Center for Stem Cell Biology and Engineering at the **University of California, Santa Barbara**, "but there are at least a couple of experiments in mouse model systems that suggest that that's the case."

Clegg is working with David Gamm, director of the **McPherson Eye Research Institute** at the University of continued>

Upcoming Features

Proteomics—April 17 ■ *Microscopy—June 5* ■ *Transcriptomics—July 31*

Wisconsin to develop strategies to differentiate iPS cells into RPE and photoreceptor cells for transplantation into patients with AMD.

The former cells are relatively simple: RPE proliferate easily, grow as a sheet, and "are used to taking a beating," Gamm says. Photoreceptors, in contrast, "are kind of the divas of the retina."

Photoreceptors have a required physical orientation, and they must form synaptic connections to function. They also are post-mitotic, Gamm notes, and fragile and difficult to purify to homogeneity. Once transplanted—and it isn't yet clear which developmental stage would be best—the cells must integrate into preformed retinal neural circuitry, something cells never normally do. As Gamm puts it, the cells are "being asked to mature on their own, without the normal cues that would normally be there, and then make connections with cells that may not be too happy to begin with."

Despite these difficulties, researchers are advancing such programs for eye and other disorders. Yet some say it is neither practical nor cost-effective to create, differentiate, and quality control iPS cells on demand. Instead, they advocate assembling banks of HLA-matched iPS cells—at least for some applications. It depends on the speed of disease progression and age of onset, says Joseph Wu, director of the **Stanford Cardiovascular Institute**. For a child with juvenile diabetes and a long life ahead, for instance, autologous cells could represent a sound investment, Wu says. "On the other hand, if you have an 80-year-old patient who has a heart attack, it probably makes less sense to create a line just for him or her." Besides, "the cells are needed more urgently in this situation," he adds.

The required size of such banks varies with a population's genetic variation. By one estimate, 150 lines could match 93% of the U.K. population, whereas 50 lines would match 90.7% of Japanese (scim.ag/15LlyY8). In the United States, CDI has recruited five donors for its bank, and two lines have been stored, Nuwaysir says. "Between those two donors, you have a match to 18% or more of the U.S. population."

Technical considerations

Yamanaka's original iPS cell study used lentiviral expression vectors to initiate cellular reprogramming. But as lentiviruses integrate their genetic material into the host genome, they can complicate downstream clinical applications.

Today, researchers have several alternatives. For a recent study into the pathophysiology of Niemann–Pick type C, a lysosomal storage disease, Rudolf Jaenisch, professor of biology at the **Massachusetts Institute of Technology**, used a Cre-excisable, doxycycline-inducible lentiviral expression system. More recently, his team favors mRNA-based reprogramming, a method that avoids genomic integration. Other RNA-based strategies include a self-replicating RNA developed by Steven Dowdy at the University of California, San Diego (and commercialized by both EMD Millipore and Stemgent) and Sendai virus, available from Life Technologies/Thermo Fisher Scientific.

iPS cells can also be made without nucleic acid initiators.

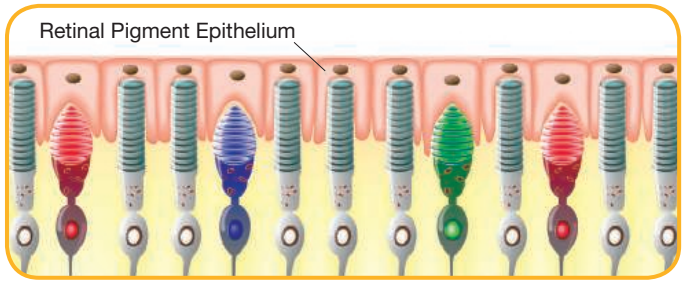

ILLUSTRATION: © DESIGNUA/SHUTTERSTOCK.COM

Because the transplanted cells are derived from the patient's own cells, no immunosuppression should be required—at least theoretically.

Lisa Ellerby at the **Buck Institute for Research on Aging** reprograms her cells by delivering purified transcription factors, a strategy that, like mRNA-based reprogramming, has been commercialized by Stemgent. In 2013, researchers in China demonstrated the ability to make iPS cells using just seven small molecules, several of which are available from STEMCELL Technologies.

At CDI, which has been awarded some $16 million from the California Institute for Regenerative Medicine to create 9,000 iPS cell lines representing 11 disease areas, iPS cells are made using episomal vectors, basically DNA plasmids that behave like eukaryotic chromosomes, Nuwaysir explains. "They have an origin of replication, so they replicate once per cell cycle like a mini-chromosome, but they're relatively inefficient and lost over time," he says, meaning by the time the cells are reprogrammed, the plasmids are long gone, leaving no genetic footprint.

Those cells will be banked at the Coriell Institute for Medical Research. But CDI, Nuwaysir says, "is focused on using iPS cells as a platform for the manufacture of terminally differentiated cells, and the use of those cells from research to preclinical applications." The company has developed protocols to reliably differentiate human iPS cells into 10 cell types, he says, including cardiomyocytes, dopaminergic neurons, and skeletal myoblasts, all of which are available under the company's iCell brand.

Researchers who wish to differentiate their own cells can purchase preformulated differentiation media for select cell types from companies such as STEMCELL Technologies and Thermo Fisher Scientific. For most cell types, though, researchers are on their own.

Rohit Kulkarni, senior investigator at the **Joslin Diabetes Center** in Boston, for instance, uses patient-specific iPS cells to study the pathophysiology of diabetes and screen for therapeutics. But first, he'll have to figure out how to turn those cells into insulin-producing beta cells, something that nobody has yet gotten exactly right, he says.

A true beta cell has distinctive anatomic, signaling, and secretory characteristics, Kulkarni explains, and iPS-derived cells often fall short of the mark. Thus, he calls them "beta-like."

Groups led by Douglas Melton at Harvard University and Timothy Kieffer at the **University of British Columbia** have had some success on that front, however. Kieffer described a seven-step protocol that could turn an iPS cell into what he called S7 cells in about six weeks. These cells, he writes in a recent publication, are similar to beta cells "but also [exhibit] notable differences," including in the kinetics of glucose response. Nevertheless, they reversed diabetes in a mouse model of the disease. Melton's team reported a 34-day, six-step method of its own for "large-scale production of functional human β cells from [human pluripotent stem cells] in vitro."

Because each cell line represents an individual with a distinct genetic background, comparing phenotypes across lines can be complicated. "You have to ask yourself, is [the phenotype] due to the variation you have anyway between different iPS cells … or is it due to the disease-relevant mutation you want to study," Jaenisch says.

Increasingly, researchers address this problem using so-called isogenic controls—cell lines that differ by a single mutation. Typically, researchers use gene-editing tools, such as CRISPR/Cas9, to either repair or insert a key mutation in a cell line. Then, by comparing the modified line against the parental line, "you can compare apples with apples," Jaenisch explains. His team has applied this approach to Parkinson's disease, identifying subtle differences between normal and mutant cells, as well as pharmaceuticals that could negate those differences.

Going 3-D

While researchers often can drive cells towards their desired endpoint, they often stumble near the goal line. "What we get from iPS are very immature cells, whether it's an islet cell or a heart cell or a neuron," says Svendsen. "They don't seem to mature to the extent they mature in the human body."

For instance, it takes 90 days to turn iPS cells into RPE, Tsang says, and 200 days to make photoreceptors. Yet even then, the cells aren't quite right: instead of hyperpolarizing in response to light, most are nonresponsive, or even depolarize.

In part, that could be a function of cellular age itself—cells may need to physically age to better mimic adult-onset diseases. ("Maybe if we grow [photoreceptors] for 300 days, then they'll be right," Tsang quips.) But, it also could be because the cells are maturing not in the human body, with all its environmental cues, but in 2-D sheets on plastic dishes.

Featured Participants

Buck Institute for Research on Aging
www.buckinstitute.org

Cedars-Sinai Medical Center
www.cedars-sinai.edu

Cellular Dynamics International
www.cellulardynamics.com

Center for Stem Cell Biology and Engineering, UC Santa Barbara
www.stemcell.ucsb.edu

Cincinnati Children's Hospital Medical Center
www.cincinnatichildrens.org

Columbia University Medical Center
www.cumc.columbia.edu

Joslin Diabetes Center
www.joslin.org

Massachusetts Institute of Technology
www.mit.edu

McPherson Eye Research Institute
vision.wisc.edu

RIKEN Center for Developmental Biology
www.cdb.riken.jp/en

Stanford Cardiovascular Institute
cvi.stanford.edu

Svendsen and colleagues demonstrated recently that iPS cells generated from lymphoblastoid cells from patients with Crohn's disease could be induced in culture to form 3-D intestinal "organoids," simply by growing them in a 3-D matrix in the presence of collagen. Now he says his lab is collaborating with Harvard researchers to develop microfluidic devices capable of simulating interfaces and interactions with other tissues and organ systems, to "create a much more dynamic living model of the disease."

Likewise, James Wells, director of the Pluripotent Stem Cell Facility at the **Cincinnati Children's Hospital Medical Center**, has turned ES and iPS cells into gastric organoids (i.e., "mini-stomachs") by delivering a precise set of growth factors in a defined sequence that models human development. "We've identified signaling pathways that we think are used in the developing embryo to induce this transition from two to three dimensions," Wells explains. The result is a "primitive gut tube," from which other gastrointestinal organs arise. Using that system, his team was able, among other things, to model *Helicobacter pylori* infection.

Wells now is extending the work to iPS cells from patients with such gastrointestinal maladies as cystic fibrosis, malabsorption syndromes, and Hirschsprung's disease. "We can actually study embryonic development in a dish and find out what goes wrong developmentally in these congenital syndromes." And at the end of the day, he adds, "it will also allow us in the future to correct the genetic defect and then generate healthy tissue."

But don't look for artificial stomachs any time soon, he says. Though researchers have had success generating relatively simple structures in a dish, the stomach and intestines are far more complex, with vasculature, neural networks, absorptive and secretory cells, and so on. Such structures could require "a Manhattan Project-level of investment in bioengineering [and] tissue engineering."

It will take years to bridge that gap, if ever. But considering how far the research community has already come since 2006, anything is possible. Says Wells, "The therapeutic use of pluripotent stem cells is no longer science fiction. It's current reality."

Jeffrey M. Perkel is a freelance science writer based in Pocatello, Idaho.

DOI: 10.1126/science.opms.p1500092

Human Class II MHC Monomer Reagents

ProM2 is a range of Human Class II MHC monomer reagents for tetramer analyses in the study of $CD4^+$ T cell immune responses. ProM2 Class II MHC Monomers are pre-biotinylated and can be readily made into MHC tetramers that allow the detection of single antigen-specific $CD4^+$ T cells accurately by flow cytometry. Class II tetramers made from ProM2 monomers can also be used to separate cells for culture, expansion, and further study. ProM2 Class II MHC monomer reagents are supported by ProImmune's expert customer service and application support, helping new users in particular to establish and optimize robust protocols in their own laboratories. The class II reagent offering complements ProImmune's existing extensive range of services for evaluating $CD4^+$ T cell responses, including ProImmune REVEAL MHC peptide binding assays, $CD4^+$ T cell and DC T cell proliferation assays, and standard immune monitoring services through ELISPOT and flow cytometry based assays.

ProImmune
For info: 888-505-7765
www.proimmune.com

Mitochondria/Metabolism Assays

The new range of 96- and 384-well phosphorescence- and fluorescence-based assays enable direct real-time analysis of mitochondrial respiration (MitoXpress Xtra), glycolysis (pH-Xtra), and intracellular oxygen concentration (MitoXpress Intra)—providing the perfect toolkit for monitoring bioenergetics, metabolism, Warburg, and mitochondrial function & toxicity. MitoXpress Xtra—an oxygen consumption assay (high-sensitivity method)—is a convenient fluorescence-based, high throughput approach to the direct real-time analysis of mitochondrial oxygen consumption rate. The easy-to-use assays measure oxygen consumption of isolated mitochondria, cell populations, small organisms, tissues, and enzymes. pH-Xtra Glycolysis Assay is a fluorescence-based assay that measures extracellular acidification. The assay detects changes in extracellular pH caused by the acid extrusion of either suspension or adherent cells. This allows convenient plate based analysis of glycolytic flux and can be used to monitor alterations in glucose metabolism and to confirm mitochondrial dysfunction.

AMS Biotechnology
For info: +44-(0)-1235-828200
www.amsbio.com

Fluorescence Microscopy

The ZOE Fluorescent Cell Imager is one of the first cell imaging systems able to deliver the power of microscopy in a system that is as easy to use as a tablet. The system includes three fluorescent channels and brightfield to simplify fluorescence imaging for cell culture applications. Fluorescence microscopes are used in traditional cell culture workflows to confirm transfection efficiency and visualize fluorescent proteins. Performing this task requires training and the process can be time-consuming. Fluorescence microscopes can take 15 minutes to warm up and the systems are often located in a separate facility that is outfitted with a darkroom. However, the ZOE Fluorescent Cell Imager's LEDs are instantly ready to use after the power is turned on. Researchers simply place their culture dish onto ZOE's stage and then access all controls using the LCD touchscreen, tapping the screen to capture images and pinching with their fingers to zoom up to 20x magnification.

Bio-Rad
For info: 800-424-6723
www.bio-rad.com/zoepr

NFκB Translocation Assay

The Amnis NFκB Translocation kit allows researchers to better study the nuclear translocation of NFκB, a transcription factor that plays a central role in regulating key mammalian cell processes, including proliferation, inflammation, immune, and stress responses. The new kit uses imaging flow cytometry to obtain statistically significant quantitative assessment of NFκB translocation as well as visual identification of the translocation at a single-cell level. The optimized kit, which works with cultured cell lines and whole blood cells, conveniently contains directly-conjugated anti-Human NFκB monoclonal antibody, 7-AAD dye, and required buffers. Using the dedicated Nuclear Localization Wizard in the IDEAS software, NFκB translocation can then be studied and quantified in an objective, statistically robust manner. The kit is designed for use with the Amnis ImageStreamX Mark II and the Amnis FlowSight imaging flow cytometers, systems that combine the quantitative power of flow cytometry with the spatial information provided by microscopy.

EMD Millipore
For info: 800-221-1975
www.emdmillipore.com/amnis

Cryopreservation Solution

PRIME-XV FreezIS DMSO-Free is a chemically defined cryopreservation solution for human mesenchymal stem/stromal cells (MSCs) free of dimethyl sulfoxide (DMSO) and animal-derived components. Amid growing concerns that DMSO may compromise the potency of MSCs, offering an effective DMSO-free cryoprotectant is an important addition to PRIME-XV product line. Researchers can now characterize cells in DMSO-free environments during basic and translational research, which may add valuable insight downstream and facilitate scale-up. PRIME-XV FreezIS DMSO-Free maintains the potency of MSCs throughout cryopreservation while sustaining comparable cell viability as solutions containing 10% DMSO. For applications where the effects of DMSO are not as critical, PRIME-XV FreezIS is offered as a 10% DMSO-containing, protein-free, chemically defined cryopreservation solution for a variety of cell types. Both cryopreservation solutions join the PRIME-XV line of cell therapy products, which are designed to offer the highest quality and performance for the culture of human stem cells and primary cells.

Irvine Scientific
For info: 800-577-6097
www.irvinesci.com/cell-therapy

Electronically submit your new product description or product literature information! Go to www.sciencemag.org/products/newproducts.dtl for more information.

Newly offered instrumentation, apparatus, and laboratory materials of interest to researchers in all disciplines in academic, industrial, and governmental organizations are featured in this space. Emphasis is given to purpose, chief characteristics, and availability of products and materials. Endorsement by *Science* or AAAS of any products or materials mentioned is not implied. Additional information may be obtained from the manufacturer or supplier.

Photo: Henrik Trygg/imagebank.sweden.se

Will you be in Stockholm this December?

(If you have a recent PhD you could be.)

Stockholm in the second week of December is a special place. The city is alive with excitement as it welcomes and celebrates the new Nobel Laureates at the annual Nobel Prize ceremony.

If you are a recent PhD graduate you could be here too, and receive a rather special prize yourself.

The journal *Science* & SciLifeLab have established The *Science* & SciLifeLab Prize for Young Scientists, to recognize and reward excellence in PhD research and support young scientists at the start of their careers. It's about bright minds, bright ideas and bright futures.

Four winners will be selected for this international award. They will have their essays published in the journal *Science* and share a new total of 60,000 USD in prize money. The winners will be awarded in Stockholm, in December, and take part in a unique week of events including meeting leading scientists in their fields.

"The last couple of days have been exhilarating. It has been an experience of a lifetime. Stockholm is a wonderful city and the Award winning ceremony exceeds my wildest dreams."
–Dr. Dan Dominissini, 2014 Prize Winner

Who knows, The *Science* & SciLifeLab Prize for Young Scientists could be a major stepping stone in your career and hopefully one day, during Nobel week, you could be visiting Stockholm in December once again.

The 2015 Prize is now open. The deadline for submissions is August 1, 2015.
Enter today: www.sciencemag.org/scilifelabprize

The 2015 Prize categories are:

- Cell and Molecular Biology
- Ecology and Environment
- Genomics and Proteomics
- Translational Medicine

Science & SciLifeLab PRIZE FOR YOUNG SCIENTISTS

For over 130 years the journal Science has been the world's leading journal of original scientific research, global news and commentary.

SciLifeLab is a collaboration among four universities in Stockholm and Uppsala, Sweden, and is a national center for molecular biosciences with focus on health and environmental research.

This prize is made possible with the kind support of the Knut and Alice Wallenberg Foundation.

Knut och Alice Wallenbergs Stiftelse

Science AAAS

SciLifeLab

FLORIDA ATLANTIC UNIVERSITY

GROUNDBREAKING RESEARCH AND EDUCATION INITIATIVE TO ESTABLISH COLLABORATIVE DEGREE PROGRAMS

Pictured from left to right: Dr. John Kelly, President, Florida Atlantic University; Rep. Mary Lynn Magar, Florida House of Representatives; David Fitzpatrick, CEO and Scientific Director, Max Planck Florida Institute for Neuroscience; James Paulson, Acting President and CEO, The Scripps Research Institute

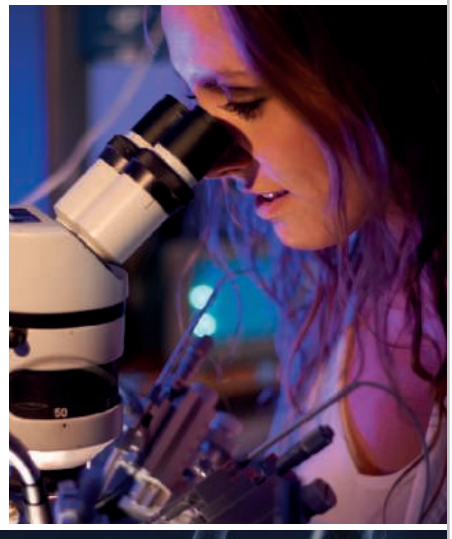

INITIATIVE WILL HELP CURE DISEASES, DEVELOP DRUGS, EDUCATE STUDENTS AND GENERATE JOBS

One of Florida's Leading Public Universities and Two of the World's Premier Research Institutions Build on Existing Relationship to Further Scientific Discovery

Florida Atlantic University, the Max Planck Florida Institute for Neuroscience, and The Scripps Research Institute will allow students to work alongside some of the world's leading scientific researchers.

FAU, Max Planck and Scripps will collaborate to develop premier STEM programs – Science, Technology, Engineering, Math – and combine FAU Jupiter's existing strengths in STEM areas, with support from the arts, to create a leading STEAM initiative.

Florida Atlantic University
www.fau.edu

Max Planck Florida Institute for Neuroscience
www.maxplanckflorida.org

Scripps Florida
The Scripps Research Institute
www.scripps.edu/florida

FAU FLORIDA ATLANTIC UNIVERSITY + MAX PLANCK FLORIDA INSTITUTE FOR NEUROSCIENCE + SCRIPPS FLORIDA™ THE SCRIPPS RESEARCH INSTITUTE

ExoQuick®: Publications delivered.

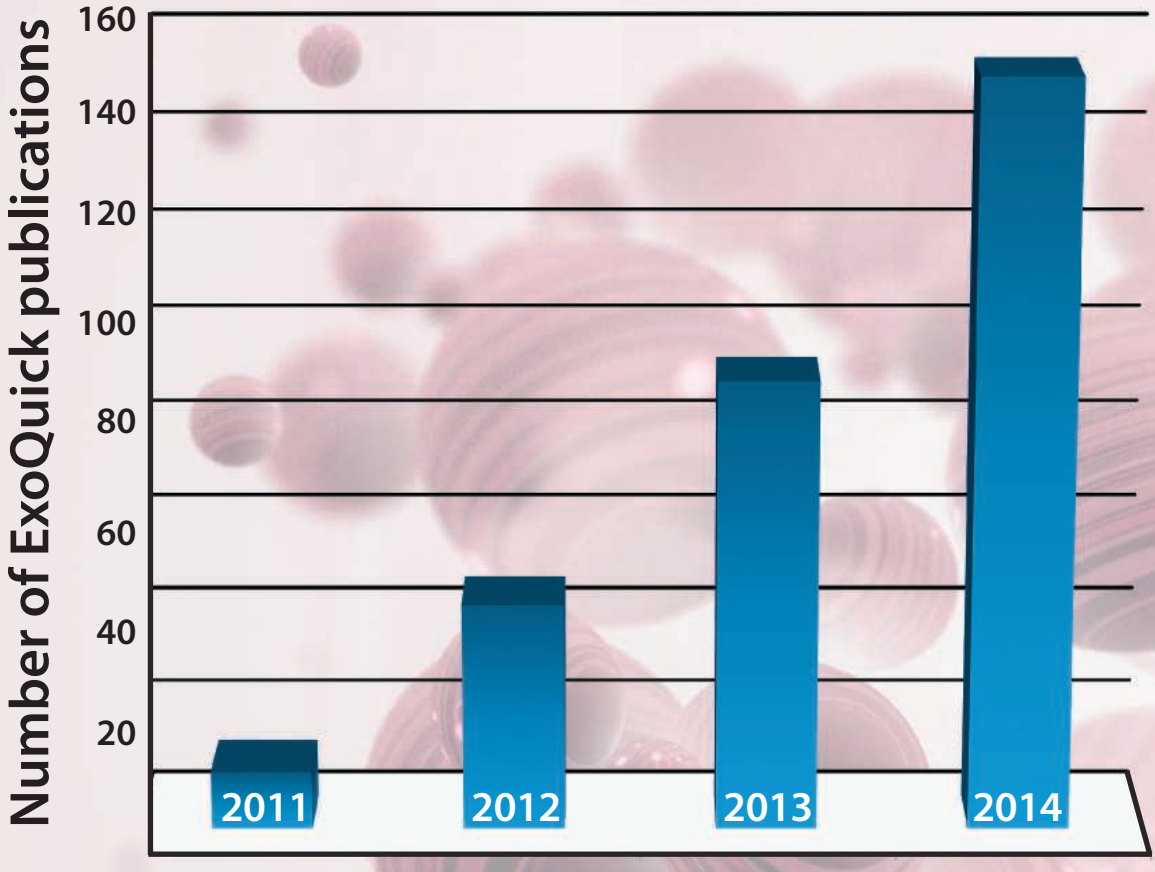

ExoQuick - The World's Most Published Exosome Isolation Reagent

Peer reviewed technology.

Need exosomes? SBI's patented ExoQuick technology enables high-throughput, scalable, quantitative isolation of exosomes without ultracentrifugation from any biofluid. Study these important extracellular signaling vesicles reliably with ExoQuick from as little as 100 µl of sample.

- Simple protocol to isolate exosomes in as little as 30 minutes
- Works with serum, media, urine, saliva, ascites fluid, CSF and more
- Compatible with miRNA profiling, NGS and Mass Spec analyses
- ExoQuick exosomes are intact and bioactive for functional studies

SBI is the only vendor to offer reagents and kits that support all aspects of exosome research—covering isolation, detection, biomarker discovery, and even exosome engineering. With a comprehensive set of tools and services to accelerate the study of exosomes, SBI puts the power of exosomes into researchers' hands.

SEE TOP CITATIONS & REQUEST FREE TEST KITS:
www.systembio.com/go-exoquick

SBI
System Biosciences

Science Careers Advertising

For full advertising details, go to ScienceCareers.org and click For Employers, or call one of our representatives.

Tracy Holmes
Worldwide Associate Director
Science Careers
Phone: +44 (0) 1223 326525

THE AMERICAS

E-mail: advertise@sciencecareers.org
Fax: 202 289 6742

Tina Burks
Phone: 202 326 6577

Nancy Toema
Phone: 202 326 6578

Marci Gallun
Sales Administrator
Phone: 202 326 6582

Online Job Posting Questions
Phone: 202 312 6375

EUROPE / INDIA / AUSTRALIA / NEW ZEALAND / REST OF WORLD

E-mail: ads@science-int.co.uk
Fax: +44 (0) 1223 326532

Axel Gesatzki
Phone: +44 (0) 1223 326529

Sarah Lelarge
Phone: +44 (0) 1223 326527

Kelly Grace
Phone: +44 (0) 1223 326528

JAPAN

Katsuyoshi Fukamizu (Tokyo)
E-mail: kfukamizu@aaas.org
Phone: +81 3 3219 5777

Hiroyuki Mashiki (Kyoto)
E-mail: hmashiki@aaas.org
Phone: +81 75 823 1109

CHINA / KOREA / SINGAPORE / TAIWAN / THAILAND

Ruolei Wu
Phone: +86 186 0082 9345
E-mail: rwu@aaas.org

ScienceCareers
FROM THE JOURNAL SCIENCE AAAS

ScienceCcareers.org

NIH National Institute of Environmental Health Sciences
Your Environment. Your Health.

Department of Health and Human Services, National Institutes of Health
National Institute of Environmental Health Sciences
Environmental Health Perspectives
Editor-in-Chief

The National Institute of Environmental Health (NIEHS), a component of the National Institutes of Health (NIH) and the Department of Health and Human Services (DHHS), is seeking exceptionally qualified candidates for the next Editor-in-Chief of Environmental Health Perspectives (EHP). EHP is a peer-reviewed, open access, monthly science journal, publishing a wide range of topics related to the impact of the environment on human health. The journal has an impact factor of 7.03 and is international in scope with readers in over 100 countries. EHP is the third-ranked journal in Public, Environmental, and Occupational Health, the fourth-ranked journal in Toxicology, and the fifth-ranked journal in Environmental Sciences. Information about EHP is available at http://ehp.niehs.nih.gov/.

The Editor-in-Chief is a full-time federal government employee who will be responsible for the science and strategic vision of the journal. The Editor-in-Chief will supervise a limited number of senior employees, including an Operations Manager who oversees the journal production and management of staff. Candidates should have a substantial background as a research scientist in a field related to environmental health sciences and extensive editorial experience in the field of scientific publishing. The ideal candidate will have a Ph.D., MD, or equivalent Doctoral degree in a field of the biological sciences or another scientific discipline, such as statistics or chemistry.

This exciting opportunity will be posted on the USAJOBS website and open for applications from **March 30 to April 17, 2015**. For questions about the position, please contact **Rick Woychik, Ph.D., NIEHS Deputy Director, rick.woychik@nih.gov**.

DHHS and NIH are Equal Opportunity Employers.

National Institutes of Health • U.S. Department of Health and Human Services

Science Careers
Cernet

"《科学》职业" 已经与**Cernet/赛尔互联**开展合作。中国大陆的高校可以直接联系**Cernet/赛尔互联**进行国际人才招聘。

请访问 **Sciencecareers.org/CER** 点得联系信息。

中国大陆高校以外的 招聘广告，或者高校的其它业务，
请与国际合作、出版副总监吴若蕾联系：
+86-186 0082 9345 rwu@aaas.org

招募学术精英，《科学》是您的不二之选 Science

Be a Leader with GSK Neuroscience

gsk do more feel better live longer

GSK Neuroscience conducts world-class research to discover medicines of global potential. We focus on areas where scientific advances have the highest chance to enable discovery of medicines for patients with brain and nerve diseases.

GSK Neuroscience has created two new Discovery Performance Units (DPUs) focusing on neuroexcitation and proof of concept. The **Neuro-Excitation DPU** based in Shanghai will focus on membrane excitability critical to a wide range of neurologic diseases. The **Neuro-Virtual Proof of Concept DPU** based in Upper Providence, Philadelphia will help GSK capitalise on discovery and therapeutic opportunities through externalisation.

We are seeking to recruit two outstanding PhD and/or MD qualified research leads for each DPU. You will have outstanding scientific achievements of international repute within neurophysiology, pharmacology, and/or medicinal chemistry. You must have strategic vision to integrate research into drug development. You must also be a highly effective leader with substantial experience of managing employees of diverse backgrounds, be values-led and dedicated to improving the well-being of patients.

To express your interest in either of these opportunities, please forward your CV together with a summary page highlighting your experience and skills that qualify you for this position to **apac.exec-recruitment@gsk.com**.

Please indicate in subject line the DPU of interest.

We regret that only shortlisted candidates will be notified.

University of Iowa Carver College of Medicine
University of Iowa Health Care

John P. Long Endowed Chair in Pharmacology - Neuroscienc

The Univesity of Iowa Department of Pharmacology seeks exceptional applicants at the senior Associate or full Professor level to hold the John P. Long Chair in Pharmacology (Neuroscience). Applicants should have an outstanding record of innovative research and academic excellence and demonstrated expertise in any area of neuroscience including systems, molecular/cellular, behavioral, neurodegenerative disorders, and pain, employing cutting edge methodologies. The candidate will join a strong and growing community of neuroscientists. The Carver College of Medicine has designated neuroscience as a strategic priority for growth and investment. Newly remodeled research space with state-of-the-art shared instrumentation is available. This position includes a 12-month salary (funded partially by the endowment), benefits and a highly competitive start-up package. All applicants must have a relevant doctoral degree and a record of accomplishment consistent with appointment as Associate Professor with Tenure or Professor with Tenure. The successful candidate will maintain a vigorous, independent, extramurally funded research program, have a desire to train students and postdoctoral fellows, and participate in departmental teaching.

To apply for this position, visit The University of Iowa website at **http://jobs.uiowa.edu**, requisition **#65982**.

The University of Iowa is an Equal Opportunity/Affirmative Action Employer. All qualified applicants are encouraged to apply and will receive consideration for employment free from discrimination on the basis of race, creed, color, national origin, age, sex, pregnancy, sexual orientation, gender identity, genetic information, religion, associational preference, status as a qualified individual with a disability, or status as a protected veteran.

Washington University in St. Louis
School of Medicine

Assistant or Associate Professor
Center for Cardiovascular Research
Diabetic Cardiovascular Disease Center

The Center for Cardiovascular Research (CCR) (http://cardiology.wustl.edu/ccr-home.html) and the Diabetic Cardiovascular Disease Center (DCDC) (http://dcdc.wustl.edu) at Washington University School of Medicine invite applications from individuals interested in developing vibrant independent research programs focused on cardiovascular physiology/pathophysiology and on delineating cardiovascular disease mechanisms, particularly diabetic cardiovascular disease. Tenure-track tenured appointments can be made at the Assistant/Associate Professor level. The CCR and the DCDC offer outstanding facilities and core resources in a vibrant, highly interactive and collaborative research environment.

Interested individuals with postdoctoral training and/or faculty experience should submit an application, including a cover letter, curriculum vitae, a summary of research interests and accomplishments, and an outline of research interests/plans, assembled in a single pdf file, online at: **http://ccrdcdc.wustl.edu**. In addition, reference letters from three individuals familiar with the applicant's work should be sent (by email) to Jeanne M. Nerbonne, PhD, CCR Director, or Jean Schaffer, MD, DCDC Director, care of Ms. Linda Lobos, Assistant to the CCR Director (**llobos@dom.wustl.edu**), before **May 31, 2015**.

Washington University is an Equal Opportunity/Affirmative Action Employer.

CENTER FOR CARDIOVASCULAR RESEARCH

DCDC

Learn more and conduct your job search the easy way.

- Search thousands of job postings
- Create job alerts based on your criteria
- Get career advice from our Career Forum experts
- Download career advice articles and webinars
- Complete an individual development plan at "myIDP"

Target your job search using relevant resources on **ScienceCareers.org**.

ScienceCareers
FROM THE JOURNAL SCIENCE AAAS

UCONN HEALTH

Tenure-Track Immunology (Diabetes) Faculty Position

The Department of Immunology at the University of Connecticut Health Center seeks an outstanding investigator for a tenure-track position at the Assistant or Associate Professor rank to establish an extramurally funded laboratory. We are specifically interested in an individual with research interests in autoimmunity of diabetes. The ideal candidate's research program should utilize immunobiological approaches and models to study autoimmune diabetes. Areas of priority include, but are not limited to, T cell tolerance and innate immunity of disease, including signal transduction, transcriptional control, and metabolism. The new hire will participate in a vibrant graduate student training program, and have access to a growing translational research community and an expanding scientific community in the capital region. Salary and start-up funds are highly competitive and numerous outstanding core facilities are available. Applicants must have a Ph.D. and/or M.D. with several years of postdoctoral training and a high impact publication record. For Associate Professor level a history of sustained extramural funding is expected. In addition to the beauty of the picturesque New England countryside, the Hartford area offers a vibrant arts and cultural scene and an exceptional outdoor sports environment. Interested applicants should apply at **https://jobs.uchc.edu/** search number 2015-692, and submit a curriculum vitae, a two-page summary of research accomplishments and interests, and the names and contact information of three references. Questions regarding this search should be directed to Anthony Vella, Ph.D., Chairman, Department of Immunology, School of Medicine, UConn Health Center, Farmington, CT. Email: **immunology@uchc.edu**. For further information on UCHC, please visit **http://immune.uchc.edu**. The deadline to submit applications is May 1, 2015.

UCHC is an Affirmative Action/Equal Opportunity Employer M/F/V/PwD

UCONN HEALTH

Tenure-Track Immunology (Tumor) Faculty Position

The Department of Immunology at the University of Connecticut Health Center seeks an outstanding investigator for a tenure-track position at the Assistant or Associate Professor rank to establish an extramurally funded laboratory. All areas of tumor immunology will be considered with emphasis on cancer immunotherapy, cancer vaccines, immune regulation of cancer, tumor tolerance mechanisms, and innate immunity during tumorigenesis. The ideal candidate's research program should include in vivo models, and be open to translational studies. The ideal candidate will participate in a vibrant graduate student training program, and have access to a growing translational research community and an expanding scientific community in the capital region. Salary and start-up funds are highly competitive and outstanding core facilities are available. Applicants must have a Ph.D. and/or M.D. with several years of postdoctoral training and a high impact publication record. For Associate Professor level a history of sustained extramural funding is expected. In addition to the beauty of the picturesque New England countryside, the Hartford area offers a vibrant arts and cultural scene and an exceptional outdoor sports environment. Interested applicants should apply at **https://jobs.uchc.edu/** search number 2015-691, and submit a curriculum vitae, a two-page summary of research accomplishments and interests, and the names and contact information of three references. Questions regarding this search should be directed to Anthony Vella, Ph.D., Chairman, Department of Immunology, School of Medicine, UConn Health Center, Farmington, CT. Email: **immunology@uchc.edu**. For further information on UCHC, please visit **http://immune.uchc.edu**. The deadline to submit applications is May 1, 2015.

UCHC is an Affirmative Action/Equal Opportunity Employer M/F/V/PwD

Are you conducting research into the sustainable use of natural resources? Do you want to contribute to the solution of urgent environmental, developmental and social problems, especially in developing and emerging countries?

If yes, then we would like to invite you to apply for the

Robert Bosch Junior Professorship Research into the Sustainable Use of Natural Resources

together with a German university or research institution of your choice. Applicants of all nationalities are welcome.

Areas addressed

We are looking for an outstanding young scientist whose research areas concern the sustainable use of natural resources. Research approaches may be based in the natural sciences as well as in the social, developmental, political, medical and public health sciences.

The research should focus on developing and emerging countries. We expect that research results should contribute to the solution of urgent environmental problems.

Scope

The successful applicant will be awarded a grant worth up to 1 million euros for a five year period, in order to set up a research group in a German research institution or university. The funds can be allocated flexibly towards covering salaries and research costs.

Candidate profile

:: excellent doctorate degree, completed no more than 5 years prior to the application deadline of 12 May 2015 (adjusted for documented parental leave)
:: compelling independent past scientific achievements and publications in peer-reviewed journals
:: international research experience
:: excellent proficiency in English
:: potential to obtain a leading position in his/her research field
:: non-German applicants should be prepared to learn German.

The application deadline is **12 May 2015.**

For further information and to apply please visit **www.bosch-stiftung.de/juniorprofessorship**

Robert Bosch Stiftung

POSITIONS OPEN

CHAIRPERSON
Department of Pharmacology
Kirksville College of Osteopathic Medicine

The Department of Pharmacology at A.T. Still University (ATSU) Kirksville College of Osteopathic Medicine invites applications for Chairperson. This is a full-time, tenure-track position. The successful candidate will report to the Dean of the College and will be responsible for envisioning, developing, and coordinating the implementation of programmatic academic innovations. Applicants must have a Ph.D. or other doctoral degree in pharmacology or a related biomedical discipline. The successful candidate will have demonstrated breadth of mature academic skills in the discipline of pharmacology and will have significant pharmacology teaching experience at the medical and/or graduate school level. The successful candidate will demonstrate consistent scholarly productivity as a biomedical researcher with success in publication and acquisition of extramural research funding. The successful candidate will have been involved in academic governance and leadership. Major responsibilities include: providing leadership to the department in the areas of research, teaching, and service; overseeing mentorship of department faculty; developing and managing department's resources and budget; providing teaching instruction in the curriculum; working collaboratively with other department chairs. Position details are described at **website: http://jobs.atsu.edu/kcom-chairperson-department-of-physiology/job/5097793.** Qualified persons should send a current curriculum vitae, a personal statement of teaching and research goals, and contact information for three to four references. Electronic submission of all materials should be directed to **e-mail: hr@atsu.edu.** *ATSU is an Equal Opportunity Employer and does not discriminate on the basis of race, color, religion, national origin, sex, gender, sexual orientation, age, or disability.*

MORRIS COLLEGE

Morris College, a private four-year Liberal Arts College in Sumter, South Carolina, is seeking to fill the following position(s):

Computer Scientist: To teach introductory Computer Science courses and introductory Cybersecurity courses and to develop courses for a concentration in Cybersecurity in an NNSA grant supported position. M.S. or Ph.D. in Computer Science with a background in Cybersecurity. Effective Immediately.

Submit a letter of application, personal resume, three letters of recommendation, and official academic transcripts to: **Director of Personnel, Morris College, 100 W. College St., Sumter, SC 29150-3599.** *Morris College is an Equal Opportunity/Affirmative Action Employer.*

By **Rachel Bernstein**

Into the wilderness

Ethan Perlstein never planned to be an entrepreneur. Ever since his college research internship, in a lab at the National Institutes of Health, he had dreamed of becoming a professor at a high-powered research institution. After completing his Ph.D. in molecular and cellular biology at Harvard and earning a Lewis-Sigler fellowship at Princeton, he seemed perfectly positioned to take that next step. "I was in the academic 1%," he says. ¶ Apparently, the academic 1% isn't good enough. When his 2-year job search yielded no offers, he was stunned and unprepared. "I was in an existential rut because I hadn't thought of a plan B," he says. He was "in the wilderness."

He started conducting his own research—a hybrid of a legacy project from his postdoc and some new exploratory work—at a bench he rented in a facility in Berkeley, California. He supported himself by consulting for a startup company developing a science-crowdfunding platform, and he lived off savings he had set aside during his postdoc. He branded himself an "indie scientist," a label he confesses is nebulous. "The indie label is really more about a spirit than a set of specific practices. It means doing things in an unconventional way and considering and being open to doing things that are not just the standard way of doing things," he says. The emphasis is on working "outside of the academic and industry monoculture."

"The indie label is really more about a spirit than a set of specific practices."

In search of a clearer path, he brainstormed with his brother, a legal entrepreneur. He also "turned to Twitter as a source of solace and support—and as an opportunity to learn, ... what would a plan B look like?" On Twitter, he commiserated with others who were struggling in the academic market and connected with rare-disease advocates. He found people he could bounce ideas off as he wrestled with his next career move. "I really feel like [Twitter] made my transition possible," he says.

Over the course of about a year, his new venture took shape: Perlstein Lab—PLab for short—a for-profit, public-benefit corporation that aims to develop treatments for rare diseases. In 2014 he incorporated, brought in $2.2 million in investments, and hired three Ph.D. scientists and a few other research staff. PLab is currently targeting two diseases, Niemann-Pick Type C and NGLY1 deficiency. Using genetic models in a variety of organisms—yeast, nematodes, fruit flies, zebrafish—PLab aims to identify candidate treatment compounds for each disease, which can then be refined and taken to the clinic with partner companies.

Perlstein never imagined himself as a startup CEO, but now that he's doing it, "I couldn't be happier," he says. "I feel like we're able to blend the best of basic and applied science. ... There are certain parts of academia that I miss, but the parts I miss the most I've tried to recreate here: things like journal club, happy hour, places where you can just kind of nerd out and be self-indulgent about the science."

Despite now being officially corporate, he hasn't given up the indie-science spirit. In the long run, he hopes PLab will be successful enough to allow him to "do what I really wanted to do all along, which is to build a truly independent science institution." He imagines something akin to the Santa Fe Institute, where researchers can go on sabbatical, interact with new people, and engage in interdisciplinary work. "But that's kind of a long-term fantasy," he says.

One year in, PLab is not quite out of the startup woods. "We've survived the birthing process, so at least there's that," he says. "We're showing the first signs that we can stand up on our own two feet." He's optimistic about the company's future, but knows from experience that he ought to hedge his bets. "Things could sour quickly," he acknowledges. Still, "maybe I'm just saying it, but I think we're in a tentatively firm position in terms of happiness, subject to contingencies." ■

Rachel Bernstein is a staff writer for Science *Careers. For more on life and careers, visit sciencecareers.org. Send your story to SciCareerEditor@aaas.org.*

ILLUSTRATION: ROBERT NEUBECKER